

AD 656569

AGARDograph 103

CASE FILE COPY

AGARDograph 103

AGARD

ADVISORY GROUP FOR AEROSPACE RESEARCH & DEVELOPMENT

64 RUE DE VARENNES PARIS 7E FRANCE

Aerodynamics of Power Plant Installation

PART 1



OCTOBER 1965

D D C
RECEIVED
AUG 18 1967
B. O.

NORTH ATLANTIC TREATY ORGANIZATION



RECEIVED

AUG 22 1967

CFSTI

AGARDograph 103

NORTH ATLANTIC TREATY ORGANIZATION
ADVISORY GROUP FOR AEROSPACE RESEARCH AND DEVELOPMENT
(ORGANISATION DU TRAITE DE L'ATLANTIQUE NORD)

AERODYNAMICS OF
POWER PLANT INSTALLATION

Published in Two Parts

PART I

Proceedings of a Specialists' Meeting, sponsored by the AGARD Fluid Dynamics Panel,
held in Tennessee, U.S.A., 25-27 October 1965

FOREWORD

With the renewed interest in new aircraft in the NATO countries it was extremely timely that the Fluid Dynamics Panel sponsored a specialists' meeting on the "Aerodynamics of Power Plant Installation".

The scope of the work presented in the papers indicates a need for further cooperation between the theoretical and experimental workers in the NATO technical community.

The meeting also reinforced the need for continuing contact between university, government, and industry workers thru the forum of the AGARD specialists' meetings.

Bernard W. Marschner
Professor, Colorado State University

SUMMARY

This AGARDograph contains a collection of the papers presented at the AGARD Specialists' Meeting on "Aerodynamics of Power Plant Installation", held at Arnold Engineering Development Center, Arnold Air Force Station, Tennessee, U.S.A., 25-27 October 1965, under sponsorship of the AGARD Fluid Dynamics Panel.

The purpose of the Specialists' Meeting was to review and discuss recent developments in the aerodynamics of power plant installation, to point out problem areas, and to provide guidance for future research and development in this field.

The collection of papers emphasizes the areas: general development trends, air inlets and nozzles, interference between propulsion system and airframe, VTOL propulsion and propulsion installations. Contributions have come from eight NATO countries.

SOMMAIRE

Cette AGARDographie réunit les exposés présentés à la Réunion des Spécialistes de l'AGARD organisée à l'Arnold Engineering Development Center, Arnold Air Force Station, Tennessee, Etats-Unis, du 25 au 27 Octobre 1965, sous l'égide du Groupe de Travail de la Dynamique des Fluides, sur le thème: "Aspects Aérodynamiques de l'Installation des Systèmes Propulsifs".

Cette réunion avait pour but de passer en revue et de discuter les progrès récents touchant l'aérodynamique de l'installation des systèmes propulsifs, de mettre en relief les différents domaines nécessitant un supplément de recherche, et d'orienter les recherches et développements futurs.

Les exposés rassemblés ici traitent en particulier des domaines suivants: tendances générales des développements, entrées d'air et tuyères, interférence entre systèmes propulsifs et cellules, propulsion des appareils VTOL et installation des systèmes propulsifs. Ces exposés représentent les contributions de huit pays de l'OTAN.

533.695.9:629.13.03

CONTENTS

	Page
FOREWORD	iii
SUMMARY	iv
SOMMAIRE	iv
1. Introductory Paper: Engine Designer's Point of View by L.G.Dawson	1

PART I

General Development Trends

2. A Discussion of Selected Aerodynamic Problems on Integration of Propulsion Systems with Airframe on Transport Aircraft by Walter C.Swan	23
3. The Feasibility of Supersonic Combustion Ramjets for Low Hypersonic Speeds by R.Hawkins	69
4. The Blunt Trailing Edge Axial-Flow Supersonic Compressor by F.Breugelmans	117
5. Measurements of Relaxation Effects in Nozzle Flow of Hot Combustion Gases by Means of a Shock Tube Technique by Th.Just	153
6. Aircraft Performance Problems Associated with Engine and Intake Installation by John Weir	173
7. Low-Drag Installation of Twin Propulsion Nozzles in the Rear of the Fuselage for Transonic and Supersonic Flight by Helmut Langfelder	195
8. Method of Net Thrust Measurement in Supersonic Flight by Theron W.Davidson	217
9. Past Flight Experience and Recent Developments in Combinations of Ramjet and Turbojet Engines by A.Gozlan	245

Air Inlets and Nozzles

- | | |
|---|-----|
| 10. Additive Drag on Inlet Cowls and its Effect on Aircraft Performance
by Joseph S. Mount | 271 |
| 11. Intake Design and Performance Around a Mach Number of 2.2
by M.C. Neale | 301 |
| 12. Fonctionnement du Piège à Couche Limite Interne d'Une Prise d'Air à Compression Supersonique Externe
by Jacky Leynaert | 325 |
| 13. A General Method for Calculating Low Speed Flow about Inlets
by John L. Hess and A.M.O. Smith | 345 |

PART II

Air Inlets and Nozzles (Continued)

- | | |
|--|-----|
| 14. An Investigation of Splitter Plates for Supersonic Twin Inlets
by John B. Peterson, Jr. | 373 |
| 15. Boundary-Layer Interaction Effects in Intakes with Particular Reference to Those Designed for Dual Subsonic and Supersonic Performance
by J. Seddon | 411 |
| 16. Possibilités Actuelles d'Etude Théorique d'Une Tuyère Supersonique à Double-Flux
by Jean-Marie Hardy | 445 |
| 17. Methods of Measuring Aerodynamic Efficiency and Thrust Vectors of Engine Exhaust Systems
by N. Scholz | 479 |

Interference Between Propulsion System and Airframe

- | | |
|---|-----|
| 18. Propulsion System Integration in Wings
by J. Lockwood Taylor | 503 |
|---|-----|

Specific Propulsion Installations

19. A Fully Integrated Propulsion System for a Supersonic Transport Aircraft
by J.E. Talbot and B. Furness 513

VTOL Propulsion

20. Jet VTOL Power Plant Experience During Flight Test of X-14A VTOL Research Vehicle
by L. Stewart Rolls 539
21. Jet Lift Intakes
by W.F. Wiles 559
22. Techniques for the Simulation of Jet-Lift Engines in Wind-Tunnel Models of V/STOL Aircraft
by Dr. Ing. Ugo Sacerdote 587
23. Aerodynamic Interference Effects with Jet Lift Schemes on V/STOL Aircraft at Forward Speeds
by John Williams and Maurice N. Wood 619
24. Lift-Fan V/STOL Propulsion and Airframe Integration
by Herbert E. Dickard 653
25. NASA Research on the Aerodynamics of Jet VTOL Engine Installations
by Richard E. Kuhn and Marion O. McKinney, Jr. 689
26. Experimental Studies of VTOL Fan-in-Wing Inlets
by U.W. Schaub 715

INTRODUCTORY PAPER

THE ENGINE DESIGNER'S POINT OF VIEW

by

L. G. Dawson

Rolls-Royce Limited, Derby, England.

THE ENGINE DESIGNER'S POINT OF VIEW

L. G. Dawson

Mr. Chairman, Gentlemen

I would like to thank you for the honour of being asked to present the opening paper for this Conference on the Aerodynamics of Powerplant Installation. I do not intend to roam through all the subjects and all the possibilities that this title calls to mind. I propose to review the way in which the engine is affected by the state of the air which is delivered to it by the powerplant installation. By giving a relatively straightforward survey of the way the flow processes inside the engine are affected by the condition of the air delivered to it, I hope I may persuade those responsible for engine installations that there are certain fundamentals about engines which we can only alter to a limited extent. As a result of this, I hope to make some small contribution towards persuading powerplant designers to give more attention to the way they deliver engine air to the compressor face.

A difficult problem on all but the simplest of installations is that of flow distortion in the engine air intake. The present approach is for the engine manufacturer to specify distortion limits and for the aircraft manufacturer to comply with these as best he may. Sometimes it is not possible to reach a satisfactory solution for the intake and engine without complicating the engine, or lowering the working line which causes penalties in fuel consumption.

To specify reliable limits for the distorted flow the engine compressor will accept, involves understanding and measuring the susceptibility of engines to non-uniform flows and generalising the test information in such a way as to make it applicable to new engine designs.

I believe that the ultimate solution to the problem of distorted flow into engines will stem from the detailed analysis of the compressor aerodynamics now possible with powerful computers, combined with testing of the type discussed in this paper.

Let us consider an area of low total pressure entering the compressor and understand what happens when the air enters the first compressor stage. One's first thought is that there will be approximately uniform static pressure over the face of the compressor and hence in the region of low total head there will be a low axial velocity. If this were true, the section of blading behind the area of low total pressure would be doing more work on the air than the rest of the blading where it passes through the area of normal flow. A low axial velocity causes the blade to do more work, that is providing it is not so low that the blade has stalled. Suppose this local increase in work exists, then the flow velocities would increase locally until the work done by the compressor blading, as it passes through the region of low total pressure, was

approximately the same as the work done over the rest of the compressor face. In fact, we do not have the normal system of flow with varying total head where the static pressure tends to be constant. At the compressor face (Fig.1) we tend to have a varying static pressure and a constant velocity. The compressor blading is tending to produce a constant pressure rise over the whole of the compressor face but, because there is a region of low total pressure, it cannot produce a constant total pressure behind it. This situation persists right through the compressor.

Our examination of the problem of distorted flows entering compressors has led us to believe that the compressor tends to behave as if it were two compressors in parallel. The low total pressure region is maintained through the compressor. We were led to this observation by the fact that we found that compressors were greatly upset by circumferential distortion of the inlet total pressure but hardly at all by radial distortion of the inlet total pressure (Fig.2).

Let us now consider the problem in more detail. The circumferential variation in inlet total pressure is illustrated in Figure 3 for a simple once-per-circuit step-down in total pressure such as could be produced by a local flow separation in the air intake. The portion of the compressor which deals with this low total pressure region is regarded as a separately operating compressor in parallel with, and having similar characteristics to, the main compressor. Both exhaust to the same static pressure at outlet. The spoiled compressor works higher up the pressure ratio flow characteristic than the unspoiled compressor. When this higher working point reaches the nominal surge pressure ratio the spoiled compressor would be expected to surge. Provided that the circumferential extent of the spoiled region is sufficient, this should in turn produce a surge of the combined real compressor.

This leads to a simple relationship between inlet total pressure distortion and the loss in surge pressure ratio.

If, as a first approximation, the exit total pressures of the two compressors are assumed the same, then the relation becomes

$$\frac{\Delta R_{12}}{R_{12}} = \frac{\Delta P_1}{P_1}$$

that is percentage loss in surge pressure ratio is equal to the percentage loss of inlet total pressure ratio in the spoiled region relative to the mean value. The latter is termed the Pressure Distortion Ratio.

To compare this forecast with test results it is first necessary to convert the generally complex inlet flow profile into an equivalent stepped profile. This involves determining an average total pressure loss in each region of deficiency in total pressure below the overall mean. The largest of these, which leads to the greatest loss of surge pressure, is obviously the significant one. On the other hand, if its angular extent is small enough the overall compressor will not surge.

A more satisfactory method is to choose an appropriate angular extent θ over which to determine the average deficiency. Then the particular θ giving the greatest average loss becomes the significant one. This leads to a value for the effective pressure distortion ratio, $\overline{\Delta P_1^\theta / P_1}$, to be used to predict the loss in surge pressure ratio.

Test results are shown in these terms for a number of high pressure compressors in Figure 4. The predicted relation is given for comparison and the approximate relation based on uniform outlet total pressure is also shown. The agreement in trend and actual value is good, to within 2% of overall pressure ratio in the majority of cases, and if anything the simplified relation gives the better agreement.

A corresponding set of test results is given in Figure 5 for low pressure compressors. In this case, although the agreement in trend is good, the best line through the results indicates that there is some additional loss of surge pressure ratio, averaging about 4% for the compressors tested. By examining in detail the behaviour of the compressors producing the largest discrepancy it was deduced that this effect was due mainly to the characteristics of the last stage.

In these cases, and to a varying extent on all low pressure compressors, the pressure rise flow characteristic reaches a maximum with reducing flow before surge occurs, as shown on the left of Figure 6. Whilst the surge condition U is achievable with uniform inlet conditions, this situation is unstable. A very small disturbance will prevent operation between the peak of the curve P and the uniform flow surge point U. The movement of last stage stall from U to P produces a corresponding loss of surge pressure ratio in the overall compressor, as shown on the right of Figure 6. This is the additional loss of 4% of L.P. compressors shown on Figure 5. It can be derived accurately for each compressor from its last stage characteristic.

The Pressure Distortion Ratio $\Delta P_1^0 / P_1$ is most useful for analysing and comparing results on different compressors. It is not, however, quite so convenient in the work of matching a given engine and intake as the Pressure Distortion Coefficient $\Delta P_1^0 / q_1$, where q_1 is the compressor face dynamic head. For a given inlet flow pattern this coefficient remains substantially constant with varying inlet mass flow. In particular a flow distortion simulator, usually a parallel inlet duct containing a system of blockages, can be described satisfactorily by a single coefficient over the full mass flow range.

Surge test results with such a simulator, producing a distortion pressure coefficient of -0.27, are shown for a typical low pressure compressor in Figure 7. The predicted surge line, including the last stage effect, is included for comparison together with the uniform flow surge line. The agreement is very good over the significant speed range and the calculated surge line tends to be pessimistic at lower speeds.

A relation between surge pressure ratio and inlet flow distortion now allows us to express the latter as an equivalent loss in performance, which in turn should suggest a particular value of distortion for optimum matching. The outcome of such performance assessments depends very much on the initial assumptions but, to appreciate the possible magnitudes involved, we can take a few typical ones.

Firstly, if it is accepted that a certain minimum surge margin is required for engine handling purposes, then any loss in surge pressure ratio must be compensated by an equivalent loss in working pressure ratio. If the engine is rematched to provide the same component efficiencies, general curves can be produced (Fig.8) expressing for example, deterioration in cruise specific fuel consumption for flight Mach numbers of 0.8, 2.2 and 3 and a fixed specific thrust at each Mach number. The effect on specific fuel consumption of a given percentage loss in engine compression

ratio diminishes with increasing Mach number, since internal compression becomes a relatively smaller part of the overall compression.

Typical distortion coefficients encountered in various types of aircraft are given in Figure 9 against the corrected engine speed at which they occur. For clarity the individual results are not shown but the limiting curves drawn are based on a very large number of test results. As these are intake tests the distortion pressure coefficient $\Delta P_1^0/q_1$ is used, for the reason mentioned earlier, and the abscissa is the percentage of maximum corrected engine speed.

For a subsonic civil aircraft with podded power plants the worst pressure distortion coefficient would in general arise during take-off at rotation and during approach.

With a good inlet contraction ratio the coefficient should be effectively zero but, owing to compromises with external power plant lines, the coefficient can be as high as 0.3. In such a case the derived loss in surge pressure ratio, 10% if applied to working pressure ratio, is worth about 2% increase in cruise specific fuel consumption.

In the case of a typical subsonic long range transport aircraft the direct operating costs would then increase by about 0.8%, using the ATA 1960 method of assessment. A weight increase of 1600 lb per power plant produces the same increase in operating costs. At this is about twenty times the weight of the average intake there is room for refinement to reduce the flow distortion. Although aircraft manufacturers will put a lot of effort into a weight reduction exercise which offers a potential saving of 100 lb per power plant, they will in general show little enthusiasm for intake modifications to reduce flow distortion, where the potential saving is far greater.

The situation on military aircraft is, usually, far worse. We have encountered distortion pressure coefficients as high as 1.0, over three times as bad as the worst civil aircraft intakes. Applying the previous general assumptions, this leads to 3.5% increase in specific fuel consumption at a typical ferry condition, around 0.8 Mach number. Here again the possibility of reducing this penalty by reduced flow distortion is worth investigating.

For comparison, Figure 9 shows also the range of typical VTOL engine intake distortions. In these cases the performance/surge margin compromises are made exceedingly difficult by the following considerations:

- (a) The thrust/weight ratio for the installed engine (including intake) must be maintained.
- (b) The surge margin must be more than a bare minimum for safety reasons.
- (c) The intake must turn the approach flow through about 90° during transition, leading to a potentially high flow distortion.

In spite of these problems we have devised and developed to a high standard several VTOL intake configurations with distortion coefficients in the civil engine intake range. An outline of this work is given in Paper 21 of this AGARDograph 103. We feel that similar efforts applied to propulsion engine intakes must be worthwhile.

One interesting power plant which we engineered for the EWR Süd VJ.101 C aircraft illustrates the value of a little refinement in the air intake design. Figure 10 shows that, for low speed flight the whole of the supersonic inlet is moved forward to leave a slot near the compressor entry. This device cost little in extra weight but produced an acceptable inlet flow, lying in the VTOL band shown on Figure 9, even with the power plant at right angles to the flight path at 100 knots.

The duty of the usual supersonic inlet is not as arduous, but the flow distortion produced under ground running and low speed flight conditions is bad enough to be worth improving by devices such as this translating inlet.

In discussing the question of the effect of distorted flow from the air intake on the engine compressor, I am conscious of the fact I have presented a somewhat simplified picture. To go beyond this would complicate the issue, and probably not give you a useful grasp of how we feel about the subject.

I want to go on now to a field which is much more difficult, the problem of hot gas going into the engine. This hot gas can come from reverse thrust on a commercial aircraft or from rocket missile and gun firing on a military aircraft. It will make the subject easier if we look at the surge line and working line characteristics of an engine in a slightly different way. The left-hand side of Figure 11 shows the normal presentation of a compressor map with pressure ratio plotted against mass flow functions. The engine working line and the compressor surge line are shown. When considering hot gas ingestion, it is much easier to look at this map from a different point of view. Every point on the right-hand map has a corresponding point on the left-hand map, but in the right-hand map we have plotted it in terms of nondimensional fuel flow instead of pressure ratio. The surge line is represented by the fuel flow required to move an engine working point up to the compressor surge point. A sudden increase in fuel, which we assume takes place so rapidly that the engine speed does not change, will move the working point vertically until the engine surges. A sudden increase in temperature, again sufficiently rapid that the engine speed does not change, would move the working point down a line through the origin. This line will intersect the surge line at some point. A detailed examination of the problem shows that the surge line is not a fixed line but tends to be a band. If a slug of hot gas goes through the compressor, while it is passing through the hot portion of the compressor it is mis-matched relative to the portion which contains the cold gas. This affects the surge line.

Figure 12 shows an attempt to introduce step changes in fuel by a rapid throttle opening and you will see that the condition where the engine surges is similar to that calculated from the compressor rig measured surge line, but does to some extent depend on whether the engine is hot or cold. Figure 13 shows a similar state of affairs on an Avon engine. Both these cases are plotted on the traditional system of pressure ratio against non-dimensional speed. Translating this diagram into a fuel-flow diagram against non-dimensional speed (Fig.14) and plotting observed results, we find that the engine will accept a higher fuel flow than that calculated for a steady-state rig compressor surge line. The engine will accept a higher fuel flow under conditions due to a decrease in combustion efficiency, which takes place during the transient.

Some years ago some extremely interesting tests were carried out by the NACA injecting slugs of hot gas into an Avon engine. Figure 15 shows diagrammatically the set-up used. It was possible with the engine running steadily, taking in cold air, to suddenly inject a large slug of hot gas and to examine what happened. Figure 16 presents a somewhat simplified picture of the results. Supposing the fuel and r.p.m. are approximately constant when the slug of hot gas first goes in, the working point moves along the line indicated. If the temperature rise injected is high enough, then the working point will enter the surge area and the engine will surge. A smaller step change in temperature will take the working point round a loop, missing the surge area. The engine will continue running but will finally adjust itself to a lower speed. Clearly, whether the engine surges or not depends on the rapidity with which the fuel flow reacts to the increase in temperature. On many occasions when we have met this type of problem due to gun firing we have fitted a control to the engine which momentarily decreased the fuel flow to the engine while the gun was firing. In spite of the hot gas entering the engine, the engine did not surge and blow out.

Up to now we have considered a slug of gas of uniform temperature. However, normally it will only be a sector of hot gas which enters the engine (Fig. 17). The situation is very similar to the sector of low pressure air entering the compressor, with one modification. The portion of the compressor which is accepting the hot gas is still behaving as a compressor in parallel with that part accepting the cold gas but, because the entry temperature is higher, it is N/\sqrt{T} lower and it is working on different characteristics. In real life the problem is complicated, since there will be a sector of increased temperature going in, with losses due to a cross flow in the intake, and all the processes discussed up to now will be acting simultaneously.

The message in all this is, of course, do not do it. In my experience we have had installations in which the engine was fed under some flight or take-off conditions with rather poor flow out of the air intake. We have had installations in which, when in full reverse after touch down on landing, the outboard engines were sprayed with hot gas from the inboard engines. We have had military installations in which when the guns were fired a series of shocks, pressure losses, cross flow and hot gas went into the engine. We finally had to solve the problem by a fuel dipping arrangement so that we decreased the fuel when the guns were firing. We do admit that the engine anatomy should be such that it can swallow birds without medication. I leave it to you to make the rest of its food digestible.

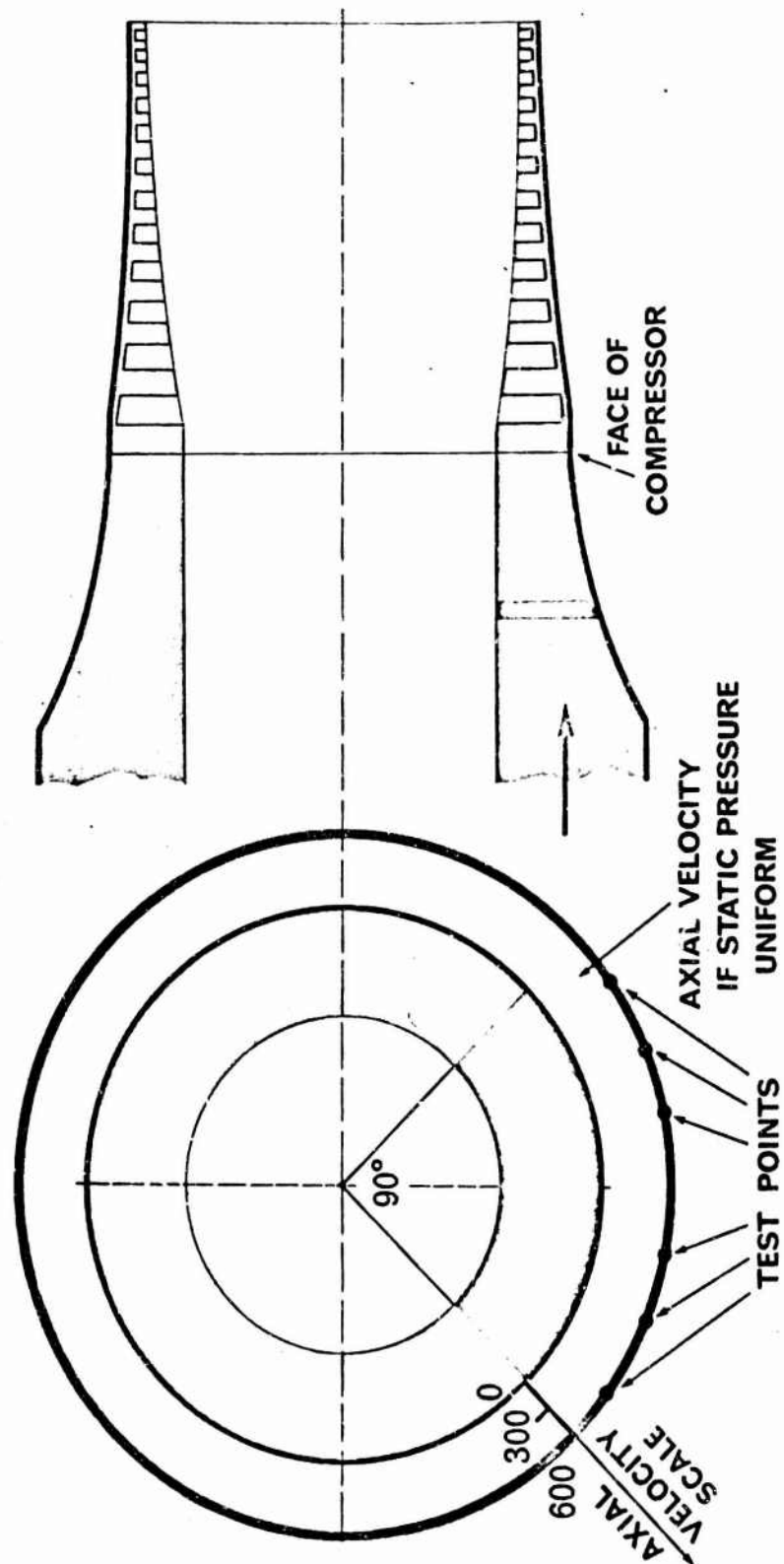


Fig. 1 Intake spoiler effects

COMPARATIVE EFFECT OF CIRCUMFERENTIAL AND RADIAL SPOILING

$$\frac{P_{\text{local}} - \bar{P}}{\frac{1}{2} \rho V^2} < -0.5 \text{ OVER } 20\% \text{ INLET AREA}$$

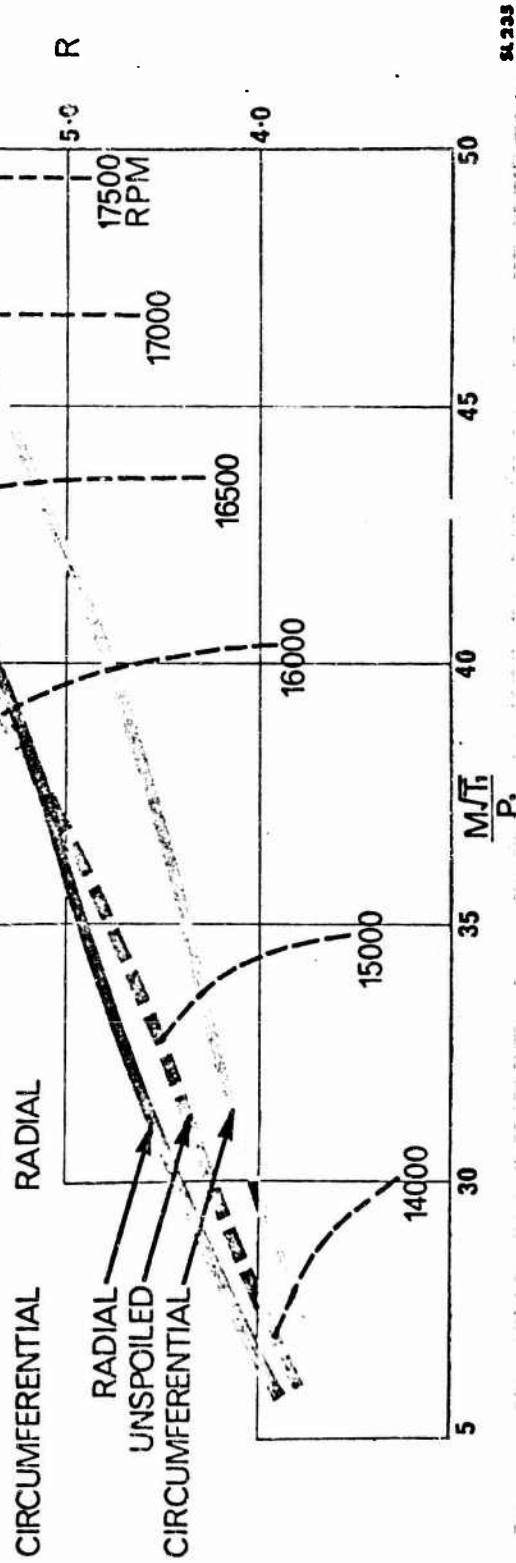
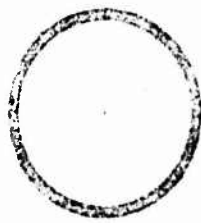


Fig. 2 Lift engine compressor

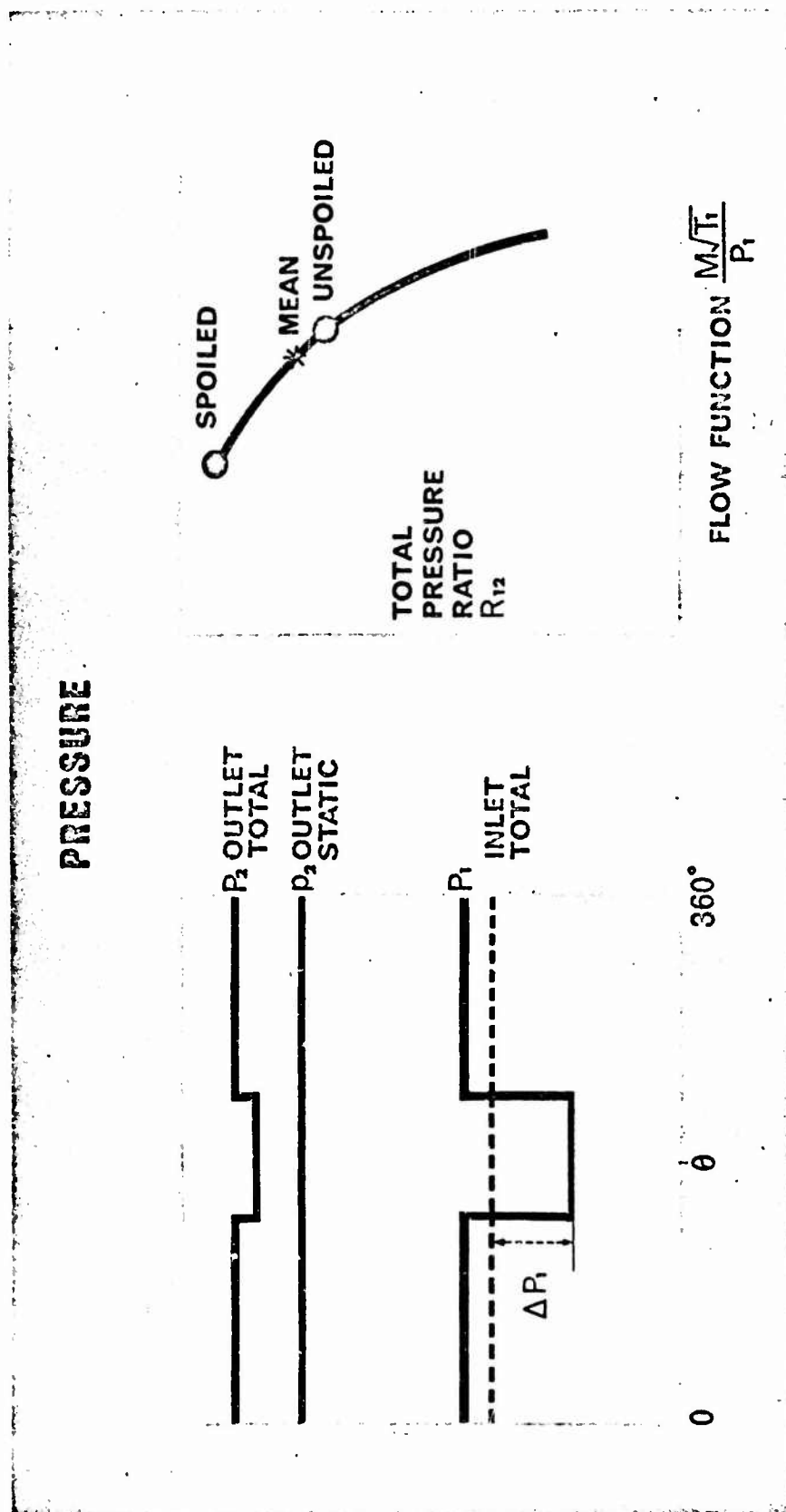


Fig. 3 Theory of two compressors in parallel

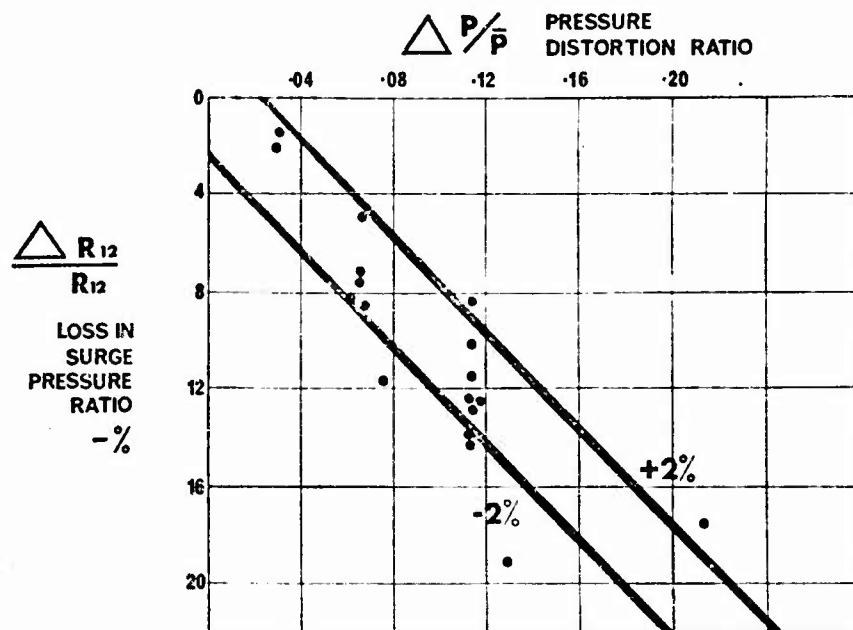


Fig. 4 Loss of pressure ratio related to inlet disturbance - H.P. compressors

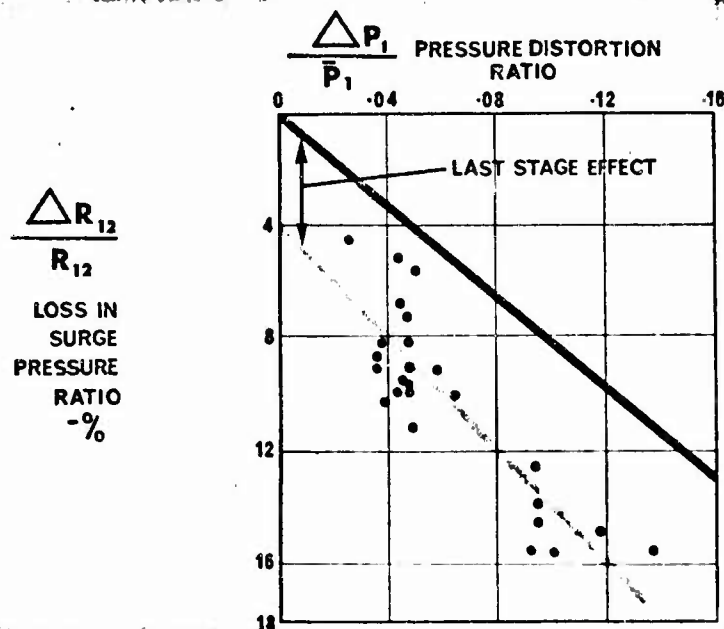


Fig. 5 Loss of pressure ratio related to inlet disturbance - L.P. compressors

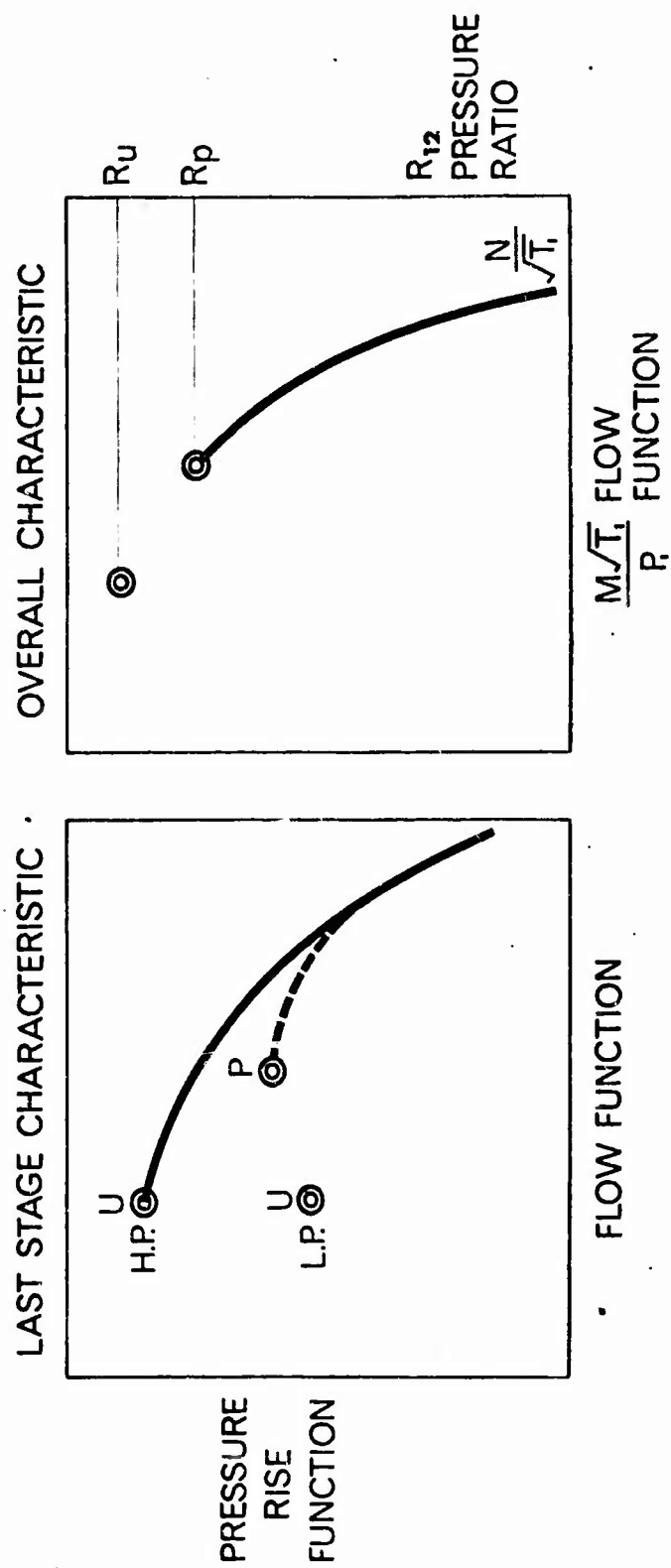


Fig. 6 High speed spolling influence of last stage

EFFECT OF FLOW DISTORTION SIMULATOR

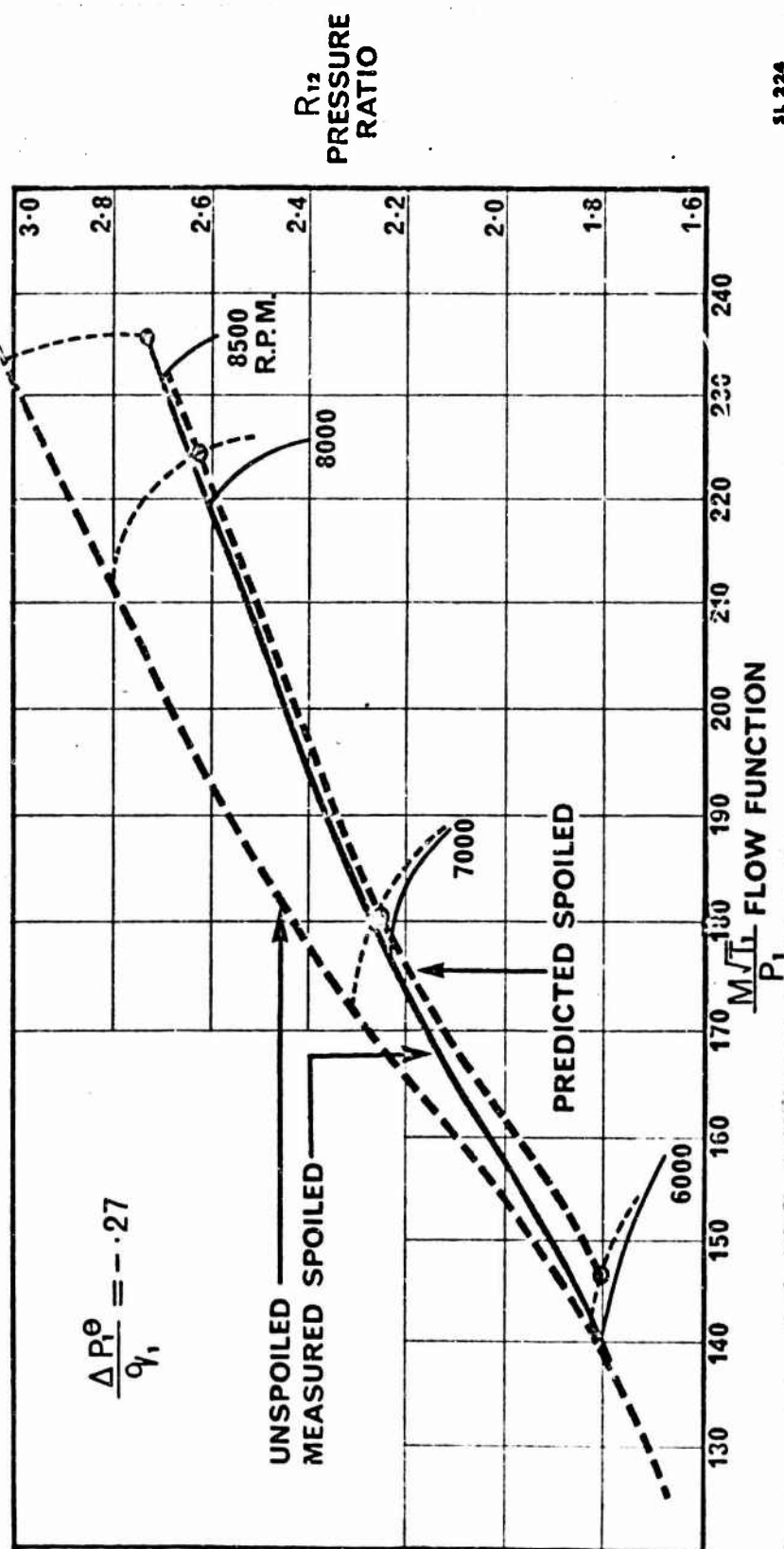


Fig. 7 Typical L.P. compressor

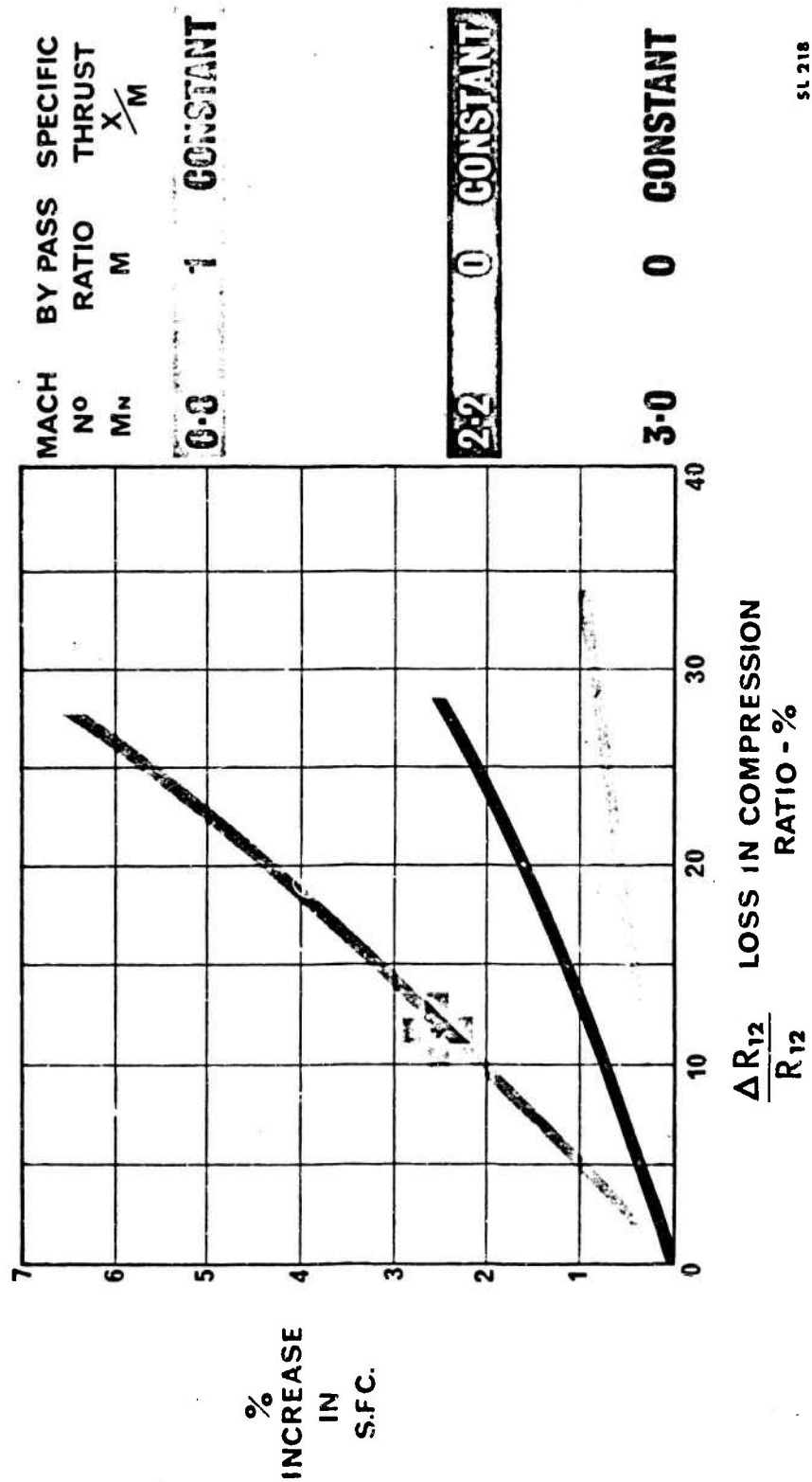


Fig. 8 Effect of loss in compression ratio on S.F.C.

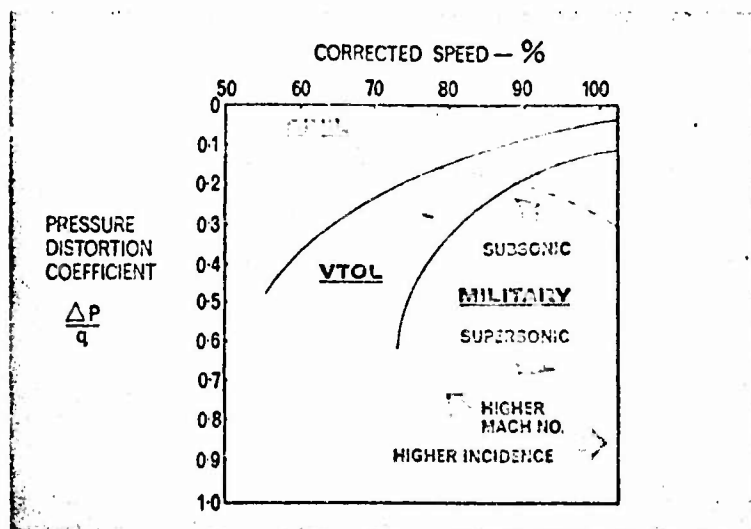


Fig.9 Typical distortion

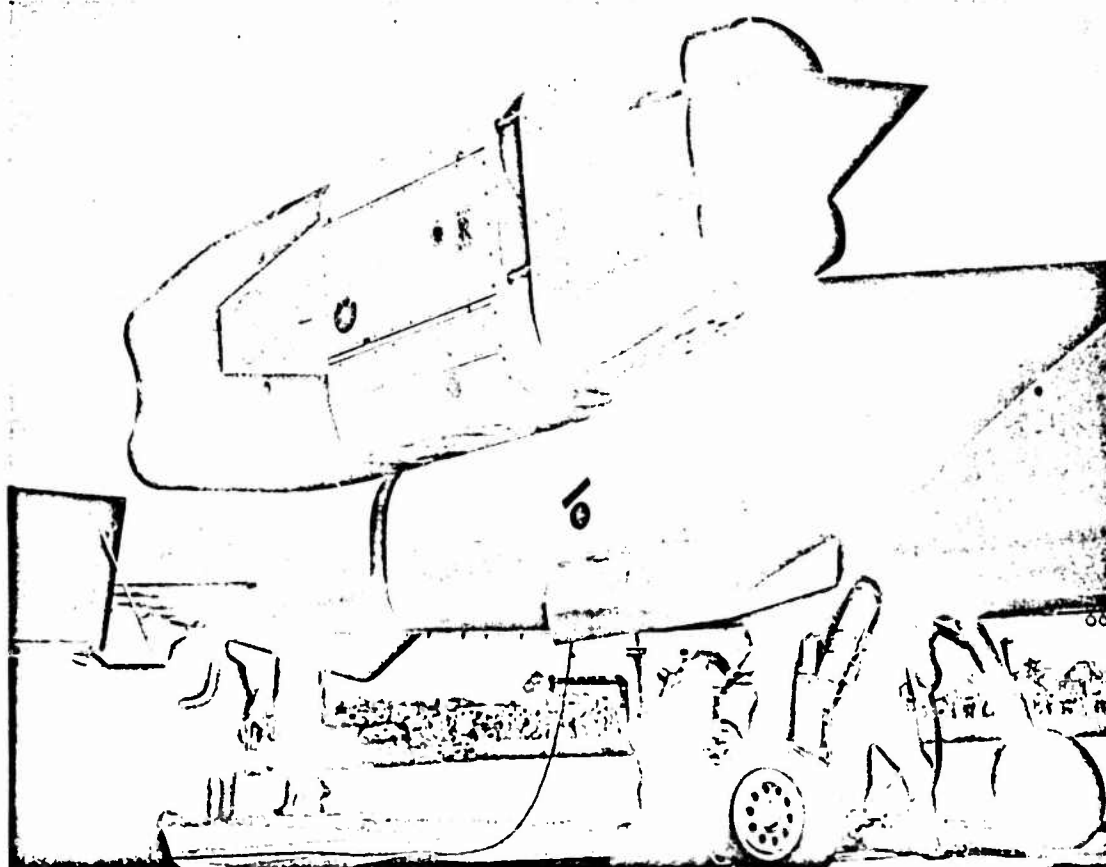


Figure 10

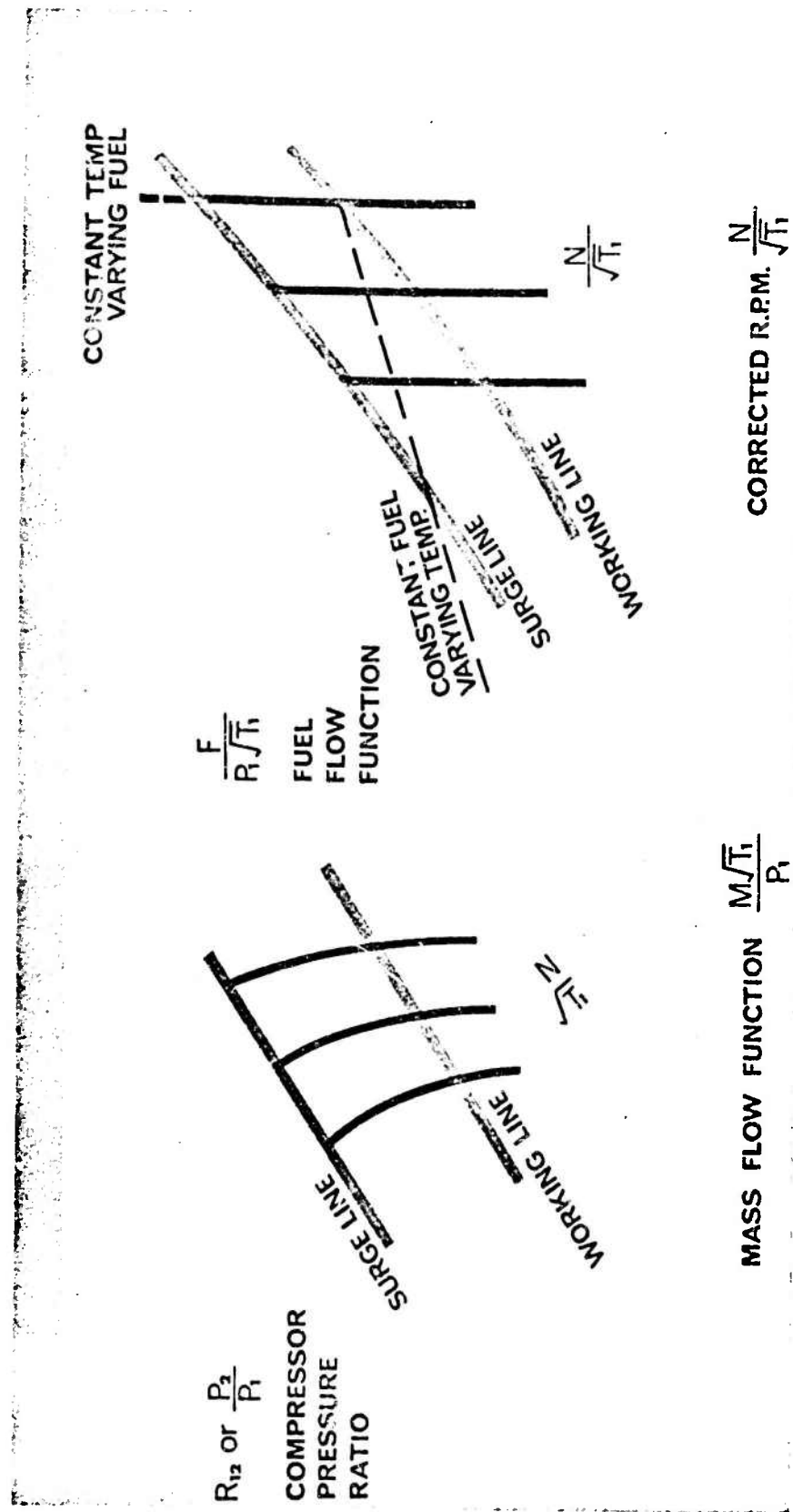


Fig. 11 Methods of mapping engine operating points

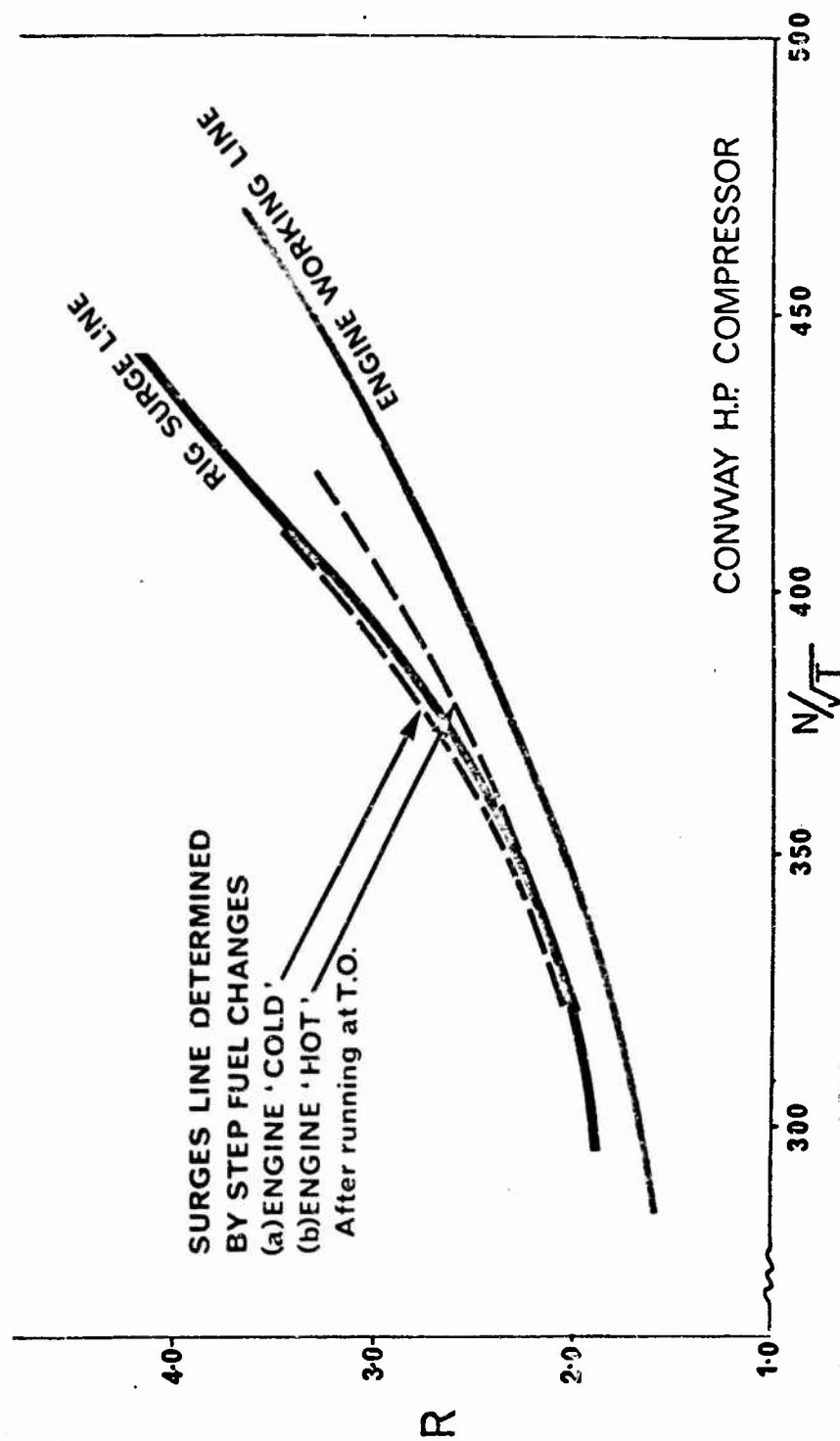


Fig. 12 Determination of surge line by step fuel changes

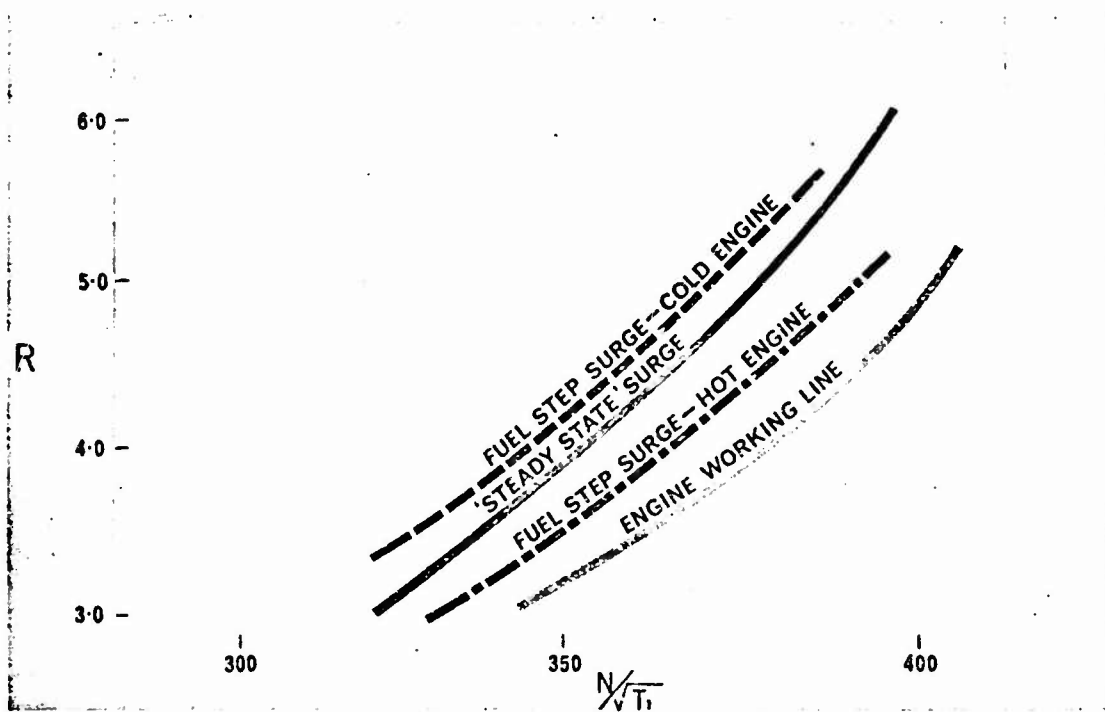


Fig. 13 Surge line determination - Avon engine

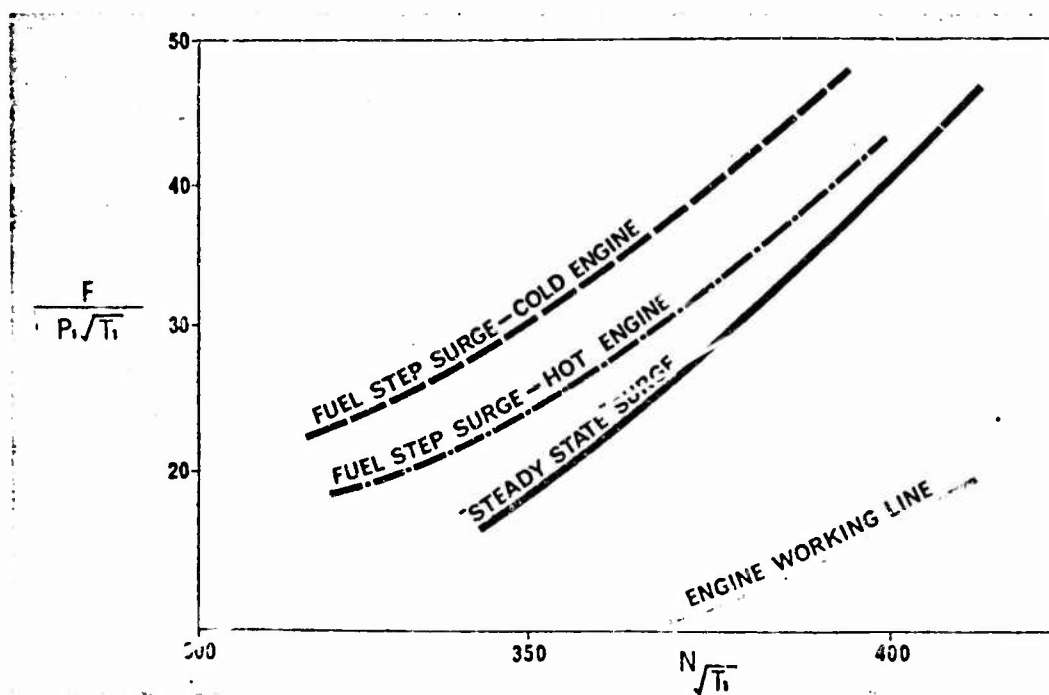


Fig. 14 Surge line determination - Avon engine

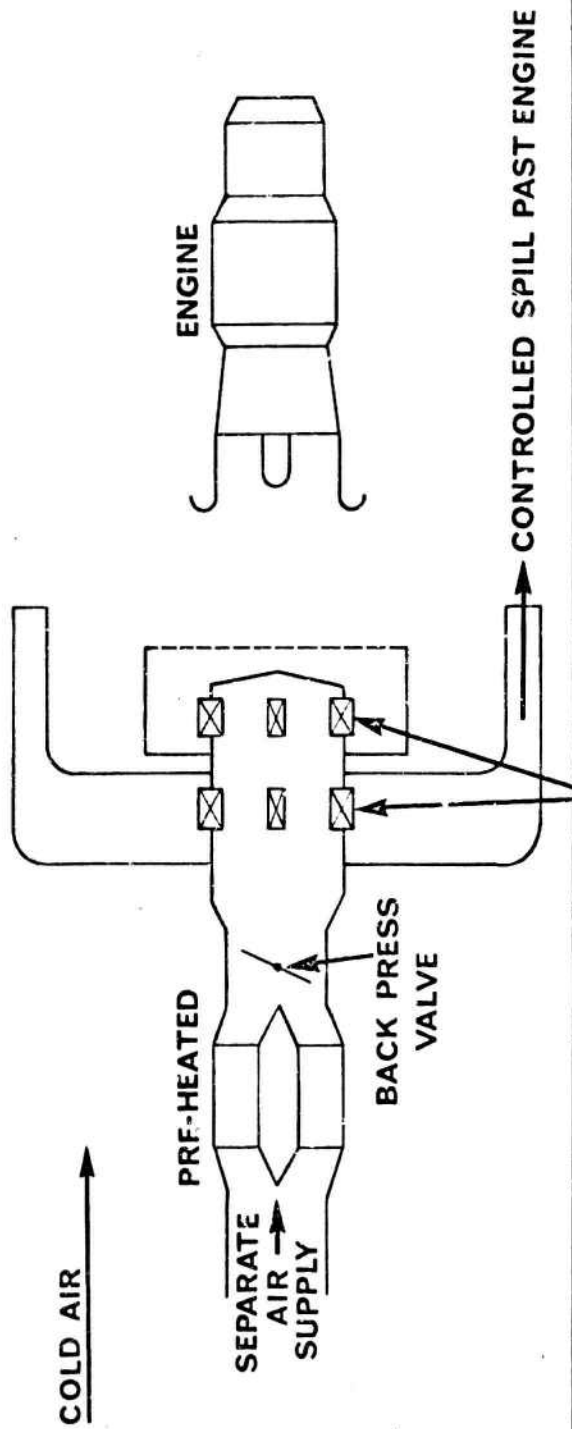


Fig. 15 Test arrangement at N.A.C.A. to subject engine to intake temperature steps

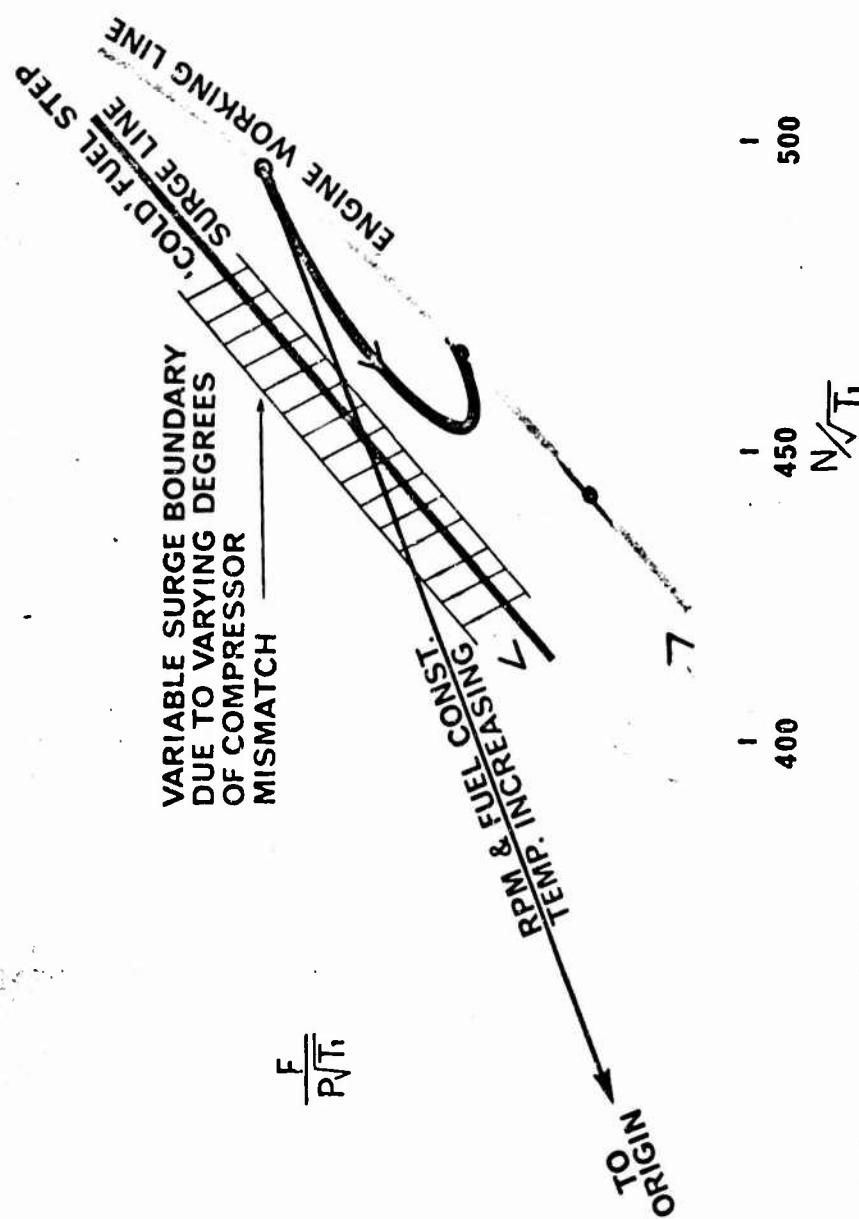


Fig. 16 Surge induced by temperature increment at engine face - Avon engine

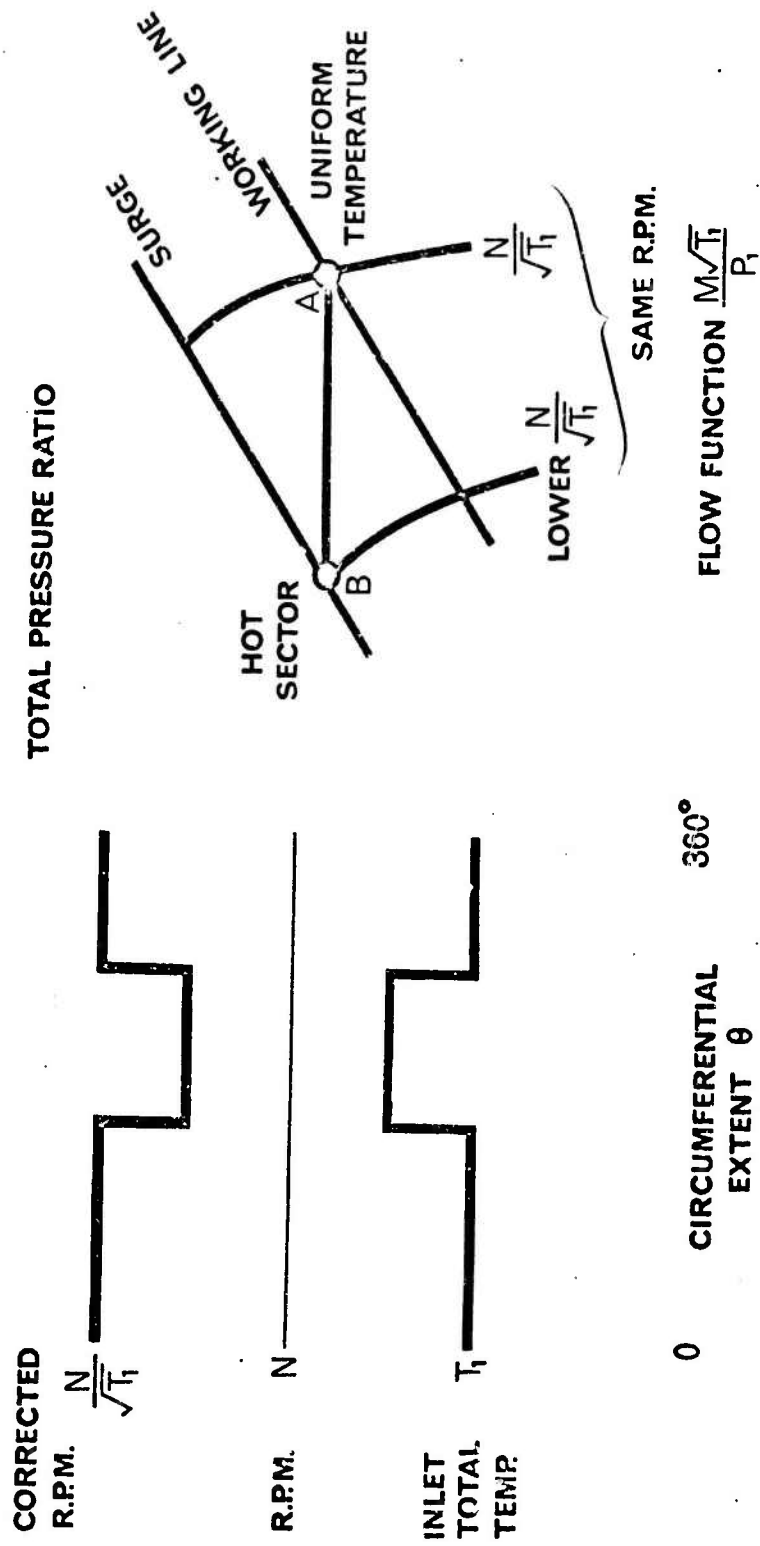


Fig. 17 Two compressors in parallel with high temperature sector at inlet

A DISCUSSION OF SELECTED AERODYNAMIC PROBLEMS
ON INTEGRATION OF PROPULSION SYSTEMS WITH
AIRFRAME ON TRANSPORT AIRCRAFT

by

Walter C. Swan

The Boeing Company, Seattle, USA

SUMMARY

This paper inspects our current knowledge on integration of engine nacelles on transport aircraft with special emphasis being placed on the aerodynamic forces which produce lift and drag. The subsonic case is treated first, showing how current aircraft drag estimates are made, and where the theory is weak. Then the supersonic case is explored with the emphasis here being placed on pressure drag due to volume and lift. Some hope for major gains are suggested. The paper suggests avenues for analytical research and points out that much room for improvement remains.

SOMMAIRE

L'auteur fait le point des connaissances actuelles sur l'intégration des fuseaux moteurs aux cellules des avions de transport, en mettant l'accent sur les forces aérodynamiques qui créent la portance, et la traînée. Il traite tout d'abord du régime subsonique, en montrant comment l'on évalue actuellement la résistance aérodynamique d'un avion, et quels sont les points faibles de la théorie. Il passe ensuite au cas du régime supersonique, en étudiant tout particulièrement la traînée de pression due au volume et à la portance. Il suggère certaines possibilités d'améliorations appréciables, ainsi que certaines orientations de la recherche analytique, et attire l'attention sur les domaines où des progrès restent à faire.

CONTENTS

	Page
SUMMARY	24
SOMMAIRE	24
LIST OF FIGURES	26
NOTATION	28
1. INTRODUCTION	31
2. THE SUBSONIC PROBLEM	32
2.1 Isolated Nacelle	32
2.2 Installed Drag	34
2.3 Theory Versus Test	34
2.4 Summary	36
3. THE SUPERSONIC PROBLEM	36
3.1 General	36
3.2 Volume Interactions	37
3.3 Interaction between Volume and Life Elements	38
3.4 Theoretical Considerations	38
3.5 The Importance of Testing	40
3.6 Promising Results	40
3.7 Summary	41
ACKNOWLEDGEMENTS	41
REFERENCES	41
FIGURES	44

LIST OF FIGURES

	Page
Fig.1 Estimated propulsion pod drag breakdown of fan-powered 707 compared with early jet powered 707	44
Fig.2 Approximate distribution of drag for commercial transports at two speeds	45
Fig.3 Typical high bypass engine nacelle	45
Fig.4 Typical fan cowl external pressure distribution	46
Fig.5 Flow model	47
Fig.6 Shadowgraph of jet flow, $M_\infty = 0.8$, fan nozzle pressure ratio, 3.6	48
Fig.7 Boattail drag coefficient versus radius of curvature	49
Fig.8 Change in airplane drag with nacelle position	50
Fig.9 External fan cowl drag	51
Fig.10 Effect of design Mach number on nacelle shape	52
Fig.11 Effect of the nacelle shape on pressure distribution and drag	53
Fig.12 Effect of nacelle location on nacelle drag increment $M = 2.7$	54
Fig.13 Volume drag	55
Fig.14 Interference between two bodies of revolution	56
Fig.15 Volume-lift interaction	57
Fig.16 Camber optimization	57
Fig.17 Comparison of airplane and theoretical models	58
Fig.18 Wing-body drag at zero lift theory - experiment	59
Fig.19 Pressure field of a body of revolution theory - experiment	60
Fig.20 Camber modification theory and experiment	61
Fig.21 Wing flow field	62
Fig.22 Effect of nacelle shape $M = 2.7$	63

	Page
Fig. 23 Lower surface oil flow pattern	64
Fig. 24 Nacelle pressure field on wing lower surface	65
Fig. 25 Effect of nacelle location theory - experiment, $M = 2.7$	65
Fig. 26 Theoretical effect of trailing edge reflex on cruise drag	66
Fig. 27 Trailing edge reflex	67
Fig. 28 Theoretical effect of nacelle size, $M = 2.7$	68

NOTATION

A_w	reference wing area
A_π	cowl cross sectional area at D_π
C	wing chord
C_D	drag coefficient
$C_{D_{Y=\infty}}$	isolated body drag coefficient
C_{Df}	friction drag coefficient
C_{Dwave}	wave drag coefficient
C_{D_b}	boattail drag coefficient
C_{Dext}	external drag coefficient
C_{D0}	drag coefficient at zero lift
ΔC_D	change in drag coefficient
C_L	lift coefficient
ΔC_L	change in lift coefficient
$\Delta C_p, C_p$	local pressure coefficient
D	afterbody diameter
d	body diameter
D_π	maximum cowl diameter
D	drag
D_{ext}	external fan cowl drag
H	afterbody boattail height
h	fan nozzle exit annulus height
L	body length; airplane lift
M	Mach number
M_∞	freestream Mach number

M_F	fan nozzle exit Mach number
P_∞	freestream static pressure
q, q_∞	$\gamma P_\infty M_\infty^2 / 2$
R	axial boattail radius of curvature
S	wingspan
S_w	reference wing area
ΔS	4 (nozzle area-inlet area)
T	thrust
V_j, V_{jet}	fan nozzle exit velocity
V_{max}	maximum profile velocity
V_∞	freestream velocity
W	airplane gross weight
X	streamwise coordinate
X_{core}	potential core length
Y	spanwise coordinate
Z	vertical coordinate
α	angle of attack
α_{body}	body incidence, degrees
β	$\sqrt{M^2 - 1}$
δ	amount of trailing edge reflex, percent of chord
γ	specific heats ratio

**A DISCUSSION OF SELECTED AERODYNAMIC PROBLEMS
ON INTEGRATION OF PROPULSION SYSTEMS WITH
AIRFRAME ON TRANSPORT AIRCRAFT**

Walter C. Swan

1. INTRODUCTION

In the commercial transport business, a difference of 5% in airplane drag can mean the loss of many millions of dollars in aircraft re-orders in any given year. This knowledge accounts for the keenly competitive and very high quality long range transports available today, such as the VC 10, DC-8, 990, and the 707, all of which are outstanding airplanes in their own right. The airline buyer is used to being offered outstanding airplanes, and hence he looks for the small differences in design which yield only slightly better fuel economy in one aircraft over another.

The commercial transport is characterized by a propulsion system which is usually encased in a nacelle, and is mounted on the wing or body structure by means of struts. Engines are not usually placed inside wings or fuselages because of airline preference. The reasons for this preference are that the podded engines provide for (i) ease of maintainability, (ii) simplified fire protection system, (iii) long term retrofit of aircraft with advanced engines, and (iv) safest wheels up landing situation when pods are located under the wing. Because of these historical prejudices this paper will restrict itself to the podded engine and its installation.

It is vital to the commercial aircraft designer that he have an accurate representation of the drag of a given configuration and that this be the best possible configuration, before he commits to development status. To anyone familiar with the laborious task of performing drag analysis, the most difficult and least understood component of this drag representation is the nacelle contribution. Not only is the isolated nacelle itself difficult to analyze and test, but the determination of the interference effect between the basic wing body and the nacelle and strut present challenging assignments.

The current subsonic commercial transports employ engines which are sized for second segment climb conditions, and whose thrust to aircraft gross weight (T/W) are in the neighborhood of 0.25. The drag attributable to the engine cowlings, struts, afterbodies, and exhaust interference accounts for 5-10% of the total net thrust of the engines at cruise. Figure 1 shows such a drag breakdown for a Boeing 707 model with current turbojet and turbofans installed, based on model and flight test results. The wing and engine are matched such that cruise occurs at altitudes close to that at which the optimum lift/drag ratio occurs. Under these flight conditions the parasitic drag (viscous, pressure, separation) and the induced drag (lifting) are about equal. Hence, the drag associated with the engines, being all parasitic, accounts for 10-20% of the viscous and pressure drag of the whole airplane. Thus, the nacelle designer has control over a fair segment of the subsonic performance of an airplane.

The supersonic transport presents an even more fertile field of opportunity. Current vehicle designs suggest installed dry T/W values of from 0.30 - 0.35, depending on the configuration, the engine size usually being based on community noise considerations. Supersonic flight requires considerably more complicated inlets and nozzles, leading to nacelle sizes which could easily account for 10-15% of the total net thrust. When one recognizes that the wing efficiency is not nearly as attractive at supersonic speeds, and that the aircraft relies heavily on the improved engine efficiencies to obtain good range, the importance of nacelle installation becomes clear.

At cruise the supersonic transport does not operate close to optimum L/D altitude. Attempts at cruising at higher altitudes result in oversizing the engine or cruising with more augmentation, either of which adds a range penalty which offsets the advantage of going to higher altitude.

Because of these matching considerations the distribution of drag is somewhat different from the subsonic airplane. Figure 2 shows a typical distribution of drag for the airplanes. Of course the absolute level of drag is much higher for the supersonic transport. From this figure it is apparent that even more control of the aircraft success is in the hands of the nacelle designer for the supersonic case.

It is now intended to discuss the current state-of-the-art in evaluating the nacelle drag attendant with each of these vehicles, without violating proprietary interests, and to point out current areas of uncertainty, and where further analytical refinement is required. Where the theory fails, gross experiment is the poor substitute, and problems associated with testing are discussed.

2. THE SUBSONIC PROBLEM

2.1 Isolated Nacelle

Figure 3 shows a typical isolated nacelle arrangement for a short duct, high bypass ratio, fan installation and identifies the items for which drag estimates must be made. This model is used in this discussion as it illustrates all the terms normally considered in nacelle drag analysis. Longer fan ducts may be used for the lower bypass arrangements. The drag of such an isolated nacelle is made up of viscous and pressure terms only, as the nacelles do not contribute to the lift of the subsonic transport. The drag buildup is now reviewed.

2.1.1 Fan Cowl Drag

Figure 4 shows the pressure distribution on a typical fan cowl. Depending on the engine thrust setting, external compression causes a fair segment of the approach stream to bypass the inlet. This bypass air, in flowing around the highly curved inlet lip, causes a large negative pressure to develop on the lip. This low pressure literally sucks the airplane through the sky. As the flow progresses back on the cowl, recovery takes place towards free-stream conditions. Near the trailing edge of the cowl a re-acceleration may occur due to curvature followed by diffusion to conditions established by interaction with the nozzle efflux boundary. Drag associated with this process is usually defined in the following manner:

- (a) Basic wetted area skin friction according to equivalent flat plate friction coefficient, C_f , versus Reynolds number with considerations allowing for roughness, and for wrapping the equivalent plate into a cylinder.
- (b) Additional skin friction associated with excess velocity caused by cowl curvature and cowl angle of attack. This term varies with throttle position.
- (c) A loss of lip suction caused by the failure of the cowl to recover the full bypass momentum. This term is dependent on throttle position and geometry of the recovery lip, and is not important for good subsonic nacelle designs.
- (d) Boattail pressure drag due to boundary layer thickening or separation. This term is dependent on throttle position as it affects the exhaust efflux boundary; throttle position also affects the state of the boundary layer approaching the boattail.

Only the first term is easily calculated from theory. Although some of the remaining terms may be calculated, they are normally developed by extensive cowl testing, using wake rakes and surface static pressure analysis.

2.1.2 Afterbody Scrubbing Drag

The use of short fan cowls in recent years has caused considerable comment on the influence of fan exhaust flow on both the isolated drag of a nacelle and on the wing-nacelle-strut interference drag. Figure 5 shows a simplified model of the flow over a short duct fan nacelle afterbody. The Boeing Company have evaluated pressure rake measurements made in this flow field together with simple boundary layer theory to calculate the skin friction drag on the afterbody. The calculated data are compared by Lawrence¹ with careful experiments where an afterbody was mounted on its own axial force balance. Consistent agreement was found in the region of interest to high bypass ratio engines.

Fortunately, engines currently under study and development have afterbodies which are shorter than the measured jet core length at cruise power. Although no suitable analysis exists for predicting pressure or velocity distributions in the core or the core length itself with any precision, because the core is composed of a complex region of shock waves and mixing flows the assumption of a constant velocity equal to V_{jet} appears adequate. Flow fields downstream from the core are even less understood. Figure 6 shows a typical shadowgraph picture of the jet flow in the core region as it proceeds down the afterbody, when exposed to external air at $M = 0.8$.

The afterbody scrubbing drag is normally considered as composed of two terms (i) the drag which would have occurred if the afterbody had been exposed to only free-stream conditions, and (ii) that drag associated with the fan stream blowing on the afterbody at a rate in excess of free stream. This second term, called the blowing drag, can be a sizeable quantity. Figure 1 shows that for a 707 type aircraft it represents nearly 50% of the total nacelle drag.

2.1.3 Afterbody Boattail Drag

The primary nozzle plug drag is usually assigned to the basic engine thrust coefficient. The plug diameter and taper are selected such that the combined wind-on thrust minus drag at cruise pressure ratio, including the afterbody, are minimized. Figure 7 shows typical experimental data on boattail drag coefficient, obtained from drag balance measurements, as a function of the curvature of the boattail. This figure shows that for R/D values less than 4 a sharp increase in drag occurs due to separation. Hence, in selecting the plug diameter and taper, the boattail radius must be considered. Usually plug half-angles of up to 15 degrees can be tolerated up to $M = 0.90$ with only skin friction drag being present.

2.2 Installed Drag

Having optimized the nacelle configuration on the isolated basis, the pod is then mounted on the wing to determine its most suitable location. The spanwise position along the wing is usually defined by the elastic characteristics of the wing and the influence of engine-out requirements on vertical tail size. Drag is not the primary consideration, and at speeds below $M = 0.90$ no significant lift contribution to the wing has been found to date from nacelle position.

Figure 8 shows typical experimental measurement of the change in airplane drag due to axial and vertical location of a nacelle at a given wing span position. This drag increment is caused mainly by changes in strut wetted area, and the supersonic velocity and diffusion which occurs both on the wing and the nacelle as the flow passes between these surfaces. It is noted that, up to $M = 0.85$, a wide choice of locations is acceptable. However, near this speed the flow becomes critical in the interference region, leading to flow separation from the nacelle afterbody boattail. For cruise speeds in the $M = 0.90$ region the nacelles want to be located far out in front of the wing leading edge. This desire presents a serious structural design problem, which may suggest another location for the engines or a more integrated design. Interference drag is seen to be a major reason why our current subsonic transports do not cruise at higher speeds.

The discussion thus far suggests that engine placement is currently an art, determined only by extensive wind-tunnel testing. No known calculation technique exists to replace wind-tunnel testing as the best means of nacelle placement in a highly compressible flow environment.

2.3 Theory Versus Test

2.3.1 General

As long as subsonic aircraft cruise at speeds below about $M = 0.85$ the above approximations are probably acceptable. However, competition could lead to increases in subsonic cruise speeds to the $M = 0.90 - 0.95$ region through the use of transonic area ruled passenger compartments and cambered and twisted swept wings. Under controlled design conditions such as these, it becomes important to reconsider the details of the flow around nacelles in order to insure that the interference drag does not become excessive due to shock-induced separations on the nacelle afterbody. Because of competition, the industry is maintaining a major effort on better understanding of the flow process around nacelles.

Model experimental programs at best are not very accurate. It is most difficult to simultaneously duplicate the inlet streamtube and the fan and primary jet efflux as they appear in flight, without using several internal and external subterfuges that rule out the determination of the absolute level of thrust minus drag from wind-tunnel tests. One usually plugs up the inlet with a forebody and pipes high pressure air to the model from a support strut, to simulate the exhaust interference for nacelle placement tests. Flow nacelles which match inlet conditions are often used for basic airplane drag tests. Internal drag estimates are subtracted from the total balance force.

2.3.2 Viscous Drag

Only recently have we been able to evaluate inlet cowls with any precision from theory. A recent large scale inlet test at Boeing (Fig.9) shows how the drag of a high bypass engine fan cowl was kept low at Mach numbers approaching $M = 0.90$ by careful control of surface conditions through a theoretical model approach. The test points shown were obtained with a special wake rake designed to span the boundary layer.

A cowl drag estimation procedure under development at Boeing consists of defining the pressure field around the inlet cowl using an inviscid, incompressible solution which is then corrected for compressibility. Using this pressure field to estimate the boundary layer, iterative procedures are followed, to define a new pressure field on the body which has the boundary layer displacement thickness superimposed. Incompressible boundary layer development is used. The leading edge is assumed laminar. The boundary layer is allowed to develop through a transition criterion to turbulent flow. Separation is indicated when the local skin-friction coefficient, C_f , appears to go to zero. A local value of C_f of zero means flow reversal is taking place.

A complicated computer network was devised by Boeing using an incompressible singularities distribution method similar to that suggested by Hough³, and by Küchemann and Weber⁴. The amount of engine flow allowed to pass through the inlet is defined by placing sources or sinks along the cowl axis. Because the setup and calculation times required to use the singularities method may be excessive, Boeing analysts are currently exploring the use of incompressible relaxation techniques, such as suggested by Allen⁵, and also finite difference techniques, such as affirmed by Lee⁶.

The boundary layer calculations can be accomplished by many methods. Thus far, we in industry have been using incompressible methods such as Schlichting⁷, or Launder⁸, with a correction for Mach numbers. However, in approaching $M = 0.90 - 0.95$, new theory will have to be devised to correct the boundary layer time history for the theoretical determination of viscous drag to be sufficiently accurate.

2.3.3 Pressure Drag

Most pressure drag estimates for subsonic nacelles have been determined from wind tunnel tests of isolated nacelle models wherein the viscous terms have been calculated and subtracted from total drag measurement. Occasionally well instrumented pressure models have been used for this purpose. Theoretical treatment has only begun to be seen in the literature.

A body immersed in an inviscid incompressible flow field experiences no pressure drag. In a real fluid, however, the boundary layer buildup causes the pressure distribution to be different, a factor which can lead to measurable pressure drag. If the boundary layer does not separate, the drag is very small. Attempts at carrying out such an exercise on a long slender body have shown that the iterative solution is difficult to converge.

The theoretical determination of the drag of separated bodies has been largely neglected, mainly because everyone tries to design away from the problem. This author believes that analytical studies of the separated flow model should be undertaken; for example, it may make considerable sense in the transonic cruise region to cut off or scallop boattail regions so as to trade controlled base pressure drag for excessive skin friction.

2.3.4 Compressibility Effects

Little has been done to apply compressible inviscid flow solutions to the nacelle problem. Emmons⁹ has suggested techniques for application of relaxation procedures to this problem. Holt¹⁵, Chushkin¹¹, Dorodnitsyn¹², among others, have shown that the method of integral relations may be useful. A third method, currently being studied in Boeing, is the use of the streamline curvature method proposed by Valentine¹³. It is too early to comment on the future of these compressible flow calculation techniques.

2.4 Summary

It is concluded that an adequate theory exists for estimating the drag of subsonic nacelle wing-body combinations. However, heavy reliance on model tests is still necessary to support the theory. As competition focuses on the $M = 0.90 - 0.95$ region, entirely new information may have to be generated, and a detailed inspection of our theoretical concepts will be required.

3. THE SUPERSONIC PROBLEM

3.1 General

Figure 10 shows typical nacelles, beginning with the high bypass dry subsonic application to the afterburning turbojet required for Mach 3.0 flight. The important point is not the engine cycle but the external shape that results from tight cowlings of these engines. As cruise Mach number increases, the nozzle area ratio required for complete expansion increases at a more rapid rate than the inlet capture area requirements for no-spillage operation. At about Mach 2.5 the ideal nozzle exit area is equal to the maximum area (over the turbine flange), resulting in a cylindrical nacelle afterbody. Below this speed the nacelle has both forebody wave drag and afterbody (boattail) wave drag. Above Mach 2.5 the ideal nozzle exit area becomes the maximum nacelle area. For an isolated nacelle, wave drag can now be reduced by limiting the nozzle exit area. Figure 11 shows the calculated pressure distribution on two isolated nacelles designed for Mach 2.70. One nacelle used an underexpanded nozzle to minimize wave drag in an effort to maximize thrust-minus-total-drag of the nacelle. The second nacelle employed a fully-expanded nozzle. Pressure coefficients

were integrated over the surface to calculate drag of the two nacelles. Nacelle number 1 appears to be the proper choice based on this calculation - but is it? The answer to this question requires further understanding of the interference of forces between the nacelle and the wing.

The importance of engine placement on total drag of a complete airplane is illustrated in Figure 12. For a given twisted and cambered wing-body combination and a tapered nacelle, variations in drag coefficient, $\Delta C_D = 0.0030$, were obtained at $C_L = 0.10$ simply by nacelle placement. This magnitude could amount to more than 20% of the total airplane drag. It is also evident that by proper placement nacelles can be installed on the airplane without any drag penalty for a given wing-body design. How is this possible?

It is the distinctive feature of supersonic flight that the zone of influence of a body is contracted laterally into a narrow space around the body. This property is the cause of significant interference forces between major components of the airplane. Favorable Interference is the study of these forces. The objective is drag reduction by the suitable arrangement of airplane components. Eggers¹⁴, Ferri¹⁵, and Migortsky¹⁶, among others, have written much on this subject and a variety of configurations based on favorable interference have been prepared. Although development of practical airplanes from these rather theoretical configurations has not been obvious, physical ideas discussed in the literature have influenced airplane design. For example, Alford and Driver¹⁷ have discussed engine-airplane integration by these methods.

In this section viscous considerations will be ignored, since they are readily determined by the methods discussed earlier, and we will concentrate on physical principles that have been presented through theoretical analysis of favorable interference on the supersonic transport. Some theory is directly applicable to defining drag and lift effects, but other aspects of nacelle integration are not currently amenable to theoretical computation.

3.2 Volume Interactions

To consider the interaction forces between engine nacelles and the rest of the airplane, it is useful to simplify our thinking by dividing these forces into components according to origin. The flow field around an airplane is then the sum of the flow fields due to individual components. Figure 13(a) shows how the flow around a wing and nacelle may be constructed by introducing an image, which ensures that the flow field of the nacelle is reflected by the wing. The method of images, used extensively to estimate wind-tunnel wall corrections, is indicated physically in Figure 14.

Drag of a body of revolution a distance Y from a wall can be estimated accurately, except very close to Mach 1.0, by determining drag of the same body at a distance of $2Y$ from an identical body. This is so because waves from the body are completely reflected back on the body from a plane solid wall. The effect of the wall can thus be replaced by that of a properly placed image. Both theory and experiment verify this fact. This method of images is used extensively in identifying the mathematical model of the supersonic drag problem.

In Figure 13(b) we see those items which contribute to the volume or thickness pressure drag of the nacelle-wing combination. These items are:

- (a) Isolated wing volume drag.
- (b) The drag of the nacelle in the presence of its image. A cylindrical nacelle would have no such drag.
- (c) The force on the lower surface of the wing caused by the nacelle and its image.
- (d) The force on the nacelle due to the presence of the wing. A cylindrical nacelle would have no such drag.

In the example shown, forces caused by the nacelle and its image reduce wing drag. The drag of the nacelle is reduced by the presence of the wing, but is increased by the image.

These concepts provide a valuable guide to understanding the effects of nacelle shape and location.

3.3 Interaction between Volume and Lift Elements

The effect of a wing's lift must be added to the effect of a wing's thickness. For this purpose the wing is idealized into a thin sheet. Forces which contribute to drag are illustrated in Figure 15. These items are:

- (a) Isolated wing drag due to lift.
- (b) Nacelle pressure acting on the wing camber line. An image nacelle is again introduced to ensure complete reflection of the nacelle pressure field on the mathematical model.
- (c) The wing lifting pressure acting upon the nacelle.

The nacelle itself is assumed to carry no lift, since it is closely aligned with the local flow direction.

In the example shown, the interference items (b) and (c) contribute drag. However, both could be reduced, as shown in Figure 16, by reflexing the wing in the vicinity of the pod. This modification will cause higher wing drag due to lift because higher incidence is required to achieve the same lift. Minimum drag stems from the correct compromise between these items.

3.4 Theoretical Considerations

In the simplest theoretical approach, the analysis of wing-nacelle integration is usually limited to these forces only; total forces are calculated by adding to the force of each isolated component additional forces due to neighboring elements, taking care to introduce such artificers as the image of a nacelle to maintain physical plausibility. Chen and Clarke¹⁸ discuss this in detail. Thus, as shown in Figure 17, a crude attempt is made to theoretically define nonfrictional drag elements of a supersonic transport by adding the models prepared for volume effects to those obtained from the lift-volume interaction.

3.4.1 Solution of Volume Elements

The interference pressure drag of volume elements have usually been determined by use of the Supersonic Area Rule Theory. This theory, which dates back to Sears¹⁹ and Lomax²⁰ among others, involves solution of a triple integral expression which requires taking the space coordinates of the aircraft configuration and transferring them into artificial coordinate systems which yield a series of equivalent bodies of revolution of the various parts of the airplane. The drag of these bodies is then transferred back to the basic coordinate system. Witcomb and others at NASA noted that for a simple slender shape, at Mach numbers near 1.0, the body of revolution can be obtained by using the actual perpendicular cuts. This has led to the popular concept which states that volume drag of a complex airplane can be minimized by maintaining the area progression perpendicular to the line of flight as smooth as possible. This thought process should not be overdone, especially for high Mach number design. The rigorous Area Rule theory must be applied in any serious design comparison. Most researchers in the supersonic transport area have programmed this calculation on the high speed computer. The only input requirements are the three-dimensional coordinates of the airplane and the application of images where needed to ensure that complete reflection of waves from the wing and neighboring nacelles are felt on each nacelle. This later statement also indicates one of the weaknesses of the calculation. A result can be obtained only for the case of no reflection (no image) or complete reflection. Many nacelle locations cause only partial reflection. Portnoy²¹ has suggested a possible solution to this problem. Figure 18 shows a typical comparison of a non-lifting wing-body with Area Rule theory, noting how reliable the theory is for the more elementary systems.

3.4.2 Interaction of Lift and Volume Elements

Lighthill²² and Ohman²³ have presented methods for computing pressure distributions on the surface of bodies of revolution and the manner in which this pressure propagates out into the near field. Figure 19 shows a comparison of theory and experiment for a body of revolution and a nonlifting delta wing. Through this theory it has been possible to estimate the interference pressure field imposed on a wing due to the pressure of a nacelle. At angle of attack it is assumed that a uniform flow field is felt by the body, corresponding to the average flow under the wing.

This approximation is currently required because the theory has been developed for use with uniform flow only.

The important problem of the cambered and twisted wing can be analyzed theoretically, using linearized supersonic lifting surface theory²⁴. In practice, attempts at using this theory have been only marginally reliable. Figure 20 shows results of a recent Boeing wing-body test in which theory and experiment did not satisfactorily agree, although the difference between configurations was quite closely estimated.

To complete the lift-volume interference forces, it is necessary to estimate the flow field at some distance from a lifting wing to obtain the effect on nacelles. Currently, methods are being explored at Boeing to accomplish this, but for the moment an assumption is being used that for small distances away from a wing the pressure at the surface propagates along straight Mach lines. This is not a very satisfactory assumption but, as can be seen from Figure 21, fair agreement with experimental results has been obtained.

3.5 The Importance of Testing

The mathematical model shown in Figure 17 clearly shows its own shortcomings. The theory can account in part for the load distribution in a wing due to camber and twist in the flow direction but it ignores the effect of wing deflection on the nacelle flow field. Also the nacelle is treated as being axisymmetric and this need not be the case. It may be desirable to yaw the nacelles and even to camber them to gain the best interference effects. Theory ignores this. The strut itself presents problems. As the nacelle is placed closer to the wing, use of a boundary layer diverter is suggested. The diverter can become a high drag item in itself.

Although complete model testing appears to be the only current solution to these problems, the techniques of nacelle testing are far from optimum. The model must be an accurate representation of the flow. Ducted nacelles must be used and then internal drag accounted for. Generally two ways exist to accomplish this. One is to design the nacelle such that the inside is a straight uniform duct and only a skin friction correction is needed. A second approach is to choke the internal flow at the exit and obtain the axial force from momentum measurement. This latter technique is quite complicated but must be used when internal geometry does not allow the model to be designed with uniform duct flow. In either case base area corrections must usually be extracted. The leading edges of the nacelle inlet must be quite sharp since they feel the highest Mach numbers. Blunt leading edges can lead to erroneous results.

3.6 Promising Results

Referring back to Figure 11, let us see what happens when we apply these two nacelles to supersonic wing-body arrangement. Figure 22 shows that due to interference the nacelle which had the highest wave drag in the isolated condition was actually quite superior when installed. The interference lift provided by the high positive pressures on the forward half of the nacelle was applied to the aft region of the wing behind the maximum thickness station, where lower surface pressures predominate, giving an increment in lift considerably in excess of that produced by the under-expanded nacelle. Actually both nacelles improved the drag of the wing-body alone. Theoretical sums made on the artificial models gave a reasonable approximation of the results obtained.

Figure 23 shows an oil flow picture of the shock pattern appearing on the underside of the wing of a typical nacelle, wing and body arrangement. The sharp interaction between the nacelles suggests that nacelles should be placed such that the interference fields intersect behind the point of maximum thickness of the wing and that certain freedom should be employed to yaw and camber the pods as desired to maximize this resulting thrust force. Figure 24 shows the theoretical distribution of pressure produced by four nacelles on a supersonic transport design. Figure 25 shows the effect of placing the nacelles forward of the maximum thickness location compared to the effect of locating them aft of the maximum thickness point.

The effect of putting reflex into the wing trailing edge in the vicinity of the pods was examined, using the theoretical tools previously discussed. Figure 26 shows that adding up to 2% reflex caused a continuing decrease in pressure drag. More reflex resulted in increased drag because of the rapid rise in isolated wing drag due to lift. The test data presented as Figure 27 show the drag reduction achieved by

trailing-edge reflex and indicates reasonable agreement with theory. In addition to this reduction in drag, trailing-edge reflex produces a nose-up pitching moment. This is beneficial since it reduces the downward tail load normally needed to trim the airplane. The engine designer and airframe configurator are at odds in several areas. This paper suggests that engines need not be concentric cylinders, but that they might have bends, kinks, and use overexpanded nozzles to optimize aircraft performance. Figure 28 shows some results from the available theory, which suggests a combination of wing reflex and either oversizing of the engine or over-area of the nozzle could lead to sizable drag reductions to the aircraft.

In conclusion, it must be stated that these thoughts have been generated without paying any attention to consequences of nacelle weight, airplane balance, structural design, or low-speed/high-lift considerations. Still, more theoretical work is needed, especially in the three-dimensional flow area.

3.7 Summary

In the supersonic case pressure forces predominate and, by intelligent use of these pressures, both lift and thrust can be obtained. At best current supersonic theory provides a guide to design, and the use of the wind tunnel is still the only way that subtle three-dimensional gains can currently be utilized.

ACKNOWLEDGEMENTS

The material in this paper has been compiled from the efforts of Robert L. Lawrence and John R. Monk of The Boeing Company in the subsonic area, and from the efforts of Armand Sigalla and Thomas H. Hallstaff of The Boeing Company of the supersonic area. Without their support this paper could not have been written.

REFERENCES

1. Lawrence, R.L. *Afterbody Flow Fields and Skin Friction on Short Duct Fan Nacelles.* AIAA Paper 64-607, 1964.
2. Lawrence, R.L. *Velocity Profiles from Compressible Wall Jets.* AIAA Paper J.2, 574, 1964.
3. Hough, G.R. *The Aerodynamic Loading on Streamline Ducted Bodies.* ASTIA AD 407148, 1962.
4. Kucheman, D.
Weber, J. *Aerodynamics of Propulsion.* McGraw-Hill, 1953.
5. Allen, D.N. *Relaxation Methods.* pp.65-91, McGraw-Hill, 1954.
6. Lee, S.C. *The Use of Finite Difference Method in Obtaining Potential-Flow Solutions.* The Boeing Company, D6-9826TN, 1962.

7. Schlichting, H. *Boundary Layer Theory*. McGraw-Hill, 1960.
8. Launder, B.E. *An Improved Pohlhausen - Type Method of Calculating the Two-Dimensional Laminar Boundary Layer in a Pressure Gradient*. ASME Paper 63-HT-26, 1963.
9. Emmons, H.W. *The Numerical Solution of Compressible Fluid Flow Problems*. NACA TN 932, 1944.
10. Holt, M. *The Design of Plane and Axisymmetric Nozzles by the Method of Integral Relations*. NIA AD 288546, 1962.
11. Chushkin, P.I. *Subsonic Flow of a Gas Past Ellipses and Ellipsoids*. Vychislitel'naya Matematika No.2, pp.20-44, 1957.
12. Dorodnitsyn, A.A. *Transactions, Third All-Union Mathematics Congress*, 1956.
13. Valentine, E.F. *An Approximate Method for Design or Analysis of Two-Dimensional Subsonic-Flow Passages*. NACA TN 4241, 1958.
14. Eggers, A.J., Jr.
Syvertson, C.A. *Aircraft Configurations Developing High Lift-Drag of Ratios at High Supersonic Speeds*. NACA RM A55L05, 1956.
15. Ferri, A.
et alii *Favorable Interference in Lifting Systems in Supersonic Flow*. Journal of Aeronautical Sciences, Vol.24, No.11, pp.791-804, 1957.
16. Migortsky, E.
Adams, G.J. *Some Properties of Wing and Half-Body Arrangements at Supersonic Speeds*. NACA RM A57E15, 1953.
17. Alford, J.
Driver, C. *Recent Supersonic Transport Research*. Astronautics and Aeronautics, pp.26-37, September 1964.
18. Chen, C.F.
Clarke, J.H. *A Study of Configurations Composed of a Body Under a Lifting Wing in Supersonic Flow*. Division of Engineering, Brown University, AFOSR TN59-1276, 1960.
19. Sears, W.R. *On Projectiles of Minimum Wave Drag*. Quarterly of Applied Mathematics, Vol.6, No.4, pp.361-366, 1947.
20. Lomax, H. *The Wave Drag of Arbitrary Configurations in Linearized Flow as Determined by Areas and Forces in Oblique Planes*. NACA RMA 55A18, 1955.
21. Portnoy, H. *The Flow Past a Delta-Wing-Half Cone Combination with Subsonic Leading Edges*. The Aeronautical Quarterly, Vol.XV, Part 4, 1954.

22. Lighthill, M.J. *Higher Approximations in Aerodynamic Theory.* Princeton University Press, Princeton, New Jersey, 1960.
23. Ohman, L. *The Application of a Lighthill Formula for Numerical Calculation of Pressure Distribution on Bodies of Revolution at Supersonic Speed and Zero Angle of Attack.* SAAB Technical Note TN-45, 1960.
24. Heaslet, M.A.
Lomax, H. *Supersonic and Transonic Small Perturbation Theory - General Theory of High Speed Aerodynamics.* Vol. VI, Section D, Princeton University Press, Princeton, New Jersey, 1954.

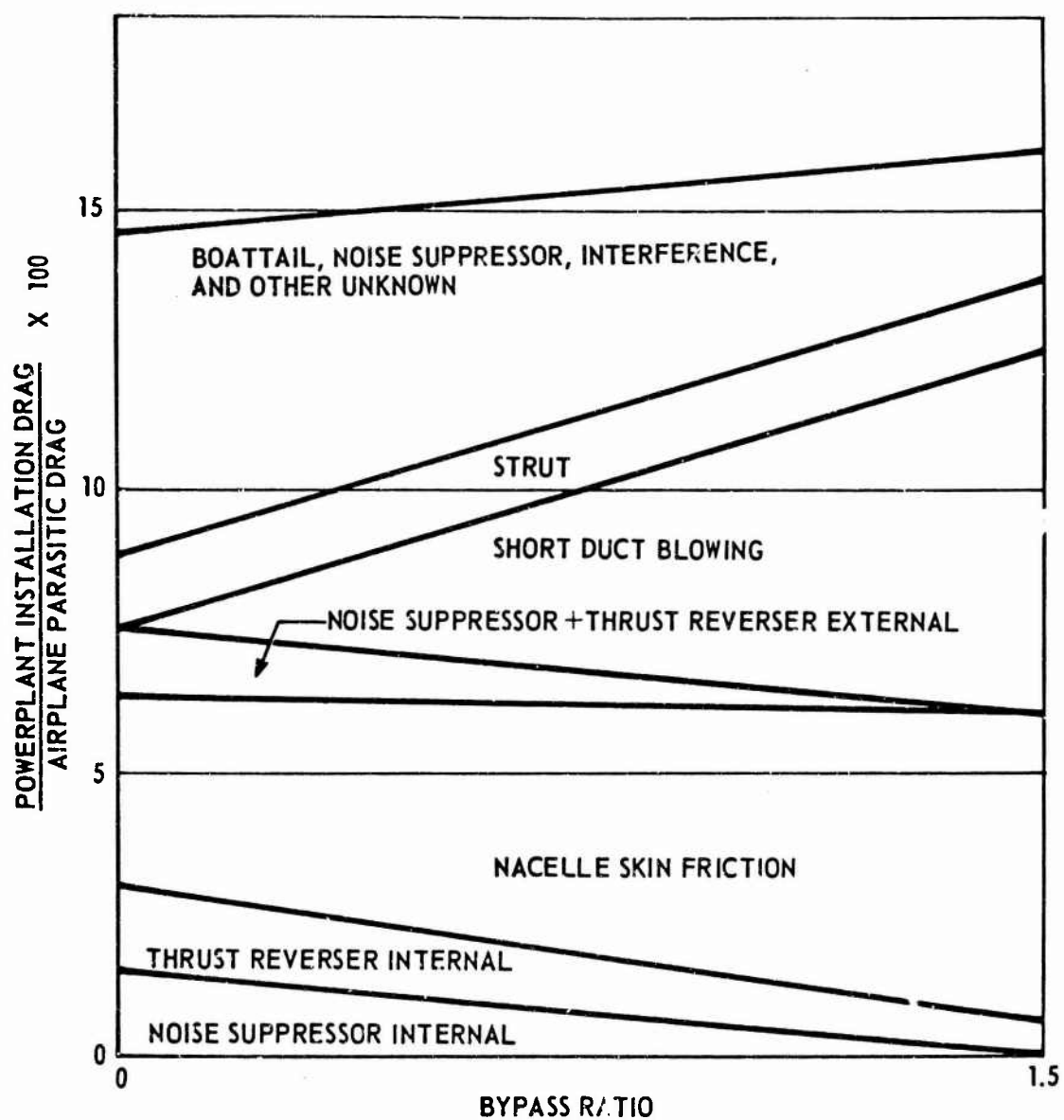


Fig.1 Estimated propulsion pod drag breakdown of fan-powered 707 compared with early jet powered 707

PARASITIC {

DRAG BREAKDOWN	M=.85	M = 2.70
FRICTION	50%	38%
FORM OR PRESSURE	15%	24%
$\frac{\partial c_D}{\partial c_L^2}$	35%	38%

Fig.2 Approximate distribution of drag for commercial transports at two speeds

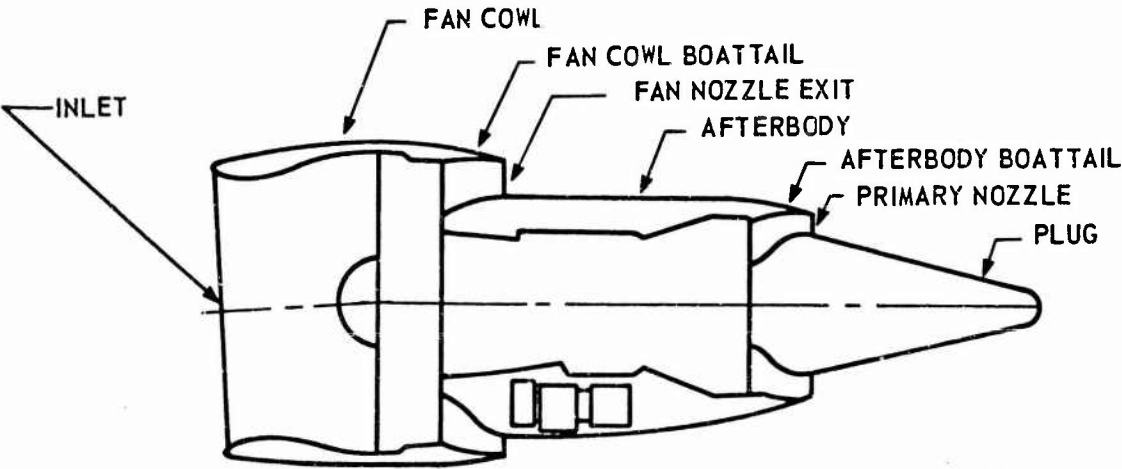


Fig.3 Typical high bypass engine nacelle

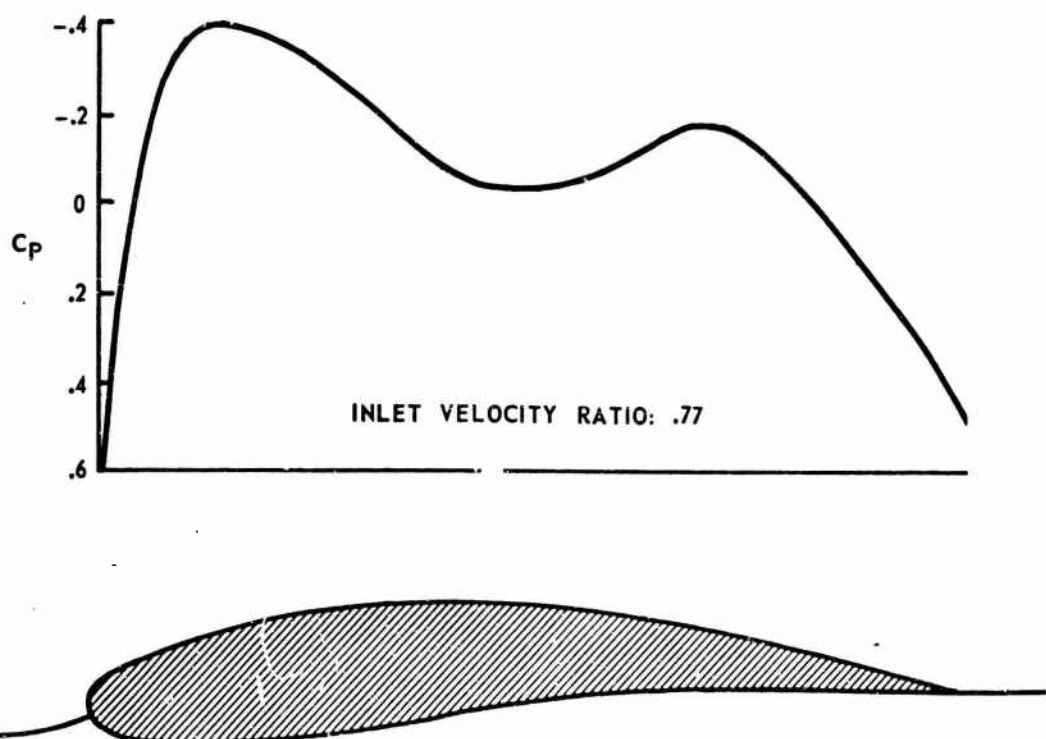


Fig.4 Typical fan cowl external pressure distribution

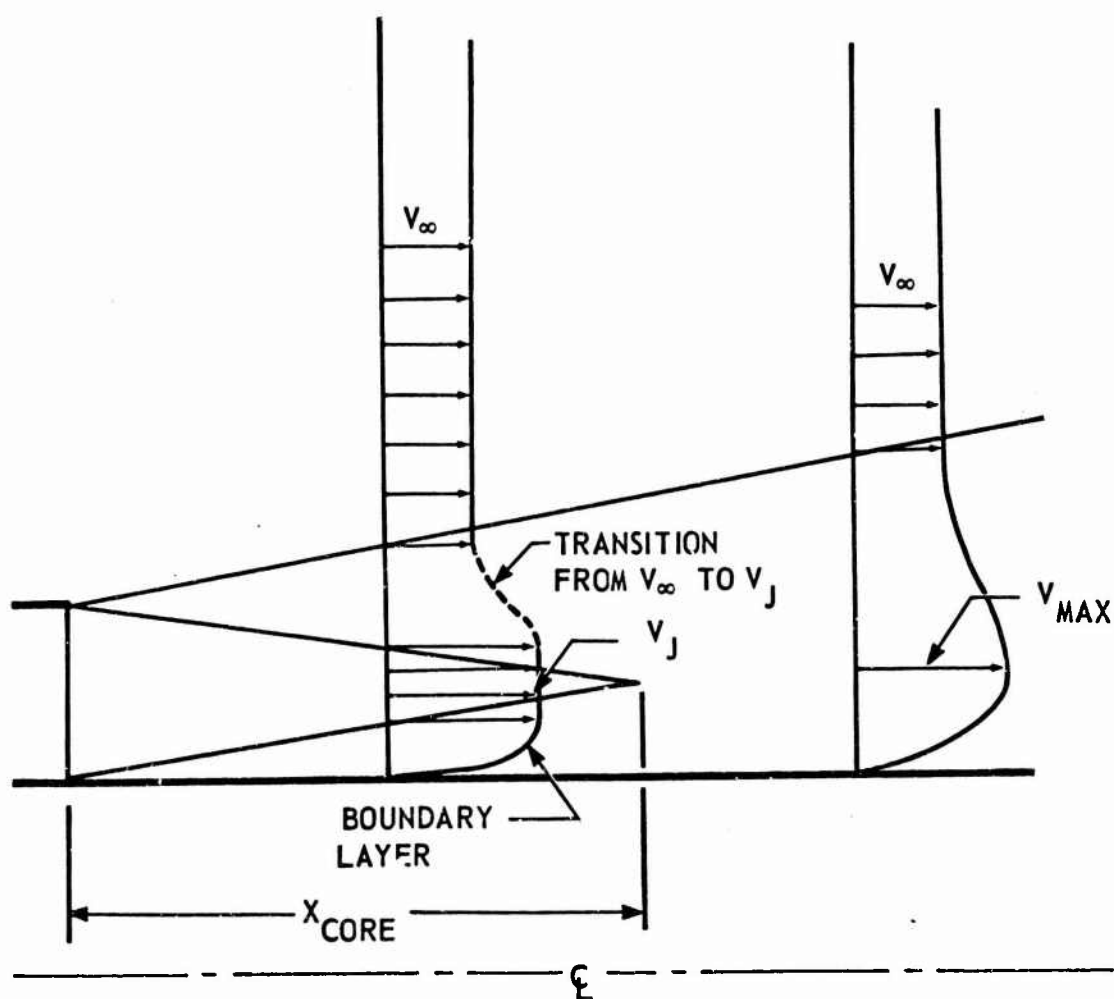


Fig.5 Flow model

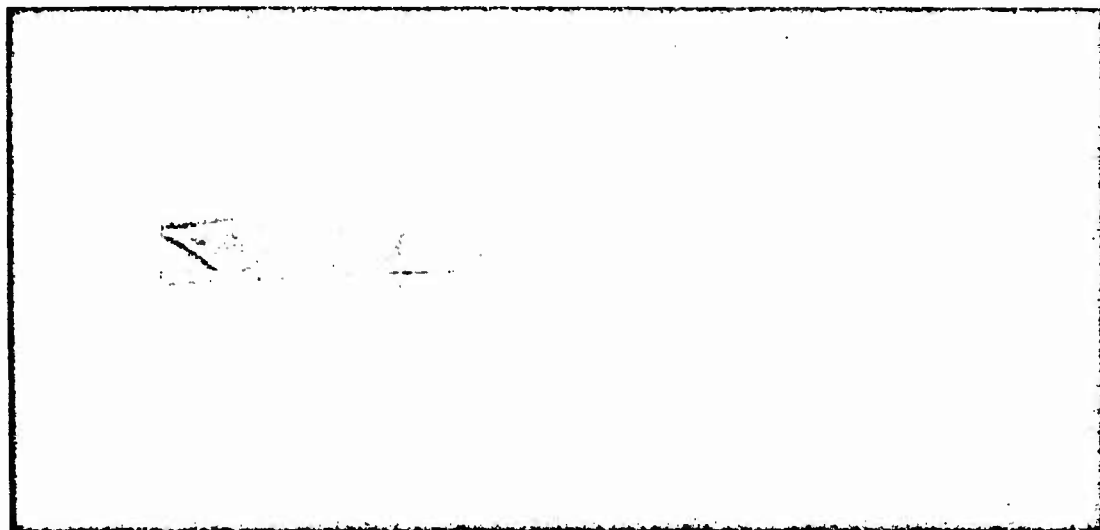


Fig.6 Shadowgraph of jet flow, $M_\infty = 0.8$, fan nozzle pressure ratio, 3.6

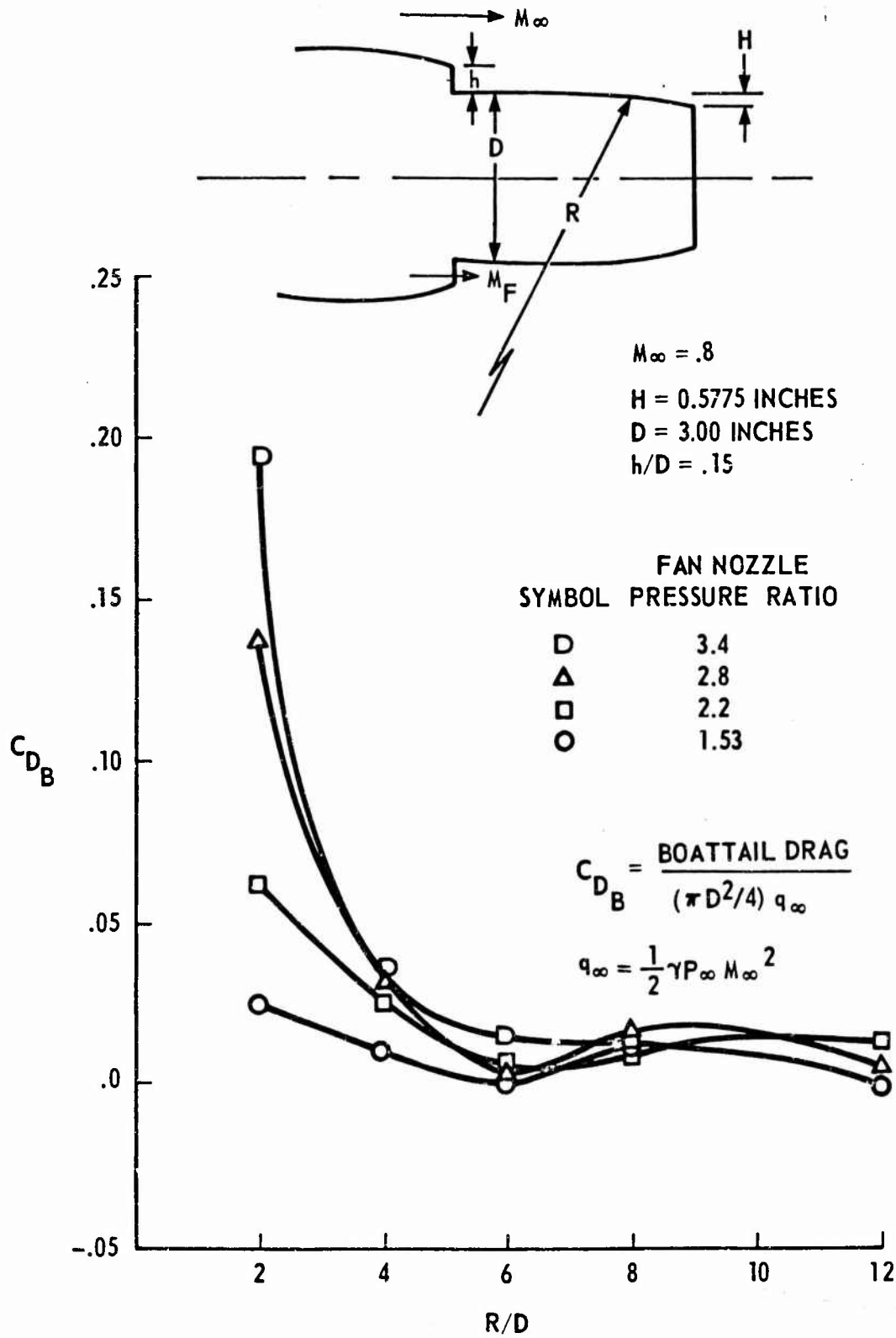


Fig.7 Boattail drag coefficient versus radius of curvature

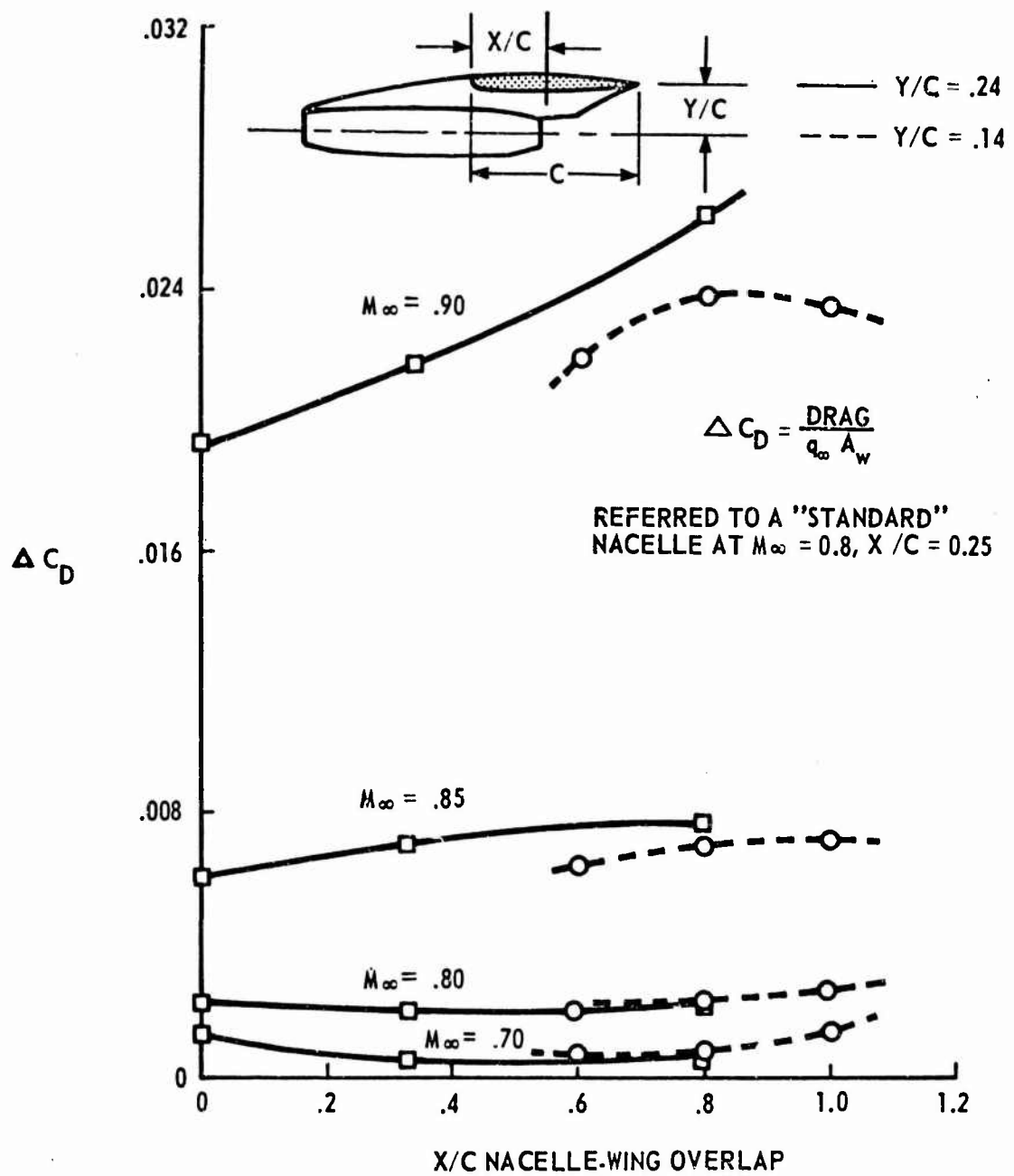


Fig.3 Change in airplane drag with nacelle position

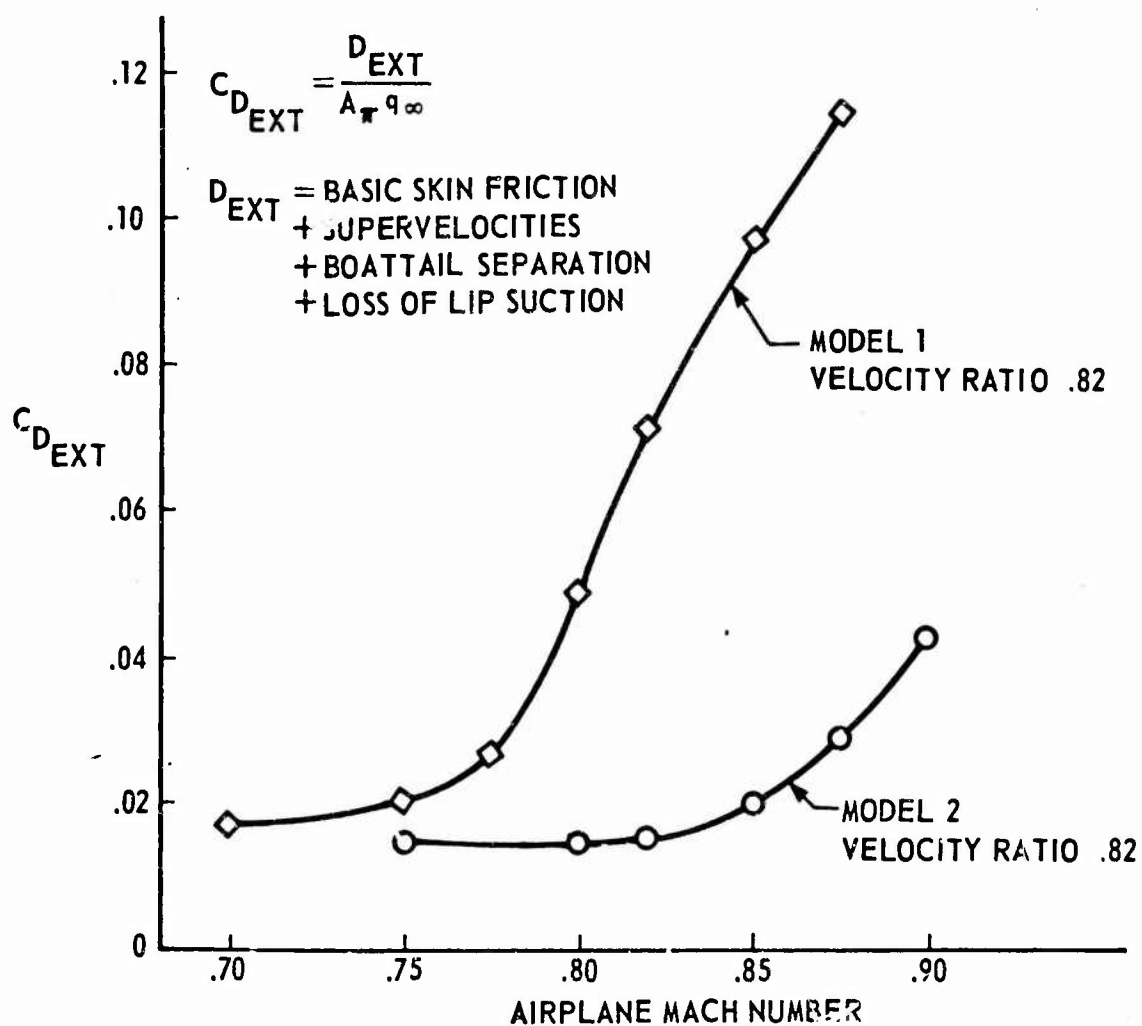
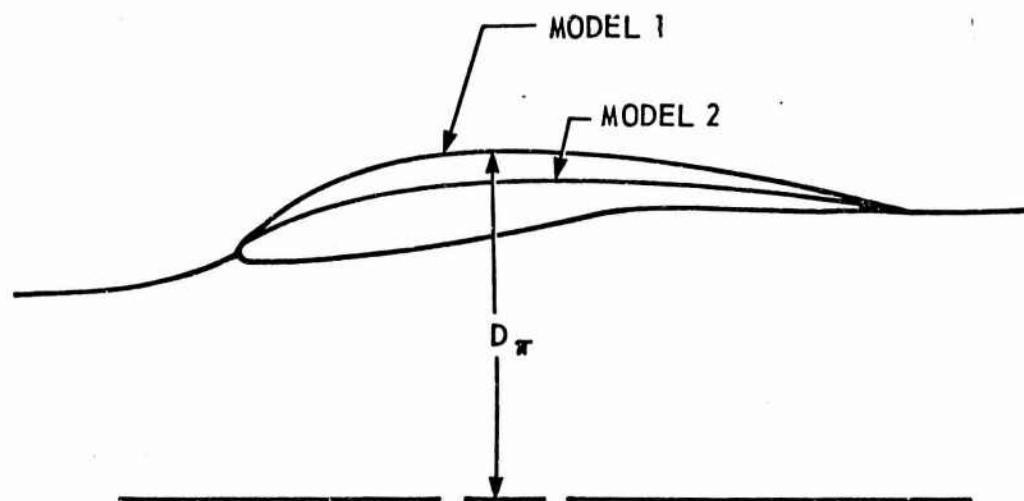


Fig.9 External fan cowl drag

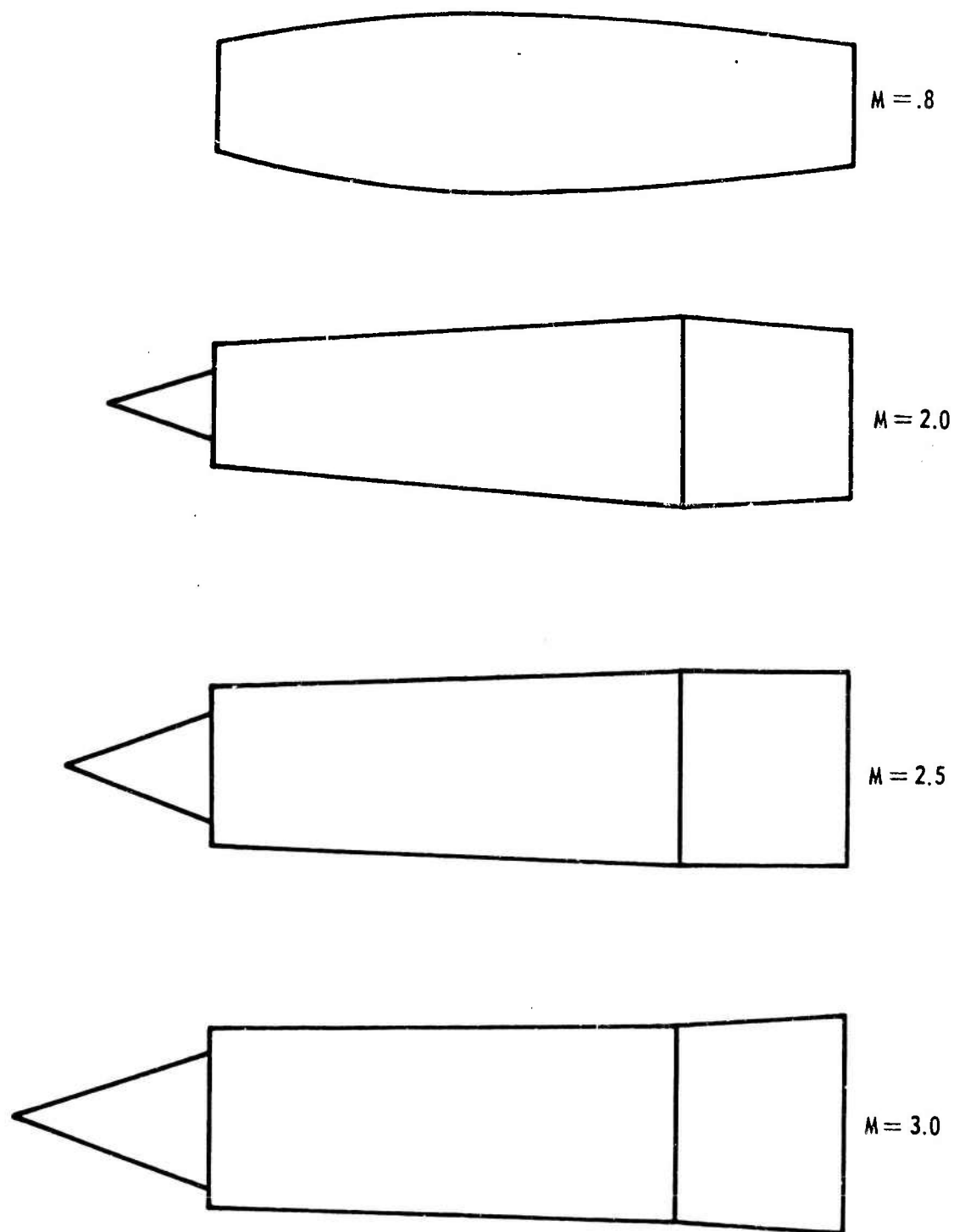


Fig.10 Effect of design Mach number on nacelle shape

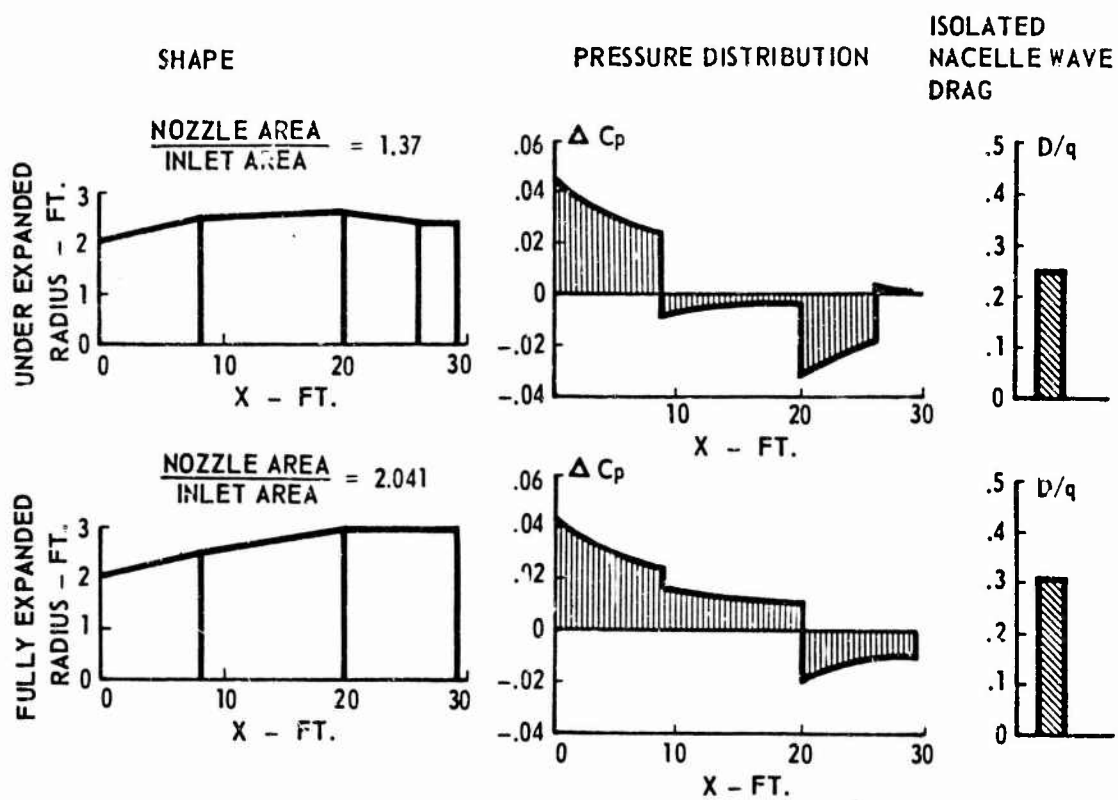


Fig.11 Effect of the nacelle shape on pressure distribution and drag

$$\Delta C_D = (C_{D \text{ WING, BODY, NACELLES}} - C_{D \text{ WING, BODY}})$$

BOEING TEST DATA

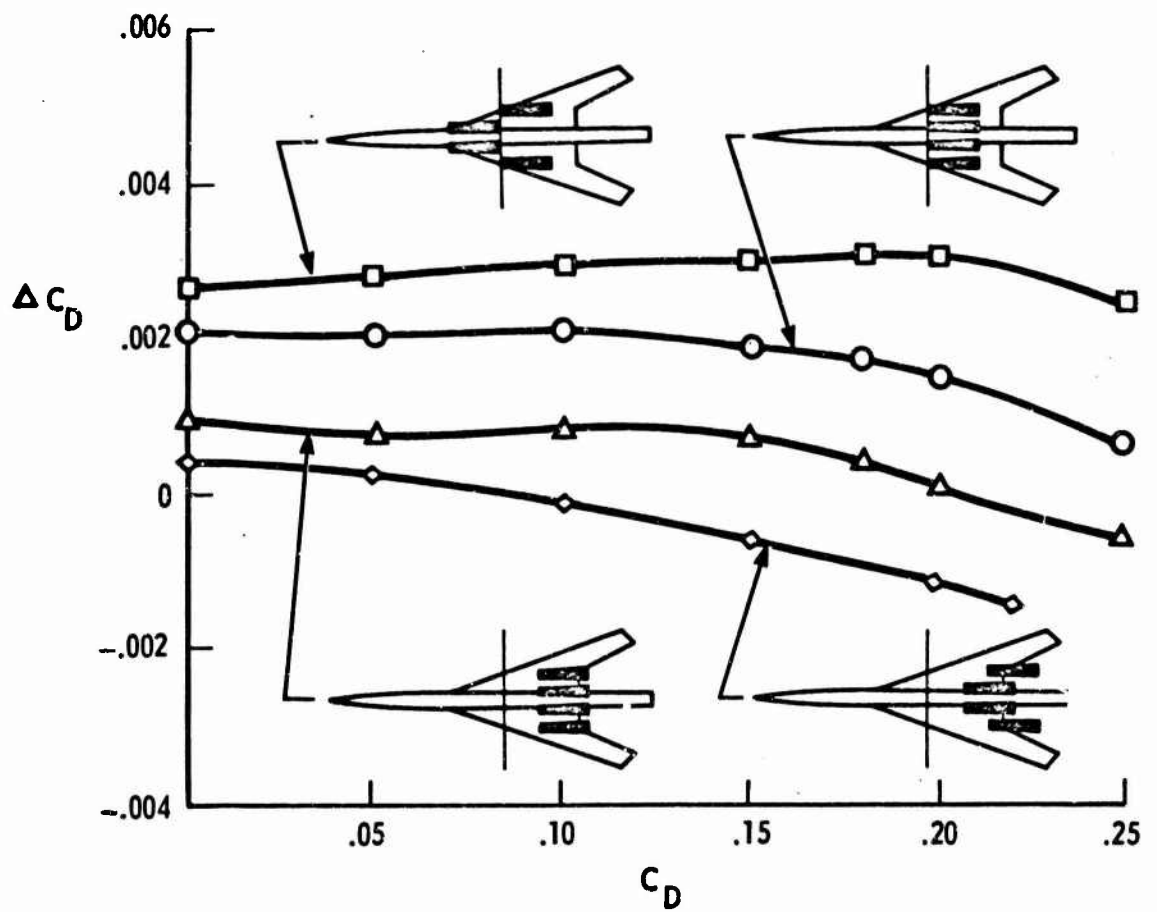
Fig.12 Effect of nacelle location on nacelle drag increment $M = 2.7$

Fig. 13 (a)

METHOD OF IMAGES

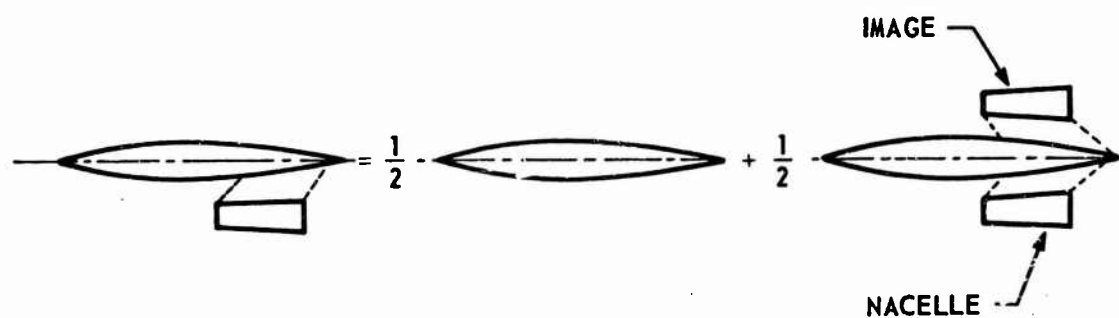


Fig. 13 (b)

INTERACTION OF FORCES

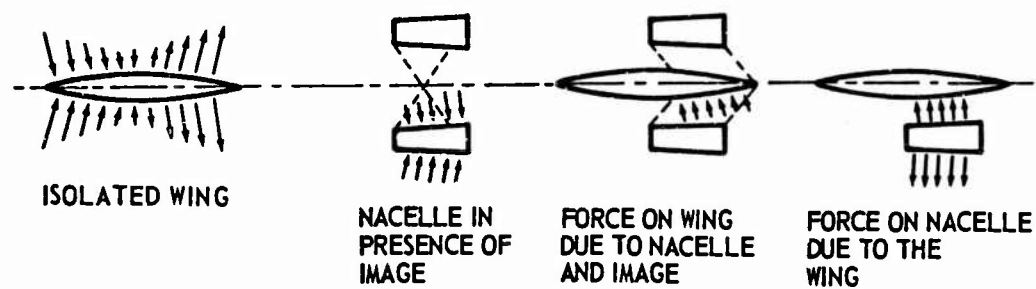


Fig. 13 Volume drag

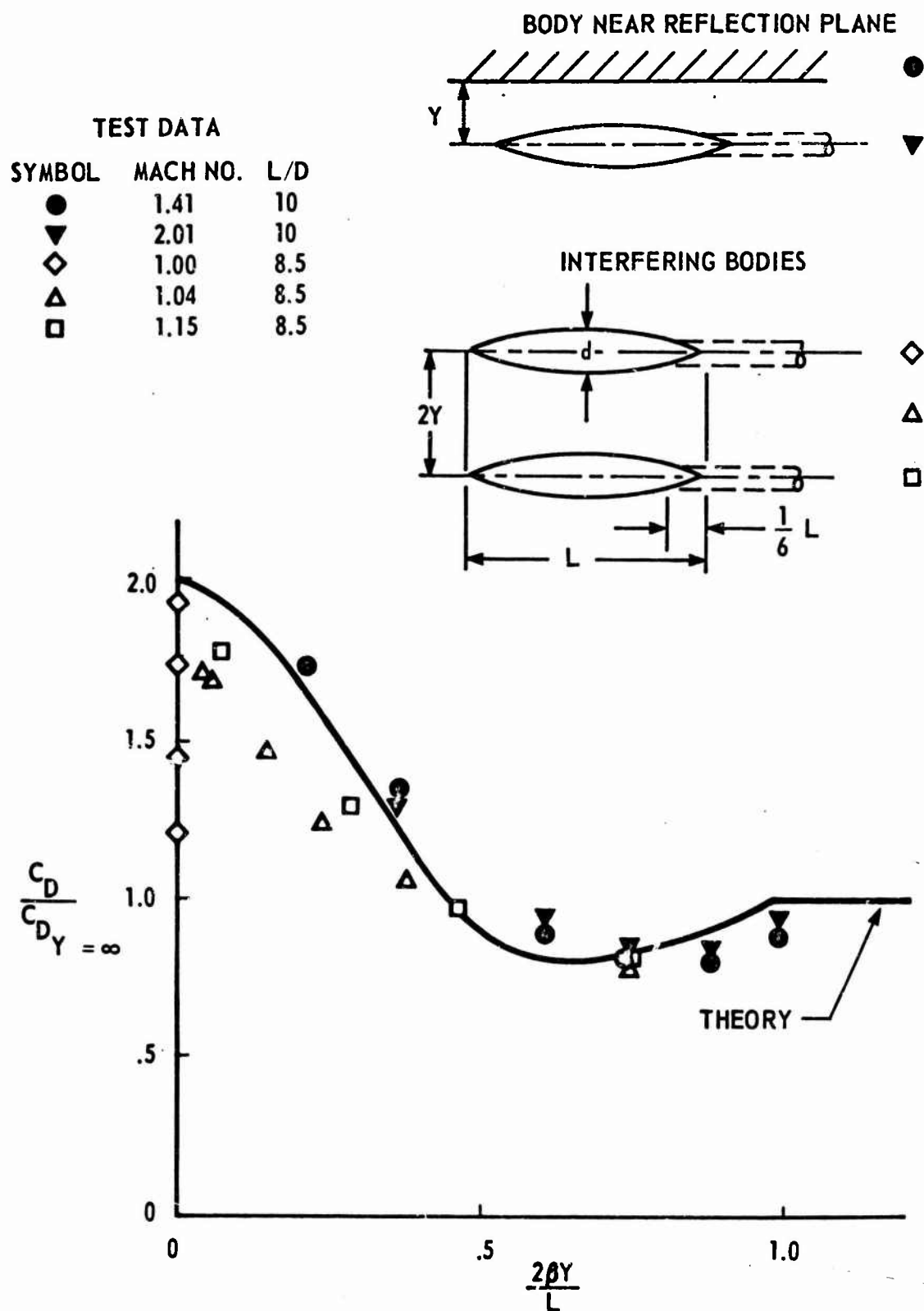


Fig.14 Interference between two bodies of revolution

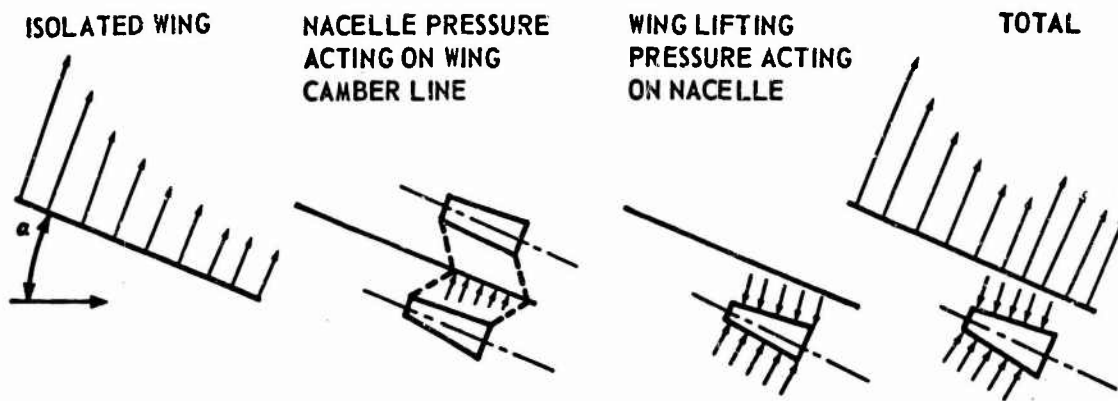


Fig.15 Volume-lift interaction

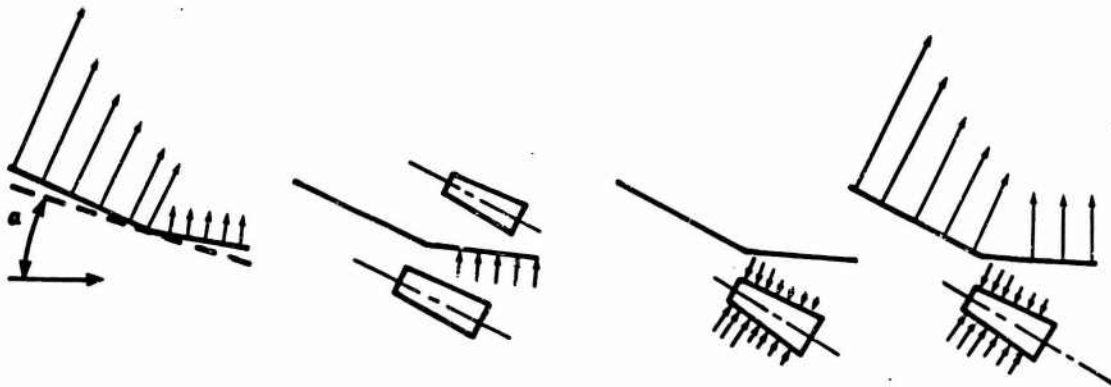


Fig.16 Camber optimization

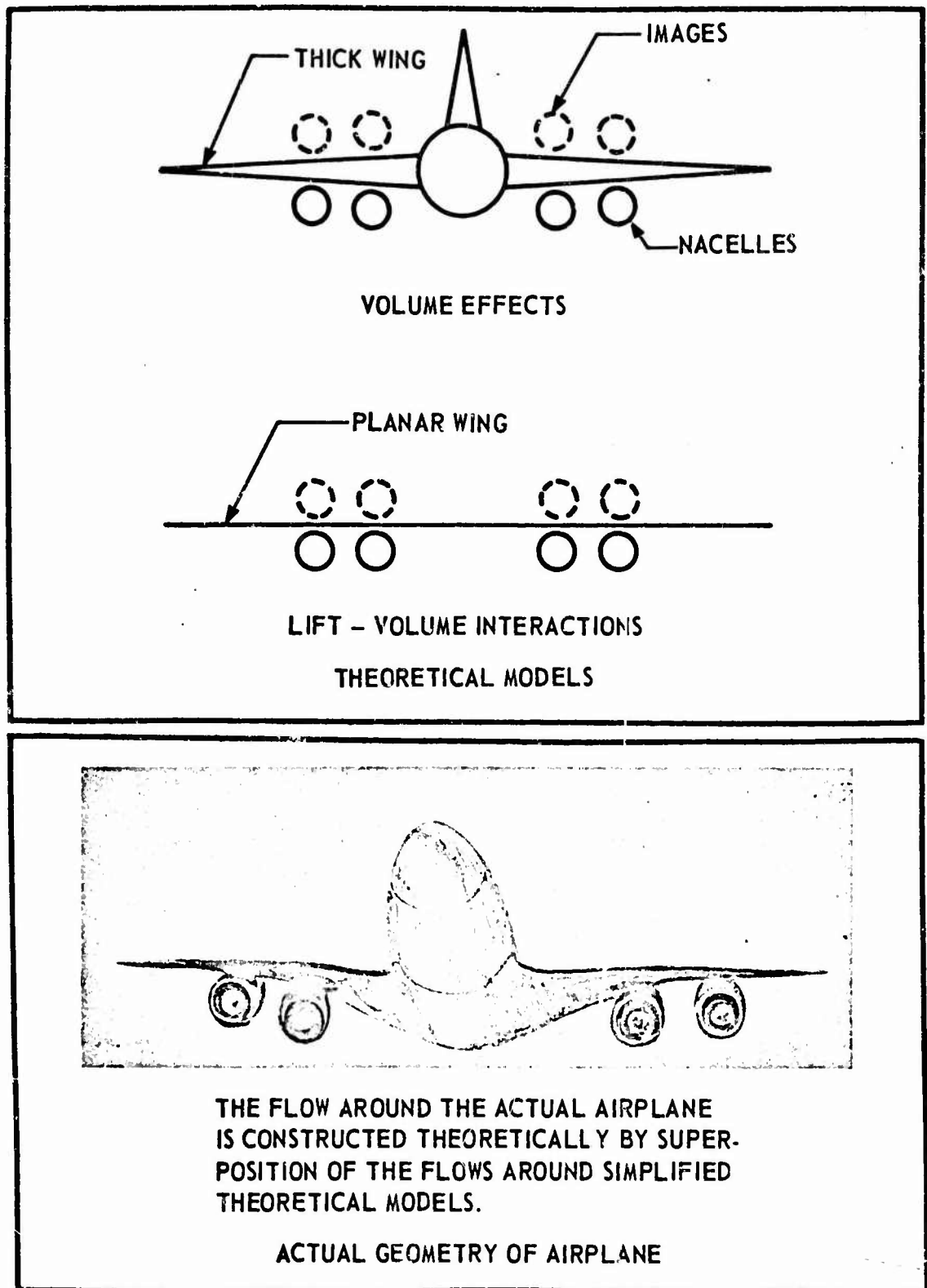


Fig.17 Comparison of airplane and theoretical models

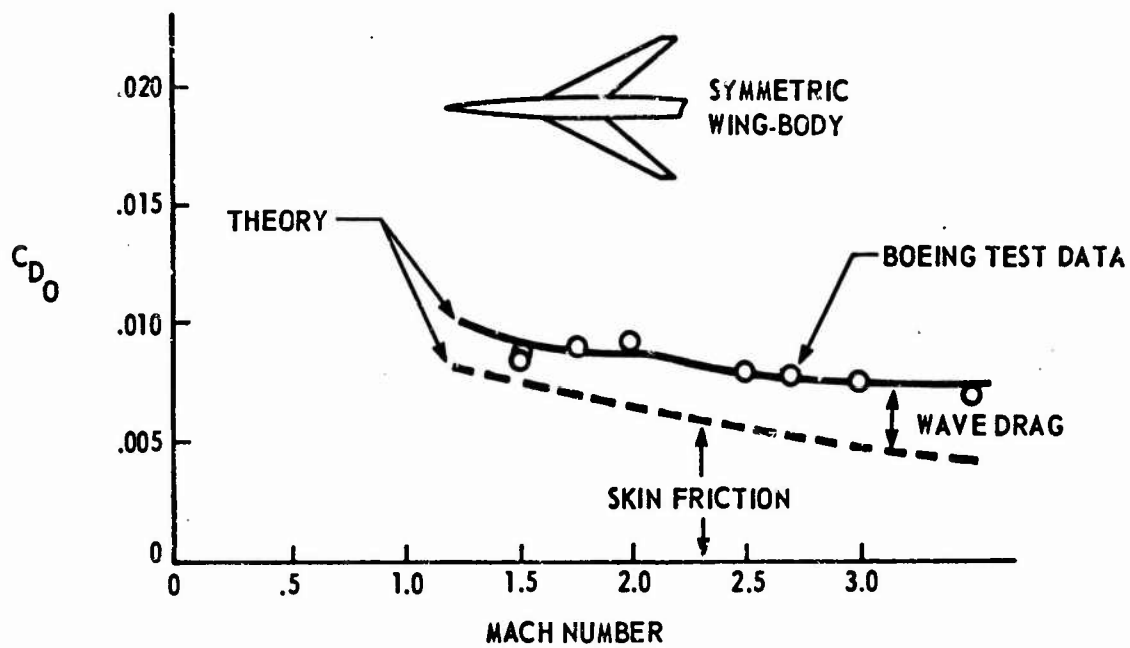


Fig.18 Wing-body drag at zero lift theory - experiment

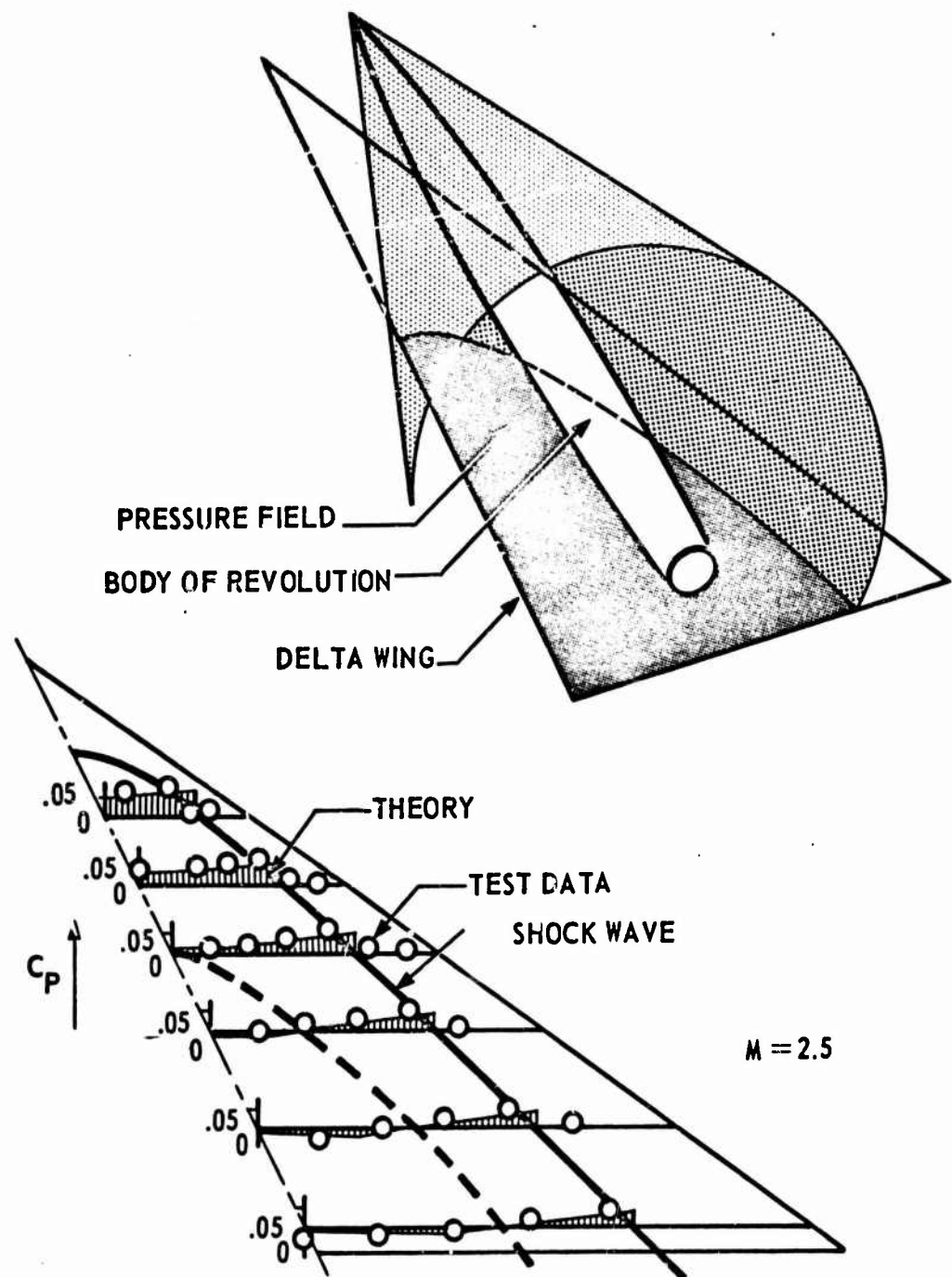


Fig.19 Pressure field of a body of revolution theory - experiment

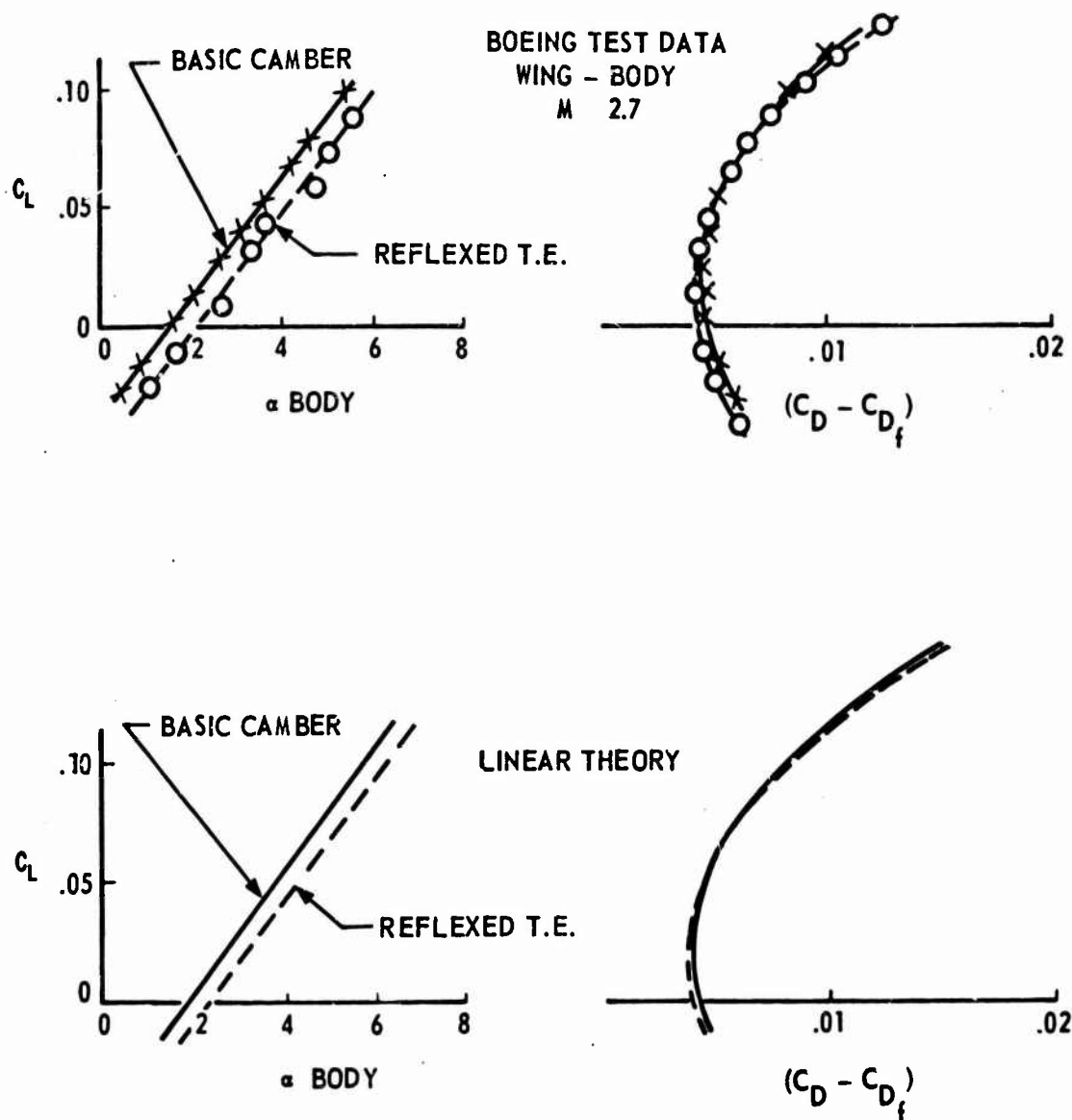


Fig.20 Camber modification theory and experiment

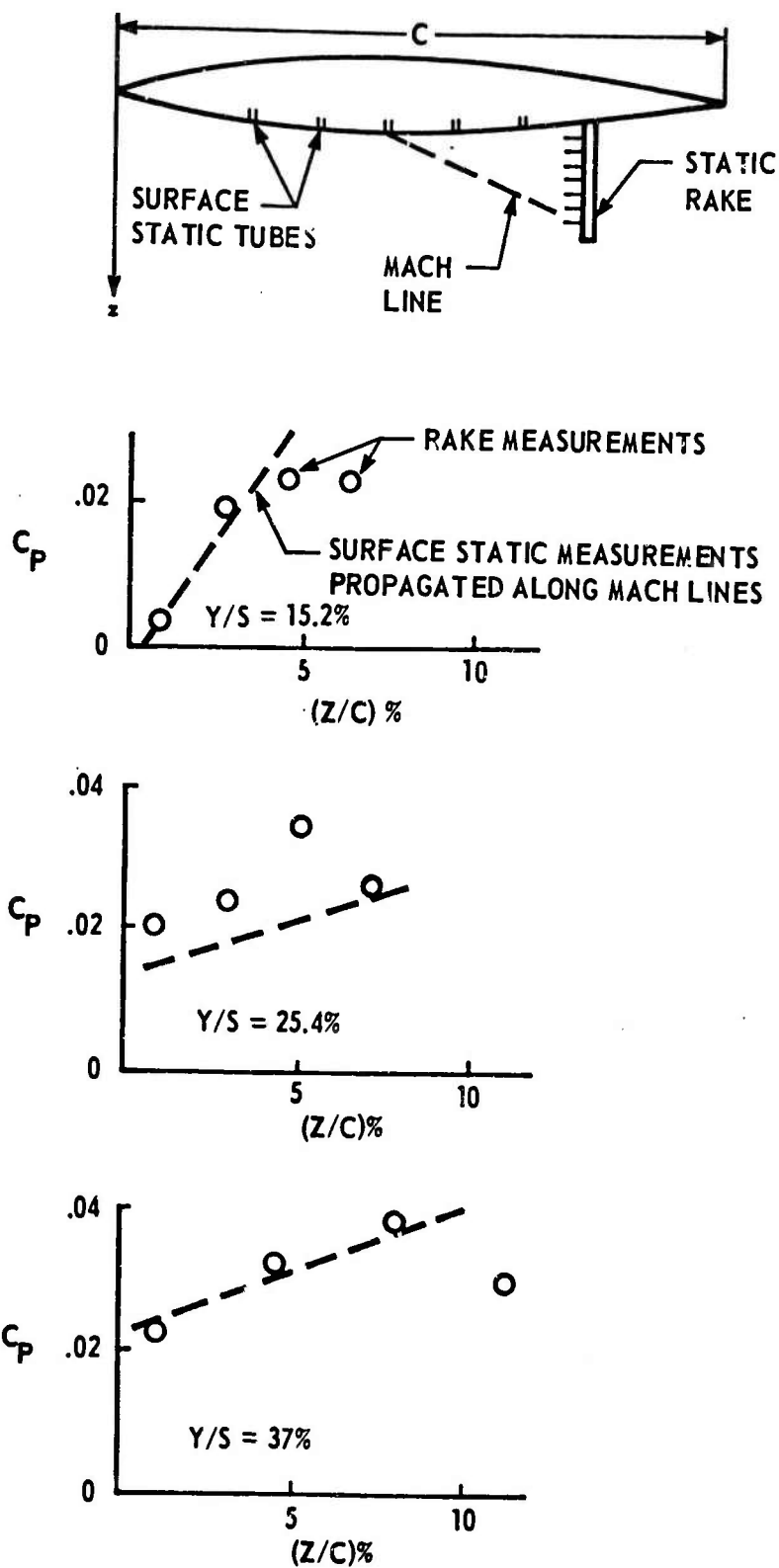


Fig. 21 Wing flow field

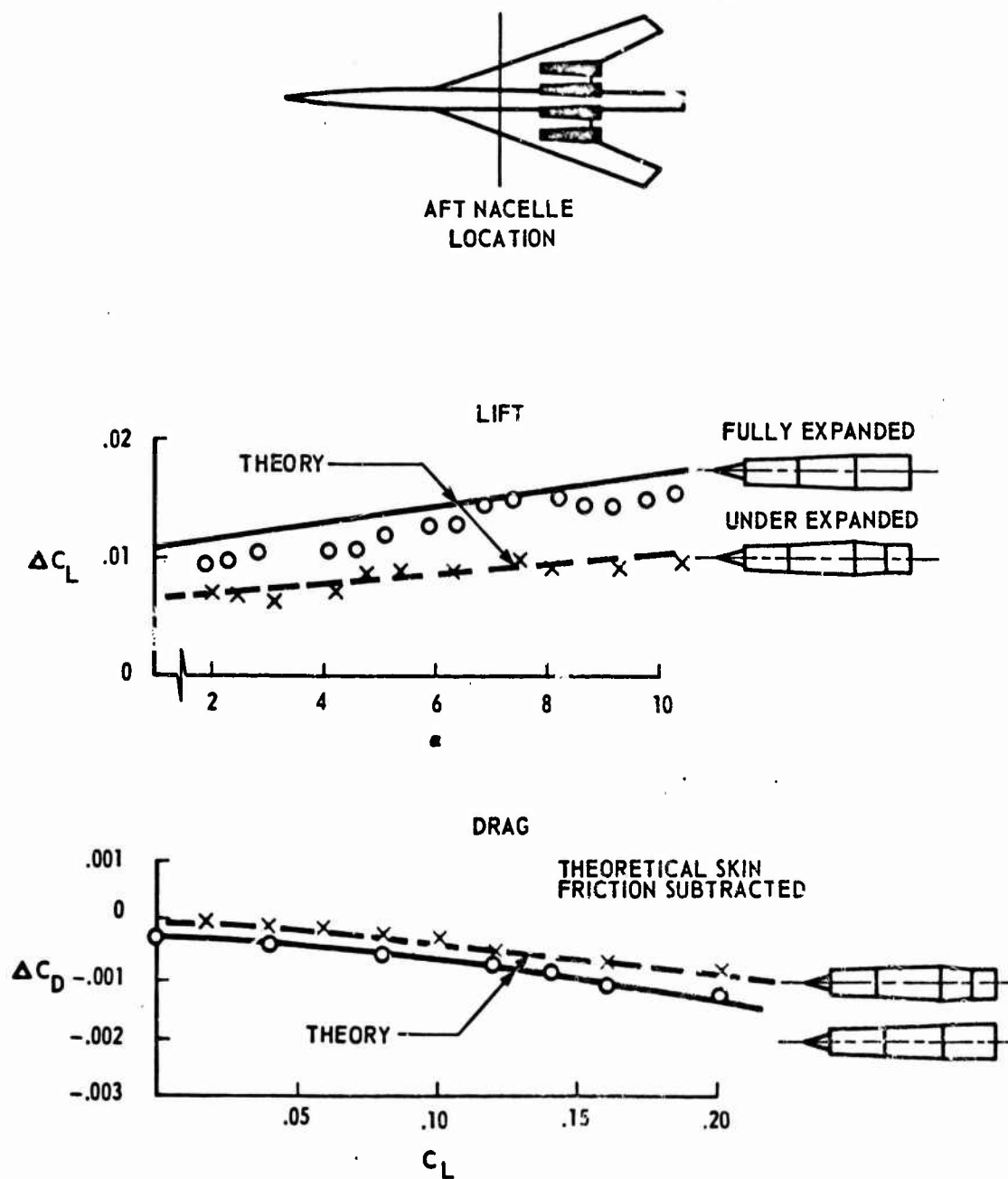


Fig. 22 Effect of nacelle shape $M = 2.7$

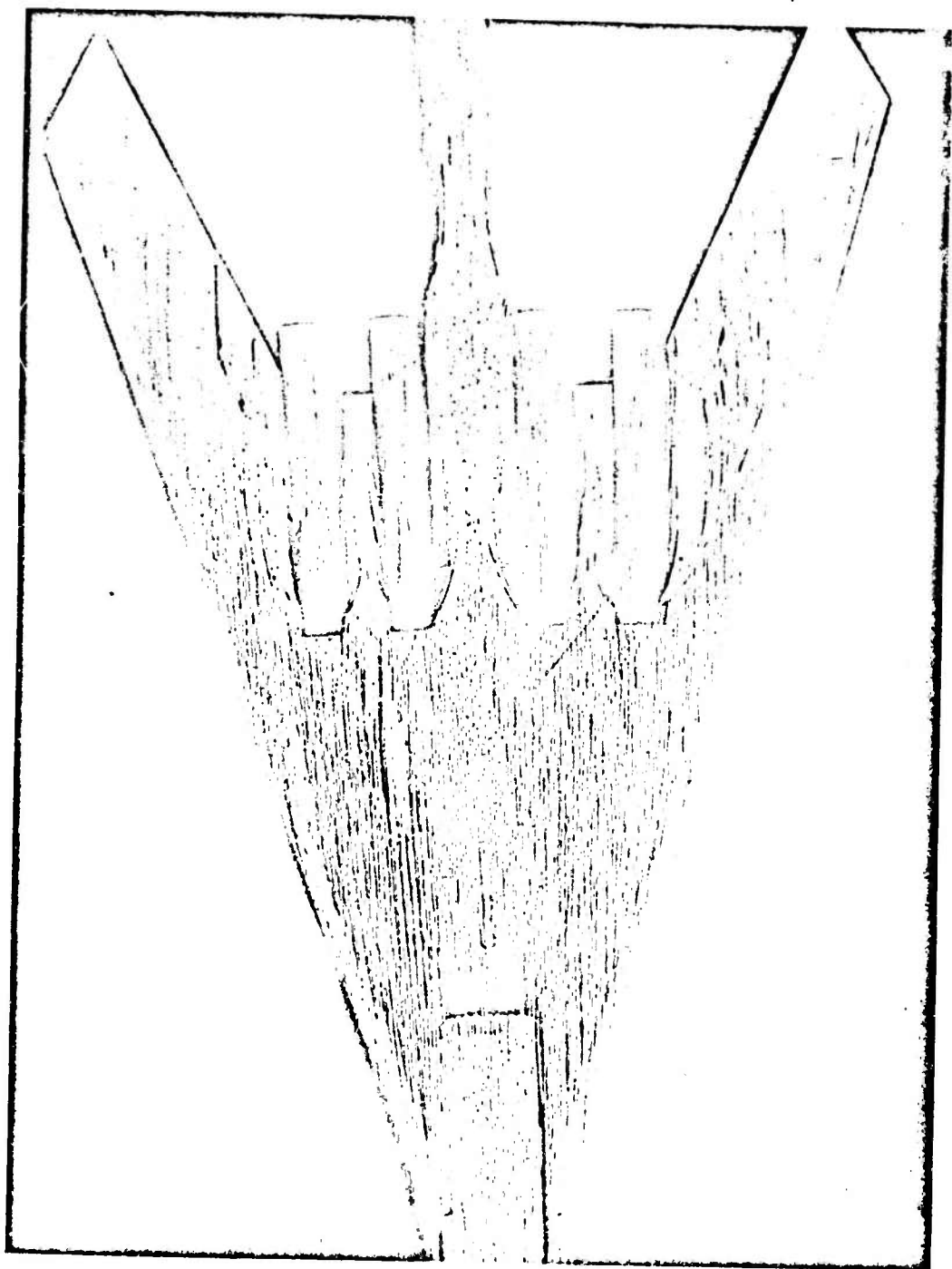


Fig. 23 Lower surface oil flow pattern

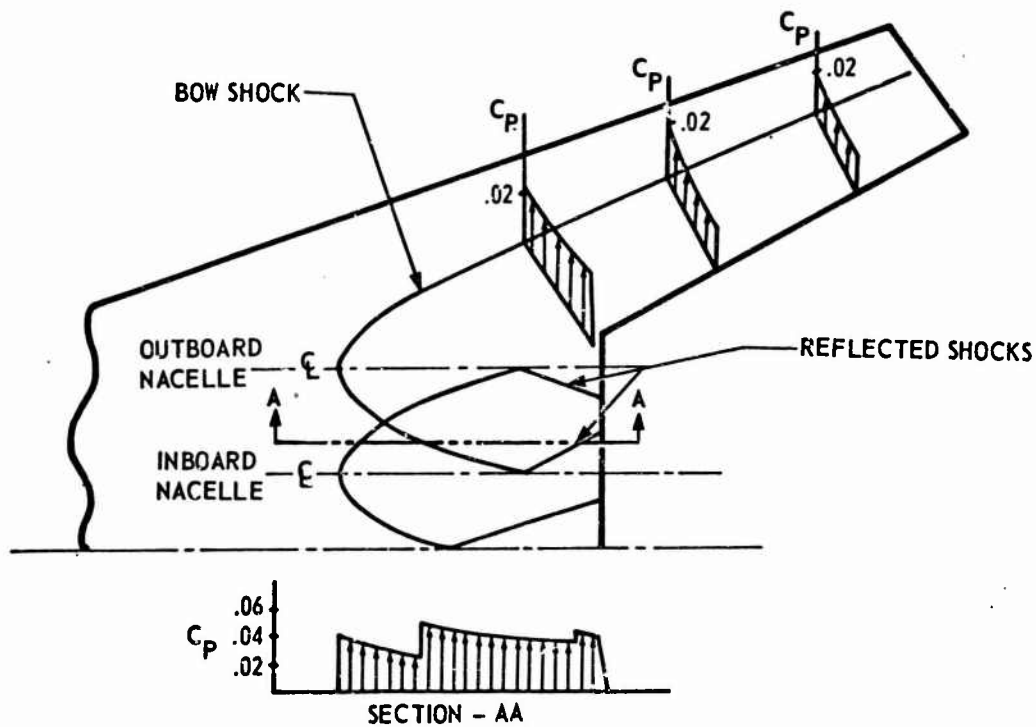


Fig.24 Nacelle pressure field on wing lower surface

FULLY EXPANDED NACELLES
THEORETICAL FRICTION SUBTRACTED.

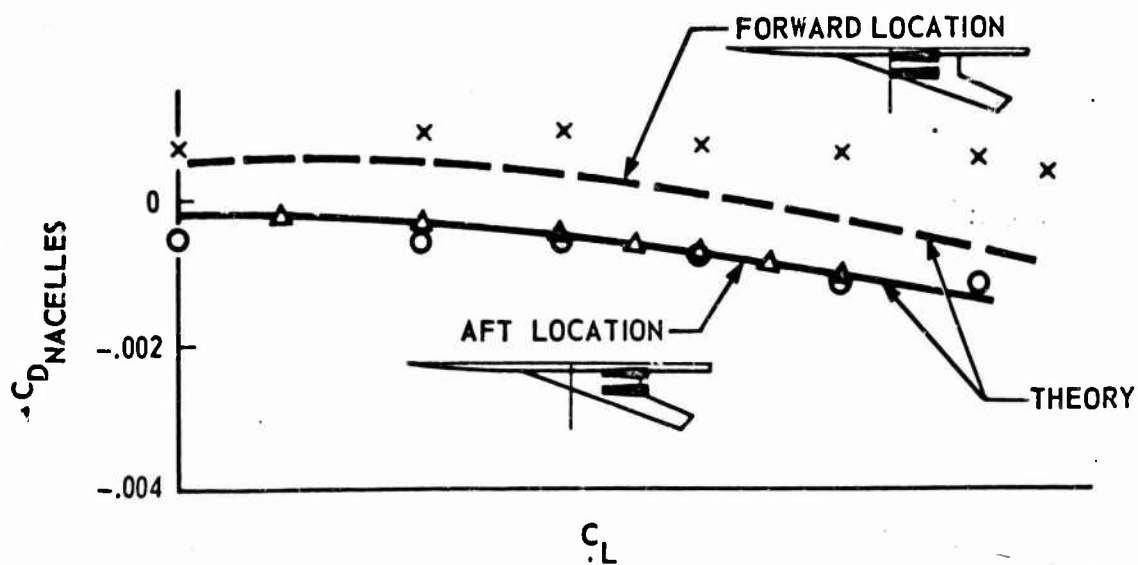


Fig.25 Effect of nacelle location theory - experiment, $M = 2.7$

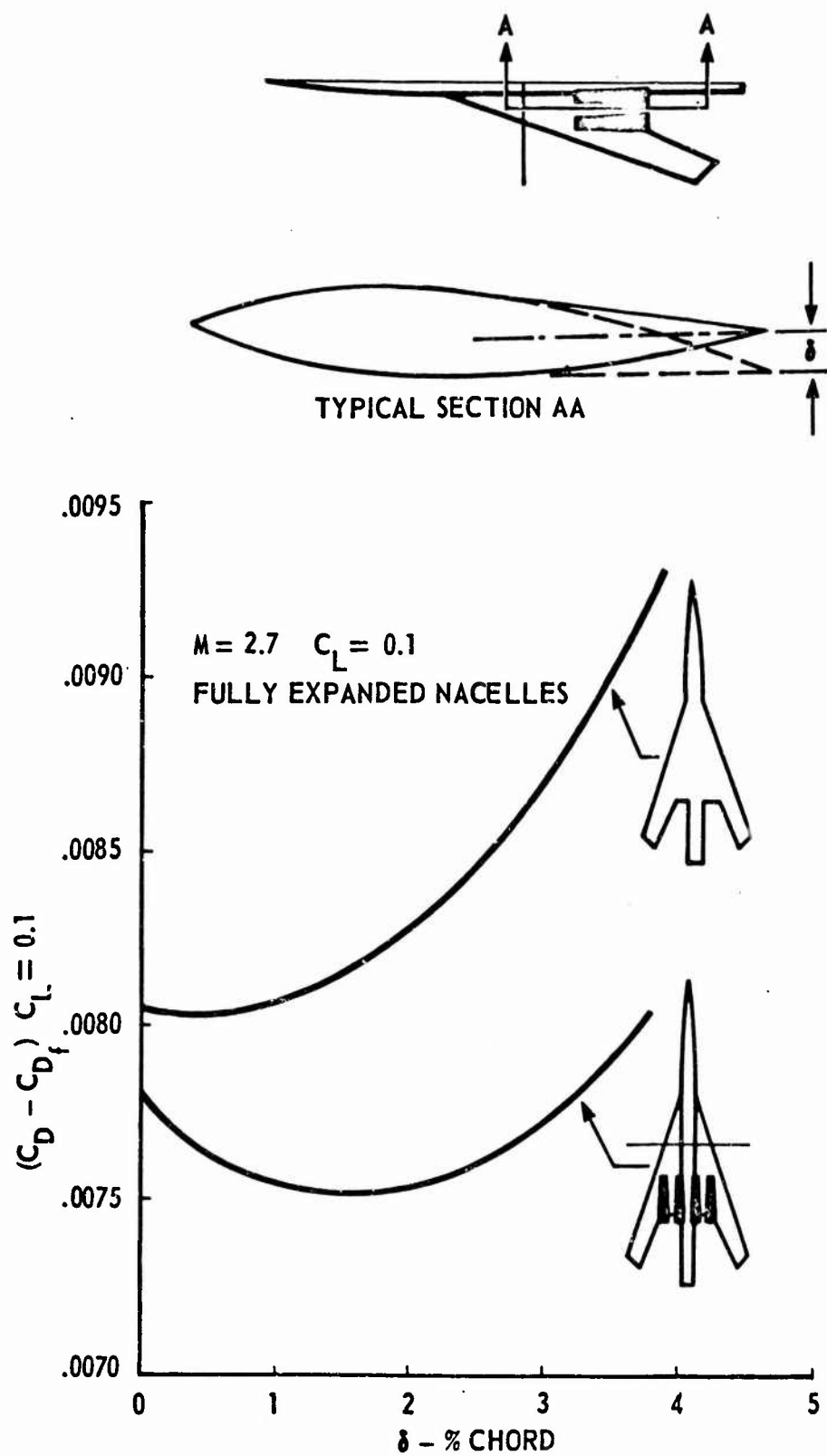


Fig. 26 Theoretical effect of trailing edge reflex on cruise drag

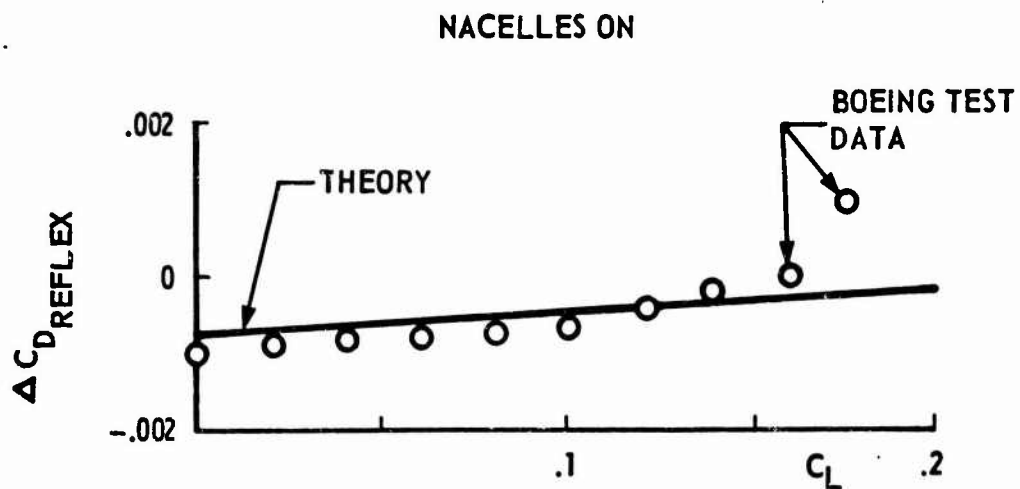
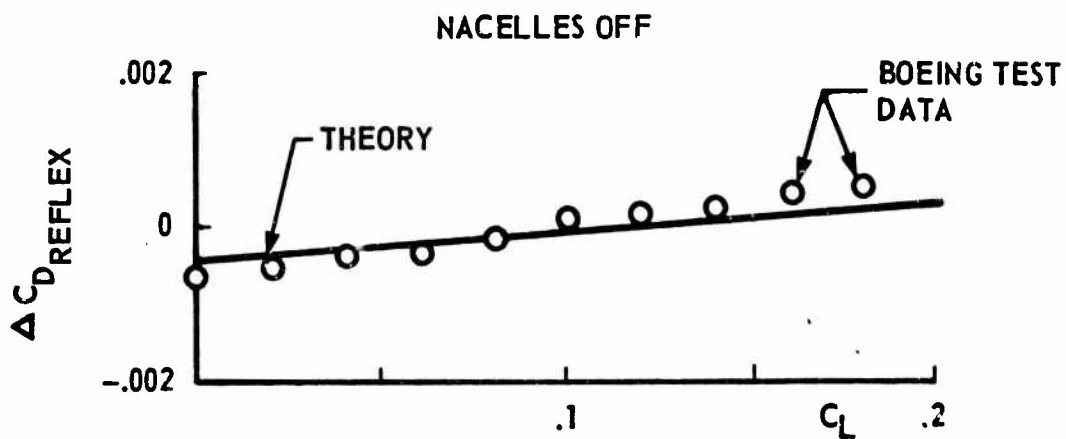
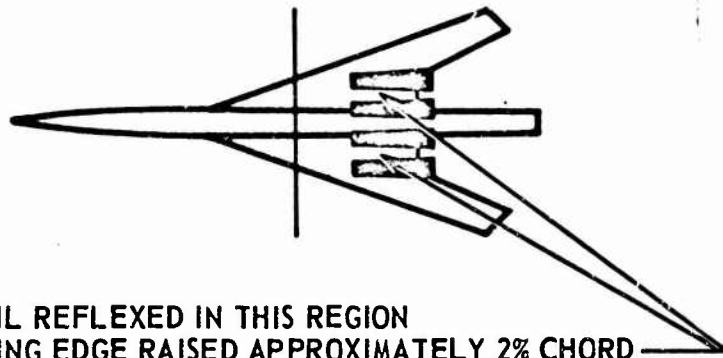
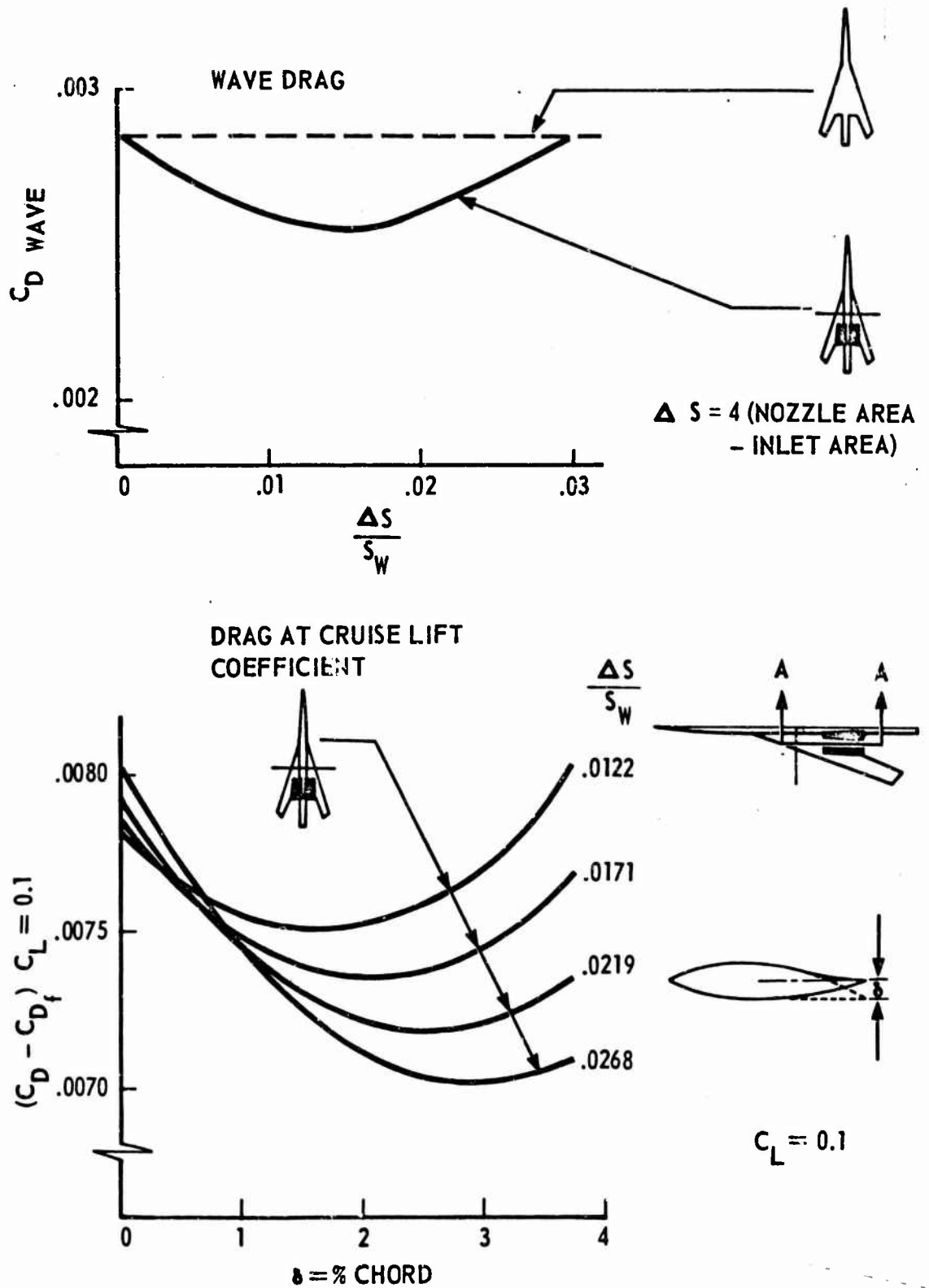


Fig. 27 Trailing edge reflex

Fig.28 Theoretical effect of nacelle size, $M = 2.7$

THE FEASIBILITY OF SUPERSONIC COMBUSTION RAMJETS
FOR LOW HYPERSONIC SPEEDS

by

R. Hawkins

Bristol Siddeley Engines.
Filton, Bristol, England.

SUMMARY

The performance of a supersonic combustion ramjet is examined in relation to that of a conventional subsonic ramjet. At low hypersonic speeds the internal performance of the two cycles are comparable, but at speeds above Mach 7, the supersonic combustion cycle should offer superior performance. Beyond Mach 9 the lack of reliable intake data makes the estimation of possible engine performance highly conjectural.

As an acceleration engine the supersonic combustion ramjet, flying at relatively low altitudes, offers possibilities unattainable with a conventional ramjet. For this application, there is a need to explore the feasibility of supersonic combustion ramjets for high supersonic speeds.

Typical entry conditions for a supersonic combustor are deduced. A detailed appraisal of available data on mixing and reaction rates is made in order to assess the feasibility of supersonic combustion, particularly at low hypersonic flight speeds.

An attempt is made to outline the most important areas in which further research on Supersonic Combustors is needed.

SOMMAIRE

Etude de la performance d'un statoréacteur à combustion supersonique comparée à celle d'un statoréacteur subsonique classique. Aux vitesses faiblement hypersoniques la performance interne des deux cycles est comparable, alors qu'aux vitesses excédant Mach 7, le cycle de combustion supersonique devrait permettre une performance plus élevée. Au-delà de Mach 9 le manque de données sûres sur les entrées d'air rend une estimation de la performance possible du réacteur très incertaine.

Comme réacteur d'accélération, le statoréacteur à combustion supersonique, volant à des altitudes relativement basses, offre des possibilités qu'un statoréacteur classique ne peut présenter. Pour une telle application, il est nécessaire d'étudier la possibilité de réalisation de statoréacteurs à combustion supersonique pour les vitesses supersoniques élevées.

Les conditions type d'entrée pour un foyer supersonique sont déduites. Il est fait une évaluation détaillée des données existantes sur les vitesses de mélange et de réaction afin de déterminer la possibilité de réaliser la combustion supersonique, en particulier aux vitesses faiblement hypersoniques.

On tente de définir les domaines les plus importants dans lesquels il est nécessaire de poursuivre les travaux sur les foyers supersoniques.

CONTENTS

	Page
SUMMARY	70
SOMMAIRE	70
LIST OF FIGURES	72
NOTATION	73
1. INTRODUCTION	75
2. INFLUENCE OF REAL GAS EFFECTS ON CYCLE PERFORMANCE	75
3. ALTERNATIVE MODES OF SUPERSONIC COMBUSTION	77
4. FUEL-AIR MIXING IN A SUPERSONIC STREAM	80
4.1 General	80
4.2 Decay Rates for Jets Immersed in an Inert Infinite Airstream	81
4.3 Decay Rates for Tangential Wall Jets in an Inert Infinite Airstream	83
4.4 Factors Influencing the Rate of Mixing	84
5. COMBUSTION IN A SUPERSONIC STREAM	85
6. FACTORS INFLUENCING INJECTOR DESIGN	88
7. CONCLUSIONS	90
REFERENCES	92
APPENDIX: Reaction Schemes and Rate Data for Hydrogen-Air Combustion	95
FIGURES	97

LIST OF FIGURES

	Page
Fig. 1 Ramjet cycle performance. Stoichiometric subsonic combustion. Kerosene	97
Fig. 2 Conventional ramjet cycle. Stoichiometric subsonic combustion. Kerosene	98
Fig. 3 Dissociation enthalpy of products as fraction of fuel calorific value. Stoichiometric subsonic combustion	99
Fig. 4 Comparison of cycles for subsonic and supersonic combustion ramjets	100
Fig. 5 Influence of surface temperature on transition Reynolds number for flat plate	101
Fig. 6 Comparison of internal thrust for stoichiometric subsonic and supersonic combustion. Ramjets. Kerosene	102
Fig. 7 Comparison of mixing rates for axial midstream injection of various gases into air for two-dimensional and axisymmetric flows [$u_j/u_e = 0.7$]	103
Fig. 8 Two-dimensional wall injection of various gases [$u_j/u_e = 0.7$]	104
Fig. 9 Number of injectors required to achieve complete mixing of hydrogen and air in combustor of specified length	105
Fig. 10 Temperature-time history of stoichiometric hydrogen-air with reaction rate scheme 2	106
Fig. 11 Reaction rate data. Reaction 9. $O_2 + M \rightarrow 2O + M$	107
Fig. 12 Temperature-time history of stoichiometric hydrogen-air reaction	108
Fig. 13 Temperature-time history of stoichiometric hydrogen-air reaction	109
Fig. 14 Calculated values of total reaction times for hydrogen-air constant pressure reaction	110
Fig. 15 Boundaries of lower end of flight range using supersonic combustion. Stoichiometric hydrogen-air	111
Fig. 16 Range of static pressures and temperature to give specific reaction times. Stoichiometric hydrogen-air	112
Fig. 17 Variation of injector blockage with M_e and M_j . Hydrogen fuel	113
Fig. 18 Injector cooling schemes	114
Fig. 19 Variation of wall temperature with coolant flow. Coolant (hydrogen) stagnation temperature 1000°K. Mach 7.0 flight conditions	115

NOTATION

A	flow area
b, F	functions in concentration decay equation (1)
h	enthalpy
λ	centre-line fuel concentration
M	Mach number
n	exponent in decay equation (1)
p	pressure
T, t	temperature
u	velocity
x	axial distance downstream of injector
γ	ratio of specific heats
ρ	density
τ_{ID}	ignition delay time
τ_R	reaction time
ϕ	equivalence ratio = $\frac{\text{fuel/air ratio}}{\text{stoichiometric fuel/air ratio}}$

Suffixes

e	denotes combustor mainstream conditions
j	denotes fuel conditions at injection

THE FEASIBILITY OF SUPERSONIC COMBUSTION RAMJETS FOR LOW HYPERSONIC SPEEDS

R. Hawkins

1. INTRODUCTION

As flight speeds increase into the high supersonic régime, the cycle temperature of conventional air-breathing engines rises rapidly. The use of turbojets or other engines having rotating machinery does not appear feasible under these flight conditions unless some degree of pre-cooling is employed. Of the air-breathing engines available, it is generally accepted that the ramjet with subsonic combustion is the best propulsion unit for high supersonic speeds.

At hypersonic speeds the attendant high cycle temperatures experienced in this form of ramjet drastically reduce its potential performance through real gas effects. Consequently there is a need to consider lowering the cycle temperature, although this apparently conflicts with the attainment of high cycle efficiency. Perhaps the most obvious way of minimizing cycle temperature is to operate at fuel/air ratios well away from stoichiometric. However the amount by which the effective overall fuel/air ratio may be reduced in a hypersonic ramjet is severely limited by performance and size considerations. An alternative method of reducing cycle temperature is to reduce the degree of diffusion in the intake, and to effect the heat addition while the airstream through the engine is still supersonic.

By changing from a subsonic to a supersonic combustor, it should be possible also to maintain the internal pressures, and hence the engine structure weight, at an acceptable level. In this way the performance advantages of flying at relatively low altitudes would be attainable.

The purpose of this report is to review the conditions under which supersonic combustion might be employed in a ramjet for low hypersonic speeds and to indicate the feasibility of such an engine as deduced from recent work in the UK and elsewhere. An attempt is made to outline the areas in which further research is needed.

2. INFLUENCE OF REAL GAS EFFECTS ON CYCLE PERFORMANCE

It has been stated that the two main incentives for considering supersonic combustion in a hypersonic ramjet are the need to minimise real gas effects, which lead to severe performance penalties in the conventional subsonic combustion cycle, and the need to keep internal pressures at a reasonable level (say less than 10 atmospheres) so that engine structure weight is not excessive. Before describing alternative supersonic combustion systems it seems appropriate to justify this statement, and to

examine what limitations are imposed on the state of the combustion gases if these requirements are to be met.

Considering first the loss of performance due to real gas effects. Cycle calculations based upon realistic component efficiencies indicate that the optimum internal performance of conventional subsonic combustion ramjets increases through the supersonic flight range, and reaches a maximum at hypersonic speeds. The performance of a family of typical kerosene fuelled ramjets is shown in Figure 1. At hypersonic speeds some uncertainty exists as to the degree of performance loss due to departure from chemical equilibrium by the exhaust gases during expansion. Theoretical analysis suggests that the lower curve in Figure 1 would be appropriate for small ramjets (capture area about 5 ft²) with an internal pressure around 10 atmospheres.

It can be seen that the fall off in cycle performance at high flight speeds, assuming fixed component efficiencies, is due almost entirely to real gas effects (dissociation) in the combustor and nozzle. The combustion of kerosene in a high temperature air stream ($t > 1000^\circ\text{K}$) results in the existence of significant concentrations of dissociation species in the combustion products (see Ref. 1). These species hold energy which in a thermally perfect gas, would be available for raising further the post-combustion gas temperature. The resulting lower combustion temperature in the real gas cycle leads to an increase in the entropy jump due to combustion: (compare the entropy changes 1-2 and 1-2' in Figure 2). There is a consequent reduction in exhaust velocity when the real gas products are expanded to ambient pressure: (compare the enthalpy changes 2-3 and 2'-3' in Figure 2 which represent the kinetic energy of the exhaust jets for the real and non-dissociating gas cycles, respectively). The corresponding reduction in internal thrust is shown as the difference between the two upper curves in Figure 1.

Taking into account the fact that the internal thrust will be further reduced by a non-equilibrium expansion process, the fall-off in performance of the conventional subsonic combustion ramjet at high speeds would appear to limit its application to flight Mach numbers below 8 or 9. Since the relative magnitude of real gas effects in a hydrogen fuelled ramjet is not materially different from that for a kerosene fuelled engine (see Fig. 3), this conclusion would still apply, in general, if the former fuel were used. (The internal thrust of a hydrogen fuelled engine is, of course, higher at a given flight condition than that of a kerosene fuelled engine because of the net differences in fuel calorific values and stoichiometric ratios.)

The loss in engine performance due to real gas effects may be reduced at high flight speed by changing to a supersonic combustion mode. Although with supersonic combustion the entropy rise due to heat addition is increased, this increment is not so great as would be the case in the absence of real gas effects. In order to minimise the entropy rise for the whole engine cycle, it is necessary to set off the increased combustor losses - including the injector and viscous losses - against a reduction in those for the intake and exhaust nozzle. Figure 4 shows the relative entropy rises (0-1) and (1-2) for an intake and supersonic combustor, with (0-1') and (1'-2'), the corresponding values for a subsonic combustion ramjet. Whether, under a given set of conditions, it would be advantageous to change from a subsonic to a supersonic combustion cycle will depend critically upon component performances, and particularly upon the improvement in the intake performance which can be effected by the change.

The increase in transition Reynolds number with flight Mach number and surface cooling, and the increasing length of the transition region at hypersonic speeds, will make intake performance relatively difficult to maintain as flight speed increases. A summary of flat plate transition data has been attempted and the results are shown in Figure 5. Experimental studies² suggest that free transition is unlikely over radiation cooled intake compression surfaces of a medium sized ramjet if the flight Mach number is much above 8. Unless a turbulent boundary layer prevails in regions of significant adverse pressure gradient, the overall compression ratio is likely to be severely restricted. Further experimental studies are necessary to determine what level of performance can be expected from intakes for both subsonic and supersonic combustion ramjets at hypersonic speeds. It is important also to determine what additional interaction losses will be incurred by the fuel injection system for a supersonic combustor. It will be necessary to ensure correct simulation of compression surface Reynolds number and equilibrium temperature ratio if the intake calibration results are to be meaningful.

3. ALTERNATIVE MODES OF SUPERSONIC COMBUSTION

No mention has yet been made of the alternative modes of supersonic combustion, or of the need to consider the various possibilities when optimising engine cycle performance. In its broadest sense supersonic combustion implies the injection of fuel and establishment of a steady reaction zone in a supersonic (or hypersonic) airstream. There are, however, several different modes of supersonic combustion which may be characterised by the precombustion conditions and by the rate at which heat is effectively released in relation to changes in combustor cross-sectional area.

Perhaps the most significant single characteristic is the ratio of the effective reaction rate to the mixing rate under the local combustor conditions. If the mixing rate is significantly greater than the reaction rate, then the combustion process is likely to be detonative. (A prerequisite for the formation of a detonation wave, whether normal or oblique, is premixing of the reactants.) If the relative rates are reversed, then the combustion process will be diffusive.

There are many practical considerations which make a detonation process unattractive. In general, the formation of a strong shock wave will leave the post-combustion gases subsonic, so that near stagnation temperatures and pressures will be achieved. This will militate against the reasons given for considering supersonic combustion. The adverse pressure gradients associated with a strong shock wave will introduce shock/boundary-layer interaction problems in the combustor. Finally, the positional control of a detonation wave may prove difficult if the engine is to be operated over a range of flight conditions giving wide variation in precombustion pressure and temperature.

Many experiments have been made to assess the feasibility of establishing a stable diffusion flame in a supersonic stream. Notable among these are those of Ferri and his co-workers⁵, who have concluded that such a mode of combustion is entirely practical. In view of this, it is not proposed to examine further supersonic combustion involving strong shock waves or detonation waves. For the remainder of this paper the meaning of supersonic combustion will be restricted to a mixing rate controlled process in which the flow remains supersonic after heat addition. Such a process characterises a supersonic diffusion flame, and may involve control by direct

mixing of the reactants, where the local static temperature and pressure are sufficiently high to give 'spontaneous' combustion, or control by convection of heat and products from a pilot into mixing reactants.

For the purposes of making simple cycle optimisation studies, several idealised supersonic combustion processes may be postulated. In all of these the flow is assumed to be one-dimensional and some parameter or function of state is assumed to have the same value before and after heat release, thereby simplifying the computational procedures.

The most obvious alternatives are

- (a) constant area combustion,
- (b) constant static pressure combustion,
- (c) constant velocity combustion,
- (d) constant Mach number combustion.

The first of these alternatives is relatively simple to achieve. In practice, it should be possible also under design point conditions, to approximate to the other supersonic combustion modes as long as the heat release is mixing-rate controlled. It remains to determine which of these alternatives are likely to be attractive from cycle performance considerations.

To make direct and meaningful comparisons between the performance attainable with different high speed engine cycles at a given flight condition is always difficult because of the complex interactions of the variables. In making the present comparisons it has proved particularly difficult in view of the inherent limitations of assuming one-dimensional flow, and because of the lack of reliable data at Mach numbers above Mach 6 or so, on component efficiencies and factors influencing them. However, an attempt has been made to be as realistic as possible in the hope that the indications may be neither unduly pessimistic or optimistic.

The relative performances of families of subsonic combustion ramjets, constant static pressure and constant area supersonic combustion engines are shown in Figure 6. Each curve represents a series of design point engines, the engines being roughly optimised to give the best possible performance at each flight Mach number consistent with the realistic component efficiencies. Allowance has been made for injector losses and internal friction losses in arriving at the performance of the supersonic combustion ramjets. The effects of non-equilibrium expansion in the exhaust nozzle have also been included.

It can be seen that, of the two cases examined, constant pressure supersonic combustion is the most attractive for replacing the subsonic combustion cycle for flight at low hypersonic speeds. The relative advantage of this mode of combustion is that the reduction in Mach number of the airstream due to heat addition is less than that which would occur in a constant area combustor. Since the post-combustion Mach number cannot fall below unity if transition to subsonic speeds ("thermal choking") is to be avoided, then the constant pressure combustor can accept a lower entry Mach number. Hence, for a given flight condition, the static temperature at

entry to the combustor will also be higher, thus reducing the entropy rise due to heat addition and giving a better cycle performance than the constant area combustor.

The advantage of a constant pressure cycle is apparent, not only in the enhanced performance obtainable, but also in that it can be employed at a lower flight Mach number than the constant area combustor. The constant Mach number cycle should be even better than the constant pressure cycle in respect of the latter advantage. (The constant velocity cycle approximates closely to the constant pressure cycle, since the velocity change across the combustor in the latter cycle is small, 3% in a hydrogen fuelled engine and 7% with kerosene.)

As flight speed increases, the performance of the constant pressure cycle, operating with a post-combustion Mach number approaching unity, diminishes due to real gas effects. At speeds above about Mach 9 it is not clear from the present studies whether the constant area cycle would be better than the constant pressure cycle. The performances of the various alternatives above Mach 9 will depend critically upon component efficiencies and, since no data exists for these speeds, it is impossible to form any conclusions, however tentative, about the relative advantages of the different cycles.

The superiority of the divergent supersonic combustor at the lower flight speeds, however, appears to be well established. The performances which might be expected from an optimised engine using this type of combustor are very good and may be expected to remain so at least to Mach 12, provided the intake performance can be maintained at these speeds.

Given the necessary practical data on fuel-air mixing rate under the flow conditions likely to obtain in a supersonic combustor, there should be no reason why the divergence of the combustor could not be designed to give near-optimum performance, as long as the combustion process is mixing-rate controlled.

Hypersonic project investigations indicate that the supersonic combustion ramjet would be very attractive for acceleration roles, for which it should be used at the lowest possible flight Mach number. Using, for example, a constant pressure cycle, the engine performance is apparently good at a flight Mach number of 5 and possibly below, while the engine internal pressure ratio is lower than that of the equivalent subsonic combustion cycle. This means that a given size of engine can be flown at lower altitudes within a certain engine maximum cycle pressure. The lower altitude confers a high thrust-drag margin and efficient acceleration. On the other hand, an aircraft with a subsonic combustion engine would have to fly some 20,000-30,000 ft higher to avoid excess internal pressures, and the loss of acceleration thrust and consequent increase in fuel consumed would be a severe penalty.

These considerations emphasise the need for research on supersonic combustion under conditions appropriate to the speed range in which the transition from a subsonic combustion cycle may be effected, i.e. in the range Mach 4 to 7.

4. FUEL-AIR MIXING IN A SUPERSONIC STREAM

4.1 General

Having established the case for supersonic combustion ramjets on the basis of cycle performance studies, the feasibility of mixing and combustion in a supersonic stream must be examined. If a medium sized supersonic combustion ramjet is to be practical, then the combined mixing and combustion lengths should be around one foot or less. A considerable body of experimental data has been examined with the object of deciding whether adequate mixing is likely to be accomplished in such a length, and to indicate what beneficial features in the injector and its environment would enhance the rate of mixing.

Numerous studies on turbulent mixing, with and without chemical reaction, have been carried out by various investigators³⁻¹⁸. Unfortunately experimental data on mixing rates appear to be confined mainly to the diffusion of non-reacting gases into an infinite mainstream. In a supersonic combustor mixing will be accompanied by chemical reactions. Also, interactions between the diffusing reactants and the duct boundaries or adjacent reaction zones appear inevitable. Consequently, in the absence of meaningful experimental data, it is impossible to determine with certainty the mixing lengths needed under a given set of conditions to achieve near complete mixing of the injected fuel. However, by assuming that reactions provide an effective sink for the diffusing fuel, and that interactions with adjacent jets do not involve the fuel, but intermediates and products, then mixing rates for the fuel into an infinite chemically inert mainstream should, at least, give the most pessimistic indication of those to be expected in a combustion chamber when the mixing is accompanied by chemical reactions. If these mixing rates are found acceptable then the prospects for short supersonic combustors will be very good.

It has been necessary for the present study to make this assumption in order to estimate mixing lengths. Clearly theoretical and experimental studies must be made of fuel-air mixing with finite rate chemistry, so that more reliable estimates are possible.

If the survey be confined, in the first instance, to tangential injection of a gaseous fuel in a downstream direction, then three injector systems are of particular interest.

- (a) A two-dimensional injector spanning the combustion chamber and giving essentially a two-dimensional midstream jet of fuel.
- (b) An injection slot at the wall of a rectangular sectioned combustion chamber, or an annular slot around the periphery of an axisymmetric chamber. In both cases the fuel would be injected as a two-dimensional jet along the combustor wall.
- (c) A midstream axisymmetric injector giving an axisymmetric jet of fuel immersed in the mainstream.

In general the change of centre-line fuel concentration with distance x due to turbulent mixing under a given set of conditions may be expressed in the simple form

$$\text{Centre-line concentration } K = \frac{F}{(x + b)^n} \quad (1)$$

where F and b are functions whose values depend upon the injector geometry, its environment, and the properties of the fuel being injected. When studying the change of concentration in the far field (i.e. at distances of some hundreds of injector heights), the constant b which is a measure of the effective potential core length is relatively unimportant. The value of the decay exponent n appears to depend mainly upon the particular injector system, i.e. whether the jet is of the type (a), (b) or (c), as listed above. Although the exponent n is a function of x , experimental results suggest that, for a jet mixing with an unbounded mainstream, it may be considered constant for all x except for a region close to the injector.

The classical Reynolds analogy assumption gives, provided that the turbulent Prandtl and Lewis (or Schmidt) Numbers are all unity,

$$K = \frac{u_e - u}{u_e - u_j} = \frac{T_e - T}{T_e - T_j} \quad (2)$$

where u = local velocity of injected gas

T = local temperature of injected gas

K = local mass concentration of injected gas,

and suffix e denotes initial mainstream values

j denotes initial values for injected gas.

Thus the dimensionless velocity, temperature (or enthalpy) and concentration profiles should all be identical at a given distance from the injector. In practice it is generally found that the profiles are similar for turbulent mixing of gases, and hence it may be inferred that the turbulent Prandtl, Lewis and Schmidt numbers are reasonably close to 1.0. This is particularly convenient since it enables general conclusions on concentration decay rates to be made from studies of velocity or enthalpy decay rates.

4.2 Decay Rates for Jets Immersed in an Inert Infinite Airstream

A simplified expression was given in Equation (1), which suggested that the change in concentration of injected gas with distance from the injector (normalised by using a characteristic dimension of the jet) involved three constants for a particular injection system. The constants K and b are related functions of the particular injector and its environment, whilst the exponent n is mainly a function of the jet form, i.e. whether two-dimensional, axisymmetric etc.

All experimental data on mixing of a tangentially injected jet show that the process is much more rapid with an axisymmetric injector than with a two-dimensional system. Data from References 7 and 14 are shown in Figure 7 for a particular jet/mainstream velocity ratio of 0.7. These experimental data are typical of all those examined.

The higher mixing rate for the axisymmetric over the two-dimensional jet is due to the fact that, in the former case, the surface area available for mixing and shear is proportionately greater. Also, the 'surface' area over which mixing occurs increases with distance for the axisymmetric jet. It is this last effect which gives rise to the steeper slope for the axisymmetric system in Figure 7.

These data appear to give a reasonably consistent picture for the mixing rates to be expected for the injection of gases tangentially into a unbounded supersonic air-stream. They suggest that the centre-line concentration of the injected gas decays exponentially according to the following laws:

$$\text{for two-dimensional midstream jets, } K \propto \frac{1}{x^{0.5}}$$

$$\text{for axisymmetric midstream jets, } K \propto \frac{1}{x}.$$

The exponents in the decay rates appear to be independent of the jet/mainstream velocity or mass flux (ρu) ratios and also of mainstream Mach number for $M < 2$ (the correlations made in References 3, 4, 5 and 8 suggest that compressibility effects may become significant when the mainstream Mach number exceeds three).

The exponents also appear to be independent of the molecular weight of the injected gas for all experimental results examined except those of Ferri and his co-workers^{5,7} for the case of hydrogen injected by an axisymmetric probe.

Forstall and Shapiro¹⁵, who studied the turbulent mixing of an axisymmetric jet of air into air for jet/mainstream velocity ratios less than unity, determined empirically that

$$\frac{u_e - u}{u_e - u_j} \propto \frac{1}{x}.$$

Schlichting⁹ has shown from theoretical considerations that the centre-line velocity of an axisymmetric jet injected into stagnant air would decay according to the relationship

$$u \propto \frac{1}{x}.$$

Ferri and his co-workers present a body of experimental results which show that, for an axisymmetric jet of hydrogen in air, the centre-line concentration decays according to the relationship

$$K \propto \frac{1}{x^2}$$

for the region between 2 and 10 injector diameters downstream of the injection point. This data is shown as the lower curve in Figure 7. Since most of the other experimental data examined covered regions much further downstream of the injector, it is

possible that the higher decay rate observed by Ferri would tend to $1/x$ at greater values of x . Alternatively, there could be an influence of molecular weight ratio, or some other parameter, which leads to a high decay rate close to the injector. In any case, the mixing rate for an axisymmetric jet in a supersonic stream needs further examination - particularly with higher supersonic mainstream Mach number.

As far as the decay of a two-dimensional midstream jet is concerned, theory⁹ suggests the exponent in Equation (1) should be $n = \frac{1}{2}$. This value may be taken as being well established experimentally. Spalding¹³ has analysed the experimental data of Forthmann on injection into a stationary atmosphere, and Weinstein, Osterle and Forstall, on injection into a moving mainstream. In both cases it was shown that the velocity decay in the far-field obeyed the law:-

$$\frac{u_e - u}{u_e - u_j} \propto \frac{1}{x^{0.5}}.$$

Recent experimental studies¹⁴ with gases of high and low molecular weight ratio gave results which also follow this law. These latter results are shown in Figure 7 and indicate how much faster the mass concentration of the light gases falls compared with heavier ones. This observation may be due in part to the fact that mixing a given volume of air in turn with equal volumes of a light and a heavy gas would result in a lower mass fraction for the lighter gas, and hence an apparently greater rate of mixing for that gas.

4.3 Decay Rates for Tangential Wall Jets in an Inert Infinite Airstream

A considerable body of experimental data is available on the rate of decay of a two-dimensional jet injected along a wall. Many of these data have been included in surveys by Spalding et al.¹⁰⁻¹².

Two theoretical models have been proposed in Reference 10 to describe the decay process for the tangential wall jet. That due to Stollery is applicable for the case where the jet/mainstream velocity ratio is less than unity. Stollery's theory, based upon a boundary-layer model for incompressible flow with zero pressure gradient, has been extended to cover compressible flow with mainstream pressure gradients by Holland⁴. This theory predicts that the enthalpy decay for the wall jet should be given by

$$\frac{h_e - h}{h_e - h_j} \propto \frac{1}{x^{0.8}}.$$

This relationship which, by Reynolds Analogy, applies also to the velocity and mass concentration decay, is well supported by all the available experimental data for regions well downstream of the injection slot. In particular, the experimental data of Price⁶ for air into air, of El-Ehwany¹⁴ for argon 12 into air, and of Hatch and Papell¹⁹ for helium into air, whose results at a velocity ratio of 0.7 are shown in Figure 8, indicate a decay exponent of $n = 0.8$.

These experimental data suggest also that the value of this exponent is independent of slot design, environment, or molecular weight ratio of the injected gas. Limited

experimental data of Morgenthaler⁶ indicate that an exponent of $n = 0.8$ describes also the far-field decay rate of hydrogen injected from a two-dimensional radial slot into a supersonic air stream at $M = 2$.

4.4 Factors Influencing the Rate of Mixing

Although a relatively simple classification of factors influencing the exponent in the mixing equation appears possible, no such simplification has yet proved possible in the case of the constant of proportionality, i.e. the function F in Equation (1). Invariably absolute mixing rates determined experimentally are higher than those predicted by theory. The more 'practical' the injector design becomes, the bigger the discrepancy between theory and experiment.

In the environment of a supersonic combustor many extraneous, but nevertheless important, influences may be expected to modify significantly the absolute mixing rates. Such factors are mixing accompanied by chemical reaction, mainstream turbulence and pressure gradients, and injector design, etc. Indications of the possible effects of some of these factors are given in Figure 8. The amount of data available is hopelessly inadequate, but the curves serve to show that the constant of proportionality F in the mixing rate equation will depend very much upon the injector design and environment, as well as upon the properties of the fuel being used. Fortunately, most of these "practical" factors lead to an increase in mixing rate, so that it should be possible to shorten significantly the injector and combustor section by developing their geometry to take advantage of these features. Price⁶ presents experimental data which shows how near-field effects associated with slot design can significantly increase the absolute mixing rates. Price also indicates the effect of large scale stream turbulence and vorticity which also serve to increase the mixing rate.

One important factor which influences the rate of mixing, and which is amenable to theoretical treatment, is the relative motion of the jet and the surrounding stream. It is generally considered that, in uniform density streams, turbulent mixing arises as a result of instabilities in the turbulent shear layer separating the two streams.

Classical mixing theories assume that the mixing is dependent on the velocity difference between the two streams and correlations have been made which purport to justify this assumption. Recent work by Alpinieri⁷ and El-Ehwany¹⁴ with streams of different density failed to detect a minimum mixing rate in the far-field when the velocities of jet and mainstream were equal. It appears possible that equality in either velocity, mass flux (ρu), or momentum (ρu^2) between jet and mainstream does not lead to minimum jet decay rates in the far-field. This problem, which must influence the design of a supersonic combustor, deserves further study over a wider range of experimental variables.

The work of Ferri⁵ indicates that the mass flux ratio $\rho_j u_j / \rho_e u_e$ may be far more significant than the simple velocity ratio u_j / u_e in describing the mixing process. This parameter has been used successfully by several workers to correlate experimental data. Assuming the mass flux ratio is an important parameter influencing the absolute mixing rate, then a constant geometry engine, fuelled to a constant fuel/air ratio, would have a fixed mixing length independent of flight speed and altitude. For, with constant fuel/air ratio, the respective mass flows through the combustor will be

$$\frac{\rho_j A_j u_j}{\rho_e A_e u_e} = \text{constant}$$

and, since A_j/A_e would be constant in a fixed geometry engine,

$$\frac{\rho_j u_j}{\rho_e u_e} = \text{constant}.$$

This feature would be a most desirable attribute in a mixing-rate controlled supersonic combustion ramjet.

On the basis of this survey, it is apparent that much remains to be done, both experimentally and theoretically, before the turbulent mixing of non-reacting compressible jets is well documented and understood. The problem of mixing with finite rate chemistry also requires detailed attention if reliable data are to be available for optimising and designing a supersonic combustion engine.

Despite the limitations in the existing data, an attempt has been made to estimate the number of injectors required to fuel a given combustor with hydrogen and achieve adequate mixing. Obviously, the shorter the duct, the larger the number of injectors required. The estimates, which have been based on data from Ferri⁵, Morgenthaler⁶ and Stollery¹⁹, are given in Figure 9.

The number of injectors required varies with the length/diameter ratio for axisymmetric injectors in a combustor of circular section, and with the length/height ratio for two-dimensional injectors spanning a combustor of rectangular section. Despite the lower mixing rates for the two-dimensional jets, the stream area covered by each injector in a rectangular combustor of high aspect ratio is so large that the number of injectors required would appear to be feasible, even for the case of a relatively short combustor.

5. COMBUSTION IN A SUPERSONIC STREAM

In general, combustion may be reaction-rate or mixing-rate controlled, depending upon which process is the slower under the local conditions. In either case, however, the chemical reactions necessary to release heat cannot proceed until reactants have mixed at least locally. In the previous section, the problem of fuel-air mixing in a supersonic stream was discussed. In this section, the time needed for reactions to occur will be examined in relation to the mean transit time of the mixture within the combustor. In order to make this study it is necessary to assume the existence of local regions of completely mixed reactants.

The overall combustion reaction may be subdivided into two régimes - an 'induction' or 'ignition delay' period, in which significant pre-flame chemistry takes place with little or no heat release, and a 'reaction' period, in which the main heat release occurs. The first comprises two body reactions which are usually either weakly exothermic or endothermic, while the second consists of three body recombination reactions which are usually strongly exothermic. The two regions are distinctly shown in Figure 10 and characteristic times, τ_{ID} and τ_R , may be ascribed to each.

Values of these characteristic times may be calculated, provided the necessary data are available, or they may be determined experimentally. At present there is a dearth of direct experimental information covering the range of compositions, pressures and temperatures of interest, although limited data are available from shock tube studies for hydrogen/air and some gaseous hydrocarbon/air mixtures (see, for example, Reference 20).

Calculation of characteristic times requires knowledge of the complete reaction scheme and rate data for all the relevant reactions. Because of the complexity of the problem, computations have, as yet, been limited to some of the simplest fuel-oxidant combinations. One of the systems which has been studied in some detail is hydrogen-air.

A list of the most probable reactions which may be used to describe the combustion of hydrogen in air, is given in the Appendix. Listed also is the particular groupings of these reactions which have been used by different investigators to calculate the overall reaction time for hydrogen-air under various conditions of pressure and temperature.

Obtaining reliable rate data for the various reactions presents more of a problem. Several surveys have been carried out and preferred data recommended, notably by Ferri⁵ and Ellis²¹.

There appears to be excellent agreement between these workers as regards the preferred rate constants for the two body collisions involved in the ignition delay zone. Some doubt appears to exist, however, as to the best values to use for the constants in the rate equations for the three body reactions. Ferri has taken alternative values of these latter constants and computed the corresponding overall reaction times. The rate data used by Ferri, together with the alternative constants for the recombination reactions, are also presented in the Appendix. Also tabulated are the rate equations recommended by Ellis²¹. It will be seen that, of the alternative schemes studied by Ferri, his preferred scheme (Scheme 2) coincides very closely with the data recommended by Ellis for all but the oxygen reaction



An examination of the available rate data for this reaction suggests that Ferri's preferred value is borne out by experiment (see Fig. 11) and is in fact slightly pessimistic compared with that recommended by Ellis²¹.

The influence on overall reaction time, of using the different values for the recombination rate constants, is illustrated in Figures 12 and 13.

Montchiloff et al.²² favour the inclusion of various nitrogen reactions in the calculation scheme. It is not felt that these are of great importance at the comparatively low initial temperatures that will subsequently be shown to be of interest.

It seems reasonable, on the above discussion, to accept Ferri's reaction times, based on the rate data given in the Appendix, together with the recombination rate constants of Scheme 2, as being reliable, and to use them in assessing the conditions under which supersonic combustion may be feasible. Following Ferri therefore, the ignition delay time and the reaction time for hydrogen air combustion will be taken as

$$\text{ignition delay time, } \tau_{ID} = \frac{8 \times 10^{-3}}{p} \exp\left(\frac{9600}{T}\right) \text{ milliseconds.}$$

$$\text{reaction time, } \tau_R = \frac{105}{p^{1.7}} \exp\left(\frac{-1.12 T}{1000}\right) \text{ milliseconds.}$$

where p is in atmospheres and T in $^{\circ}\text{K}$.

By summing these, the overall reaction times under given local initial conditions of static pressure and static temperature may be obtained. Using the combustor entry conditions, the resultant times should be relevant to a constant pressure combustion process. Figure 14 shows the total combustion time as a function of initial temperature, over the range $600 - 2400^{\circ}\text{K}$, for combustor pressures of 0.1, 1.0 and 10 atmospheres. These curves show clearly the need for the local initial mixture temperature to be in excess of about 1000°K , and the combustor pressure to be as high as possible. Whether, under a given set of inlet conditions, the overall reaction time will be short enough will depend upon the mean residence time within the combustor.

Figure 15 summarises the combustor entry conditions which would obtain at a given flight Mach number. An intake kinetic energy efficiency of 0.96 has been assumed and the stratospheric temperature has been taken as the ambient static temperature before compression. To a very close approximation, a line of constant static post-compression temperature (t_1) corresponds also with a line of constant intake compression ratio (p_1/p_0). In Figure 15 the average compression ratio for the range of flight Mach number covered has been quoted for each line of constant combustor entry temperature.

The quasi-thermal choking limit (assuming one-dimensional flow) for a constant pressure supersonic combustor burning a stoichiometric hydrogen-air mixture, is shown also in Figure 15. It may be seen that the lowest possible combustor entry velocity will be about 3500 ft/sec. With a combustor length of about 1 ft this means a mean residence time of the order 10^{-3} to 10^{-4} sec. Reference to Figure 14 will show that, for the total reaction time to be less than this residence time, the combustor inlet temperature must be greater than 1000°K and the combustor pressure must be greater than one atmosphere. The necessary combustor entry pressure-temperature requirements, to ensure the reaction time is shorter than the residence time, are defined more precisely in Figure 16.

Referring to Figure 15 it may be seen that the combustor temperature requirement may be met at flight speeds above Mach 6, providing the combustor entry Mach number is no greater than 2. To ensure the internal pressure does not fall below one atmosphere at this flight speed, the flight must be made below 100,000 ft altitude. The need for a low combustor Mach number emphasises the necessity of a divergent combustor to avoid transition to subsonic flow.

At flight speeds above 6, by maintaining the combustor entry Mach number at 2, and the flight altitude not greatly in excess of 100,000 ft, the combustor temperatures and pressures should be sufficiently high to ensure an adequate margin between overall reaction time for hydrogen and combustor residence time. The use of a piloted combustion system would be advantageous at flight Mach numbers between 6 and 7, and might be necessary at higher speeds if the altitude were such that the combustor pressure fell much below one atmosphere.

At flight speeds below Mach 6, it would appear that a piloted system will be essential if supersonic combustion is to be feasible within a length of order 1 ft. Limitations imposed by phenomena akin to thermal choking make the supersonic combustion cycle in which the internal flow is everywhere supersonic impractical below hypersonic speeds. However, at these speeds, the internal pressures which would result if the internal flow were transonic would not be excessive except at low altitudes. Consequently, it might be possible to design a supersonic combustion ramjet for low hypersonic speeds which could operate satisfactorily with transonic internal flow at the low end of the flight speed range.

Experimental studies by Townend²⁷ indicate a possible means of piloting a supersonic combustor, by utilising the wakes formed downstream of a blunt-based body. If each injector is provided with a suitable base in which stabilization might be effected, it should prove possible to achieve a mixing-rate controlled combustion process when the local static temperature is well below 1000°K. Further experimental work is required to develop an effective injector/stabiliser geometry of low blockage.

6. FACTORS INFLUENCING INJECTOR DESIGN

From the preceeding considerations of the uncoupled mixing and reaction processes, several important features are necessary if a mixing-rate controlled supersonic combustor is to be feasible at low hypersonic flight speeds. These features are

- (a) a divergent combustion chamber to permit the highest possible combustor entry pressures and temperatures without imposing restrictions on the effective heat release,
- (b) for a combustor with a small length to height (diameter) ratio mid-stream fuel injections will be required,
- (c) three-dimensional flow in the region of the fuel injection orifices greatly enhances the rate of mixing,
- (d) the use of a gaseous fuel of low molecular weight and high velocity relative to the local air stream will be conducive to high mixing rates,
- (e) a piloted combustion system will be essential for flight speeds much below Mach 7.

In addition to these requirements it is considered important to expand the fuel to a pressure close to, or below, the local combustion chamber static pressure. The implications of these requirements on injector configuration and its blockage are discussed below.

The type of mid-stream injector which has been examined is basically that shown in Figure 18, but having a bluff base surrounding the fuel injection orifice. Although, from overall performance considerations, kerosene may be equally as attractive as hydrogen as a fuel, from cooling considerations liquid hydrogen is far superior to kerosene. For this reason the present study has been confined to hydrogen.

For a hydrogen-air mixture of overall equivalence ratio ϕ , the following mass flow ratio holds:

$$\frac{\rho_J u_J A_J}{\rho_e u_e A_e} = 0.0292 \phi$$

where suffices e and J refer to the mainstream (air) and jet (hydrogen) respectively.

Assuming fuel and air pressures to be equal at the injection point, and that both gases are ideal, it may be shown that

$$\frac{1}{\phi} \sqrt{\left(\frac{T_e}{T_J}\right) \frac{A_J}{A_e}} = 0.11 \frac{M_e}{M_J} \sqrt{\frac{1 + \frac{\gamma-1}{2} M_e^2}{1 + \frac{\gamma-1}{2} M_J^2}}$$

where M = Mach number

T = stagnation temperature.

The above relationship enables the total fuel jet to airstream area ratio (A_J/A_e) to be determined. The expression on the left-hand side is plotted in Figure 17 as a function of M_e and M_J .

It may be seen that, in order to minimise the blockage caused by the fuel injectors, it would be advantageous to have a high jet Mach number and low stagnation temperature for the hydrogen at injection, and a low Mach number and high stagnation temperature for the local airstream. In general, these requirements are compatible both with mixing requirements and with the expected conditions in a supersonic combustion ramjet designed for low hypersonic flight speeds. The following table lists a set of conditions considered typical for flight speeds of Mach 5 and 7, and assumes the fuel has been used as a coolant.

Flight Mach number	5	7
Mach number M_e at combustor entry	2.0	2.5
Altitude	80,000 ft	80,000 ft
Combustor inlet total temperature T_e	1,300°K	2,340°K
Combustor inlet static temperature t_e	720°K	1,040°K
Equivalence ratio	1	1
Assumed intake efficiency (η_{KE})	0.96	0.96
Local static pressure ($P_e = P_J$)	14.2 lb/in ²	38.5 lb/in ²
Assumed jet stagnation pressure P_J	1,000 lb/in ²	1,000 lb/in ²
Assumed jet stagnation temperature T_J	1,000°K	1,000°K
Jet Mach number M_J at injection	3.44	2.78
Area of combustor occupied by fuel nozzles	3.8%	5.8%

The values of the jet exit areas given will be significantly less than the injector blockage area. In an actual combustor, it is likely that the flame will have to be stabilised on the rear end of the injectors and this will involve increasing the area of the injectors at their downstream ends. It is considered that the total blockage of the injectors will be between 30 and 50% of the combustor area. This will mean that the injectors must be considered as part of the intake compression system.

It is seen that, if an engine is to be operated with stoichiometric fuel/air ratio, the hydrogen will probably be injected at a high Mach number - about Mach 3. This high Mach number means that the velocity of the hydrogen will be very high and much greater than that of the air, because of the high speed of sound in hydrogen. The large velocity difference between the streams should aid in promoting rapid mixing and will contribute to the specific impulse of the engine.

Since the injectors must be placed in a high enthalpy airstream, they must be cooled in some way. Consideration has been given to methods of cooling injectors and three methods have been studied:

regenerative cooling
film cooling
transpiration cooling.

In each case it has been assumed that the injectors will be cooled by the fuel passing to the engine. Schematics for the three methods of cooling are shown in Figure 18, and results of simple analyses of the alternative methods of cooling are shown in Figure 19.

If a maximum acceptable injector wall temperature of 1300°K be chosen then, provided the engine fuel flow does not fall below stoichiometric, either regenerative or transpiration cooling would apparently be adequate. Film cooling appears to be marginal with a stoichiometric hydrogen flow, and inadequate if the engine fuel flow is reduced.

For an engine in which the fuel flow is to be reduced, there seems little to choose between regenerative and transpiration cooling. However, the leading-edge cooling would be more difficult if regenerative cooling is employed.

7. CONCLUSIONS

- (i) The performance of a conventional subsonic combustion ramjet is severely reduced at hypersonic speeds by real gas effects in the combustor and nozzle. Despite this, the conventional ramjet appears to be capable of high performance, at least to Mach 7 and possibly to Mach 8. Its applications in this speed range appear to be limited only by internal pressure (and hence structure weight) considerations.
- (ii) By changing to a mixing-rate controlled supersonic combustion cycle, the performance penalty incurred by lowering the cycle temperature is not as great as it would be in the absence of real gas effects. Provided the

intake, fuel injector and combustor friction losses can be held at reasonable levels, the performance of a supersonic combustion ramjet will be competitive with that of the conventional ramjet at the lower end of the hypersonic speed range, and superior to it at Mach numbers above about 7. The internal pressures for a supersonic combustion ramjet will be typically about half an order of magnitude lower than those for a conventional ramjet.

- (iii) At flight speeds above 8, where it may be difficult to ensure a fully developed turbulent boundary layer over the intake compression surfaces, the possible performance of any air-breathing engine must remain conjectural until more quantitative intake studies have been made under simulated flight conditions.
- (iv) For cruise applications of long duration where the maximum flight Mach number may be limited to low hypersonic speed (say less than Mach 7) by aircraft skin temperature considerations (see Ref. 26), the supersonic combustion cycle appears to have little to offer over the conventional cycle. If this aircraft limitation can be relaxed, possibly by employing regenerative cooling or transient cooling techniques, then flight will be possible at hypersonic speeds where supersonic combustor performance appears more attractive.
- (v) For acceleration roles where it is desirable to operate the aircraft at the lowest possible altitudes, the internal pressures experienced by a conventional ramjet become prohibitive at hypersonic speeds. For these applications, the supersonic combustion cycle would confer large acceleration possibilities unattainable with the conventional cycle due to engine structural weight.
- (vi) If, in any application, a supersonic combustion cycle was preferred, it would generally be desirable to employ this mode of combustion at the lowest possible flight Mach number. To avoid thermal choking at low hypersonic speeds it will be essential to design for a mixing-rate controlled process in a divergent combustion chamber. The divergence should be at least sufficient to give constant pressure combustion.
- (vii) A piloted supersonic combustion system will be necessary to ensure a mixing-rate controlled process at flight speeds below about Mach 7. Research must be carried out to determine the characteristics of low blockage piloted combustion systems in airstreams having velocity around 4000 - 4500 ft/sec, static pressures between 0.2 and 2 atmospheres, and static temperatures from 500°K upwards.
- (viii) Existing experimental data suggest that adequate mixing may be achieved within a reasonable length provided the fuel injection velocity is high and that there are sufficient injector/pilot zones to cover the engine combustor section. For a two-dimensional engine, one injector slot may be required for each 2 to 3 in of the combustor height. Consequently, assuming minimum combustor length, mid-stream fuel injector/stabilisers will be required for all but the very smallest engines. The blockage of mid-stream injectors incorporating a piloting system will be relatively high, so that integration of the injectors with the intake compression shock system may be necessary.

- (ix) In a supersonic combustion ramjet operating at low hypersonic speeds the chemical reaction rates will be comparable with the expected mixing-rates, so that strong coupling between the two processes is to be expected. Although theoretical studies of fuel-air mixing with chemical reactions must be carried out, it will be essential to make experimental studies to amass data upon which reliable combustor designs and performance estimations can be based. Exploratory experimental work is required to develop injectors to give maximum mixing-rate with adequate stabilisation, whilst minimising the local disturbances caused by the injector array. It will be very important to consider the internal losses incurred by such injectors when making engine performance and optimisation studies.
- (x) Performance estimations suggest that for certain applications a hydrocarbon fuel may be just as suitable as hydrogen in a supersonic combustion ramjet. Consequently, studies should not be confined to hydrogen.
- (xi) The limitations of assuming one-dimensional flow in a mixing-rate controlled supersonic combustor must be examined critically - not only in relation to cycle performance and optimisation studies, but also with regard to defining and determining component performance.

REFERENCES

1. Hawkins, R.
Fox, M.D. *An Investigation of Real Gas Effects Relevant to the Performance of a Kerosene Fuelled Hypersonic Ramjet.* Bristol Siddeley Engines Limited, BSEL Report AP 5127, February 1963.
2. Fry, W.A.S. *The Gun Tunnel as an Intake Test Facility and Preliminary Assessment of Ramjet Intake Performance at $M = 10$.* Bristol Siddeley Engines Limited, BSEL Report AP 5146, October 1965.
3. Spalding, D.B. *The Plane Turbulent Mixing Layer with Non-Uniform Density.* Unpublished Imperial College Report, July 1964.
4. Holland, M.J. *The Correlation of Film Cooling Test Data for Compressible Flow in Regions of Mainstream Pressure Gradient.* Bristol Siddeley Engines Limited, BSEL Report AP 5186, October 1963. ARC. 25363.
5. Ferri, A. *Review of Problems in Application of Supersonic Combustion.* Journal of the Royal Aeronautical Society, September 1964.
6. Morgenthaler, J.M. *Supersonic Mixing of Hydrogen and Air.* Applied Physics Laboratory, Johns Hopkins University.

7. Alpinieri, L.J. *Turbulent Mixing of Coaxial Jets.* AIAA Journal, September 1964.
8. Price, R.B. *Summary of the First Series of Tests of a Small Scale Film Cooled Ramjet Exhaust Nozzle.* Bristol Siddeley Engines Limited, BSEL Report AP 5192, November 1963. ARC 25,362.
9. Schlichting, H. *Boundary Layer Theory.* McGraw-Hill, 1960.
10. Spalding, D.B.
et alii *Film Cooling in Incompressible Turbulent Flow - Proposals for Theoretical Models of the Film Cooling Process.* ARC 25,309, 1963.
11. Spalding, D.B.
et alii *Film Cooling in Incompressible Turbulent Flow - Examination of Experimental Data for the Adiabatic Wall Temperature.* ARC 25,311, 1963.
12. Cole, E.H.
Peerless, S.J. *Film Cooling in Incompressible Turbulent Flow - A Revised and Collective Presentation of the Data for the Adiabatic Wall Temperature.* ARC 25,310, 1963.
13. Spalding, D.B. *Theory of Rate of Spread of Confined Turbulent Pre-Mixed Flames.* Seventh Symposium (International) on Combustion, 1958. Butterworths, London, 1959.
14. El-Ehwany, A.A.M.
Stollery, J.L. *A Note on the Turbulent Mixing of a Two-dimensional Gas Stream Exhausting into a Moving Stream of Different Density.* Unpublished Imperial College Report, December 1964.
15. Forstall, W.
Shapiro, A.M. *Momentum and Mass Transfer in Coaxial Gas Jets.* Journal of Applied Mechanics, Vol.17, 1950.
16. Kleinstein, A. *On the Mixing of Laminar Turbulent Axially Symmetric Compressible Flows.* Polytechnic Institute of Brooklyn, PIBAL Report ARL 63-108, June 1963.
17. Ferri, A.
et alii *Theoretical and Experimental Investigation of Supersonic Combustion.* Polytechnic Institute of Brooklyn, PIBAL Report ARL 62-467, September 1962.
18. Hatch, J.E.
Papell, S.S. *Use of a Theoretical Model to Correlate Data for Film Cooling or Heating an Adiabatic Wall.* NASA-TN D-130, 1959.
19. Stollery, J.L. *A Correlation of Some Experimental Data on the Length of the Potential Core Region.* Imperial College Report IC/HRJ/13.

20. Steinberg, M.
Kaskan, W.E. Fifth Symposium (International) on Combustion, pp.664-672, Reinhold, New York, 1955.
21. Ellis, G.E.
Bahn, G.S. *Engineering Selection of Reaction Rate Constants for Gaseous Chemical Species at High Temperatures.* Fall Meeting, Western States Section, Combustion Institute, 1962.
22. Montichiloff, I.M.
et alii *An Analytical Method of Computing Reaction Rates for H₂-Air Mixtures.* Ninth Symposium (International) on Combustion, pp.220-240, Academic Press, 1962.
23. Duff, R.E. *Calculation of Reaction Profiles Behind Steady State Shock Waves. 1, Application to Detonation Waves.* Journal of Chemical Physics, p.1193, June 1958.
24. Nicholls, J.A. *Stabilisation of Gaseous Detonation Waves with Emphasis on the Ignition Delay Zone.* Ph.D. Thesis, University of Michigan, 1960.
25. Das Gupta, N.C. *High Temperature Combustion of Hydrogen.* McGill University, Report SCS.36, August 1961.
26. Sinnott, C.S. *Factors Affecting the Surface Temperature of Hypersonic Aircraft.* Journal of the Royal Aeronautical Society, October 1963.
27. Townend, L.H.
Reid, J. *Some Effects of Stable Combustion in Wakes Formed in a Supersonic Stream.* In "Supersonic Flow, Chemical Processes and Radiative Transfer", Pergamon, 1964.

APPENDIX

Reaction Schemes and Rate Data for Hydrogen-Air Combustion

Possible Reactions for Hydrogen-Air Combustion

Reaction	
1	$\text{H} + \text{O}_2 \rightarrow \text{OH} + \text{O}$
2	$\text{O} + \text{H}_2 \rightarrow \text{OH} + \text{H}$
3	$\text{OH} + \text{H}_2 \rightarrow \text{H}_2\text{O} + \text{H}$
4	$2\text{OH} \rightarrow \text{H}_2\text{O} + \text{O}$
5	$\text{O}_2 + \text{H}_2 \rightarrow 2\text{OH}$
6	$\text{H}_2 + \text{M} \rightarrow 2\text{H} + \text{M}$
7	$\text{H}_2\text{O} + \text{M} \rightarrow \text{H} + \text{OH} + \text{M}$
8	$\text{OH} + \text{M} \rightarrow \text{H} + \text{O} + \text{M}$
9	$\text{O}_2 + \text{M} \rightarrow 2\text{O} + \text{M}$
10	$\text{H} + \text{O}_2 + \text{M} \rightarrow \text{M} + \text{HO}_2$
11	$\text{NO} + \text{M} \rightarrow \text{N} + \text{O} + \text{M}$
12	$\text{N}_2 + \text{O} \rightarrow \text{NO} + \text{N}$
13	$\text{O}_2 + \text{N} \rightarrow \text{O} + \text{NO}$
14	$\text{O}_2 + \text{N}_2 \rightarrow 2\text{NO}$

Preferred Reaction Schemes of Various Workers

Investigators	Preferred Reaction Scheme
Ref. 23	1 - 9
Ref. 24	1 - 9
Ref. 5. (and all Polytechnic Institute of Brooklyn (PIBAL) and General Applied Science Lab. (GASL) work)	1, 2, 3, 4, 6, 7, 8, 9
Ref. 25	1, 2, 3, 10
Ref. 22	1, 2, 3, 6, 7, 9, 11, 12, 13, 14

Reaction Rate Data

Reaction	Rate Constants Used by Ferri ⁵ (mole/cc) ⁻¹ sec ⁻¹	Rate Constants Recommended by Ellis ²¹ (mole/cc) ⁻¹ sec ⁻¹
1	$3 \times 10^{14} \exp \left(-\frac{3810}{T} \right)$	$4 \times 10^{14} \exp \left(-\frac{9080}{T} \right)$
2	$3 \times 10^{14} \exp \left(-\frac{4030}{T} \right)$	$3 \times 10^{14} \exp \left(-\frac{3030}{T} \right)$
3	$3 \times 10^{14} \exp \left(-\frac{3020}{T} \right)$	$3 \times 10^{14} \exp \left(-\frac{1260}{T} \right)$
4	$3 \times 10^{14} \exp \left(-\frac{3020}{T} \right)$	$3 \times 10^{14} \exp \left(-\frac{1260}{T} \right)$
6	$\frac{C \times 10^{19}}{T} \exp \left(-\frac{54,000}{T} \right)$	$\frac{10^{21}}{T^{1.5}} \exp \left(-\frac{52,000}{T} \right)$
7	$\frac{D \times 10^{21}}{T} \exp \left(-\frac{62,200}{T} \right)$	$\frac{10^{23}}{T^{1.5}} \exp \left(-\frac{58,000}{T} \right)$
8	$\frac{E \times 10^{19}}{T} \exp \left(-\frac{52,000}{T} \right)$	$\frac{10^{21}}{T^{1.5}} \exp \left(-\frac{51,000}{T} \right)$
9	$\frac{2.9 \times 10^{19}}{T} \exp \left(-\frac{60,600}{T} \right)$	$\frac{1.4 \times 10^{25}}{T^{2.5}} \exp \left(-\frac{59,600}{T} \right)$

The recombination in rate constants for Reactions 6 - 8 (in left-hand column) used by Ferri and based upon his own survey of experimental data are listed below. Ferri suggests the larger values of C, D and E (given by Scheme 3) are most appropriate but gives no justification. The overall reaction times given in the present paper are based upon the constants given in Scheme 2.

Alternative Sets of Constants	C Reaction 6	D Reaction 7	E Reaction 8
Scheme 1	1.85	0.966	0.8
Scheme 2	9.25	9.66	8.0
Scheme 3	20.8	30.6	25.3

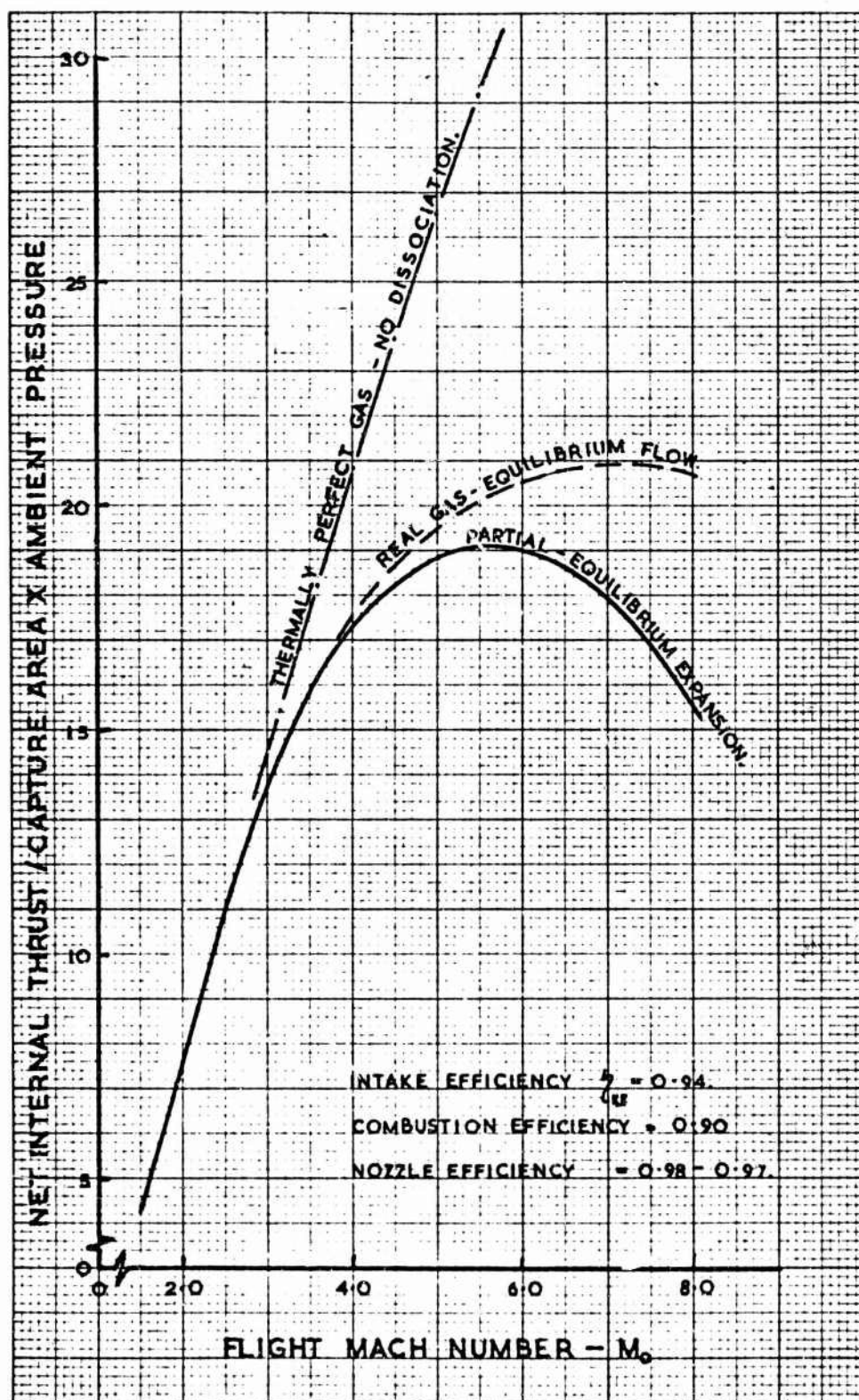


Fig.1 Ramjet cycle performance. Stoichiometric subsonic combustion. Kerosene

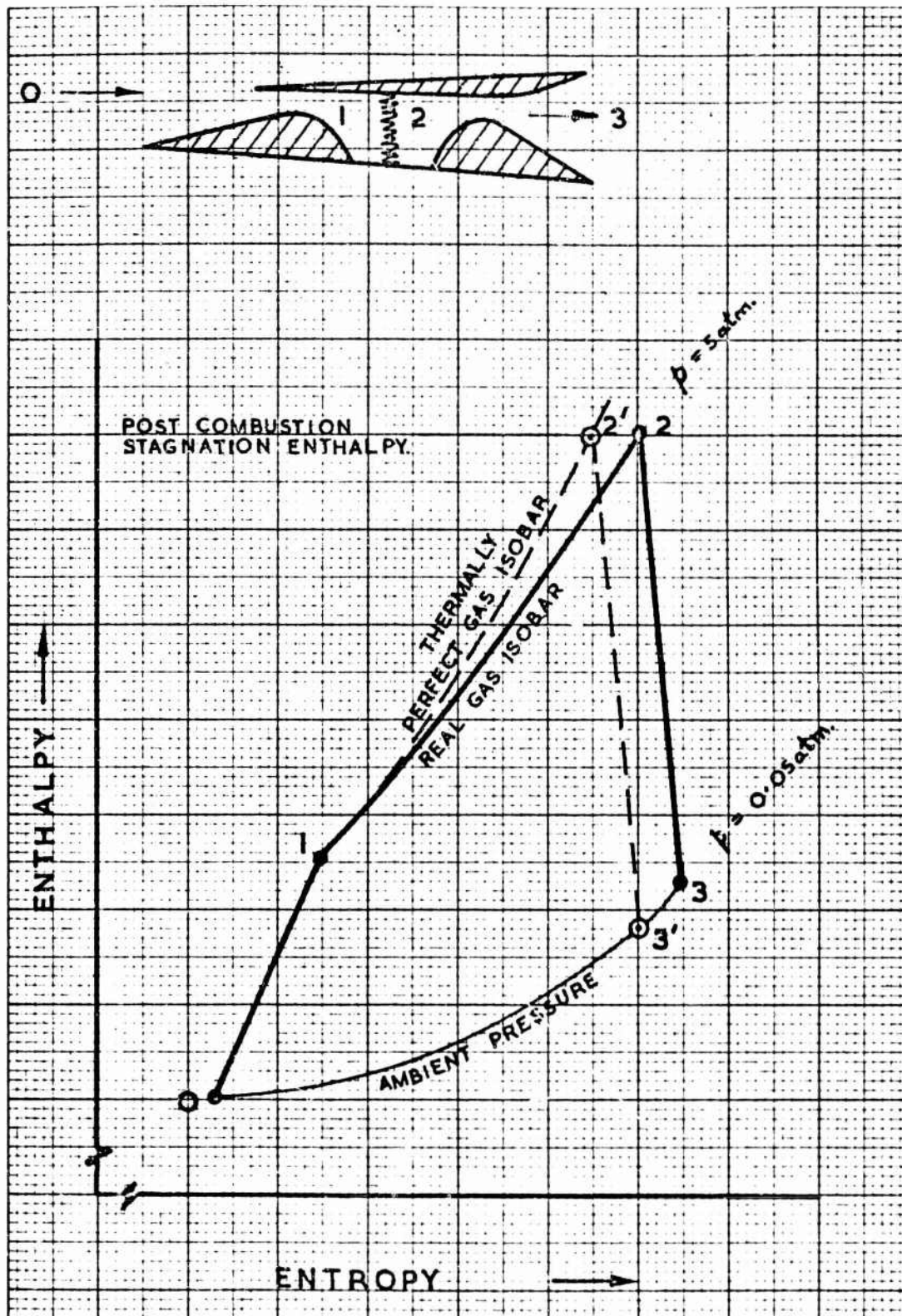


Fig. 2 Conventional ramjet cycle. Stoichiometric subsonic combustion. Kerosene

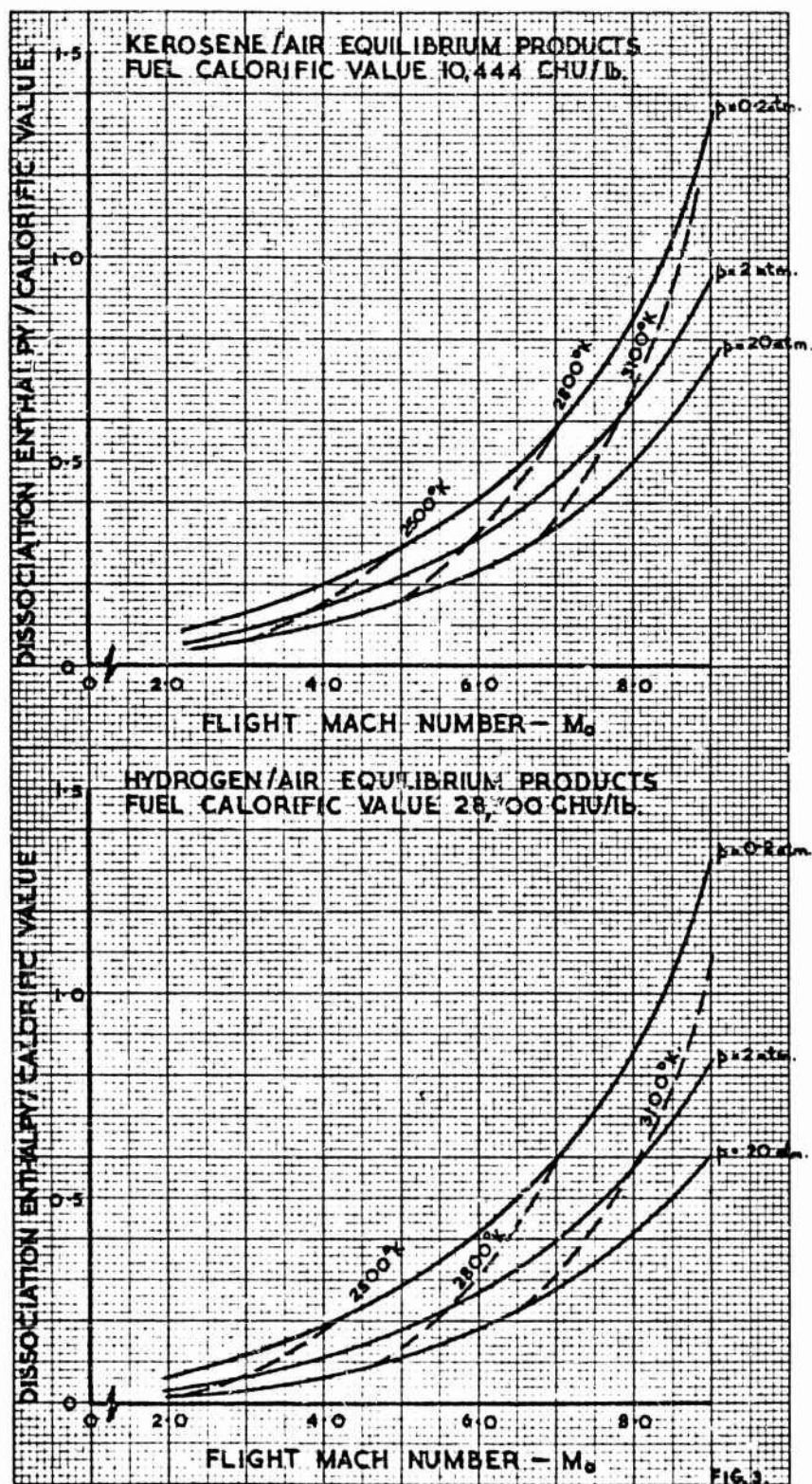


Fig. 3 Dissociation enthalpy of products as fraction of fuel calorific value.
Stoichiometric subsonic combustion.

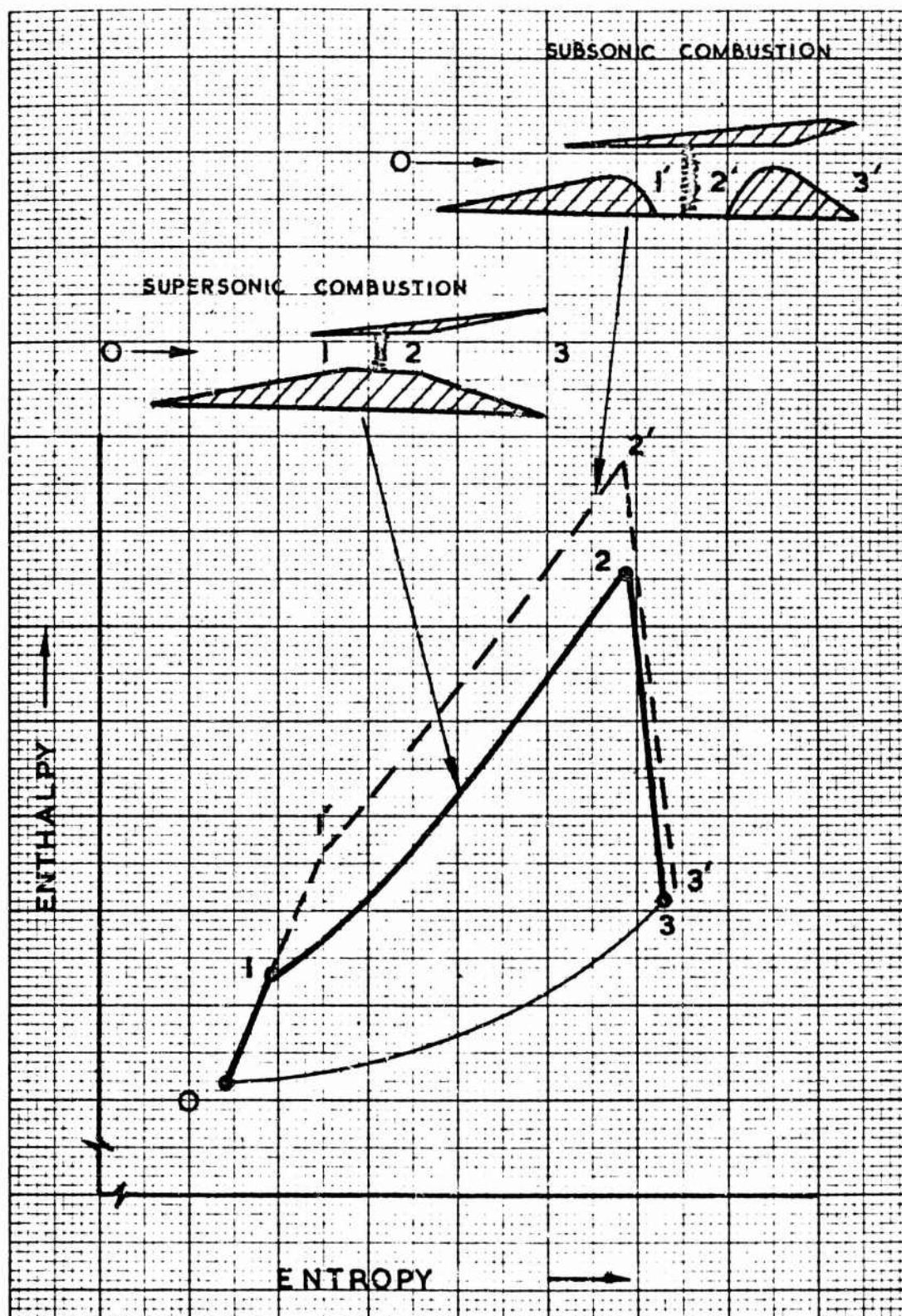


Fig. 4 Comparison of cycles for subsonic and supersonic combustion ramjets

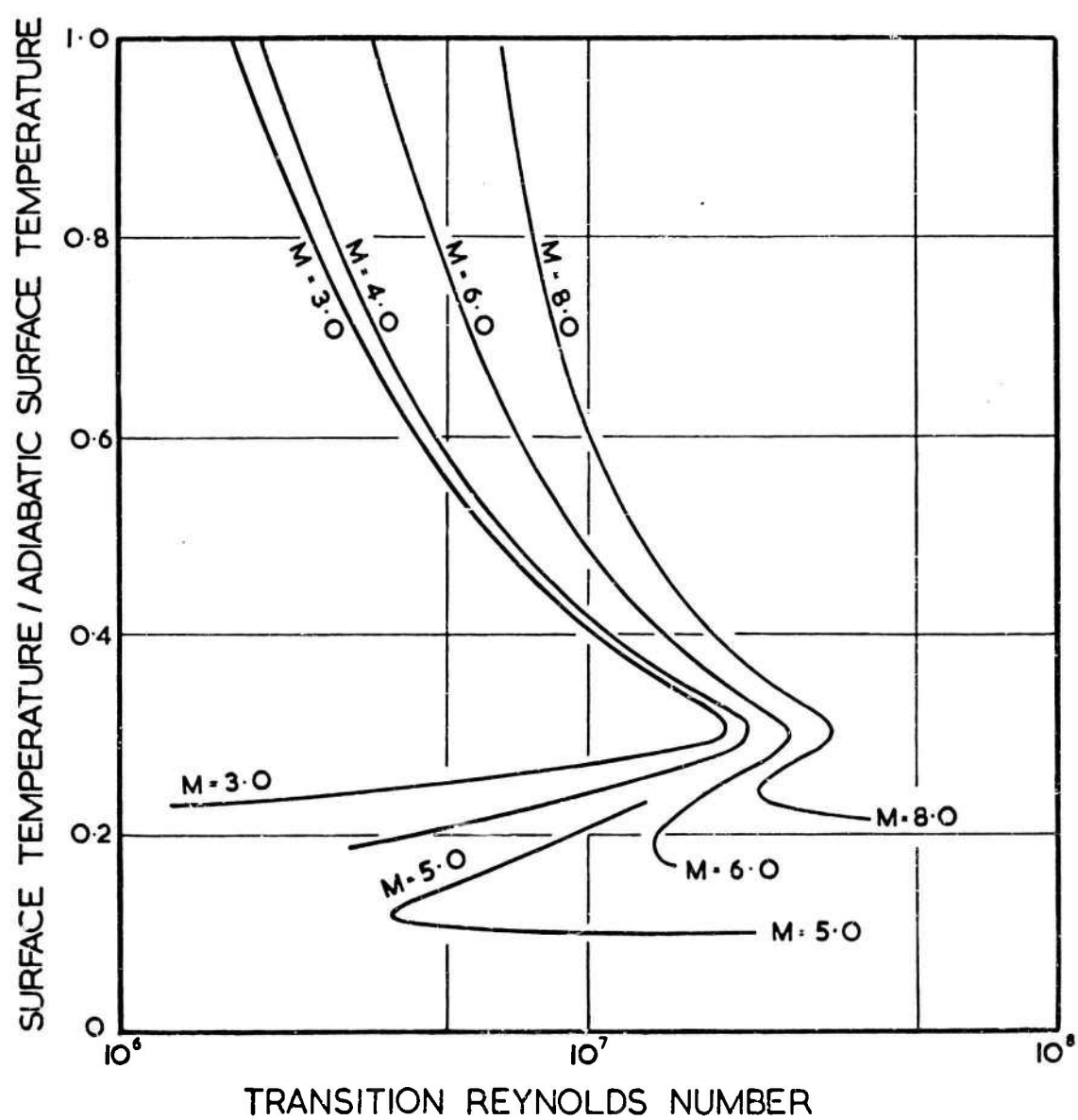


Fig.5 Influence of surface temperature on transition Reynolds number for flat plate

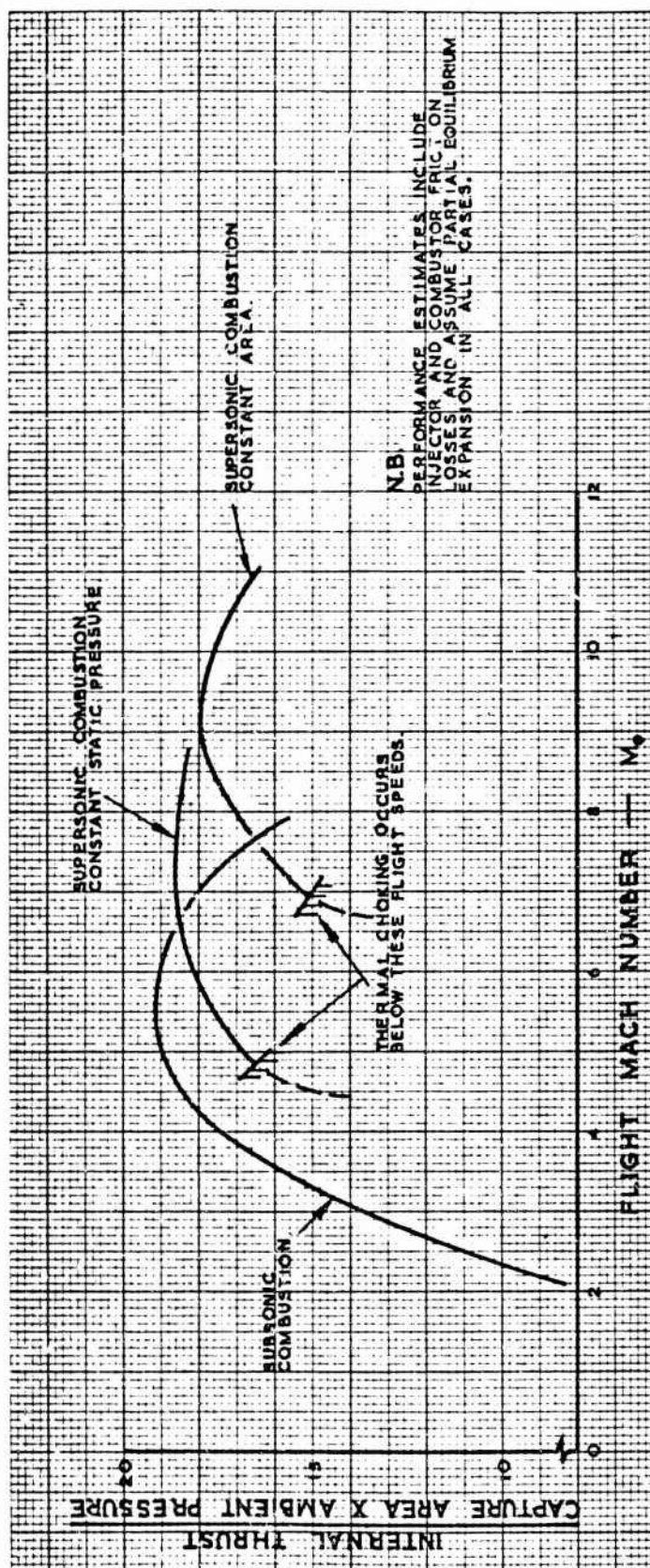


Fig. 6 Comparison of internal thrust for stoichiometric subsonic and supersonic combustion. Ramjets. Kerosene

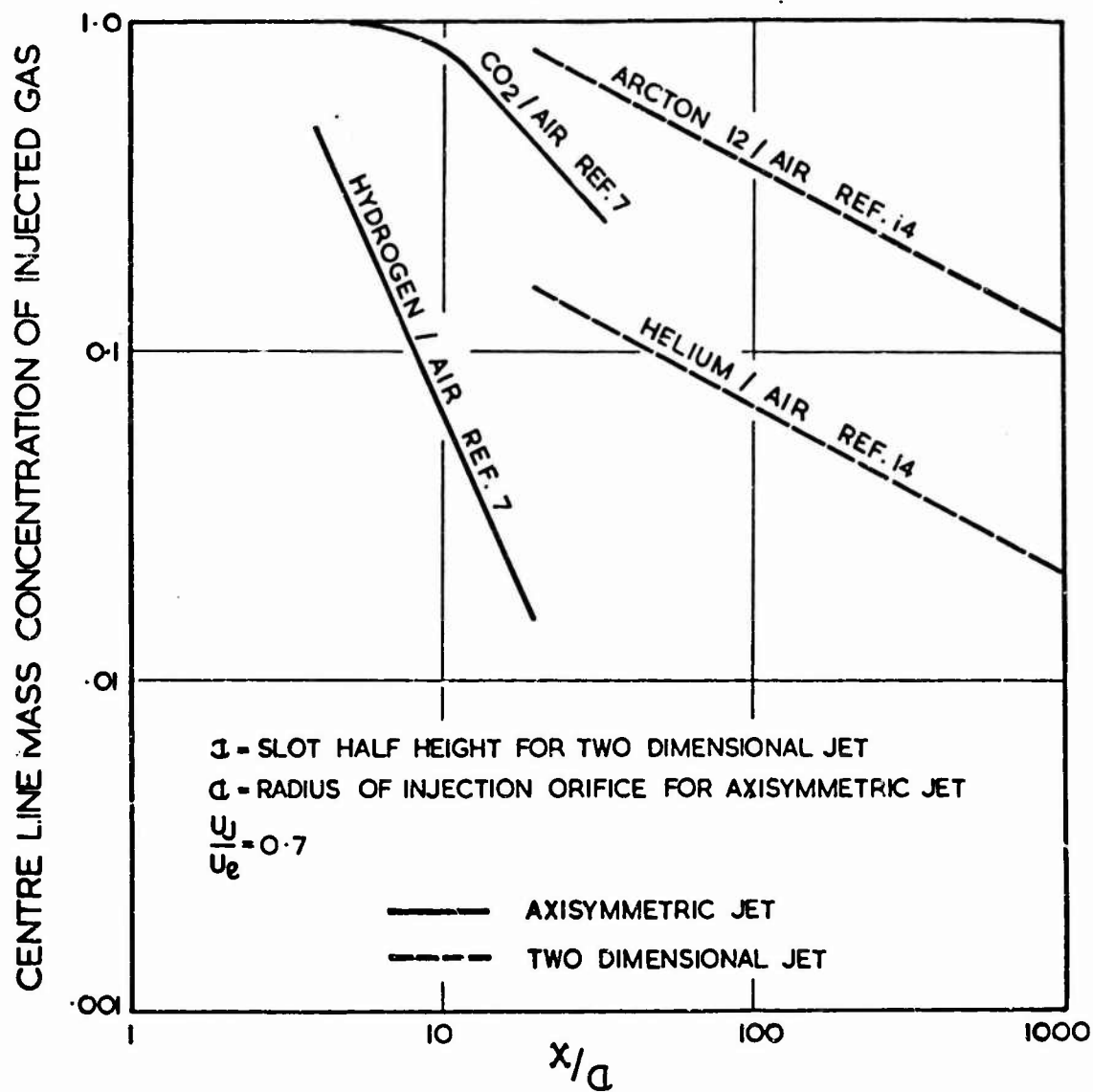


Fig. 7 Comparison of mixing rates for axial midstream injection of various gases into air for two-dimensional and axisymmetric flows [$u_j/u_e = 0.7$]

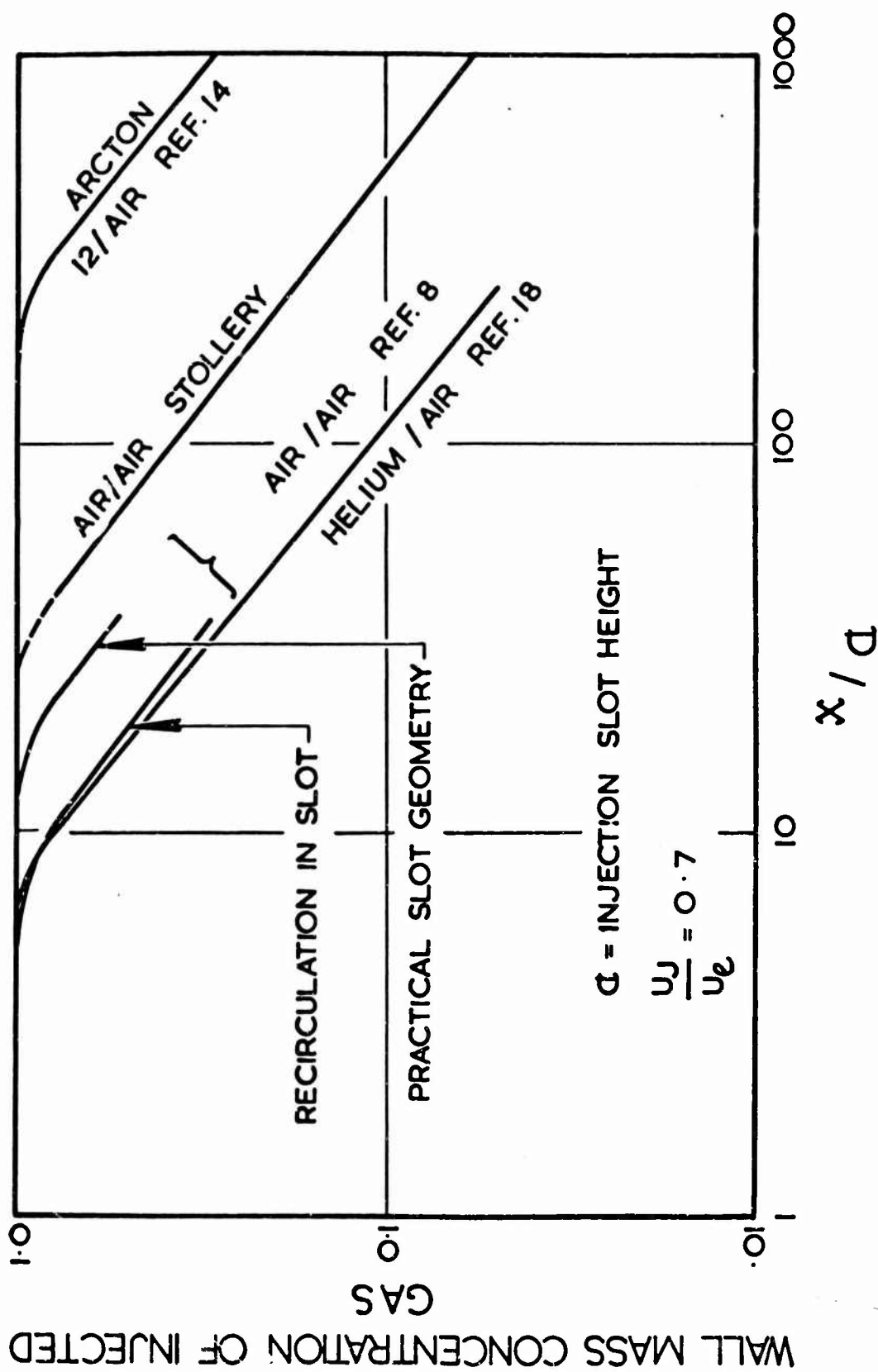


Fig. 8 Two-dimensional wall injection of various gases [$u_j/u_e = 0.7$]

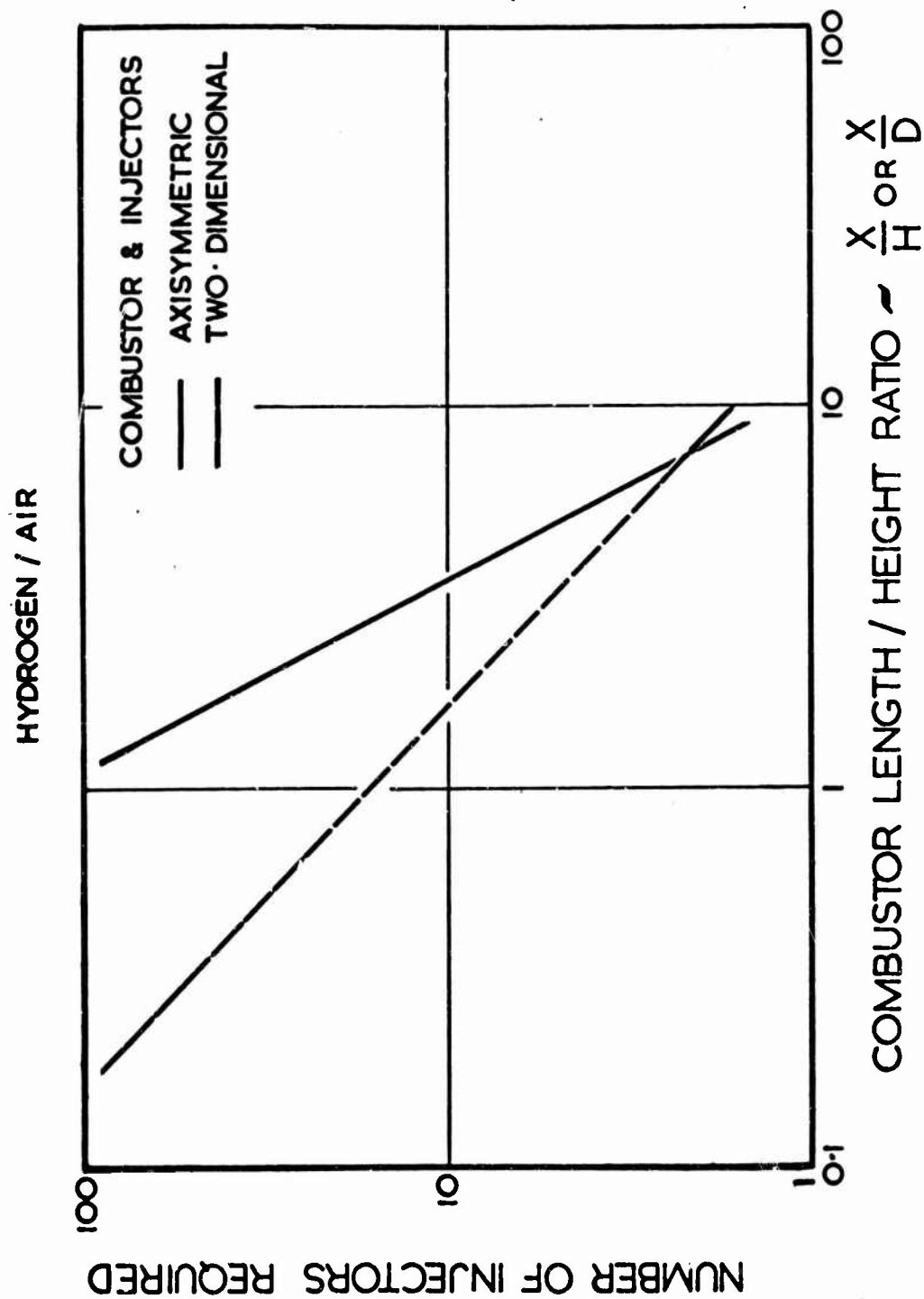


Fig. 9 Number of injectors required to achieve complete mixing of hydrogen and air in combustor of specified length. (Based on data given in Reference 5)

$P = 1.0 \text{ ATM.}$

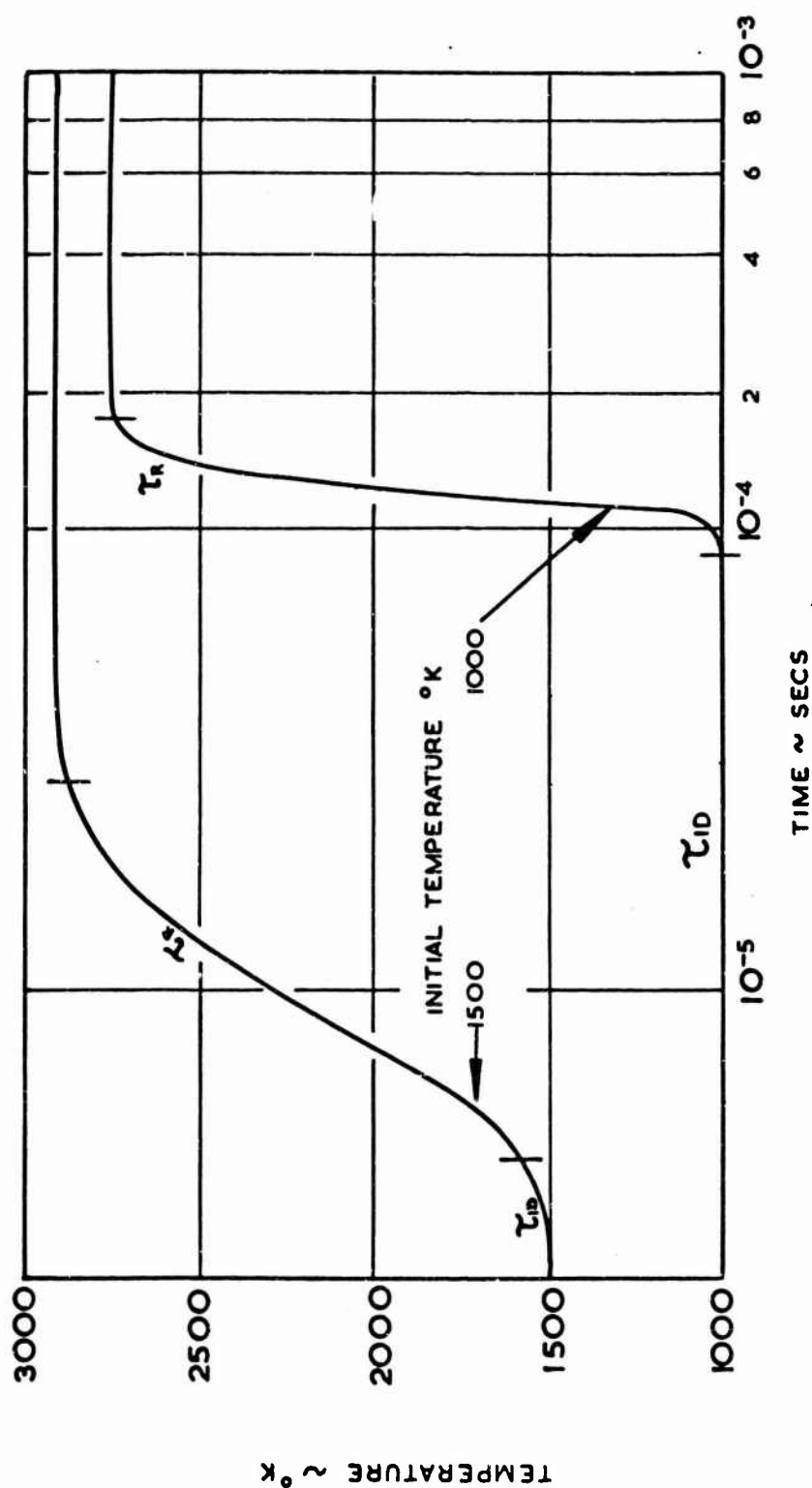


Fig. 10 Temperature-time history of stoichiometric hydrogen-air with reaction rate scheme 2 (Reference 5)

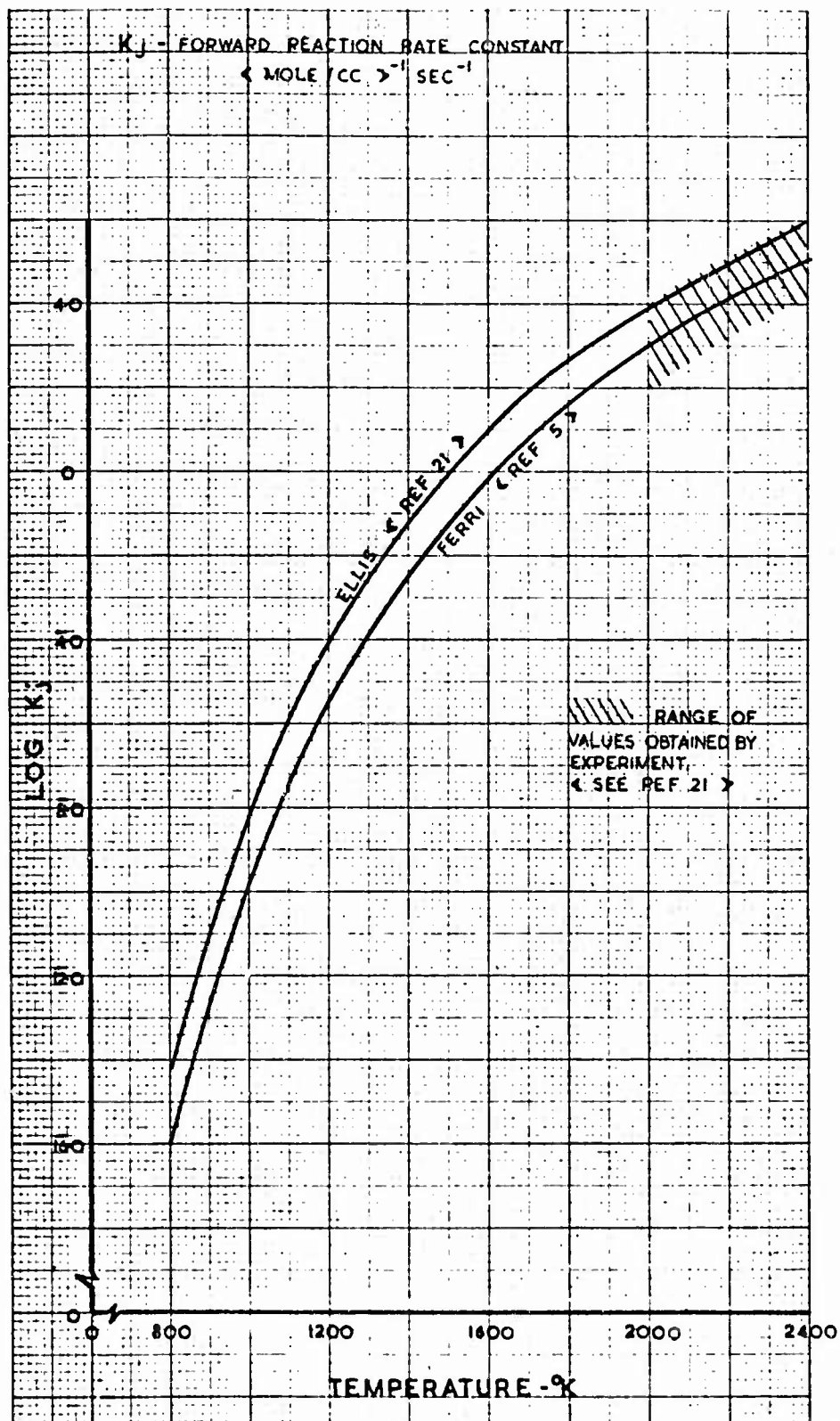


Fig.11 Reaction rate data. Reaction 9. $O_2 + M \rightarrow 2O + M$

P: O. 2 ATM.

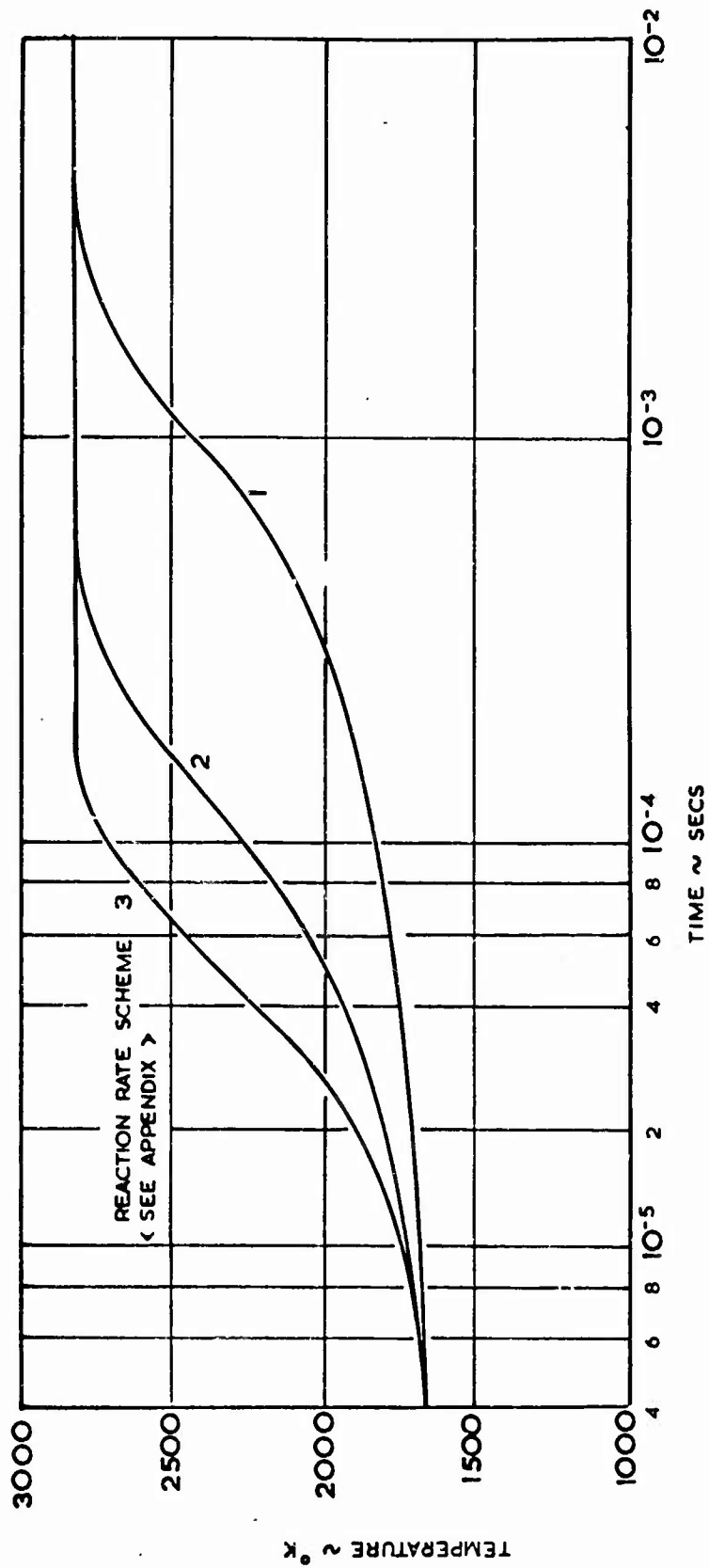


Fig. 12 Temperature-time history of stoichiometric hydrogen-air reaction (Reference 5)

P = 4.7 ATM.

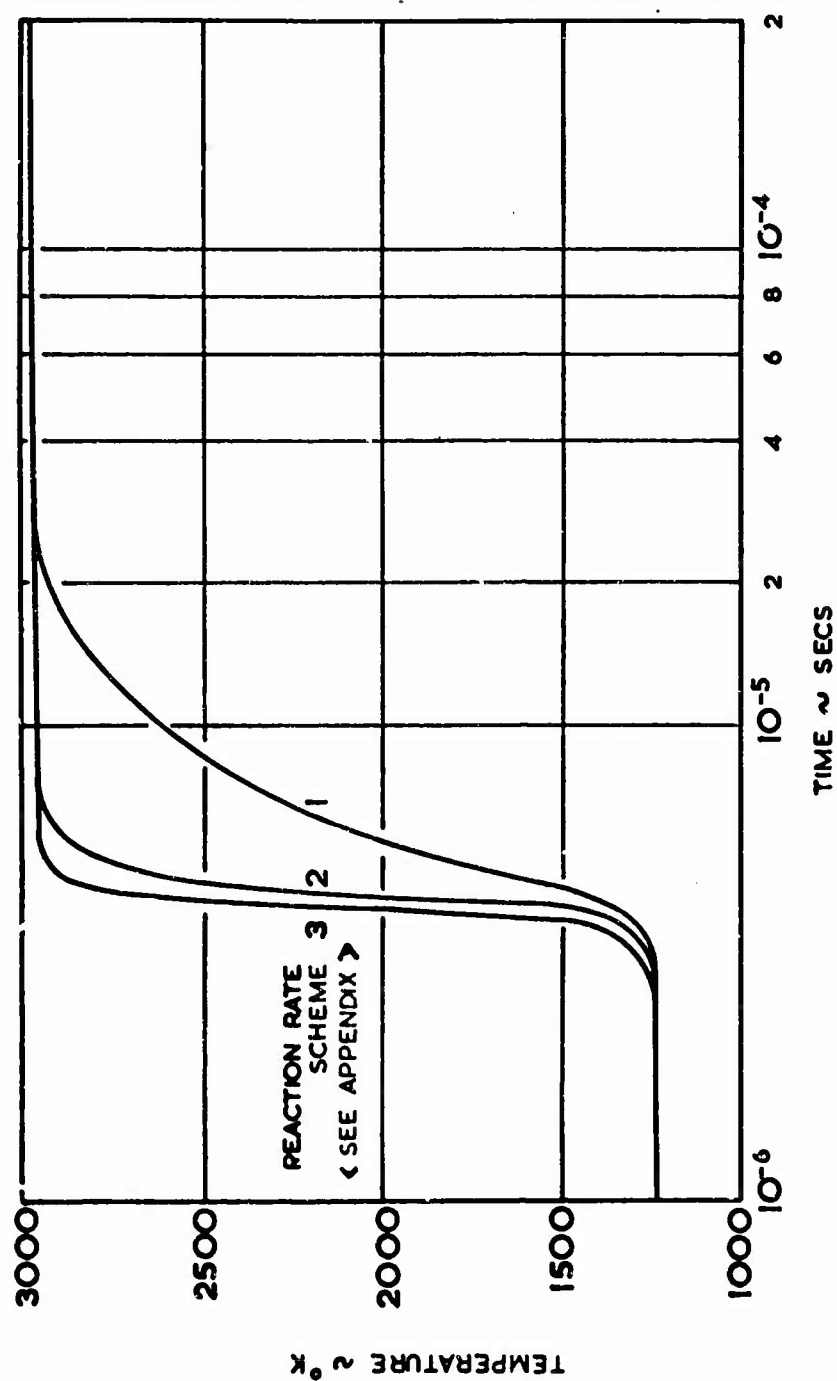


Fig. 13 Temperature-time history of stoichiometric hydrogen-air reaction (Reference 5)

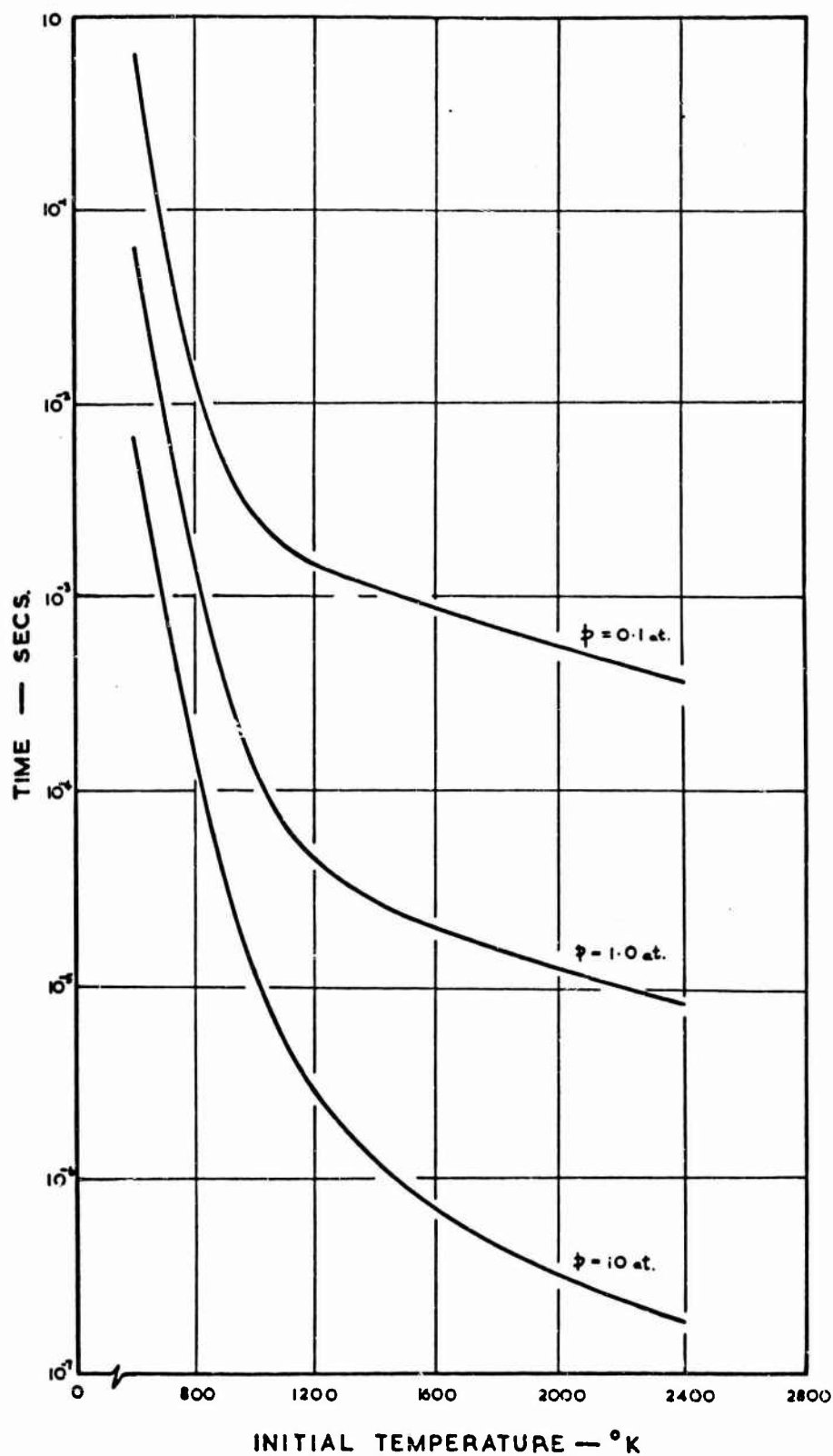


Fig. 14 Calculated values of total reaction times for hydrogen-air constant pressure reaction

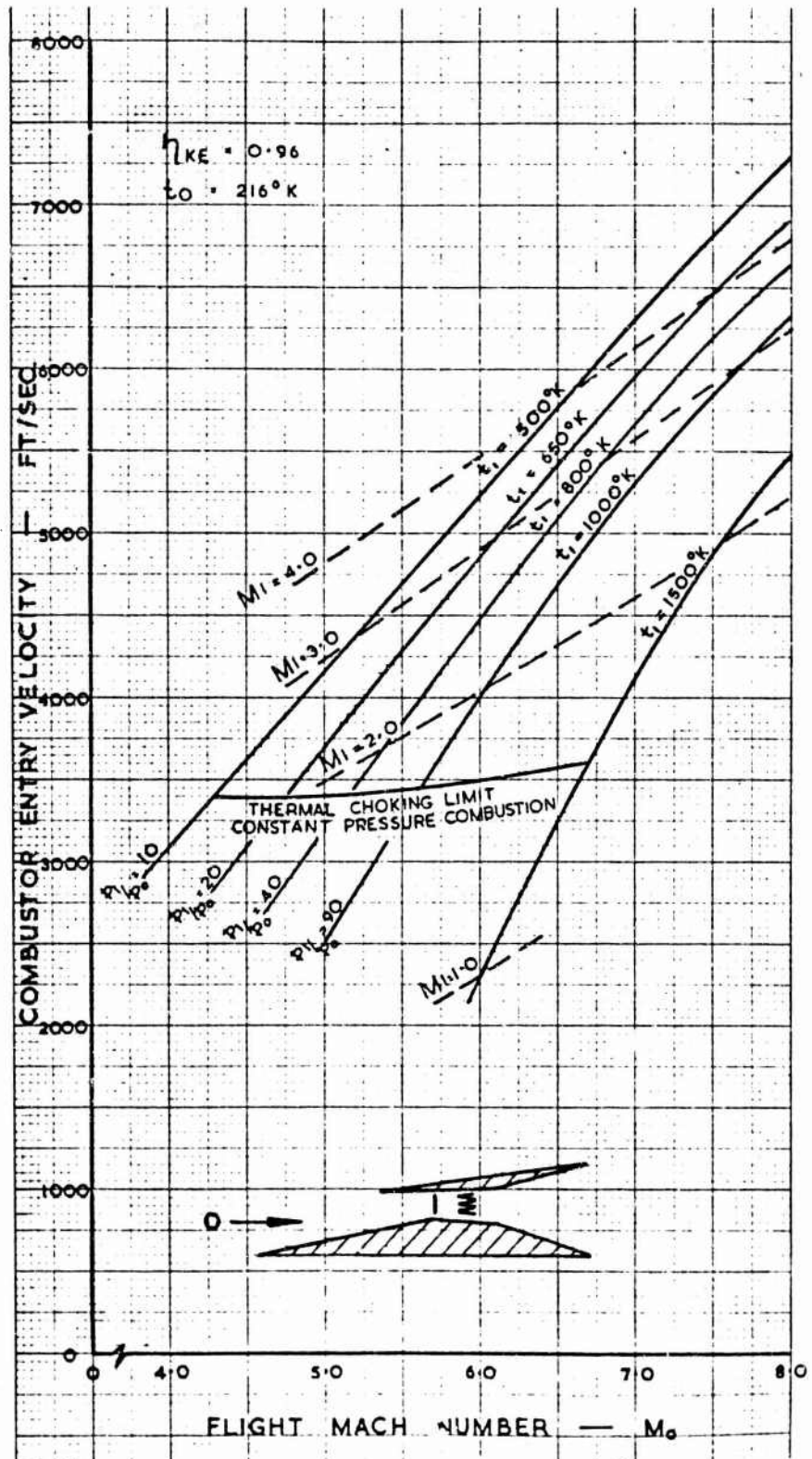


Fig.15 Boundaries of lower end of flight range using supersonic combustion.
Stoichiometric hydrogen-air

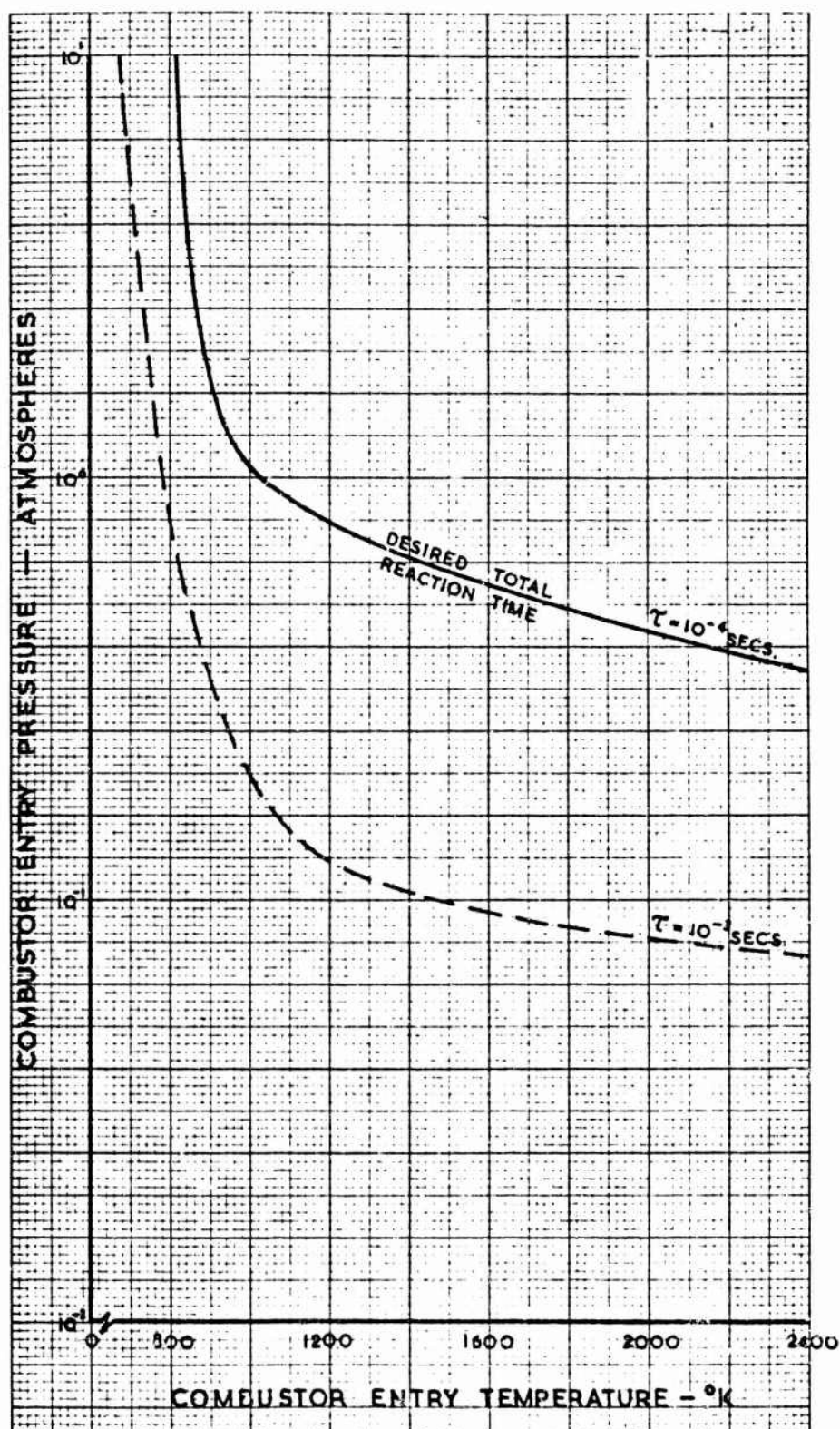


Fig.16 Range of static pressures and temperature to give specific reaction times.
Stoichiometric hydrogen-air

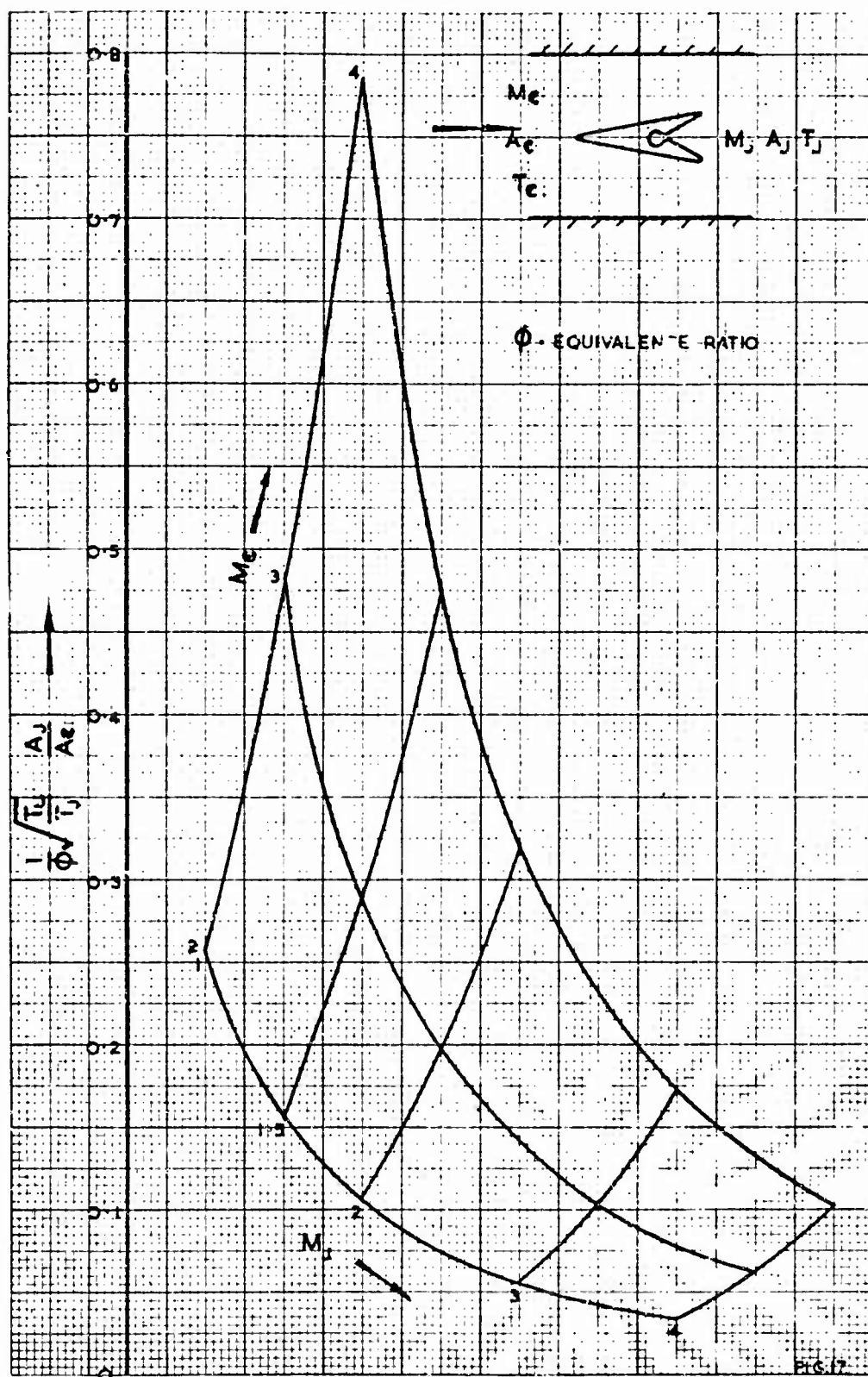
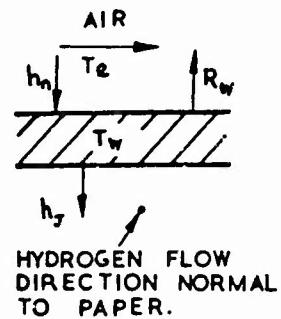
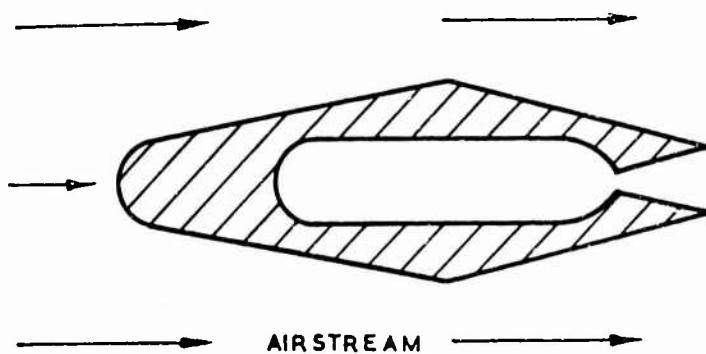
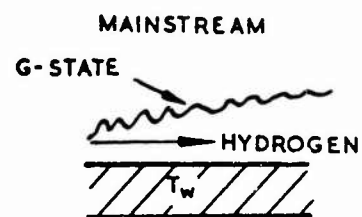
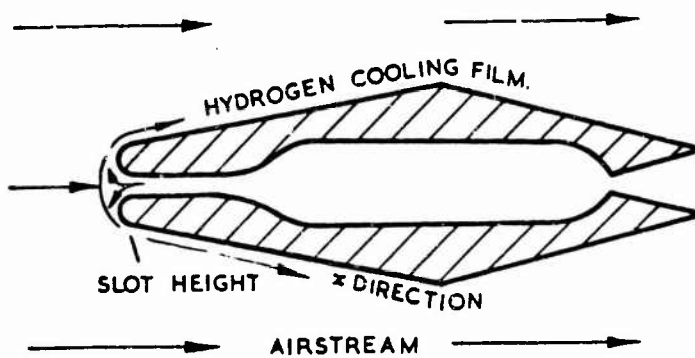


Fig. 17 Variation of injector blockage with M_e and M_j . Hydrogen fuel

REGENERATIVE COOLING.



FILM COOLING



TRANSPIRATION COOLING

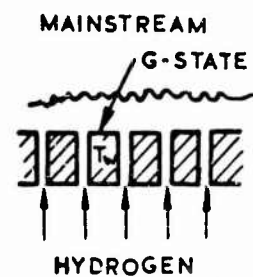
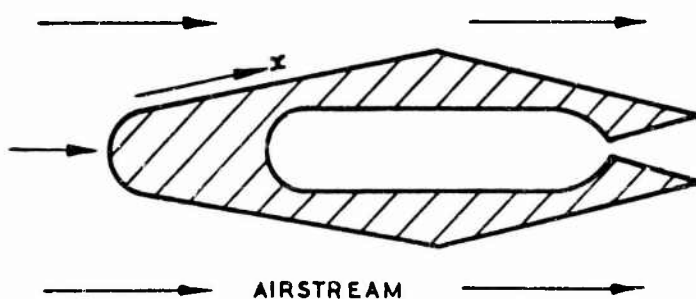


Fig. 18 Injector cooling schemes

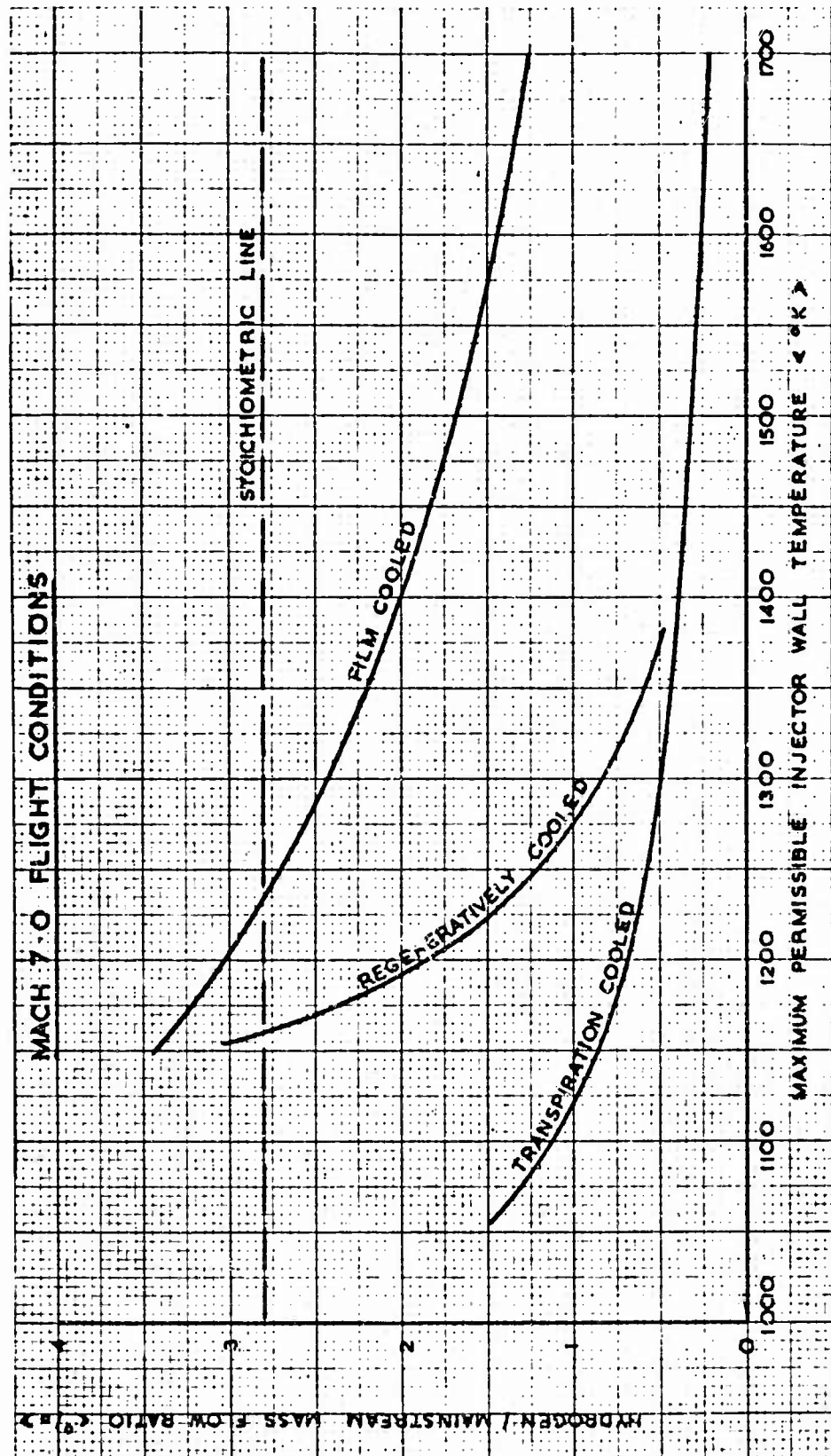


Fig. 19 Variation of wall temperature with coolant flow. Coolant (hydrogen) stagnation temperature 1000°K. Mach 7.0 flight conditions

THE BLUNT TRAILING EDGE AXIAL-FLOW
SUPERSONIC COMPRESSOR

by

F. Breugelmans

von Kármán Institute for Fluid Dynamics,
Rhode-Saint-Genèse, Belgium

SUMMARY

A 40 cm tip-diameter rotor, using blunt trailing edge blades was designed to produce a total pressure ratio of 3.5 at a tip Mach number of 1.70. Some general observations are made on the flow in pipes of constant area, ducts of the P-A power family and flows through sudden area enlargements. Both subsonic and supersonic Mach numbers are considered. The influence of Mach number, divergence of the channel, sudden area increase and back pressure on the flow behaviour is discussed. The supersonic cascade experiments are presented from the point of view of pipe flow. The rotor investigation was carried out up to 92% of the nominal speed and had to be stopped there, owing to mechanical problems. The blade section performance is analyzed from the point of view of pipe flow and compared to theoretical results. All the data obtained on stalling incidence and losses are compared. The tests were carried out in a mixture of freon 12 and air and were converted into air equivalent performance¹⁷. No inlet guide vanes and no stator have been used so far.

SOMMAIRE

On a mis au point un rotor avec pales de 40 cm de diamètre aux extrémités et bord de fuite émoussé en vue d'obtenir un rapport de pression total de 3,5 à un nombre de Mach de 1,70 en bout de pales. Dans une première partie, l'auteur rappelle certaines notions d'ordre général sur les écoulements dans les conduites de surface constante, les canalisations du type P-A (pression-surface) et sur les écoulements en présence d'extensions soudaines de surface. Il envisage les cas des vitesses subsoniques et supersoniques, et étudie l'influence du nombre de Mach, de la divergence du canal, d'une augmentation subite de surface, et d'une contre-pression, sur le comportement de l'écoulement. Dans une seconde partie, l'auteur présente une série d'expériences sur grilles d'aubes supersoniques, du point de vue de l'écoulement à l'intérieur des conduites. L'expérience sur rotor a été menée jusqu'à une vitesse équivalant à 92% de la vitesse nominale et dut être arrêtée pour des problèmes d'ordre mécanique. La performance de la section de pale est analysée du point de vue de l'écoulement dans la conduite et comparée aux résultats théoriques. Enfin, toutes les données recueillies sur l'incidence de décrochage et les déperditions sont comparées. Les expériences décrites ont été menées dans un mélange fréon 12 et air et converties en performances équivalentes pour un milieu composé uniquement d'air¹⁷. On n'a utilisé jusqu'ici ni aubes directrices ni aubes fixes aux entrées d'air.

CONTENTS

	Page
SUMMARY	118
SOMMAIRE	118
LIST OF FIGURES	120
NOTATION	121
1. INTRODUCTION	123
2. GENERAL CONSIDERATIONS	124
2.1 Flow in Constant-area Ducts	124
2.2 Flow in P-A Power Family Ducts	125
2.3 Flow in Sudden Area Enlargements	126
2.4 Application	126
3. EXPERIMENTAL RESULTS	127
3.1 High Speed Cascade Investigation	127
3.2 Rotor Tests	128
3.3 Comparison of Low Speed and High Speed Data	129
4. CONCLUSIONS	130
ACKNOWLEDGEMENT	130
REFERENCES	130
FIGURES	132

LIST OF FIGURES

	Page
Fig.1 Different types of supersonic passages	132
Fig.2 Pressure ratio through an oblique shock emerging from a turbulent boundary layer	133
Fig.3 Pipe flow characteristics	134
Fig.4 Relation between mass flow coefficients in front of and behind a normal shock	135
Fig.5 P-A power family ducts with pseudo-shock. $\gamma = 1.2$	136
Fig.6 Dump-diffusion loss coefficient. $\gamma = 1.4$, $A_2/A_1 = 1.37$ (rotor mid-section)	137
Fig.7 Dump diffusion loss coefficient. $\gamma = 1.4$	138
Fig.8 Back pressure influence on P/P_0 distribution	139
Fig.9 Pseudo-shock length in front of the shock position ^a	139
Fig.10 Static pressure distribution	140
Fig.11 Static pressure distribution	142
Fig.12 Maximum mass-averaged rotor performance	144
Fig.13 Local total pressure ratio and adiabatic efficiency ($0.88 N_d$)	145
Fig.14 Rotor outlet flow distribution ($0.88 N_d$)	146
Fig.15 Absolute flow outlet angle and mach number ($0.88 N_d$)	147
Fig.16 Radial distribution of the static pressure ratio at full throttle	148
Fig.17 Static pressure distribution downstream of the rotor	149
Fig.18 Variation of stalling incidence with M_{1r}	150
Fig.19 Analysis of rotor and cascade loss coefficient	151
Fig.20 A rotor consisting of 32 passages	152

NOTATION

A	area
\bar{c}_f	average value of the friction coefficient
c	chord
d	diameter
i	incidence angle
M	Mach number
\dot{m}	mass flow rate
N_d	design speed
P	static pressure
P_0	total pressure
R	radius
α	absolute flow angle
γ	specific heat ratio
ϵ	P-A power family parameter
η	adiabatic efficiency
$\bar{\omega}$	total pressure loss coefficient

Subscripts

1	initial conditions
is	isentropic
$*$	critical
1	inlet plane
2	exit plane

THE BLUNT TRAILING EDGE AXIAL-FLOW SUPERSONIC COMPRESSOR

F. Breugelmans

1. INTRODUCTION

A supersonic compressor is defined as a compressor utilizing supersonic relative inlet flow over the whole blade height; one or more blade rows can have supersonic inlet conditions.

As early as 1937, the use of normal shocks was recognized by Weise as a means of obtaining high static pressure rises through one single row of compressor blading.

The work of Kantrowitz¹ in 1942 on supersonic cascade starting, earlier diffuser studies and his discussion on possible supersonic compressor configurations started the NACA program in this field, which lasted until 1957.

The design of a supersonic compressor is based more on the supersonic diffuser design than on conventional criteria. The blade concept is replaced by the supersonic passage, designed to fulfil the diffuser requirements.

The different types of passages used are (Fig. 1)

the converging-diverging diffuser as used in supersonic wind tunnels, also called the Donaldson-Kantrowitz diffuser;

the converging passage;

the converging-diverging diffuser with external compression, as used in ramjet intakes, conical and spike-type diffusers;

the constant-area duct, as used in aircraft intakes.

The main problems encountered in supersonic compressors are, first of all, shock-wave boundary-layer interaction, which induces separation and makes the shape of the trailing edge ineffective. Secondly, a starting problem for the establishment of the supersonic flow in the passage.

Poor off-design performance and an unsatisfactory exit flow distribution make a suitable stator design difficult and limit the operating zone of interest.

The difficulties can be easily understood by remembering the complicated systems incorporated in the air intakes to adapt them better to each flight Mach number. These systems cannot be built-in in a blade row, because the design has to be a compromise for the Mach number range covered.

In 1959, Johnson, von Ohain, Lawson and Cramer⁵ proposed the constant-area duct as a suitable means of supersonic diffusion in compressors. A slightly divergent passage, described by circular arcs, at a high solidity was chosen. The main idea was to establish a multiple shock pattern as encountered in ducts and called pseudo-shock. A sudden area enlargement occurred at the rotor outlet to produce the dump diffusion in the downstream annular area. Tests were performed at ARL using a wheel with a 13.3 cm tip diameter. The results turned out to be very promising and an investigation on a 40 cm wheel was carried out at the von Kármán Institute for Fluid Dynamics (VKI) and sponsored by Aeronautical Research Laboratories (Melbourne) through the European Office of Aerospace Research. The tests were conducted in a mixture of freon 12 and air.

Although all the difficulties mentioned cannot be avoided entirely, the following positive features are worthy of notice:

no starting problems occurred in the supersonic range of operation,

good subsonic and transonic operation was found,

the blunt trailing edge and the corresponding dump diffusion process are comparable to the shock-induced separation occurring in other types of blading.

2. GENERAL CONSIDERATIONS

2.1 Flow in Constant-area Ducts

One normal shock does not always describe the transition from supersonic to subsonic flow in a duct. The mechanism is more complicated than the simple discontinuity of a normal shock wave. A gradual transition from supersonic to subsonic flow is obtained in ducts. The discrepancy from a normal shock is due to the boundary layers at the walls of the duct, in which the flow is retarded by viscous actions.

Assuming a uniform inlet flow distribution, the boundary layer starts growing at once at the duct inlet. The longer the pipe, the more the boundary layer develops, until it fills the whole section of the duct. The uniform core decreases at the same time and finally disappears. The flow is now in the fully developed pipe flow. These effects occur also in pipes with variable area.

The static pressure obtained through a normal shock can only be supported by the boundary layer near Mach 1 (Fig. 2). Otherwise, the change is achieved through a λ -shock. For higher Mach numbers the X-shock extends more and more into the central core of uniform flow and reduces the normal shock extension. Finally the uniform part of the flow is replaced by an X-shock pattern. The multiple shock pattern observed in these cases is due to the static pressure rise difference which exists between the λ -shock and the normal shock in the central core. Restoration of these pressures creates supersonic conditions again, which are favourable for repeating the process and establishing a multiple shock system, called pseudo-shock.

Only for Mach numbers close to unity and thin boundary layers is the normal shock a possible configuration. For higher Mach numbers a multiple shock pattern is produced.

The pseudo-shock losses are produced by the shock pattern and especially by the dissipation process from the central core to the boundary regions. The overall entropy increase is nearly the same as for a normal shock under the same inlet conditions. The static pressure rise approaches the normal shock value.

At subsonic entrance velocities, the boundary layer growth decreases the effective flow area, producing a slow pressure decrease and velocity increase.

The pressure distribution in pipes for different flow rates and specific heat ratios are computed. Figure 3 gives the ratio of static to total inlet pressure as a function of the pipe length and for the flow rates m/m_{is}^* from 1.00 to 0.80. A specific heat ratio of 1.20 is used. There are theoretically three possibilities for a given flow rate, assuming a suitable pipe length: first, a subsonic inlet flow and acceleration up to sonic velocity, causing choking; second, a supersonic inlet flow with a shockless diffusion to sonic conditions (this is more a theoretical case), and finally, a supersonic inlet flow with the shock system (which places the working point on the subsonic curves) producing a possibility of reacceleration of the flow. These observations mean that, when the pipe length is given, depending on the required flow rate, there exists a supersonic diffusion without multiple shocks, a supersonic diffusion with shock system with reacceleration in the subsonic flow part and finally choking due to the sonic conditions at the duct exit. For example, a duct with an $4\bar{c}_f(L/d)$ value of 0.08 can have a slight supersonic diffusion for a $m/m_{is}^* = 0.80$, supersonic diffusion with shock system for $m/m_{is}^* = 0.96$ and a choked flow condition for a 0.98 value of m/m_{is}^* .

A few remarks must be made on the use of these diagrams. The choice of a suitable and realistic value of \bar{c}_f is very important in relation to the experimental data; also, in the case of a shock system a different value of m/m_{is}^* has to be used in the subsonic flow régime compared to the initial supersonic inlet value. This is because the initial total pressure is taken as reference throughout the whole process, which would give higher static pressure ratios than the normal shock at the same Mach number. The relation between the two values of m/m_{is}^* is presented in Figure 4. The calculations of these theoretical curves was based on the theory developed in Section B of Reference 7.

2.2 Flow in P-A Power Family Ducts

The actual passage used in the rotor is not a constant-area duct. Therefore, some observations on ducts with variable area must be made. A variation of cross section would have no effect on a normal shock, which is a purely local phenomenon, due to its extremely small thickness. A pseudo-shock, with a finite axial extension, is of course affected by area changes.

In the case of ducts of the P-A power family, defined by

$$pA^{\epsilon/(\epsilon-1)} = \text{constant}$$

the conditions before and after the transition process can be correlated in a similar way as for the constant-area duct. In fact $\epsilon = 1$ gives a constant area duct and $\epsilon = 0$ a constant pressure duct. Cases of arbitrary area variation cannot generally be solved, but a result can be obtained by numerical integration.

The variation of the static pressure ratios and area ratio with Mach number are presented in Figure 5. The parameter between the pressure and area distribution curves is ϵ . The assumption of pseudo-shocks is made and the example is calculated for a specific heat ratio of 1.20. The values of $P_2/P_1 > 1$ have a physical meaning, as otherwise they correspond to an entropy decrease. For a divergent duct, $\epsilon < 1$, a pseudo-shock is already possible at $M < 1.0$, giving a static pressure increase. This would be impossible for a constant-area duct or if the pseudo-shock consisted of a normal shock. Calculations of the curves presented in Figure 5 are based on the formulae developed in Section B of Reference 7.

2.3 Flow in Sudden Area Enlargements

A second feature of the actual passage is the dump diffusion caused by a sudden area enlargement. Calculation of the static pressure rise and Mach number after complete mixing and the total pressure ratio through the dump diffusion process is by the method of Reference 10. The calculation of these parameters was performed for $\gamma = 1.40$ and 1.20 in the case of subsonic and supersonic inlet velocities at the sudden area enlargement. In the case of supersonic inlet velocities at the sudden area increase (or correspondingly at the blade passage outlet) one has an additional variable, i.e. the static pressure ratio in the dump diffusion process.

From these data the total pressure loss coefficient can be calculated and is presented in Figure 6 for $\gamma = 1.40$. Concerning the influence of γ , higher shock losses and lower dump diffusion losses are observed for $\gamma = 1.20$ compared to $\gamma = 1.40$. The static pressure ratios achieved in the dump diffusion and through a normal shock are smaller for $\gamma = 1.20$.

In Figure 6 the dump diffusion loss coefficient is presented for a sudden area enlargement, as encountered at the rotor mid-section. The region under the line AB represents points with a higher than normal shock static pressure rise. Supersonic outlet velocities should be avoided to keep losses low, except if a very high static pressure rise can be achieved.

The influence of the variation of the area ratio is shown in Figure 7 for the subsonic and supersonic velocities. A rapid increase of the losses with A_2/A_1 is seen.

It is evident that the conclusion on the necessary static pressure rise for better efficiency has to be seen also from the point of view of pipe flow and pseudo-shock location, which is closely related to the back pressure imposed.

2.4 Application

Normal shocks are observed in rectangular ducts up to a Mach number of 1.20. Thereafter, the bifurcated shock appears with a multiple shock system ($M = 1.45$) and, at Mach numbers of the order of 1.80 with thick boundary layers, the X-type pattern is observed.

A qualitative picture of the static pressure variation along the duct axis is given in Figure 8. As the back pressure increases the static pressure rise starts earlier in the duct; the extension of the pseudo-shock system is decreased and the

maximum obtainable pressure rise increases. The maximum static pressure is observed for an unstarted flow in the duct and corresponds almost to the normal shock value. The pressure decrease, once the maximum static pressure is reached, is due to the boundary layer growth in the subsonic flow case, as mentioned in Section 2.1. The flow behaves exactly as predicted in Figure 2, the supersonic diffusion (as seen in the lower common curve) and the subsonic reacceleration (the upper curves). The extension of the shock system as a function of its starting point (related to the applied back pressure) is obtained from experiments and is shown in Figure 9. A shock length of 6 to 8 diameters is observed in the Mach number range from 1.7 to 2.2; but, due to the back pressure, this required length can be reduced to 4 diameters with the shock starting point located at 2 diameters from the duct entrance⁶.

The blunt trailing edge blade passage, used for the supersonic compressor, has a length to width ratio of 6.17, based on the length of the mean camber line at mid-radius. A rectangular passage of 3.0 cm height and 2.6 cm wide is achieved, the equivalent cone angle of the passage considered as a diffuser is 3° divergent. The blade wedge angle is 8° , the maximum blade thickness is at 100% of x/c (Fig.1) and the camber angle is 32° at mid-radius.

This type of blade is a result of the realization of pipe flow based on the constant-area duct, corrected to obtain a divergent passage to avoid starting problems and to compensate for boundary layer growth in subsonic operation. At the same time it provides a wider and better operating range, as seen in Section 2.2 but increases the loss level and furnishes an additional static pressure rise in the dump diffusion process downstream of the passage (Section 2.3).

3. EXPERIMENTAL RESULTS

3.1 High Speed Cascade Investigation

A cascade investigation on the rotor mid-radius blade section at Mach numbers of 1.45 and 1.67 was carried out. The main parameter was the back pressure, as will be shown.

The static pressure distribution for a Mach number of 1.45 and an incidence angle $i = 4^\circ$ demonstrates the influence of the back pressure on the shock pattern inside the passage. Maximum back pressure in Figure 10(a) gives an unstarted flow, and Figures 10(b),(c) and 11(a),(b),(c) are obtained with further decrease in back pressure. The distributions of Figures 2 and 8 are found again. An accelerated flow is observed at the minimum back pressure case of Figure 11(c) and the pseudo-shock is outside the given geometrical passage length. At the maximum back pressure the pseudo-shock is expelled from the passage (Fig.10(a)). No starting difficulties were observed during the cascade operation.

The corresponding schlieren pictures show the multiple shock system, which starts with a normal shock bifurcated at the ends. One has to allow for a supersonic entrance region where oblique shocks are formed on the blade leading edge and reflected on the blade suction surface. Figure 10(a) shows that a shock system is possible inside the blading at Mach numbers smaller than one for a diverging passage, as anticipated in Section 2.2.

The static pressure ratio obtained, including the dump diffusion, was 2.20 for $M = 1.45$ and 2.42 for $M = 1.67$.

An increase of incidence angle increases the distance at which the first oblique shock hits the suction surface and reduces the available length for the pseudo-shock, which results in a smaller static pressure rise inside the passage. No influence is observed in an incidence range from 0° to 7° .

The total pressure losses are high and decrease rapidly with increase of back pressure. A fairly large amount of the overall losses is introduced by the dump diffusion. In Section 3.3 the losses are compared to the rotor and low speed data and an analysis is made of the relative importance of shock, profile and dump diffusion losses.

3.2 Rotor Tests

The 40 cm tip diameter wheel had a constant hub/tip ratio of 0.85 and a blade solidity of 3.16 at the mid-radius. A blade inlet angle of 61° , a stagger angle of 45° and a camber of 32° is achieved at the mean section. The sudden area enlargement at the passage exit is 1.37. The rotor consisted of 32 passages (Fig. 20).

The design speed was defined for an axial inlet Mach number of 0.80 and a relative inlet Mach number of 1.70 at the tip radius, which gives 22,760 r.p.m. $= N/\sqrt{\theta}$ in air.

A length/width ratio of 6.17 and an equivalent cone angle of 3° is obtained for the passage; this gives an outlet to inlet passage area ratio of 1.32, measured perpendicular on the mean camber line.

The downstream traverses are done one axial chord (8 cm) downstream of the rotor.

The maximum mass-averaged values of the total and static pressure ratios and the adiabatic efficiency, converted into air equivalent values, are presented in Figure 12. The full supersonic operation starts around $75\% N_d$, while Mach numbers high enough to obtain a multiple shock system are reached around $85\% N_d$. A much steeper increase in static pressure ratio is also noticed there. The adiabatic efficiency compares favourably with other supersonic designs, excluding impulse rotors.

A slight instability was observed near sonic operation, where the normal shocks are in front of the leading edges. Instability, accompanied with a high vibration level, was also observed at a given throttle setting in the 85% to $92\% N_d$ range when increasing the throttle from minimum to maximum. It is assumed that it corresponds to the transition from pseudo-shock outside towards the shock system inside the passage when increasing the back pressure.

An example of the variation of the local parameters as measured in a mixture of freon 12 and air, is a test at 88% of the nominal speed. Different throttle valve settings are represented. The local maximum value of total pressure ratio and adiabatic efficiency change from hub to tip region as the throttling increases (Fig. 13). The outlet flow diagram (Fig. 14), in the form of a vector diagram, shows the axial Mach number (M_{Ax}) distribution as influenced by an increase in total pressure ratio. Absolute outlet angles α_2 and Mach numbers M_2 show a small

influence on M_2 and a serious redistribution of α_2 . It is clear that, although the blade height is small, the passage cannot be treated as a two-dimensional one.

Overall static pressure ratios, from hub to tip radius, are well above the normal shock values at high compression ratios, because they include the dump diffusion static pressure rise. The almost horizontal distribution at the higher N_d values is found again when applying a lower back pressure. A reason for this can be that the Mach number is high enough at the tip to have a shock system with a certain axial extension, while at the hub a normal shock exists. This gives, when seen section by section, a gradual pressure rise at the tip and a more abrupt pressure rise at the hub, followed by a reacceleration as occurs in a subsonic flow in ducts. This will result in a change of the spanwise pressure distribution inside the passage and explains the lower than normal shock value observed at the tip radius for 92% N_d . At higher inlet Mach numbers, where the pseudo-shock system is established over the whole blade height, a further important increase in the static pressure distribution is expected, which should confirm the trend of the curve in Figure 12.

During the cascade investigation, a lower than inlet static pressure could be obtained at the passage outlet, due to the equivalent effect of a too short pipe for the back pressure applied. Similar behaviour is observed in the rotor (Fig. 17), where the pressure distribution was measured on the hub casing at different downstream locations. It confirms the cascade tests and principle of pipe flow on which the design is based.

3.3 Comparison of Low Speed and High Speed Data

The mid-section of the rotor was tested in a very wide Mach number range in rotor and cascade configurations. The low speed data were obtained in a two-dimensional cascade model and as mid-section performance of a scaled-down rotor model tested in water. From $M = 0.60$, the mid-section performance of the rotor as tested in the freon 12-air mixture is used and is completed with high speed cascade data up to $M = 1.50$ (Fig. 18).

The stalling incidence i_g decreases with the Mach number and reaches a minimum value around $M = 1.0$. Thereafter higher incidences can be allowed as the Mach number increases. The discrepancy between the experimental points and the limit for an attached shock is probably due to the formation of a bow wave.

The losses $\bar{\omega}$ can be divided in shock losses ($\bar{\omega}_s$), profile losses due to friction in the passage ($\bar{\omega}_p$) and dump diffusion losses due to the sudden area enlargement ($\bar{\omega}_d$).

The losses are presented as a function of the static pressure rise realized with the relative inlet Mach number as parameter. The losses measured in the high speed cascade are also added in Figure 19. The shock loss variation as presented is corrected for the higher than inlet Mach number which occurs at the shock location due to the blade curvature. The $\bar{\omega}_d$ are the values obtained from calculations (Fig. 6) and used for the minimum loss point of the curve. By subtraction, a constant profile loss of 5% is found. The minimum diffusion loss coefficient varies between 5% and 15% when sonic velocity is approached at the passage outlet. The discrepancy between rotor and cascade data for what concerns the minimum loss line is due to the margin which is left to keep the rotor out of stall and surge.

The detailed investigations of rotor and cascade are presented in References 9, 10, 11, 12 and 16.

4. CONCLUSIONS

- (i) The concept of using pipe flow to obtain supersonic diffusion in rotors is confirmed.
- (ii) The back pressure plays an important rôle, deciding whether or not the shock system will be inside or outside the passage.
- (iii) Although the losses are high, a reasonable efficiency is obtained because of the high work exchange.
- (iv) Considerable static pressure ratios are obtained by the combined effect of pipe flow and dump diffusion.
- (v) The accelerating or decelerating mode of operation, as found in cascades, is confirmed in the rotor tests.
- (vi) An improvement of the design must be based on a wider exploration of the possibilities of pipe flow in variable-area ducts and on a variation of the sudden area enlargement at the rotor exit, to optimize static pressure increase, outlet flow and the overall loss coefficient.
- (vii) The analysis made of pipe flow and sudden area enlargement and experimental results show that improved design will be towards a smaller sudden area increase and less turning at the tip of the blading.

ACKNOWLEDGEMENT

The work reported in this document has been sponsored by the Office of Aerospace Research (OAR) under grants AF EOAR 63-84/64-4, through the European Office of Aerospace Research (EOAR) of the United States Air Force.

REFERENCES

- 1. Kantrowitz, A. *The supersonic axial-flow compressor.* NACA ACRL 6-DC, April 1946.
- 2. Graham, R.C.
et alii *Investigation of off-design performance of shocks in rotor-type supersonic blading.* NACA RM E51C22, 1951.
- 3. Fejer, A.A.
Wenzlau, W.D. *Supersonic cascade studies.* University of Toledo, TR AE 1, June 1951.

4. Beder, E.
Buhler, R.D. *A study of a cascade system for supersonic flow diffusion.* Wright Air Development Center, WADC 54-261, May 1954.
5. Jahnsen, L.J.
Hartmann, L.J. *Investigation of supersonic compressor rotors designed with external compression.* NACA RM E54G27a, July 1954.
6. Johnson, E.G.
et alii *A blunt trailing edge supersonic compressor blading.* Wright Air Development Center, WADC TN 59-269, August 1959.
7. Emmons, H.W. *Fundamentals of gas dynamics.* Princeton Series, Vol. III, Princeton University Press, 1958.
8. - *Characteristics of normal shock waves in the throat of induction systems having precompression inlets.* United Aircraft Corp. Research Laboratories, R 0790-13, 1956.
9. Breugelmans, F. *Preliminary investigation of a blunt trailing edge blade cascade in the S-3 supersonic cascade tunnel.* von Kármán Institute for Fluid Dynamics, VKI IN 8, Jan. 1964.
10. Hermann, P. *Further investigation of a blunt trailing edge cascade in the S-3 supersonic wind tunnel.* von Kármán Institute for Fluid Dynamics, VKI IN 9, June 1964.
11. Breugelmans, F. *Performance of the blunt trailing edge blade rotor R-32.* von Kármán Institute for Fluid Dynamics, VKI IN 12, part 1, March 1965.
12. Breugelmans, F.
Klock, R. *Blade section performance of the blunt trailing edge rotor R-32.* von Kármán Institute for Fluid Dynamics, VKI IN 12, part 2, April 1965.
13. - *ASME Journal of Engineering for Power*, July 1961.
14. Fejer, A.A.
Heath, G.L. *Supersonic cascade studies.* ARL 125, 1961.
15. Fejer, A.A.
et alii *An investigation of constant area supersonic flow diffusion.* ARL 64-31, 1964.
16. Weisbuch, A. *Performances hydrodynamiques à la ligne moyenne d'un rotor d'aubages à bord de fuite épais.* von Kármán Institute for Fluid Dynamics, VKI IN 10, Jan. 1965.
17. Hartmann, M.J.
Wilcox, W.W. *Problems encountered in the translation of compressor performance from one gas to another.* ASME, June 1956.

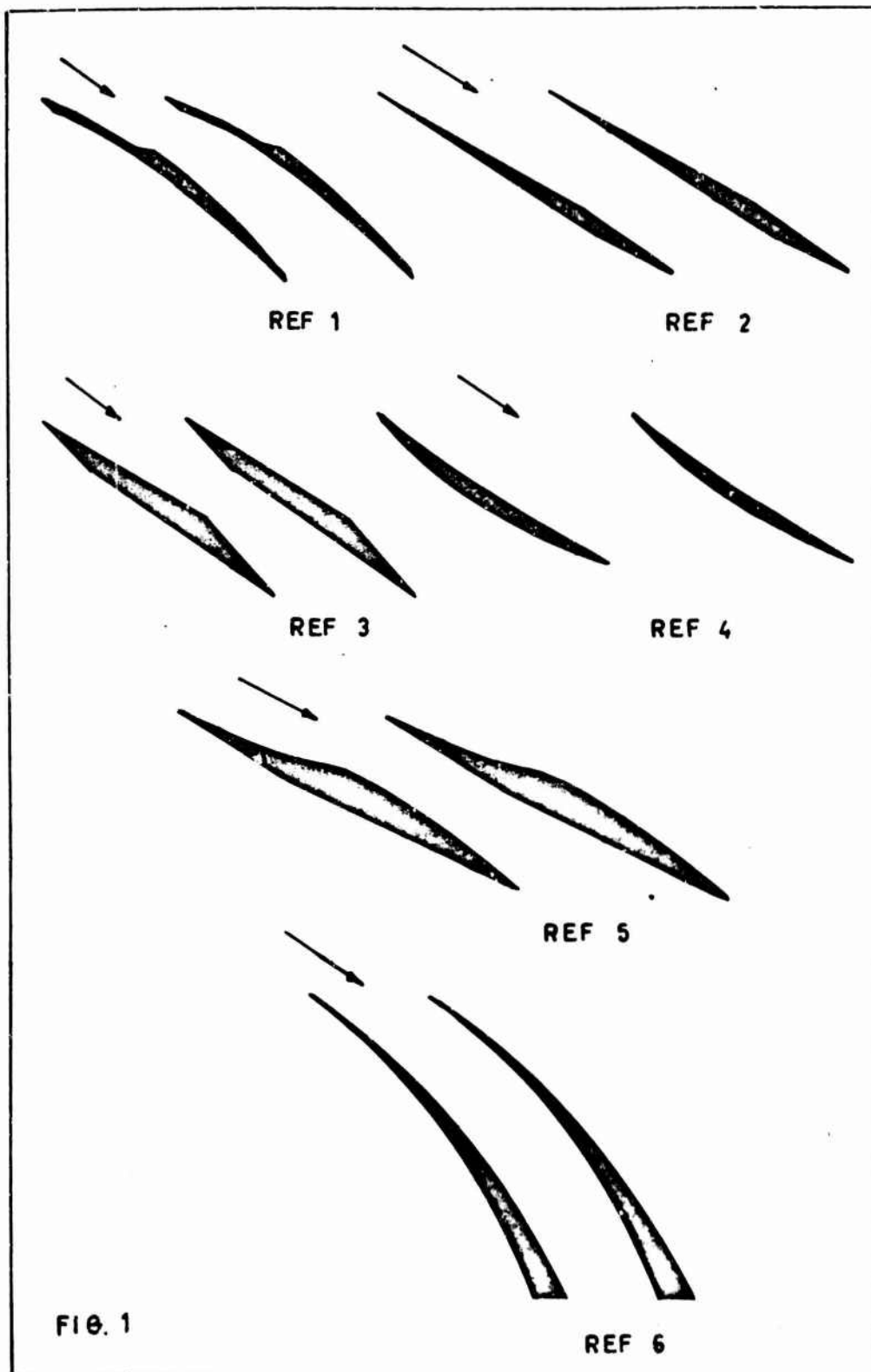


Fig.1 Different types of supersonic passages

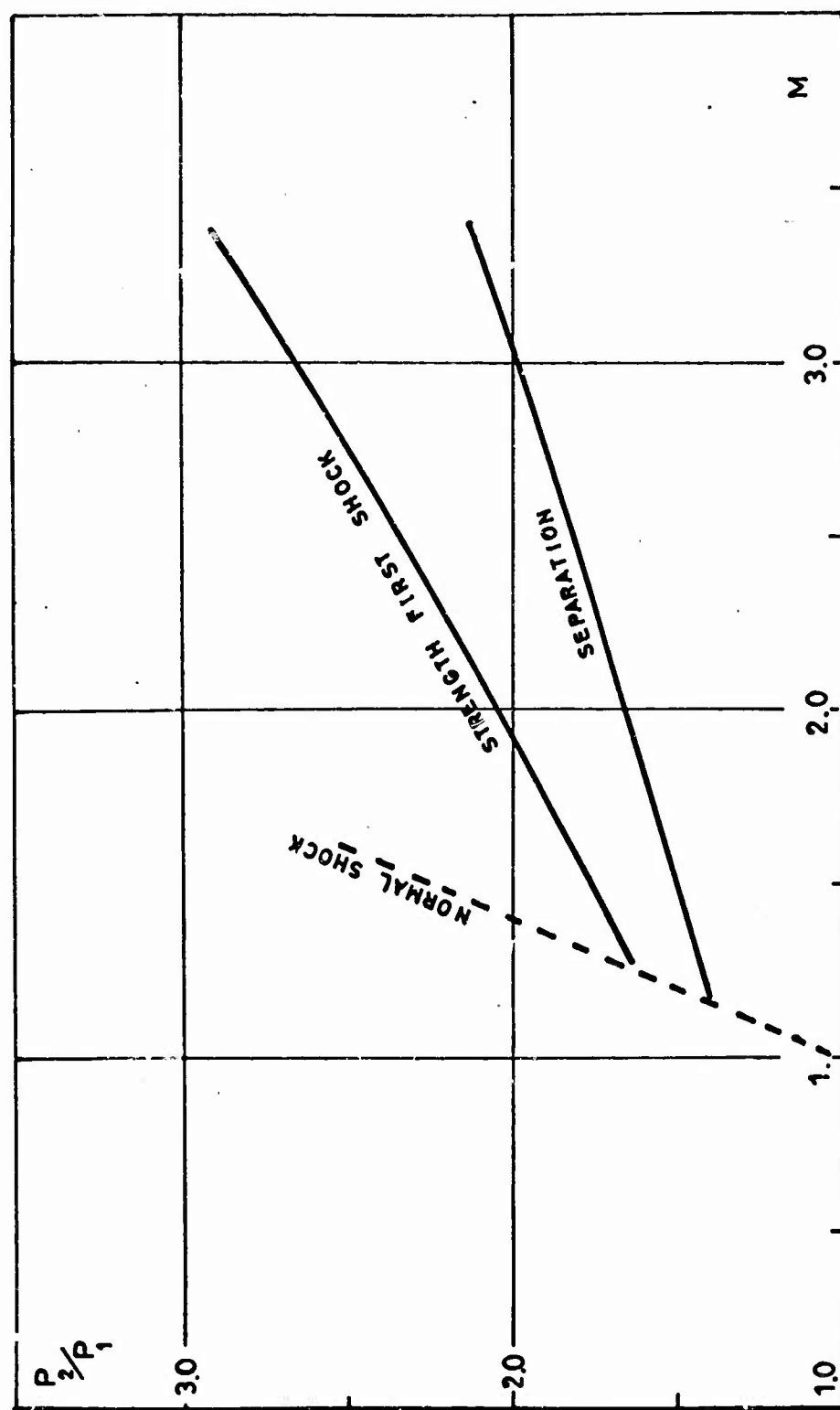


Fig. 2 Pressure ratio through an oblique shock emerging from a turbulent boundary layer

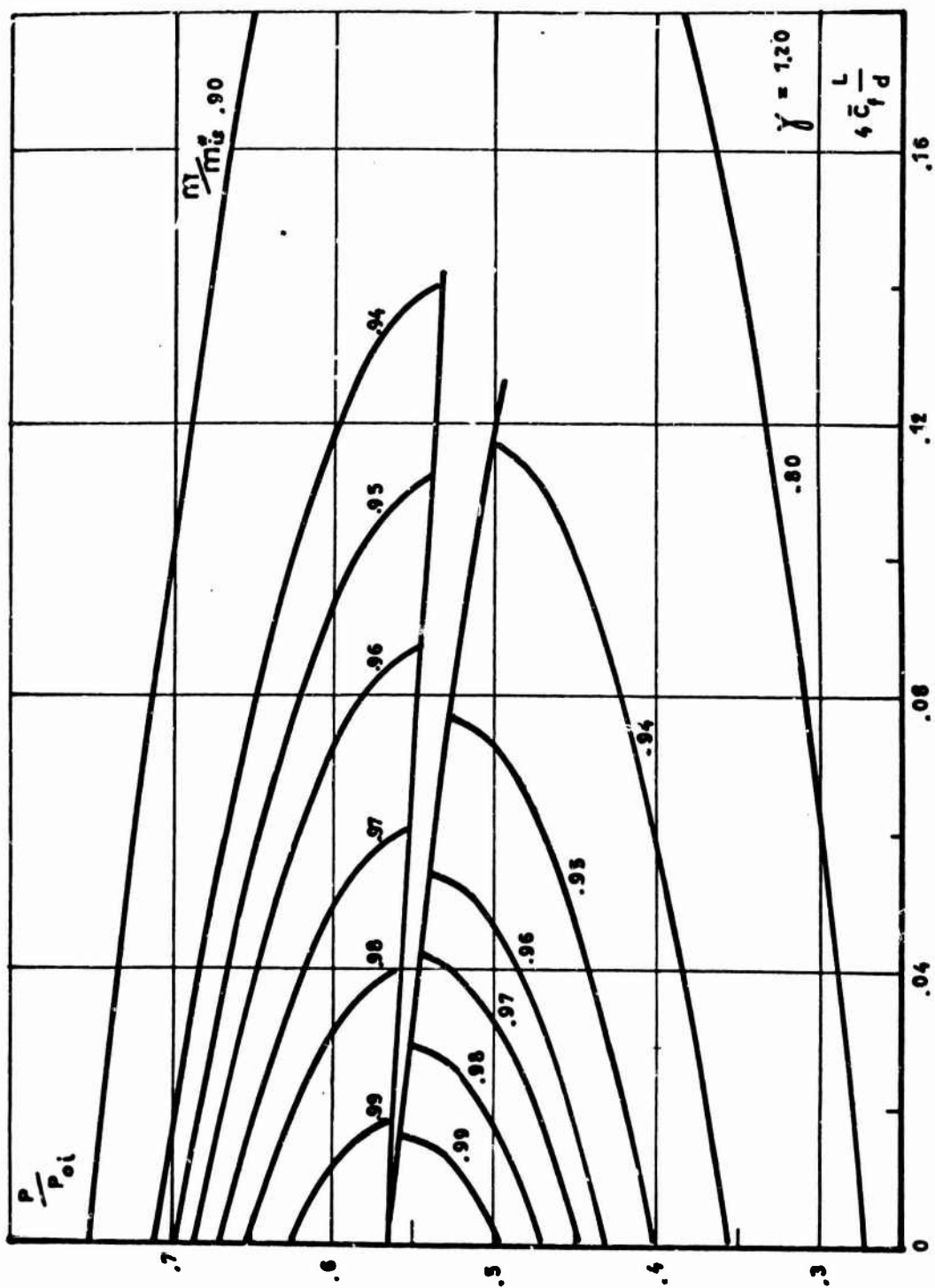


Fig. 2 Pipe flow characteristics

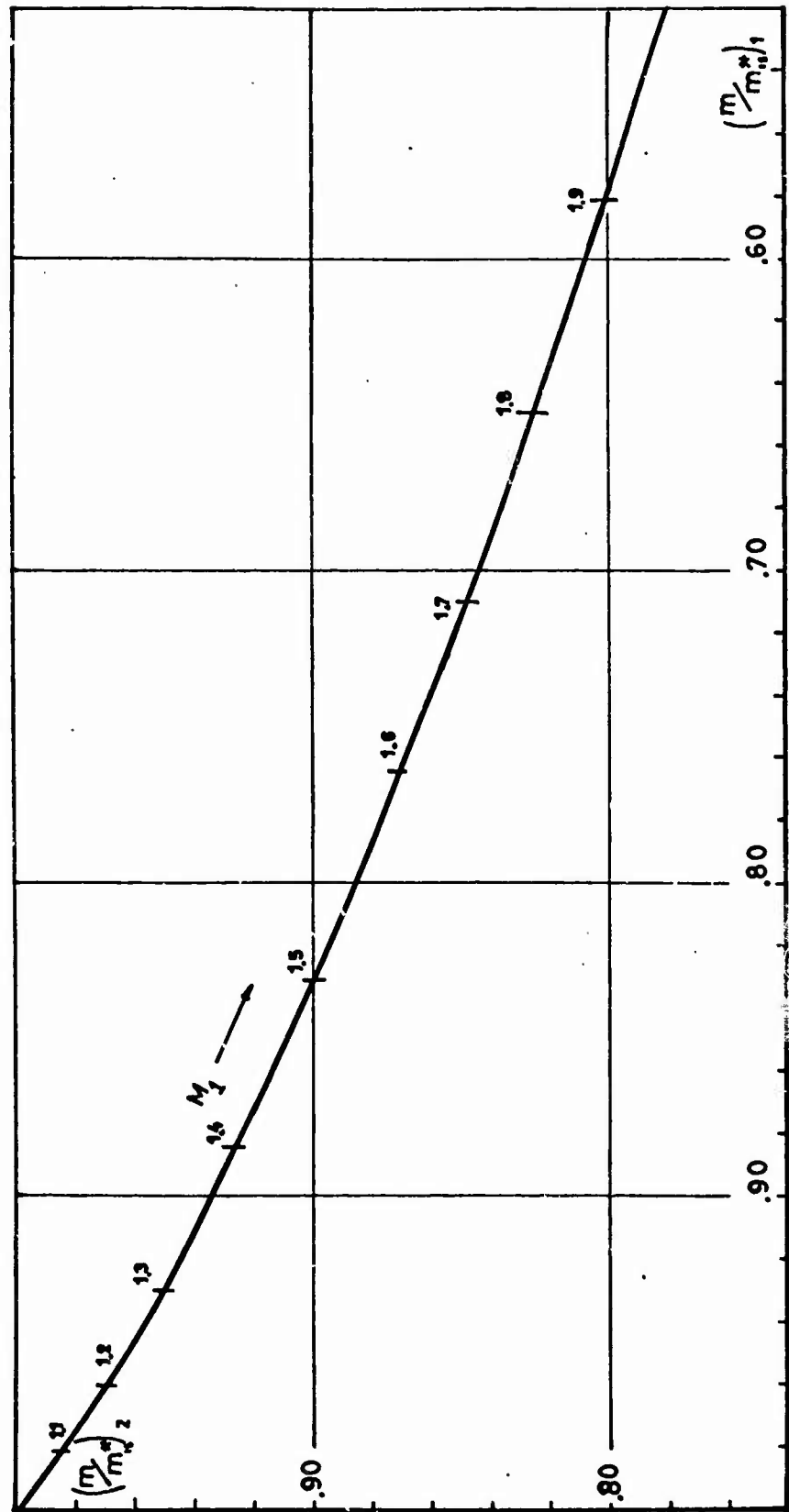


Fig. 4 Relation between mass flow coefficients in front of and behind a normal shock

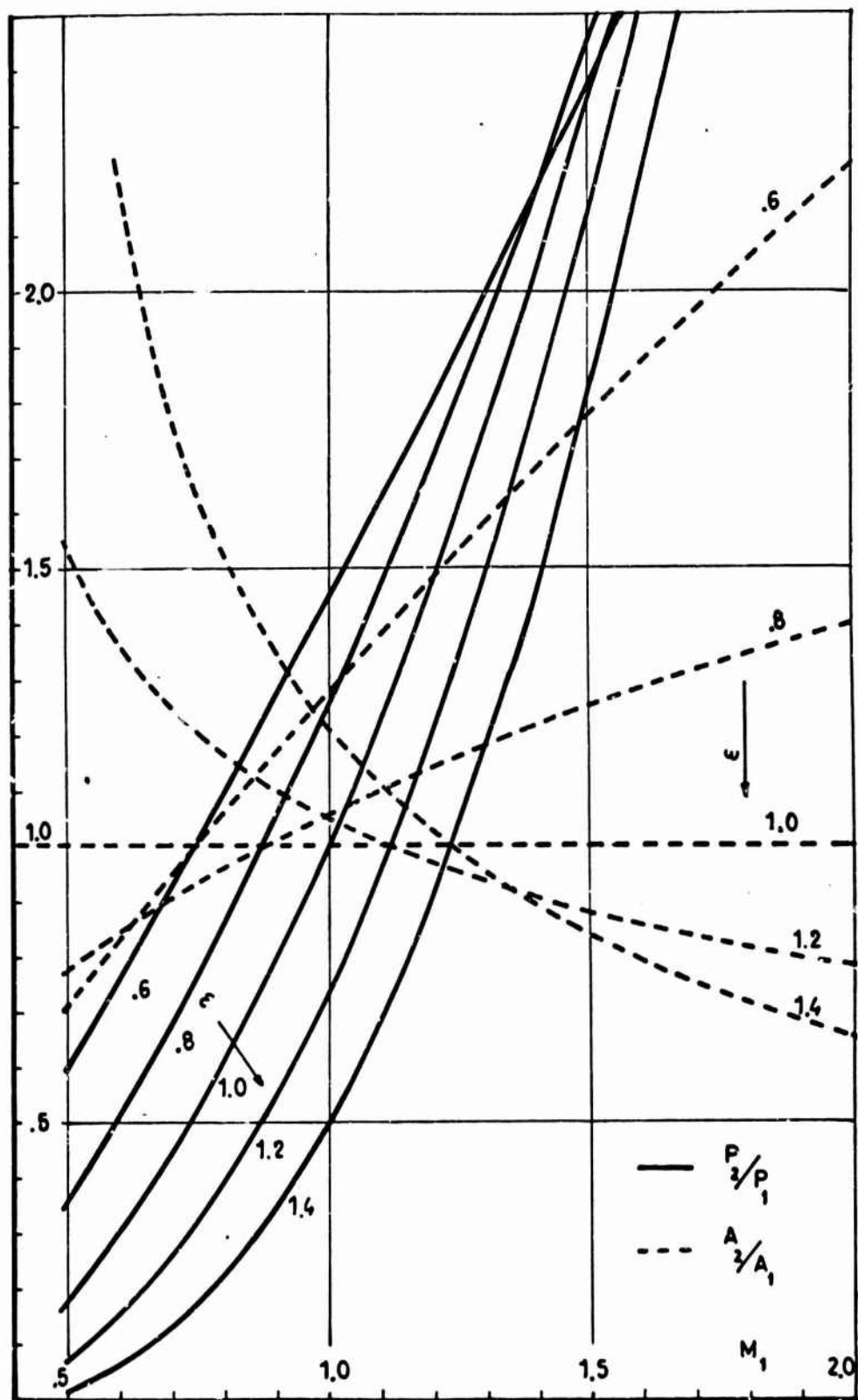


Fig. 5 P-A power family ducts with pseudo-shock. $\gamma = 1.2$

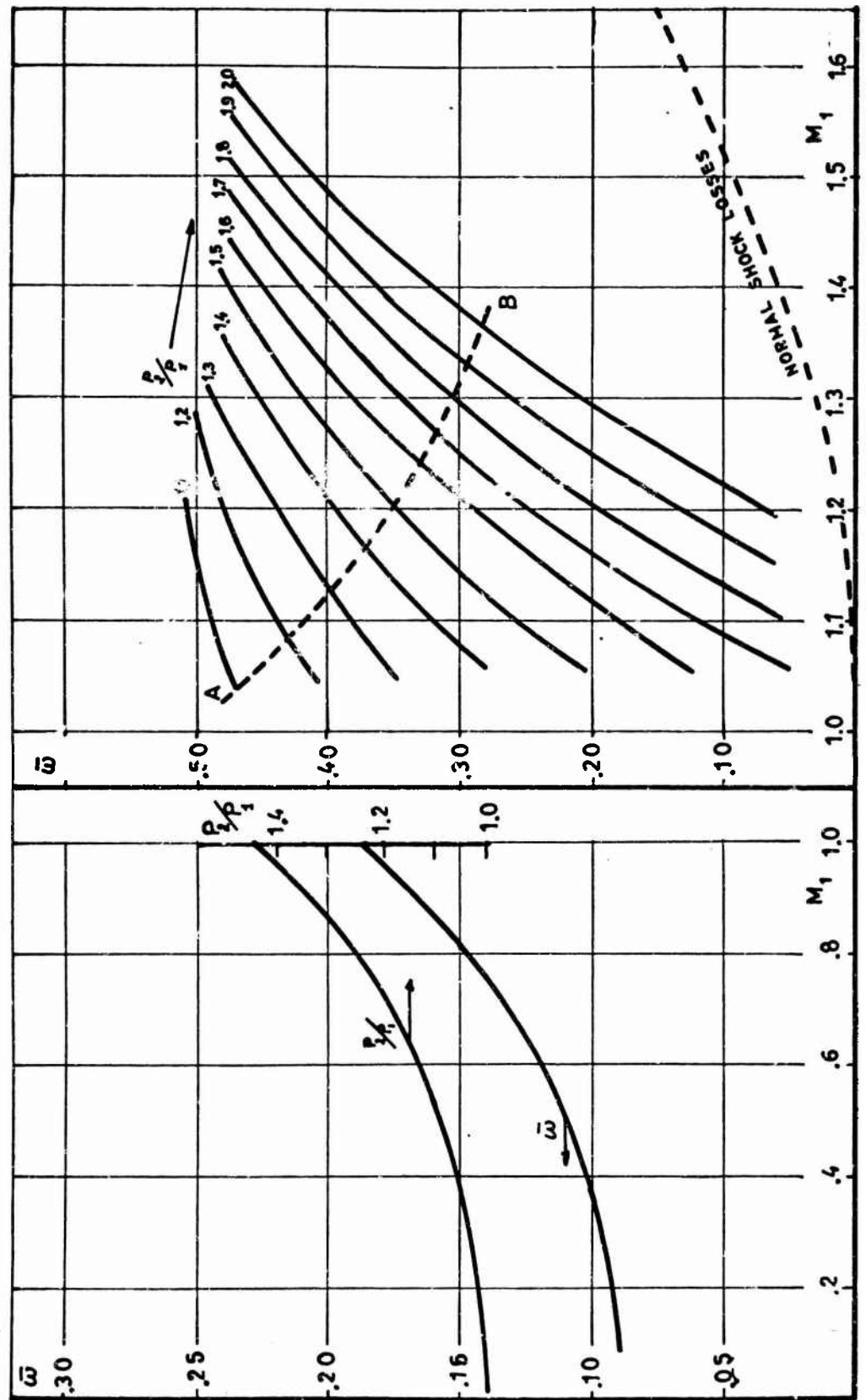


Fig. 6 Dump-diffusion loss coefficient. $\gamma = 1.4$. $A_2/A_1 = 1.37$ (rotor mid-section)

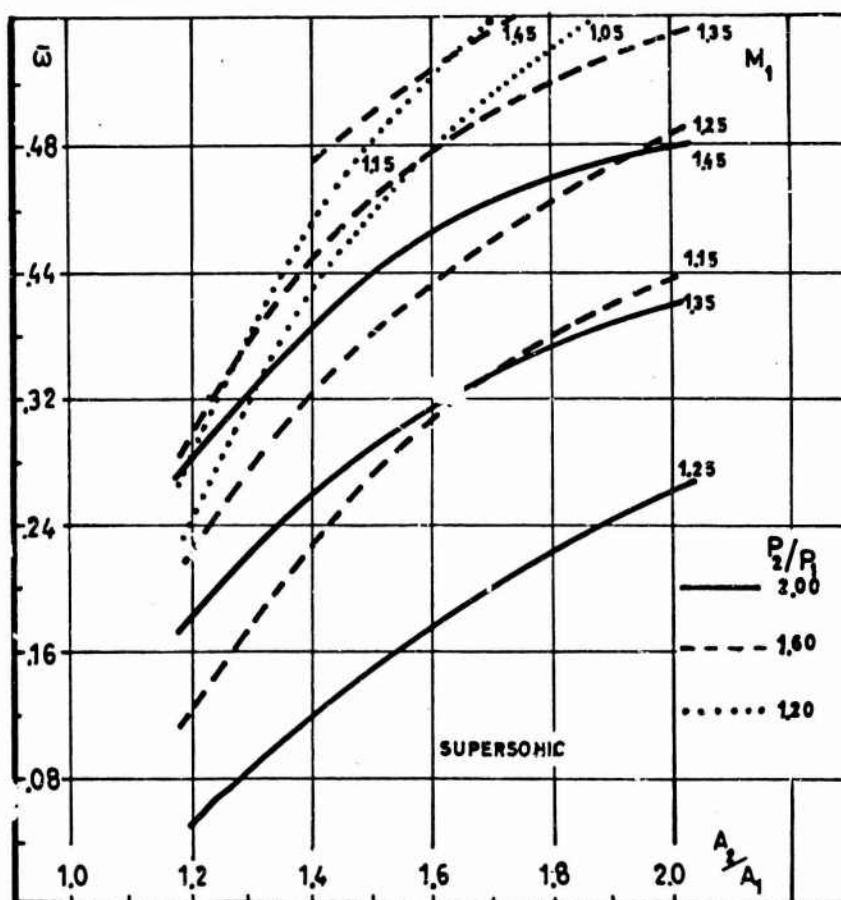
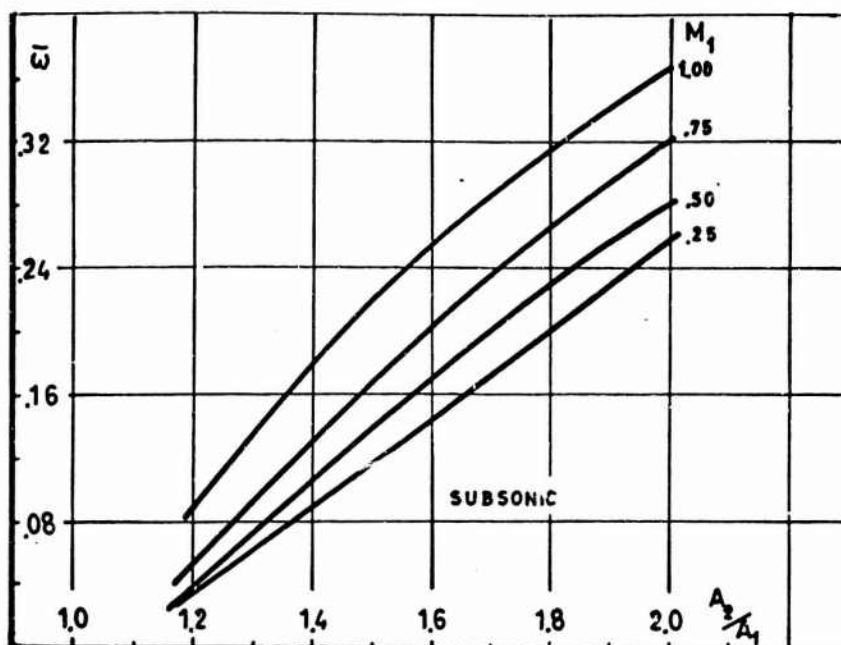


Fig.7 Dump diffusion loss coefficient. $\gamma = 1.4$

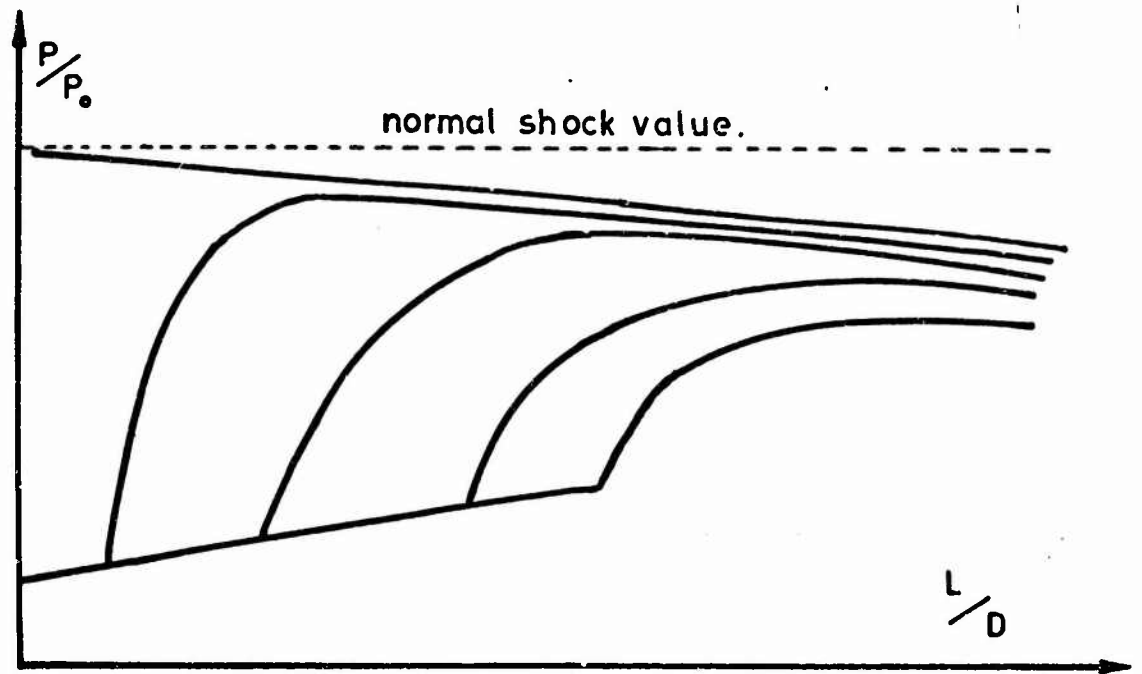


Fig.8 Back pressure influence on P/P_0 distribution

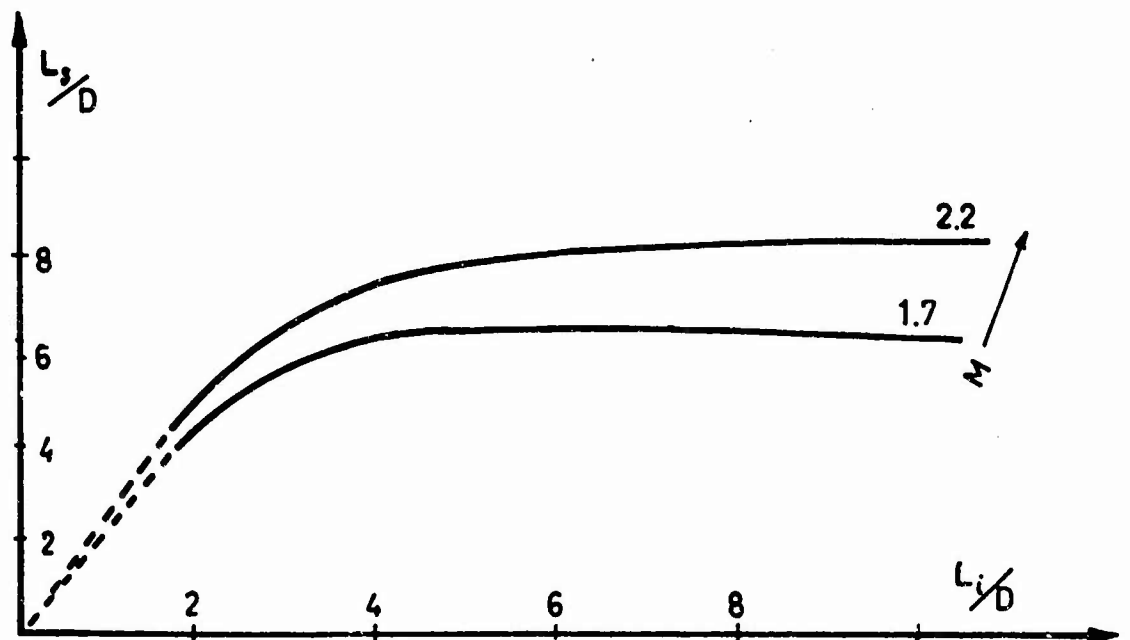


Fig.9 Pseudo-shock length in front of the shock position^a

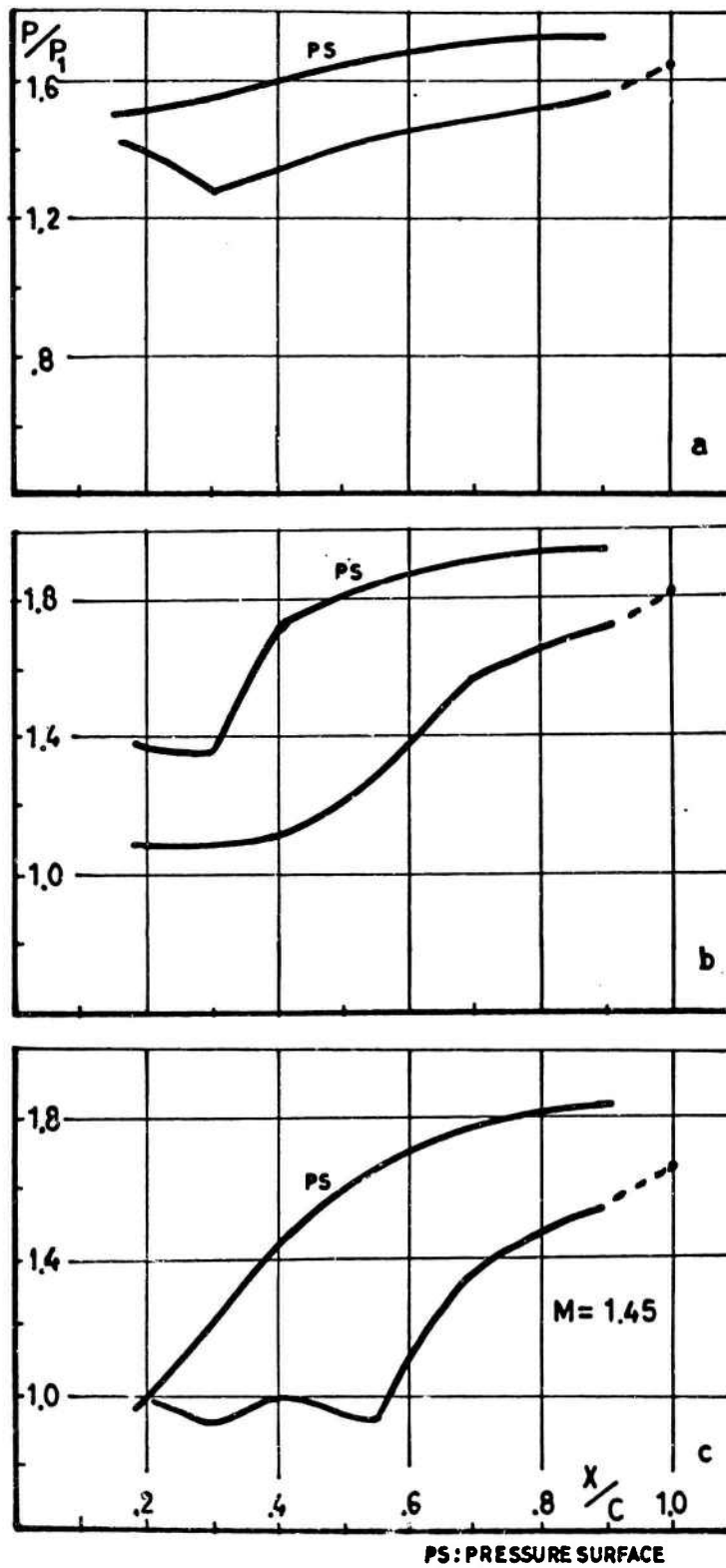
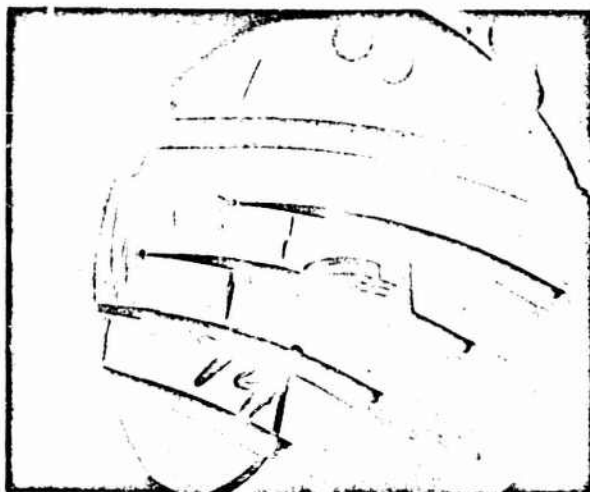


Fig. 10 Static pressure distribution
(The corresponding schlieren photographs are on the facing page)

(a)



(b)



(c)



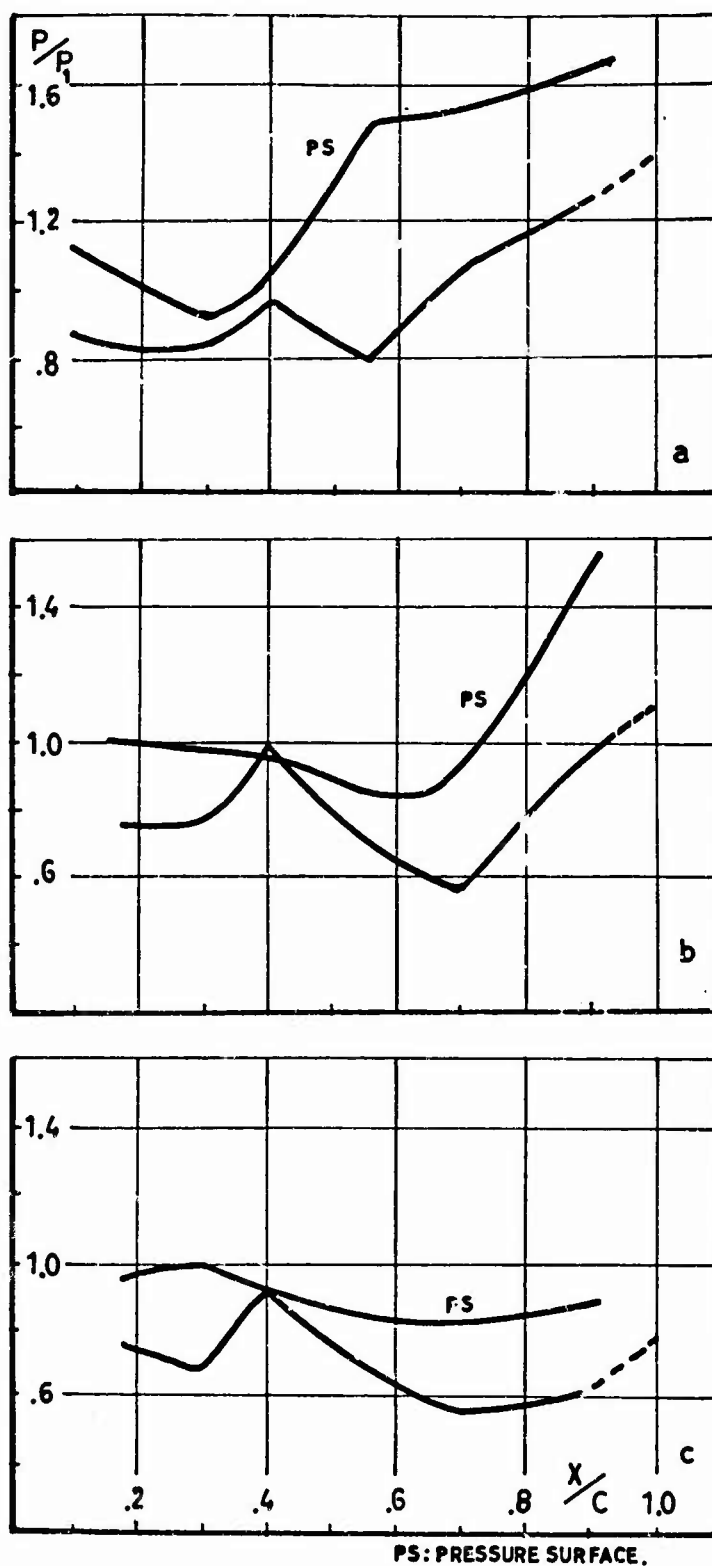


Fig. 11 Static pressure distribution
(The corresponding schlieren photographs are on the facing page)

(a)



(b)



(c)



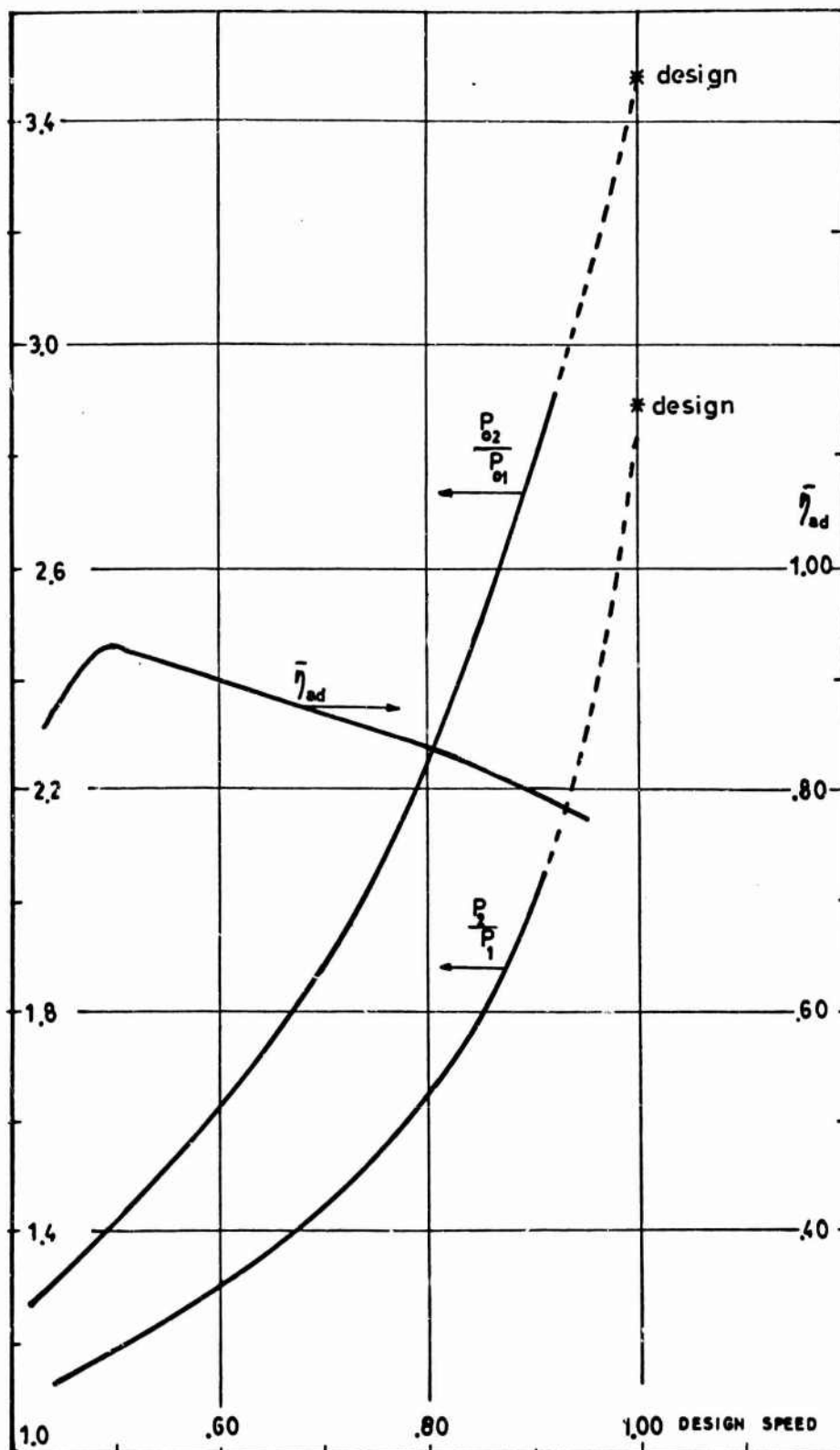


Fig. 12 Maximum mass-averaged rotor performance

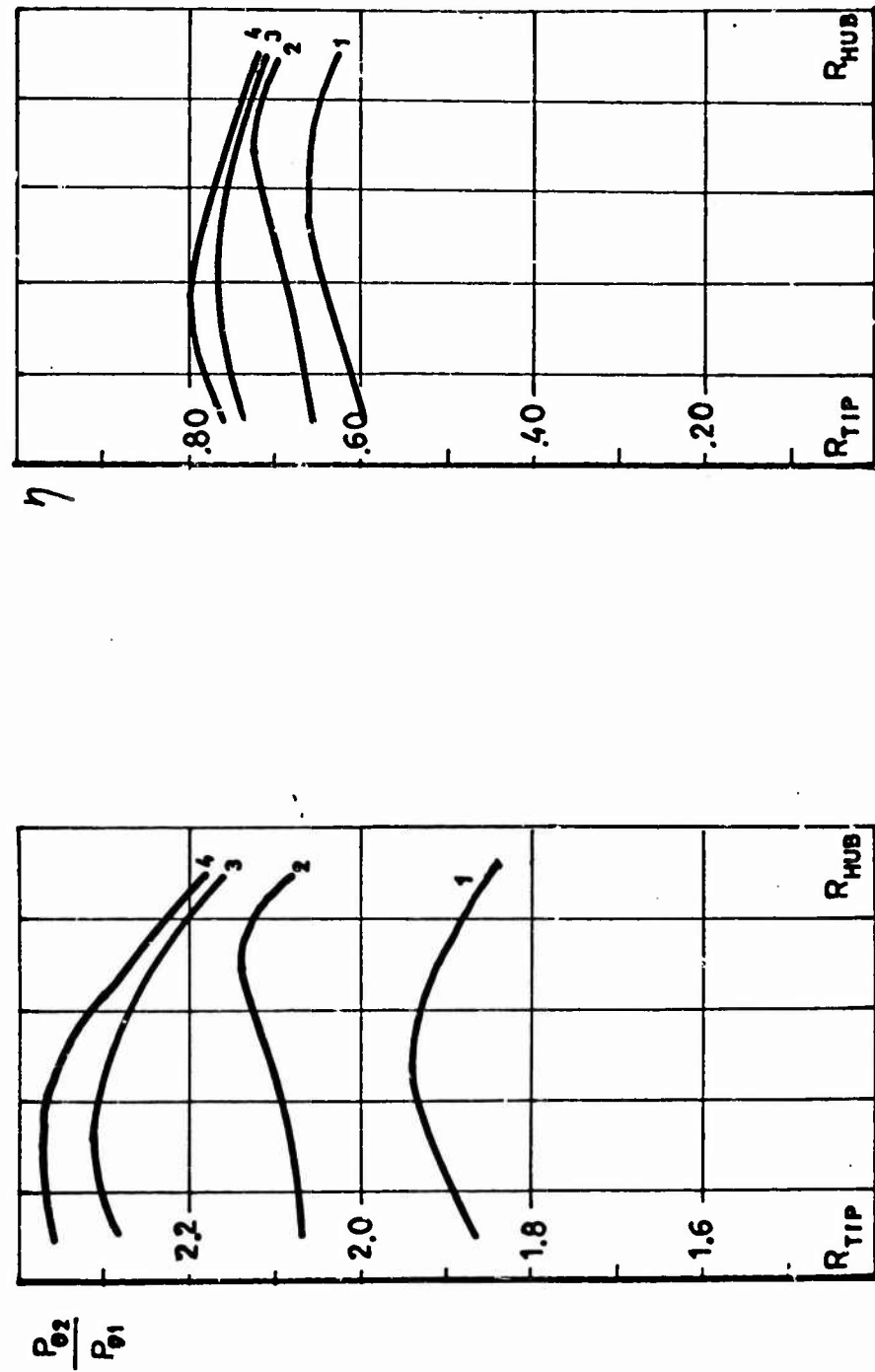


Fig. 13 Local total pressure ratio and adiabatic efficiency (0.88 η_d)

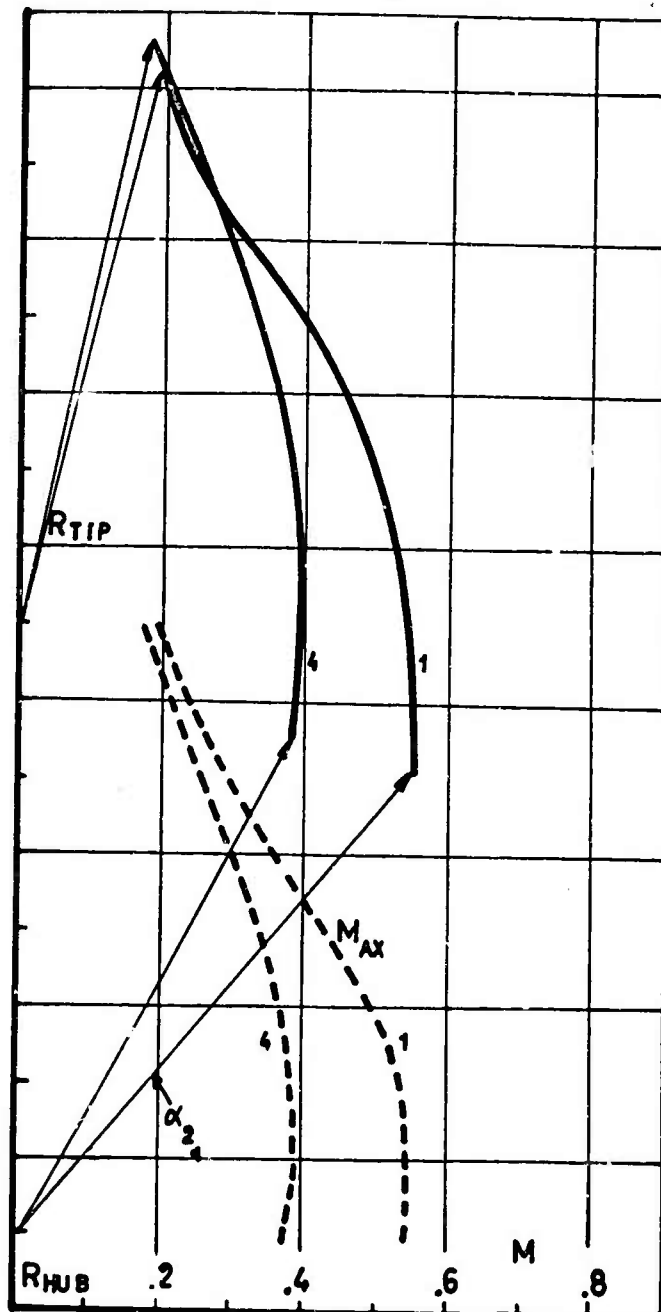


Fig. 14 Rotor outlet flow distribution ($0.88 N_d$)

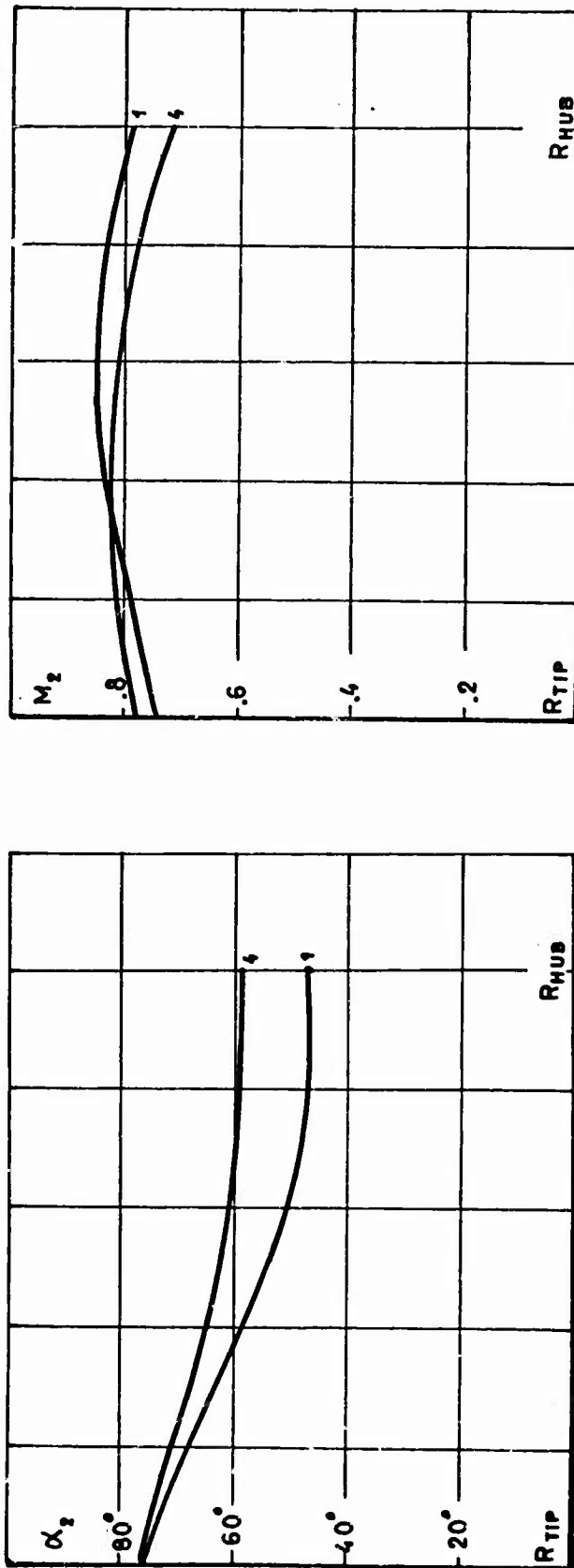


Fig. 15 Absolute flow outlet angle and mach number ($0.88 N_d$)

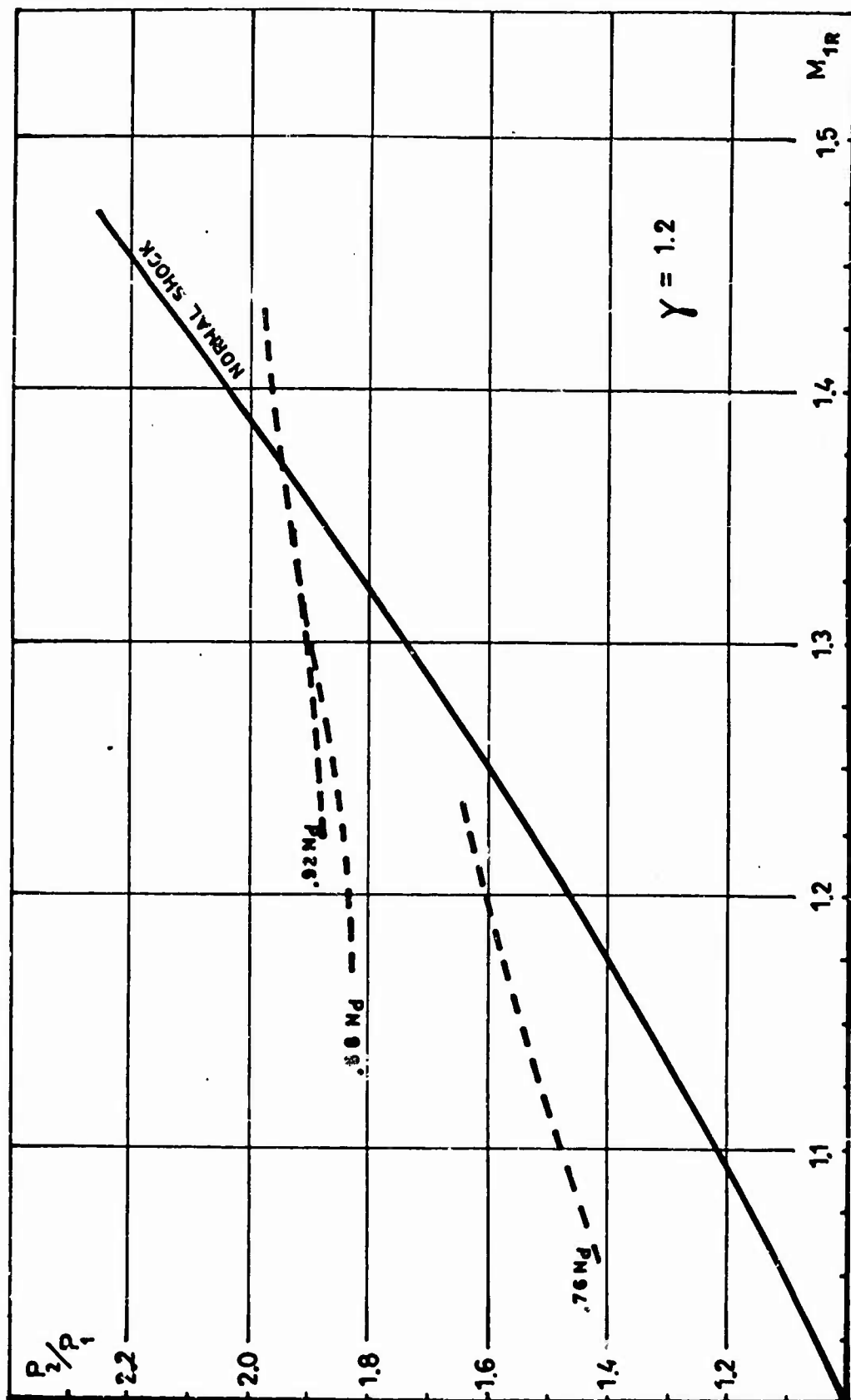


Fig. 16 Radial distribution of the static pressure ratio at full throttle

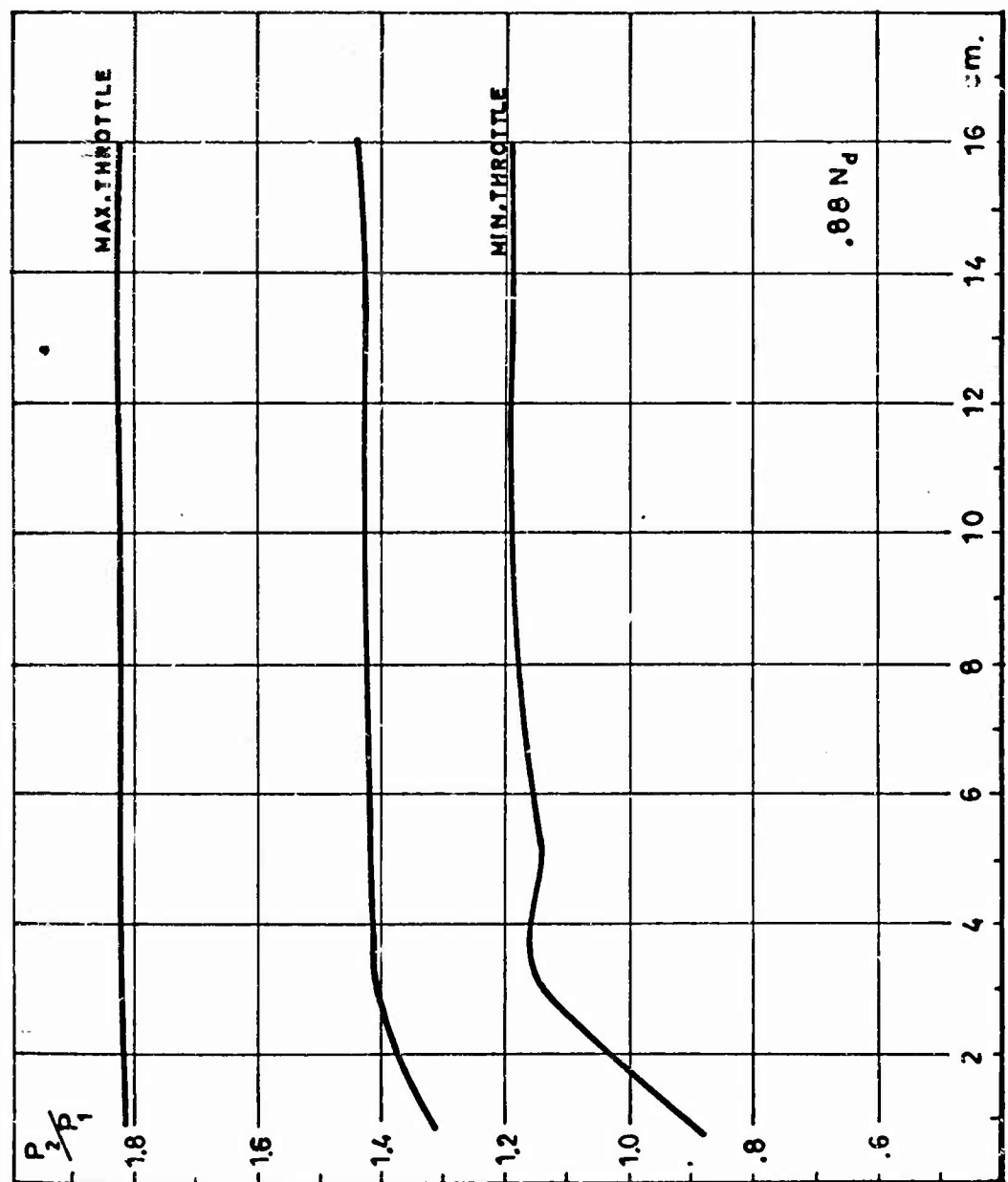
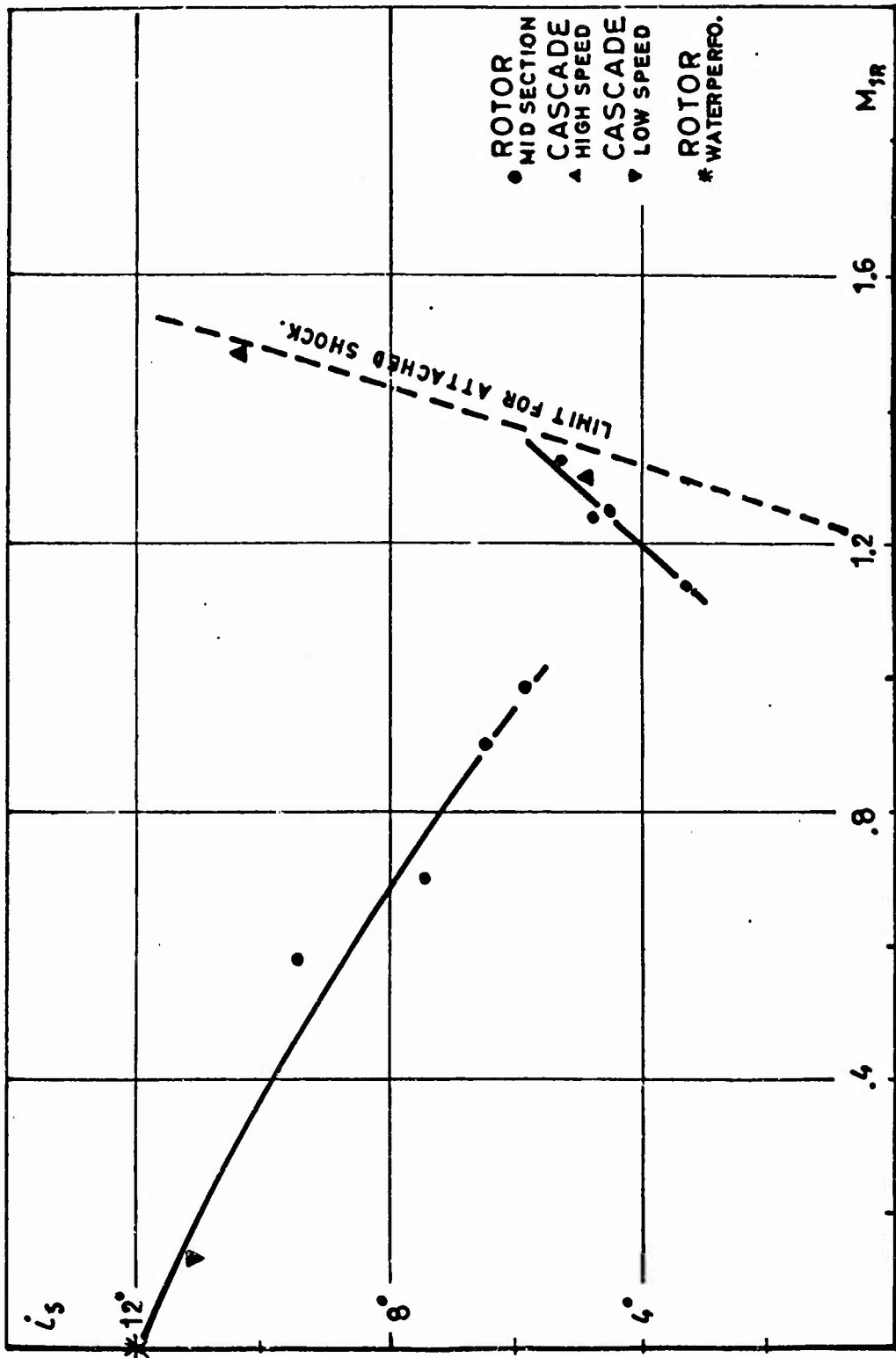


Fig. 17 Static pressure distribution downstream of the rotor

Fig.18 Variation of stalling incidence with M_{1R}

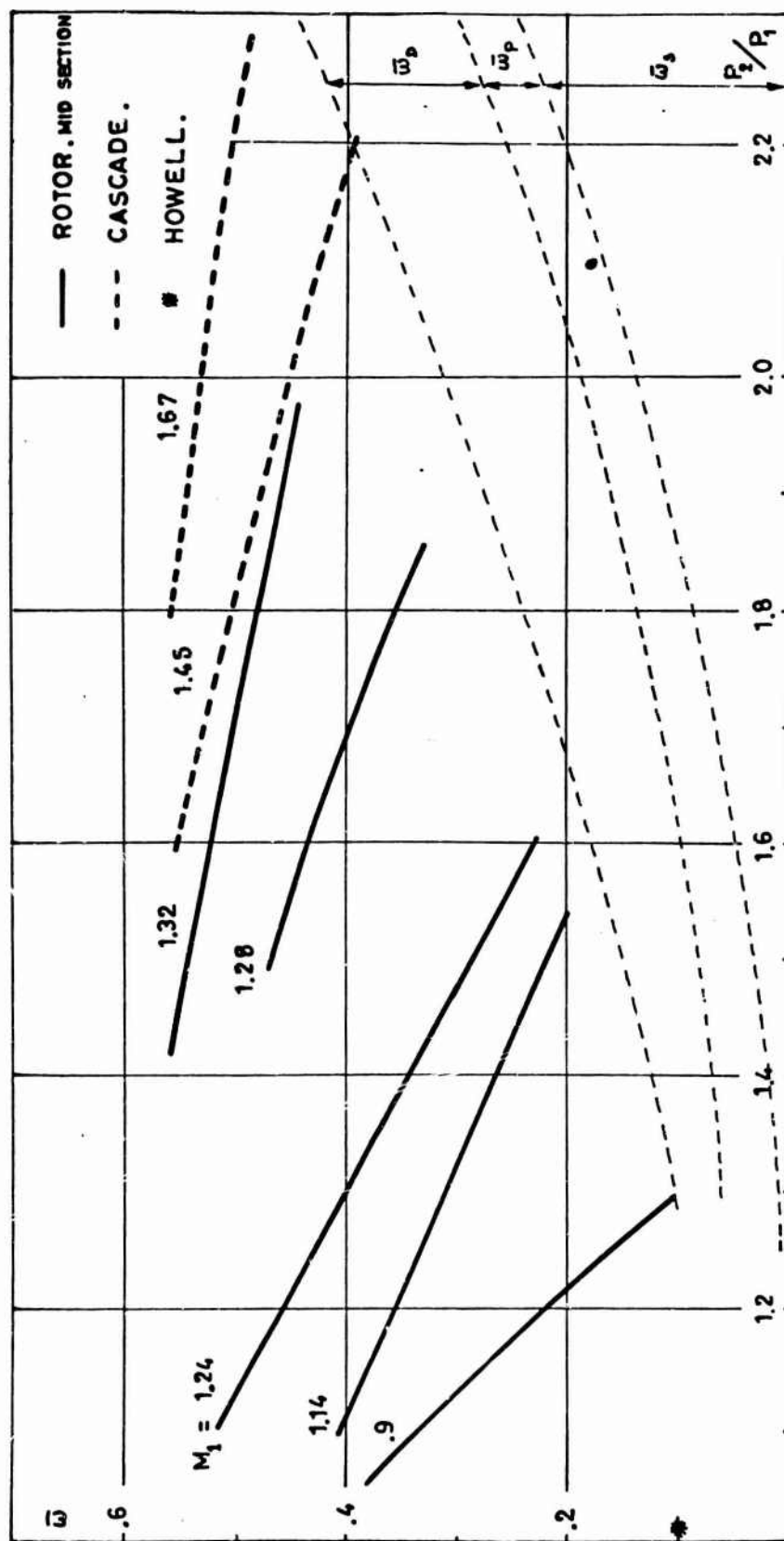


Fig. 19 Analysis of rotor and cascade loss coefficient

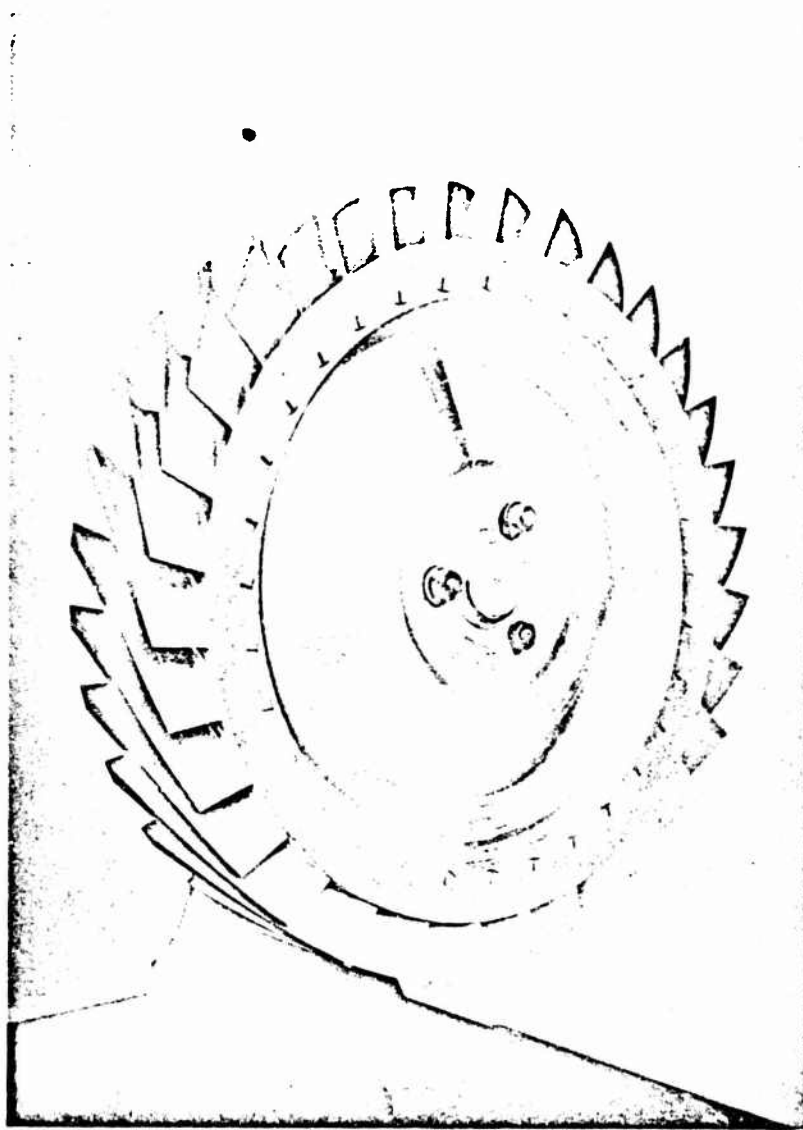


Fig. 20 A rotor consisting of 32 passages

MEASUREMENTS OF RELAXATION EFFECTS IN
NOZZLE FLOW OF HOT COMBUSTION GASES BY
MEANS OF A SHOCK TUBE TECHNIQUE

by

Th. Just

Deutsche Versuchsanstalt
Für Luft- Und Raumfahrt E.V.,
Porz-Wahn, Germany

SUMMARY

The paper describes a modified line reversal technique which permits measurement of temperatures during short time intervals in relaxing nozzle flow. The high temperatures of combustion gases needed were produced by shock-driven detonations in a shock tunnel. Preliminary results are given.

SOMMAIRE

Au cours de cette communication, nous décrivons une technique modifiée du renversement des raies qui nous a permis de mesurer les températures pendant de brefs laps de temps dans un écoulement en cours de relaxation à l'intérieur d'une tuyère. Les températures élevées des gaz de combustion qui étaient nécessaires à l'expérience ont été produites à l'aide de détonations induites par choc dans un tube à choc. Les premiers résultats obtenus sont exposés.

CONTENTS

	Page
SUMMARY	154
SOMMAIRE	154
LIST OF FIGURES	156
1. INTRODUCTION	157
2. EXPERIMENTAL APPARATUS	157
2.1 Shock Tunnel (Detonation Tube, Nozzle and Tank)	157
2.2 Gases Used, Filling Procedure and Injection of Sodium-Containing Salts	158
2.3 The Ignition of Detonations in Section B	158
2.4 Time of Constant Flow	159
3. MEASUREMENTS	159
3.1 Pressure Measurements	159
3.2 Measurement of Temperature. The Optical Arrangement	159
3.3 The Determination of Temperatures at Different Positions Relative to the Nozzle Throat	160
4. CRITICISM OF THE METHOD	163
5. FUTURE PROGRAMME	164
REFERENCES	165
FIGURES	166

LIST OF FIGURES

	Page
Fig.1 Shock tunnel	166
Fig.2 Apparatus for production of sodium-containing air flows	166
Fig.3 Stoichiometric mixture of acetylene - hydrogen - air. Trace A, pressure ahead of membrane and nozzle inlet. Trace B, pressure ahead of nozzle inlet	167
Fig.4 Optical arrangement	168
Fig.5 Stoichiometric mixture of acetylene - hydrogen - air. Trace A ₁ , chopped light without gas. 500 μ sec/cm. Trace A ₂ , chopped light with emitting gas. 200 μ sec/cm. Trace B, pressure at measuring position	169
Fig.6 Temperatures behind the nozzle throat. Air-fuel mixture	170
Fig.7 Temperatures behind the nozzle throat. Oxygen-propane mixture	171

MEASUREMENTS OF RELAXATION EFFECTS IN NOZZLE FLOW OF HOT COMBUSTION GASES BY MEANS OF A SHOCK TUBE TECHNIQUE

Th. Just

1. INTRODUCTION

Because of lack of precise kinetic data on the main chemical reactions in nozzle flow of combustion gases there is an urgent need to measure the well-known relaxation effects in nozzle flow. Data are especially needed for fuel-air mixtures; for example, the information is necessary for the proper design and development of projected hypersonic aircraft. For the determination of relaxation effects, it was decided to measure temperatures along the nozzle. A kind of shock tunnel was built, with a nozzle at the end of a shock tube, and this apparatus turned out to be much less expensive than a conventional combustion chamber with preheated air. Further advantages are as follows: The apparatus can be built quite quickly. A shock tunnel is relatively flexible in using different fuels, initial conditions and nozzles. The high temperatures required are easily produced by using shock-driven detonations. Mass flow rates of 1 kp/sec or even more are achieved. The diameters of the nozzle throats are in the order of 10 cm.

In the following sections a brief description is given of the apparatus and of preliminary results, the experiments having started only a few months ago.

2. EXPERIMENTAL APPARATUS

2.1 Shock Tunnel (Detonation Tube, Nozzle and Tank)

The detonation apparatus consists of three parts (Fig.1). The high pressure section A is 3 m long and has an inner diameter of 90 mm. The second part B, filled with the combustible gases, has a diameter equal to that of part A and is 9 m long. These sections are separated before detonation by a plastic membrane. At the end of section B is the nozzle C and finally, at its exit, the big tank D. The diameter of the tank is 1 m and the length 3 m. Nozzle and tank are evacuated and separated from section B by a thin aluminium-membrane before detonation. In the work described here, two nozzles were first used, the half-angles of the divergent parts being 8 and 16 degrees respectively. For our first experiments we used simple cone-shaped nozzles and the diameter of the throat was chosen as 80 mm. The overall length of the two nozzles is nearly 90 cm. At different positions (see Section 3.3.2) ahead of and behind the nozzle throat we installed several windows and their diameters were 18 and 22 mm. These minimum values fitted exactly the aperture of our monochromator.

2.2 Gases Used, Filling Procedure and Injection of Sodium-Containing Salts

In all cases we used hydrogen in the high pressure section A. We performed measurements with several mixtures of propane-oxygen and of acetylene-hydrogen-air. The latter mixtures were in all cases chosen with equal amounts of acetylene and hydrogen. This is similar to the most hydrocarbons in kerosene.

In preparing the mixtures flow meters were used. The accuracy was $\pm 1.5\%$ of the different compounds. The detonation tube was not filled directly, but a 25 litre glass balloon was used as a storage bottle. In this way we were able to perform three measurements with precisely the same mixture.

The difficult problem of injection of suitable amounts of sodium salts into the gases was solved by using boiling salt melts. Sodium nitrite (NaNO_2) was put into a brass container and heated by a commercial immersion heater. Above 300°C we could produce, in the apparatus shown in Figure 2, a stable "aerosol". The air or oxygen blew at the surface of the melt (1). The outflowing aerosol at (2) was cooled at (3) in order to prevent dangerous ignition at the mixing point with the fuel gases. The brass container was put into a bigger steel cylinder and between the walls is a thermal insulator. Thus we overcame the difficulties with the packing materials, because at temperatures above 100°C we found sodium nitrite extremely aggressive. The temperature at the top of the outer steel cylinder was well below 100°C . Therefore we could use cheap and conventional packings.

2.3 The Ignition of Detonations in Section B

To achieve the maximum usable blowing time of the gases through the nozzle, pressure and temperature behind the front of the detonation wave should be constant*. This demand can be fulfilled, using shock-driven detonations, under two conditions:

- (i) The velocity of the expanding hydrogen must be equal to the velocity of the burnt gases behind the detonation wave. In this case the pressure and temperature between the detonation front and the contact surface remains constant.
- (ii) The initial shock, produced after bursting of the membrane between sections A and B, passing through the unburnt gases should be strong enough to ignite the fuel-oxygen mixture quickly.

The suitable pressure ranges in sections A and B can be calculated easily, using the well known conservation equations (Hugoniot curves, etc.) and kinetic data concerning the ignition behaviour of the fuel-oxidizer mixtures. Experimentally we obtained satisfactory results using, in section A, 18-20 atm of hydrogen and, in section B, initial pressures of 90 to 130 mm mercury of the test mixtures. We thus measured, at the nozzle inlet, pressures of the burnt gases in the range 4 to 6 atm.

* The zone just behind the detonation wave in which the chemical equilibrium is attained is a good approximation for our purposes.

2.4 Time of Constant Flow

The time interval of constant flow was calculated taking into account the sonic velocities, the initial pressure values in sections A and B and the length of both sections. We calculated time intervals for different mixtures of 1.5 to 2 msec and measured usable intervals of 0.9 to 1.4 msec.

3. MEASUREMENTS

3.1 Pressure Measurements

The pressure in front of and behind the nozzle throat was measured at different positions. Piezo-quartz pressure detectors were used and the time resolution was better than $10\ \mu\text{sec}$.

Measurements of the low pressures downstream of the nozzle throat were at first greatly disturbed by the inevitable wall vibrations of the detonation tube. We were able to reduce this effect by embedding the detonation tube nearly 1 m in front of the nozzle inlet into a cube of concrete of length 1.5 m, height 1.5 m, width 1.2 m. The accuracy thus obtained was $\pm 2\%$ and $\pm 3\text{--}4\%$ for low pressures in the range of 0.1 to 0.5 atm. Figure 3 shows a typical example of an experiment with stoichiometric air-acetylene-hydrogen mixture. Both pressures were measured ahead of the nozzle throat, trace A at 30 cm and trace B at 10 cm. Trace A shows clearly the reflection of a weak shock coupled with a rarefaction wave at the bursting membrane which separates the nozzle and the detonation tube before the detonation. Trace B originates from the pressure detector located behind the bursting membrane but ahead of the nozzle throat. The steady value of the pressure during a time interval of more than 1 msec is satisfying.

3.2 Measurement of Temperature. The Optical Arrangement

The well-known method of the reversal of atomic resonance lines seemed to us most suitable. We shall not outline the theoretical background here, but recapitulate that the temperature of the gas is equal to the calibrated black-body temperature of a tungsten filament lamp as soon as the selected spectral line (Na-D) which the hot gases are emitting cannot be seen against the continuous background emitted from the lamp. Due to the short time of constant flow in the nozzle we cannot hope to pick up the true matching point exactly.

Therefore we decided to use two tungsten lamps at different estimated temperatures and to interpolate the point of reversal. One lamp has a "temperature" which is a little lower than that of the gas, the other lamp has a slightly higher temperature. Thus we have, in the first case, emission of the line relative to the background and, in the second one, slight absorption. The apparatus is shown in Figure 4.

The radiation of the lamps L_1 and L_2 is reflected in exactly the same direction by means of a semi-transparent mirror M_t . The light falling on the entrance slit of a monochromator is chopped by a rotating chopper Ch and picked up at the exit slit of the monochromator M by a photomultiplier RCA 931 A. The chopper has an odd number of teeth so that the radiation of the lamps is chopped alternately. We used

41 teeth, 200 mm wheel diameter and 50 rev/sec. In this way each lamp is "switched" on and off every 200 μ sec (see Fig. 5). The "dead time" between the change from one lamp to the other is relatively long (200 μ sec) and in future vibration diaphragms with an upper frequency of 15 kHz will be used. To ensure that precisely the same steric angle of gas and lamp radiation was used, a screen was mounted in front of the lens C with a hole of the same cross-section as that of the radiation from the lamps at this point.

The monochromator M4GII was manufactured by Zeiss. Its ratio of focal length to effective diameter is 10.8 and the slit height is 10 mm. The dimensions of all lenses and the windows in the nozzle walls were selected to give maximum intensity at the exit slit of the monochromator. The pictures of the filaments on the entrance slit were 11 mm high and the aperture of the monochromator was completely filled with light. We found a suitable signal to noise ratio* with entrance and exit slit widths of 20 μ . This corresponds to a spectral slit width of 4.5 Å (for comparison, the Doppler-width of the sodium D-line is nearly 0.04 Å at 2500°K).

The lowest temperature which can be measured with an accuracy of $\pm 1.5\%$ with this apparatus was found to be 2000°K. Beyond this value the sensitivity decreases rapidly, due to the exponential dependence on temperature of the sodium line and black-body radiation. To extend the lower limit we shall use in future a monochromator with greater energy output and higher resolution. The highest temperature which we can measure was found to be nearly 2500°K to 2600°K, and this depends on the use of the semi-transparent mirror M_t . Without this mirror we might go up to 2800°K, but in this case we cannot use the easy method of interpolation between the radiation of two different lamps. We shall try to use Xenon high pressure lamps in conjunction with calibrated filters to extend the upper limit well beyond 3300°K.

3.3 The Determination of Temperatures at Different Positions Relative to the Nozzle Throat

3.3.1 *The Temperature Just Ahead of The Nozzle Inlet*

As already pointed out, we cannot measure temperatures higher than 2500 to 2600°K with our line reversal method. In the present tests we calculated the temperatures behind the incident detonation wave and behind the reflected shock at the nozzle inlet.

The pressure behind the incident detonation wave was measured and, using the hydrodynamic equations and thermodynamic data, the corresponding temperature was calculated. In addition, the velocity of the incident detonation wave was measured and the corresponding temperature was calculated in another way. Generally both values agreed well within $\pm 2\%$. The temperature behind the weak reflected shock at the nozzle inlet was calculated under the assumption of isentropic compression of the gases. This seems reasonable because the pressure ratio of incident and reflected shock is within the range 1.2-1.8.

* Bandwidth of the amplifier 0-20 kHz.

In general, this procedure was not quite satisfactory but, on the other hand, the author performed direct measurements some years ago of the temperature behind detonation waves and found good agreement with the predicted values. In that work temperatures were measured from OH band-spectra. In future we shall use either this method or the reversal method with Xenon lamps, as mentioned earlier.

3.3.2 Determination of the Temperatures Behind the Nozzle Throat

The tungsten lamps were calibrated with a pyrometer and we obtained in the usual way the variation of black-body temperature with lamp current, with an error of $\pm 1.0\%$.

The second calibration curve needed is the photomultiplier output at the monochromator as a function of lamp current. The result was straight lines in a double-logarithmic plot. The corresponding curves obtained with emitting or absorbing hot gas were also straight lines to a good approximation; therefore interpolation was easy. In some cases at the highest temperatures (2600°K) the matching point has to be obtained by extrapolation, because we cannot get absorption with the "hotter" lamp without destroying the lamp too quickly. The losses of the semi-transparent mirror, lenses and windows must be taken into account.

We found a surprisingly good repeatability of the temperatures at the various positions behind the throat and so it was not necessary to measure these temperatures at the same time.

Figure 5 shows a typical oscillograph of an experiment with a stoichiometric mixture of air-acetylene-hydrogen. The relevant data were as follows.

Nozzle: 8° half-angle
80 mm throat diameter.

Window: 11 cm behind throat. Nozzle diameter at this position, 109 cm.

Initial pressure: 90 mm mercury.

Trace A_1 shows the intensity of both lamps without gases and trace A_2 shows the intensities with sodium D-line radiation. The relative emission and absorption can be seen. Trace B shows the pressure at the position of the windows. Taking into account the inevitable wall vibrations the pressure is constant within $\pm 3\%$.

Table I summarizes the results of a number of experiments with the same stoichiometric mixture. The reproducibility is within $\pm 0.7\%$. The relevant data are as follows.

Mixture: 0.0587 acetylene
0.0587 hydrogen
0.883 air.

Nozzle: 8° half-angle.

Throat: 8 cm diameter.

Initial pressure in section B of shock tunnel: 90 torr.

Hydrogen pressure in section A: 18 atm.

The position behind the throat is given by d/d_{th} , where d_{th} is the throat diameter.

TABLE I

d/d_{th}	Pressure in front of throat (atm)	Pressure at d/d_{th} (atm)	Temperature (°K)
1.36	4.3	0.49	2255
			2220
			2240
			2250
1.77	4.3	0.28	1970
			1980
			1980

In Figure 6 we show the results of the measurements with the air-fuel mixture. The composition of the mixture was 88.3% air, 5.87% acetylene and 5.87% hydrogen. The curves of equilibrium and frozen composition were calculated with the aid of the tables of Sanger-Bredt¹ and Bristol Siddeley². The measured values are near the frozen composition curve. This may be explained partly by the "dilution" of the reacting gases with the nitrogen of the air. In contrast, propane-oxygen mixtures show measured values near the equilibrium curve.

In Figure 7 are shown the results of the measurements with an oxygen-propane mixture. The mixture contained 8.24% propane and 91.76% oxygen, corresponding to an equivalence ratio of 2.25. We plotted the measured temperature against the ratio of diameter at the measuring position to the throat diameter. The temperature at the nozzle inlet was calculated from pressure measurements as already explained. In addition we calculated the curves of equilibrium and of frozen composition, using Reichert's tables³. The measured values are near to the curve of equilibrium composition. In future we shall develop a computer programme, which includes kinetic data of the main chemical reactions and we hope then to approximate the measured values of the temperatures as a function of nozzle geometry.

Possible objections concerning the validity of the measured temperatures are discussed briefly in the next section.

* In the nozzle of a hypersonic aircraft we must probably expect temperatures nearer to the equilibrium curve. In this case the nozzle is much larger and therefore the time of residence of the gas is longer.

4. CRITICISM OF THE METHOD

Obviously we must take care of boundary-layer effects and of inhomogeneities of temperature due to the conical shape of our nozzles. (Across any section perpendicular to the nozzle axis the Mach number varies slightly.)

The influence of the boundary layer does not seem to us very serious and we try to justify this statement by the following arguments. We measured in a range where the gas layers are optical thick. In this region it is a good approximation that the total absorption W is proportional* to \sqrt{Nl} , where l is the length of the layer and N is the number of sodium atoms per cubic centimetre.

For a rough estimate, if we divide the total layer of the gas into two parts with different temperatures, where l_1 is the thickness of the central region and l_2 the thickness of both boundary layers, then we can easily derive the following equation at the effective reversal point:

$$K_L = K_{l1} \left\{ \frac{\frac{W_1^*}{\Delta\omega_D} - \frac{W_2}{\Delta\omega_D} \left(1 - \frac{K_{l2}}{K_{l1}}\right)}{\frac{W_1^*}{\Delta\omega_D}} \right\}$$

K_{l1} , K_{l2} are the Planck constants for radiation at sodium wavelength and at the actual gas temperatures T_1 and T_2 . K_L is the measured value for the average temperature T_L .

The total absorption W_1 is defined as

$$\frac{W_1}{\Delta\omega_D} = \frac{1}{\Delta\omega_D} \int_0^\infty \left[1 - \exp(-k_{1\omega} l_1) \right] d\omega$$

where l_1 = thickness of layer

ω = frequency = $2\pi\nu$

$k_{1\omega}$ = absorption coefficient (at T_1 and N_1) per frequency interval

$\Delta\omega_D$ = doppler half-width of sodium under the given conditions.

The symbol W^* denotes an average value over both layers, l_1 and l_2 .

$$W^* = \int_0^\infty \left[1 - \exp \left\{ k_{1\omega} l_1 \left(1 + \frac{k_{2\omega} l_2}{k_{1\omega} l_1} \right) \right\} \right] d\omega$$

* The ratio of collision-width to Doppler-width of the sodium line is of the order of 1.6 to 0.8.

If we assume a boundary layer of 10% of total diameter and a decrease in Nl at the boundary of at least a factor of 100, then we get

$$K_L \approx K_{L1} (1 - 0.1) = 0.9 K_{L1}$$

$$W_1^* \approx W_1$$

$$\frac{N_1 l_1}{N_2 l_2} \approx 100.$$

Therefore, as mentioned above, $W_1/W_2 \approx 10$.

$$T_2 < T_1; \quad \frac{K_{L2}}{K_{L1}} \ll 1$$

because K_L depends exponentially on temperature.

$K_L \approx 0.9 K_{L1}$ corresponds to a measured temperature, which is roughly 1% too low compared with T_1 corresponding to K_{L1} .

Therefore it is estimated that temperature is not very seriously affected by this effect.

Taking into account the inhomogeneous flow due to the cone-shaped nozzle, we estimated in a similar way the deviations of the measured temperature from the arithmetic mean. We concluded that, according to this effect, the measured temperature would be too low by 1 - 2% compared with the arithmetic mean.

In addition we made measurements with argon filled and contaminated with sodium in section B (Fig.1). The calculated and measured temperatures behind the throat agreed within 2.5%. The temperature at the nozzle inlet was calculated from pressure and velocity measurements of the incident and reflected shock waves. The accuracy of these values is within $\pm 3\%$; therefore this proof should be conservative.

We shall now try to develop an apparatus which allows us to colour only central parts of the flow fields.

5. FUTURE PROGRAMME

We shall investigate experimentally the effect of nozzle geometry on temperature along the nozzle, for various mixtures; mixtures of hydrogen-air are of special interest. We hope to be able to develop, from these results, semi-empirical rules useful in the design of hypersonic aircraft.

By means of a computer programme we shall try to fit the measured data to reasonable values of the velocity constants of the chemical reactions.

* At the cooler boundary the concentration of sodium atoms decreases rapidly, probably more rapidly than was assumed in our estimate.

REFERENCES

1. Sanger-Bredt, I. *Thermodynamische Gemischeigenschaften von Oktan-Luft-Feuergasen unter Gleichgewichtsverhaltnissen bei Temperaturen bis zu 4000°K. Mitteilungen aus dem Forschungsinstitut fur Physik der Strahlantriebe e.V. No.17, Stuttgart 1959.*
2. McIntyre, R.W.
Metcalf, H. *Tables of the Equilibrium Composition of Kerosine-Air Combustion Products up to 6000°K. Bristol Siddeley L.T.D., Report AP 5122, 1963.*
3. Reichert, H. *Enthalpy Charts: For Dissociating Gas Mixtures in the Temperature Range 600° to 4000°K. ARC R & M 3015, 1957.*
4. Mitchell, G.
Zeemansky, W. *Resonance Radiation and Excited Atoms. Cambridge University Press, 1961.*
5. Unsold, A. *Physik der Sternatmospheren. Springer Verlag, 1955.*

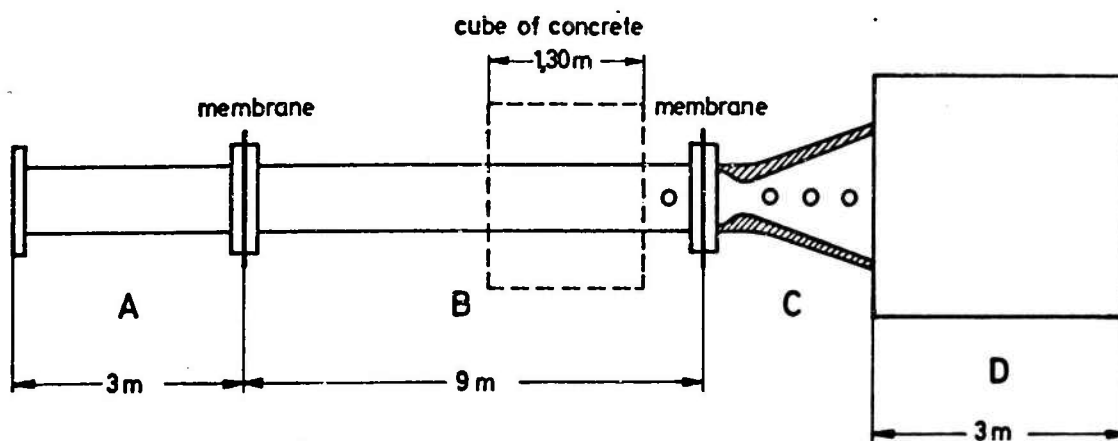


Fig.1 Shock tunnel

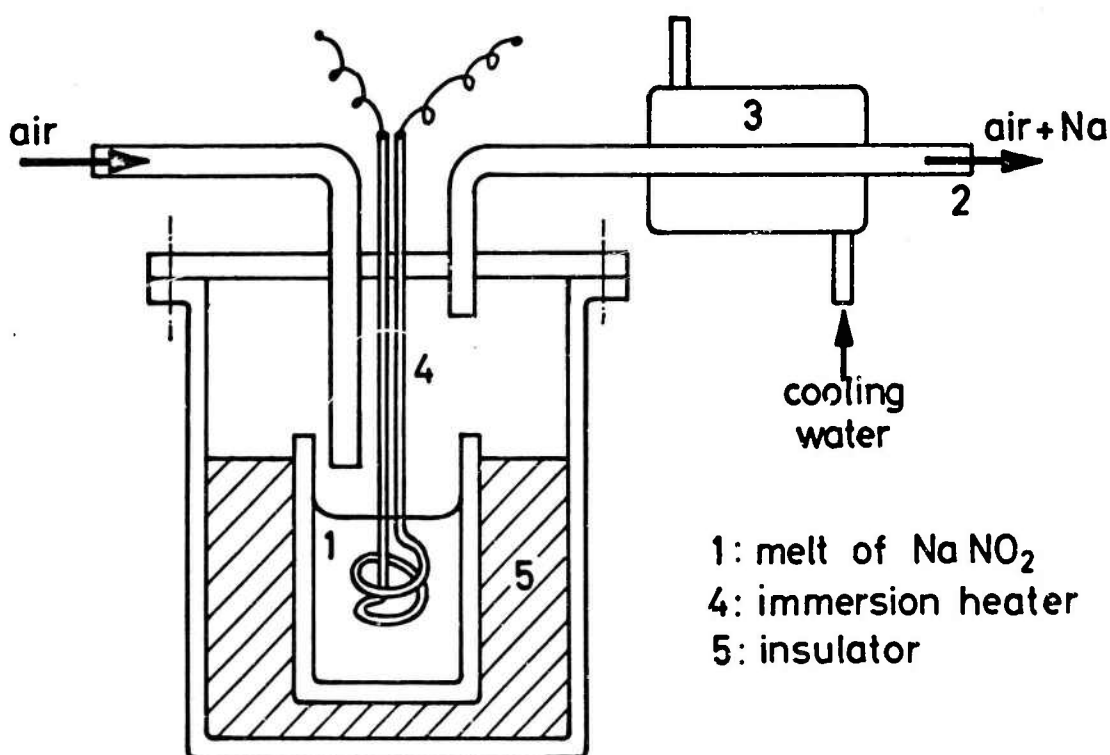


Fig.2 Apparatus for production of sodium-containing air flows

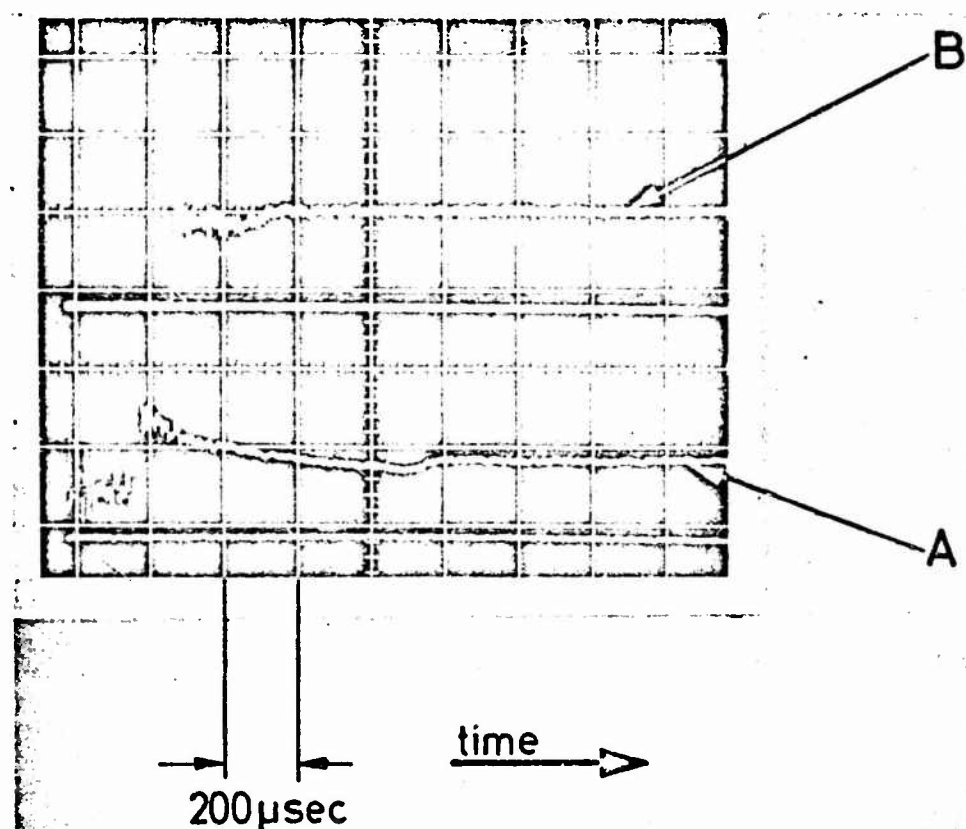


Fig.3 Stoichiometric mixture of acetylene - hydrogen - air. Trace A, pressure ahead of membrane and nozzle inlet. Trace B, pressure ahead of nozzle inlet

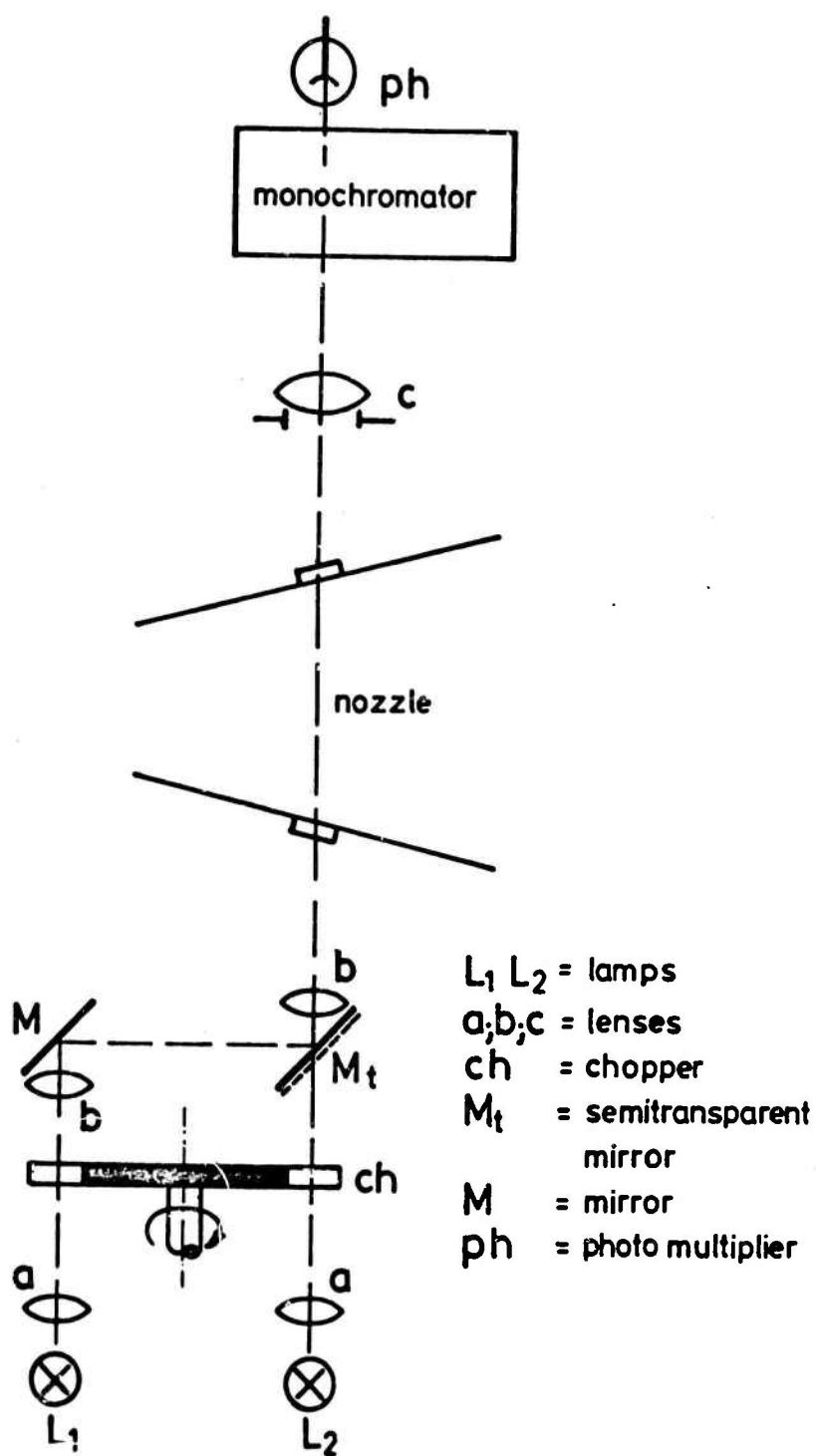


Fig.4 Optical arrangement

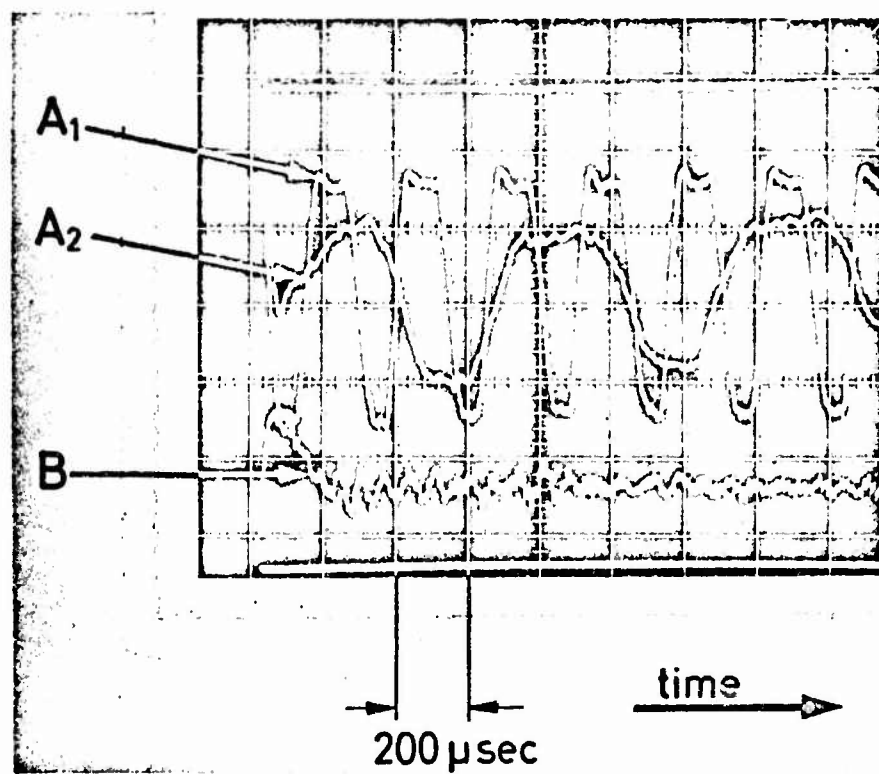


Fig.5 Stoichiometric mixture of acetylene - hydrogen - air. Trace A₁, chopped light without gas. 500 μsec/cm. Trace A₂, chopped light with emitting gas. 200 μsec/cm. Trace B, pressure at measuring position

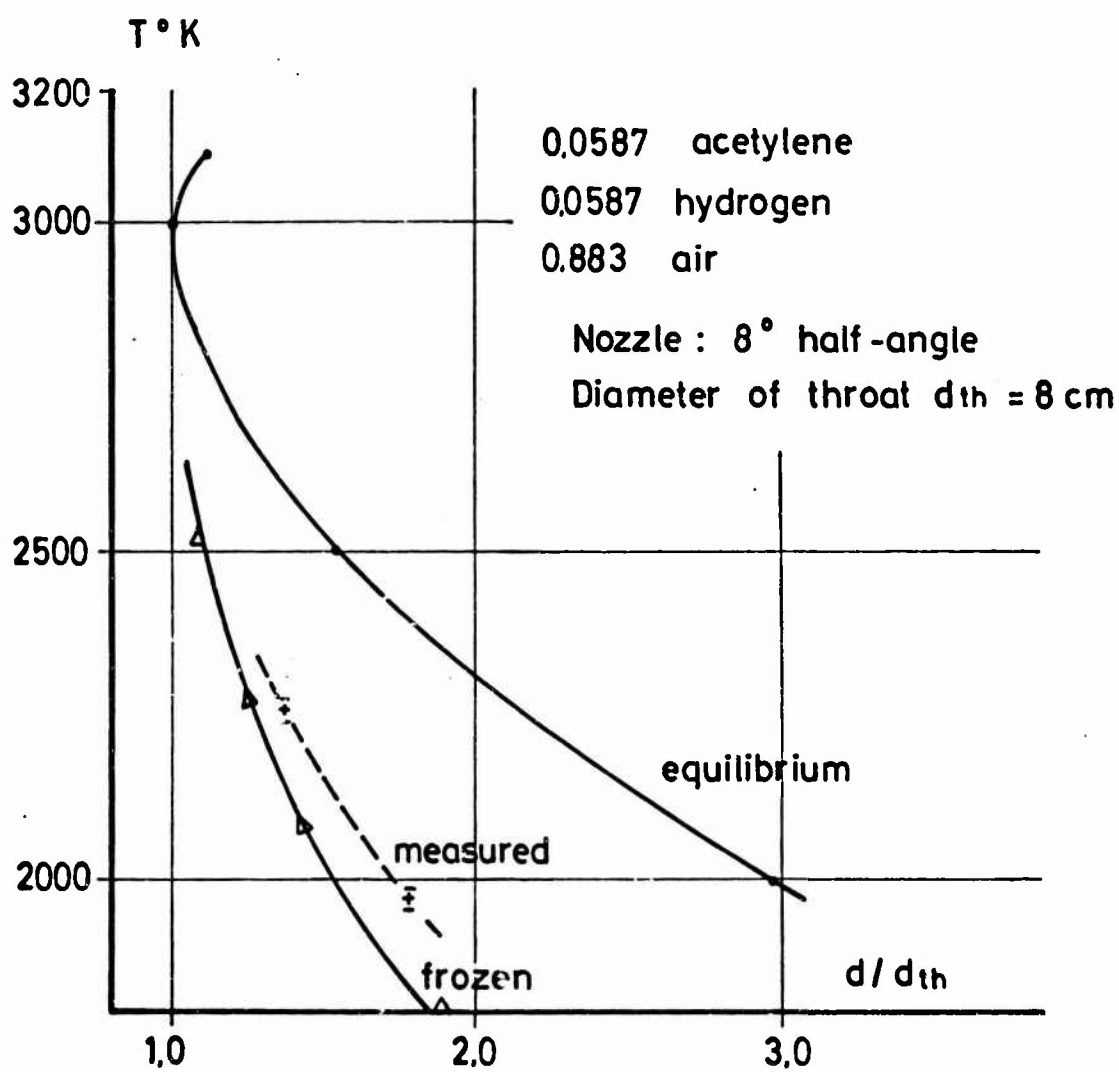


Fig.6 Temperatures behind the nozzle throat. Air-fuel mixture

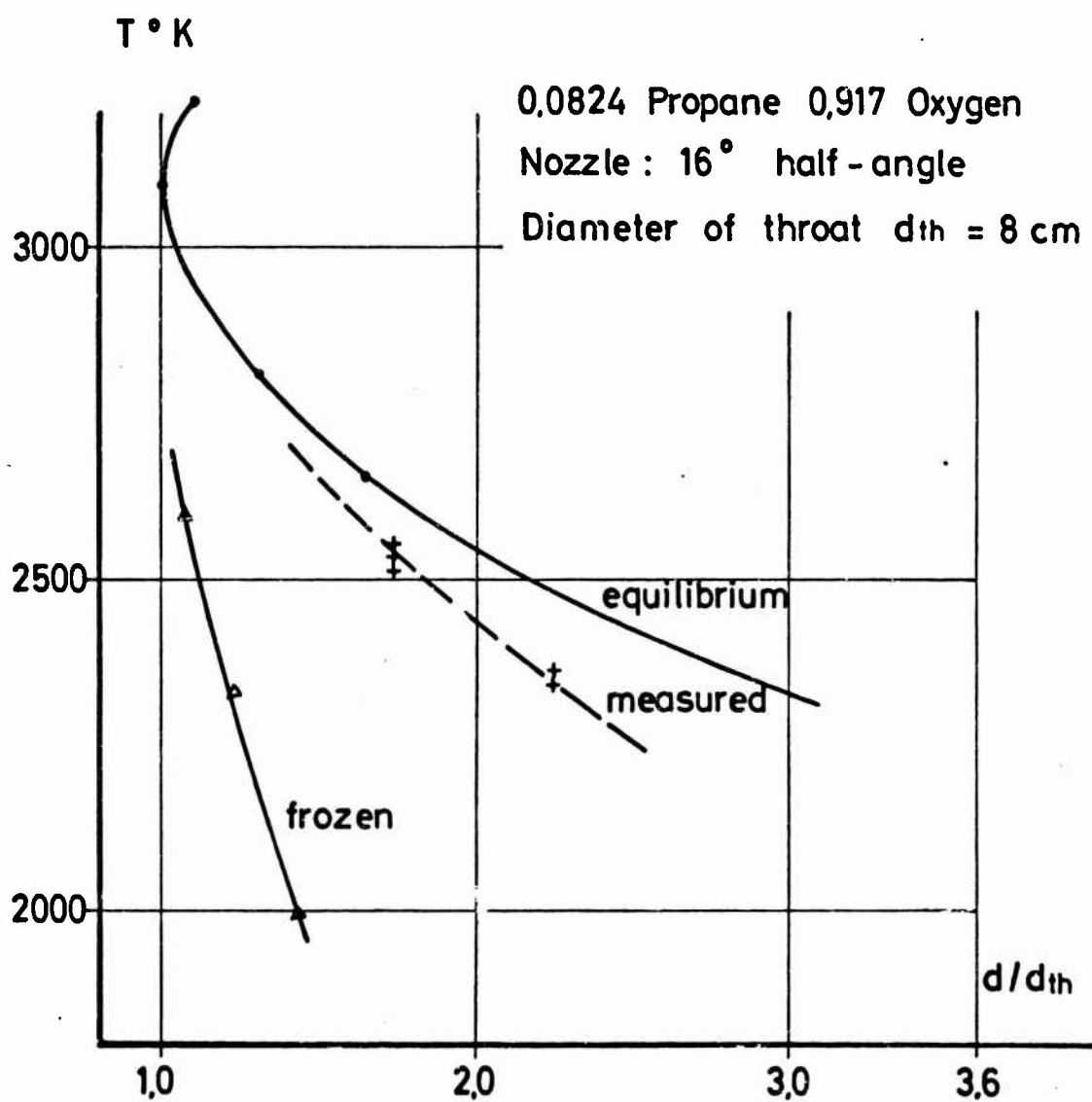


Fig.7 Temperatures behind the nozzle throat. Oxygen-propane mixture

AIRCRAFT PERFORMANCE PROBLEMS ASSOCIATED
WITH ENGINE AND INTAKE INSTALLATION

by

John Weir

British Aircraft Corporation (Operating) Limited, Warton Aerodrome,
Nr. Preston, Lancashire, England

SUMMARY

The compromise between subsonic and supersonic requirements of the intake and afterbody-nozzle design is discussed for aircraft which spend most of their time at subsonic cruise conditions but which still retain the ability to accelerate rapidly to $M = 2.0$ and beyond. The usual approach of designing the intake and nozzle for supersonic speeds and then minimising the penalties that result at subsonic speeds is questioned. The approach which first fulfils subsonic requirements, accepting some supersonic penalties, is considered in more detail. Sufficient data exist to illustrate the attractions of this approach but much more testing is required, particularly on jet interference on afterbody drag at supersonic speeds and on intake boundary-layer bleed drag at subsonic speeds.

SOMMAIRE

L'auteur étudie le compromis à établir entre impératifs subsoniques et supersoniques dans la mise au point de l'entrée d'air et de la tuyère de la partie arrière pour les avions volant le plus fréquemment à des vitesses de croisière subsoniques mais conservant toutefois la possibilité d'atteindre rapidement $Mach = 2.0$ et davantage. Il conteste l'attitude habituelle qui consiste à concevoir une entrée d'air et une tuyère pour des vitesses supersoniques puis à réduire au minimum les inconvénients qui en résultent en régime subsonique. Il étudie plus en détail la solution consistant à satisfaire tout d'abord aux impératifs subsoniques, en acceptant certaines servitudes aux vitesses supersoniques. On dispose d'une masse suffisante de résultats pour illustrer les avantages de cette solution, mais un complément d'expériences s'impose, en particulier en ce qui concerne l'interférence du jet avec la traînée de la partie arrière aux vitesses supersoniques et la traînée créée par la purge d'air de la couche limite des entrées en régime subsonique.

CONTENTS

	Page
SUMMARY	174
SOMMAIRE	174
LIST OF FIGURES	176
NOTATION	177
1. INTRODUCTION	179
2. DESCRIPTION OF THE PROBLEMS	179
2.1 Afterbody-Nozzle Problem	179
2.2 The Intake Problem	180
3. AFTERBODY DRAG AND NOZZLE THRUST	180
3.1 Subsonic Speed	180
3.2 Supersonic Speed	181
4. INTAKE EFFICIENCY AND BLEED DRAG	183
4.1 Subsonic Speed	183
4.2 Supersonic Speed	183
5. DISCUSSION AND FURTHER WORK REQUIRED	184
5.1 Afterbody Drag	184
5.2 Intake Design	184
6. CONCLUSIONS	185
REFERENCES	186
APPENDIX: Analysis of Flight-Measured Profile Drag at Subsonic Speeds.	187
FIGURES	188

LIST OF FIGURES

	Page
Fig.1 Afterbody drag	188
Fig.2 Boattail and base drag	189
Fig.3 Rate of change of boattail drag with base pressure ($M = 0.9$)	190
Fig.4 Jet interference on boattail wave drag	191
Fig.5 Effect of boundary-layer bleed on side-intake performance	192
Fig.6 Comparison of flight-measured and estimated drag at subsonic speed (plotted against S_{wet}/S_{wing})	193
Fig.7 Comparison of flight-measured and estimated drag at subsonic speed (plotted against A_{bleed}/S_{wing}).	194

NOTATION

A_{bleed}	fuselage bleed frontal area
A_m	afterbody maximum cross-sectional area
β	final boattail angle
C_{Db}	base drag coefficient, referenced to A_m
$C_{D\beta}$	boattail drag coefficient, referenced to A_m
C_{Da}	afterbody drag coefficient = $C_{D\beta} + C_{Db}$ referenced to A_m
C_{Do}	aircraft profile drag coefficient, referenced to wing area
$\Delta C_{D\beta} / \Delta C_{pb}$	rate of change of boattail drag with base pressure
ΔD	drag change from drag of basic intake (see Section 4.2)
d_b	base diameter
d_j	jet diameter
d_m	maximum afterbody diameter
δ	fuselage boundary-layer thickness
h	fuselage boundary-layer bleed height
H_j	jet total pressure
M	Mach number
\dot{m}_0	intake capture mass flow
\dot{m}_{bleed}	intake throat bleed flow
p_∞	ambient static pressure
T_j	jet total temperature
S_{wet}	aircraft wetted area
S_{wing}	aircraft gross wing area
X, X_0	thrust (see Section 4.2)

AIRCRAFT PERFORMANCE PROBLEMS ASSOCIATED WITH ENGINE AND INTAKE INSTALLATION

John Weir

1. INTRODUCTION

The design compromise between subsonic and supersonic aircraft performance has been our concern now for many years, but recent times have seen much interest in tactical strike aircraft for which the prime requirement is for good high subsonic speed and high- and low-level performance, but which still require the ability to accelerate rapidly and cruise for some time at Mach numbers of 2.0 and above. This paper considers one approach to the compromise on the intake and afterbody-nozzle design for such an aircraft. Most of the model test data referred to later have been available for many years, but the current trends in mixed subsonic-supersonic aircraft perhaps make them more relevant than they were at the time the tests were first completed.

2. DESCRIPTION OF THE PROBLEMS

Before going on to outline the various compromises that face the designer, one requires some idea of the relative importance of subsonic versus supersonic drag and intake pressure recovery. For a mixed mission with an acceleration to supersonic speeds followed by a short cruise the following rates of exchange apply approximately. The effect on fuel required for a given sortie of a 1% change in subsonic drag is the same as a 3-4% change in supersonic drag. Or again a 1% change in subsonic drag is the same as a 2% change in supersonic intake efficiency. These are only round figures, which will vary according to the partsortie deemed most important and the aircraft maximum Mach number, but they serve to illustrate the need for particular attention to the subsonic design.

2.1 Afterbody-Nozzle Problem

There are two approaches to the afterbody-nozzle problem for a mixed subsonic-supersonic aircraft. The first is to design for good supersonic performance by the use of variable convergent-divergent or ejector nozzles to give maximum engine thrust, which leads at the same time to reduced rear fuselage wave drag because of the lower afterbody slopes. The losses in internal thrust which then arise at high subsonic speeds are minimised, either by reducing the ejector or convergent-divergent nozzle exit area or by filling it with air from the main intake or from intakes located in the rear fuselage just upstream of the nozzle. This appears to have been the solution adopted on many supersonic aircraft to date and, while subsonic thrust losses can be

avoided by variable geometry nozzles, this has sometimes been achieved, initially at least, at the expense of subsonic afterbody drag. Subsequent modifications to the nozzle to avoid the drag finally lead to a longer, more complex and heavier nozzle than was ever envisaged.

The second approach is to design for minimum subsonic afterbody drag, with a plain convergent nozzle, and then to make maximum use of favourable jet interference, which can arise at supersonic speeds, to minimise the rear fuselage wave drag and regain some of the underexpanded convergent nozzle thrust on the afterbody. This is the approach considered in this paper; it is not of course an approach that would be considered for a moment for a supersonic transport where a large percentage of the fuel is used at one particular supersonic Mach number.

2.2 The Intake Problem

Turning now to intake design, one is faced with a wealth of information concerning intake pressure recovery at high Mach numbers and the drags of various types of fuselage boundary-layer systems which is more than adequate for initial design studies of intakes designed primarily for supersonic speeds. This appears to have led to bleed requirements being fixed entirely from supersonic considerations and, consequently, bleed flows at subsonic speeds are often in excess of the minimum required. When faced with the design of an aircraft considered here, one has either to compromise the supersonic intake performance by decreasing bleed sizes below the optimum in order to avoid the extra drag due to unnecessary bleed flow at subsonic speeds or one has to consider some form of bleed which can be reduced at Mach numbers when it is not required.

3. AFTERBODY DRAG AND NOZZLE THRUST

3.1 Subsonic Speed

According to inviscid potential flow theory, the drag of a closed body of revolution is zero at sub-critical Mach numbers. In practice the drag consists mainly of skin friction plus a small form or pressure drag due to the modification of the inviscid pressure distribution by the boundary layer. For a non-closed body, with bluff base where the external flow must separate, the pressure drag is much more important and may be several times the skin friction drag. It arises because the rear separation alters the base and boattail pressures. The afterbody pressure drag is then defined as the sum of the boattail plus base pressure drags.

These remarks still hold when part of the base is replaced by a jet, but, if the exit static pressure is sufficiently high, the afterbody drag can become negative.

3.1.1 Model Test Results

There has been a fair amount of systematic model testing to investigate the afterbody drag of axisymmetric bodies of revolution with a convergent sonic jet at high subsonic and transonic speeds. The data has been generalised in Reference 1 and is used in Figures 1 and 2 to illustrate the variation of afterbody drag with certain geometrical variables. Figure 1 presents the afterbody drag coefficient as

a function of d_b/d_j , d_b/d_m , and the final boattail angle, β . d_j , d_b , and d_m are respectively the jet, gross base, and maximum body diameters. The jet total-to-static pressure ratio is 3.0 and the jet total temperature 1200°F. An indication of the magnitude of the afterbody drag relative to the total profile drag is given in Figure 1 for a typical aircraft.

The main trends with afterbody geometry can clearly be seen and lead to the following design requirements for minimum afterbody drag at subsonic speeds:

- (i) The aircraft rear fuselage should be faired as close as possible to the engine primary nozzle, i.e. minimum base area. Note that this ensures minimum d_b/d_j and minimum d_b/d_m .
- (ii) A moderate amount of fuselage boattailing. The correlation of Reference 1 says nothing about the detailed shape of the afterbody but, since all model results were on bodies with smooth gradually-increasing boattail angle, this assumption is implicit in the use of Figures 1 and 2 for drag prediction. Furthermore, although increasing boattail angle β up to 20° is generally favourable, separation of the flow on the boattail becomes increasingly likely as the angle is increased. It is felt that the use of boattail angles greater than about 15° should be avoided unless specific tests on a configuration are available which simulate the detailed shape and the correct boundary-layer development.

The correlation of Reference 1 can also be used to break down the total afterbody drag into its components of boattail drag $C_{D\beta}$ and base drag C_{Db} . Figure 2 shows this for $\beta = 10^\circ$ and we can at once see that, in this case, the base drag is a negative or thrust force. Similar plots for lower boattail angles would show this base thrust decreasing and eventually becoming a positive drag force.

There is one final point from Reference 1 which may be useful for practical design purposes. For a given geometry the boattail drag $C_{D\beta}$ is shown to be a function only of the base pressure and not the way in which a particular base pressure is produced either by varying the jet pressure ratio or replacing the jet by a sting of varying diameter. $C_{D\beta}$ decreases as the base pressure increases and, furthermore, the rate of change of boattail drag with base pressure increases as the boattail angle increases (see Figure 3).

In other words, any geometrical change or flow change, such as base fairings, base bleed, jet pressure ratio, which alters the base pressure and drag, will have a corresponding and generally larger change in boattail drag, and these changes will become rapidly more important as the boattail angle is increased.

3.2 Supersonic Speed

At first sight it appears that the requirements for low subsonic afterbody drag inevitably give rise to high supersonic wave drag because of the high boattail angles and low d_b/d_m which results. Furthermore, the underexpanded convergent nozzle, which is ideal for subsonic flight, becomes more and more inefficient as the Mach number and jet pressure increase.

In practice, however, the presence of this high pressure jet at the rear of a boattailed fuselage produces an interference which reduces the wave drag. This interference arises in the following way. The external flow along the afterbody meets the expanding jet and is deflected, forming a shock wave. The pressure rise of the shock feeds upstream through the subsonic part of the boundary layer, increases the pressures on the afterbody and hence reduces the drag. If the shock interaction is strong enough the boundary layer may separate, and the upstream influence is then larger. This phenomenon can almost be regarded as a convergent-divergent nozzle with the separated layer forming fluid walls with the thrust produced by the expanding jet acting on the afterbody.

The interaction is governed by, among other things, the strength of the shock, which in turn depends on the local pressures and flow angles just upstream and downstream of the base. A more detailed description is found in References 2 and 3, but high afterbody boattailing and small base area (hence higher base pressure) both increase the shock strength and hence the magnitude of the favourable interference. We can now see that the geometrical requirements for low afterbody drag at subsonic speeds are also the requirements for maximum favourable jet interference at supersonic speeds.

Systematic series of wind-tunnel tests corresponding to those already discussed at subsonic speeds are not available at supersonic speeds, but there are sufficient results to get some idea of the drag changes.

Figure 4 shows results reproduced from Reference 2 for three afterbodies (A, B and C). The first afterbody represented a highly-boattailed convergent nozzle configuration; the other two were intended to simulate convergent-divergent nozzles of different area ratios and they had correspondingly lower boattail angles and smaller rearward-facing afterbody area (see sketch on Figure 4). The measurements of boattail wave drag shown in Figure 4 show clearly that the jet interference on the convergent nozzle afterbody is at least large enough to counter the increase in wave drag relative to the convergent-divergent afterbodies within the jet pressure range which is of interest.

The increase in thrust from the convergent-divergent nozzles B and C was not measured in these tests. These two afterbodies would therefore be superior to A by the amount of this thrust increase.

A further series of tests, in which the nozzle thrust was accounted for, is reported in Reference 4. Here a highly-boattailed convergent nozzle afterbody was fitted with terminal fairings (similar to Whitcomb bodies) which extended downstream of the base. This was a deliberate attempt to increase the jet interference. Tests were completed at $M = 2.0$ and above, and the overall thrust minus drag was compared with the performance of a convergent-divergent nozzle of area ratio 2 with a zero boattail angle. The convergent nozzle afterbody came within 2-3% (of the ideal isentropic thrust) of the convergent-divergent nozzle at $M = 2.0$ and was only 5% down at $M = 2.5$.

Both these series of tests are isolated examples, but they at least serve to indicate the need for more systematic tests and appear to offer the possibility of a very satisfactory compromise for a mixed subsonic-supersonic aircraft.

4. INTAKE EFFICIENCY AND BLEED DRAG

There are two most commonly used ways of preventing the boundary layer from entering a fuselage side-mounted intake for both subsonic and supersonic aircraft. The boundary layer can either be taken between the intake and the fuselage side and immediately diverted above and below the intake or it can be ducted away and discharged overboard or into the engine bay for cooling. These are often referred to as diverter and scoop bleeds respectively.

4.1 Subsonic Speed

The philosophy on most aircraft in the past seems to have been to play safe and raise the intake out of the boundary layer, even for purely subsonic aircraft. Both diverter and scoop bleeds have commonly been used, but there is scarcely any published direct evidence on the drag penalties of these bleed systems at subsonic speeds. A look at flight-measured zero lift drags on 22 jet aircraft suggests that it can sometimes be appreciable. The Appendix contains details of this analysis.

Briefly, estimates for the important drag-producing items are made in a consistent manner for all the aircraft. The unaccounted drag, that is the difference between measurements and estimates, seems to be related strongly to the intake installation. The unaccounted drag is much larger for aircraft with fuselage side-mounted intakes than for aircraft with nose intake, and the suggestion is made that this drag can, partly at least, be related to the boundary-layer bleeds, and in particular to the size of the bleed.

The drag levels implied by this analysis are large and range up to 20% and 30% of the aircraft zero lift drag. The Appendix contains a fuller discussion of these values.

From subsonic considerations, then, the boundary-layer bleeds should be kept as small as possible, and it seems likely that some part of the boundary layer will be allowed to enter the intake. Careful attention to diffuser design will be required to minimise the chance of any ensuing separation, especially when the entry flow is subject to the pre-entry retardation at cruise conditions.

4.2 Supersonic Speed

At supersonic speeds intake bleed requirements are conditioned by shock boundary-layer interactions both on the fuselage and on the intake compression surface at the intake throat, and the penalties for inadequate bleed can be more severe than at subsonic speeds. Most current aircraft raise the intake out of the fuselage boundary layer and deal with subsequent interactions with a bleed on the compression surface or at the intake throat. There is, however, a substantial amount of test data, for example in Reference 5, on the combined effects on pressure recovery and drag of different amounts of fuselage and throat bleed. Some results from Reference 5 on a 14° single ramp intake at $M = 2.0$, reproduced in Figure 5(a), show that, provided there is adequate removal of the boundary layer at the intake throat, the same total pressure recovery can be obtained with the fuselage boundary-layer bleed varying from one third to complete removal. Similar results are obtained at lower Mach numbers, the main difference being that performance is less sensitive to amounts of bleed flow anyway.

The picture is much the same when the bleed drags as well as intake efficiency are taken into account. Taking the basic intake as the one with complete fuselage boundary-layer removal and zero throat bleed, Figure 5(b) presents, for the other configurations, the thrust minus the difference in drag from the basic intake, divided by the thrust of the basic intake. At low throat bleed flows there is little to choose between one third and complete boundary-layer removal.

The advantage of using a combination of fuselage and throat bleed is apparent when we realise that the throat bleed mass flow can easily be controlled and can be stopped completely when it is probably not required at subsonic speeds. Thus we have a simple variable bleed system which gives the best performance at supersonic speeds and keeps the penalties at subsonic speeds to a minimum.

5. DISCUSSION AND FURTHER WORK REQUIRED

5.1 Afterbody Drag

The ease with which the requirements for good subsonic and supersonic performance, discussed in Section 3, can be achieved in practice depends very much on the engine designer. The operating mechanism for the variable primary nozzle often makes it impossible to fair in the fuselage to give minimum base area without using excessive boattail angles which are certain to lead to flow separation. Recent years have seen large improvements in engine specific fuel consumption, but further substantial improvements in overall propulsive efficiency from better engine-airframe integration seem likely, provided engine designers are made aware of the problems and there is co-operation sufficiently early in the design.

On the model testing side, there is clearly a need for more tests on ways of increasing supersonic jet interference either by straightforward afterbody design or by terminal fairings. The latter may be particularly appropriate for a twin-jet afterbody, when some of the base area between the nozzles can be faired out probably with beneficial effects on both subsonic and supersonic performance.

5.2 Intake Design

It goes without saying that the arguments put forward on boundary-layer bleed drag need substantiating by wind-tunnel tests. At the same time other forms of boundary-layer control need developing, especially for half-cone intakes for which the ideas of Section 4.2 cannot easily be applied. The requirement is for a bleed system which can be varied, especially between subsonic and supersonic operation. Flush type fuselage boundary bleeds, such as suction or blowing just ahead of the intake, may be appropriate, and the degree of complexity necessary will obviously depend on the Mach number range of the aircraft.

It is equally possible that tunnel tests on the subsonic drag of conventional diverter and scoop bleeds will lead to ways of reducing the drag so that the frontal area of the bleed may become less important.

Finally, there has been no discussion of intake additive drag at subsonic speeds, which is particularly important on a low-level subsonic cruise because of the low

intake velocity ratio. Once again one is faced with choosing between subsonic and supersonic performance. Lip blunting required for low subsonic drag will give increased supersonic drag. A survey of intake additive drag was made in Reference 6, and the author concluded that a systematic series of tests were required and went on to describe a model programme. The same author is contributing a paper on intake additive drag at this meeting⁷.

6. CONCLUSIONS

The design of a mixed subsonic-supersonic military aircraft raises difficult problems concerned with compromise necessary between subsonic and supersonic requirements of intake and engine performance.

This paper suggests that an approach which concentrates on achieving good subsonic performance is worth considering and that the supersonic penalties are not as large as may first appear.

Much wind-tunnel work is still required, especially on jet interference on afterbody drag at supersonic speed, side-intake boundary-layer bleed drag at subsonic speeds, intake additive drag at subsonic speeds and the effect of lip blunting on supersonic drag.

REFERENCES

1. McDonald, H.
Hughes, P.F. *A Correlation of High Subsonic Afterbody Drag in the Presence of a Propulsive Jet or Support Sting. Journal of Aircraft, Vol. 2, pp. 202-207, May-June 1965.*
2. Englert, G.W.
et alii *Effect of Jet-Nozzle Expansion Ratio on Drag of Parabolic Afterbodies. NASA RM E54B12, 1954.*
3. Cartwright, E.M.Jr.
Kochendorfer, F.D. *Jet Effects on Flow Over Afterbodies in Supersonic Stream. NASA RM E53H25, 1953.*
4. Norton, H.T.Jr.
Keith, A.L.Jr. *Effect of Base Bleed and Terminal Fairings on the Performance of Exhaust-Nozzle - Afterbody Combinations at Mach numbers of 1.93, 2.55 and 3.05. NASA TN D-539, November 1960.*
5. Campbell, R.C. *Performance of Supersonic Ramp-Type Side Inlet with Combinations of Fuselage and Inlet Throat Boundary-Layer Removal. NASA RM E56A17, 1957.*
6. Mount, J.S. *The Effect of Inlet Additive Drag on Aircraft Performance. Paper presented at the AIAA Transport and Operations Meeting, Seattle, August 1964. AIAA Paper No. 64-599.*
7. Mount, J.S. *Additive Drag on Inlet Cowls and its Effect on Aircraft Performance. Pages 271 to 300 of this AGARDograph 103, 1965.*

APPENDIX

Analysis of Flight-Measured Profile Drag at Subsonic Speeds

Available information on the subsonic profile drag of jet-engined aircraft over the last fifteen years shows that the measured drag varies from as little as 5-10% above the basic skin friction drag to as much as 60-70% in some cases. Closer inspection of this data suggests that much of this extra-to-friction drag is related to the intake and engine installation in the form of afterbody and some kind of intake drag.

The analysis proceeds by making the best estimates for the known drag-producing areas in a consistent manner for all 22 aircraft. This estimate is made up as follows:

- (i) Skin friction drag.
- (ii) Form or pressure drag which allows for the effect of pressure distributions on skin friction and for the effect of the boundary layer on the inviscid pressure distribution.
- (iii) Afterbody drag obtained from Reference 1. Figure 6 shows the measured minus estimated drag divided by the measured drag, against the total wetted area or the gross wing area. There is no significance in this latter quantity, it serves merely to spread the data out. It is immediately apparent that the unexplained drag is appreciably higher for aircraft with side-mounted intakes than for aircraft with nose intakes. The only feature which seems capable of producing this higher drag is the fuselage boundary-layer bleed normally employed for side intakes, and if this is so then one would expect the unexplained drag to be dependent to some extent on the amount of bleed, and also on the way in which it is disposed. Figure 7 shows the unexplained drag against the fuselage bleed frontal area divided by gross wing area. There is a marked trend with bleed size; not surprisingly the scatter is fairly large and represents a bleed drag equivalent to a minimum of 25% momentum loss of the bleed flow to a maximum of full momentum loss. This reflects the variety of bleed and disposal systems employed, and very likely other sources of drag which are not accounted for.

It is possible that some of this drag is not due to the bleed itself but is the result of interference of the intake pressure field with that of the front fuselage or canopy, but it has not been possible to demonstrate this.

Different assumptions about how to calculate the basic skin friction drag, whether to apply compressibility factors, what Reynolds number to use when this varied during the flight tests, do not materially alter Figure 7. They do change the level of $(C_{D0} - C_{D \text{ estimate}})/C_{D0}$ but the dependence on the type of intake installation is still there.

Finally the arguments for carefully balancing subsonic bleed drag against supersonic pressure recovery for the type of aircraft under discussion do not depend entirely on the large momentum losses implied by the above analysis. On a typical aircraft, a bleed drag equivalent to as little as 10% momentum loss, which on past experience does not seem easy to achieve, can still contribute 5-10% of the subsonic profile drag.

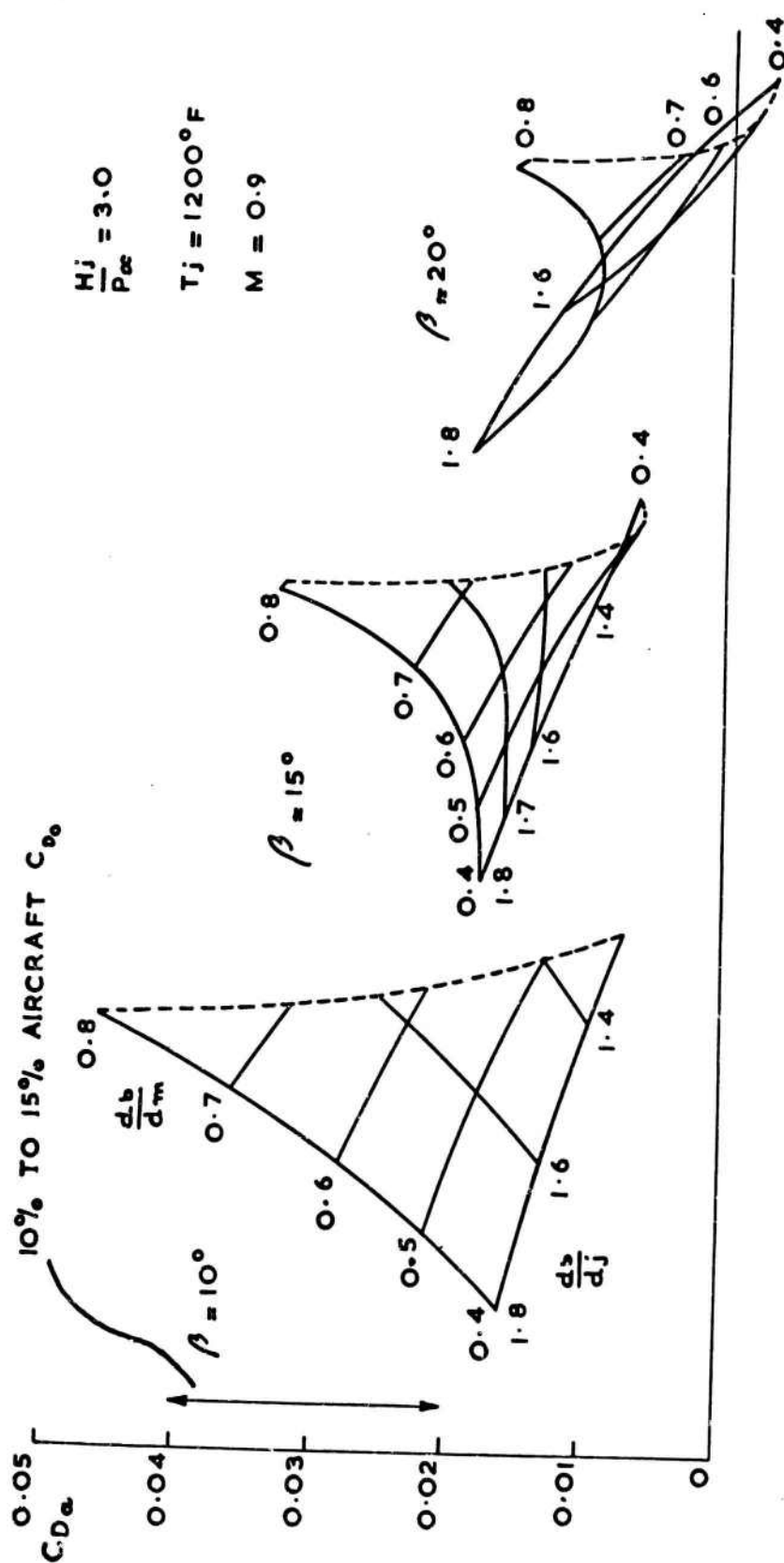


Fig. 1 Afterbody drag

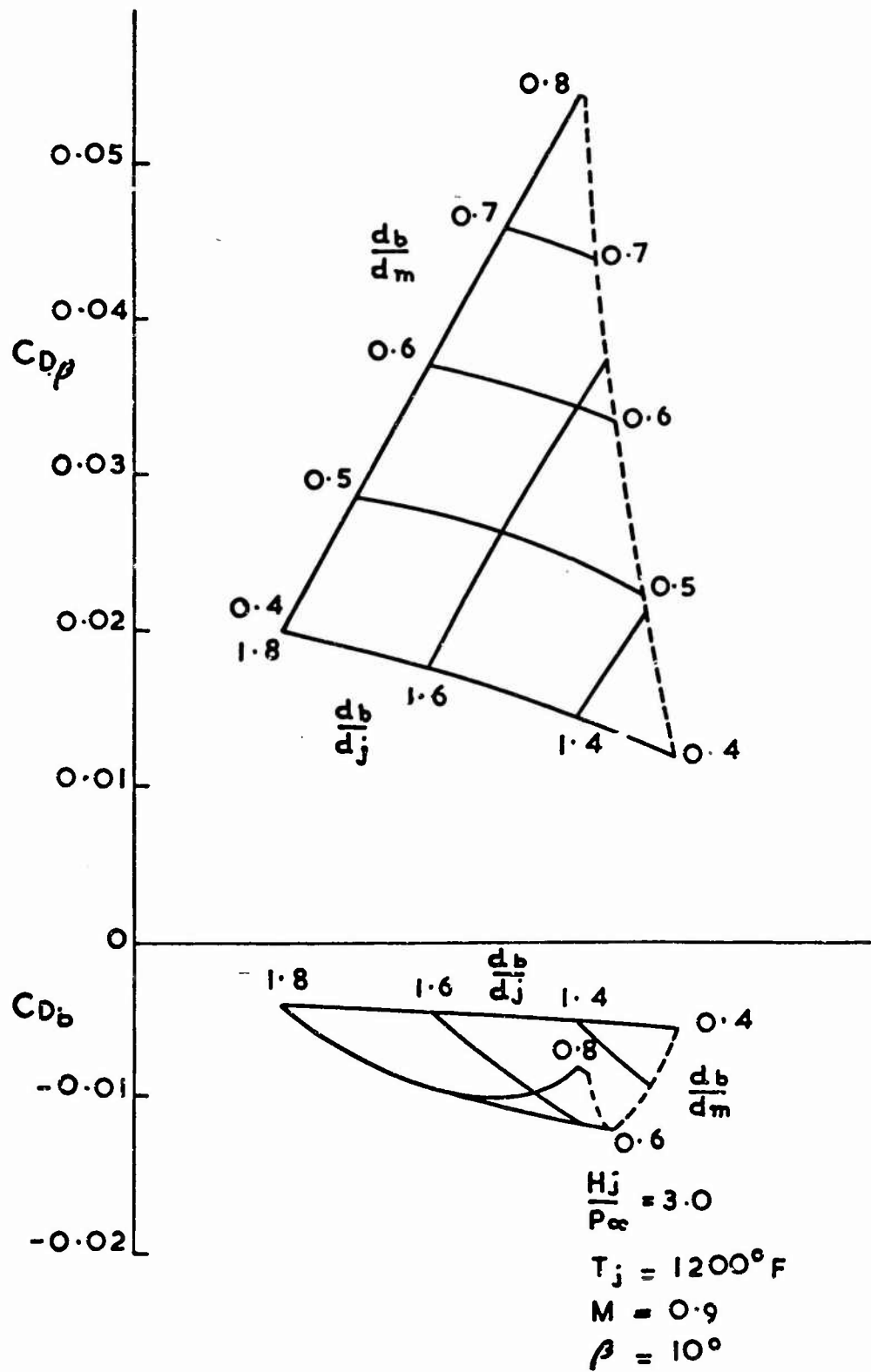


Fig.2 Boattail and base drag

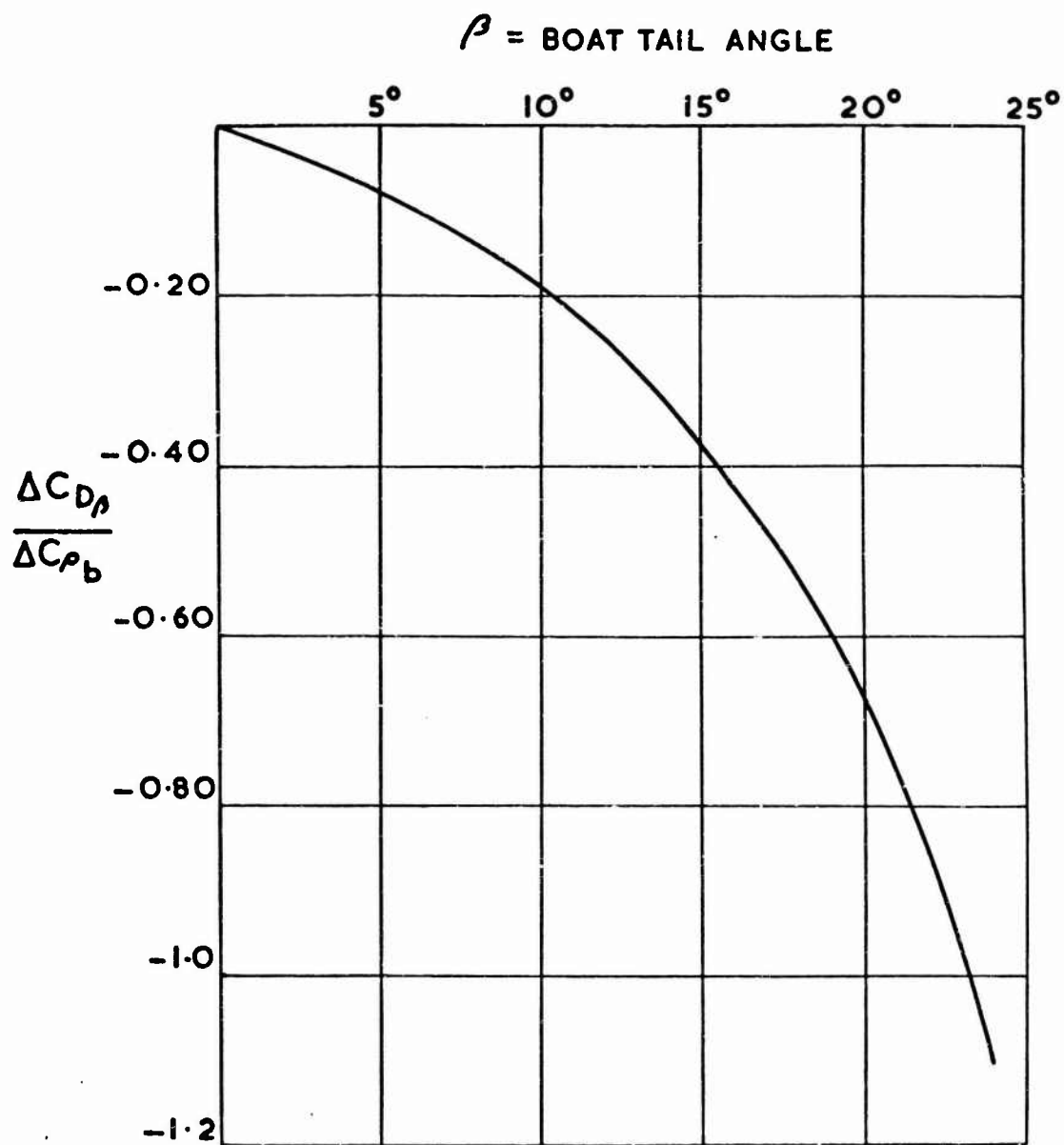


Fig. 3 Rate of change of boattail drag with base pressure ($M = 0.9$)

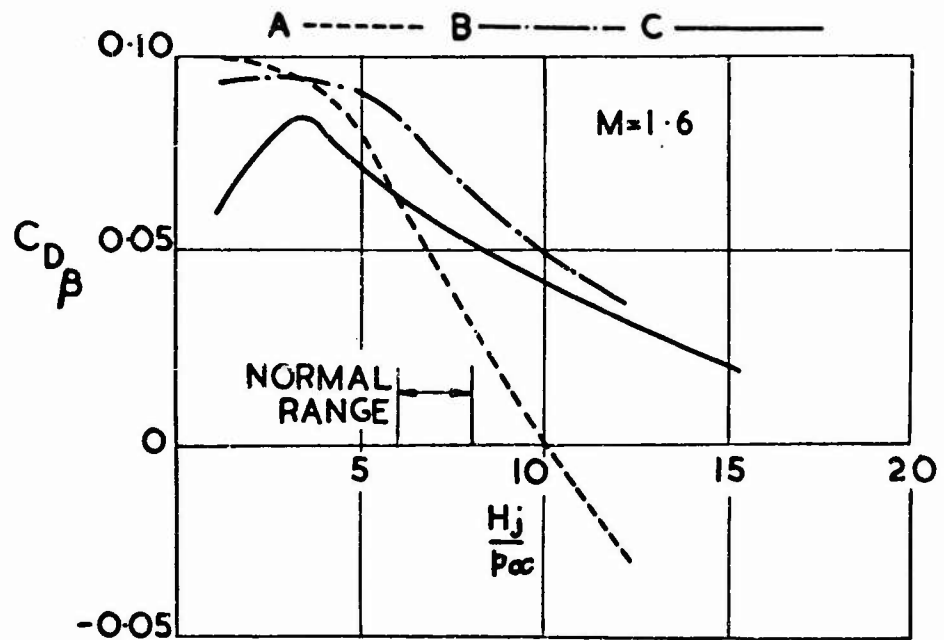
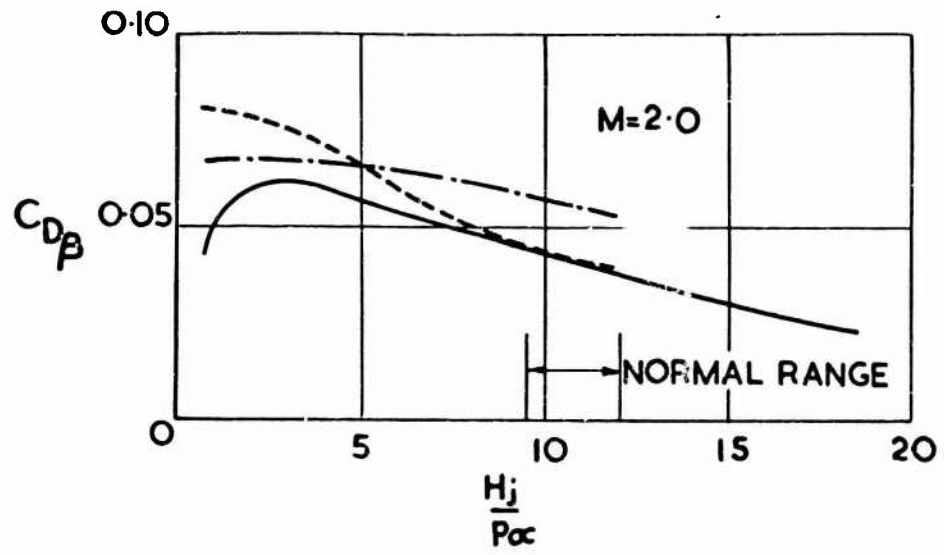


Fig. 4 Jet interference on boattail wave drag

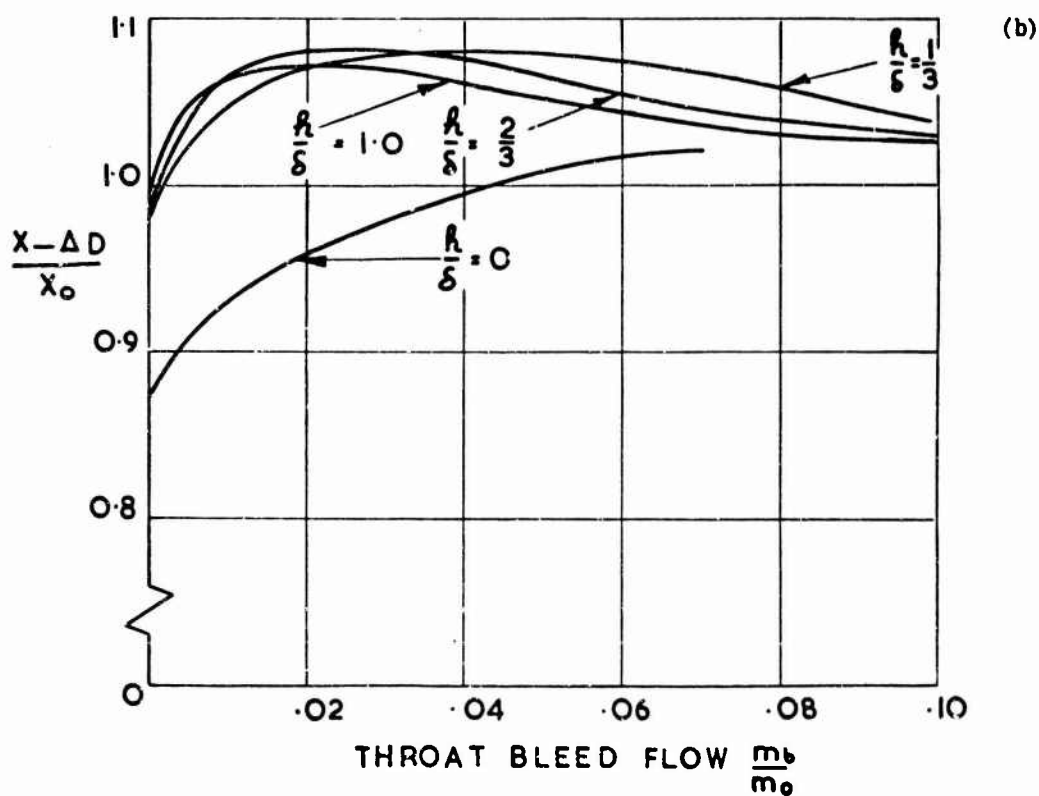
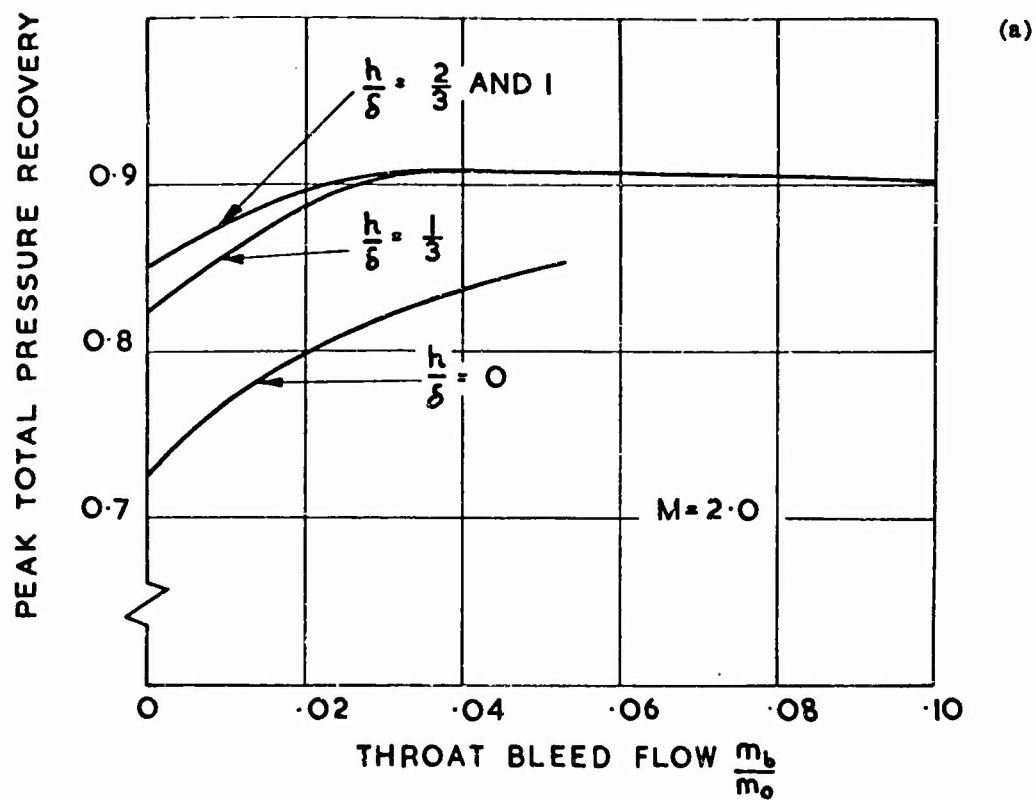


Fig. 5 Effect of boundary-layer bleed on side-intake performance

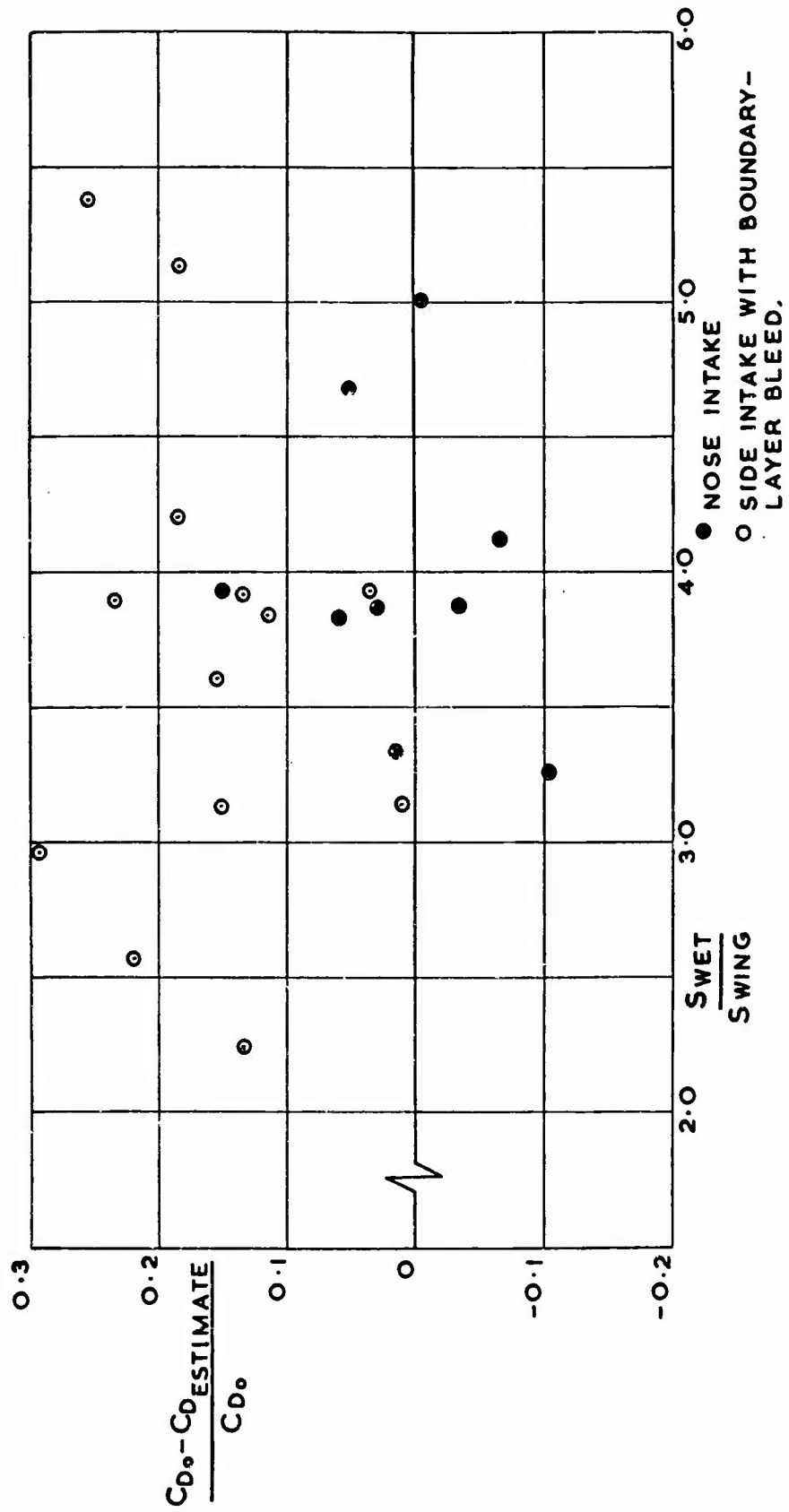


Fig. 6 Comparison of flight-measured and estimated drag at subsonic speed
(plotted against S_{wet}/S_{wing})

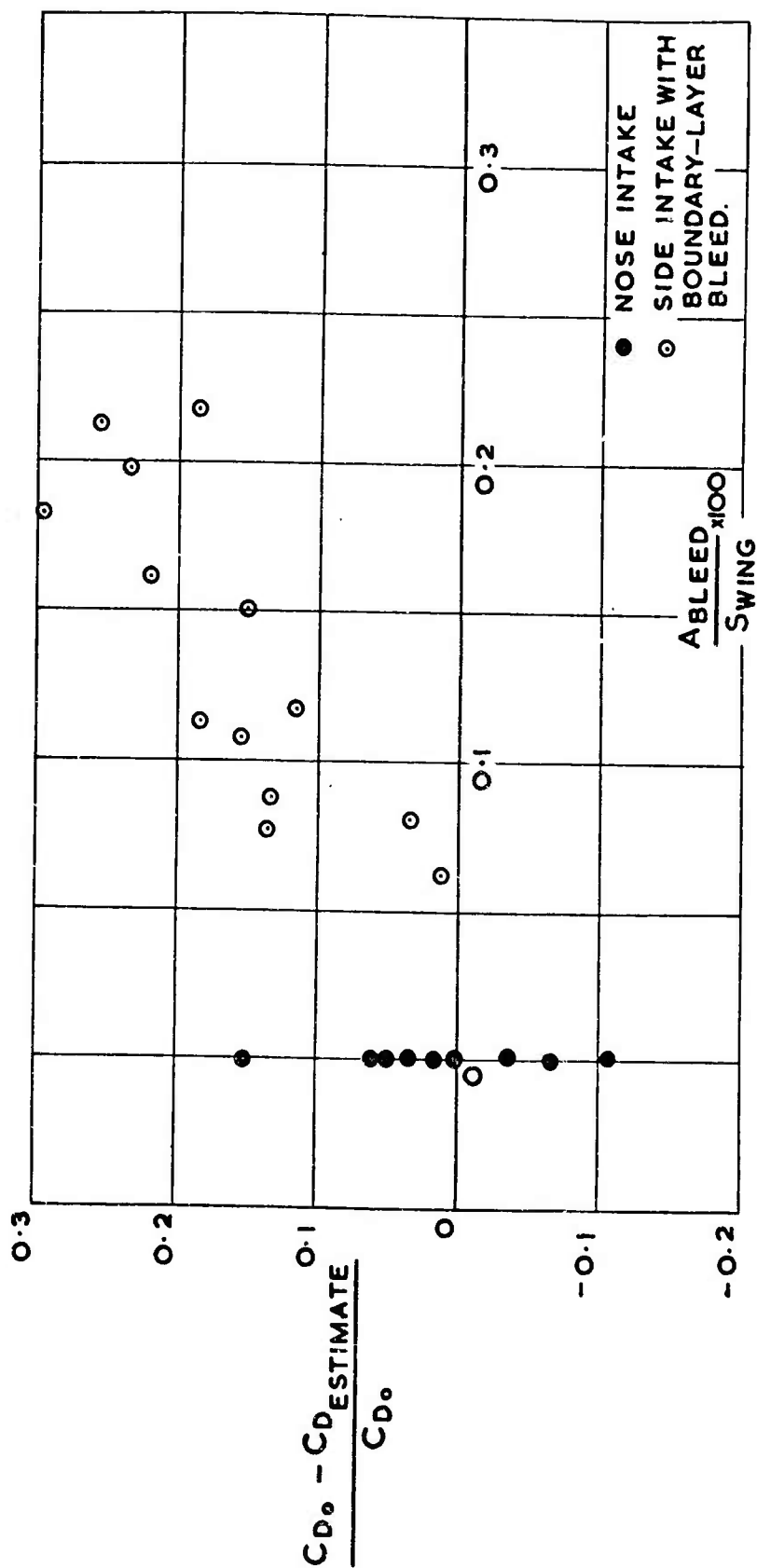


Fig. 7 Comparison of flight-measured and estimated drag at subsonic speed
(plotted against A_{bleed}/S_{wing})

LOW-DRAG INSTALLATION OF TWIN PROPULSION NOZZLES
IN THE REAR OF THE FUSELAGE FOR TRANSONIC
AND SUPERSONIC FLIGHT

by

Helmut Langfelder

Entwicklungsring Süd GmbH, München, Germany

SUMMARY

A very large number of parameters influences the low-drag installation of twin engine nozzles in the rear of the fuselage. Because of the many possibilities systematic investigations are likely to lead to useful results only when they are based on the demands of a specific configuration. For the project of a medium tactical fighter, various models were tested by Entwicklungsring Süd. Since a better insight into the basic problems is given by pressure distribution measurements than by attempting to make force measurements with a balance, a technique that causes difficulties, pressure measurements were made in this case on the afterbody, the base and the internal and external nozzle surfaces in order to understand the flow. A twin propulsion nozzle installation requires careful attention to the shape of the boattail, since the drag associated with this in the transonic range may be much larger than the base drag. Base drag was comparatively small in the case investigated. The influence of ejector nozzles with venting of base areas was also investigated, but the advantage of such an installation is doubtful at transonic speeds. The purpose of the ejector nozzle is mainly the increase of thrust obtained at supersonic speeds because of its divergent nozzle section. The results of these investigations of boattail and base pressure drags, and of the secondary ejector drag, are presented and discussed, together with some comments on ejector nozzle behaviour. The problem of the best solution for the integration of propulsion nozzles into the rear of the fuselage remains unsolved in many practical cases and the pertinent problem areas are therefore briefly reviewed.

SOMMAIRE

Un très grand nombre de paramètres interviennent dans l'installation, à faible traînée, de tuyères de réacteurs, jumelées à l'arrière du fuselage. En raison de nombreuses possibilités, des recherches systématiques ne peuvent mener à des résultats utiles que si elles sont basées sur les exigences d'une configuration particulière. Dans le cadre d'un projet d'appareil de combat tactique moyen, différentes maquettes ont été expérimentées par EWR. Une meilleure compréhension des problèmes fondamentaux étant obtenue au moyen des relevés de distributions des pressions, plutôt que par la mesure des forces à la balance, technique qui soulève des difficultés, des mesures de pression ont été effectuées sur l'arrière-corps, la base et les parois interne et externe de la tuyère pour comprendre l'écoulement. L'installation de tuyères de propulsion jumelées exige qu'une attention particulière soit accordée à la forme du rétreint, la traînée qui en résulte pouvant être considérablement plus grande que la traînée de base. La traînée de base était assez faible dans le cas étudié. L'influence des tuyères avec effet de trompe a également été étudiée, mais les avantages de ce type d'installation sont douteux aux vitesses transsoniques. L'objet de la tuyère à double flux est principalement l'augmentation de la poussée obtenue aux vitesses supersoniques grâce à son divergent. Les résultats de recherche portant sur la traînée du rétreint et de la base, ainsi que la traînée secondaire de la tuyère à double flux sont présentés et discutés, avec quelques remarques sur le comportement de la tuyère à double flux. Le problème de la meilleure intégration possible des tuyères de propulsion à l'arrière du fuselage n'a pas reçu de solution dans bien des cas concrets, les difficultés qu'il présente sont brièvement passées en revue.

CONTENTS

	Page
SUMMARY	196
SOMMAIRE	197
LIST OF FIGURES	199
NOTATION	200
1. INTRODUCTION	201
2. TEST METHODS	202
2.1 Description of Models	202
2.2 Boundary Layer on the Afterbody	203
2.3 Method of Drag Analysis	203
3. RESULTS	203
3.1 Base Pressure Drag	203
3.2 Boattail Pressure Drag	204
3.3 Secondary Ejector Drag	205
3.4 Effect of Ejector Nozzle on Thrust	205
4. CONCLUSIONS AND UNSOLVED PROBLEMS	206
REFERENCES	206
FIGURES	207

LIST OF FIGURES

	Page
Fig. 1	Twin propulsion ejector nozzle installation
Fig. 2	Geometry of afterbody and nozzles
Fig. 3	Boundary layer on afterbody
Fig. 4	Method of drag analysis
Fig. 5	Effect of jet pressure ratio on base pressure drag
Fig. 6	Base pressure drag. Axial force coefficient
Fig. 7	Boattail pressure drag. Axial force coefficient
Fig. 8	Boattail pressure distribution. $M = 0.92$
Fig. 9	Boattail pressure distribution. $M = 2.0$
Fig. 10	Secondary drag of ejector
Fig. 11	Expansion in ejector nozzle
Fig. 12	Effect of ejector nozzle on primary thrust

NOTATION

M_0	free-stream Mach number
δ_0	boundary layer thickness
r_0	radius of equivalent body of revolution
α	angle of incidence
p	local static pressure
p_∞	free-stream static pressure
p_{11}	static pressure in nozzle exit plane
p_{0s}	total pressure of primary flow in nozzle
q_∞	free-stream dynamic pressure
C_D	drag coefficient (axial force) in drag units
C_p	pressure coefficient
H	altitude
G_s	secondary mass flow
G_p	primary mass flow
S_p	primary thrust
T.E.	trailing edge

LOW-DRAG INSTALLATION OF TWIN PROPULSION NOZZLES IN THE REAR OF THE FUSELAGE FOR TRANSONIC AND SUPERSONIC FLIGHT

Helmut Langfelder

1. INTRODUCTION

The installation of two engines side by side in the rear fuselage is of great interest in current fighter aircraft design. The closure problem of the rear body for supersonic aircraft with reheat engines, which are also expected to operate efficiently at subsonic speeds without reheat, is made difficult by the fact that the variable nozzles required have very different exit areas for these two cases. When a twin propulsion nozzle arrangement is used further complexities arise. Large base areas between the nozzles, generally thought to be detrimental, can then only be avoided by geometrically complicated fairing shapes in the boattail region and possibly venting of the base.

During the early design stages of the VJ 101 X-1 and X-2 various studies were done by EWR to solve similar problems for the twin-engine tilting wing-tip pods of that aircraft. Since in that case a short rear body was of paramount importance, considerable base area seemed unavoidable. The pressure distribution testing carried out then showed that pure base drag might not be large for high-speed subsonic flight and that indeed excessive boattailing, in particular necking-in in the region between the engines, could be unsuitable. Some of this work is reported in Reference 1.

For a later project of a tactical fighter aircraft at EWR, these results were used to develop some general guide-lines for aerodynamic design of low-drag twin-nozzle installations in the rear of the fuselage. In most practical cases even close cowlings of the engines does not result in a long enough boattail without adding considerably to the overall length of the fuselage. Therefore, if boattail angles are to be kept below about 10° , a blunt base should be accepted and the nozzle exit plane offset from it. This effect can be increased by recessing the base. An aerodynamic ejector nozzle using secondary air ducted to it from flush rear fuselage boundary layer intakes seemed particularly suitable as a variable nozzle for the reheat engines.

Such a nozzle consists of a variable primary engine nozzle and an ejector shroud providing the divergent nozzle section for full expansion at the high jet pressure ratios occurring during supersonic flight. For non-reheat engine operation the region around the jet, required to accommodate the increased nozzle exit area for the supersonic case with reheat, is partly occupied by a good external shroud boattail and partly by an annulus vented by the secondary flow. The theory of such nozzles is discussed in Reference 2.

To gain some insight into the aerodynamics of the rear body and the nozzle flow, models were designed for testing in both transonic and supersonic tunnels. Force testing by using internal balances in flow models is a complicated technique with multiple sources of error. As it was desired to have some understanding where local drags occur and by what specific means they might be reduced, an extensive pressure plot was considered to be a better way to tackle the problem.

2. TEST METHODS

2.1 Description of the Models

Figure 1 shows the twin propulsion ejector nozzle installation proposed for the aircraft. Models were built for testing in the Transonic (8 ft x 9 ft) and Supersonic (27 in x 30 in) Tunnels of the Aircraft Research Association, Limited, England (ARA). Both models used were equipped with pressure measuring points on the afterbody, the base, the ejector shroud and some pressures could be measured inside the nozzles. The number of pressure points indicated on the figure refer to the transonic model, which was more fully instrumented, the total number of measuring points used on the supersonic model being about half. The installation in the aircraft provided flush secondary air-intakes arranged circumferentially at a station forward of the vertical tail to supply the secondary air flow to the ejector nozzles. For the transonic model this air flow was simulated by diverting some of the pressurized air ducted to the model through a sting and a forebody. The supersonic model was not designed for secondary air flow. For these tests unheated air was used, as this was not expected to introduce basic errors. The geometry of the afterbody and the nozzles is shown on Figure 2, in which the two basic configurations for the models can also be seen. The non-reheat configuration was used for most of the tests in the Transonic Tunnel and the reheat configuration applies to the model in the Supersonic Tunnel. Additional geometric variations were the so-called "recessed" base, which meant that the plane of the base could be moved upstream to a point about half a nozzle exit diameter from the trailing edge of the boattail, or the "bluff" base could be tested, where this plane was close to the trailing edge of the boattail; further, the external ejector shroud could be removed, leaving a convergent primary nozzle. The design of the ejector nozzle was based on the results of Reference 2, which show that the shroud length is critical when both the conditions of parallel exit flow and negligible mixing within the ejector are to be fulfilled.

The equivalent body of revolution is also indicated on Figure 2 to give an idea of the closure of the rear. Somewhat less than half the total cross-sectional area is closed by the boattail, leaving a fifth for the base. The nozzle exit area difference for non-reheat and reheat geometries is 10% of the total maximum cross-sectional area of the afterbody. This area is occupied by the external ejector shroud with a boattail of about 10° . The equivalent boattail angle is only 4° but, due to certain requirements of the engine installation, especially on the underside of the fuselage, boattail angles of about 11° were required locally.

The models were provided with both vertical and horizontal tails at representative settings because some significant influence on the boattail pressure distribution was expected. The pressure distributions shown later demonstrate that the tail surfaces can have a large effect on the rear body aerodynamics.

The ratio of maximum cross-section of the model to the tunnel cross-section was about 4.5% for the transonic and 3.2% for the supersonic model.

2.2 Boundary Layer on the Afterbody

The boundary layer approaching the boattail was investigated on the underside of the model near the plane of symmetry. The profile shown on Figure 3 indicates a turbulent boundary layer. The thickness is summarized on the table below Figure 3. For most practical flight cases the boundary layer would not be expected to be nearly as thick. This will have to be considered in relation to incidence effects, which apply mainly to the boattail pressure distribution. However, the general nature of the conclusions should not be greatly affected by this discrepancy.

2.3 Method of Drag Analysis

A summary of the method of drag analysis is given on Figure 4, where an attempt is made to isolate the drag contributions of the various elements of the flow. The thrust definition required in conjunction with these drags refers to the stream thrust of the primary jet only. The primary jet boundary indicated in the figure is not precisely known and the primary flow will certainly not be isentropic. Indeed the lack of symmetry of the internal shroud pressure distribution indicated that quite a complicated shock system is involved in the expansion process of this jet after it leaves the convergent primary nozzle. This will be further discussed in Section 5.4. However, other tests have shown that the assumption of a parallel flow at the exit applies in ejector nozzles of this type and, therefore, a more or less uniform static pressure can be assumed at the exit plane. For the known primary and secondary mass flows, the flow area of the secondary stream at that station can then be calculated and the secondary ejector drag terms can be estimated from a knowledge of the static pressure p_{11} at the exit, obtained from the internal shroud pressure distribution.

The external ejector shroud pressure could contribute to the drag for the non-reheat configuration. But this contribution is very small and, in the results shown later it has been included in the secondary ejector drag term.

The largest contribution to drag can be expected from the boattail and base pressure distributions. These are in the form of axial force coefficients, obtained by integration of the pressure distribution, which is sufficiently well defined by an adequate number of pressure-measuring points.

3. RESULTS

3.1 Base Pressure Drag

The pressure drag due to the base is considerably affected by primary jet pressure ratio and Mach number. In Figure 5 the effect of pressure ratio is shown for the two important cases of low-level flight at $M = 0.92$ and supersonic flight with reheat. In the former case the curve obtained is the typical base pressure variation with

pressure ratio, showing a steep increase of pressure (decrease of drag) as the pressure ratio varies from the value corresponding to "jet off" to small blowing pressures, followed by a decrease of pressure (increase of drag) as the pressure ratio increases further. At pressure ratios corresponding to real flight conditions (about 2.5 to 3.0), the base pressure is about the same as for the "jet off" condition. The behaviour of the reheat configuration at $M = 2.0$ is different. There a steady decrease of drag occurs with pressure ratio of the primary jet and, for p_{08}/p_{∞} about 8 - 10, representative for such a flight condition, the drag is only about a third of the "jet off" case. Also shown on the diagram is the effect of the recessed base. This approximately doubles the thrust obtained from the base for $M = 0.92$ and also decreases the base drag somewhat for the supersonic flight condition. To give an idea of the order of magnitude of the base drag, it can be compared with estimated skin friction drags of the aircraft, which would be about 12 drag units for $M = 0.9$ and 10 drag units at $M = 2.0$.

Not shown on the diagram is the effect of removing the ejector shroud. For $M = 0.92$ this results in an increase of drag about equal to the difference of drag between the two base geometries.

The effect of Mach number and secondary flow in the ejector nozzle on the base drag is shown on Figure 6, which refers to the recessed base. It is interesting to note that at high subsonic speeds the base provides some thrust and this is increased when the ejector nozzle is operated with secondary flow. The transonic drag rise Mach number for the base contribution is very high, not less than $M = 0.92$. However at small supersonic Mach numbers considerable base drag occurs with this installation. In the supersonic reheat case, base drag seems to increase with Mach number. For the pressure ratios which correspond to real flight conditions the ejector shroud has not much effect. Further incidence effects on the base drags were found to be very small in all cases.

3.2 Boattail Pressure Drag

The pressure distribution on the afterbody is an important element of drag, due to the boattailing in that region. The flow is required to undergo considerable compression near the trailing edge of the boattail to approach the low drag experienced by idealized shapes. The axial force coefficient of the afterbody boattail is shown on Figure 7 as a function of flight Mach number. Incidence affects the drag, decreasing C_D as angle of attack increases. The jet itself does not influence the pressure distribution greatly. As can be seen on the diagram, relatively high drags are experienced on the boattail, the order of magnitude being about 60% of friction drag of the aircraft for flight at $M = 0.9$ at sea level and 35% at $M = 2.0$. The drag rise in the transonic region commences early. The type of pressure distribution obtained for subsonic Mach numbers is indicated on Figure 8 for $M = 0.92$. The C_p -distribution is plotted for longitudinal rows as shown on the sketch. The location of the vertical tail in the plane of symmetry is seen to affect the pressures near it, comparing row 1 with 2 and 3. The horizontal tails are situated between rows 9 and 10 and they also seem to have a considerable effect. For $C_p < -0.18$ the flow can be considered supersonic. As can be seen, large supersonic regions of expansion exist on the afterbody with a shock system just upstream of the trailing edge where ambient static pressure, or in some parts a little above ambient static pressure, is obtained. The large expansion regions and the poor

compression following it explain the high drag experienced on the boottail. Better shapes are required, especially on the lower half of the afterbody. The aircraft with this particular shape of afterbody gave a ratio of 1.46 of total drag to that of the equivalent body of revolution of the same wetted area and thickness ratio.

The conditions at $M = 2.0$ are shown on Figure 9. Only very slight compression occurs in this case and the ambient static pressure is not obtained on the surface. Between rows 5 and 6 the horizontal tail affects the pressure distribution.

3.3 Secondary Ejector Drag

The secondary drag of the ejector in terms of the axial force coefficient is given on Figure 10, which is based on estimated conditions for the installation in the aircraft. The secondary air is taken on board through flush boundary layer intakes. Experimental results for the pressure recovery of such intakes were used and an internal ducting loss equal to the entry dynamic pressure was assumed. The secondary drag is based on free-stream conditions for the intake momentum. At $M = 0.92$ a secondary mass flow of 3% of the primary flow gives the minimum drag. Curves for practically no secondary air flow and for $G_s/G_p = 0.03$ are given for the non-reheat transonic configuration.

The secondary air flow in the ejector nozzle is not choked and is practically isentropic within the ejector. At Mach numbers below about 0.85 there is no benefit in having any secondary flow from the point of view of drag. The drag rises very steeply when a Mach number of 0.92 is exceeded. For supersonic flight the secondary ejector drag is relatively small.

3.4 Effect of Ejector Nozzle on Thrust

The ejector nozzle in the non-reheat configuration is operated at pressure ratios $P_{0s}/P_{0\infty}$ ranging from about 1.5 to 4. At pressure ratios above about 4 instability occurs with secondary air flows less than 2%. The primary flow overexpands slightly, as shown on Figure 11, for a pressure ratio of 2.5. This overexpansion is a function of the secondary air flow. The thrust obtained from the nozzle is somewhat less than that of the ideal convergent nozzle. On Figure 12 it is seen that a loss of thrust of about 1.5% must be expected from this installation in the transonic range.

For the reheat configuration some cooling secondary air flow will be required to protect the shroud. A flow of about 1% is sufficient for this purpose. Instability of the internal nozzle flow in this configuration occurs at low pressure ratios of about 3 to 4, but again, as tests have shown, this will be avoided by having a secondary air flow of about 2%. For supersonic flight with reheat at altitude the pressure ratios will be greater than about 7, but when accelerating through the transonic range pressure is lower, or when throttled instability would occur if insufficient secondary flow is available. When the nozzle is operated with the correct secondary flow of about 2%, the ejector nozzle produces more thrust than the ideal convergent nozzle, as seen on Figure 12. At Mach numbers around 2.0 a gain of 6 - 7% can be expected.

4. CONCLUSIONS AND UNSOLVED PROBLEMS

The propulsion nozzle installation described in this paper should not be regarded as an optimum solution for the problem of finding a low-drag twin engine arrangement in the rear of the fuselage for an aircraft operating both in the transonic and supersonic speed range. To obtain efficient propulsion with reheat at higher Mach numbers, the performance for non-reheat flight at $M = 0.92$ has been compromised. The ejector nozzle is not as efficient as a simple convergent nozzle in that speed range. The drag on the rear body is mainly due to an unsatisfactory pressure distribution on the boattail at high subsonic Mach numbers, where the desired compression is not obtained efficiently in this case, especially on the underside of the fuselage. The base itself produces thrust at a Mach number of 0.92 and this can be increased by recessing the base. Improved shapes of the boattail will lead to considerable reduction of drag and it is not necessary to avoid a bluff base altogether. In practical cases many constraints for the cowlings of the engines will have to be taken into account. For V/STOL aircraft, for example, deflection of the cruise engine thrust will make it particularly difficult to improve the boattailing of the underside. In some cases it may be possible to integrate the fuselage boattail with the nozzle and use it as part of the expansion surface of the jet itself. Ramp nozzles, for example, may be adapted for this type of application. In any case it will be necessary to investigate further which nozzles give really satisfactory performance at transonic speeds, while effectively giving convergent-divergent nozzle performance at supersonic Mach numbers. This problem is a very involved one, since careful weight estimates of the variable nozzles are required before a proper choice can be made. The type of variable ejector nozzle discussed here is a comparatively simple and short one. Aerodynamically superior proposals often turn out prohibitively heavy, since they may require additional linkages and longer leaves.

For military aircraft the infra-red radiation from the reheat nozzle and jet poses further problems not discussed here. This aspect could assume considerable importance in the final choice of the type of nozzle.

REFERENCES

1. Aulehla, F. *Heck-aerodynamik einer Triebwerksgondel mit zwei nahe zusammenliegenden Strahlen.* pp. 226-232, WGLR Jahrbuch 1963.
2. Pearson, H. et alii. *A Theory of the Cylindrical Ejector Supersonic Propelling Nozzle.* Journal of the Royal Aeronautical Society, Vol. 62, October 1958.

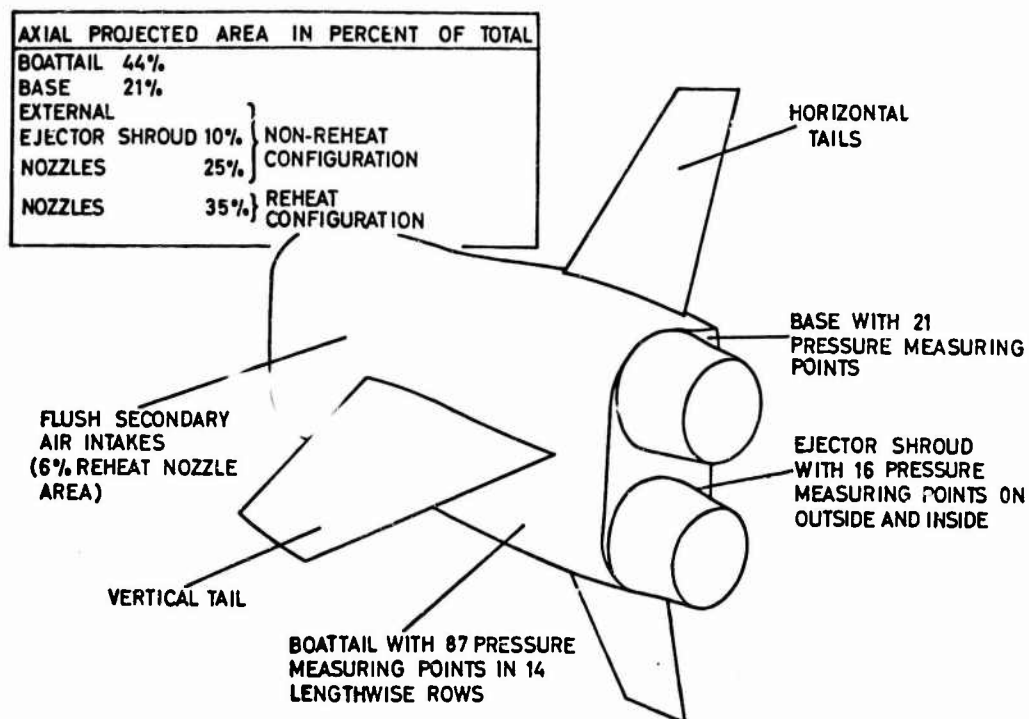
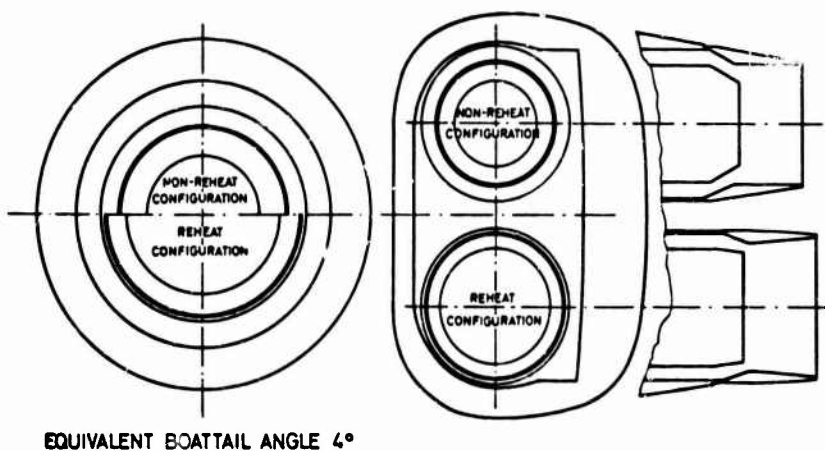


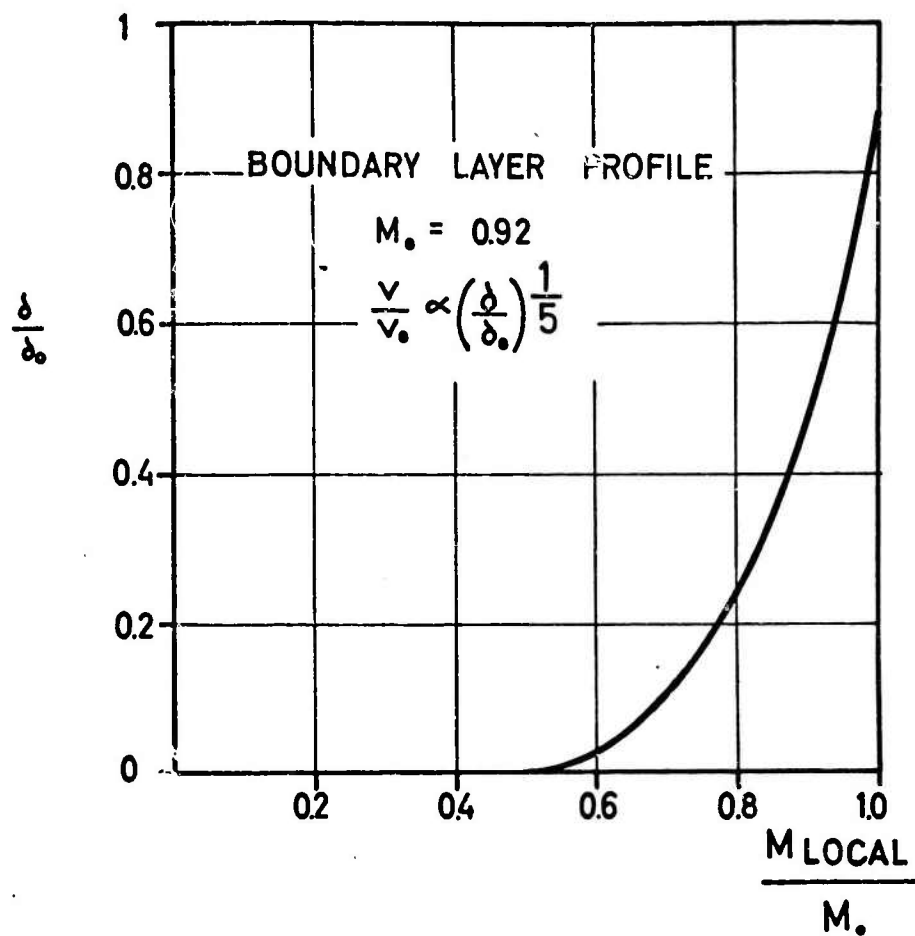
Fig.1 Twin propulsion ejector nozzle installation

EQUIVALENT BODY OF ROTATION



	NOZZLE GEOMETRY	
	NON-REHEAT CONFIGURATION	REHEAT CONFIGURATION
EJECTOR SHROUD LENGTH		
PRIMARY NOZZLE DIA	0.8	0.66
NOZZLE EXIT DIAMETER		
PRIMARY NOZZLE DIA	1.46	1.26

Fig.2 Geometry of afterbody and nozzles

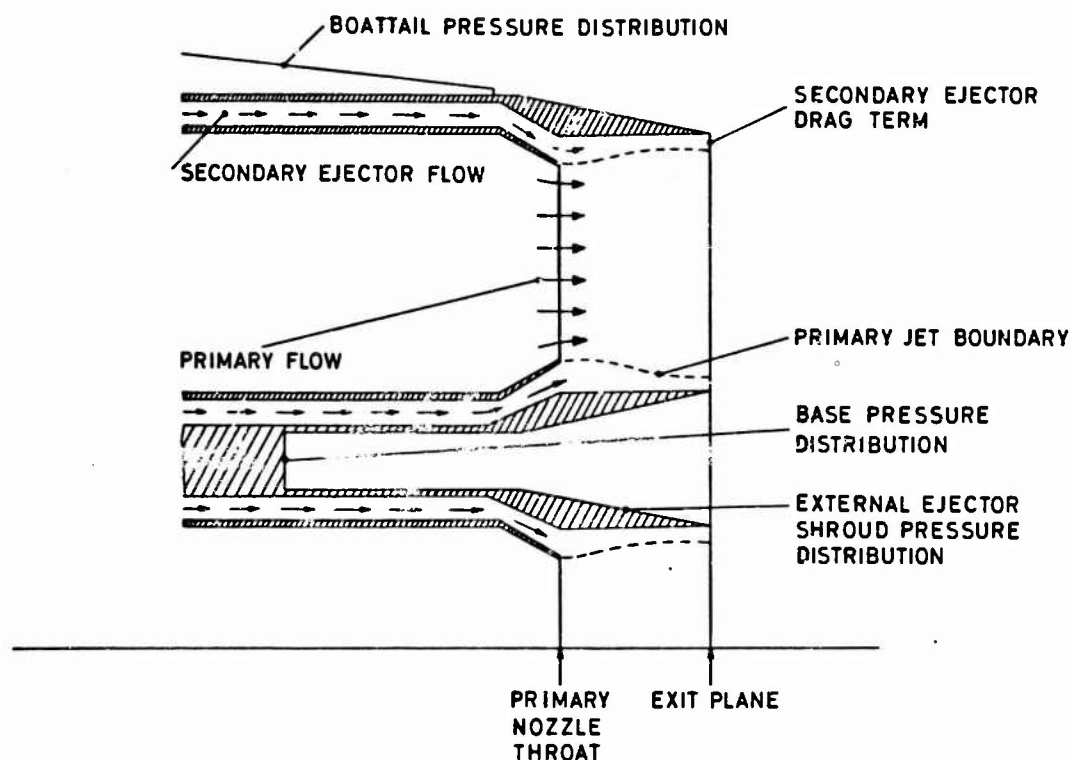


BOUNDARY LAYER THICKNESS

$\delta_\infty/\%$ TABLE 1

M	TRANSONIC MODEL	SUPERSONIC MODEL
0.6	0.25	—
1.35	0.28	—
1.8	—	0.21
2.2	—	0.22

Fig.3 Boundary layer on afterbody



DRAG TERMS

1. BASE PRESSURE DRAG - INTEGRATED PRESSURE DISTRIBUTION (21 POINTS) YIELDING AXIAL FORCE COEFFICIENT
2. BOATTAIL PRESSURE DRAG - INTEGRATED PRESSURE DISTRIBUTION (87 POINTS) YIELDING AXIAL FORCE COEFFICIENT
3. EXTERNAL EJECTOR SHROUD PRESSURE DRAG - INTEGRATED PRESSURE DISTRIBUTION (8 POINTS) YIELDING AXIAL FORCE COEFFICIENT
4. SECONDARY EJECTOR DRAG TERM - MOMENTUM AND PRESSURE TERM CALCULATED BY ESTIMATING NOZZLE STATIC EXIT PRESSURE FROM INTERNAL SHROUD PRESSURE DISTRIBUTION (8 POINTS) AND EFFECTIVE SECONDARY FLOW AREA IN THE EXIT PLANE FROM FLOW PARAMETERS WITH THE ASSUMPTION OF PARALLEL FLOW AT THE OUTLET.

Fig.4 Method of drag analysis

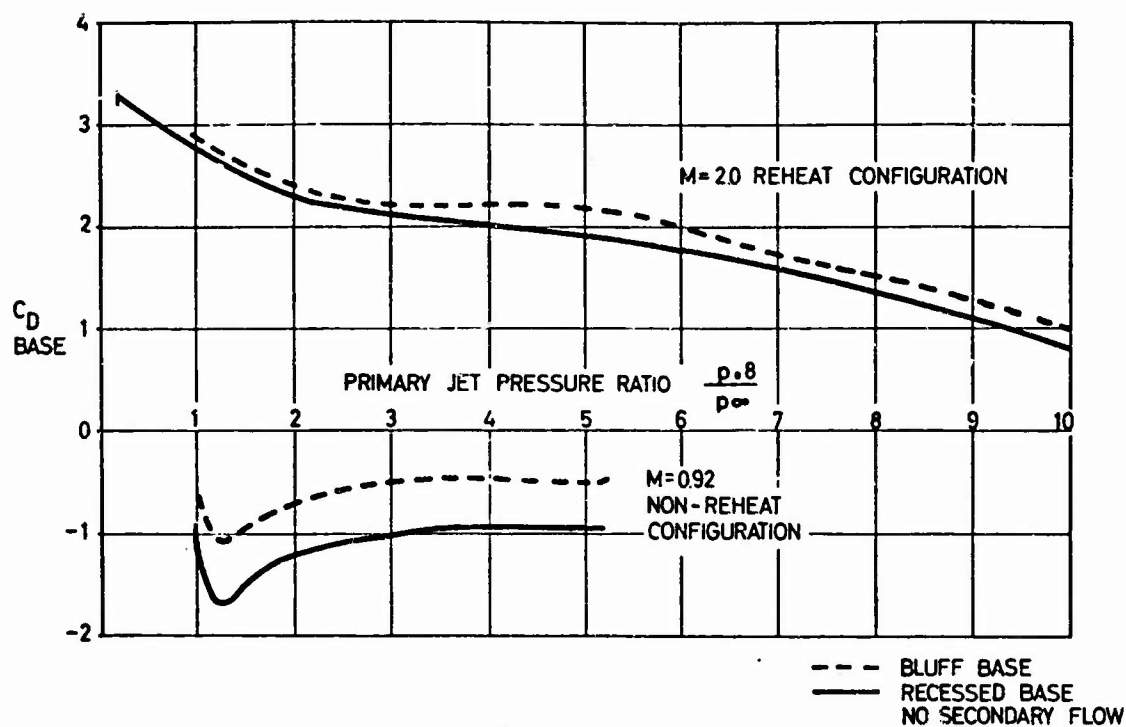


Fig. 5 Effect of jet pressure ratio on base pressure drag

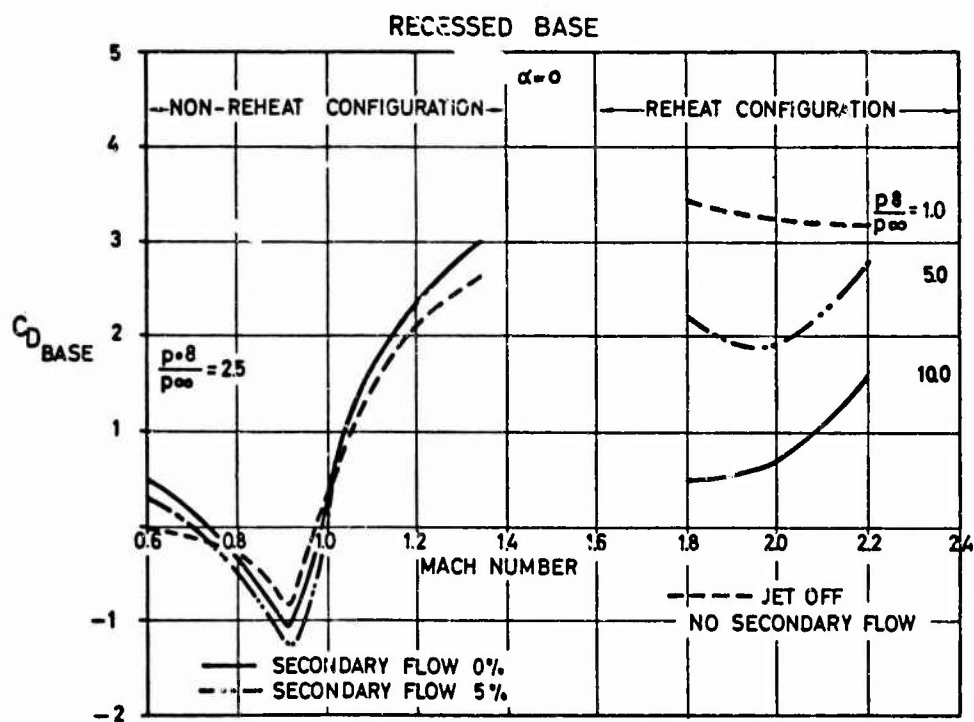


Fig. 6 Base pressure drag. Axial force coefficient

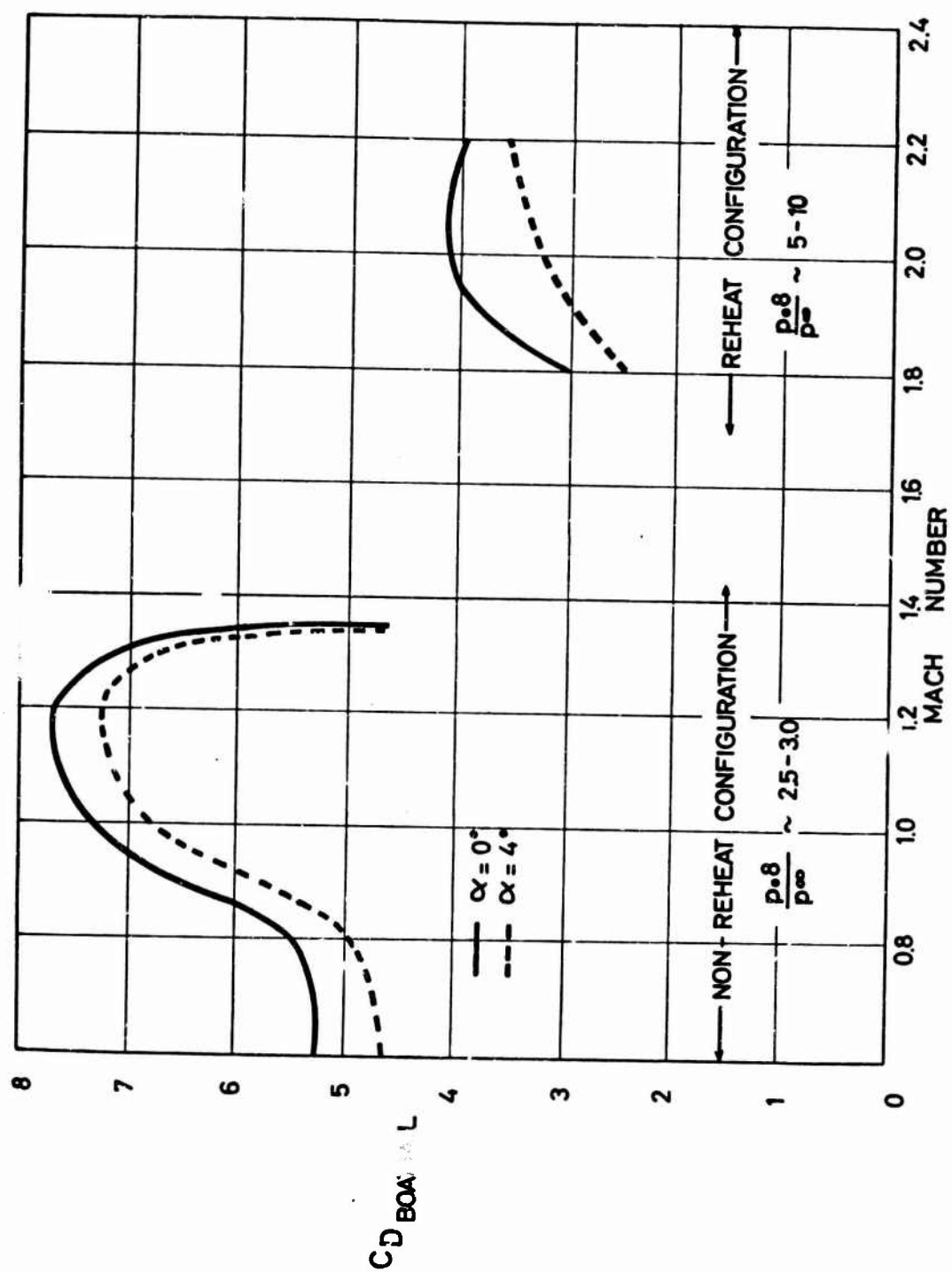


Fig. 7 Boattail pressure drag. Axial force coefficient

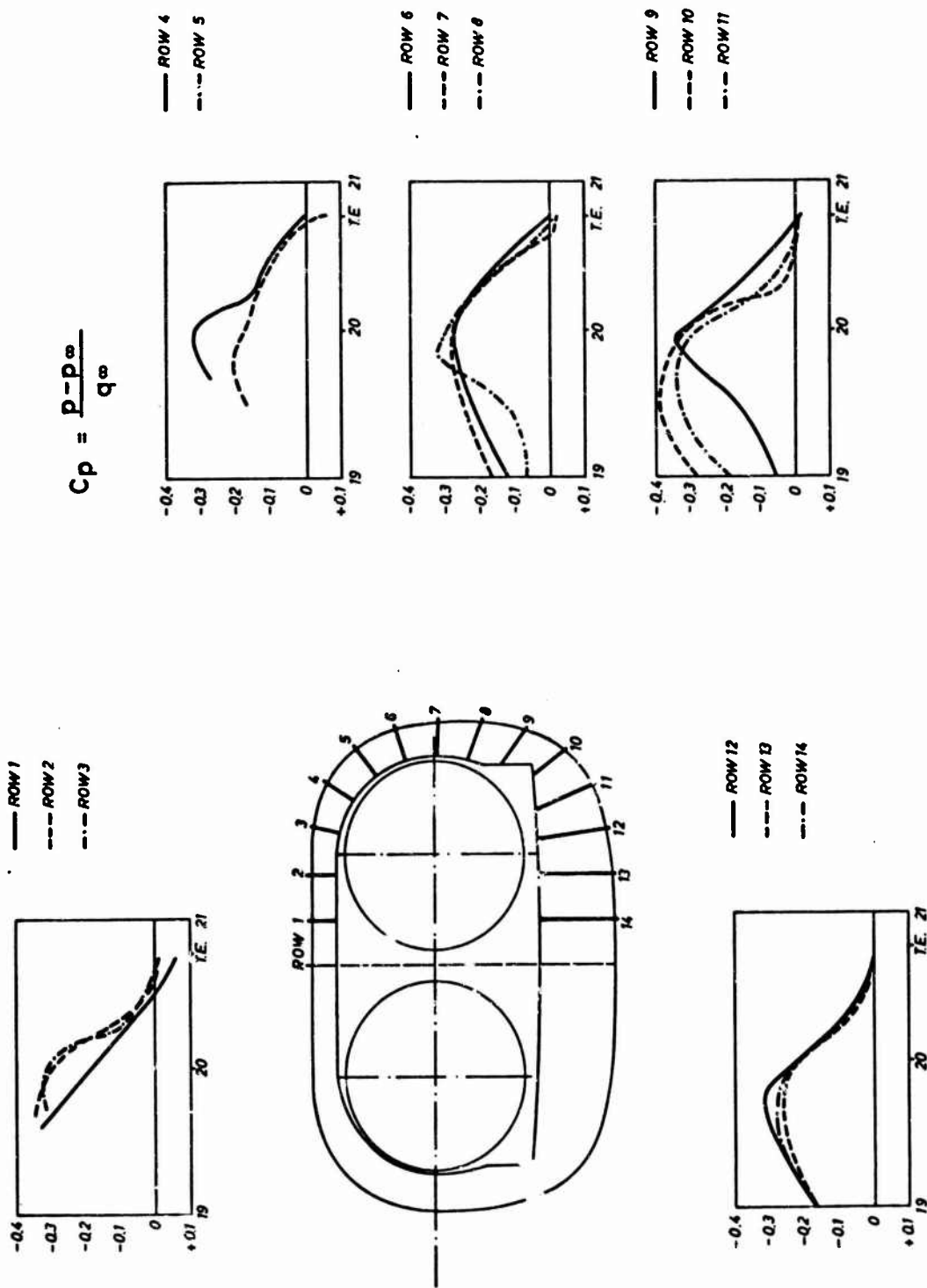


Fig. 8 Boattail pressure distribution. $M = 0.92$

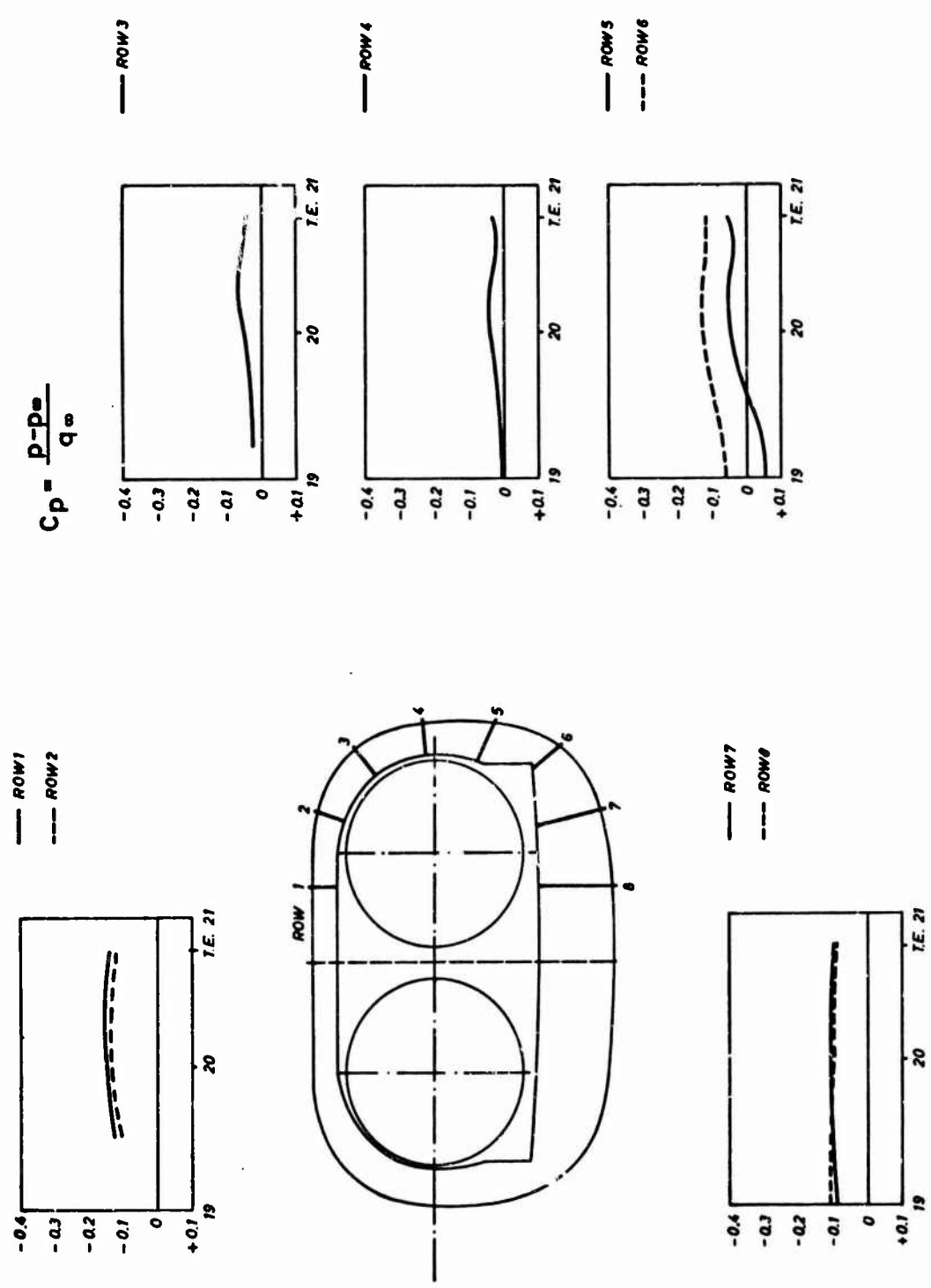


Fig. 9 Foattail pressure distribution. $M = 2.0$

ASSUMING FLUSH INTAKES FOR SECONDARY FLOW AND LOSS OF
ENTRY DYNAMIC PRESSURE FOR INTERNAL DUCTING

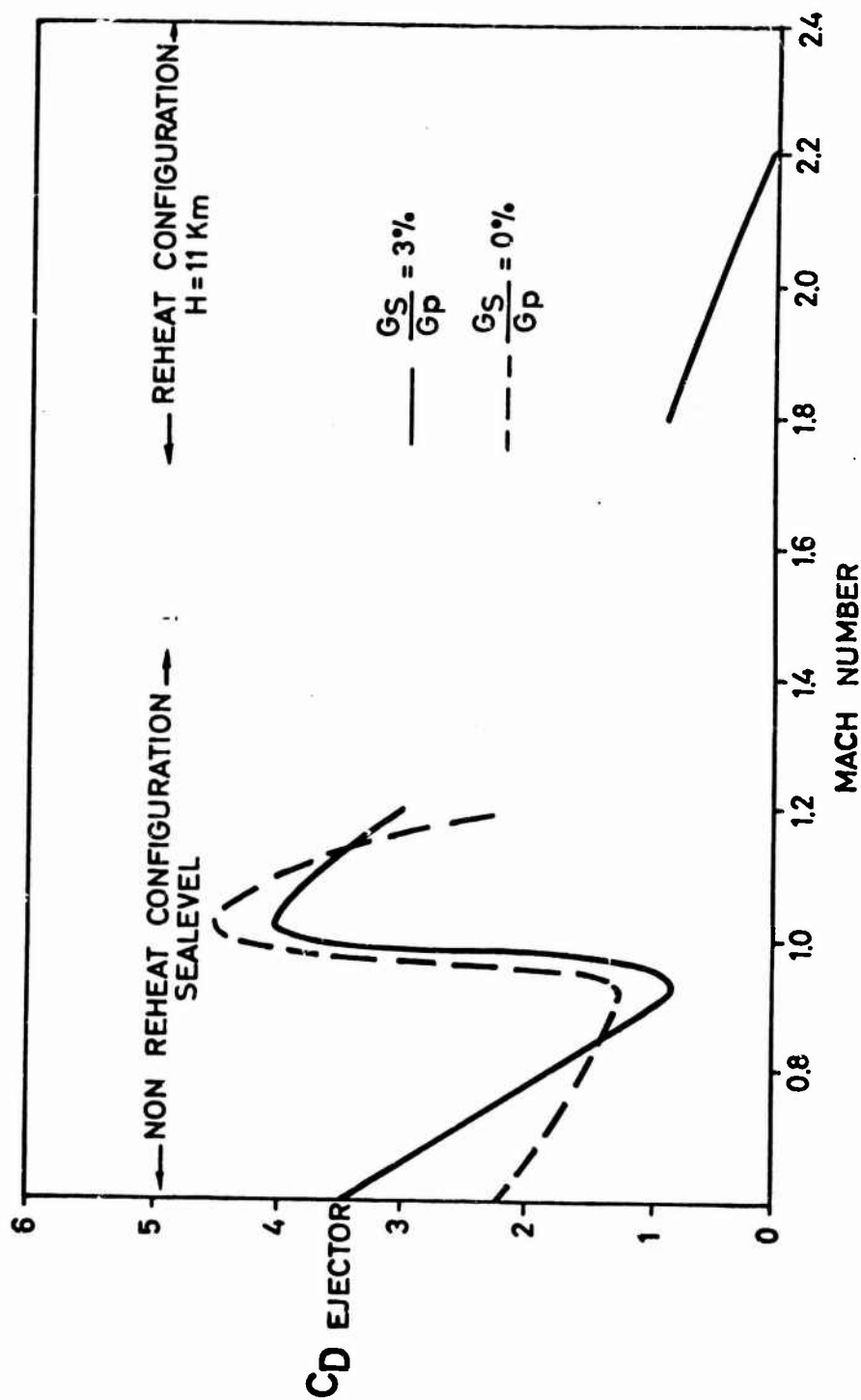


Fig. 10 Secondary drag of ejector

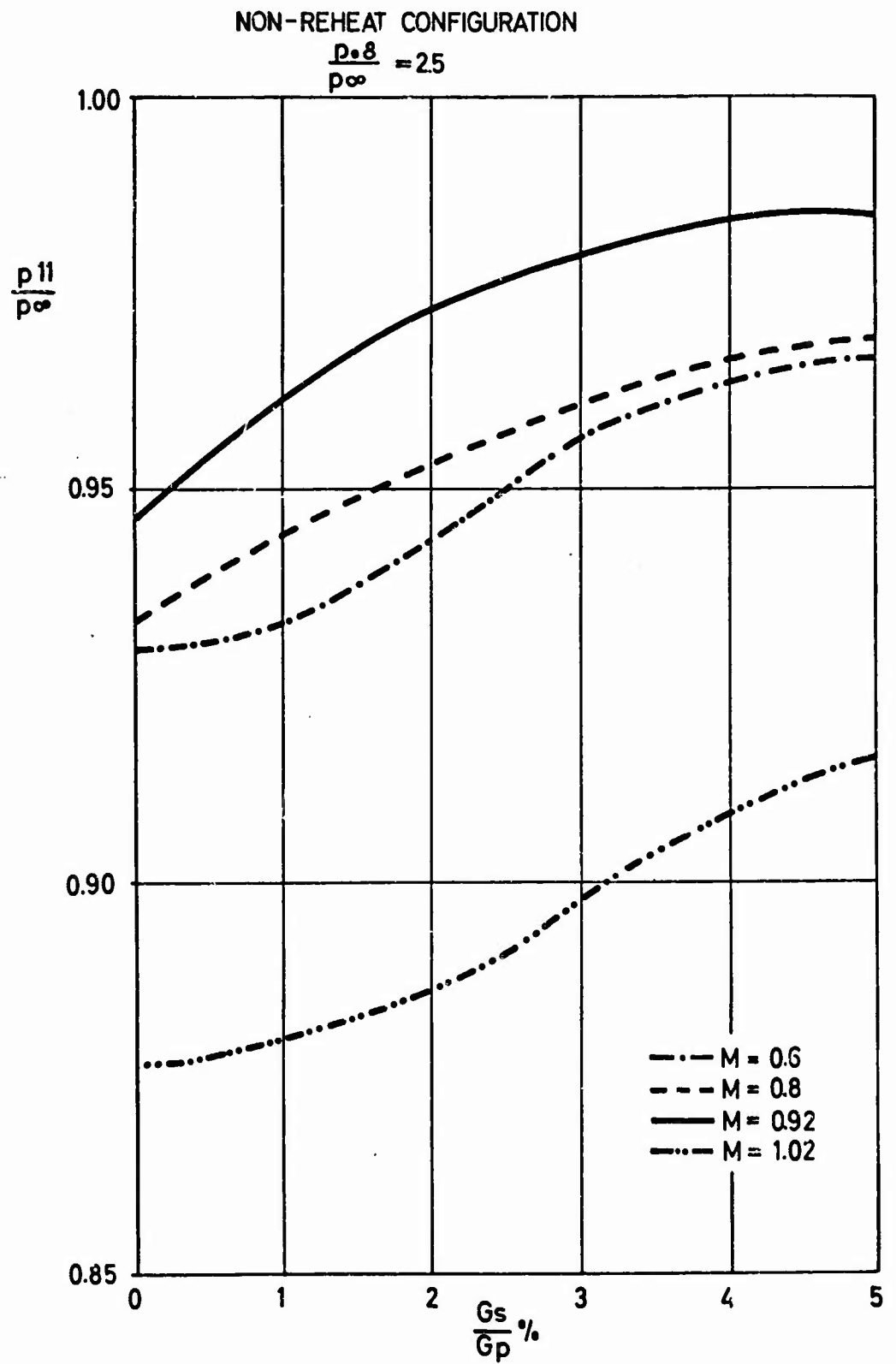


Fig. 11 Expansion in ejector nozzle

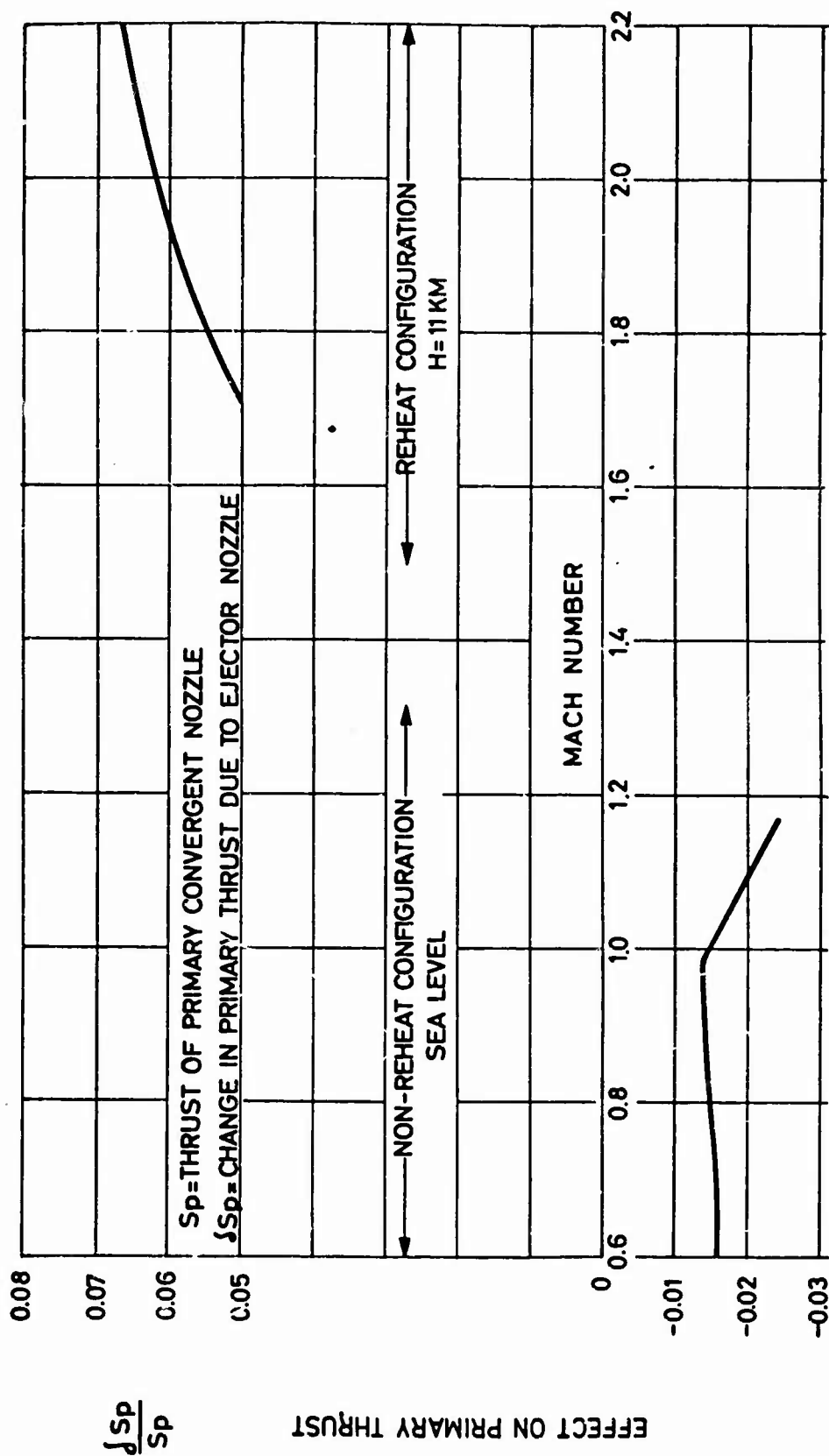


Fig. 12 Effect of ejector nozzle on primary thrust.

METHOD OF NET THRUST MEASUREMENT
IN SUPERSONIC FLIGHT

by

Theron W. Davidson

Naval Air Test Center, Patuxent River, Maryland, USA

SUMMARY

The feasibility and accuracy of the Traversing Rake System, which samples pressures and temperatures through the engine exhaust has been established. Initial results show data to be within 2-3% gross thrust and 4-5% net thrust. This accuracy is expected to be maintained with the new automatic data acquisition and processing system. This system, which utilizes airborne magnetic tape, analyzes and plots thrust and drag data in a matter of minutes. The rake promises developmental and research application bypassing extensive engine test cell calibrations.

SOMMAIRE

On a établi la valeur pratique et la précision du Traversing Rake System (TRS) qui permet des échantillonnages de pressions et de températures le long de l'échappement du réacteur. Les premiers résultats montrent que l'exactitude des données obtenues est de 2 à 3% pour la poussée globale, et de 4 à 5% pour la poussée nette. On compte maintenir ce degré de précision avec le nouveau système automatique d'acquisition et de traitement des données. Ce système, qui utilise des bandes magnétiques aéroportées, analyse les informations sur la poussée et la trainée et en trace le graphique en quelques minutes. Il semble que le TRS puisse trouver dans le domaine de la recherche et des développements, des applications permettant d'éviter un travail considérable d'étalonnage de cellules d'essais de moteurs.

CONTENTS

	Page
SUMMARY	218
SOMMAIRE	218
LIST OF FIGURES	220
NOTATION	221
1. INTRODUCTION	223
2. NET THRUST APPLICATIONS	223
3. GAS GENERATOR METHOD	224
4. TRAVERSING RAKE METHOD	225
4.1 Design Requirements	225
4.2 Description	225
4.3 Installation	226
5. TEST INSTRUMENTATION	226
5.1 Photopanel	226
5.2 Pilot's Panel	227
5.3 Oscillograph	227
6. EARLY TEST RESULTS	227
7. ACCURACY	228
8. SUPERSONIC TEST RESULTS	229
9. DATA REDUCTION	230
9.1 Initial Process	230
10. AUTOMATIC DATA PROCESSING SYSTEM	231
11. CONCLUSIONS	231
REFERENCES	232
FIGURES	233

LIST OF FIGURES

	Page
Fig.1 Traversing rake head	233
Fig.2 Assembled traversing rake system	233
Fig.3 Two installed rake systems	234
Fig.4 Automatic machine plot of corrected profiles of various parameters in the jet with respect to engine nozzle radius; both left and right engine data superimposed, utilizing separate rake systems	235
Fig.5 Pressure profiles across the jet for eight subsonic airplane Mach numbers	236
Fig.6 Comparison of rake gross thrust and laboratory gross thrust	237
Fig.7 Comparison of rake net thrust with internal method net thrust	237
Fig.8 Automatic machine plot of corrected supersonic profiles of various parameters in the jet with respect to engine nozzle radius	238
Fig.9 Mach number profiles across the jet for subsonic and supersonic flight	239
Fig.10 Pressure profiles across the jet for subsonic and supersonic flight	239
Fig.11 Gas flow parameters across the jet for subsonic and supersonic flight	240
Fig.12 Gross thrust per unit area across the jet for subsonic and supersonic flight	240
Fig.13 Sample machine plot of temperature and pressure profiles before lag corrections	241
Fig.14 Temperature profiles across the jet for subsonic and supersonic flight	241
Fig.15 Temperature profile across the jet from magnetic tape and fully automatic data reduction program	242
Fig.16 Typical pressure profile across the jet from magnetic tape and fully automatic data reduction program	243

NOTATION

M	Mach number
W_G	gas flow, lb/sec
A	unit area, ft ²
P	pressure, lb/ft ²
F_G	gross thrust, lb
EPR	exhaust pressure ratio
NATTS	(Trenton) Naval Air Turbine Test Station

Subscripts

t	total
s	static

METHOD OF NET THRUST MEASUREMENT IN SUPERSONIC FLIGHT

Theron W. Davidson

1. INTRODUCTION

If there is any one common thing that both aerodynamicists and propulsion engineers need it is clear and careful definition of thrust and drag that they can agree upon. It is not the purpose of this paper to offer such a definition, but one must be chosen in order to discuss net thrust. It should be remembered that propulsive forces and drag forces acting on an aircraft are related and can influence each other. Gross thrust produced by the engine nozzle influences the boattail and base drag on some installations. In addition to the ram drag involved in taking engine air aboard, there may be other drags, such as spillage, cowl, boundary-layer removal and auxiliary air drag, all of which are influenced by the amount of engine airflow. These extra forces are accounted for either by subtracting from the net thrust or by adding to the basic aircraft drag. Net thrust is defined as the difference between engine gross thrust and the ram drag of the engine airflow.

The whole system of getting at net thrust, by accounting for air, is much like the grocery clerk checking and weighing items when you leave the supermarket. He purchased the stock and placed it on the shelves for your use. He paid plenty for it, and he must charge you more if he is to make a profit. His profit is like our net thrust. Now the grocer has his checking problems too. The stock boy raids the cookie jar and the ice cream box. When refrigeration fails, spoiled milk goes down the drain and meat in the garbage. Even the tiny mouse sneaks away a little cheese. How accurate is the figure he calls "profit", and what is his real profit?

2. NET THRUST APPLICATIONS

Net thrust is a tool needed in all phases of the research, design and evaluation of airplanes. The airframe manufacturer designs an airplane with a specific engine in mind because he needs a specific propulsive force. The engine inlet ducts must be suited to the engine, and the whole propulsion system must be properly mated to the airframe. Wind-tunnel engineers are constantly looking for in-flight verification of their drag predictions to serve as a calibration for future work. They need to know what the net thrust is, so drag can be adequately defined. The test and development engineers need it to isolate causes of performance deficiencies early in an airplane development program. An accurate measurement of net thrust can help determine responsibility for non-compliance of performance guarantees, and it can be used to reduce the scope of flight testing, especially for airplanes with many different external loadings. Presently the fleet pilots are predicting mission ranges

and cruise control data from "drag count" charts that have been prepared from data based on the knowledge of net thrust.

For several years the Naval Air Test Center (NATC) at Patuxent River, Maryland has been actively engaged in the development of a satisfactory method for measuring in-flight net thrust for turbojet airplanes. The two most satisfactory methods studied were the Gas Generator method and the Traversing Rake method. Both methods are presently in use and are undergoing continual refinement. The instrumentation for both methods was installed on the same airplane so that two independent calculations of net thrust were available for any given test.

3. GAS GENERATOR METHOD

The Gas Generator method was refined and programmed for the Datatron Digital Computer by NATC¹. It is presently in standard use for performance determinations of airplanes powered by J79-GE-8 engines. This is an internal method, utilizing many coefficients and calibration curves. It is restricted to evaluations involving only those engine types for which extremely complex and extensive laboratory calibrations have been made.

The J79 engine calibrations were conducted in the Tullahoma laboratory. The engine was instrumented with pressure rakes, taps, and thermocouples to measure the gas-flow profiles at virtually every station. The characteristics of each measured station were then related to single-probe reading for a "calibration". The single probes at the various stations comprise an "instrumented" engine, the performance of which is calculated through the use of the calibration curves.

Along with the standard airplane performance instrumentation of airspeed, altitude, r.p.m., fuel flow, fuel used, and outside air temperature, the instrumentation of the calibrated engine included: (i) compressor inlet total pressure and temperature, (ii) exhaust nozzle position (area), (iii) inlet guide vane position, (iv) secondary air total pressure, and (v) turbine discharge total pressure and temperature.

Including the enumeration of input data, there are 55 computer data reduction exercises for the nonafterburning operations and 37 for afterburner operations. These computations involve such relationships as: (i) airflow vs. engine speed for various inlet guide vane schedules; (ii) tailpipe pressure loss, with respect to temperature and pressures, at both the turbine-out and exhaust stations; (iii) compressor discharge static pressure vs. turbine-out total pressure with respect to turbine-out Mach number; (iv) engine inlet airflow vs. engine speed with respect to compressor face total pressure; (v) airflow corrections for Reynolds number effect and variable stator positions; (vi) exhaust-system pressure loss vs. a turbine discharge-flow function with respect to effective discharge area and the exhaust-to-turbine absolute temperature ratio; (vii) thrust-weight flow-temperature functions vs. jet nozzle pressure ratio; (viii) secondary-pressure ratio vs. primary-pressure ratio with respect to nozzle area and a function involving secondary and primary weight flow and temperature ratios; and (ix) gross-thrust coefficient vs. primary-pressure ratio with respect to nozzle area and a function involving secondary and primary weight flow and temperature ratios.

When the lengthy laboratory tests have been performed for a given engine model, the data reduction procedures can be accomplished rapidly by machinery.

4. TRAVERSING RAKE METHOD

Many concerns, both military and industrial, have attempted to measure thrust with a traversing rake, but most have abandoned the idea. In order to utilize all the experience available on the subject these concerns were contacted for background on problem areas. It was apparent that emphasis should be placed on designing a system from the "ground up", so that the final package could be installed on different airplanes with a minimum of customizing, either of the aircraft or of the system, and so that it have as little detriment to aircraft performance as possible.

4.1 Design Requirements

Some problems of the past generation of rakes had to be overcome in order for the system to provide: (i) a rake arm that would not bend or warp in the jet from either blast or heat; (ii) small enough pressure probes to permit a side-by-side design for the measurement of both total and static pressures at the same radius and in the same plane; (iii) a position-indicating system accurate to within 0.10 in of nozzle radius; (iv) an actuating system that would produce a steady sweep at all times; (v) pressure responses that would produce an accurate indication of exit area in the measurement plane; and (vi) reliable temperature readings that would be made simultaneously with the pressure readings throughout the measurement plane.

In addition to these and other design improvements, a low-lag, high-response temperature probe was installed on the rake. The temperature probe makes possible the determination of mass flow at the nozzle exit. The thermocouple in the shielded tip is composed of iridium and 60% iridium-40% rhodium wire. It has consistently measured temperatures up to 3600°R during six-second sweeps.

4.2 Description

The traversing rake system is composed of a hydraulic rotary actuator, a torque shaft assembly that is coaxial with the actuator, and a rake. The rake measures total and static pressures, and temperature. Figure 1 is a close-up of the traversing rake head. The temperature probe is the single probe on the end of the rake arm. The total pressure probes are the same length as the temperature probe. The static orifices of the static pressure probes are located so that all readings of temperature and pressure are made in the same plane. The length, size, and spacing of the probe were designed for both subsonic and supersonic flow. The system was calibrated in a wind tunnel.

Figure 2 shows an assembled traversing rake system. The torque shaft is hollow so the pressure lines may run through it. The length of the torque shaft can be altered for any installation and the position of the rake on the torque shaft is adjustable. This design permits an adjustable sweep, so that the probes can be air cooled in any particular installation. It further provides the flexibility to measure airflow patterns at various distances aft of the nozzle exit.

The sweep rate can be varied by changing the size of certain restrictors in the hydraulic lines. Desirable sweep times are 10 - 20 sec per sweep in nonafterburning operation and 5 - 6 sec in afterburner. The successive sweeps, one in each direction, produce an accurate basis for pressure and temperature-lag determinations.

Figure 3 shows two separate traversing rake systems installed in the North American Vigilante. The rakes are in the down position. For a test run they are swung upward into the pockets, and after a few moments of cooling they are swung back through the exhaust to the starting position in the free air stream.

4.3 Installation

The installation of the traversing rake system presented no unusual difficulties. The structure of the aircraft was modified to withstand the loads imposed by the rake operation. The location of the actuating system on the test vehicle was found to be very important because the system is subjected to long periods of high temperature and vibration during supersonic flights. Engine growth and any engine flap extensions must be considered to provide for sufficient clearance at all times.

Once the rakes were installed and calibrated, there were no major operational difficulties, except for the lack of proper cooling between swings during afterburner operation. The rakes were repositioned to permit better cooling between swings, and $\frac{1}{2}$ -in air lines were routed to the actuator compartments. For extended supersonic testing, it is necessary to position the actuators so that the rake head will be completely clear of the jet exhaust at the end of each swing.

An automatic cycling system is being considered for future installations to guard against subjecting the rake to extreme temperature for too long a time. On one of the Mach 2 flights the rake arms and heads were severely damaged when the sweep direction was changed several times before the rakes were allowed to reach cooling air.

5. TEST INSTRUMENTATION

Quantities measured for a typical twin-engine airplane are shown below. The same general measurements are made for the fully automatic data acquisition and reduction program.

5.1 Photopanel

- Airspeed
- Altitude
- Compressor inlet total pressure, left and right engine
- Engine r.p.m., left and right engine
- Exhaust gas temperatures, left and right engine
- Exhaust nozzle position, left and right engine
- Frame count
- Fuel flow, left and right engine
- Fuel flow, left and right afterburner core
- Fuel flow, left and right afterburner annulus

Fuel temperature, left and right engine
Fuel temperature, left and right afterburner
Fuel used, both engines
Fuel used, left and right afterburner
Inlet guide vane position, left and right engine
Outside air temperature
Secondary air total pressure, left and right engine
Time count
Turbine outlet total pressure, left and right engine.

5.2 Pilot's Panel

Airspeed
Altitude
Engine r.p.m., left and right engine
Exhaust gas temperature, left and right engine
Fuel used, both engines
Frame count
Mach number
Outside air temperature
Time count.

5.3 Oscillograph

Left engine reference pressure
Left engine bottom total pressure
Left engine top total pressure
Left engine bottom static pressure
Left engine top static pressure
Left engine iridium-iridium rhodium tip temperature
Left engine reference temperature
Left engine position
Right engine reference pressure
Right engine bottom total pressure
Right engine top total pressure
Right engine bottom static pressure
Right engine top static pressure
Right engine iridium-iridium rhodium tip temperature
Right engine reference temperature
Right engine position.

6. EARLY TEST RESULTS

Extreme care was exercised during the initial flight tests of the traversing rake program to insure the best possible accuracy. Eight stabilized runs at various airspeeds were made at 25,000 ft to provide the data in the first analysis. Each run provided complex data for performance and fuel consumption for both the internal Gas Generator method and the Traversing Rake method. The ratio of airplane weight to the pressure ratio (altitude ambient pressure to sea-level standard pressure) was kept relatively constant in order to keep a constant lift coefficient from run to run.

Analysis was based on the fact that in stabilized level flight the thrust is equal to drag. Rake traverses were made on both engines at the same time for each stabilized flight data point. Two sweeps were made on each engine for each run. The flight Mach numbers ranged from 0.94 to 0.56 in approximately even increments. At no time during the tests could the pilot detect any change in the characteristics of the test vehicle while the rakes were being traversed.

Figure 4 is a photograph of the machine plots for the first flight run. It is important to remember that the left and right rake installations were completely separate systems. Figure 4 shows all the data for both engines on the same plot. Each profile is composed of eight superimposed plots; that is, it contains the bottom-to-top and top-to-bottom traverses for each of two engines, with two static and two total pressure readings per traverse. During this run the throttle positions of the two engines were closely matched. Since the left and right rake installations are completely separate systems, this particular run displayed two important features of a rake system. First, two separate systems can give identical results with no "juggling" of data. Second, acceptable data for a multiple engine airplane can be obtained with a single traversing rake system, provided all engine settings are properly matched.

The symmetry of the profiles about the centerline of the jet is worthy of note. It is characteristic of good installation techniques and accurate lag corrections. On the left-hand edge of the plots, the rakes are entering the jet from the local freestream. Here, the Mach number will be in the vicinity of the flight Mach number but not identical to it because of boundary flow. The pressure profiles, consistent with the Mach number profiles, start in the local free stream. The total pressure decreases as the rake approaches the wake and becomes equal to the static pressure at the edge of the jet. In this case the total pressure rises to its greatest value about the first 3 in inside the jet. As the rake comes out of the jet on the right (top of the swing) it goes into a static area. Here the Mach number is zero, showing the absence of local airflow. Also, the static pressure is less than ambient, belying the presence of base drag.

Figure 5 shows the family of pressure profiles for various airplane speeds. These are tracings of the machine plots. The first pressure profile of Figure 5 is the same as that in Figure 4. The static pressure profiles, despite their low magnitude, reveal many important flow characteristics. As in Figures 4 and 5, the static pressure is higher in the center of the jet than in any other portion. It reveals that the air is more dense in the center and that a correspondingly high airflow may result. From the highest static pressure to the lowest static pressure there is expansion of the gases. In Figure 4, expansion occurs from the center of the jet out to a radius of about 8 in. From this point to the edge of the jet, however, the pressure rises again, indicating that the jet was overexpanded in the measurement plane. This can be a useful tool, indeed, to the engineer responsible for nozzle and ejector design.

7. ACCURACY

The altitude test chambers of the Trenton Naval Air Turbine Test Station (NATTS) were used to verify the over-all accuracy of the rake system. Figure 6 shows the

close agreement between the rake-measured gross thrust and the gross thrust measured by NATTS. Both the Pratt & Whitney J57 and the GE J79 engines were used in the tests, with and without afterburning. Only the ambient pressure readings of the test cell were common to both data-reduction programs. The lines on Figure 6 are for 3% variation. The majority of data agreed within 1 or 2%. The laboratory tests thus proved the rake system on the ground and endorsed it as a basis with which to compare other methods in flight.

Figure 7 compares the in-flight net thrust of the internal method to the net thrust of the traversing rake method. For all practical purposes they are the same. Certain minor assumptions were incorporated in both programs. The fuel flow, for instance, is additional mass flow injected into the system after the intake of air. On a weight basis, it is assumed in the internal method that the leakage airflow is equal to the fuel flow that is added to the system. This assumption is fairly valid and has little effect on the over-all result. Both the fuel flow and leakage airflow are in the order of $\frac{1}{2}$ to $1\frac{1}{2}\%$ of the total gas flow. Bleed airflow, that is, the airflow taken from the engine system to do other work, is estimated by the airframe contractor to be in the order of $\frac{1}{4}\%$ of total airflow. With the traversing rake refinements, it was assumed that the leakage air plus bleed air for the test vehicle was the same as the fuel flow. Extra measurements of any bleed airflow, air leakage and static pressures in the base area will permit an even more precise determination of in-flight net thrust.

Accuracies to within 2 - 3% gross thrust and 4 - 5% net thrust are apparent from the studies so far. Early results from the new automatic data acquisition and data reduction system using airborne magnetic tape promises to hold this accuracy. Improvements are constantly being incorporated and will be published as significant advances are made.

8. SUPERSONIC TEST RESULTS

To demonstrate the integrity of the traversing rake system, performance data were collected for eleven airplane loadings at various altitudes and Mach numbers. This comprised a total of 42 flights during which 1244 successful rake traverses were made. The later portion of the program was devoted to supersonic testing. Typical supersonic profiles are presented in Figures 8 - 14.

Figure 8 shows the machine plot of Mach number of the jet exhaust M , mass flow per unit area W_g/A (lb/sec/ft²), total and static pressures P_t , P_s (lb/ft²) and gross thrust per unit area F_g/A (lb/ft²) for both subsonic and supersonic flight. The data for the various plots shown for a given flight Mach number were generated at the same time.

Figures 9 - 12 present similar data for 4 different Mach numbers to show how the profiles change with flight requirements. The nozzle radius refers to the radius of the measured circle (exhaust) in the measurement plane and is 6 - 12 in behind the engine tail pipe. Hence, for the J79 engine, these measurements are taken in the divergent portion of the convergent-divergent aerodynamic nozzle. Subsonically, the exhaust area increases with flight Mach number while the actual engine nozzle decreases in size. This continues until maximum thrust without afterburner is

reached. When afterburner is selected, the nozzle extends toward the full open position with an extension of about 8 in.

The Mach number profiles of Figure 9 display interesting patterns of supersonic flow in the jet. For the higher subsonic flight speeds, the Mach number in the center of the jet is considerably lower than in the area a few inches inside the edge. The corresponding increase in static pressure, as previously explained, shows that the air is more dense near the center. Even though the Mach number is lower in the center, the increased density more than compensates for the lower gas velocity, with the result that there is a substantial rise in total gas flow (mass flow) in the center of the jet. The exhaust gas speed is supersonic for both subsonic and supersonic flight speeds and, of course, as the airplane nears its maximum velocity the two speeds approach the same magnitude.

Typical total and static pressure profiles are given in Figure 10. These pressure curves are the backbone of the analysis, for these data, along with the temperature inputs, form the basis of the other profiles. In the subsonic family of Figure 5, note that the edges of the jet show how the area of the exhaust in the measurement plane changes with respect to flight Mach number M and exhaust pressure ratio EPR . With these pressure profiles and a measurement of temperature for each increment of area, the gas flow per unit area can be integrated across the measurement plane to give a total mass flow. Mass flow is related to both gross and net thrust.

Figures 11 and 12 show the total gas flow and gross thrust per unit area as a family of curves; the marked similarity between the two families is obvious. Each of these profiles is integrated within the limits of the area in the measurement plane to obtain gross thrust and exit airflow for each engine for any given flight run. From the total exit airflow, the ram drag of the airplane is computed for the appropriate flight speed, and in-flight net thrust is defined.

9. DATA REDUCTION

9.1 Initial Process

In the beginning, a photopanel recorder and an 18-channel oscillograph were used to record the airplane and engine performance parameters. The data reduction of the traversing rake data was divided into three parts^{2,3}.

Part I, input data was made up of the oscillograph and photopanel readings plus the various calibrations. A sample output of Part I is shown in Figure 13, which is a machine plot of temperature and pressure vs. nozzle radius for the determination of lag corrections. This plot is for one engine, and it displays two static pressure, two total pressure, and temperature readings for both sweeps. Sweeps in both directions for the same test run are required to account for lag. Each pressure and temperature measurement is associated with a unique radial distance from the center of the nozzle area (in the measurement plane). Figure 14 shows typical temperature profiles after the appropriate lag corrections have been made.

Part II utilized the corrected pressure and temperature profiles of Part I, along with weighted area curves and appropriate thrust equations, to compute the following

parameters with respect to nozzle radius: (i) Mach number, (ii) total gas flow per unit area (mass flow), (iii) corrected total-pressure and corrected static-pressure, and (iv) gross thrust per unit area. Figure 4 is a machine plot of the Part II output for the left engine of the first flight test point. The centerline of the nozzle bisects the chart and runs through "zero" on the nozzle radius scale.

Part III of the data-reduction process involved integrating the total gas flow per unit area and the gross thrust per unit area curves within the limits of the jet boundaries of the measurement plane.

10. AUTOMATIC DATA PROCESSING SYSTEM

The initial data-reduction process for one thrust point for a twin-engine airplane took about 32 man hours and 8 hours of computer time. The newly developed automatic data processing system, using airborne magnetic tape, allows us to do the same work in 20 minutes with less than 4 minutes of computer time. The system was designed and programmed by the Flight Test Division, Naval Air Test Center, Patuxent River, Maryland. The system involves data acquisition via an airborne analog magnetic tape, analog to digital conversion, computer processing on the IBM 7030-Stretch System, high speed printing and cathode ray tube plotting. The system is presently being used by two separate activities, one government and one commercial, with good results.

Figures 15 and 16 are photographs of the very first automatic system results from the cathode ray plotter. These data were recorded behind a TF-30 engine at sea-level static conditions. Transducers with a too long response time of 10-12 seconds for full scale have caused a minor problem in data fairing; however, this problem will be corrected by differential pressure transducers with quick response characteristics. The transducer response problem is more clearly seen in Figure 16 as the data should superimpose to make a single profile for each set of probes. Figures 15 and 16 are "Part I" plots and are analogous to Figure 12 of the initial process.

A large amount of traversing rake data for the TF-30 engine, with and without afterburner, will be processed in October and November 1965. Comparison will be made with the data acquired simultaneously by the laboratory. Thrust readings behind the blow-in-door ejector nozzle will be analyzed and compared with data from wind tunnel studies. The rake is presently set up in the test cell to measure temperatures and pressures at various distances downstream of the engine to give data for an exhaust nozzle effectiveness study. Two completely automatic systems are being installed in the Navy F-111B airplane and one in the Navy A-7A airplane for in-flight performance evaluations. Thus, the traversing rake with its new automatic data processing system promises to be an extremely useful tool in both the design and testing of airplanes.

11. CONCLUSIONS

The traversing rake concept of measuring net thrust in flight has been evaluated for feasibility and accuracy, utilizing a North American Vigilante airplane in subsonic and supersonic flight. The system provided exceptional accuracy of thrust measurement for the test engines which had convergent-divergent aerodynamic nozzles with large secondary airflows.

The system can aid greatly in the establishment of a firm basis for the verification of other concepts, such as ground calibrations and internal methods. It has potential for noteworthy developmental and research applications that need not resort to lengthy engine test cell calibrations. No longer are the stringent requirements for exacting and time-consuming data reduction blocking the usefulness of the traversing rake method; the procedures have been committed to a new automatic data acquisition and reduction system, using airborne magnetic tape. The new computer program, that can reduce and plot the data in a matter of minutes, is presently being used in two different engine test cells. In-flight net thrust tests, using the traversing rake system, on the F-111B and the A-7A airplanes are scheduled for 1966. Also a method of evaluating nozzle efficiencies through use of the traversing rake system is under study.

REFERENCES

1. Davidson, T.W. *Development of a Satisfactory Method for Measuring In-Flight Thrust of Turbojet Aircraft. Gas Generator Method.* Naval Air Test Center, Flight Test Technical Memorandum 1-61, March 8, 1961.
2. Haines, D.W.
Monsko, R.P. *Development of a Traversing Rake System for Measuring In-Flight Thrust of a Turbojet Powered Aircraft, Phase II.* Grumman Aircraft Engineering Corporation, Rept. FA-B7-111-1-007, October 1961.
3. Brovetto, R.L.
Haines, D.W. *Development of a Traversing Rake System for Measuring In-Flight Thrust of a Turbojet Powered Aircraft, Phase III.* Grumman Aircraft Engineering Corporation, Rept. FA-B7-111-1-008, March 1962.

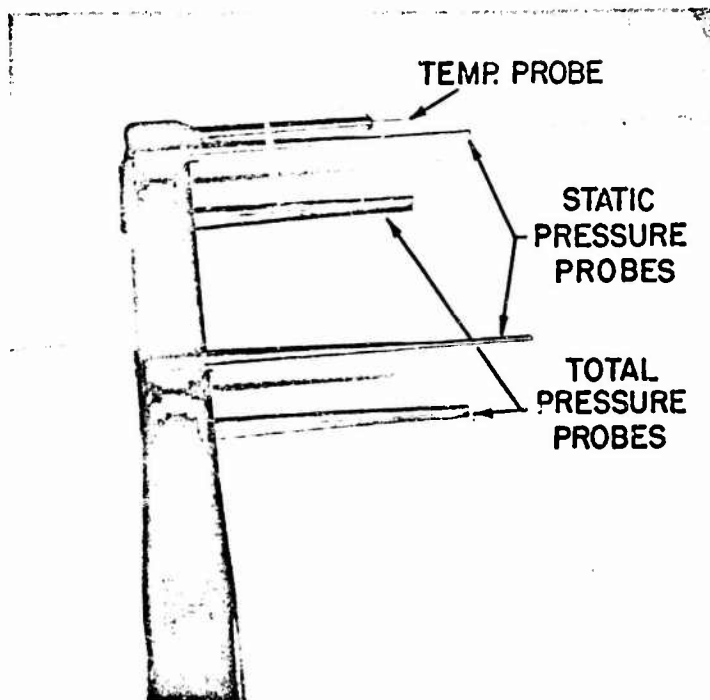


Fig. 1 Traversing rake head

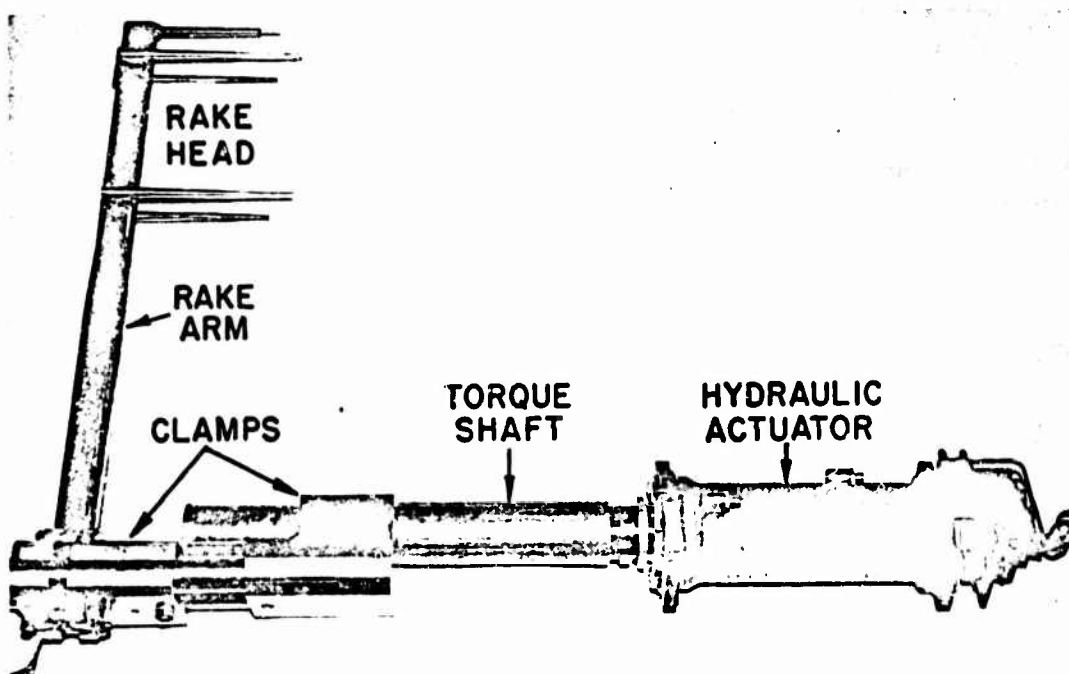


Fig. 2 Assembled traversing rake system

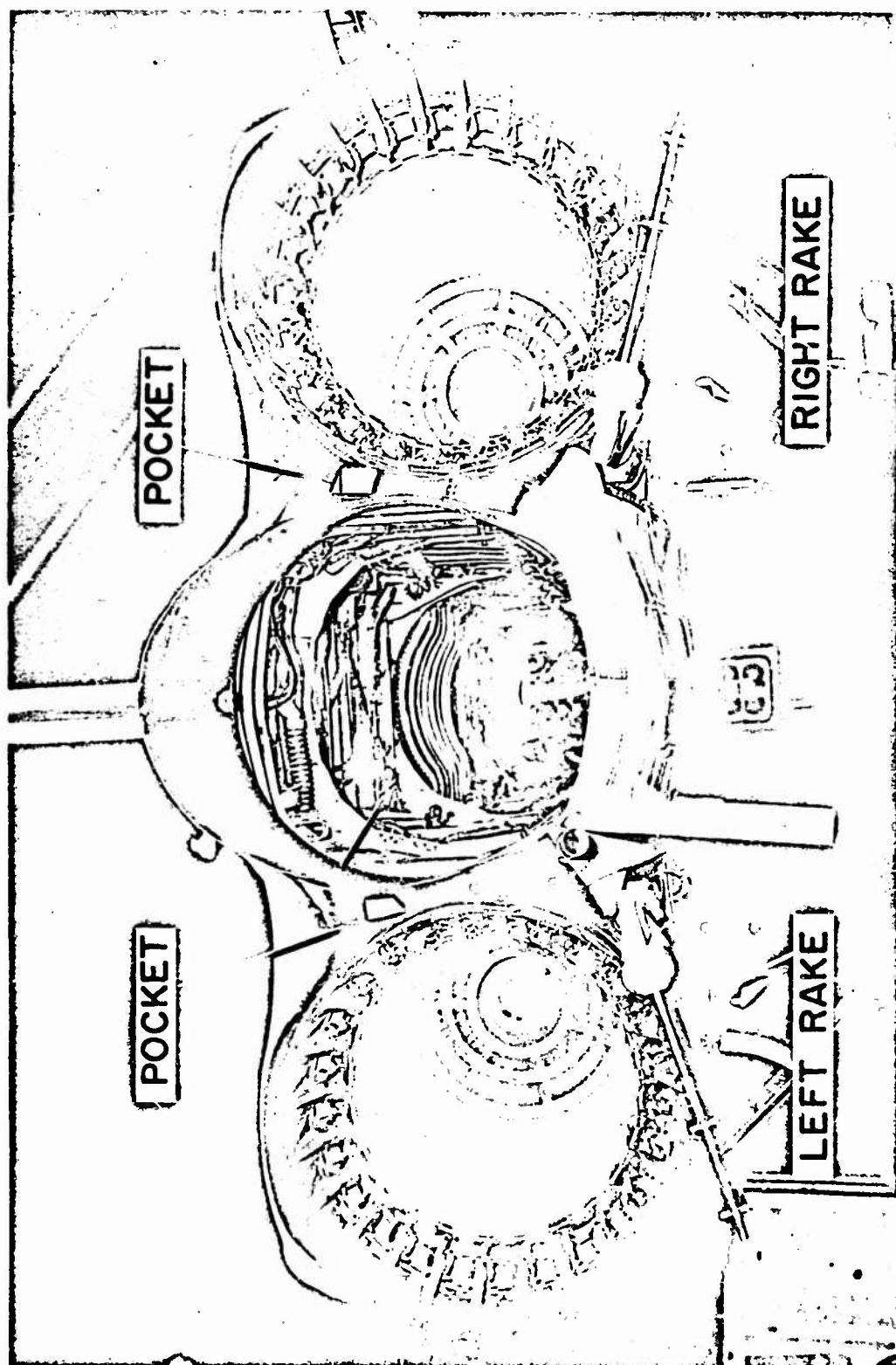


Fig. 3 Two installed rake systems

BOTH LEFT AND RIGHT ENGINES

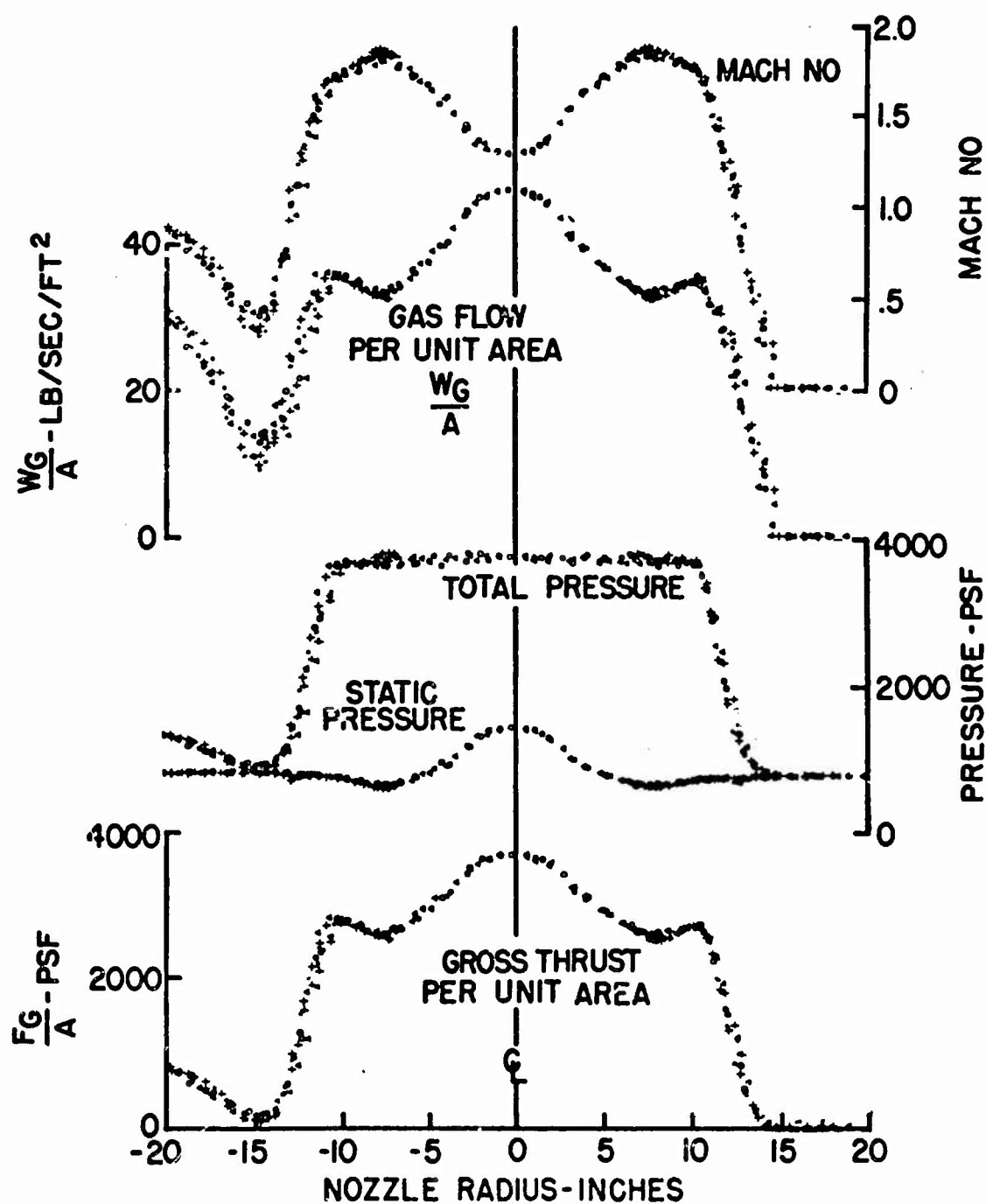


Fig. 4 Automatic machine plot of corrected profiles of various parameters in the jet with respect to engine nozzle radius; both left and right engine data superimposed, utilizing separate rake systems

J79 ENGINE

25,000 FT
 .56-.94 MACH NO
 2.2-4.2 EPR

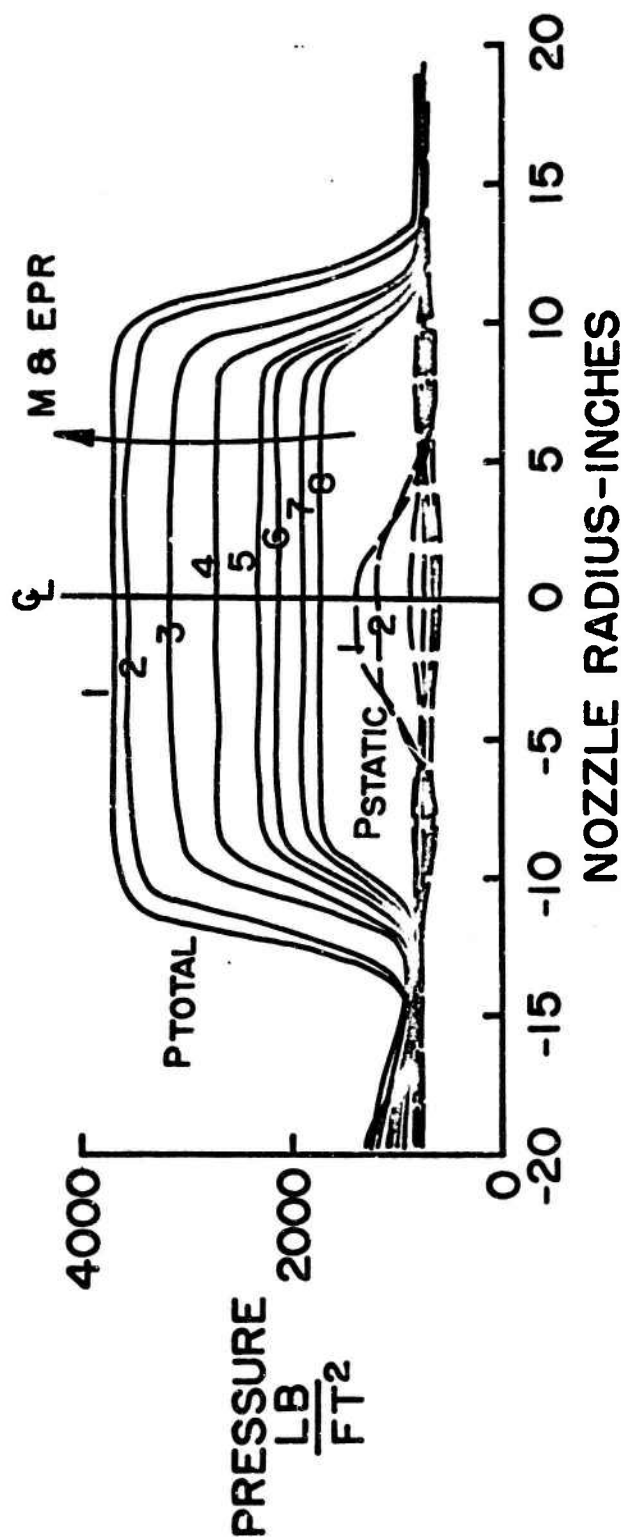


Fig. 5 Pressure profiles across the jet for eight subsonic airplane Mach numbers

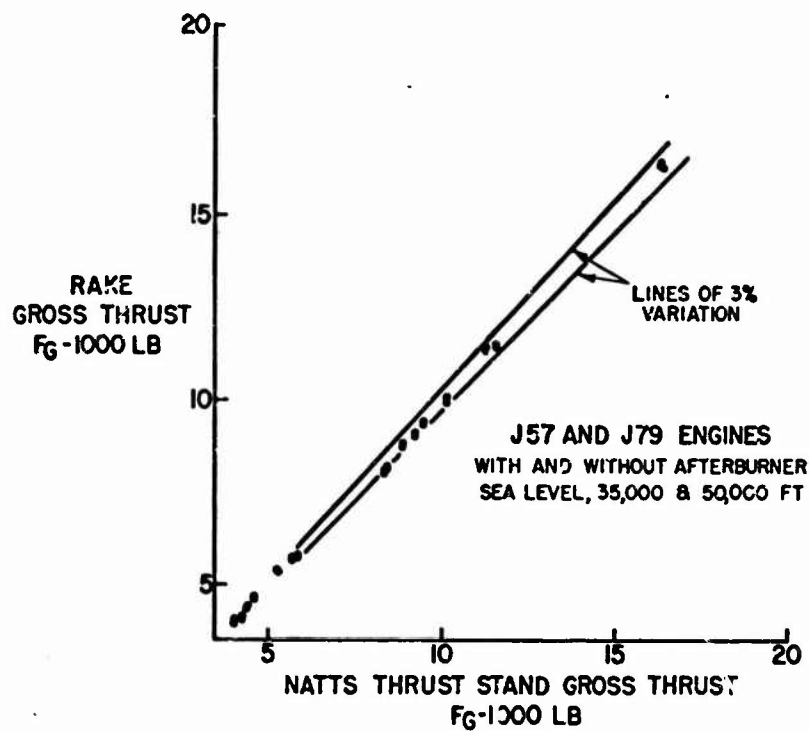


Fig.6 Comparison of rake gross thrust and laboratory gross thrust

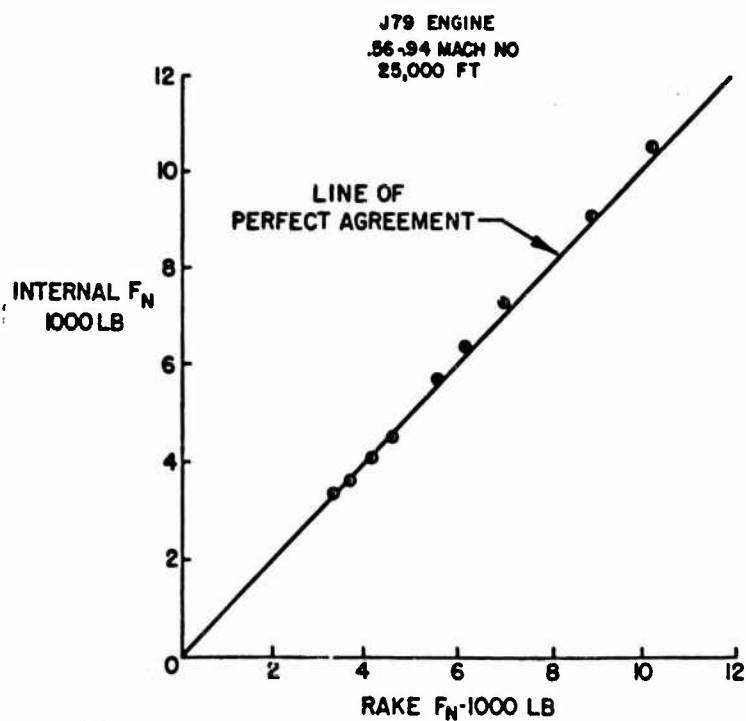


Fig.7 Comparison of rake net thrust with internal method net thrust

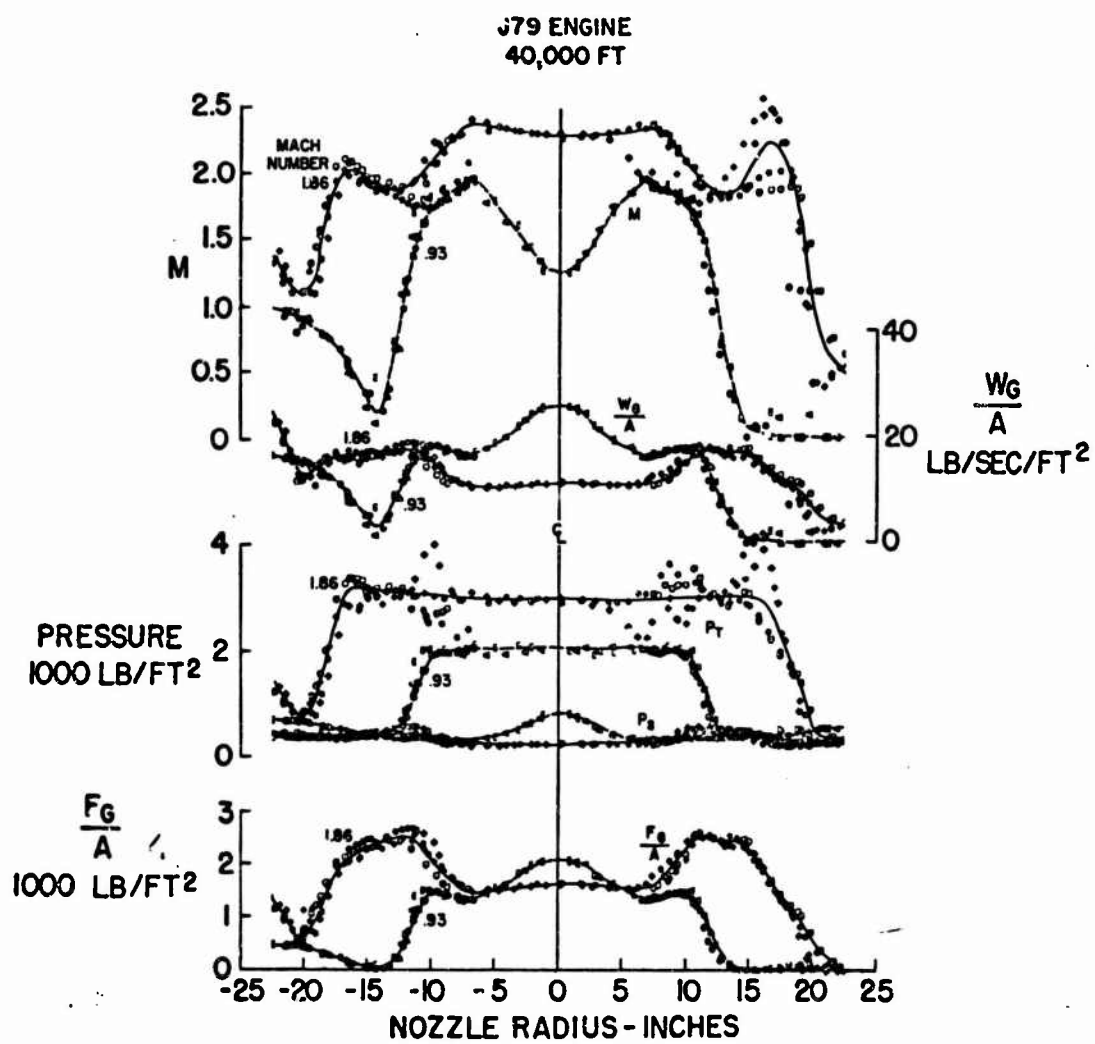


Fig.8 Automatic machine plot of corrected supersonic profiles of various parameters in the jet with respect to engine nozzle radius

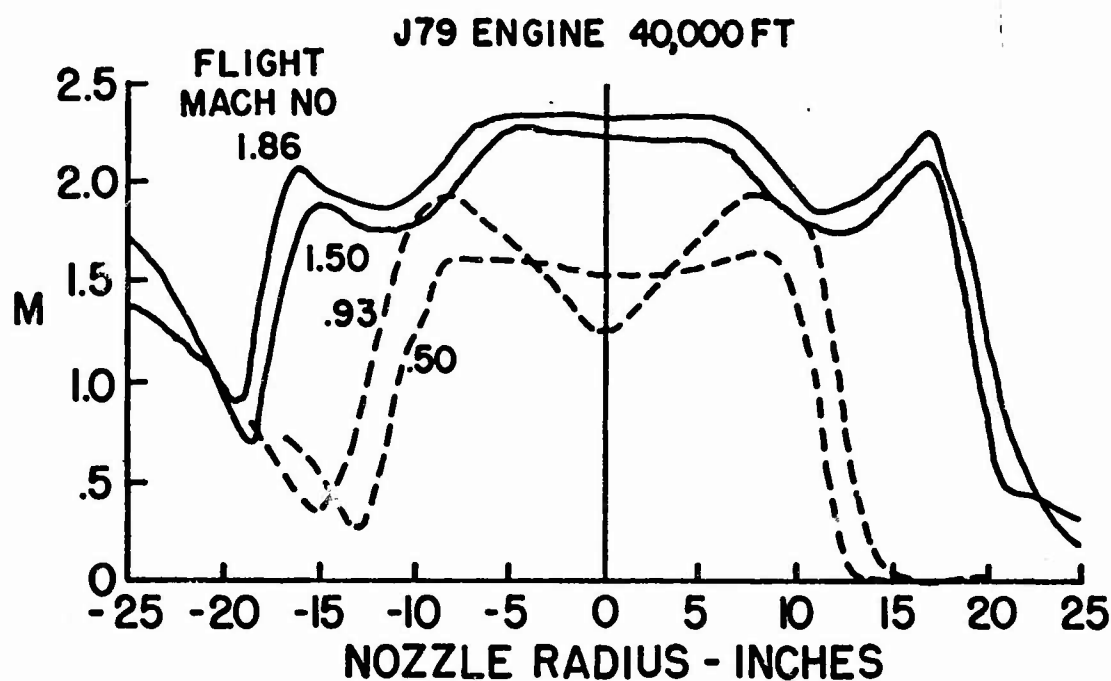


Fig. 9 Mach number profiles across the jet for subsonic and supersonic flight

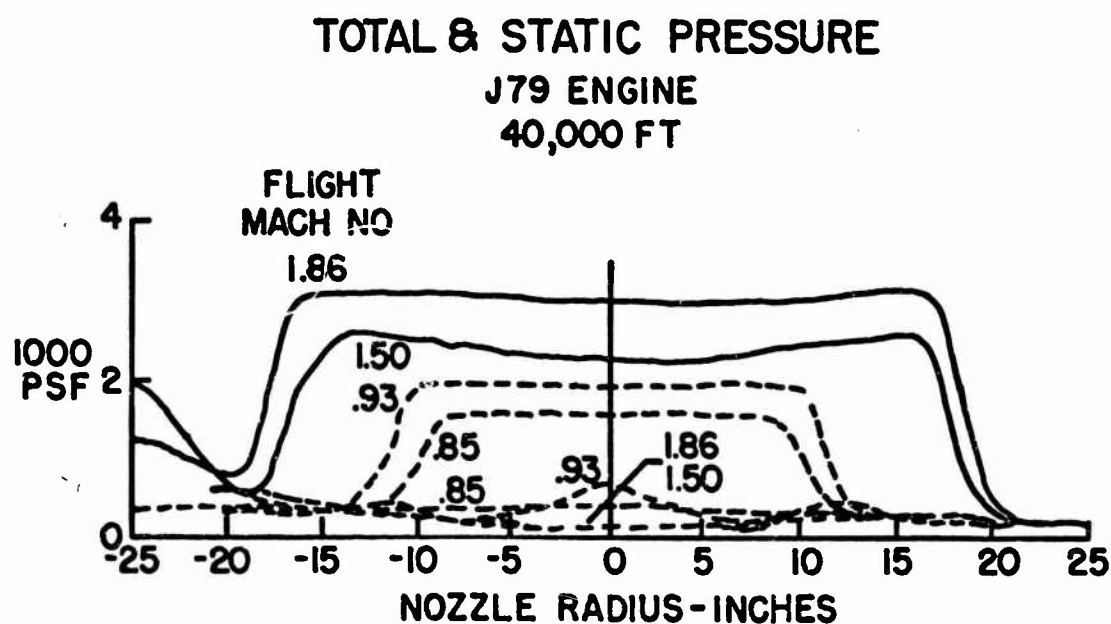


Fig. 10 Pressure profiles across the jet for subsonic and supersonic flight

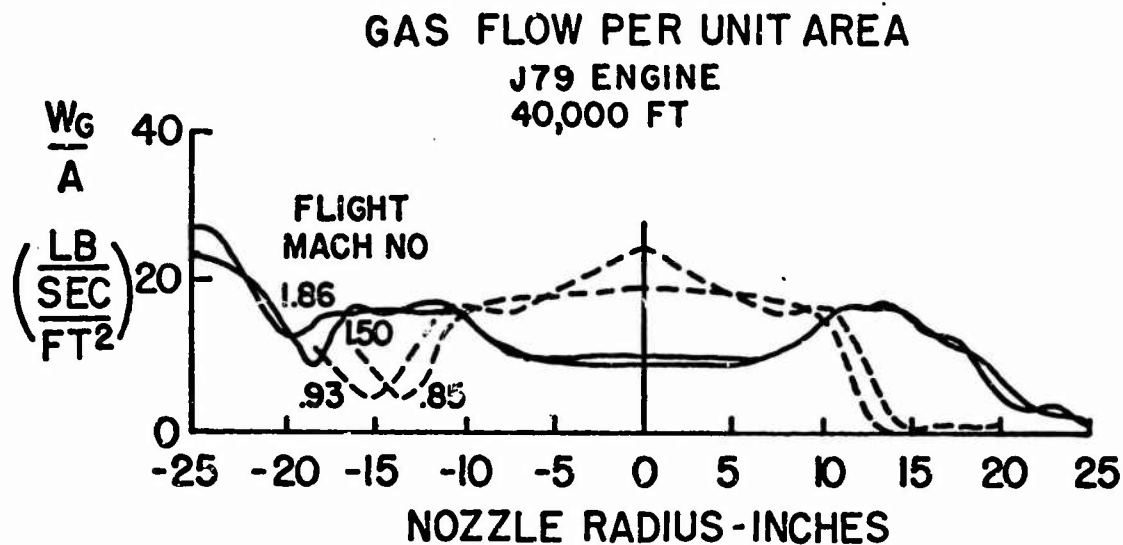


Fig.11 Gas flow parameters across the jet for subsonic and supersonic flight

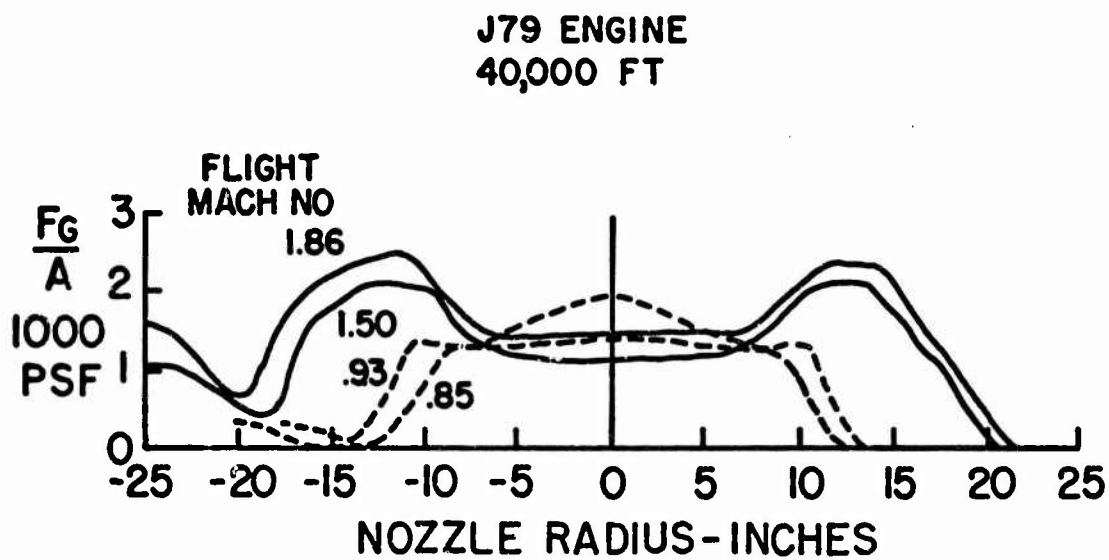


Fig.12 Gross thrust per unit area across the jet for subsonic and supersonic flight

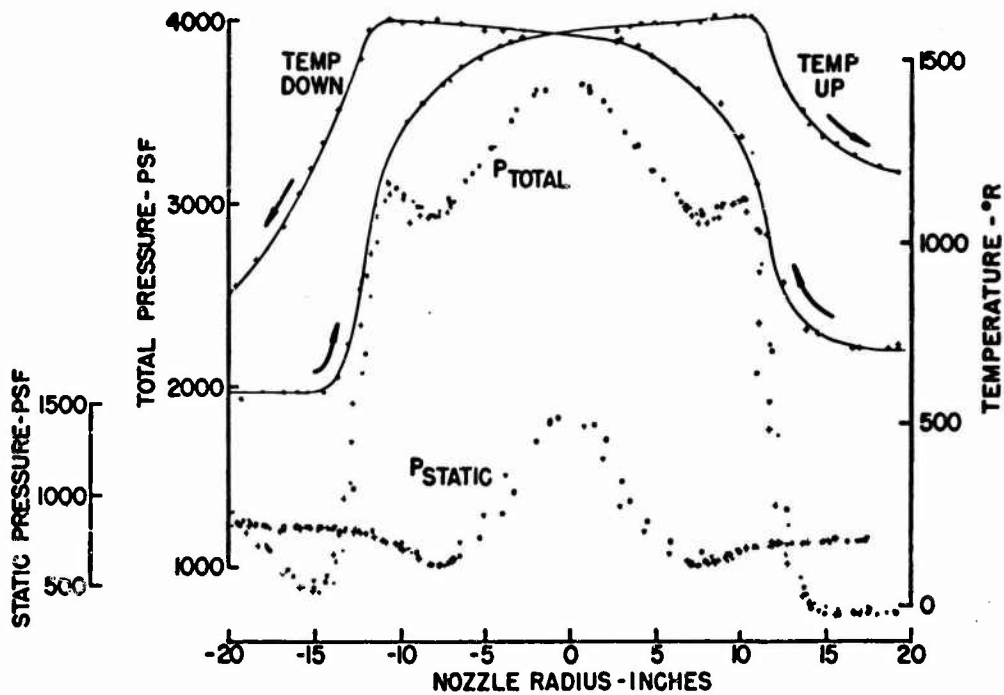


Fig. 13 Sample machine plot of temperature and pressure profiles before lag corrections

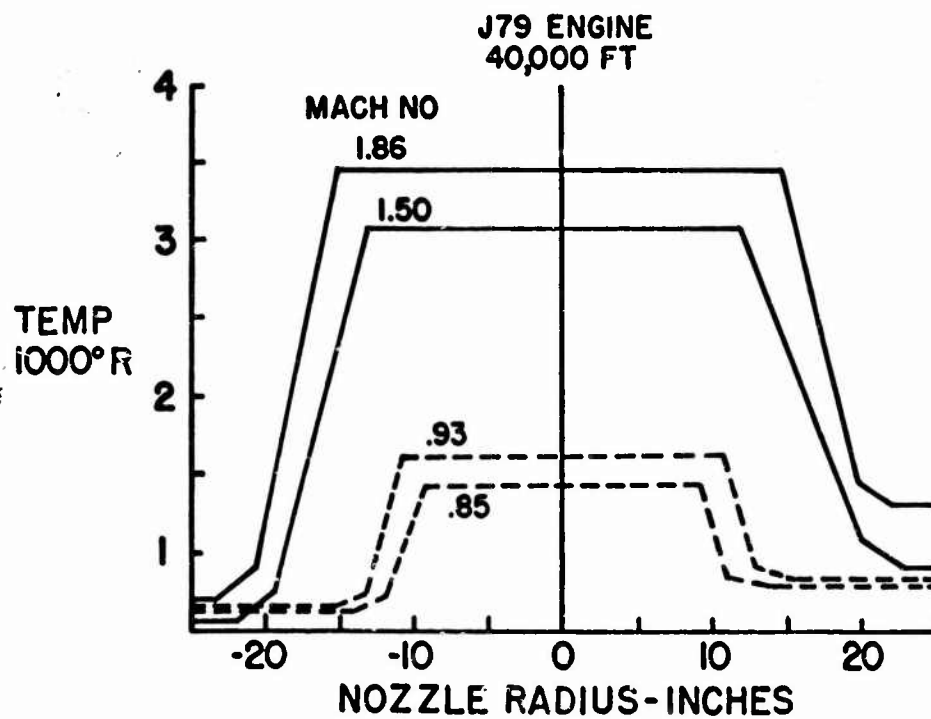


Fig. 14 Temperature profiles across the jet for subsonic and supersonic flight

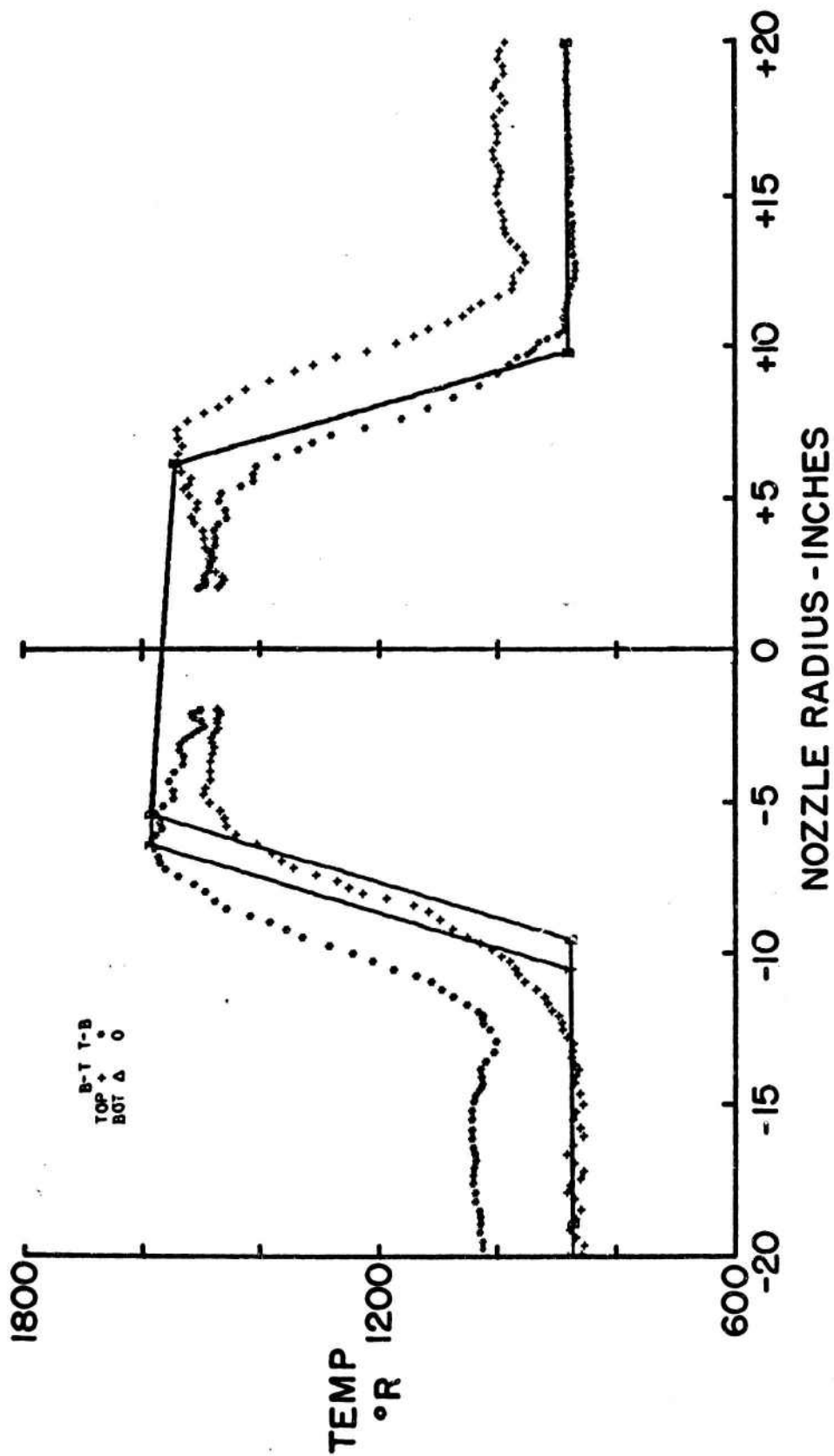
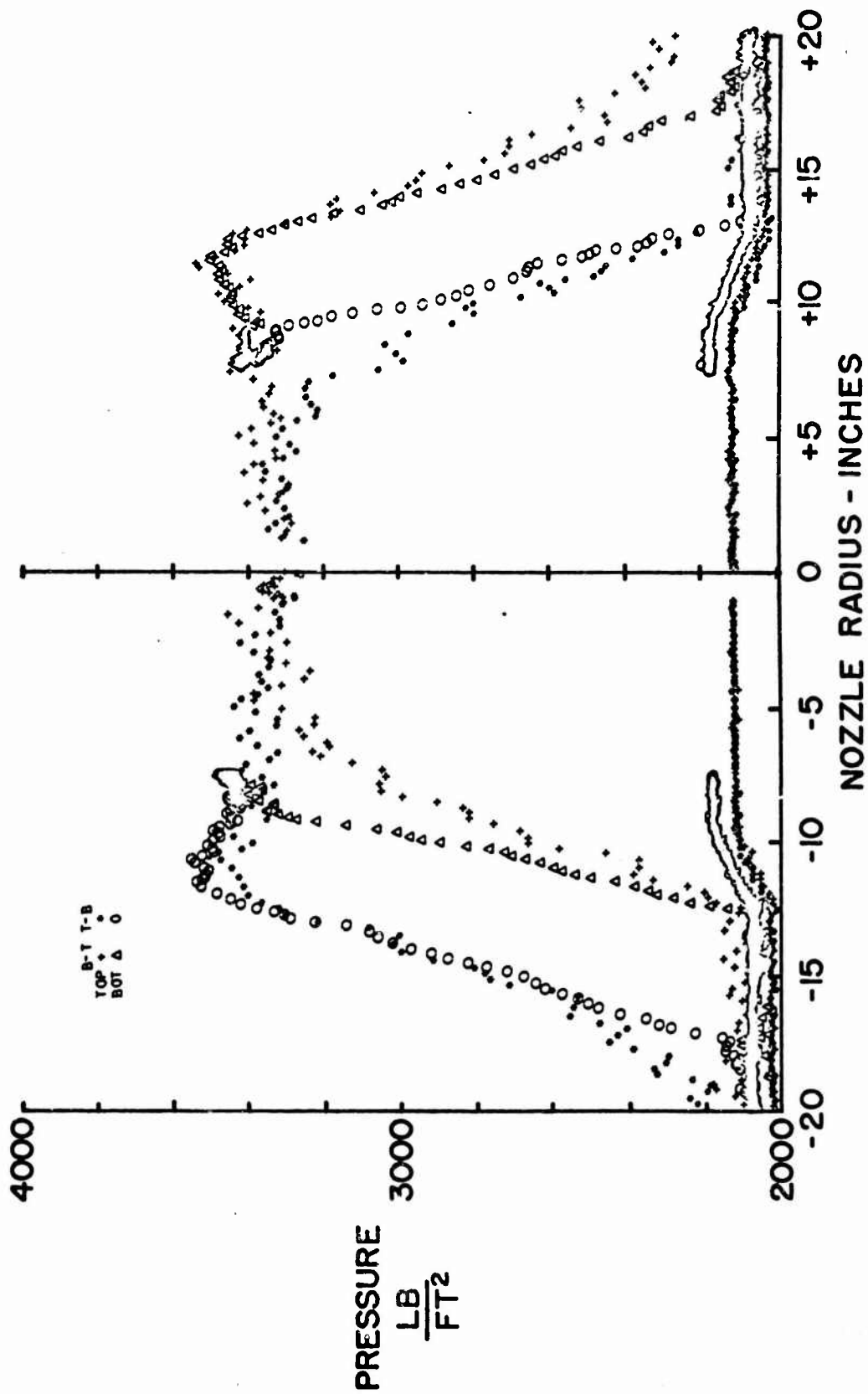


Fig. 15 Temperature profile across the jet from magnetic tape and fully automatic data reduction program



**PAST FLIGHT EXPERIENCE AND RECENT DEVELOPMENTS IN
COMBINATIONS OF RAMJET AND TURBOJET ENGINES**

by

A. Gozlan

Nord-Aviation, Châtillon-sous-Bagneux, Seine, France

SUMMARY

For any type of engine, operation and performance are subject to limitations which are related to material properties, aerodynamics, thermodynamics etc. Therefore, trying to meet the often conflicting requirements of the various phases of the flight profile is all the more difficult when the Mach number range is wide. From the desire to extend the domain of application of airbreathing powerplants stemmed studies of composite engines where advantage was taken of the good performance of turbo-engines at low and moderate Mach numbers and that of the ramjet at high Mach number, integration in the same powerplant proving superior to separate systems. Such combinations did not generally raise much more than academic interest except in France where even supersonic flight testing could be conducted with the Griffon, a turbo-ramjet-powered, 1953-designed, Mach 2.2 experimental aircraft. Beyond the original straightforward Griffon concept novel studies, both theoretical and experimental, were and still are conducted, the most recent being under contracts with the Air Force Systems Command, USAF. In the paper a general approach to the problem of compound powerplants is set forth, the experience gained with the Griffon flight-testing is summarized and the results of the latest research work are presented. Furthermore, it is shown how additional sophistication, involving the use of cryogenics, might extend the efficient operating range into the hypersonic régime, while taking advantage of the most recent advances in this field.

SOMMAIRE

S. Le fonctionnement et la performance de tout réacteur comporte des limitations qui tiennent aux propriétés des matériaux ou à des effets aérodynamiques ou thermodynamiques. Il est donc d'autant plus difficile de satisfaire aux conditions, souvent contradictoires, imposées par les différentes phases du profil de vol, que le domaine des nombres de Mach est plus étendu. Du désir d'étendre le domaine d'application des moteurs atmosphériques sont nées des études de moteurs combinés réunissant les avantages des turbo-réacteurs, réalisant de bonnes performances à des nombres de Mach faibles ou modérés, à ceux des stato-réacteurs aux nombres de Mach élevés, leur intégration en un même moteur s'avérant supérieure à deux systèmes séparés. Ces combinaisons n'ont généralement pas suscité autre chose qu'un intérêt théorique, si ce n'est en France où l'on a même pu réaliser des essais supersoniques avec le Griffon, avion à turbo-stato-réacteurs, conçu en 1953, pour Mach 2,2. Faisant suite au premier Griffon très simple, de nouvelles études, tant théoriques qu'expérimentales, ont été et sont menées, jusqu'aux plus récentes, placées sous contrat avec l'Air Force Systems Command de l'USAF. Exposé d'une conception générale du problème des moteurs combinés, des résultats d'essais en vol avec le Griffon, ainsi que des résultats de recherche récents. De plus, on montre que certains perfectionnements, tels que emploi de cryogéniques, pourraient étendre la plage de fonctionnement jusqu'au régime hypersonique tout en profitant des plus récents progrès réalisés dans ce domaine.

CONTENTS

	Page
SUMMARY	246
SOMMAIRE	247
LIST OF FIGURES	248
NOTATION	249
TEXT OF THE PAPER	251
FIGURES	258

LIST OF FIGURES

	Page
Fig.1 The turbo-ramjet powered Griffon 02 airplane in flight	258
Fig.2 Side view of Griffon 02	259
Fig.3 Drag and thrust coefficient along a typical flight profile	260
Fig.4 Evolution of Nord-Aviation turbo-ramjet	261
Fig.5 Typical turbofan-ramjet engine. Side view	262
Fig.6(a) Supersonic and transonic performance characteristics	263
Fig.6(b) High supersonic performance characteristics	264
Fig.7 Models of turbofan inlet cowl	264
Fig.8 Engine inlet pressure distribution	265
Fig.9 Flow mixer	266
Fig.10 Pressure profiles (upstream of the combustion chamber)	267
Fig.11 Typical flight programme	268
Fig.12 Turbofan-ramjet with LOX injection. Specific impulse and specific thrust. Nozzle velocity coefficient = 0.95, shifting equilibrium, stoichiometric, fuel: JP1, inlet efficiency: MILE5008-B	269
Fig.13 Model of an aerospace vehicle (ERNO + Nord-Aviation + SNECMA)	270

NOTATION

A_a	aircraft reference area
A_0	air capture area
C_D	drag coefficient
C_T	engine thrust coefficient
F	thrust
F_0	sea level static thrust
g	acceleration due to gravity
L/D	lift/drag ratio
P_{00}	sea level pressure
q	dynamic pressure
R	range
I_s	specific impulse
I'_s	specific impulse of excess thrust
V	flight velocity
W	all-up weight
z	altitude

PAST FLIGHT EXPERIENCE AND RECENT DEVELOPMENTS IN
COMBINATIONS OF RAMJET AND TURBOJET ENGINES

A. Gozlan

This paper ranges under the general heading of "Combined Propulsion Cycles" in the programme of this AGARD meeting on "Aerodynamics of Powerplants". It will deal only with airbreathing composite engines, more specifically with those involving the combination of ramjet and turbomachinery.

Airbreathing composite engines have existed for a long time in industry and aeronautical applications appeared during World War II when turbosuperchargers were added to piston engines. The merger was eventually complete with the turbo-compound engine which dominated long-range transportation until the emergence of the turbojet-powered airliner.

The need for a composite engine is generally felt in trying to meet the requirements of a given flight programme. Any type of engine shows performance characteristics (thrust and specific impulse) that change following a particular trend when the flight conditions vary. There are also particular limitations imposed on its internal operation, such as those resulting from excessive pressure or temperature, or even from internal flow mismatching. The weight taken on by the complete powerplant when such an engine is used is significant. All of those characteristics are dependent on the state of the art. The airframe manufacturer in charge of a project has also to know whether such a type of engine is available in the required thrust range or how long it would take to develop it, as well as the cost.

Taking these things into account, the selection of a propulsion system aims generally at minimizing the total propulsion weight (powerplants plus fuel) over the flight profile of the mission considered. If the use of a single engine type results in falling not very far from the optimum, this is preferred for the sake of simplicity. But such may not always be the case, for instance when the Mach number range is wide. Resort may then be made to the use of different engine types, showing different performance trends and different limitations to their operation. Separate engines can be considered. This generally leads to poor design, for instance because of the increased bulk and unnecessary duplication of some components. On the contrary, making common to both engine types as many components as possible is very attractive and results in clean design. Taking advantage of each engine type where it fits best, while integrating both in the same powerplant, is a good proposition for a composite engine.

But it is not the purpose of this paper to dwell on philosophy. We have rather to bring out the interest and the potentialities of composite airbreathing engines while presenting some examples of the combination of ramjet and turbine engines, on which some practical experience has been gained.

The first example is the turbo-ramjet of the well-known Griffon (Fig.1), the only turbo-ramjet-powered aircraft that has ever flown supersonically.

It is a delta-winged aircraft, designed in 1953 to meet the requirements of a light interceptor program. It weighed about 15,000 lb. 330 experimental flights were carried out and it attained a Mach number of 2.2. Only structural limitations on the airframe prevented it from flying at even higher Mach numbers. When the centre of interest shifted from airplanes to missiles the project was phased out. The flight programme was then carried on for engine development and later as an investigation on kinetic heating. The Griffon eventually entered the Museum while still being one of the fastest of exist. g airplanes.

Figure 2 is a side view of its powerplant. It consists essentially of a coaxial arrangement of ramjet and turbojet with common air inlet and exit nozzle. Part of the captured air is spilled around the turbojet to feed the ramjet combustion chamber which surrounds the turbojet. This is a SNECMA Atar 101 E3 dry turbojet with 7,700 lb static thrust, Mach limited to 1.85. No need for variable geometry, either for the inlet or the nozzle, arose. In fact the inlet efficiency resulting from the combination of the oblique shock from the fuselage spike and the normal shock at the inlet face was quite acceptable. Also, along the climb path, air inlet and exit nozzle remained well matched, the airflow requirements for the ramjet and the turbojet varying with opposite trends.

The fuel pump for the ramjet was driven by the turbojet but the fuel control system of the ramjet was independent, the control parameter being the equivalence ratio.

The airplane took off on turbojet power only. The ramjet was ignited at about Mach 0.5. Considerable acceleration resulted, permitting rapid passage through the transonic range and supersonic climb. On attaining the Mach number limit of the turbojet (1.85) the r.p.m. was progressively throttled down to 90% of the maximum.

Flight experience confirmed that both types of engine operated almost independently and no detrimental interference effect was ever observed. The turbojet did not even react to the shut-down of the ramjet.

The aircraft was very easy to handle, as were the engine controls. Operation at angle of attack proved satisfactory, much to the surprise of the USAF pilot who achieved near-3g turns at about Mach 1.6, when flying the Griffon for the first time.

Such results are made clearer by looking at Figure 3. It shows the drag of the Griffon along a typical climb acceleration profile. The lowest curve gives the thrust coefficient of the turbojet and the upper curve the thrust coefficient of the turbo-ramjet. It shows that considerable excess thrust was available. As a reference is also plotted the thrust coefficient of the Atar 101 G, which was the afterburning version of the Atar 101 E3, used on the Griffon. At high Mach number the turbo-ramjet delivers about three times the thrust of this afterburning turbojet. Needless to say, the weight of three afterburning turbojets would have been incompatible with the 15,000 lb total weight of the aircraft, and in any case the turbojets were limited to Mach 1.85.

The performance characteristics were not essentially different from the estimated figures. Combustion chamber blow-off limits were slightly better than those expected.

That no interference effect was noticed at the turbojet inlet is probably due to its central position. Only the ramjet flow was influenced by wall effects, and ramjet combustion chambers are generally less sensitive to flow distortion than are turbojets.

Interference between the turbojet exit and the ramjet flow was negligible in flight. It was as if both flows were independent, showing the same static pressure along the duct. The turbojet flow could then be thought of as a convergent-divergent channel having no walls but some variable geometry. At take-off mixing existed, causing more air to enter the inlet because of the ejector effect. Thrust loss resulted, the air inlet lips not being designed for the zero-velocity case. A tolerable loss was obtained through adjustment of the distance between turbojet convergent flow and turbo-ramjet nozzle exit.

In flight, even when the ramjet was not operating, the total pressure at the turbojet face was not very different from that generated by the external shock-wave pattern of the inlet. The annular duct around the turbojet cowl formed a throat that could be choked when operating the ramjet cold or at lean mixtures. Supercritical operation was then characterized by a shock wave located between this throat and the ramjet combustion chamber. In such conditions no disturbance could reach the turbojet inlet.

Considerable experience was also gained from the study of transients as far as the structure strength was concerned. The openings of all the compartments existing in the turbo-ramjet had to be dimensioned according to the volume in order to prevent high pressure differences being generated on both sides of each wall when suddenly shutting off the ramjet.

From the viewpoint of safety, it is interesting to note that in case of engine failure there was no risk of inlet buzz or instability. In such a case the inlet would become supercritical.

A somewhat unexpected effect was the noise level reduction observed when lighting the ramjet at low altitude. Early measurements showed this to amount to about 6 dB, but unfortunately no systematic investigation could be made, emphasis being by then on the heat transfer programme.

As to the sonic boom, we never experienced any reaction from the public. This is possibly due to the fact that acceleration always occurred when climbing, and also to the small size of the aircraft. But engine whine at low altitude sometimes caused reactions. No investigation was made of any of these phenomena.

During the time that flight test results were accumulating with the Griffon, serious thought was given on how to extend the range of application of composite engines to higher Mach numbers while using turbine engine types that were either in existence or being developed. A new configuration was designed, the turbofan-ramjet engine, and its derivation is shown in Figure 4. The coaxial configuration of the original design is maintained. Here also air inlet and exit nozzle are common, but variable geometry is mandatory for both. The turbojet is replaced with a turbofan. Part of

the air supplied by the inlet is spilled around the turbofan cowl and mixes with the turbofan secondary flow in an annular mixing chamber from which the resulting flow feeds an annular combustion chamber wrapped around the turbofan rear section. Reheat of the turbofan primary flow may also be provided and there are variable flaps at the exit of the secondary flow of the turbofan. Three modes of operation are then possible. When closing the ram air duct the engine operates as a turbofan. When closing the secondary flow exit the engine operates as a ramjet. Operation as a turbofan-ramjet is the third mode, with the flaps positioned in the "mixer" configuration. Figure 5 gives further details.

At take-off the engine is operated as a turbofan, with possible reheat on both flows. Above a certain value of the air stagnation temperature, which may correspond to a supersonic or a subsonic Mach number, depending on the altitude and the turbofan design, the engine may be operated in the mixed flow mode, thereby gaining in thrust. As the flight Mach number increases the proportion of ram air feeding the mixer increases too. Also, when approaching the Mach limit of the turbofan, which can be between Mach 2.5 and 3, the r.p.m. is progressively slowed down. The flaps close the secondary flow exit and the turbofan may then be made to idle or even to windmill, the composite engine running as a pure ramjet.

Such a composite engine is considered to be limited to those applications where the thermal problems resulting from kinetic heating can be solved by careful selection of present-day materials, insulation techniques and the proper use of the hydrocarbon fuel as a heat sink. Depending on the flight programme, the limiting Mach number would probably be somewhere between 4 and 4.5. For such extreme conditions it would be advisable to close the turbofan inlet and a mechanical closing device can actually be stored inside the inlet cowl.

This second type of combined propulsion cycle, the turbofan-ramjet engine, raised interest at the AFSC, which sponsored additional work, both theoretical and experimental. Many configurations based on various turbofans were studied and Figure 5 shows one of them. Their performance characteristics were also computed and typical results are given in Figures 6(a) and 6(b).

The experimental work concentrated on those components that were peculiar to the cycle. Aerodynamic tests permitted us to investigate the zones of interaction of the various flows, such as the turbofan inlet, the flow mixer and the primary flow exit. The combustion chamber also merited special investigation.

Figure 7 shows three models for the turbofan inlet cowl that were aerodynamically tested at Centre d'Essais de Propulseurs (CEP), Saclay. The intermediate model proved the best. Figure 8 gives the total pressure distribution at the turbofan face and in the ram duct in the three operating modes.

Development work on the mixer led to the configuration shown in Figure 9. This staggered-flaps system achieves correct mixing over a short length. Figure 10 gives the total pressure profiles obtained in the diffuser just upstream of the combustion chamber for various values of the fan pressure increase, which correspond to various flight Mach numbers.

As regards the primary flow exit, the tests led to the conclusion that very little mixing with the adjoining flow issuing from the combustion chamber took place, and that the performance characteristics had to be calculated as if no mixing occurred.

Much more complicated is the problem of the combustion chamber, for which the requirements are rather stringent. It has to operate up to Mach 4 over a very large range of equivalence ratio to meet the needs from lean supersonic cruise to rich acceleration. A full-size section of the combustion chamber has been tested at Les Gatines, a 15,000 h.p. facility where various configurations could be investigated up to Mach 2 simulated conditions. The design was then frozen. The combustion chamber is now under test up to Mach 4 at CEP, Saclay. This is our largest test centre for air-breathing engines, with more than 200,000 installed horsepower, and is run by the French Government. The tests are expected to be completed before the end of the year. The early results of the "hot" runs are promising.

The philosophy underlying the third combined propulsion cycle, now described, is much the same as for the first two. In fact this is a derivation of the turbofan-ramjet engine just described. It aims at extending its use to even higher Mach numbers, around Mach 6 when hydrocarbons are considered. The added sophistication is liquid oxygen (LOX) injection. In its simplest version the system essentially consists of injecting liquid oxygen upstream of the annular combustion chamber of the turbofan-ramjet, thereby allowing more fuel to be burnt. This does not markedly affect the pressure. The nozzle throat area is increased in proportion to the resultant mass and temperature increases. The exit flow momentum is increased, producing additional thrust. The operation of the air inlet is unaffected by LOX injection and the momentum of the captured air remains unchanged. The specific impulse would obviously be smaller than that of the plain turbofan-ramjet, taking on some intermediate value between that of a ramjet and that of a rocket, depending on the amount of excess thrust needed. Liquid oxygen being a cryogenic can also help solve the problem of cooling the engine components. Also the injection system can be used only if and when it is required and exactly at the optimized rate.

The effect of a combined propulsion cycle may be considered by trading-off engine performances characteristics against powerplant weight.

For very high Mach number application the powerplant size is not determined by take-off requirements but by the requirements in flight.

Supersonic cruise is governed by the two following equations:

$$A_0 C_T = A_a C_D$$

and

$$\frac{dW}{W} = \frac{dR}{VI_S(L/D)} \quad (\text{Breguet})$$

(The $(1 - V^2/V_S^2)$ correction is disregarded here).

Climb-acceleration is governed by two more equations:

$$I'_s = I_s \left(1 - \frac{A_a C_D}{A_o C_T} \right)$$

$$\frac{dW}{W} = \left(\frac{dz}{V} + \frac{1}{g} dV \right) \frac{1}{I'_s}$$

where I'_s is the specific impulse of the excess thrust and z is the altitude.

A_a characterizes the powerplant size and the significance of I'_s is well brought out. The last equation also shows that climb should preferably take place at the highest velocity at a given altitude.

As C_T decreases when the flight Mach number increases, whereas C_D usually shows a very gentle decrease, the engine size must increase. The use of LOX injection permits an increase of C_T while maintaining A_o at a reasonable value, at the expense of decreased I_s .

Figure 11 gives the main characteristics of a typical flight profile. It is dominated by the sonic boom intensity, the dynamic pressure, which is indicative of the strength of the airframe structure, and the powerplant duct pressure, which is indicative of the strength of the powerplant structure. There are also thermal limitations not represented here.

When the Mach number is slightly supersonic it is generally found that the engine size is determined by the transition requirements. When the Mach number increases the cruise condition determines the engine size, but above Mach 4 the acceleration condition dominates. It might then prove preferable to accept some decrease in I_s , using LOX injection, while maintaining the size of the engine to that corresponding to Mach 4.

Figure 12 gives typical performance characteristics of a turbofan-ramjet with LOX injection; the specific impulse is plotted against thrust coefficient. The minimum thrust corresponds to the zero-injection case.

The application of such a combined propulsion cycle has been considered for a space vehicle studied jointly by ERNO (Germany) Nord-Aviation (France) and SNECMA (France).

Figure 13 is a photograph of the model of such a two-stage re-usable, manned vehicle, in which the second stage is mounted under the belly of the first stage. It is powered by rockets using liquid hydrogen and liquid oxygen.

The first stage is powered by four turbofan-ramjet powerplants with LOX injection. The vehicle takes off with the powerplant operating in the turbofan-mode, turns to the mixed flow mode after transition up to Mach 2.5, and then to the pure ramjet mode. Above Mach 4 LOX injection is progressively added, the maximum rate being attained when just pulling out before separation, which takes place between Mach 6 and 7.

Other types of combined propulsion cycles can be and have been envisaged, but it was not the purpose of this paper to discuss their relative merits. It was only intended to show by example how, while using the current state of the art, some practical propulsion problems have been or can be solved.

This does not mean that very advanced technology must be neglected, and consideration has been given to liquid hydrogen and its use in turbo-scamjets.

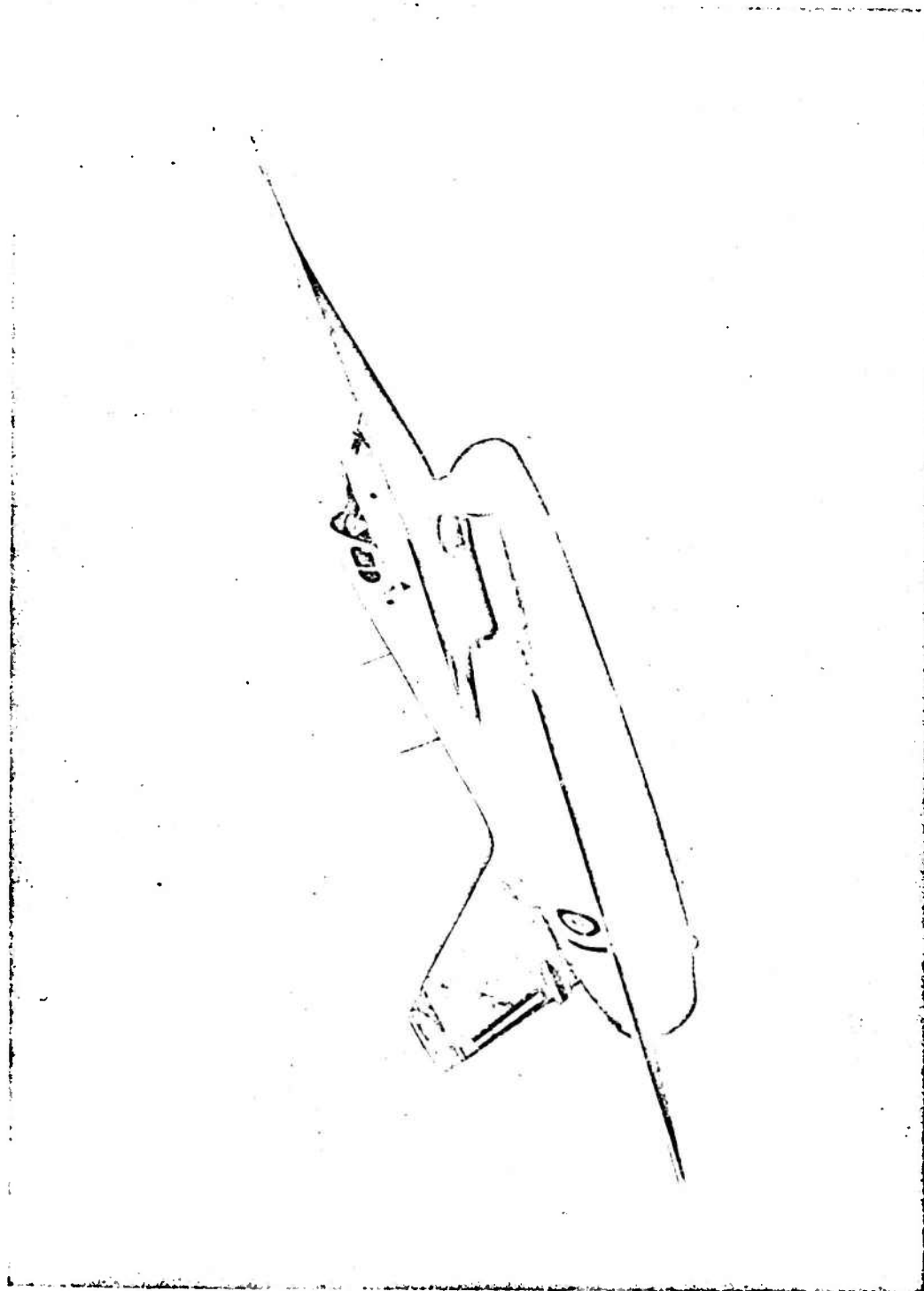


Fig. 1 The turbo-ramjet powered Griffon 02 airplane in flight

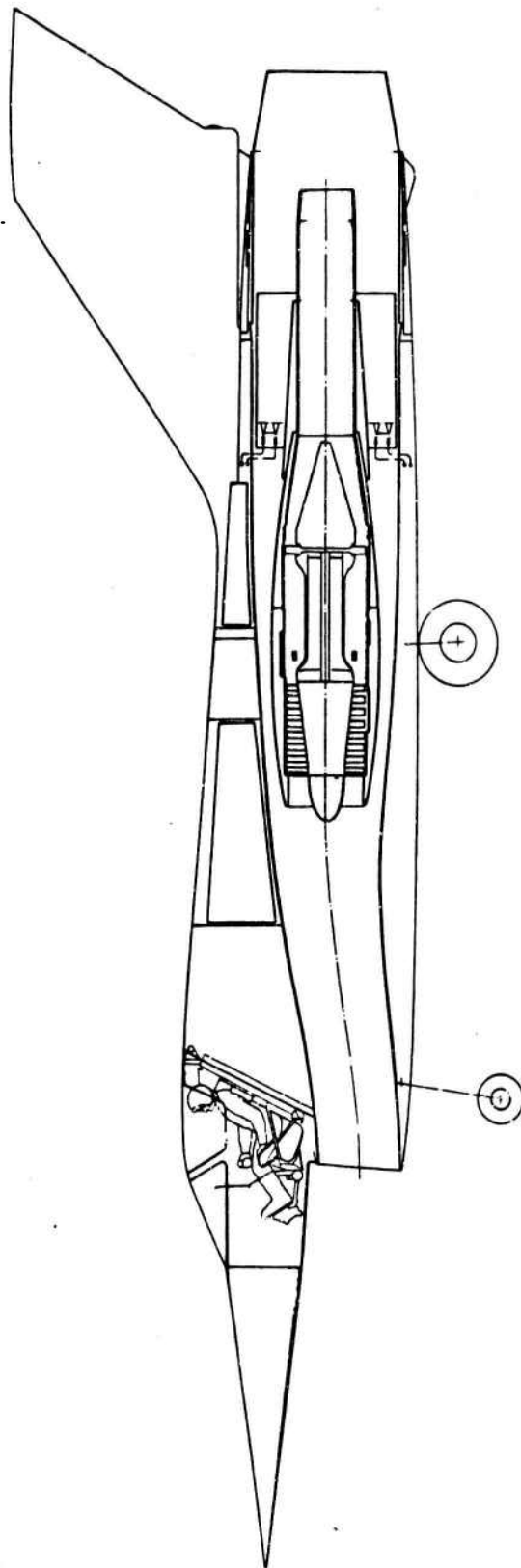


Fig. 2 Side view of Griffon 02

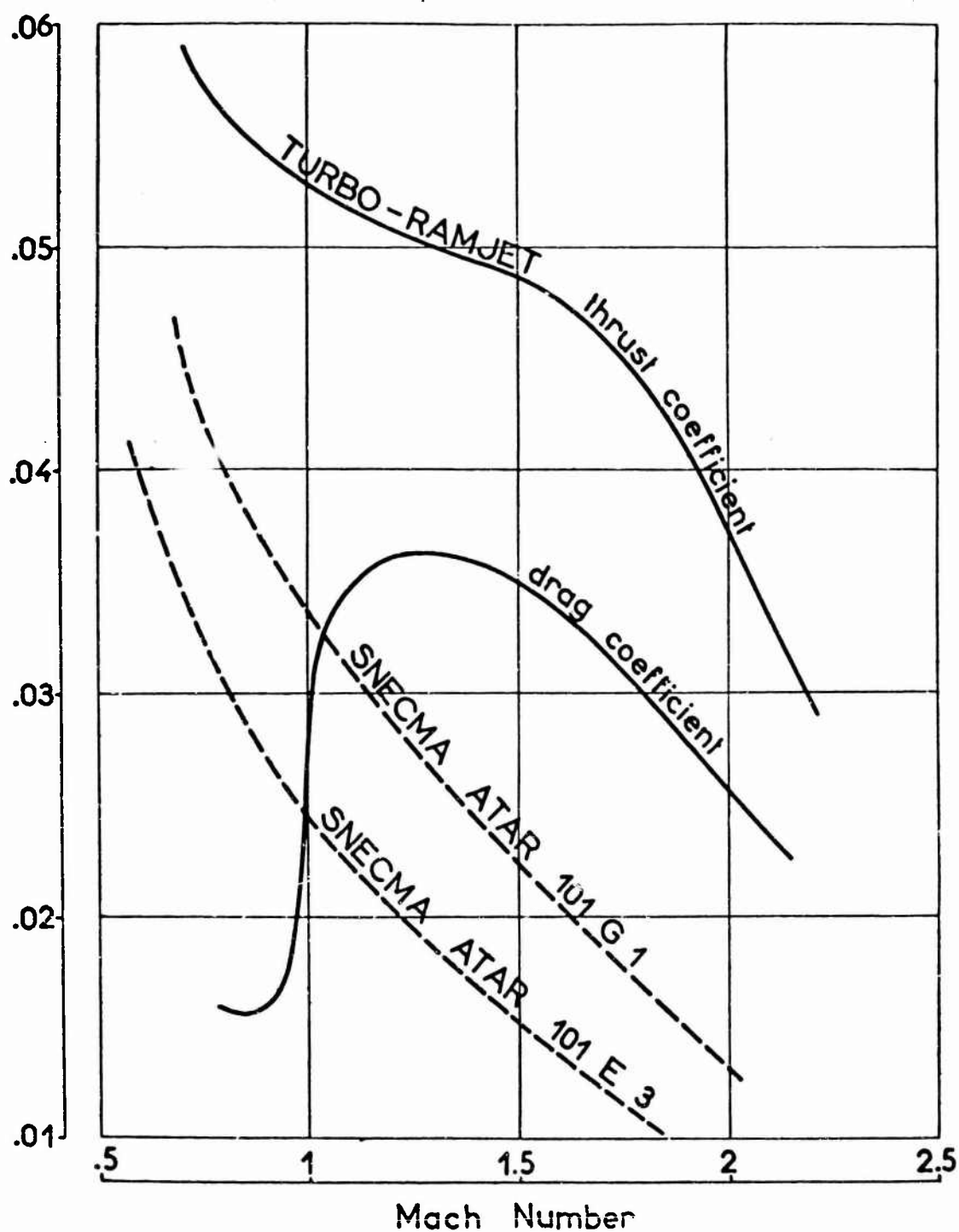
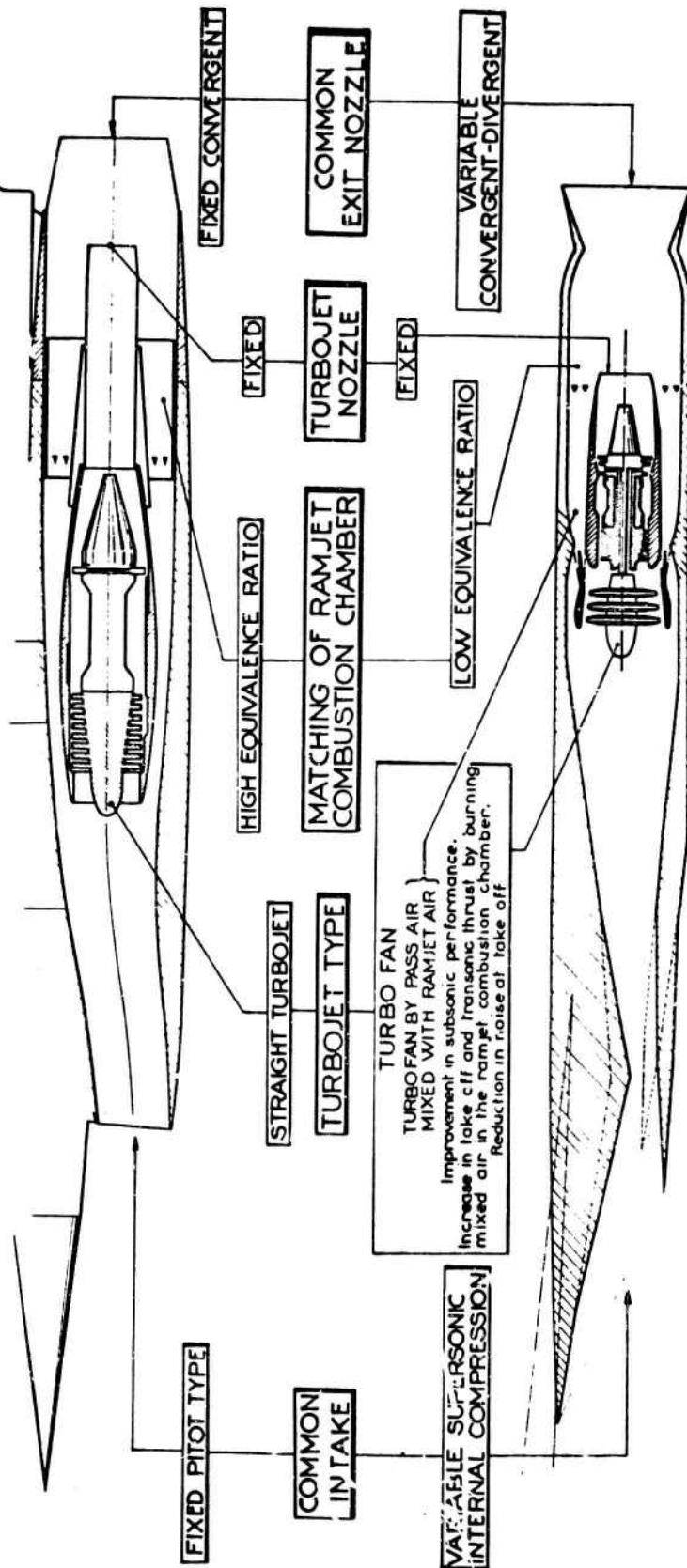


Fig. 3 Drag and thrust coefficient along a typical flight profile

CRIFTON COMBINATION[1954] MACH 2 FIGHTER

Low weight. Noise at take-off not important. Large thrust for normal operation and transonic acceleration



TURBOFANRAMJET ENGINE

Low SFC. for cruise. Large thrust for transonic acceleration. Low noise level at take-off

Fig. 4 Evolution of Nord-Aviation turbo-ramjet

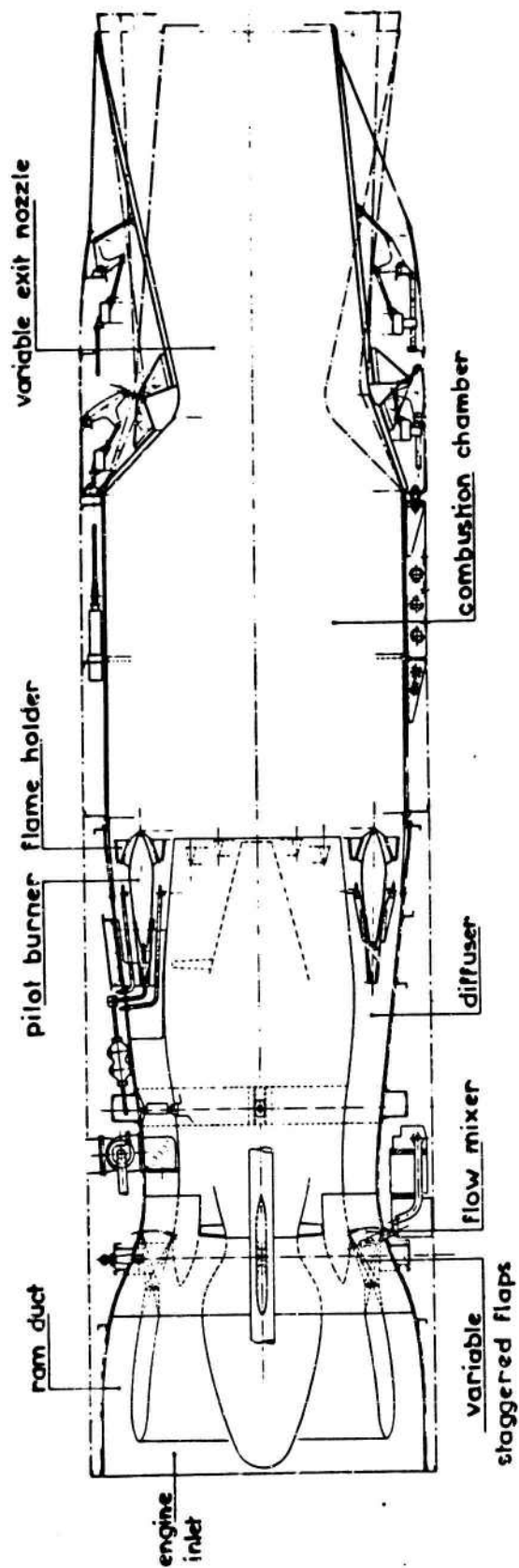


Fig. 5 Typical turbofan-ramjet engine. Side view

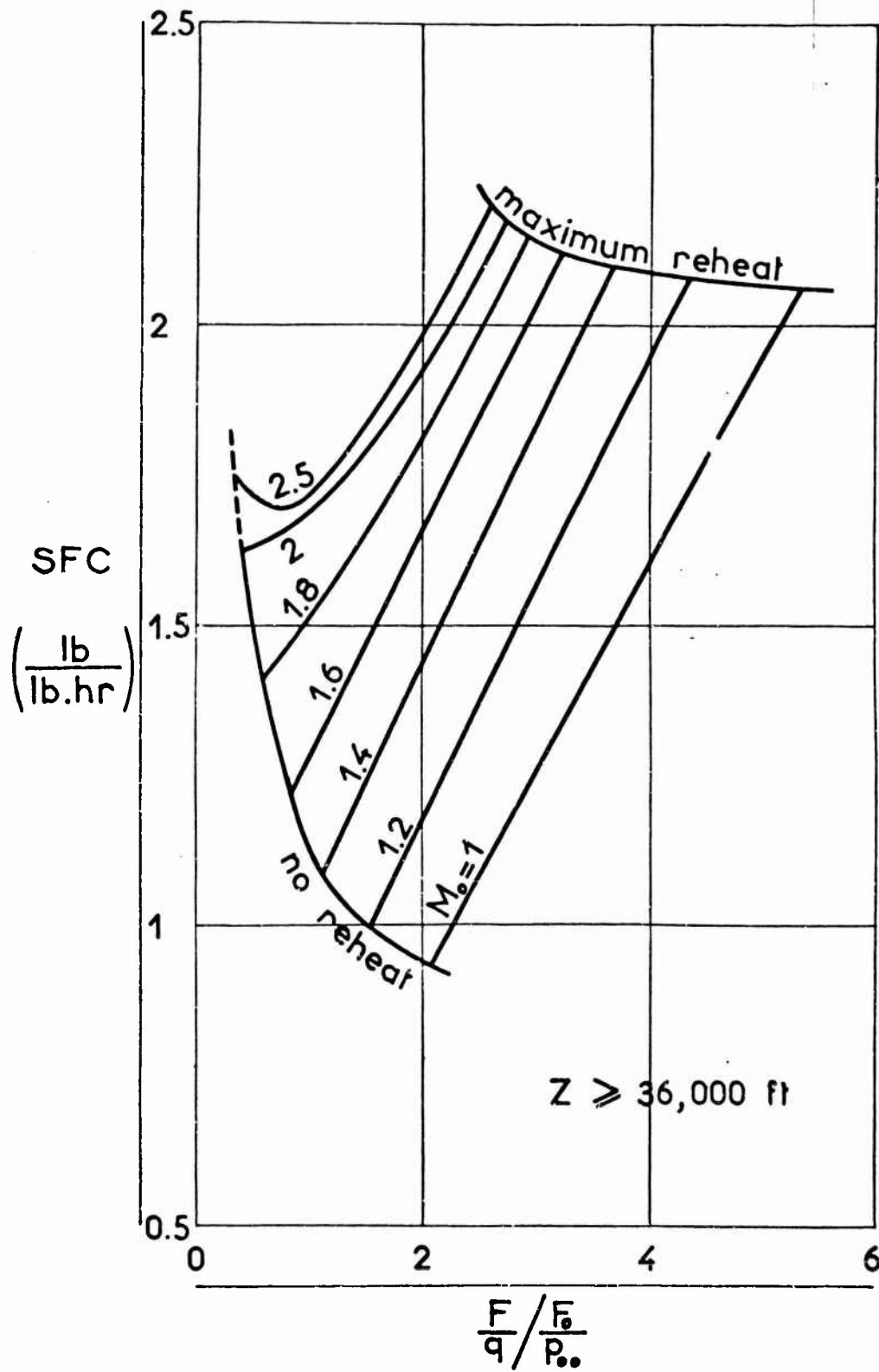


Fig.6(a) Supersonic and transonic performance characteristics

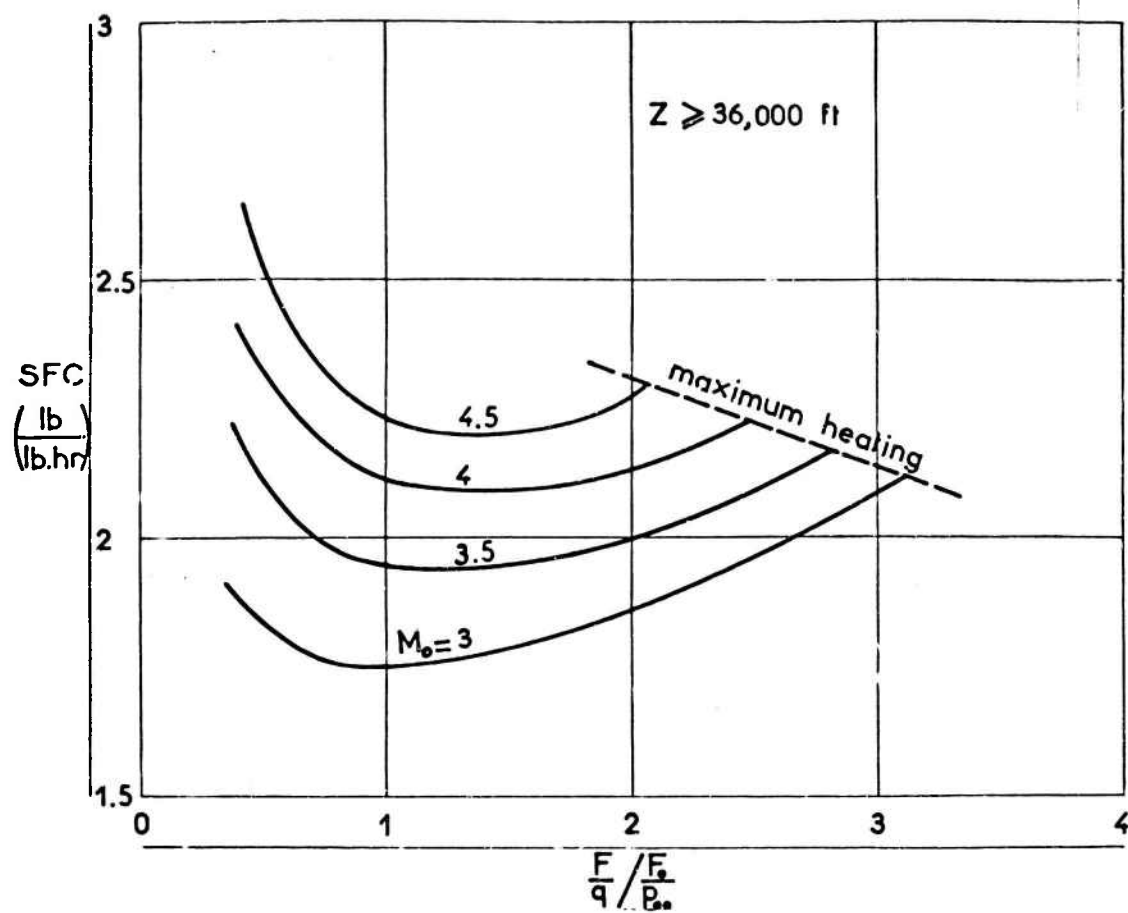


Fig. 6(b) High supersonic performance characteristics

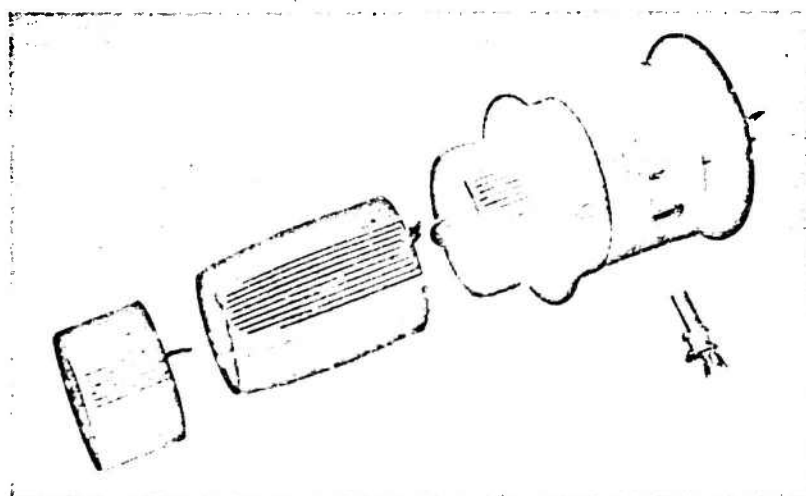


Fig. 7 Models of turbofan inlet cowl

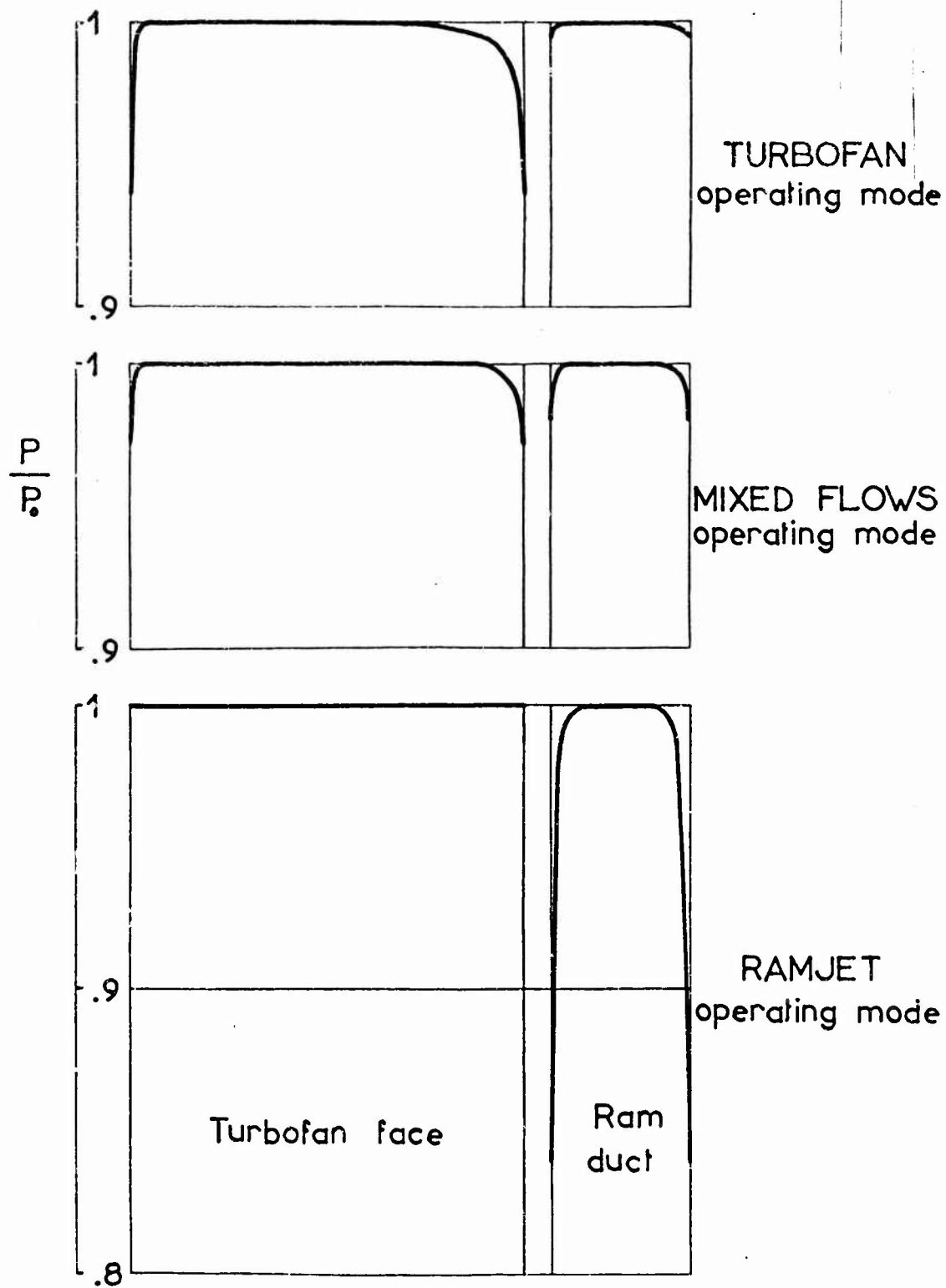


Fig.8 Engine inlet pressure distribution

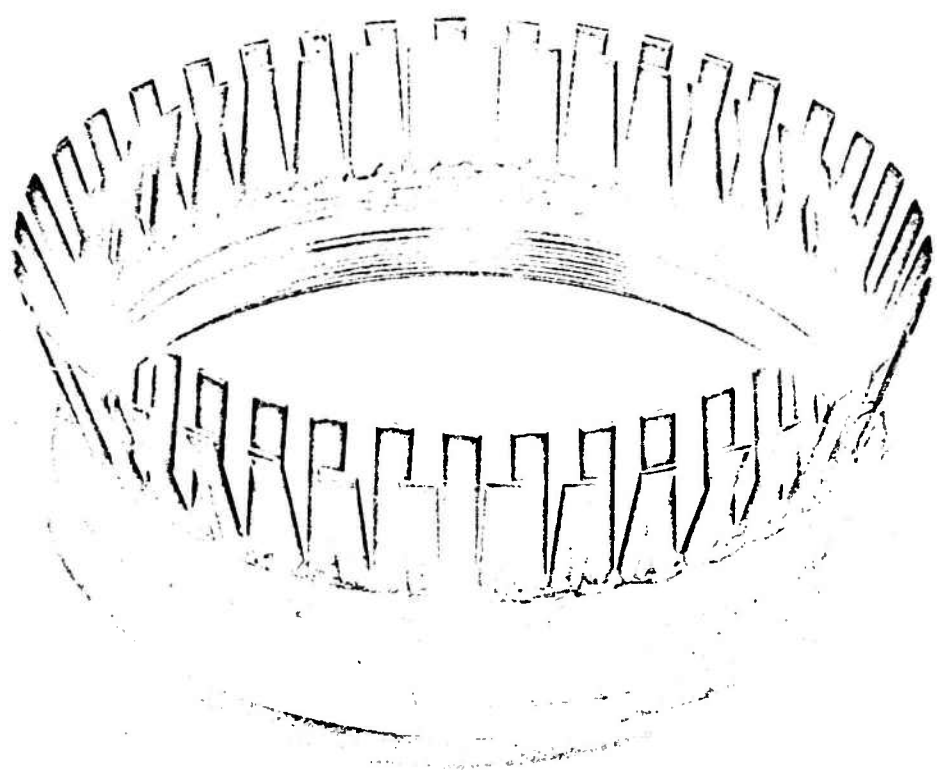


Fig.9 Flow mixer

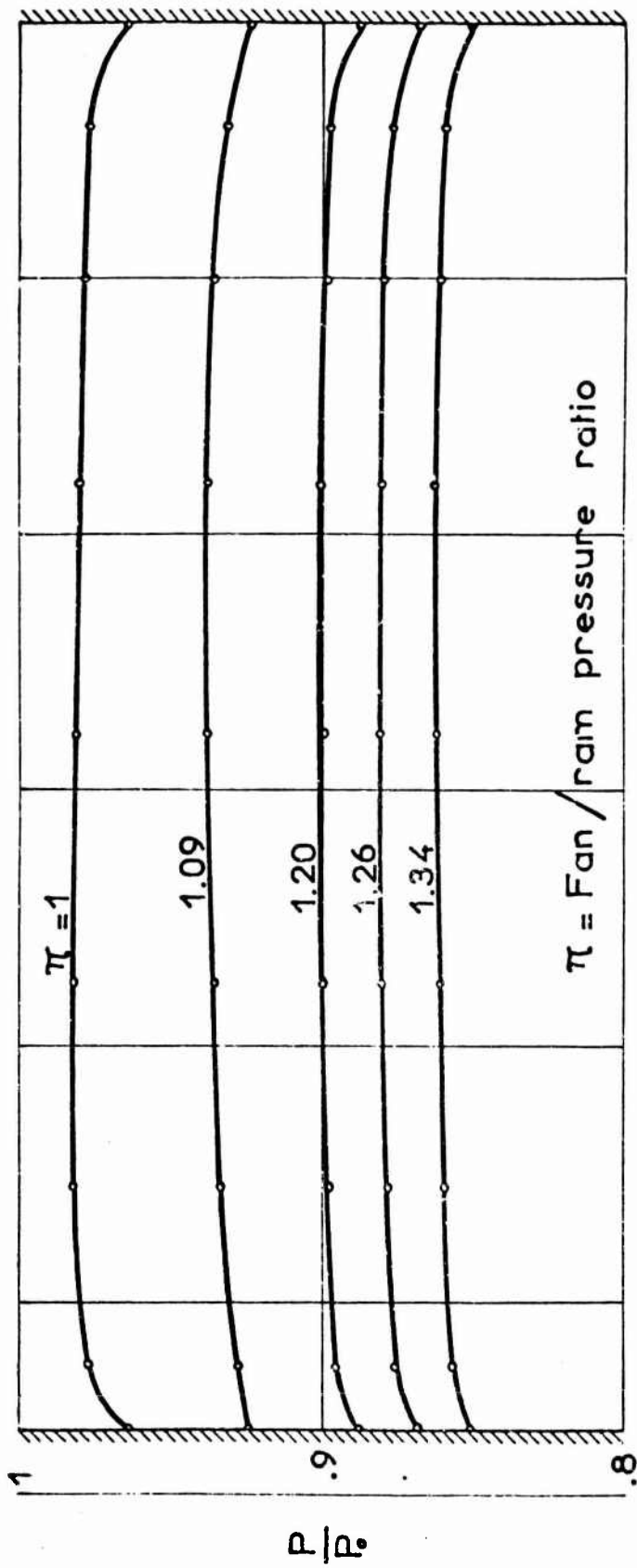


Fig. 10 Pressure profiles (upstream of the combustion chamber)

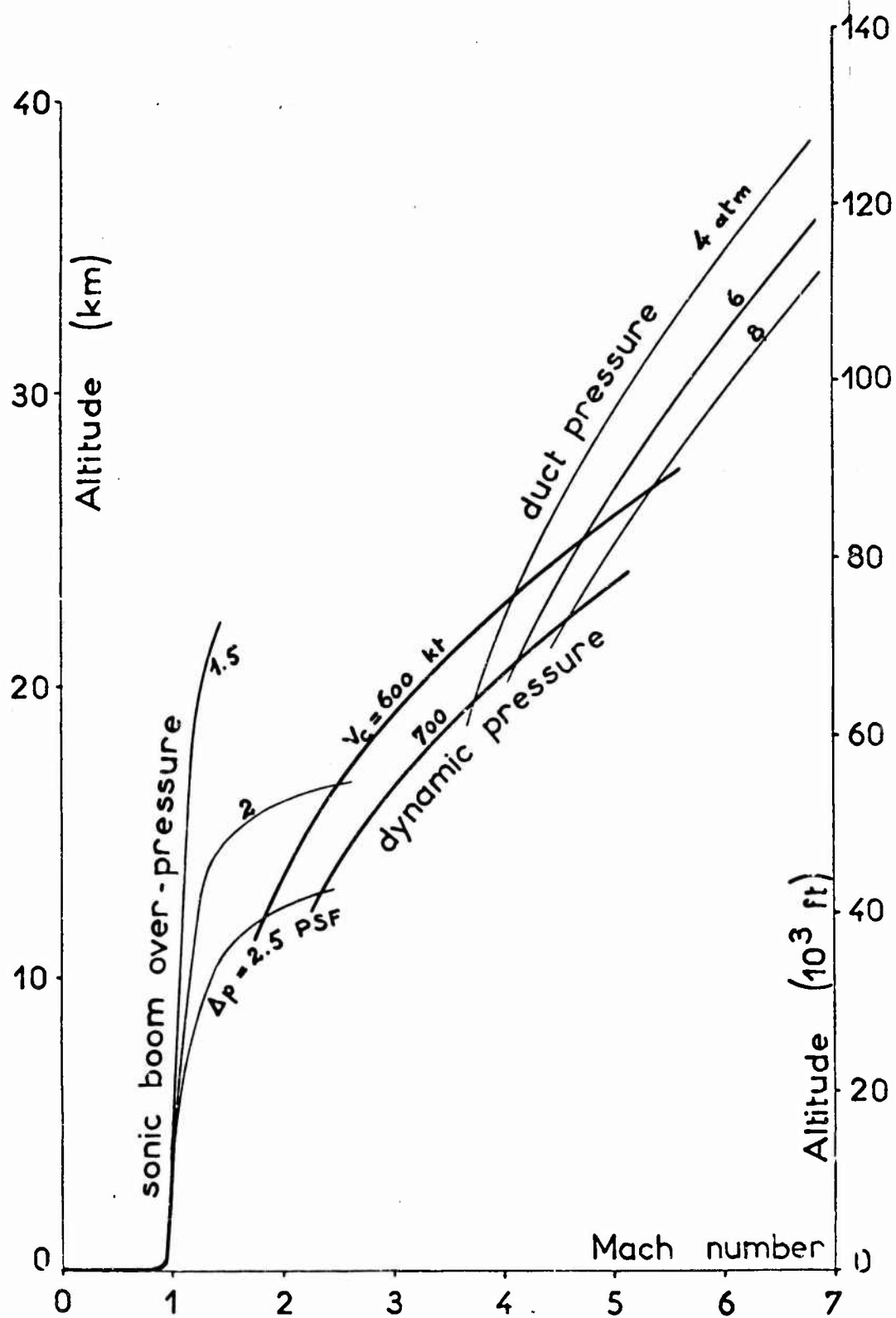


Fig. 11 Typical flight programme

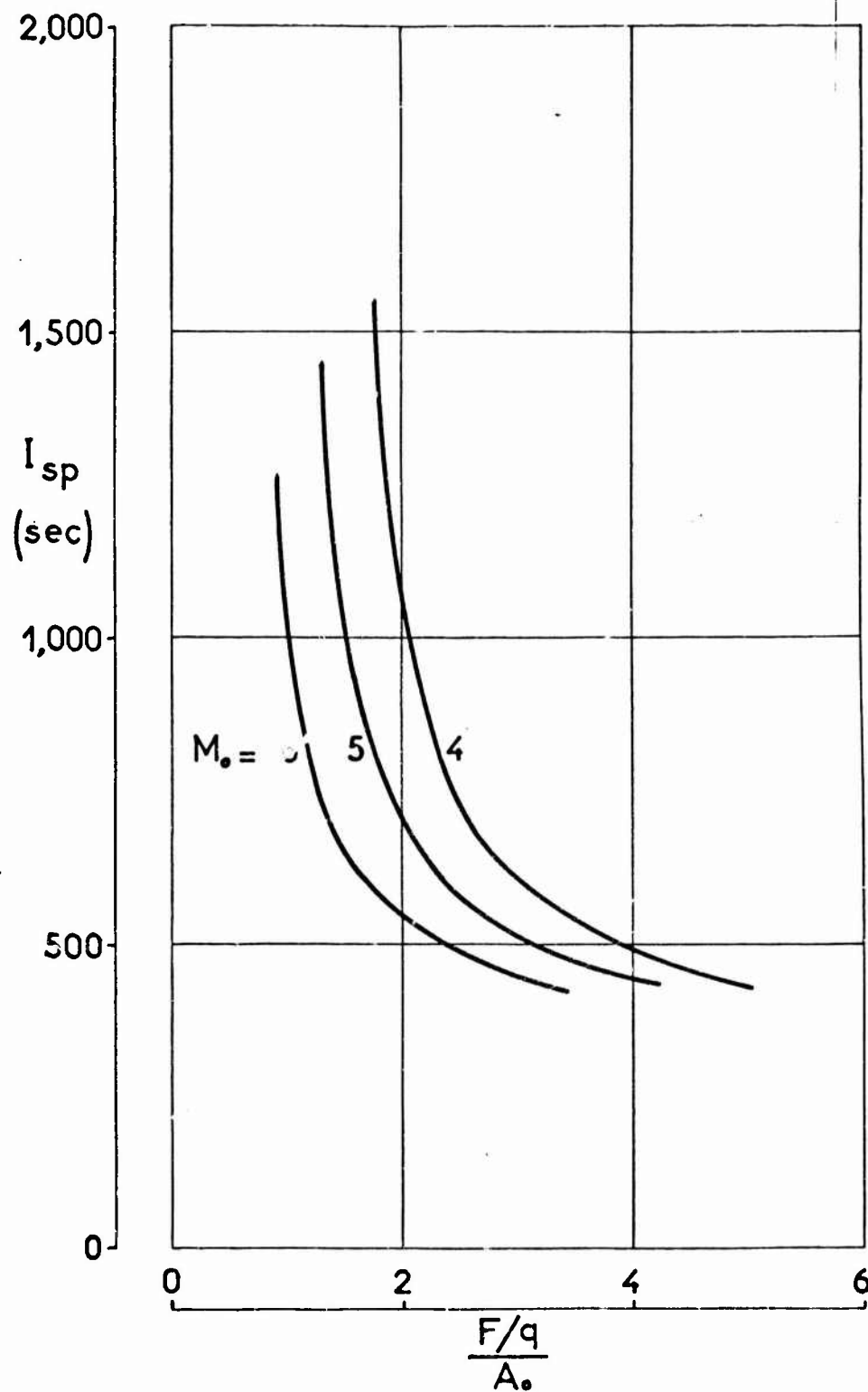


Fig. 12 Turbofan-ramjet with LOX injection. Specific impulse and specific thrust.
 Nozzle velocity coefficient = 0.95, shifting equilibrium, stoichiometric,
 fuel: JP1, inlet efficiency: MILE5008-B

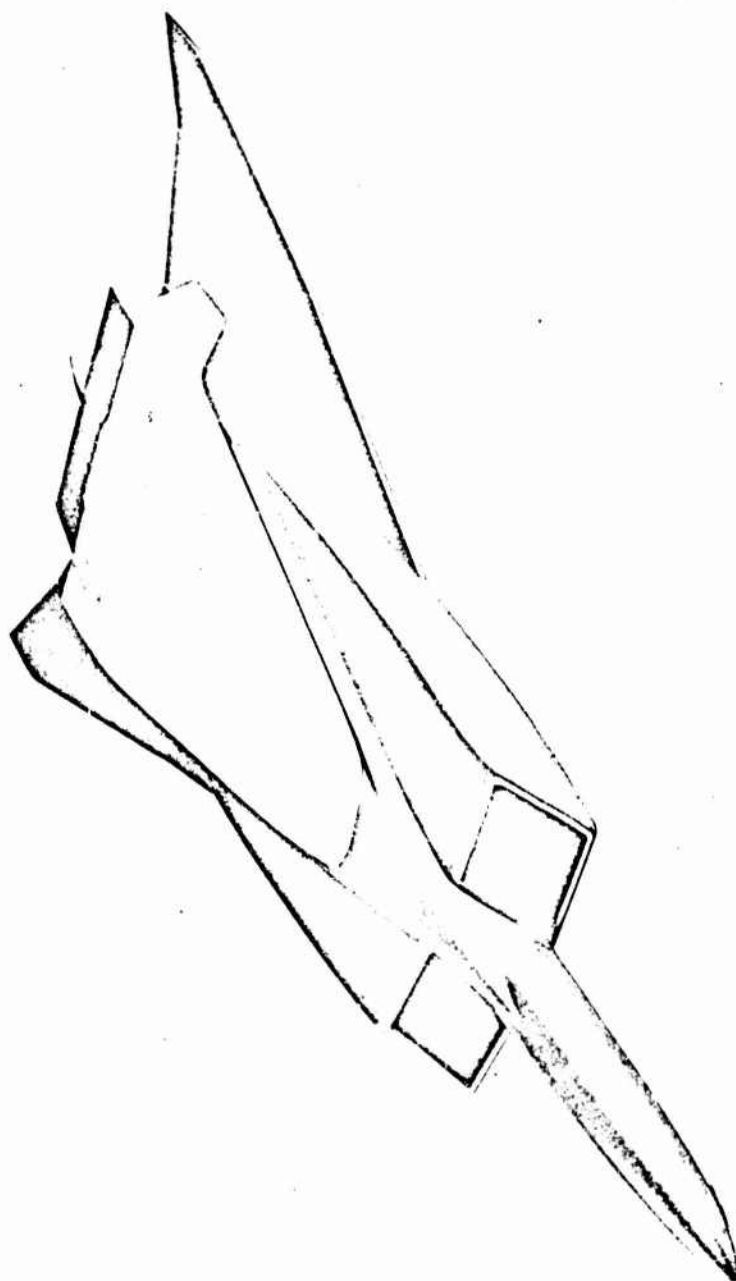


Fig.13 Model of an aerospace vehicle (ERNO + Nord-Aviation + SNECMA)

ADDITIVE DRAG ON INLET COWLS
AND ITS EFFECT ON AIRCRAFT PERFORMANCE

by

Joseph S. Mount

North American Aviation, Los Angeles, California, U.S.A.

SUMMARY

If the operational requirements for a turbojet-powered aircraft require the inlet to operate off-design at reduced inlet mass-flows, the theoretical additive drag can be significant in magnitude, compared to the basic aircraft drag. This could be equivalent to large penalties in range. Proper cowl design will allow much of this potential drag increment to be cancelled by a cowl suction force. For subsonic inlets at subsonic Mach numbers, test results show that about 30% of the theoretical additive drag can be recovered with a reasonably short and thin cowl. For the same subsonic inlets at low supersonic Mach numbers, about 50% - 60% can be recovered. For supersonic inlets at subsonic Mach numbers, the amount of theoretical additive drag cancellation that can be achieved is probably less, varying from 0 to 60% for a limited number of configurations recently tested. However, the configurations showing the best cancellation had higher basic drag levels. Further study of both subsonic and supersonic data will be needed to provide a satisfactory method of evaluating the various effects.

SOMMAIRE

Lorsque la définition des performances d'un avion à turboréacteurs exige que la prise d'air fonctionne hors adaptation avec des débits réduits, la traînée additionnelle calculée peut atteindre des valeurs importantes par rapport à la traînée de base de l'appareil, ce qui pourrait se traduire par d'importantes réductions du rayon d'action. Le calcul convenable du carénage permet d'éliminer en grande partie cet accroissement possible de traînée par une force d'aspiration du carénage. Pour les prises subsoniques aux nombres de Mach subsoniques, les résultats d'essais montrent que 30% environ de la traînée additionnelle calculée peuvent être récupérés grâce à un carénage modérément court et mince. Avec ces mêmes prises subsoniques aux nombres de Mach faiblement supersoniques, près de 50 à 60% peuvent être récupérés. Pour les prises supersoniques aux nombres de Mach subsoniques, la traînée additionnelle calculée qui peut être éliminée est sans doute moindre, de 0 à 60% pour quelques configurations récemment expérimentées. Cependant pour la configuration réalisant la plus forte récupération, la traînée de base était la plus élevée. Une étude plus poussée des résultats, en subsonique et en supersonique, est nécessaire pour définir une méthode satisfaisante d'évaluation des différents effets.

CONTENTS

	Page
SUMMARY	272
SOMMAIRE	272
LIST OF FIGURES	274
NOTATION	275
1. INTRODUCTION	277
2. QUANTITATIVE PERFORMANCE EFFECTS	278
3. REDUCTION OF LOSSES	279
4. TEST METHODS	279
5. SUBSONIC INLETS	280
6. SUPERSONIC INLETS	281
REFERENCES	283
FIGURES	284

LIST OF FIGURES

	Page
Fig. 1 Streamline approaching cowl	284
Fig. 2 Additive drag of a spike inlet	285
Fig. 3 Theoretical additive drag for a supersonic transport	286
Fig. 4 Mission penalties for $K_{ADD} = 1.0$	286
Fig. 5 Typical variation of drag with MFR	287
Fig. 6 Inlet cowl nomenclature	288
Fig. 7 Subsonic additive drag model	289
Fig. 8 Subsonic cowls	290
Fig. 9 K_{ADD} for straight cowls	291
Fig. 10 K_{ADD} for NACA Series 1 cowls	292
Fig. 11 K_{ADD} for short thin cowl, modified NACA-1 contour	293
Fig. 12 Supersonic additive drag model	294
Fig. 13 Interchangeable components	295
Fig. 14 Effect of cowl angle on drag	296
Fig. 15 Effect of cowl contour on drag	297
Fig. 16 Effect of ramp movement on drag	298
Fig. 17 Effect of cowl movement on drag	299
Fig. 18 K_{ADD} for ramp-type supersonic inlet. Mach 0.85, 10° contoured cowl	300

NOTATION

A	area
A_c	inlet capture area, measured in a plane perpendicular to the flight direction
A_1	flow area at inlet throat
A_{LE}	projected area perpendicular to the flight direction, taken at the lip leading edge station
A_0	area of the streamtube approaching the inlet, taken at free-stream conditions
C_p	pressure coefficient P/P_0
D	diameter or drag
F_g	gross thrust, $(W/g)V + (P - P_0)A$, taken at the jet exit conditions
F_n	net thrust, $F_g - (W/g)V_0$
M	Mach number
MFR	mass-flow-ratio; A_0 divided by a reference area. In this paper, the reference area used for subsonic inlet data is A_{LE} and for supersonic inlet data either A_c or A_1
P	pressure
q_0	freestream dynamic pressure, $\frac{1}{2}\rho_0 V_0^2$
r	radius
V	velocity
W	airflow, lb/sec
ρ	density
θ	angle
<i>Subscripts</i>	
s	surface
$1,1$	inlet throat
o	freestream
p	projected

ADDITIVE DRAG ON INLET COWLS AND ITS EFFECT ON AIRCRAFT PERFORMANCE

Joseph S. Mount

1. INTRODUCTION

Theoretical additive drag, D_{ADD} , as used in this discussion, is the force, in the flight direction, acting on the streamtube of air approaching a jet engine inlet. It will be further defined as measured relative to a certain base level of aircraft drag. The normal reference used is that level of drag which exists when the average Mach number of the air entering the inlet at the leading edge station is equal to free-stream Mach number (in other words, when the mass-flow-ratio (MFR) of the inlet, based on the leading edge station, equals 1.0).

It is well known that, under many flight conditions, the theoretical additive drag force is partially cancelled out (for purposes of computing the net propulsive effort exerted on the aircraft by the propulsion system) by a change in the suction forces acting on the cowl lip.

This paper presents the results of some recent tests aimed at obtaining empirical design data on the magnitude of this suction force.

The physical situation for a podded spike inlet is shown in Figure 1. Mathematically, D_{ADD} is defined, as in Figure 2, as the integrated force on the external streamline. It is equal to the algebraic sum of the momentum and pressure terms acting on the streamtube freebody. (The equation for a two-dimensional, or ramp inlet is identical in form. For a open-nose, or pitot inlet, the only change is the disappearance of the final term involving the surface pressure on the shock-generator.)

The effective cancelling out of a portion of the D_{ADD} term may be conveniently handled by an empirically-determined correction factor, K_{ADD} . Thus the equation for propulsion system net effort, F_{NE} , becomes

$$F_{NE} = F_N - (K_{ADD} D_{ADD}) - D_{BP} - D_{AUX}$$

where $F_N = F_g - \frac{W}{g} V_0$ = nozzle gross thrust - ram drag of engine air

D_{BP} = drag of bypass air taken into the inlet for matching purposes and shock control.

D_{AUX} = drag of auxiliary air taken into the inlet for such purposes as structural cooling, component cooling, and boundary layer control.

As may be seen, a value of 1.0 for K_{ADD} signifies no cancellation. A value of 0 indicates complete cancellation. It is desirable to have K_{ADD} as low as possible. Efforts toward minimizing K_{ADD} become focused on the detail design of the inlet lip.

Before discussing ways to minimize K_{ADD} , it is appropriate to ask: "Just how high is D_{ADD} and what would its effect be on performance if K_{ADD} were equal to 1.0?"

2. QUANTITATIVE PERFORMANCE EFFECTS

The more off-design conditions (from the inlet point of view) that appear as prime operating points for the aircraft, the larger effect additive drag will have on aircraft capability. The off-design condition is usually typified by the engine's demand for air, as expressed in terms of freestream tube area, being considerably less than the inlet can capture; i.e., a low mass-flow condition. Examples of off-design conditions for specific types of vehicles are:

Supersonic Transport

- (a) Transonic acceleration at high enough altitude to avoid unacceptable sonic booms. (This condition will establish engine size.)
- (b) Subsonic cruise for secondary leg of split route.
- (c) Maximum economy hold.

V/STOL Transport

- (a) Subsonic cruise at reduced power with certain arrangements of fan-type engines of large air-handling capacity sized for lifting.

Strategic and Tactical Penetrators

- (a) Extended transonic or high-subsonic low altitude penetration with inlets and engines capable of some reasonable supersonic performance.
- (b) Rate-of-climb transonically to effectively accomplish alternate supersonic missions.

Figure 3 has been prepared as an example of how theoretical additive drag compares to basic aircraft drag for a supersonic transport design. The lower solid curves represent basic aircraft drag for matched inlet operation. The theoretical additive drag increment for 100% r.p.m. is shown cross-hatched for both subsonic and supersonic operation (supersonic acceleration and cruise are done at 100% r.p.m.). For the subsonic case, an additional cross-hatched area is shown indicating the large increment in D_{ADD} that would result from reducing power to 25%. On this field of reference, points representative of the D_{ADD} increments associated with subsonic cruise (50% power) and subsonic loiter (20% power) have been spotted in. It may be seen that D_{ADD} gets to be about 16% as large as the basic aircraft drag during acceleration, about 13% as large during subsonic cruise and about 32% as large during subsonic loiter.

Figure 4 is a bar chart summary for the three vehicles listed above. It shows what additive drag would mean to "off-design" vehicle performance if the entire theoretical

additive drag term were to actually appear as a drag force on the vehicle. It is obviously profitable to seek reduction in potential losses of this magnitude.

3. REDUCTION OF LOSSES

Of course, in approaching a propulsion design problem, the inlet airflow capability should always be matched to the engine airflow requirement, with considerable attention directed toward keeping the theoretical additive drag low. The means employed may include variable geometry for the compression surfaces, variable geometry for the cowl, variation in the engine operating point, variable geometry for engine components, and bypassing. All of these approaches involve penalties in weight, complexity, cost, and/or thrust. The decision of how much air to spill externally involves trading off these penalties against the term $K_{ADD} \times D_{ADD}$. As with any trade studies, the results can be no more valid than the inputs and, since a thorough trade in this area involves a large expenditure of engineering manhours, it is appropriate to ask "How accurately can $K_{ADD} \times D_{ADD}$ be determined?"

In the case of D_{ADD} , the answer is "at least as accurately as the other terms in the net propulsive effort equation", since it is purely a theoretical function of engine airflow and dimensional factors. In the case of K_{ADD} , the answer depends upon the applicability of the particular test data available to the cowl configuration being considered and, additionally, upon the probable accuracy of the test data itself. Thus, it comes down to a matter of sifting the test data available, examining trends, and arriving at the best conclusions possible. For purposes of the discussion to follow it is probably best to deal with subsonic and supersonic inlets sequentially. First however, it would be well to describe the three ways in which test data may be taken to determine K_{ADD} .

4. TEST METHODS

The typical increase in drag with decreasing MFR of a given aircraft (or model) at a fixed Mach number is shown in Figure 5. The curve starts from a basepoint value at $MFR = 1.0$ (which may be an extrapolated point) and rises to the left. Knowing the airflow through the inlet from appropriate downstream measurements, the theoretical D_{ADD} may be calculated from the governing relationships. The basepoint drag at $MFR = 1.0$ is then subtracted from the measured data and an "adjusted measured" curve is obtained as shown. The ratio of the drag from the adjusted curve to that from the D_{ADD} curve is then K_{ADD} for a given MFR. In practice, data scatter can be significant at MFR near 1.0. However, since D_{ADD} approaches zero here, accuracy in K_{ADD} is less important than at lower MFR.

Measured drag may be obtained in any one of three ways for a wind tunnel model. The most preferred way is by use of an accurate force balance. Another way of "measuring" (in quotes because it is not a direct measurement) the change in drag with MFR is by integration of the static pressure profile on the lip, as obtained from a large number of flush orifices.

A third (and least preferred) method involves the use of one or more cowl pressure rakes extending outward from the cowl surface far enough aft so that the local static

pressure is not affected by changes in MFR and preferably where it is equal to or very near freestream pressure. Obviously, for complex shapes, complete coverage is impossible with the latter two methods. However the second method is often useful where, as so often happens, installation of a balance interferes with proper internal ducting and the third method can be employed where, in addition, the cowl is physically too small to allow installation of an adequate number of static pressure orifices.

5. SUBSONIC INLETS

Many subsonic inlets are of the pitot type, while others will have one or two sides adjacent to aircraft surfaces. Many are essentially circular in cross-section, whereas others may depart from this simple shape in varying degrees. The cancellation of D_{ADD} can be studied for all, using wind tunnel models and various measurement techniques. Most of the data available to the author has been produced by round, or near-round pitot inlets.

An inlet cowl profile may be defined by the geometrical symbols shown on Figure 6. Using these symbols, X/D describes the cowl length to the point of maximum external cross-section and d/D describes its thickness. The inner and outer surfaces may be described in a variety of different ways, as by leading edge radii (if circular or elliptical), cowl angle (if straight) or by coordinates (if a faired or generated surface). An added real life complication which confronts the engineer attempting to use or categorize the data is the fact that external fairing requirements aft of the inlet crown often require that different cuts in the fore-and-aft direction have different thicknesses, lengths and even profiles. In general it is usually true that aerodynamic cross-section constraints generally are forcing in the direction of thin short cowls (high d/D and low X/D), while the desire to avoid internal flow separation during takeoff is generally forcing in the direction of generous internal radii (high r_1/d). These restraints greatly limit the ability of the designer to choose a good external lip profile - good, that is, from the point of additive drag cancellation.

A model was built at North American Aviation specifically for investigating additive drag cancellation (Fig.7) and a number of different pitot-type cowls (Fig.8) were tested at subsonic and transonic Mach numbers in July of 1964. The model, described in more detail in References 1 and 2, employed both a drag balance and cowl static pressure orifices. Drag changes measured by the two methods compared very favorably. K_{ADD} data obtained from this model is presented in Figures 9 - 11, together with comparable data from other sources as noted.

In Figure 9 data from straight (i.e. conical) cowls is presented. The North American data (cowls A and C of Figure 8) is compared with some older NACA force balance data³ taken at very low Mach numbers on a cowl that was both thinner and shorter than the NAA model. None of the data show really acceptable additive drag cancellation, except for the bluntest cowl (lip radius one-twentieth of the inlet diameter at the leading edge) at the lowest (0.3) test Mach number. A cowl with intermediate blunting (cowl B of Figure 8; $r/D_{LE} = 0.011$) was also tested. However, K_{ADD} was not significantly lower than that of the sharp cowl, indicating that appreciable rounding is required before good additive drag cancellation can be achieved with straight cowls, even at low Mach numbers.

A potpourri of other relatively ancient data from various models¹ indicated that, for relatively thick ($d/D = 0.3$ to 0.8) and long ($X/D = 0.5$ to over 2.0) ducted bodies, K_{ADD} could certainly be kept below 0.5 and possibly below 0.1 for subsonic operation at reasonable, i.e. above 0.5 , MFR. What is required is careful contouring of the lip and external cowl to provide separation-free acceleration of the external flow around the cowl presumably to the lowest peak surface Mach number possible. Two additional cowls were run in the July 1964 test period, employing an NACA Series 1 external contour and round lip, $r/D_{LE} = 0.011$ and 0.050 . As with all of the models of Figure 8, the internal duct was cylindrical. Results are shown in Figure 10 and are encouraging, indicating K_{ADD} may be kept below approximately 0.2 for a reasonable range of MFR at Mach numbers below 0.9 .

Some data obtained in June 1965 on a much thinner ($d/D = 0.91$) and shorter ($X/D = 0.16$) cowl at 0.85 Mach number is presented in Figure 11. Since the primary purpose of the test was not cowl drag measurement, the third method of cowl drag calculation mentioned previously - that of computing momentum change from cowl external rake readings - was used. Therefore the data cannot be considered of high reliability, particularly since the shortness and thinness of this cowl would lead one to predict a higher value than that obtained in the 1964 tests. However, the low value of K_{ADD} , 0.06 , obtained is certainly encouraging. This cowl employed a NACA series 1 contour modified at the leading edge by a radius, as shown in the figure.

6. SUPERSONIC INLETS

Subsequent to the subsonic inlet testing of July 1964, the USAF Aero-propulsion Laboratory at Wright Field sponsored a test of a series of two-dimensional ramp-type supersonic inlets. The inlets were nominal Mach 3.0 designs and testing was carried out at Mach 0.7 to 2.2 in August 1965 in the NASA Ames $6\text{ ft} \times 6\text{ ft}$ Supersonic Wind Tunnel. The model (Fig. 12) employed the same flow-measuring section as the subsonic model previously described, with a large variety of interchangeable ramps, sideplates and cowls (Fig. 13). Prior to this program, the only available data¹ for a ramp-type supersonic inlet indicated that $K_{ADD} = 0.70$ could be expected between Mach 0.9 and 1.6 .

Results of preliminary analysis on a portion of the test data are shown on Figures 14-18. (In Figures 14-17 MFR is defined as A_0/A_C , since variations from a basepoint capture area geometry are of interest. In Figure 18, MFR is based on inlet area A_1 - a more logical reference for K_{ADD} comparisons.) The effect on spillage drag of modifying cowl shape, changing cowl angle and changing ramp angle are demonstrated. Data are presented for $M_0 = 0.85$ and 1.3 . The basic model is that of a Mach 3.0 inlet which would operate shock-on-cowl at design point. The initial ramp angle is 5° .

Figure 14 shows the effect on drag coefficient of straight cowls having 6° and 10° external angles. The drag coefficient used in this and in later figures is:

$$\frac{D}{q_0 A_C} = \frac{D_{ADD} + \text{External model drag}}{q_0 A_C}$$

where A_c is the design point capture area of the inlet. Thus, the unrecovered portion of additive drag is clearly defined by the increase in drag coefficient as mass-flow-ratio is reduced. The data show that a reasonably large cowl angle is desirable both subsonically and transonically.

Figure 15 shows a comparison of a 10° straight cowl and a circular arc contoured cowl having a leading edge tangent angle of 10° . These data and other data not presented here show that contouring reduces drag.

Thus, a good cowl shape is a contoured cowl having a relatively large leading edge angle. Other data not included show that a 15° contoured cowl is even better than the 10° cowl subsonically and equally as good as the 10° cowl transonically.

Figure 16 shows the effect on drag coefficient of raising the second external ramp from an angle of 5° to 9° and to 12° . Both subsonically and transonically, large spillage quantities (decreases in MFR) are obtainable for relatively small drag increases. Calculations, based upon empirical losses for bypass systems, show that the drag associated with bypassing the same amount of air would be twice as high at Mach 1.3 and even greater at Mach 0.85.

Figure 17 shows the effect on spillage drag of employing a variable inlet cowl. Data are presented for the 10° circular arc cowl in its 0° , -5° and -10° rotated positions.

Again, large drag decreases are obtainable at the lower MFRs by varying inlet geometry. Envelope curves through the end points of the variable ramp and cowl drag curves would show that the drag levels are quite similar for the two methods. The variable ramp method is slightly superior for the mass-flow range tested. Since nearly all such supersonic inlets necessarily have variable external ramps, a low drag spillage device is normally available without added weight or cost.

Figures 14-18 represent the extent to which the new data on the supersonic inlets have been studied. When the analysis is complete a much clearer picture should be available. At this date it is not apparent, for instance, what the most useful reference area will be for comparing drags of the various configurations. For subsonic operation it is probably reasonable to define MFR as A_0/A_1 and to refer drag comparisons at reduced mass flows back to the condition of $MFR = 1.0$, i.e. $M_1 = M_0$. This was done for the Mach 0.85 variable ramp data of Figure 16. A K_{ADD} was computed, as for the pitot inlets discussed earlier, by dividing the measured drag by the theoretical open-nose additive drag. Results are shown in Figure 18. It is seen that cancellation of the theoretical D_{ADD} is not as good for the higher ramp angles although, when drag itself is considered, the higher angles are to be preferred. Thus K_{ADD} of itself is not an adequate criterion for evaluating a cowl shape. It is probably true, for both supersonic and subsonic designs, that a certain amount of "built-in headwind", i.e. drag at some baseline value of inlet airflow, is required to get good additive drag cancellation. It is hoped that further study of the data will provide a uniform analytical/bookkeeping approach that will satisfy the requirements both of the external aerodynamicist, for establishing and categorizing drag changes due to inlet effects, and of the propulsion specialist, for accurately predicting the performance of the internal airflow system.

REFERENCES

1. Mount, J.S. *The Effect of Inlet Additive Drag on Aircraft Performance.* AIAA Paper 64-599, Transport Aircraft Design and Operations Meeting, Seattle, August 10-12, 1964.
2. Petersen, M.W.
Tamplin, G.W. *Open Nose Additive Drag Test Results at Subsonic and Transonic Speeds.* Report NA-64-921, North American Aviation, Inc./Los Angeles Division, December 1964.
3. Blackaby, J.R.
Watson, E.C. *An Experimental Investigation at Low Speeds of the Effects of Lip Shape on the Drag and Pressure Recovery of a Nose Inlet in a Body of Revolution.* NACA Ames, TN 3170, April 1954.
4. Baals, D.D.
et alii *The Development and Application of High Critical-Speed Nose Inlets.* NACA Langley, Report 920, 1948

Note:

NACA - National Advisory Committee for Aeronautics (Predecessor of NASA, National Aeronautics and Space Administration).

AIAA - American Institute of Aeronautics and Astronautics.

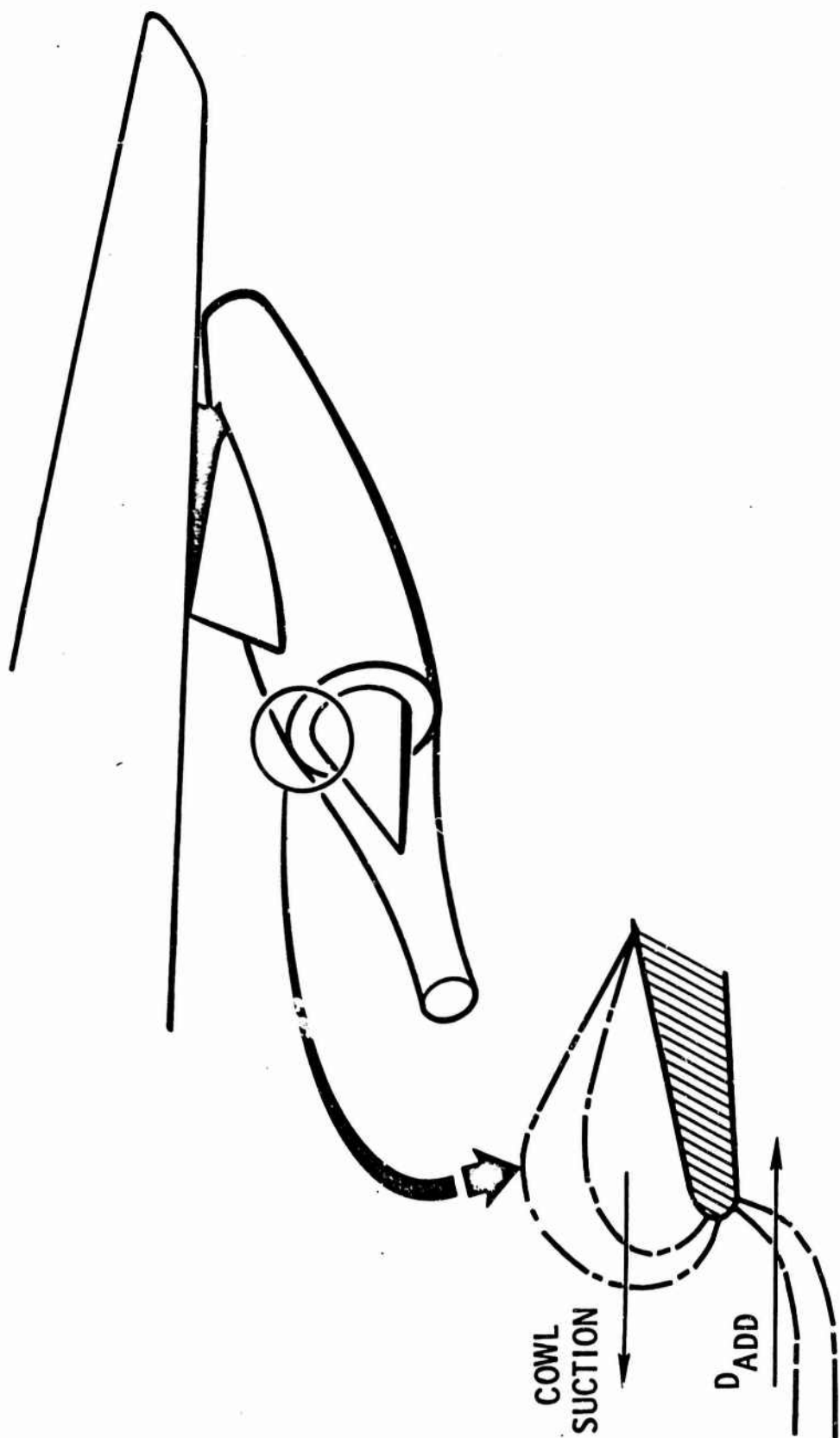
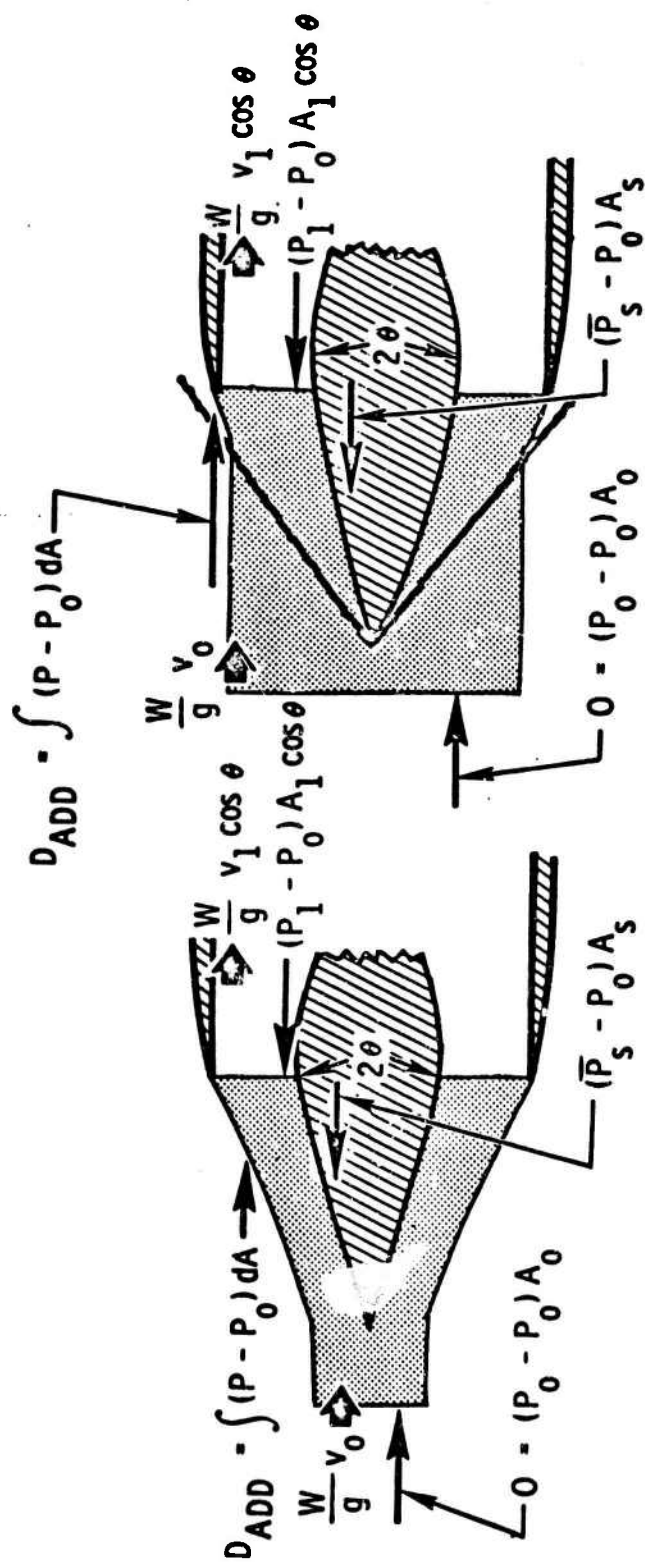


Fig.1 Streamline approaching cowl



(A) SUBSONIC

(B) SUPERSONIC, TERMINAL SHOCK INSIDE

$$D_{ADD} = \left[\frac{W}{g} v_1 + (P_1 - P_0) A_1 \right] \cos \theta - \frac{W}{g} v_0 + (\bar{P}_s - P_0) A_s$$

Fig. 2 Additive drag of a spike inlet

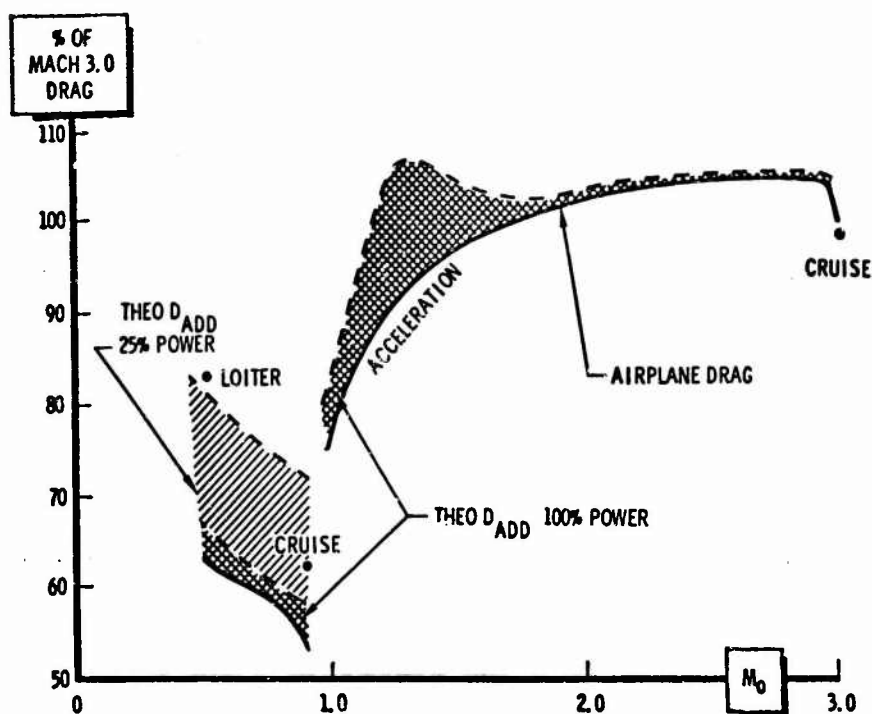


Fig. 3 Theoretical additive drag for a supersonic transport

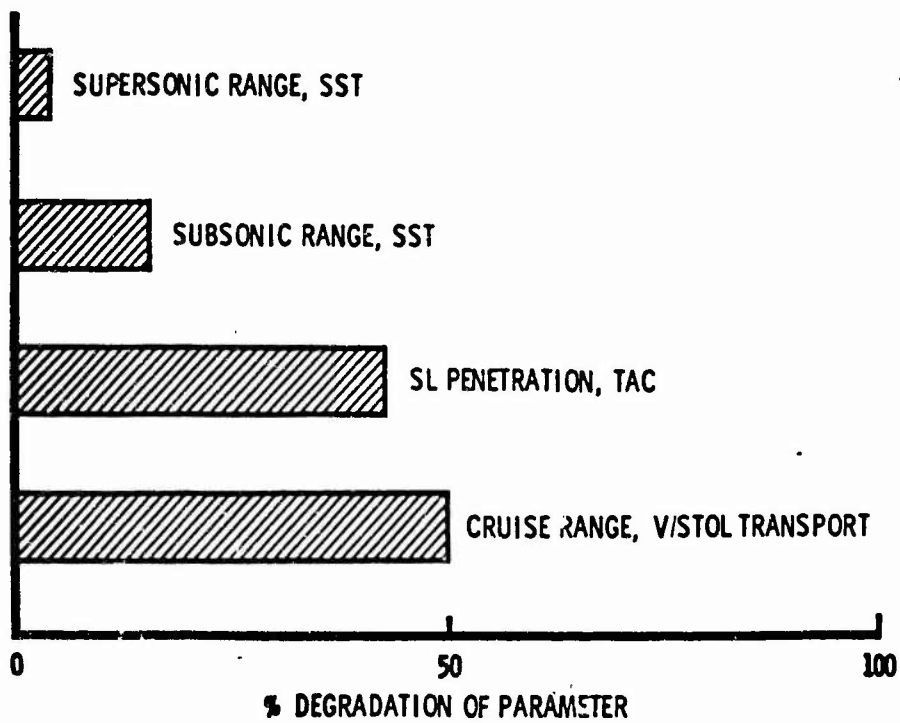


Fig. 4 Mission penalties for $K_{ADD} = 1.0$

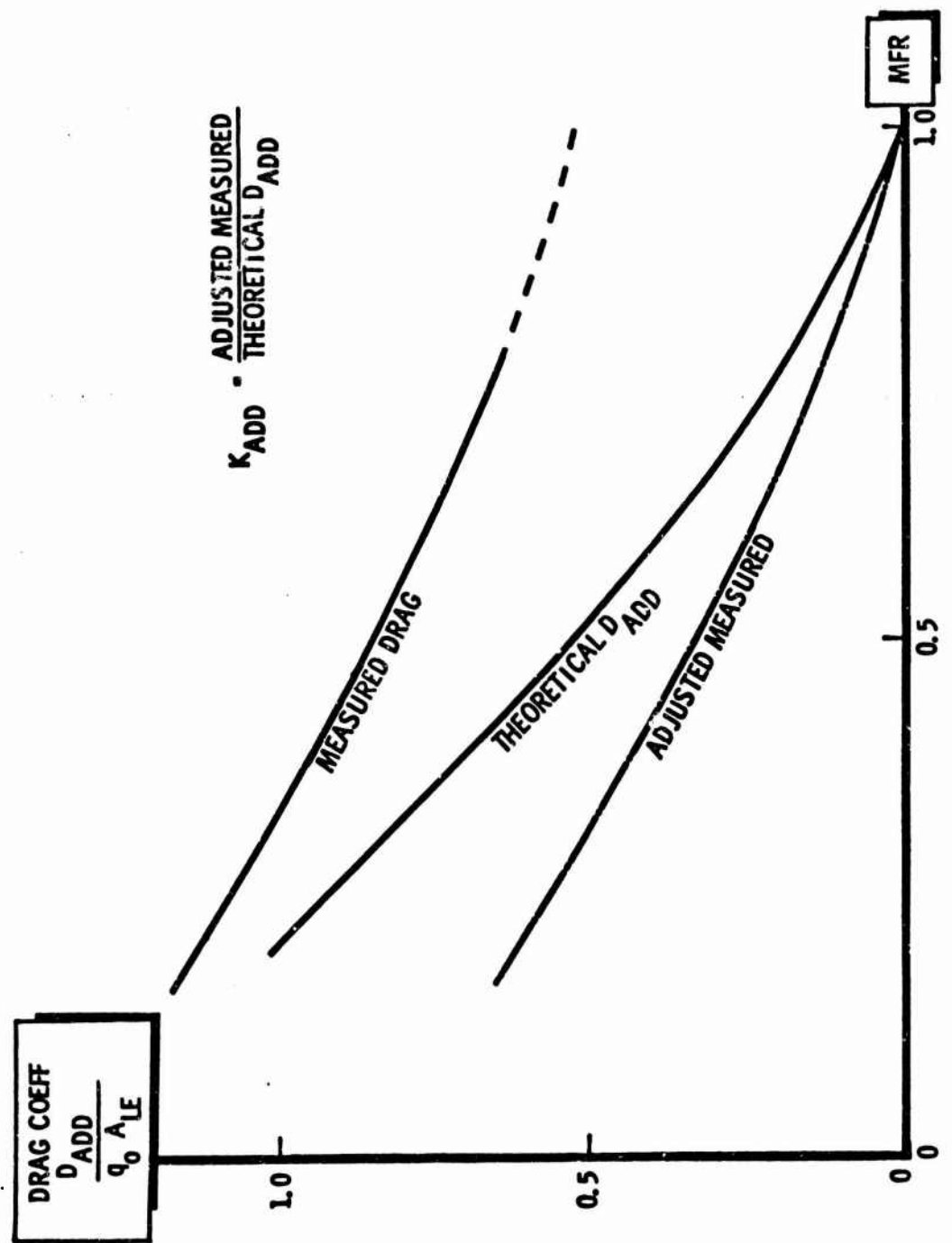


Fig. 5 Typical variation of drag with MFR

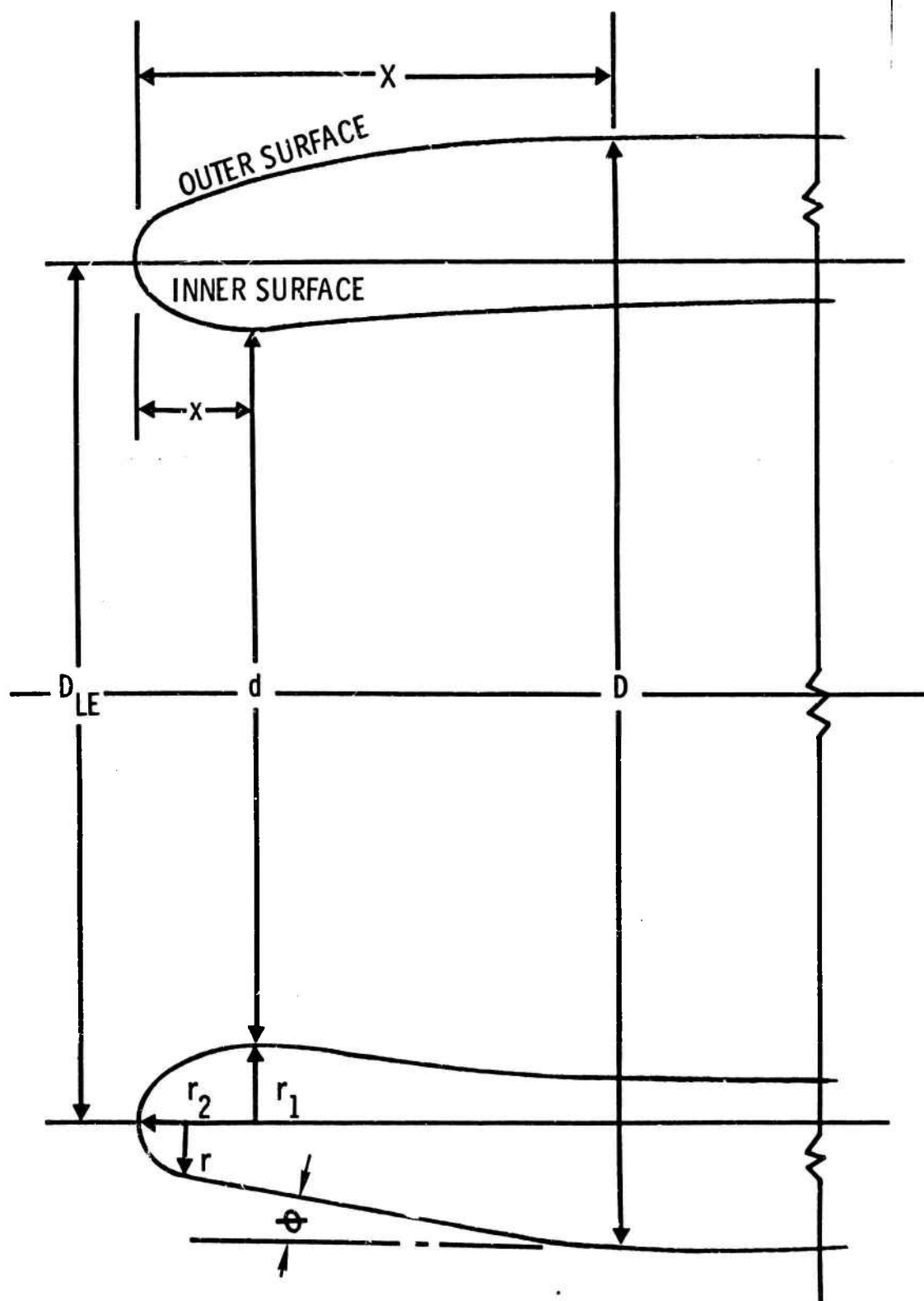


Fig.6 Inlet cowl nomenclature

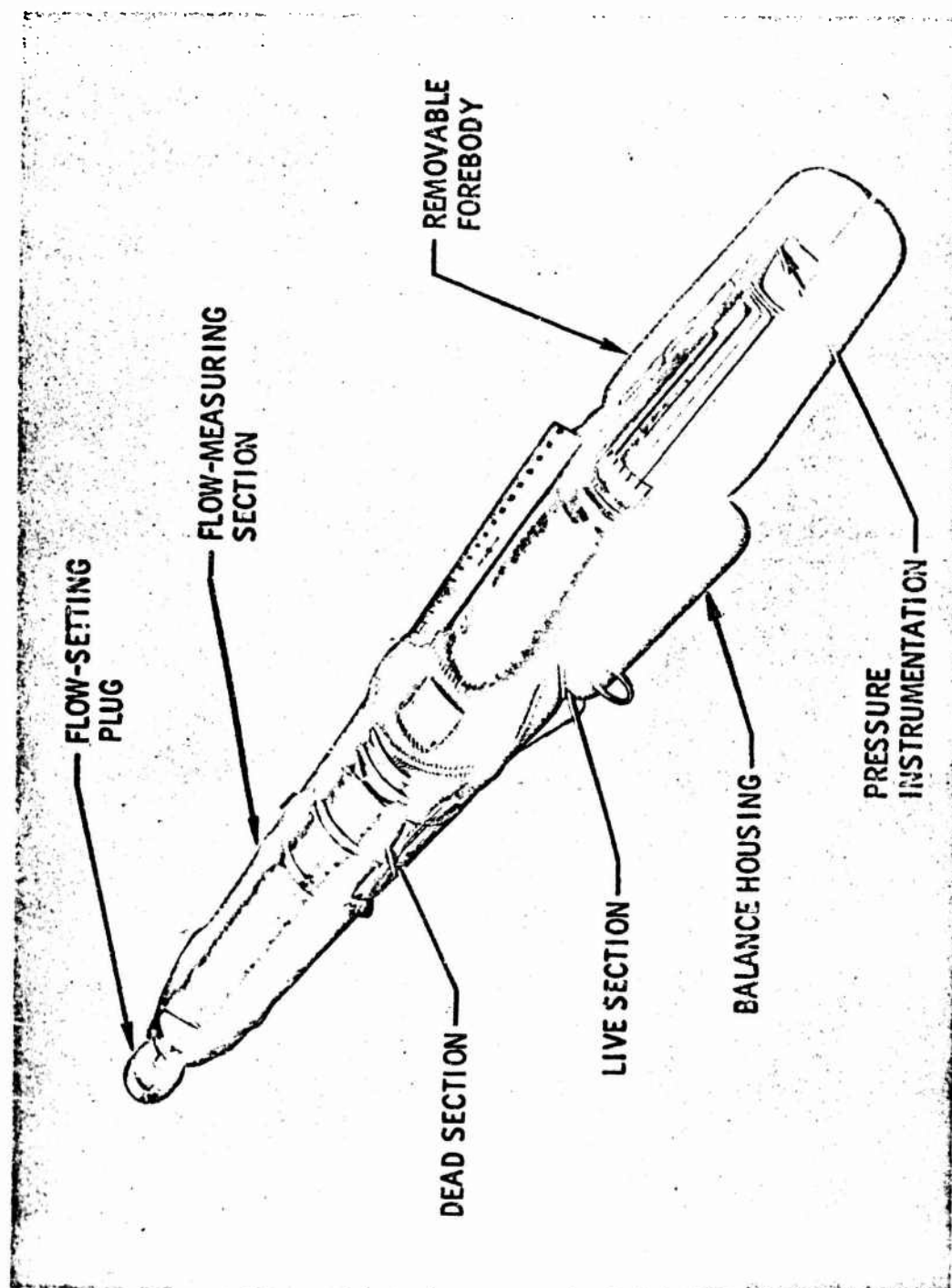


Fig. 7 Subsonic additive drag model

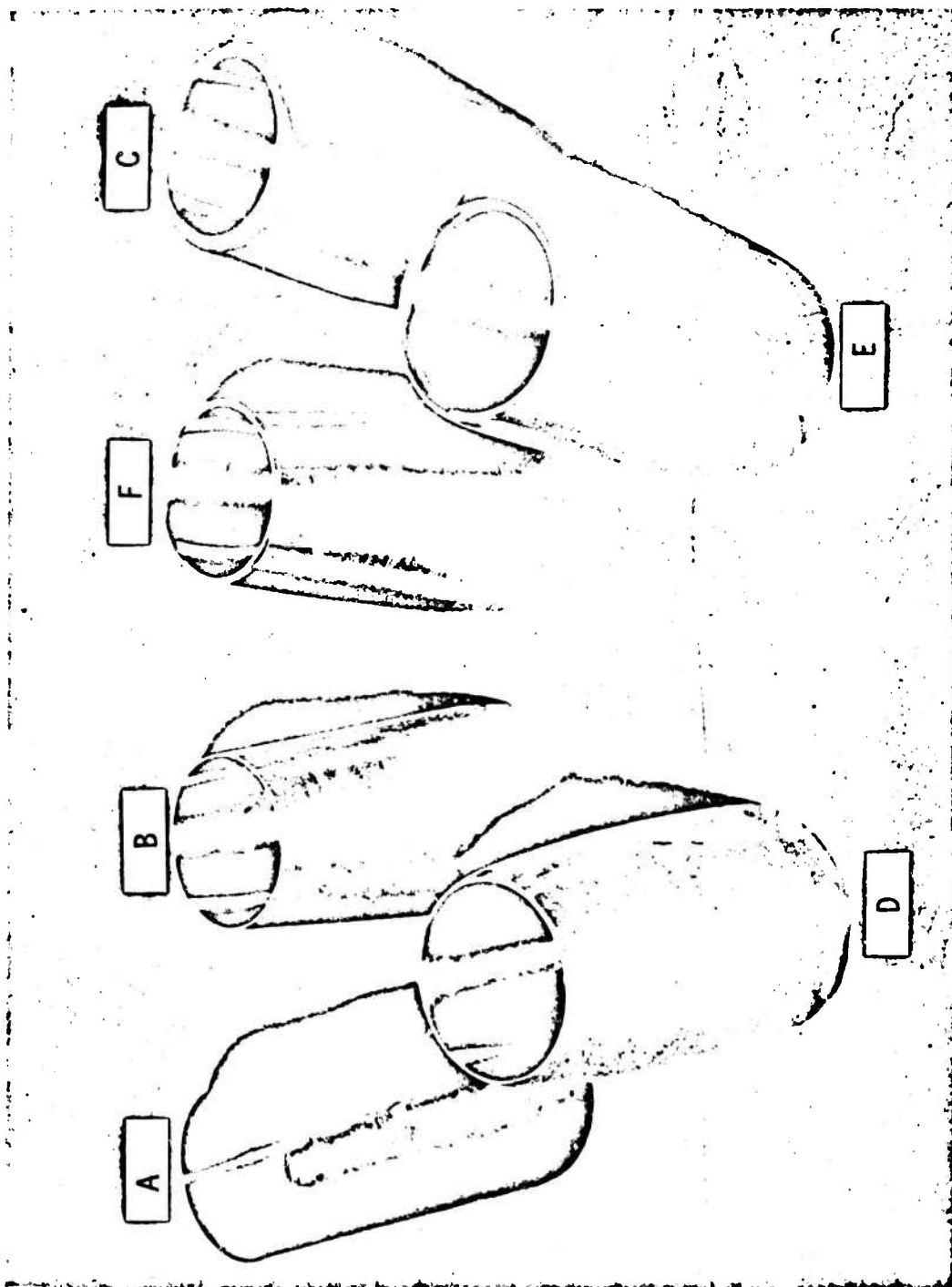


Fig. 8 Subsonic cowls

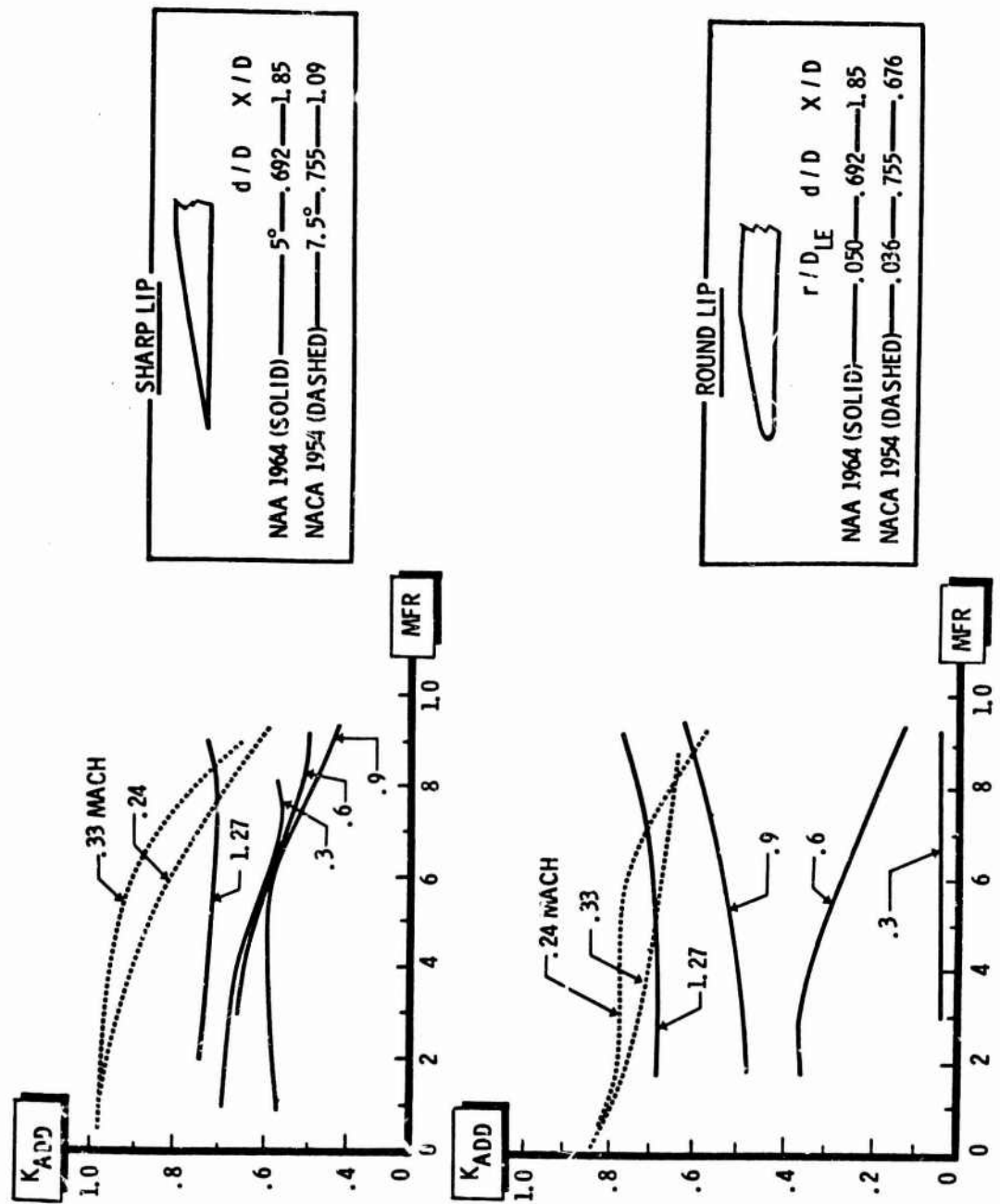


Fig. 9 K_{ADD} for straight cowls

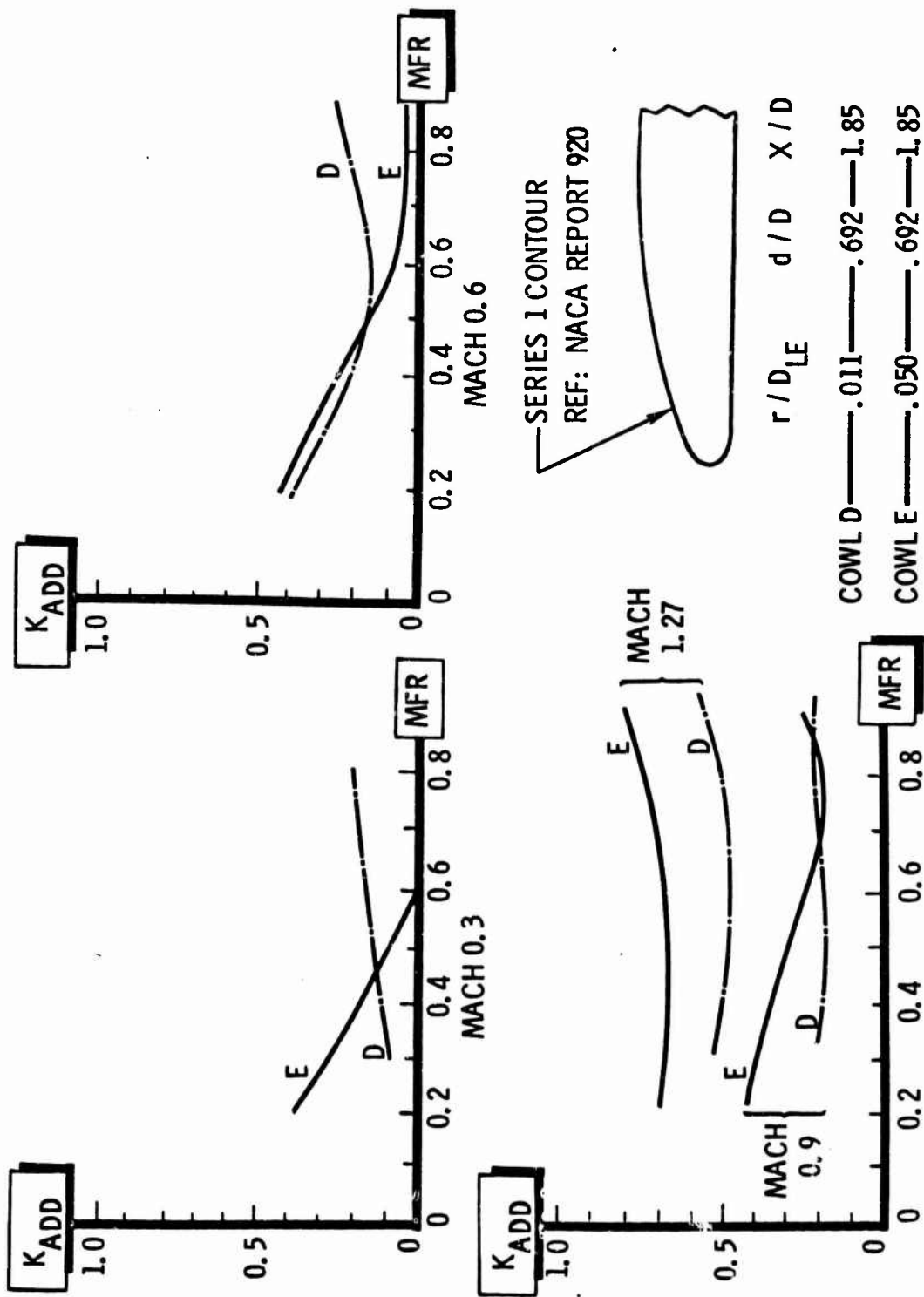


Fig. 10 K_{ADD} for NACA Series 1 cowls

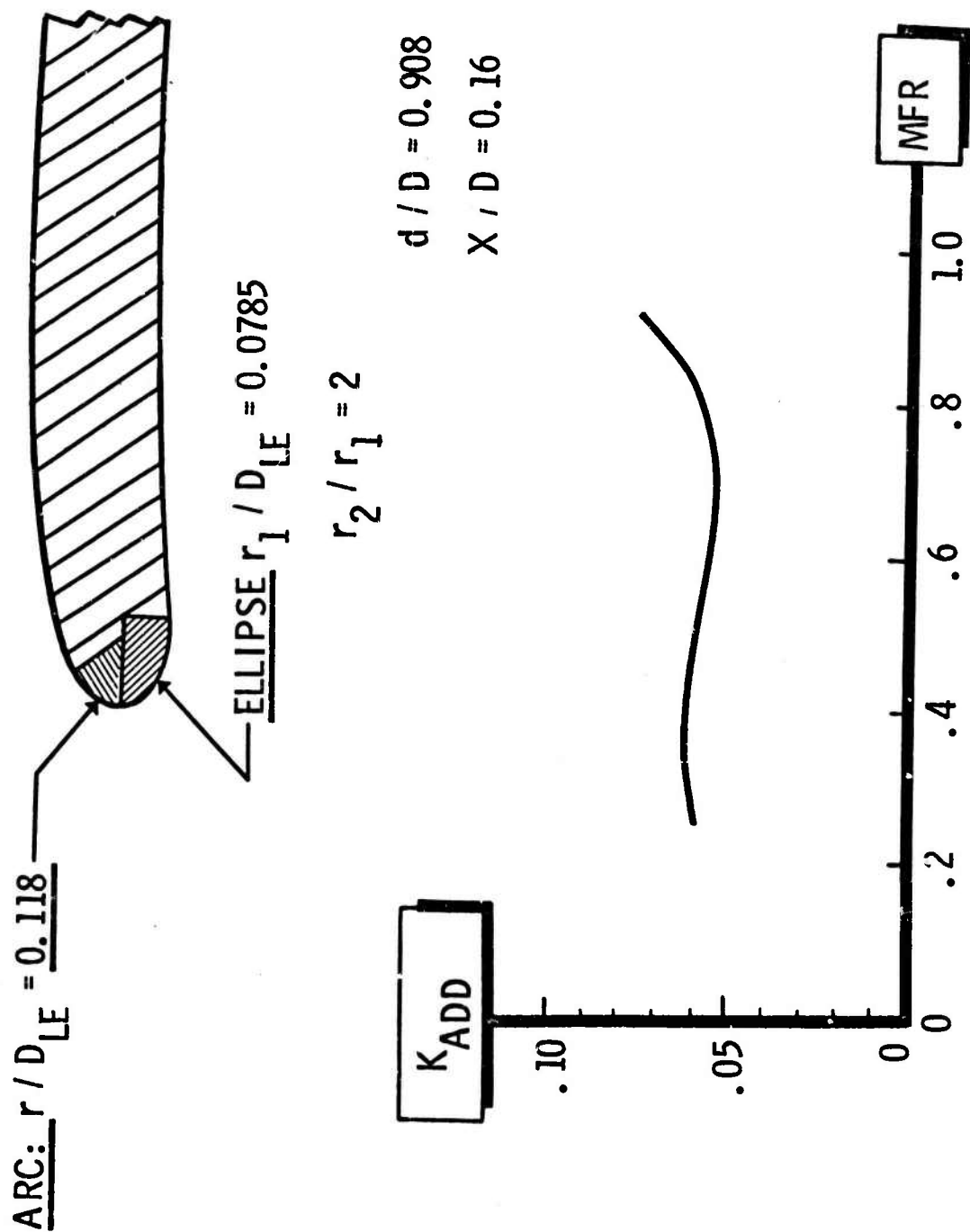


Fig.11 K_{ADD} for short thin cowl, modified NACA-1 contour

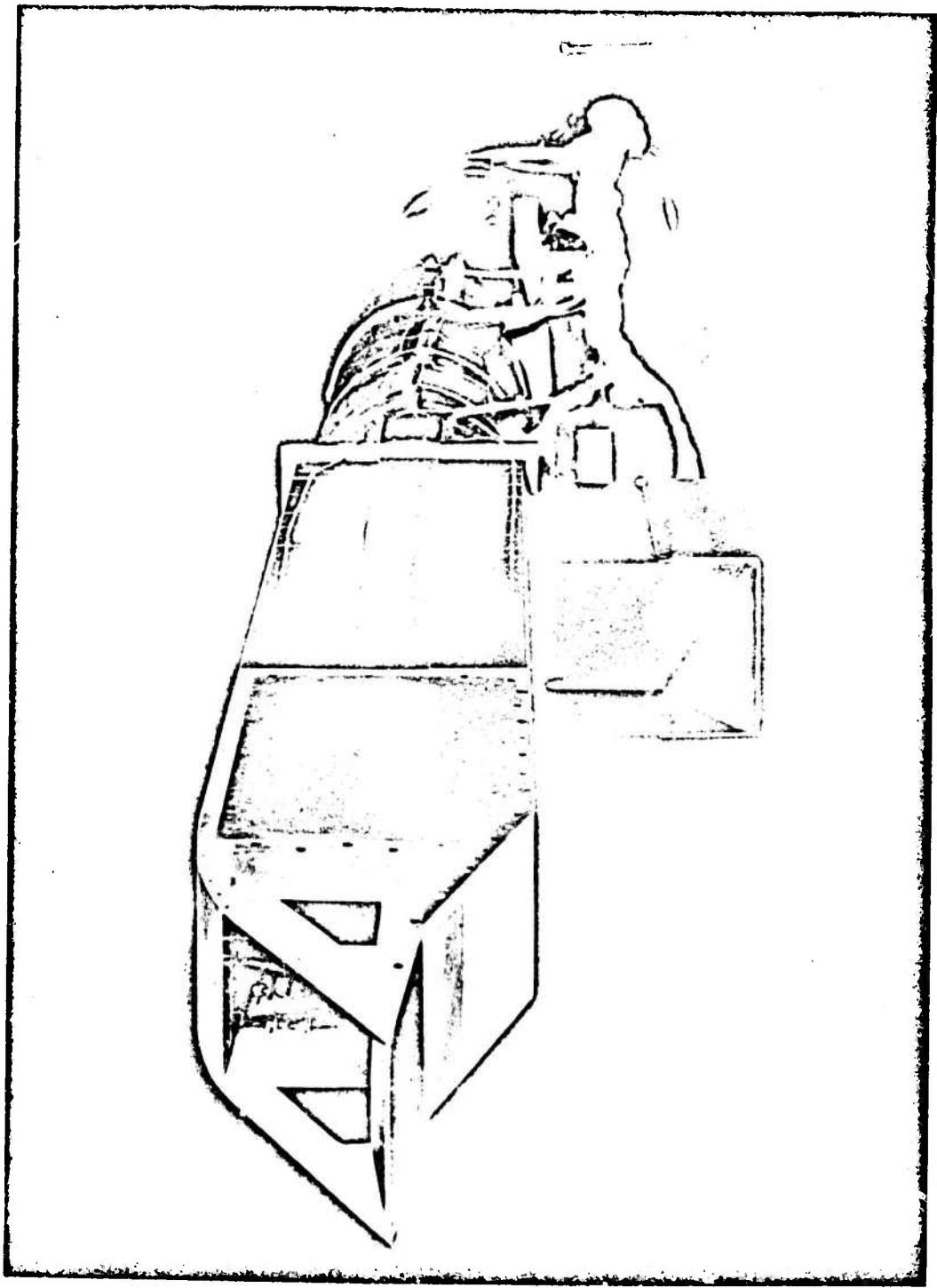


Fig. 12 Supersonic additive drag model

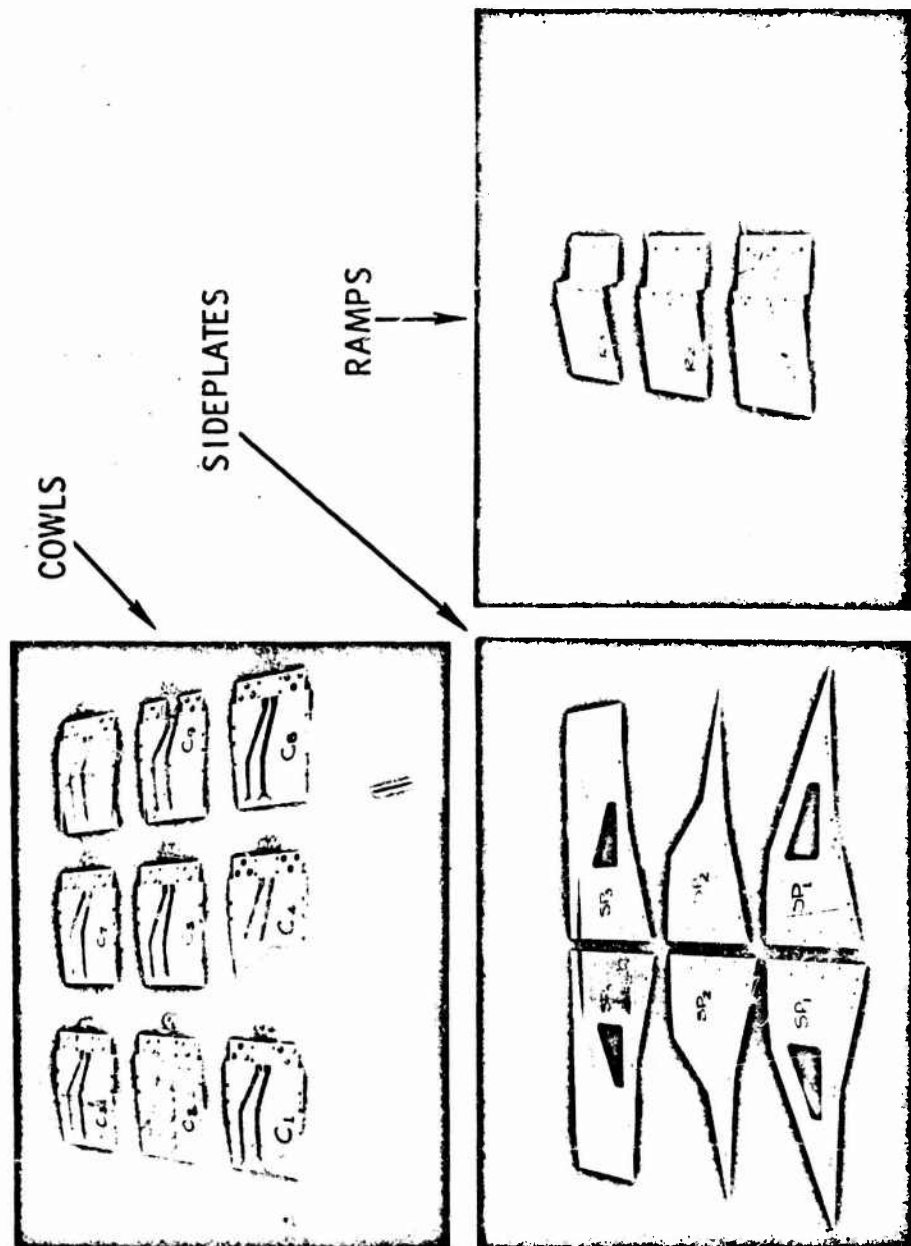


Fig. 13 Interchangeable components

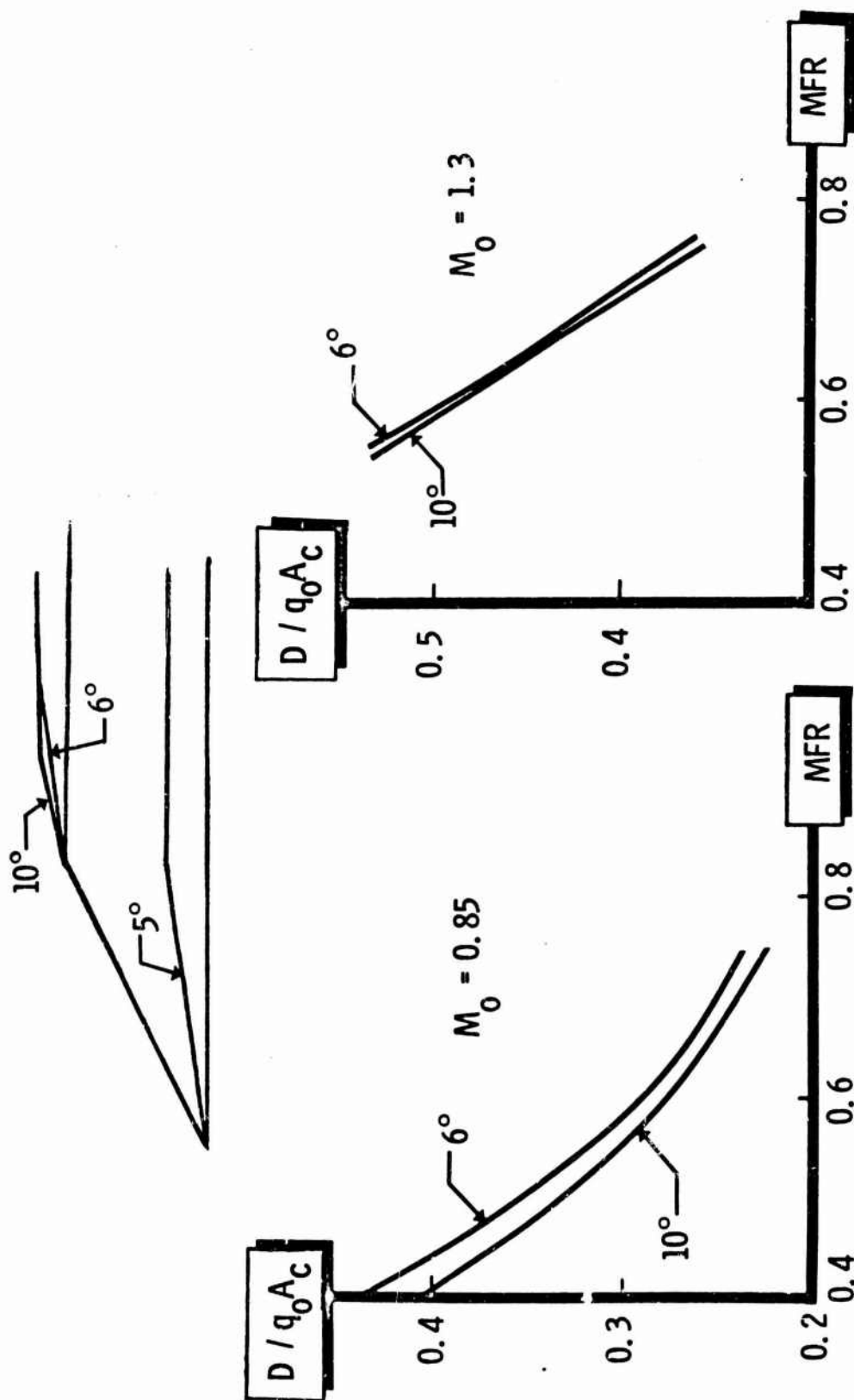


Fig. 14 Effect of cowl angle on drag

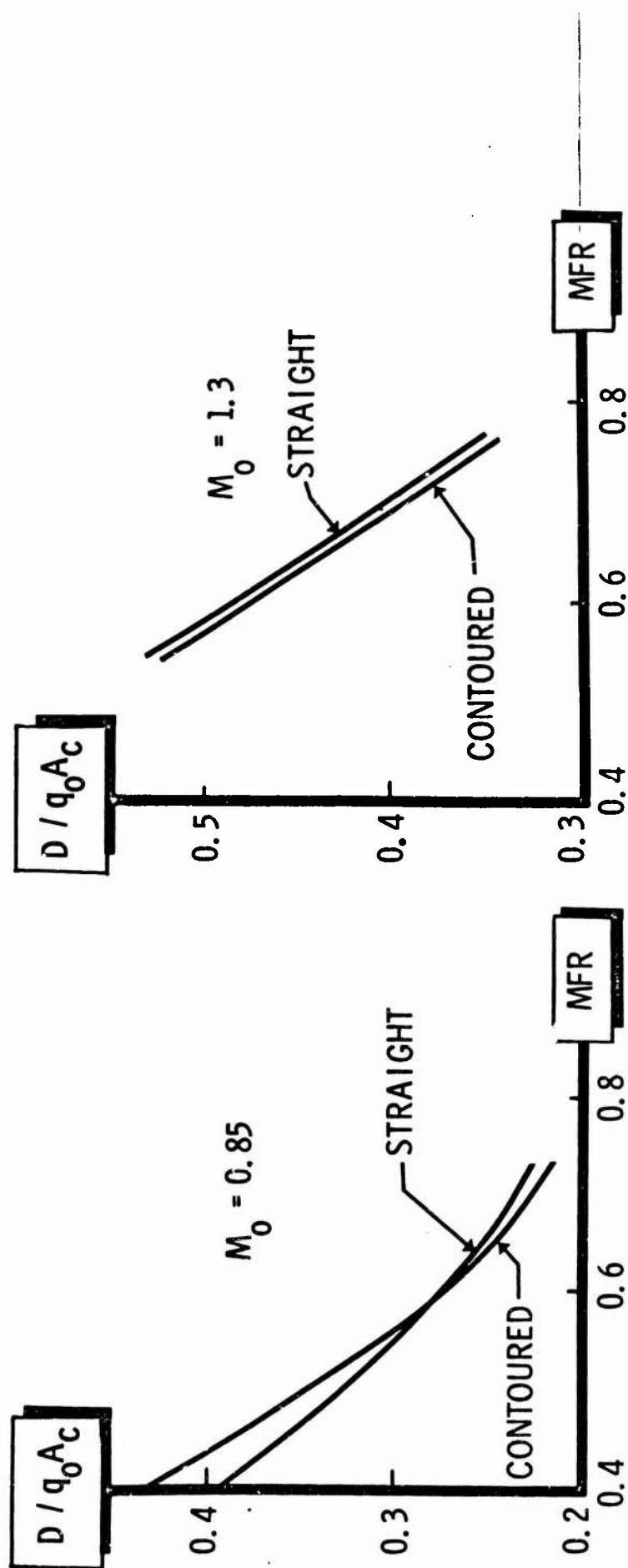
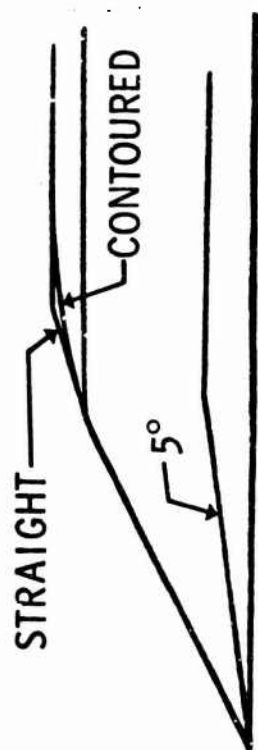


Fig. 15 Effect of cowl contour on drag

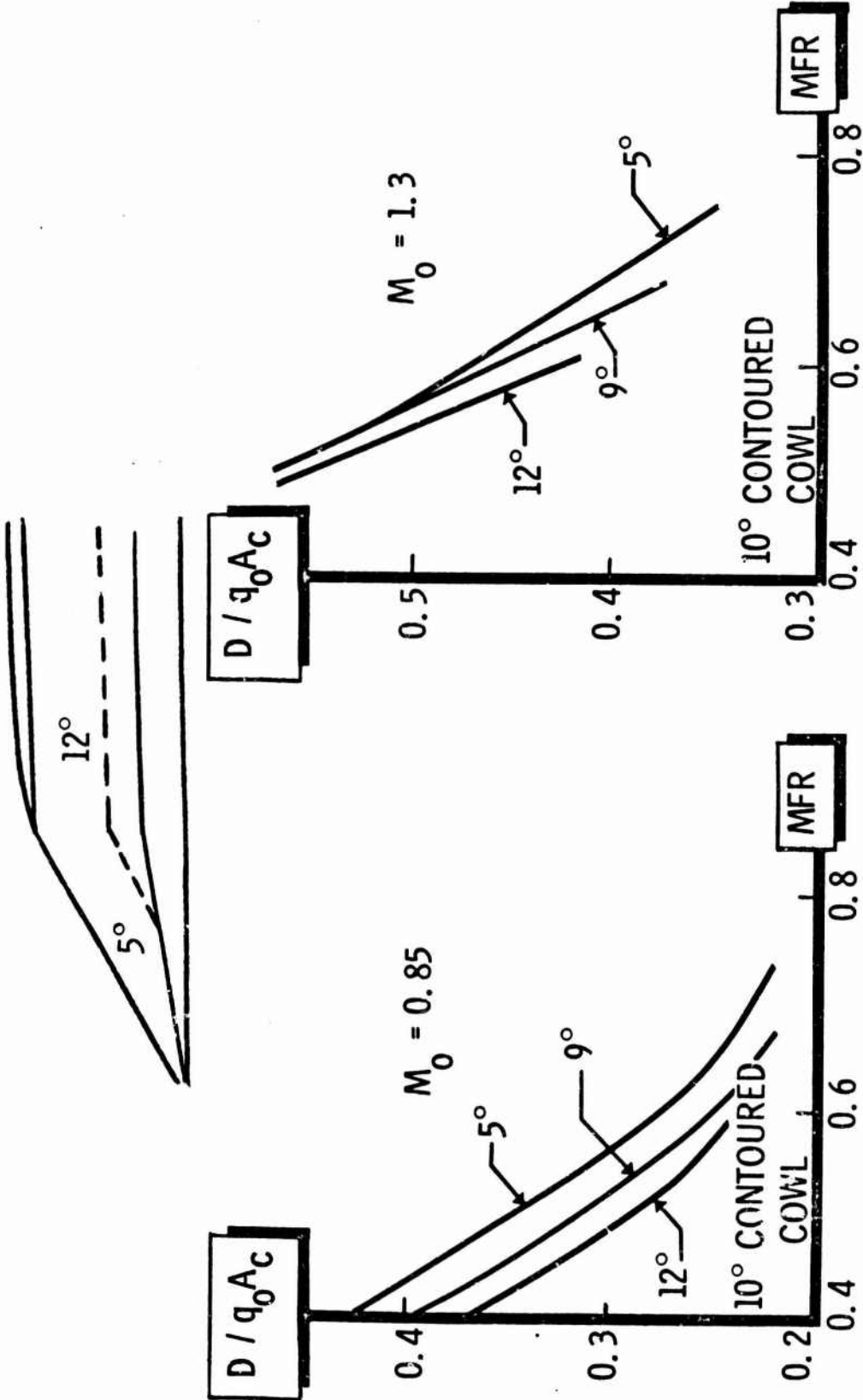


Fig. 16 Effect of ramp movement on drag

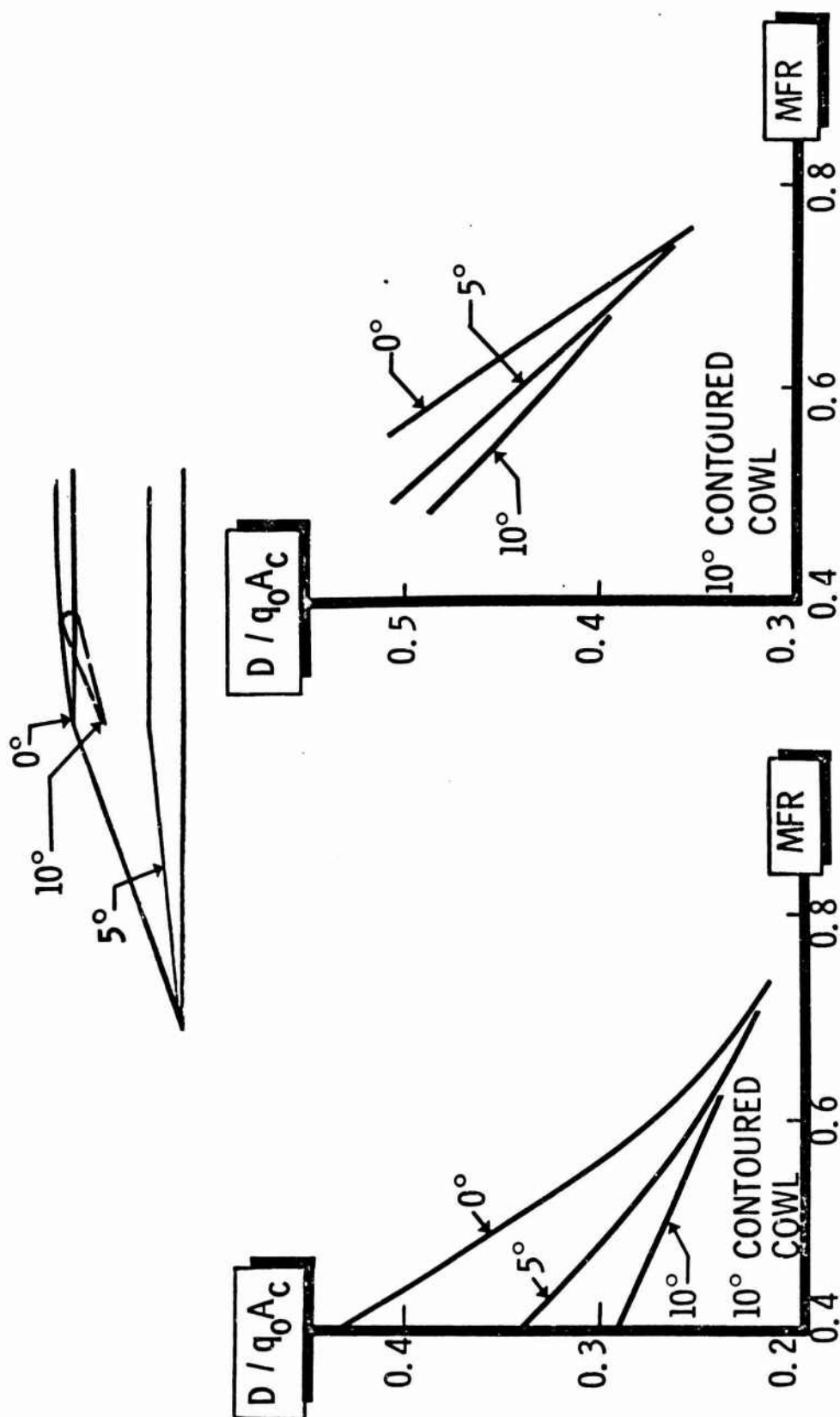


Fig. 17 Effect of cowl movement on drag

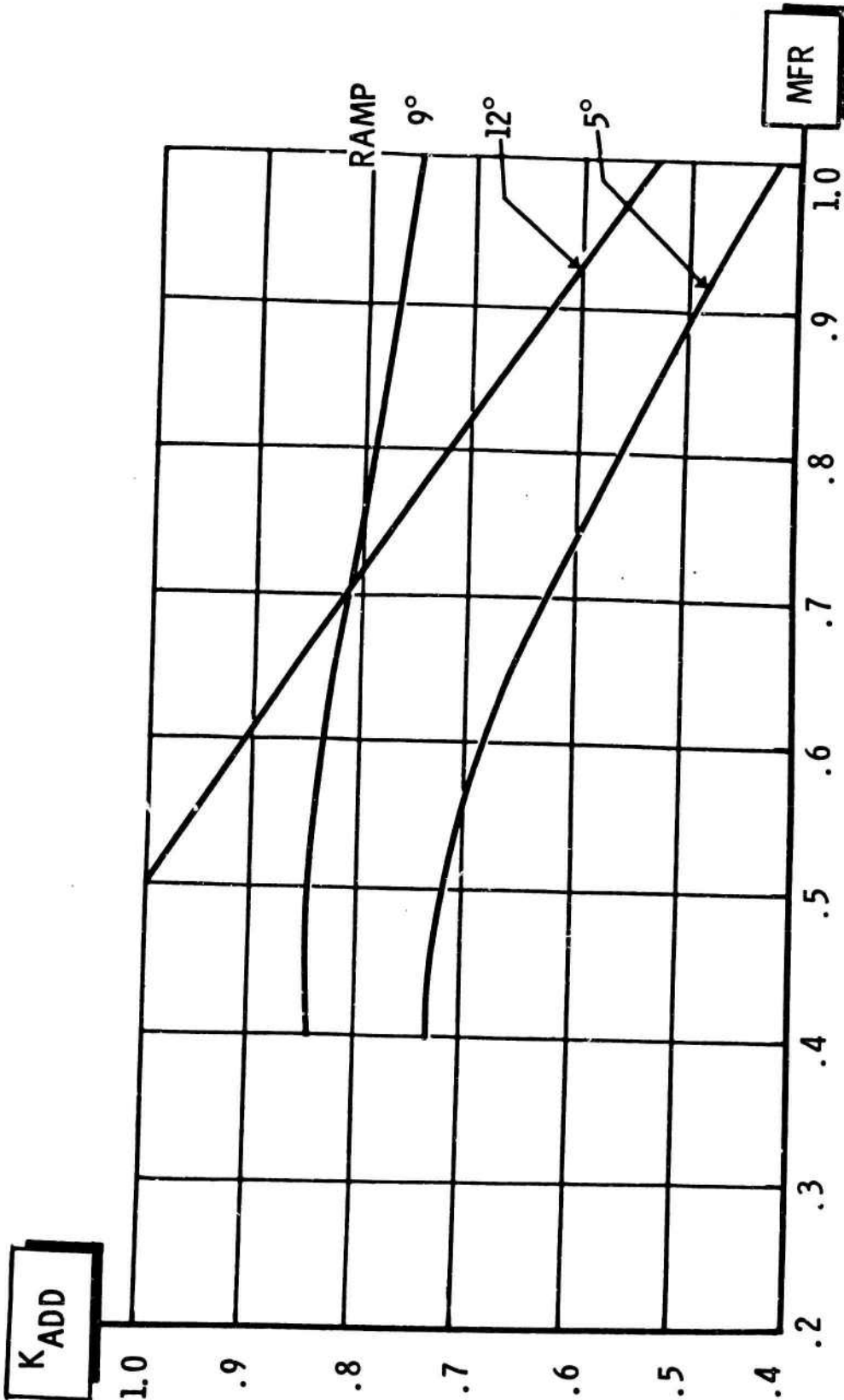


Fig. 18 K_{ADD} for ramp-type supersonic inlet. Mach 0.85, 10° contoured cowl

INTAKE DESIGN AND PERFORMANCE AROUND A MACH NUMBER OF 2.2

by

M.C.Neale

National Gas Turbine Establishment, Pyestock, Hants, UK

SUMMARY

The paper considers the selection of a shock geometry for a two-dimensional intake for operation at $M = 2.2$. Either combined external/internal compression or all external compression arrangements are possible, and preliminary theoretical arguments point the need for experimental information to assist the choice. Appropriate test programs are described. It is concluded that the external compression geometry is to be preferred. Some areas for further research are indicated.

SOMMAIRE

Considérations sur le choix d'une géométrie de l'onde de choc pour une prise bidimensionnelle fonctionnant à $M = 2,2$. Des dispositions à compression externe/interne ou à compression entièrement externe sont également possible. Les arguments théoriques doivent être complétés par des données expérimentales pour permettre le choix. Des programmes d'essais appropriés sont décrits. On en conclut que la géométrie à compression externe est préférable. Les travaux à poursuivre sont indiqués.

CONTENTS

	Page
SUMMARY	302
SOMMAIRE	302
LIST OF FIGURES	304
1. INTRODUCTION	305
2. POSSIBLE SHOCK GEOMETRIES FOR A PARTICULAR INSTALLATION	305
3. EXPERIMENTAL INVESTIGATION OF COMBINED EXTERNAL/INTERNAL COMPRESSION DESIGN	306
3.1 Model Description	306
3.2 Experimental Pressure Recoveries	306
3.3 Stability and Control Aspects	307
3.4 Subcritical Performance	308
4. EXPERIMENTAL INVESTIGATION OF EXTERNAL COMPRESSION DESIGNS	309
4.1 Model Description	309
4.2 Experimental Results	310
5. THE CHOICE OF GEOMETRY FOR OPERATION AT $M = 2.2$	312
6. CONCLUSIONS	314
ACKNOWLEDGEMENTS	314
REFERENCES	314
FIGURES	315

LIST OF FIGURES

	Page
Fig. 1 Aerodynamic profiles. Combined external/internal compression intakes	315
Fig. 2 Throat flow. Combined external/internal compression intake	316
Fig. 3 Intake characteristics. Combined external/internal compression	317
Fig. 4 Aerodynamic profiles. External compression intakes	318
Fig. 5 Further aerodynamic profiles. External compression intakes	319
Fig. 6 Throat flow. External compression intakes	320
Fig. 7 External compression intake performance - I	321
Fig. 8 External compression intake performance - II. Effect of throat radius	322
Fig. 9 External compression intake performance - III. Reynolds number effects	323

INTAKE DESIGN AND PERFORMANCE AROUND A MACH NUMBER OF 2.2

M. C. Neale

1. INTRODUCTION

The attractions of the external compression intake at Mach numbers up to about 1.8 are well known. It is possible to design for a high theoretical shock recovery without either the difficulties associated with internal compression or an excessive cowl wave drag. At higher Mach numbers the role of internal compression is more clear. High shock recoveries demand some internal compression if steep cowl angles are to be avoided. But at what flight Mach number does internal compression begin to pay off? Much must depend upon the intended application. For a military aircraft having only limited supersonic capability it might be preferable to optimise the intake for subsonic operation and accept the ensuing penalties at supersonic speeds. On the other hand, the intakes of an aircraft intended for long range at a supersonic cruise Mach number, though requiring good performance at low speeds, demand particular attention at the design condition. It is with this type of intake that the present paper is concerned, and in particular it is concerned with the internal aerodynamics of two-dimensional intakes operating in the Mach number range between 2.0 and 2.2.

2. POSSIBLE SHOCK GEOMETRIES FOR A PARTICULAR INSTALLATION

In selecting a two-dimensional shock geometry a choice has to be made between all external compression and combined external/internal compression designs. Both permit incorporation in the two-dimensional box installation and also the throat area variation necessary for engine matching over a range of flight speeds and engine flow requirements. Moreover, both offer very similar theoretical shock recoveries. When considering some of the other factors influencing the choice of shock geometry it has first to be borne in mind that underwing installations may operate within the wing compression field. Thus the "effective" free stream Mach number, so far as the intakes are concerned, can be lower than the flight Mach number. The difference can amount to 0.1 of a Mach number, or perhaps more at $M = 2.2$, and is a worthwhile bonus for the intake designer.

Theoretically the cowl angle, and thus the wave drag, of the combined external/internal compression design can be reduced to zero. However, it has not been possible to exploit fully the feature in installations considered by the author because at $M = 2.2$ some outward inclination of the cowl has always been necessary to accommodate the engines. "Hiding" the intake behind the engine at this flight speed requires the engine to be partly buried in the wings.

The modified ramp bleed slot shown in Figure 1 produced a large improvement in performance, primarily by virtue of its beneficial effect on the sidewall boundary layers. Throttle adjustment now permitted the normal shock to be brought close to the theoretical position, whereas previously a premature normal shock expulsion had always occurred from a position some distance downstream in the subsonic diffuser. As a result the pressure recovery with about 3% bleed rose from the earlier maximum of 83% to 87% with the geometry of Figure 1(a) and to 88½% with the geometry of Figure 1(b). Moreover the recovery for a given bleed flow was now the same with both subsonic diffusers - an important result in the light of the restrictions that tend to govern the size of practical installations.

Further tests incorporated a wide variety of sidewall bleed arrangements. An array of inclined perforations gave the most favourable result and, for a given total bleed flow (i.e., ramp plus side-walls), increased the earlier levels of pressure recovery by about 1%.

The final tests were conducted at the relatively high Reynolds number of 3.25×10^6 ; this yielded a further ½% on pressure recovery. In this way a maximum pressure recovery of 90.9% was obtained, the corresponding bleed being 6.4% of the capture flow. At a lower bleed flow of 3.4% the recovery was 90%, which in terms of overall power plant performance may be a more attractive operating condition. The corresponding theoretical shock recovery was approximately 95%, so that the extra to shock losses ranged between 4 and 5%. Retrospectively it can be seen that this stage of development was reached by arranging (a) the model configuration to give the maximum possible theoretical shock recovery, and (b) the shock geometry to correspond as closely as possible with the theoretical pattern. Departures from the theoretical shock arrangement invariably entailed performance penalties. Movement of the normal shock downstream from the position for maximum pressure recovery naturally reduced performance. Focusing the internal oblique shock downstream of the subsonic diffuser lip reduced the maximum pressure recovery by an amount corresponding closely with simple calculation based on shock losses. Focusing upstream of the lip tended to induce a form of instability in which the internal shock structure pulsed intermittently between the throat and some position upstream. This phenomenon is discussed in Section 3.4.2.

3.3 Stability and Control Aspects

The stability characteristics of intakes with internal compression are of especial concern in view of the fundamental instability of the normal shock in the convergent duct upstream of the throat. In consequence a degree of supercritical operation is frequently advocated to provide a control margin. Figures 2(a) and 2(b) show schlieren photographs of the throat flow with the intake running critically and also supercritically to a degree corresponding with a 1½% reduction in pressure recovery. The shock movement to reach the supercritical condition is only small but it does produce a deterioration of the velocity profiles at the diffuser exit. To minimise this experiment suggests that the Mach number upstream of the normal shock should be reduced as far as possible - an end desirable also on the count of improving pressure recovery.

Both the geometries shown in Figure 1 were "self-starting". Thus, after forward shock expulsion it was not necessary to cycle the geometry to re-establish the internal flow, an opening of the mass flow regulating throttle sufficed. This property derives first from the close correspondence between the internal contractions tested and the

theoretical limiting contractions for self-starting¹, and second from the large increase in bleed flow accompanying shock expulsion. The increased bleed reduces the effective contraction but, as will be seen, also contributes to the mechanism of a particular form of subcritical instability.

3.4 Subcritical Performance

Figure 3 shows a large difference between the subcritical characteristics of the two geometries of Figure 1. With the geometry of Figure 1(a) a reduction of subsonic diffuser mass flow immediately drove the intake into a violent instability, irrespective of the form of bleed slot or subsonic diffuser. With the geometry of Figure 1(b), however, a violent instability was not initiated until the subsonic diffuser mass flow had been reduced by about 10% and had passed through three distinct flow régimes. These can be defined with reference to Figure 3 as:

- (a) the first subcritical range extending from A to B,
- (b) the second subcritical range extending from B to C,
- (c) the third subcritical range extending from C to D.

3.4.1 The First Subcritical Range

Throttling the intake from the critical point enabled the normal shock to be moved progressively upstream from the position for critical operation shown in Figure 2(a) to the position shown in Figure 2(c). The upstream movement of the normal shock raises the static pressure at entry to the bleed slot, so increasing the bleed flow by an amount corresponding with the reduction in main diffuser mass flow. This procedure was reversible. Thus re-opening the throttle permitted a return to critical operation or any intermediate subcritical condition.

3.4.2 The Second Subcritical Range

This flow régime was initiated by throttling the intake very slightly beyond the condition corresponding with the flow pattern of Figure 2(c) and point B on Figure 3. The régime was characterised by an intermittent pulsing of the shock structure between the throat and some position upstream. Continued throttling at first increased the frequency of the pulses from an initial level of one about every ten to twenty seconds. Subsequently the pulses occurred less frequently as the shock system gradually stabilised slightly upstream of the cowl tip at a position corresponding roughly with Figure 2(d) and point C in Figure 3. The pressure recovery was then approximately 1% less than at the critical point, whilst the bleed had increased from 3 to 6% of the capture flow as a result of the increased static pressure at entry to the slot.

Initiation of the instability is believed to be associated with the behaviour of the sidewall boundary layer in the region of the bleed slot. Earlier work² had indicated that the much improved performance of the modified bleed slot resulted largely from the slot's ability to evacuate the sidewall secondary flow generated immediately upstream of the internal oblique shock. Now, as the normal shock advances upstream from the critical position not only does it tend to restrict the sidewall secondary flow into the slot (and so tend to reproduce the original ram scoop slot geometry) but also it markedly increases the local static pressure gradient to be

negotiated by the sidewall boundary layer en route to the subsonic diffuser. Although other factors may contribute, the upstream pulse of the shock is therefore ascribed primarily to a breakdown of the sidewall secondary flow in the region of the bleed slot.

The self-starting characteristic of the intake referred to earlier would ensure the return downstream of the shock system from the upstream limit of its excursion - at least until throttle closure precluded ingestion of the full capture plane stream tube.

3.4.3 The Third Subcritical Range

Throttling the intake from the condition corresponding with Figure 2(d) and point C in Figure 3 enabled the terminal shock to be moved progressively upstream on the ramp surface. As the shock moved further away from the bleed slot the lambda feet became more marked, both the pressure recovery and the bleed flow stayed approximately constant, and the forespill increased. Figure 3 shows that 7% of the critical capture flow could be spilled in this way; this illustrates the observation noted in the following discussion on external compression intakes, that of large amounts of fore-spill at the datum condition (which, as Figure 1(b) shows, applies to the geometry in question) making possible large stable subcritical margins. At point D on Figure 3 an instability was induced which became progressively more violent with further throttling. Studies of the shock geometry suggest a reasonable correlation between the onset of instability and entry to the subsonic diffuser of a vortex sheet formed at the intersection of the ramp oblique and terminal shocks³.

4. EXPERIMENTAL INVESTIGATION OF EXTERNAL COMPRESSION DESIGNS

4.1 Model Description

Little need be said about the mechanical aspects of the model since in all material respects it was similar to the combined external/internal compression design just described. External compression shock geometries could be investigated readily using the same basic model "chassis" by the substitution of suitably designed front end components.

The fundamental principle applied to the aerodynamic design was the employment of a strong solution oblique shock at the cowl; this is shown schematically in Figure 4(a). With a strong solution shock the initial internal inclination of the cowl can be reduced to an angle finally limited by detachment of the internal shock from the cowl lip. In practice boundary layer growth both on the ramp and inside the cowl restricts the minimum cowl angle to a figure somewhat higher than that predicted by inviscid theory.

The preceding considerations lead to an interplay between the initial cowl angle and the supersonic turning on the ramp - in other words between drag and shock recovery. A further design feature is the rate of turn downstream of the cowl lip; its effect on performance is considered in Section 4.2. Figures 4 and 5 illustrate some typical aerodynamic designs that were included in the test programme. These indicate the forms of bleed slot that were used throughout the tests. The upstream and downstream limits

of the slot lie approximately flush with each other on an arc drawn concentrically with the cowl: some effects of departing from the flush slot will be discussed later.

4.2 Experimental Results

For test convenience the first experiments were made at a total pressure corresponding to a Reynolds number based on free stream conditions and intake capture height of approximately 1×10^6 . Maximum pressure recoveries were achieved with a bleed of about 3%, and ranged from approximately 93% at $M = 2.0$ with the geometry of Figure 4(b) to 89.5% at $M = 2.2$ with the geometry of Figure 4(c). Rather higher figures can be obtained with increased supersonic turning on the ramp but, it is deduced, at the expense of a substantial increase in the internal cowl angle⁴.

Figure 6(a) shows a schlieren photograph of the throat flow of the intake shown in Figure 4(b) when running at $M = 2.0$ with a bleed of 4%, a pressure recovery of 93%, and the bleed slot arranged to be truly flush in the sense defined previously. The strong oblique shock is clearly evident. As shown it is inclined at 75° to the ramp surface as compared with the figure, based on inviscid theory, of 82° . The discrepancy is attributed to the increase of flow deflection at the cowl resulting from boundary layer growth on the ramp and cowl surfaces and perhaps, too, on the sidewalls.

With the truly flush slot the bleed flow could not be reduced below slightly less than 2% of the capture flow without the cowl shock being expelled upstream and consequent cowl spillage. However a slight increase of throat height effected by moving the diffuser lip from position X to position Y in Figure 4(b) enabled the bleed to be reduced to only 1%. Although at this condition the pressure recovery had deteriorated to 90.4%, the throat flow was stable and, as Figure 6(b) shows, the cowl lip shock remained perfectly clean. Reducing the throat height by moving the diffuser lip to position Z in Figure 4(b) reduced the pressure recovery for a given bleed by about 1%. However the subcritical stability was markedly improved. Whereas the flush bleed provided virtually zero stable subcritical range, the stepped slot obtained with the diffuser in position Z allowed the main diffuser mass flow to be reduced by up to 5% without instability. Similar results have been noted elsewhere⁵.

Although the shock geometry of the design just discussed was designed to form on the cowl lip, viscous effects caused the focal point to lie slightly outside the capture stream tube. Tests with the ramp shock system focused accurately on the cowl lip were marked not only by zero stable subcritical range but also by an inability to stabilise the throat flow at the critical point; throttle closure led directly from supercritical operation to instability. The application of pitch in the sense tending to move the ramp shocks away from the cowl lip and outside the capture stream tube lead to immediate improvements in stability. Shock geometries with large amounts of pre-entry spill (and thus substantial pre-entry drag penalties) provided large stable subcritical margins. Typical of such geometries are those shown in Figures 4(c) and 5, which at their design Mach number of 2.2 permitted stable subcritical margins, without any intermediate form of instability, of over 10%. Figure 6(c) shows a schlieren photograph of such an intake operating at $M = 2.2$ in the stable subcritical mode.

The intake shown in Figure 5 was tested at $M = 2.2$ with two different ramps. The first featured compression by three discrete shocks totalling 23° of supersonic turning,

whereas in the second the same total turning comprised two discrete shocks and finally a profiled turn arranged to give 9° of isentropic compression. The latter design gives the lowest overall theoretical shock recovery because, although the total pressure recovery through the ramp compression system is higher than that given by the three-shock design, the increased losses from the cowl shock arising from the higher terminal supersonic Mach number more than outweigh this gain. On test, however, Figure 7(a) shows that, throughout the experimental range of bleed flow, the isentropic ramp gave the higher pressure recovery of the two. Traverses at the subsonic diffuser exit revealed that, although the total pressures in the mid-span region were almost equal in both cases, near the sidewalls the total pressure with the isentropic design was some 2% higher than with the three-shock ramp. It thus appears that the introduction of isentropic compression provides a beneficial influence on the sidewall boundary layers and on the uniformity of the flow at the diffuser exit.

All the preceding tests were made with subsonic diffusers corresponding closely with the two used in the tests of the combined external/internal compression design and, where directly comparable tests were made, the external compression geometries gave results substantially independent of diffuser length. Of the two diffusers the shorter is probably of the most practical import because of the premium on weight and space in so many installations, and with diffusers of this length Figures 5(a) and 7(b) illustrate the possible gains from design refinement. The overall length from cowl lip to exit plane of the two diffusers shown superimposed in Figure 5(a) is the same but, whereas in one the diffusion is concentrated on one wall, in the other the diffusion is distributed equally about the diffuser centre line. (It is to be noted that by suitable adjustment at the throat the symmetrical diffuser was accommodated within the same external envelope as the asymmetric design.) The two upper curves in Figure 7(b) show that throughout the experimental range of bleed the symmetrical design gave the higher pressure recovery of the two. The difference is only slight - approximately 0.6% - but, in the light of the tendency of improvements in flow uniformity at the diffuser exit to accompany improvements in pressure recovery, these changes can be very worthwhile. The lower curve in Figure 7(b) shows the effect of shortening the asymmetric diffuser by the simple expedient of reducing its axial dimensions by one-third. Although the fall in pressure recovery is now significant so, probably, are the rewards for more intelligent design.

A further design feature is the radius by which the flow is turned downstream of the cowl lip and directed towards the compressor face. Figure 8 shows three different throat radii which were tested in conjunction with the same ramp and subsonic diffuser, the latter being the shortest of the three diffusers mentioned in the previous paragraph. For simplicity the two larger cowl radii are quoted approximately on the figure; the actual cowl profiles tested were composites of an initial straight and a subsequent arc. Downstream of the ramp surface the throat profile was varied so that in all cases it was concentric with the cowl. Figure 8 shows that reducing the cowl radius from approximately 4 to approximately 3.2 capture heights (and thereby reducing the forward projected area of the cowl) reduced the pressure recovery by about 0.7%. Irrespective of the bleed, a further reduction of cowl radius to 2.4 capture heights resulted in forward expulsion of the cowl shock and consequent forespill; calculation shows that, with this radius, the minimum internal duct area immediately upstream of the bleed slot is insufficient to pass the full capture flow. The cowl shock was re-attached to the lip by moving the leading edge of the bleed slightly upstream. This had the effect of slightly modifying the throat shock structure from a simple

strong solution shock similar to that shown in Figure 6(a). Near the cowl it continued to correspond closely with the theoretical strong solution, but towards the ramp it gradually weakened, so that overall it assumed a curved form. As Figure 8 shows, the pressure recovery with this geometry was about 1% below that obtained with the largest radius tested. A further penalty was that the bleed flow pressure recovery was, at about 35% of free stream total pressure, some 5% below the level typical of the other external compression geometries tested. This probably reflects a reduced static pressure at entry to the bleed slot consequent on the changed shock formation. The bleed recovery might have been improved by extending the slot downstream, although perhaps at the expense of pressure recovery.

The preceding results were all obtained at a Reynolds number, based on free stream conditions and intake capture height, of approximately 1×10^6 . Results of tests at higher Reynolds numbers are shown in Figure 9. There is a significant Reynolds number effect with both the short and the symmetrical subsonic diffuser throughout the experimental range of bleed flow. More particularly, though, the effect is amplified at low bleed flows in the short diffuser, when viscous effects could be expected to be most important. In engineering aircraft installations the intake designer may be properly concerned with minimising bleed flows and is frequently driven to shorter subsonic diffusers than he would wish. Thus Figure 9 emphasises the importance of reproducing representative Reynolds numbers in tests aimed at simulating accurately full-scale conditions.

5. THE CHOICE OF GEOMETRY FOR OPERATION AT $M = 2.2$

Pressure recovery for a given bleed flow can be taken as a first yardstick of intake performance. Although obviously over-simplified it does at least indicate a level of internal performance. Looking first at the combined external/internal compression design, a pressure recovery of 90% has been demonstrated with a bleed of only 3.4%. These figures entailed testing at high Reynolds numbers and the provision of sidewall bleed. Reducing the Reynolds number to 1×10^6 would, on the test evidence, reduce the pressure recovery to about 89%. This represents an extra to shock loss of about 6%.

Turning to the external compression intake, a pressure recovery of 89% was achieved at a Reynolds number of 1×10^6 without exceeding an initial cowl angle of 10° and with a bleed only marginally in excess of the 3.4% just quoted for the combined external/internal compression design. The extra to shock loss here is approximately 3%. Thus, although the external compression geometry gave the lowest extra to shock loss of the two, the pressure recoveries for a given bleed flow at $M = 2.2$ were closely comparable.

Flow stability provides a second basis for comparison. In the external compression design, subcritical stability was only achieved at the expense of some pre-entry drag. The margin of stability increased with the amount of pre-entry spill, although no doubt there is scope for studies aimed at securing the largest margin of stability for the least drag. Subcritical stability is not usually associated with designs featuring internal compression, but a small margin has been demonstrated under certain conditions. Larger margins would demand supercritical operation, so implying penalties on pressure recovery and outlet flow uniformity. To these might be added some pre-entry drag. Assessing the relative magnitudes of the penalties that have been described is

difficult, but the preceding remarks indicate that with both shock geometries stability was only obtained at a price.

Studies of supersonic aircraft projects reveal the considerable significance of the penalty arising from cowl drag. In this respect the combined external/internal compression intake shows to distinct advantage, and more especially if a measure of integration between power plant and wing permits the cowl wave drag to be reduced to zero.

These arguments can be elaborated but, confined as they are to performance at the design condition, can lead to conclusions that are perhaps somewhat academic. It is the widening of the argument to embrace off-design performance that, in the author's view, highlights the real shortcomings of the combined external/internal compression design; that is its relative inflexibility and complication. The performance figures quoted for the combined external/internal compression intake relate to a design that is regarded as very highly tuned, in the sense that the internal oblique shock has to be accurately focused on the downstream lip of the bleed slot, at which point it meets the normal shock. Moreover, to obtain the highest recovery the geometry requires the complication of sidewall bleed. The reproduction of the shock geometry over a range of ramp angles and Mach numbers, as opposed to one particular flight condition, appears far from straightforward.

In disposing of the spill flows that can arise at off-design conditions the external compression design exhibits flexibility in the variety of techniques that are theoretically possible. These include doors in the subsonic diffuser, adjustment of the ramp to deflect flow externally past the cowl, and increased evacuation via the bleed. The combined external/internal compression design is much less flexible. The shock focusing requirement precludes the use of the ramp as a mass flow trimming device to cater, for example, with spill flows arising from variations of ambient temperature during constant Mach number cruise, whilst, to judge from the results described, the capacity for deflecting spill into the bleed is extremely limited.

It appears therefore that at a flight Mach number of 2.2 there is a balance to be drawn between potentially low drag, relative inflexibility and perhaps poor off-design performance on the one hand, and a relatively flexible installation featuring a rather higher drag on the other. A quantitative assessment of these factors is not easy, but the demands of flexibility in operation must weigh heavily and, especially in an installation where engine and wing are not fully integrated, so that the cowl wave drag cannot be eliminated, the external compression design appears in a very favourable light.

At Mach numbers lower than 2.2 the balance between the conflicting factors outlined above swings more emphatically towards the external compression intake. The case for the combined external/internal compression design becomes much more clear at those flight Mach numbers beyond 2.2 when, irrespective of any integration between the power plant and fuselage, the engine can be completely hidden behind the intake. More especially is this so when the intake capture plane dimensions so exceed the compressor diameter that not only can the engine be hidden but also such diverter passages and ducts that might be required to by-pass air around the engine at off-design conditions.

6. CONCLUSIONS

For long range cruise operation at $M = 2.2$ with a power plant installation which precludes the elimination of cowl wave drag, the external compression intake is preferred to the alternative combined external/internal compression design.

The performance of the external compression intake is subject to many variables, some of which have been investigated experimentally, and all of which need to be considered in optimising a design for practical application. Among the many subjects which could well figure as targets for research programmes, two particularly are selected for mention here:

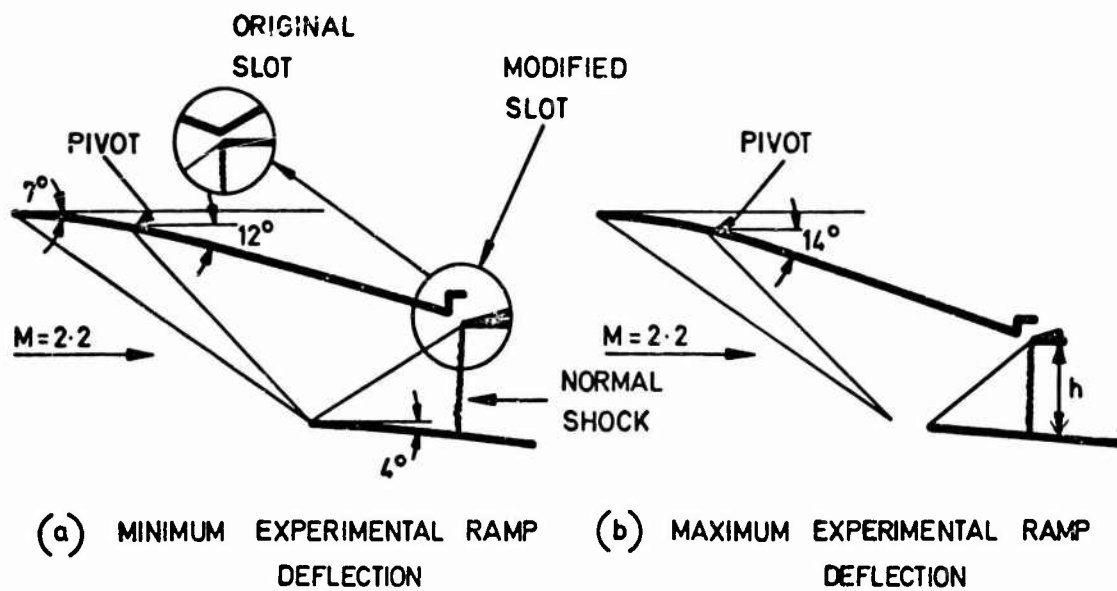
- (a) The study of boundary layer bleed techniques, permitting effective boundary layer control with minimised bleed penalties not only at the design point but throughout the full range of flight conditions.
- (b) The study of spill techniques aimed at permitting intake operation at both design and off-design Mach numbers, over a wide mass flow range, with minimum interference with the internal performance of the intake and minimum external drag penalty.

ACKNOWLEDGEMENTS

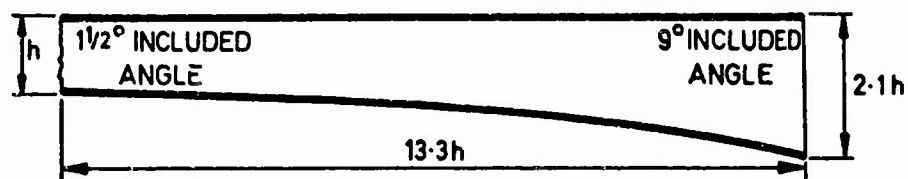
Acknowledgement is made to many colleagues at the National Gas Turbine Establishment, and in particular to Mr. P. S. Lamb, for assistance with the work on which this paper is based.

REFERENCES

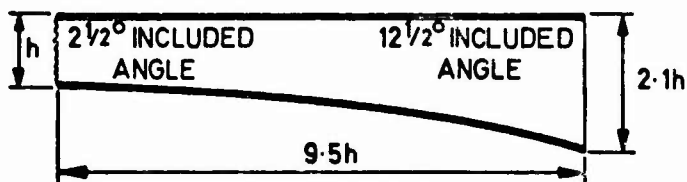
1. Howarth, L. (Editor)
Part XI by Holder, D.W.
et alii
Modern Developments in Fluid Mechanics. High Speed Flow. Vol. II, XI Experimental Methods. Section I, Wind Tunnels and Moving Bodies. Art. 7. Clarendon Press, Oxford 1953.
2. Neale, M.C.
Lamb, P.S.
Tests With a Variable Ramp Intake having Combined External/Internal Compression and a Design Mach number of 2.2. ARC Current Paper (to be published).
3. Ferri, A.
Nucci, L.
The Origin of Aerodynamic Instability of Supersonic Inlets at Subcritical Conditions. NACA RM L50K30, January 1951.
4. Vargo, D.J.
et alii
Investigation of a High Performance Top Inlet to Mach number of 2.0 and at Angles of Attack to 20° . NACA RM E57, A21, March 1957.
5. Lewis, W.J.
Private communication, 1964.



SUPERSONIC COMPRESSION GEOMETRIES



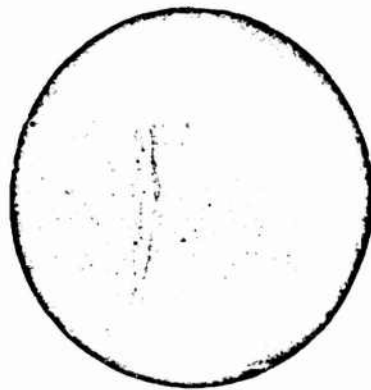
(c) LONG SUBSONIC DIFFUSER



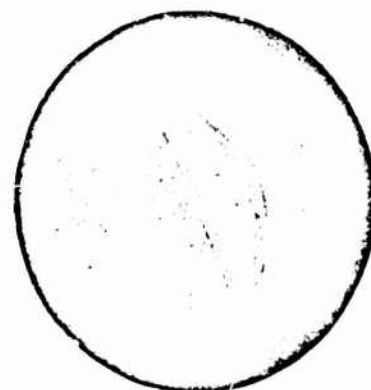
(d) SHORT SUBSONIC DIFFUSER

SUBSONIC DIFFUSERS

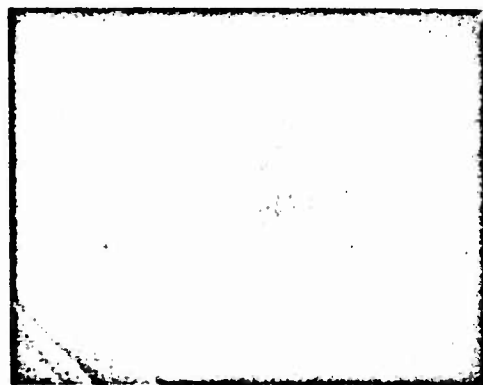
Fig.1 Aerodynamic profiles. Combined external/internal compression intakes



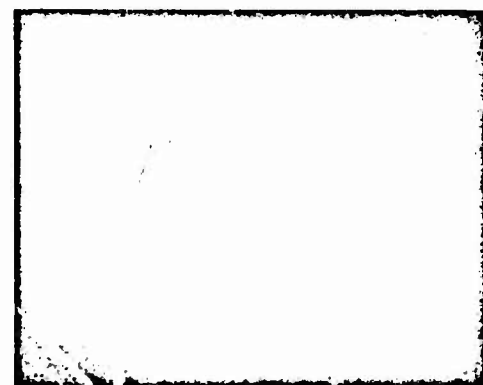
(a) INTAKE CRITICAL



(b) INTAKE SUPERCRITICAL



(c) INTAKE SUBCRITICAL



(d) INTAKE SUBCRITICAL

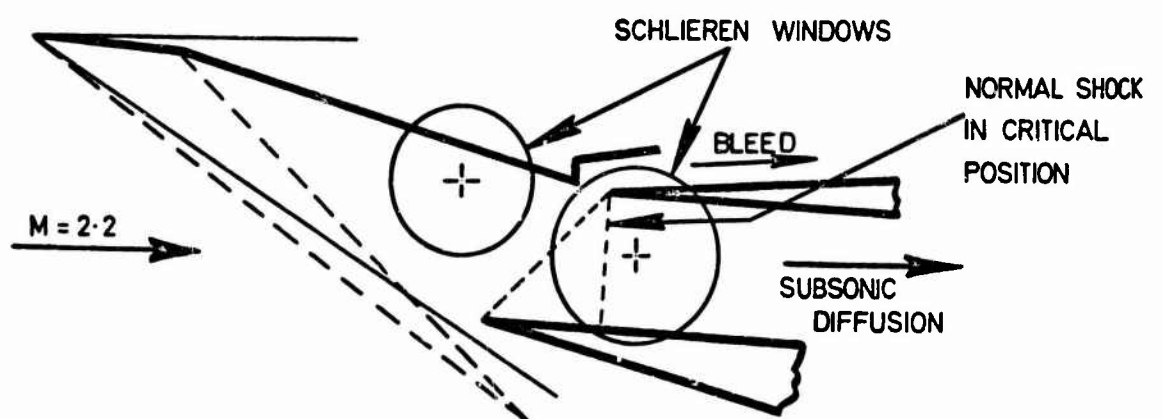


Fig.2 Throat flow. Combined external/internal compression intake

$Re = 1 \times 10^6$: $M = 2.2$
 2% BLEED FLOW WITH INTAKE CRITICAL

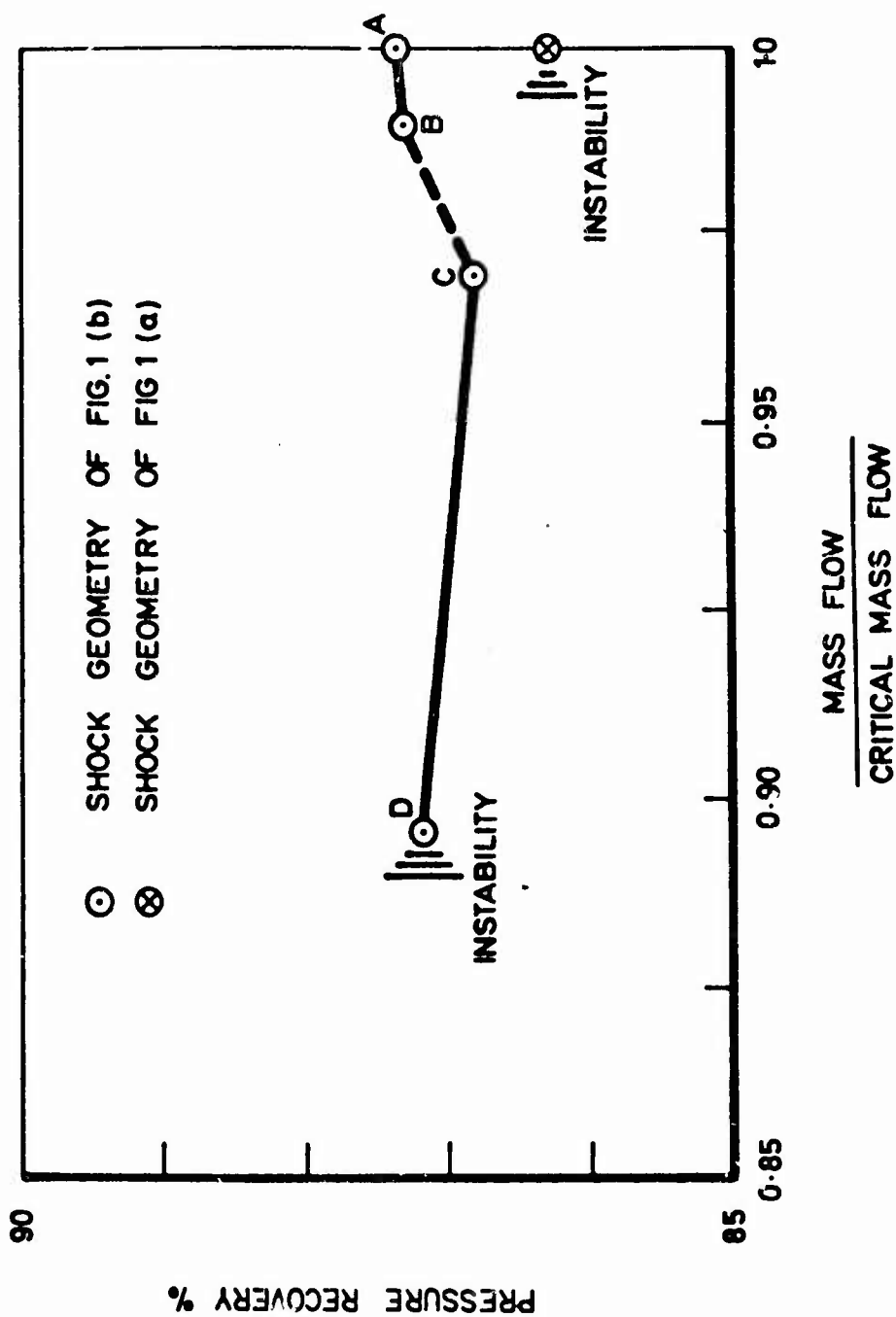
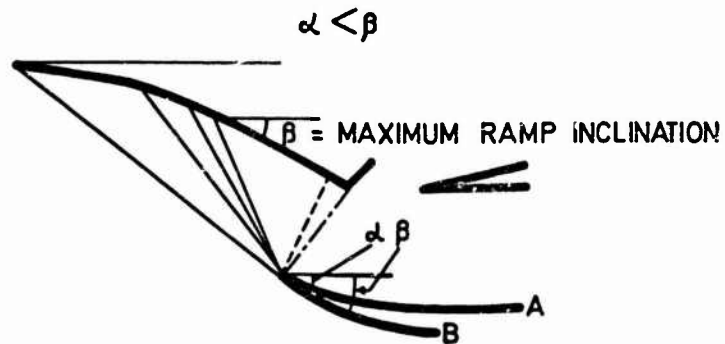


Fig. 3 Intake characteristics. Combined external/internal compression



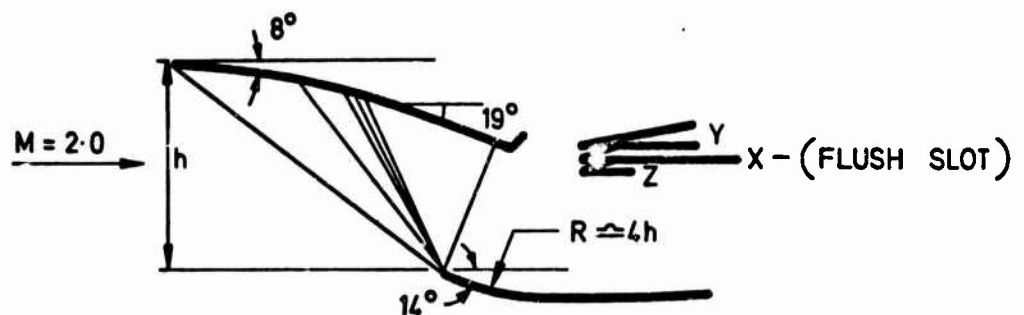
GEOMETRY A FOR STRONG SOLUTION OBLIQUE SHOCK. COWL ANGLE = α

-----RELATED SHOCK

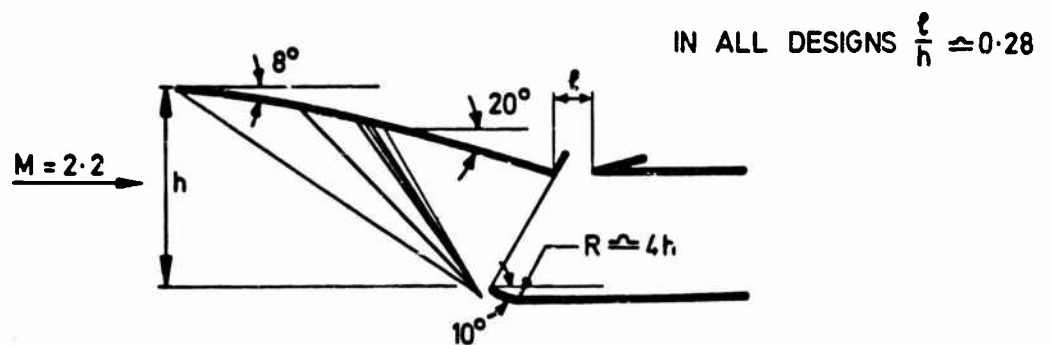
(a)

GEOMETRY B FOR NORMAL SHOCK. COWL ANGLE = β

-----RELATED SHOCK

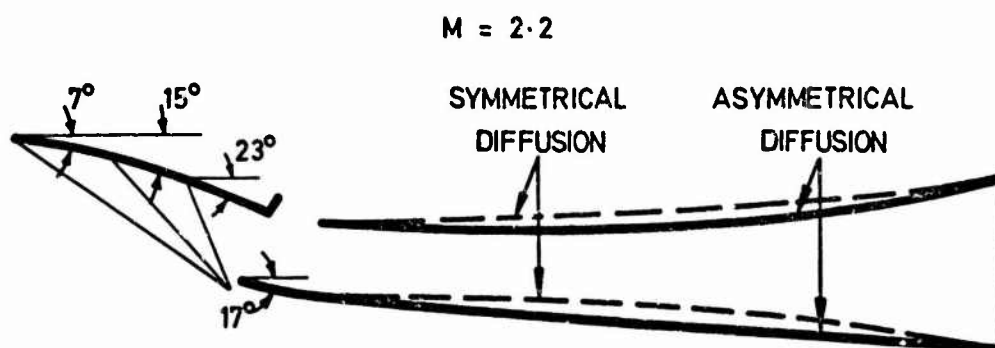


(b) $M = 2.0$ GEOMETRY SHOWING DIFFERENT DIFFUSER TIP POSITIONS

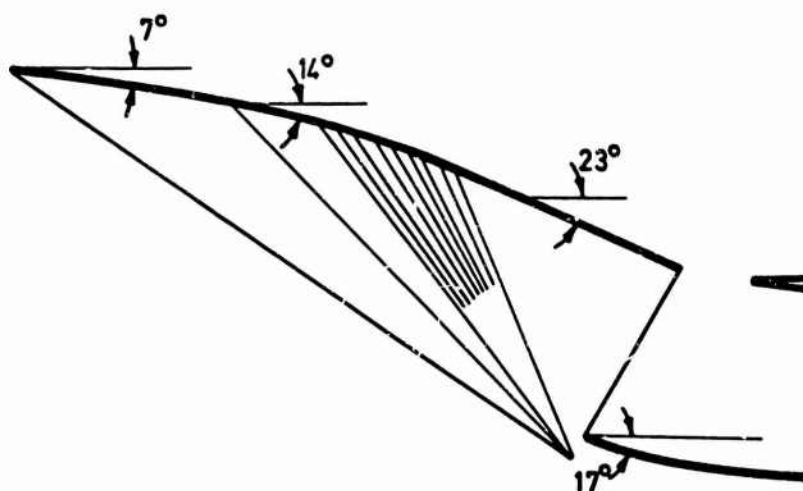


(c) $M = 2.2$ GEOMETRY WITH 10° COWL ANGLE

Fig. 4 Aerodynamic profiles. External compression intakes

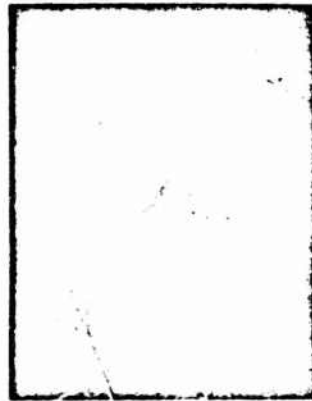


(a) THREE SHOCK RAMP : 17° COWL ANGLE : SUBSONIC DIFFUSER LENGTH AS IN FIG. 1 (d)

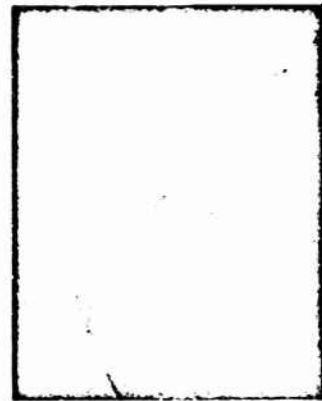


(b) RAMP WITH PARTIAL ISENTROPIC COMPRESSION : 17° COWL ANGLE

Fig. 5 Further aerodynamic profiles. External compression intakes



(a) BLEED FLOW = 4%



(b) BLEED FLOW = 1%



(c) STABLE SUB-CRITICAL OPERATION

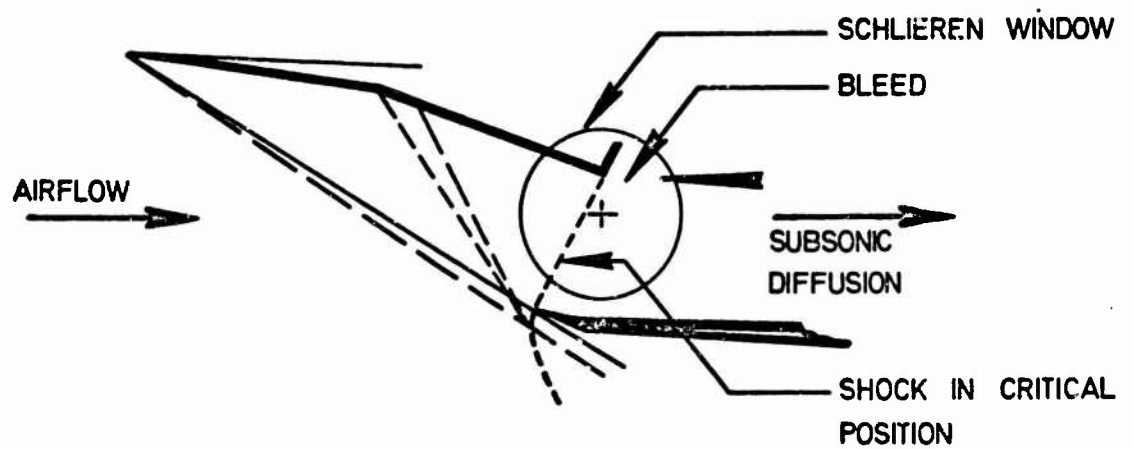
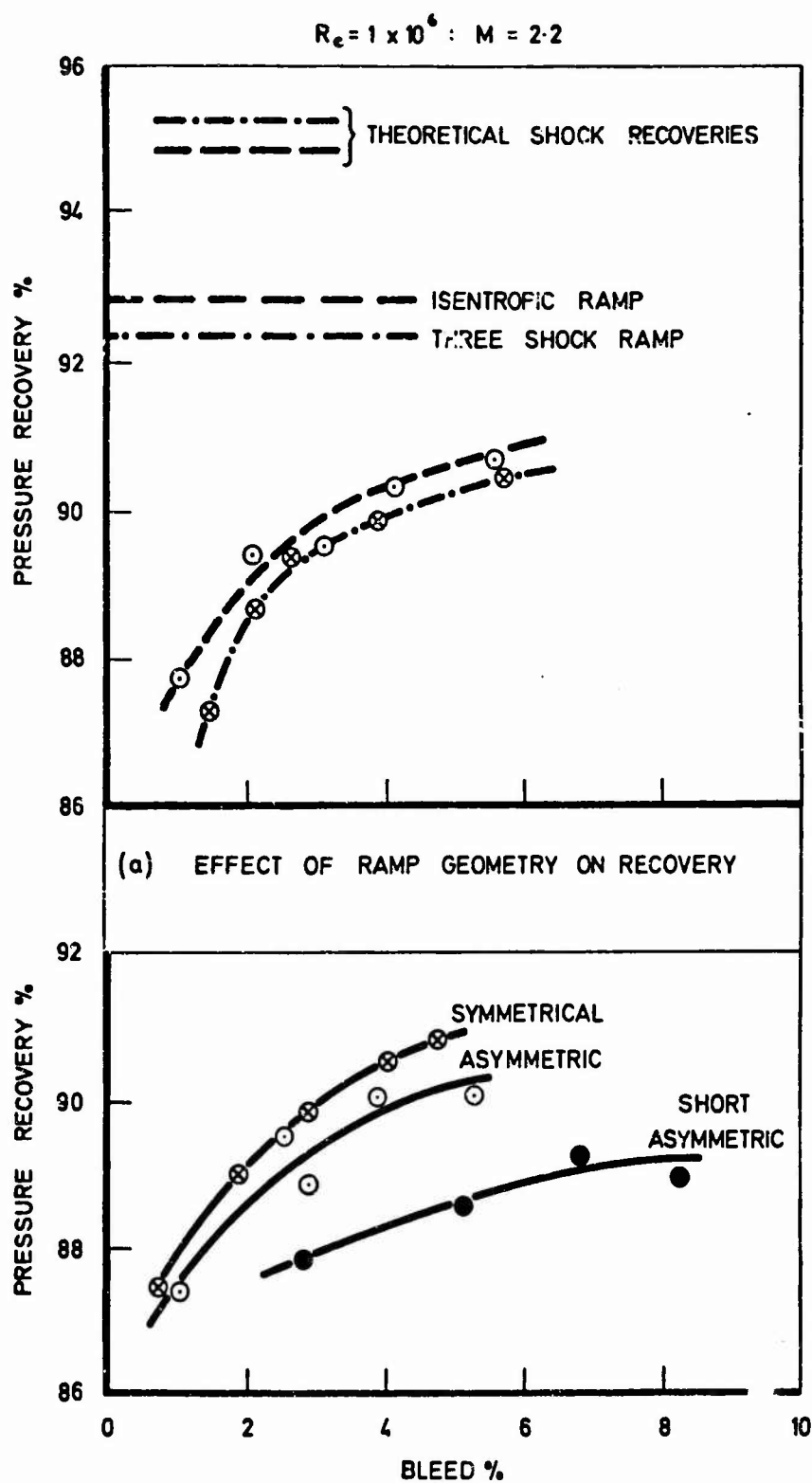


Fig.6 Throat flow. External compression intakes



(b) EFFECT OF SUBSONIC DIFFUSER GEOMETRY ON RECOVERY

Fig.7 External compression intake performance - I

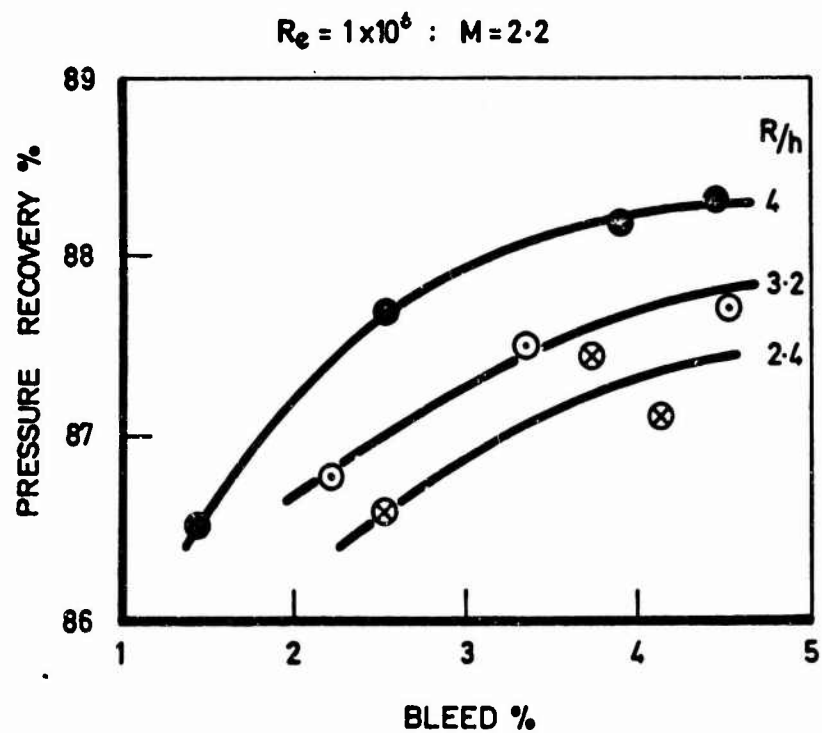
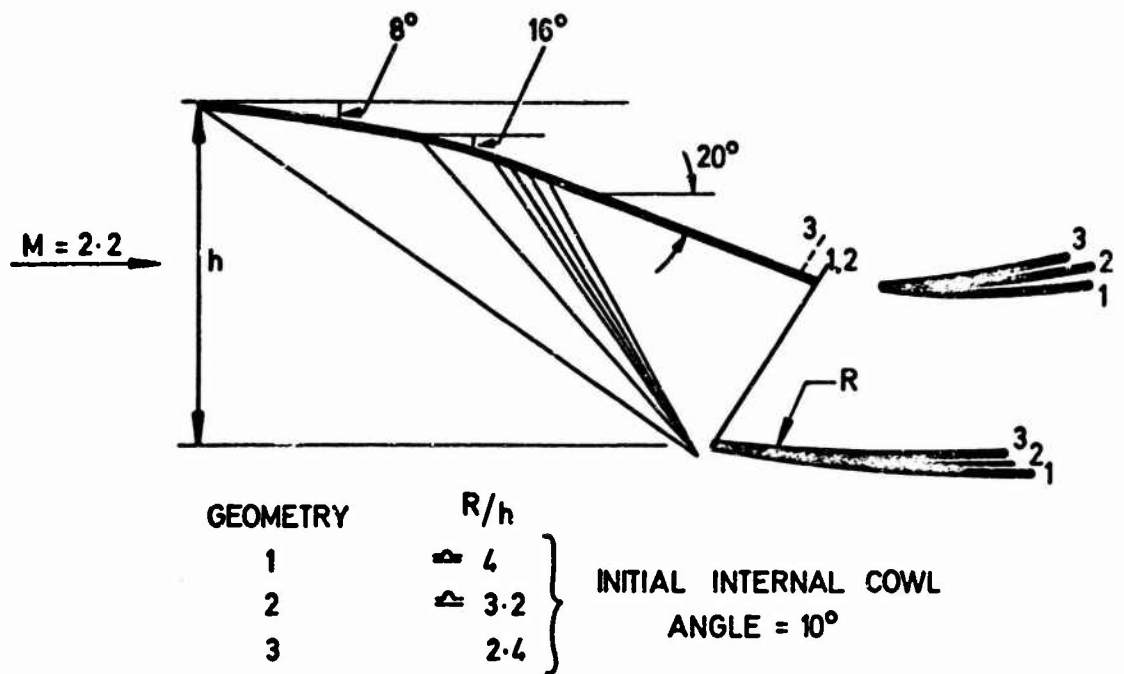


Fig.8 External compression intake performance - II. Effect of throat radius

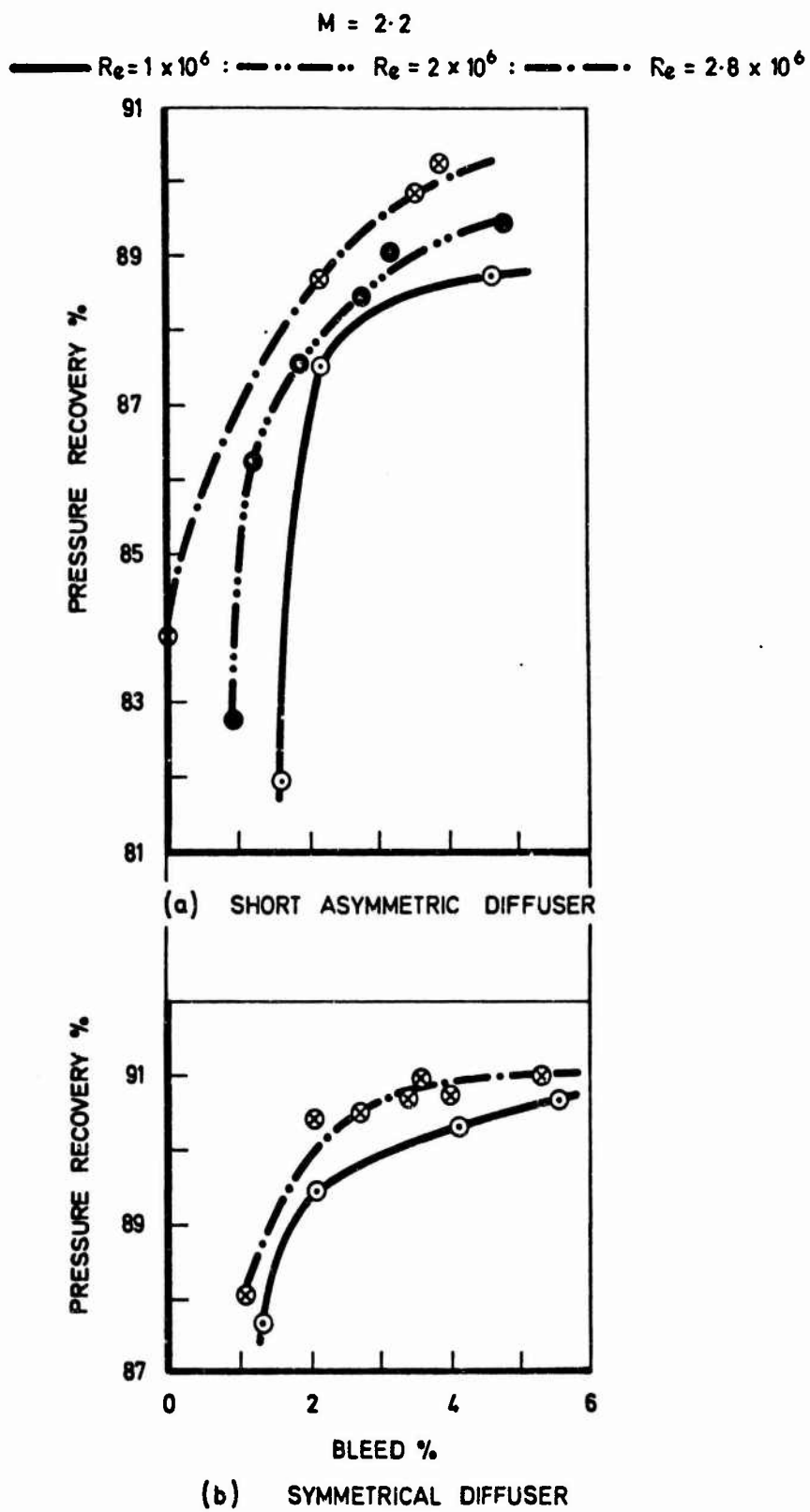


Fig.9 External compression intake performance - III. Reynolds number effects

FONCTIONNEMENT DU PIEGE A COUCHE LIMITE INTERNE D'UNE
PRISE D' AIR A COMPRESSION SUPERSONIQUE EXTERNE

par

Jacky Leynaert

Office Nationale d' Etudes et de Recherches Aéronautiques,
Chatillon-sous-Bagneux, Seine, France

SOMMAIRE

La structure de l'écoulement dans une prise d'air à compression supersonique externe de faible pente de carène et munie d'un piège à couche limite interne placé à l'origine théorique du diffuseur subsonique ne correspond pas en fait au schéma classique d'une compression supersonique terminée par un choc droit; on observe, au contraire, que le choc effectif est oblique et incurvé, et qu'au niveau du piège se produit une détente transsonique limitée. La frontière de l'écoulement au-dessus du piège est constituée d'une couche de mélange isobare: le débit du piège est concentré en un jet formé au point de recollement de cette couche de mélange sur le bord d'attaque du diffuseur. L'étude des conditions d'équilibre au point de recollement montre que le débit du piège est déterminé en fonction du débit du moteur. Lorsque ce débit diminue, le débit du piège augmente, de sorte que le piège joue le rôle d'une by-pass automatique évitant l'entrée de la prise d'air en régime subcritique. La déformation de la courbure du choc d'entrée et l'adaptation de la détente transsonique interne font que l'efficacité reste constante dans la plage où peut jouer ce phénomène; l'étendue de cette plage dépend du débit maximum permis par le circuit d'évacuation de l'air secondaire. En régime normal, un écart de réglage de ce débit n'a qu'un effet local, et ne réagit pas sur l'écoulement en fin de diffuseur. La description détaillée de ces phénomènes permet d'expliquer l'évolution des caractéristiques globales de la prise d'air et facilite la recherche d'une solution donnant un écoulement d'efficacité et d'uniformité optimales à la sortie du diffuseur.

SUMMARY

The structure of the flow in an external supersonic compression air intake of small lip angle and provided with a boundary-layer trap located at the theoretical subsonic diffuser origin does not correspond in fact to the standard pattern of a supersonic compression terminated by a normal shock. On the contrary, we observe that the actual shock is oblique and curved, and that a limited transonic expansion occurs over the trap. The boundary of the flow under this expansion is formed by a constant-pressure mixing layer; the bleed mass flow is concentrated in a jet originating near the re-attachment point of this mixing layer on the diffuser leading-edge. The study of the flow equilibrium conditions at the re-attachment point shows that the bleed mass flow rate is determined as a function of the engine mass flow rate. When the latter decreases, the bleed mass flow rate increases, so that the trap acts like an automatic by-pass, and thus the subcritical régime is avoided. The evolution of the shock curvature and of the extent of the internal transonic expansion maintains a constant efficiency within the range of application of this phenomenon. This range depends upon the maximum mass flow rate allowed by the secondary air exhaust system. Under normal working conditions, a slight variation in the mass flow control has only a local effect, and does not affect the flow at the diffuser exit. The detailed description of these phenomena helps to explain the evolution of the overall characteristics of the inlet, and facilitates work towards a solution giving the best efficiency and uniformity in the compressor entrance plane.

TABLE DES MATIERES

	Page
SOMMAIRE	326
SUMMARY	327
LISTE DES FIGURES	329
NOTATION	330
1. INTRODUCTION	331
2. DESCRIPTION GENERALE DE L'ECOULEMENT DANS LA PRISE D'AIR	331
3. FONCTIONNEMENT DU PIEGE A COUCHE LIMITE INTERNE	332
3.1 Réglage de l'Aspiration par le Piège	333
3.2 Compensation des Fluctuations du Débit Principal	334
3.3 Limites de Fonctionnement	335
4. CARACTERISTIQUES GLOBALES	336
5. INFLUENCE DES PARAMETRES GEOMETRIQUES SUR LES CARACTERISTIQUES GLOBALES	337
6. CONCLUSION	338
REFERENCES	339
FIGURES	340

LISTE DES FIGURES

		Page
Fig. 1	Description générale de l'écoulement et du débit du piège	340
Fig. 2	<div style="display: flex; justify-content: space-between;"> <div> <p>①-② Réglage de la section critique du piège</p> <p>③-④ Effet de by-pass contrôlé</p> </div> <div> <p>①-③ Effet de by-pass automatique</p> </div> </div>	341
Fig. 3	Limites de variations de p_b dans le domaine de fonctionnement correct	342
Fig. 4	Courbes caractéristiques globales	343

NOTATION

M	nombre de Mach
M_T	nombre de Mach caractéristique du choc terminal (T)
p_{10}	pression d'arrêt isentropique à l'infini amont
p_{12}	pression d'arrêt isentropique en fin de diffuseur
p_A	pression au point d'arrêt (A)
p_b	pression dans la cavité du piège à couche limite interne
A_c	section critique de l'écoulement en fin de diffuseur
A_{cb}	section critique de l'écoulement par le piège interne
Indices ① ② ③ ④	conditions d'écoulement relatives aux ① ② ③ ④ de la Figure 2 (Section 3.2)
Indice '	conditions d'écoulement relatives à la plus grande valeur de A_{cb} dans les comparaisons de la Figure 4 (Section 4)
η	efficacité de la prise d'air $\eta = p_{12}/p_{10}$
η_b	efficacité du piège à couche limite $\eta_b = p_b/p_{10}$
ϵ	coefficient de débit de l'écoulement interne, défini Figure 4
ϵ_b	coefficient de débit du piège, défini Figure 4

FONCTIONNEMENT DU PIEGE A COUCHE LIMITE INTERNE D'UNE PRISE D'AIR A COMPRESSION SUPERSONIQUE EXTERNE

Jacky Leynaert

1. INTRODUCTION

Malgré de nombreuses années d'études et de pratique du vol supersonique le problème des prises d'air est encore loin d'être bien résolu. En fait seule la partie supersonique de l'écoulement se prête aisément à des calculs exacts sur des formes simples bidimensionnelles ou axisymétriques; il n'en est pas de même des formes tridimensionnelles qui présentent souvent un certain intérêt. Pour définir la partie transsonique et subsonique, il faut aussi avoir recours à des règles encore empiriques, dégagées d'études expérimentales laborieuses^{1,2,3}. C'est le cas par exemple de la forme du piège à couche limite interne aménagé au pied du choc terminal d'une prise d'air à compression supersonique externe. Les essais comparatifs d'aspiration de la couche limite par une paroi continue perforée ou de captation par des pièges avec ou sans effet Pitot ont montré que cette dernière disposition était la plus favorable⁴. Les recherches poursuivies par l'Onera dans le cas d'un nombre de Mach de vol de l'ordre de 2, ont confirmé et précisé ce point de vue⁵; en même temps qu'elles ont permis de comprendre le mécanisme de fonctionnement du piège interne⁶. Cette analyse sera présentée ici dans le cas d'une prise d'air bidimensionnelle.

2. DESCRIPTION GENERALE DE L'ECOULEMENT DANS LA PRISE D'AIR

La prise d'air est du type classique (Fig. 1(a)); une rampe profilée assure une compression progressive de l'écoulement supersonique dont les ondes focalisent sur la lèvre de la carène, au nombre de Mach d'adaptation, afin d'éviter toute traînée "additive". Le profil interne de la carène à une pente de lèvre inférieure à la pente locale de l'écoulement incident, et une courbure accentuée, de façon à minimiser la traînée externe. Un diffuseur subsonique ralentit ensuite l'écoulement jusqu'au plan d'entrée compresseur.

Le piège à couche limite est aménagé à l'entrée du diffuseur, sous la forme d'une large ouverture prolongeant le profil de compression supersonique. Dans cette région, l'écoulement subit une déviation brutale et une augmentation importante de pression et passe du régime supersonique au régime subsonique; l'aspiration d'un certain débit par le piège permet d'éviter le décollement de la couche limite qui en résulterait.

L'examen de l'écoulement (Fig. 1(a)) montre que la configuration classique d'une compression supersonique terminée par un choc droit n'est pas respectée. On observe en effet que le choc d'entrée est en fait un choc oblique incurvé vers le diffuseur à

l'approche du piège interne. Dans la cavité du piège règne une zone d'eau morte de pression p_b . Cette pression est, suivant le cas, inférieure ou supérieure à celle de l'écoulement incident, ce qui provoque soit une détente soit une compression locale au voisinage de l'origine du piège D. Le schéma de la Figure 1(a), est donné dans le cas de pressions identiques donc sans qu'il y ait de déviation.

Le choc oblique d'entrée rencontrant la frontière isobare de l'eau morte, une détente se forme à son point d'impact et provoque une déviation de l'écoulement principal qui, le long de la frontière conserve la même pression p_b c'est à dire pratiquement le même nombre de Mach M_T , la perte de pression d'arrêt isentropique à travers le choc oblique étant peu élevée.

La détente supersonique interne s'atténue progressivement lorsqu'on s'écarte du piège et peut ne pas s'étendre jusqu'à la carène au voisinage de laquelle, dans ce cas, l'écoulement reste subsonique; une ligne sonique incurvée limite alors la région supersonique. Un choc droit (T) met fin à cette détente immédiatement avant le bord aval du piège. L'intensité de ce choc s'atténue progressivement lorsqu'on s'écarte de la ligne de mélange et s'évanouit sur la ligne sonique.

En aval du pied du choc, la frontière de l'écoulement subsonique prend une courbure très brusque pour compenser par effet centrifuge le gradient de pression entre l'eau morte et l'écoulement principal recomprimé par le choc. L'écoulement recolle ensuite sur la paroi du diffuseur subsonique. La courbure du choc d'entrée et l'intensité du choc transsonique dépendent de la géométrie du système. On peut réussir à définir ces conditions de manière telle que la combinaison des deux chocs donne sur chaque ligne de courant sensiblement la même perte de pression génératrice. On obtient alors en fin de diffuseur un profil uniforme de pression d'arrêt et de vitesse. L'efficacité globale de la configuration atteint 0,94 à $M = 2$.

Le débit aspiré dans l'eau morte est concentré dans sa quasi-totalité en un jet attaché au bord aval du piège. Un débit minimum doit être assuré pour éviter un décollement dans le diffuseur et améliorer l'efficacité par élimination de la couche limite incidente, fortement épaissie le long de la frontière de l'eau morte. Le schéma local des lignes de courant est représenté par la Figure 1(b).

Soit P la ligne de courant qui aboutit au point d'arrêt A. La partie de l'écoulement située au-dessous de cette ligne peut vaincre la compression locale qui s'établit autour de A et s'écouler normalement dans le diffuseur. Les particules fluides plus lentes s'écoulant au-dessus sont au contraire refoulées dans la cavité du piège. Elles se détendent dans le piège pour former un jet étroit pouvant atteindre localement des vitesses supersoniques et perdant ensuite son énergie cinétique sous l'effet de la viscosité et des ondes de choc éventuelles. Nous reviendrons plus en détail sur l'écoulement au voisinage de A, à l'occasion de l'étude plus générale du mécanisme de fonctionnement du piège que nous allons aborder.

3. FONCTIONNEMENT DU PIÈGE A COUCHE LIMITE INTERNE

L'observation révèle qu'il existe un domaine, que nous appellerons domaine de fonctionnement normal de la prise d'air, jouissant des propriétés suivantes: D'une part, le réglage de l'aspiration par le piège ne modifie pas le débit aspiré (débit secondaire), mais agit seulement sur la pression p_b de l'eau morte. Ce réglage

n'affecte pas non plus l'efficacité de l'écoulement principal. D'autre part, le piège peut jouer le rôle d'un by-pass automatique pour compenser les fluctuations du débit principal.

Ces deux aspects de fonctionnement du piège seront étudiés successivement; les limites de leur domaine d'application, - domaine de fonctionnement normal - seront ensuite précisées.

3.1 Réglage de l'Aspiration par le Piège

Etudions ce qui se passe lorsque sans changer le réglage du débit principal (section critique A_c = constante), on réduit progressivement la section critique A_{cb} du débit secondaire. L'évolution de l'écoulement est représentée par les schémas ① et ② de la Figure 2.

On constate expérimentalement les faits suivants:

la pression p_b s'élève mais le débit principal et le débit secondaire sont inchangés,

dans le piège, la partie supersonique du jet (J) s'est réduite sous l'effet de l'augmentation de p_b ,

la couche de mélange s'est déformée légèrement dans le sens de la compression de l'écoulement extérieur, mais sa longueur et le nombre de Mach moyen de l'écoulement extérieur ayant relativement peu varié, le profil des pressions d'arrêt à l'amont du recollement en A est conservé.

Cette compression se traduit à son tour par:

une légère déviation en D,

un raidissement du choc d'entrée (E) qui devient plus accentué à l'approche de piège,

une réduction du domaine transsonique et du nombre de Mach de détente interne, corrélativement, une diminution de l'intensité du choc terminal (T).

Globalement, il y a compensation des effets de E et T, et l'écoulement principal reste invariant. En particulier, le profil des pressions d'arrêt en aval de T, et l'efficacité sont inchangés.

Pour expliquer l'invariance du débit secondaire dans cette plage d'ajustement de A_{cb} , revenons au schéma de l'écoulement au voisinage de A (Fig.1(b)).

On pourrait considérer a priori sur ce schéma que trois éléments concourent à la détermination de la ligne de courant séparatrice (P): le profil des pressions d'arrêt de l'écoulement incident et les champs de pression de part et d'autre de A, dans le diffuseur et dans l'eau morte. Mais en fait, la présence d'un domaine supersonique dans le jet (J) a pour effet de protéger le point d'arrêt A, et la région subsonique qui l'entoure, des variations de p_b ; la pression de l'eau morte p_b n'est alors qu'un facteur secondaire de l'équilibre considéré. Le partage de l'écoulement ne dépend donc pratiquement que de deux autres facteurs, le champ de pression à l'entrée du diffuseur et le profil des pressions d'arrêt amont dans la zone de mélange et

l'écoulement non visqueux qu'elle limite. Or, nous avons observé que ces éléments étaient invariants pour une évolution limitée de la pression p_b . Si le débit secondaire est assez faible, la ligne de séparation (P) est la ligne de courant de la couche de mélange de pression d'arrêt isentropique p_A ; cette pression au point d'arrêt A étant déterminée par le champ de pression aval, il en résulte donc bien que la ligne de séparation (P) et par conséquent le débit secondaire, sont conservés.

On reconnaît dans ce schéma l'idée directrice des théories actuelles du recollement d'une couche de mélange isobare sur une paroi⁷, mais ici les phénomènes sont plus complexes du fait de la présence des chocs E et T et d'un écoulement aval subsonique; de plus, ces propriétés s'étendent à des débits aspirés supérieurs à ceux de la couche de mélange incidente, ce qui déborde le cadre de ces théories.

3.2 Compensation des Fluctuations du Débit Principal

Que se passe-t-il maintenant si, sans changer le réglage de l'aspiration par le piège (section critique A_{cb} constante), on fait varier le débit de l'écoulement principal (section critique A_c)?

Reprenons (Fig. 2) le cas du schéma ① pour lequel la section A_{cb} est la plus ouverte, et supposons que l'on diminue A_c ; nous obtenons le schéma ③: les nombres de Mach dans le diffuseur étant réduits, les pressions à l'entrée du diffuseur sont plus élevées. La nouvelle ligne de partage (P') est donc située comme l'indique la Figure 2 ③ par rapport à P, le débit passant par le piège augmente.

Le débit volume du piège étant maintenu constant (A_{cb} fixé), la pression dans le piège p_b croît proportionnellement au débit.

L'augmentation de la pression p_b se traduit, pour l'écoulement principal, par le passage à une nouvelle configuration qualitativement identique, au débit aspiré près, à la dernière configuration du cas précédent (Fig. 2 ②) obtenue pour le même niveau de pression p_b . Le phénomène de compensation de l'intensité des chocs E et T conserve le profil des pressions d'arrêt en aval de T.

En fonctionnement normal, la ligne de partage initiale (P) est située en dehors de la couche de mélange proprement dite. Le profil des pressions d'arrêt de l'écoulement non visqueux étant alors à peu près uniforme, l'élimination d'une part supplémentaire du débit ne modifie pratiquement pas l'efficacité.

En définitive, la diminution du débit principal, toutes choses égales par ailleurs, se traduit par l'augmentation correspondante du débit du piège et de la pression d'eau morte, l'efficacité globale restant constante.

On voit ainsi que le piège peut jouer le rôle d'un by-pass automatique pour compenser les fluctuations du débit principal.

Ce fonctionnement a évidemment des limites assez étroites (de l'ordre de 4% du débit, comme nous le verrons) mais si l'on dispose d'un dispositif de réglage de la section critique A_{cb} du piège, on peut étendre largement ce rôle de by-pass.

En effet, reprenons le dernier cas considéré (schéma ③ de la Figure 2) et supposons que l'on désire diminuer davantage le débit principal ($A_{c1} < A_{c3}$) en conservant une pression de piège constante ($p_{b4} = p_{b3}$) de façon à bénéficier du même schéma générale de l'écoulement principal et pratiquement de la même efficacité: il suffit pour cela d'ouvrir A_{cb} en proportion du supplément de débit évacué dans l'eau morte par diminution du débit principal.

La comparaison des schémas ③ et ④ de la Figure 2 montre qu'une nouvelle ligne de partage (P'') s'établit alors sous l'effet de pressions de refoulement plus élevées dans le diffuseur mais que pour le reste, l'écoulement est inchangé, la pression du piège ayant été rétablie par l'ouverture de A_{cb} .

Nous avons raisonné jusqu'à présent dans l'hypothèse où l'aspiration par le piège était réglée par sa section critique A_{cb} . En fait, il est possible, dans certain cas, de disposer d'un système plus souple, par exemple, si l'on rejette le débit secondaire à l'arrière du moteur par une fente aménagée en aval du col d'une tuyère convergente-divergente; dans ce cas, les conditions d'extraction sont commandées par le régime du moteur qui définit en même temps le débit d'entrée, et ces conditions jouent en partie de la même façon qu'une adaptation automatique de la section critique de décharge A_{cb} (Refs. 8,9).

3.3 Limites de Fonctionnement

Nous avons décrit le principe du fonctionnement de la prise d'air dans son domaine d'adaptation; il nous faut maintenant en préciser les limites.

3.3.1 Limites du Débit Secondaire, à p_b Constante

Nous avons vu que la forme générale de l'écoulement était définie par la pression p_b dans le piège; en particulier, si un débit secondaire variable est extrait à pression p_b constante, la structure de l'écoulement demeure inchangée. Cette propriété ne subsiste qu'entre deux limites:

vers les grands débits passant par le piège, il est probable qu'un décollement dans le diffuseur du côté de la carène, finirait par apparaître, bien que, pour le cas particulier étudié, les essais jusqu'à 20% de débit passant par le piège n'aient pas permis d'atteindre cette limite;

vers les petits débits, lorsque la couche de mélange incidente n'est plus largement aspirée dans le piège, il se produit dans le diffuseur une dégradation progressive du profil des pressions d'arrêt le long de la paroi, et une diminution de l'efficacité.

L'épaisseur de cette couche de mélange croît à peu près linéairement en fonction de la longueur du piège. Pour un piège très étendu de longueur égale par exemple à 75% de la hauteur d'entrée de la prise d'air, le débit à éliminer pour bénéficier de l'efficacité maximale atteint 6,5% du débit total. Une diminution de ce débit au-dessous de cette valeur n'a cependant comme nous l'avons dit qu'un effet modéré.

Il faut aller jusqu'à des débits secondaires très faibles, de l'ordre de 1%, pour voir apparaître un large décollement de l'écoulement dans le diffuseur.

3.3.2 Limites de p_b

Le domaine des valeurs de p_b acceptables pour un fonctionnement correct possède à son tour deux limites:

vers les faibles pressions de piège (Fig.3(a)), la réaccélération supersonique interne, qui se manifeste par une première détente au point de décollement D et une seconde au point d'impact de E sur la frontière libre, conduit à un choc T de plus en plus intense, tandis que E tend à devenir stationnaire. Le phénomène de compensation de E et de T ne joue plus. La perte d'efficacité qui en résulte est assez progressive et commence à se traduire par une plus forte interaction du choc T avec les couches limites latérales de la prise d'air.

Vers les fortes pressions de piège (Fig.3(b)) le choc d'entrée après s'être redressé, est refoulé en amont des lèvres de la carène. La détente supersonique au pied de ce choc sur la frontière libre est très réduite, et fait place à une succession de petites zones de détentes transsoniques suivies chacune de leur choc $T_1, T_2 \dots$. Lorsque le choc E qui émerge de l'entrée rencontre le faisceau focalisé de la compression supersonique amont, une ligne de glissement prend naissance; dès que cette ligne de glissement passe à l'intérieur de la prise d'air, le pompage apparaît (J.Ferri).

Notons à ce propos que le pompage a généralement une fréquence qui est relation avec le temps de propagation des perturbations depuis l'entrée jusqu'à l'obstacle qui règle le débit principal en fin de diffuseur, mais il arrive, pour certaines configurations particulières que le col aérodynamique formé entre le carène et la frontière fluide du piège joue le même rôle que le col de sortie; le pompage prend alors une fréquence beaucoup plus élevée, et une amplitude réduite. L'on a pu ainsi déceler des cas de pompage à 2500 cycles par seconde en soufflerie, pour une maquette à l'échelle 1/10 environ de l'avion; la configuration étudiée avait d'abord été jugée stable, car l'observation stroboscopique ne permettait plus de déceler aucun phénomène; ce sont ultérieurement des mesures de pression à court temps de réponse qui ont mis en évidence ce type de pompage.

4. CARACTERISTIQUES GLOBALES

Il est maintenant utile de rassembler les éléments du fonctionnement de la prise d'air que nous venons de décrire, sur un graphique donnant l'évolution des grandeurs globales caractéristiques.

Nous avons reporté planche 4 en fonction du coefficient de débit de l'écoulement principal, ϵ , l'efficacité de la prise d'air, η , le coefficient de débit du piège, ϵ_b , et son efficacité, η_b , qui est encore égale à la pression de l'eau morte, rapportée à p_{10} , comme on a pu le vérifier (le jet du piège perd dans l'eau morte toute son énergie cinétique). La définition de ces grandeurs est précisée sur la Figure 4.

Pour simplifier, nous avons tracé les résultats pour deux valeurs seulement de la section critique A_{cb} du débit du piège, supposées fixées a priori, et situées, dans le domaine de fonctionnement normal de la prise d'air.

Prenons d'abord le cas de la plus petite section A_{cb} . L'élément BC de la courbe d'efficacité η représente la plage de compensation à efficacité quasi-constante du débit principal par le débit du piège, comme on peut le vérifier sur la courbe donnant ϵ_b en fonction de ϵ , dont la pente est - 1.

De A à B, la détente supersonique interne conduit à une valeur élevée du nombre de Mach du choc T et l'efficacité s'effondre.

De C à D, le choc est refoulé en amont de l'entrée (régime subcritique), et le débit principal décroît plus vite que n'augmente le débit secondaire.

L'efficacité du piège, η_b , suit la même loi que ϵ_b , puisque A_{cb} étant donné, η_b est proportionnel à ϵ_b .

Donnons maintenant à A_{cb} la valeur supérieure. Aux points A'B'C'D' respectivement de même pressions de piège p_b que les points ABCD précédents, l'écoulement aux points homologues est semblable, mais pour chaque point le débit piège est augmenté proportionnellement à A_{cb} , et le débit principal est réduit d'autant. Ceci se traduit par un décalage de la courbe (η, ϵ) vers la gauche.

Lorsqu'on considère le fonctionnement de l'ensemble du fuseau moteur, il apparaît qu'une solution souhaitable d'adaptation de la prise d'air aux conditions variables de débit imposées par ailleurs consiste à se placer constamment en des points tels que BB'. Ces points sont caractérisés par une efficacité élevée, une déviation nulle de débit en amont de l'entrée (trainée "additive" nulle) et une marge de sécurité vis à vis du pompage constante. Ils correspondent à des configurations d'écoulement interne semblables, de même pression p_b . Pour maintenir ce régime en vol de croisière, il suffit par conséquent d'assurer l'invariance de cette pression, (ou d'une manière plus précise, l'invariance du rapport de cette pression à la pression ambiante).

5. INFLUENCE DES PARAMETRES GEOMETRIQUES SUR LES CARACTERISTIQUES GLOBALES

Il nous reste à faire quelques remarques sur l'influence des paramètres géométriques de la prise d'air. Revenons au schéma général de l'écoulement (Fig. 1). Nous ne connaissons pas de méthode théorique pour le calcul de l'écoulement répondant à des conditions aux limites données (formes de paroi et débits principaux et secondaires), ni pour prévoir par exemple, les conditions d'apparition du régime subcritique. Or le principal écueil rencontré dans les essais des prises d'air de ce type, notamment lorsqu'on cherche à réduire la trainée de carénage externe, c'est que, dans certains cas, l'expulsion du choc, et le pompage qui en résulte, se produisent avant même que le piège ait pu fonctionner correctement; les performances de la prise d'air sont alors très médiocres.

Faute de théorie pour prévoir ces phénomènes, indiquons quelques observations expérimentales sur une configuration particulière; on a noté comme ayant tendance à provoquer cette expulsion prématurée du choc, les éléments suivants:

un déplacement vers la carène du bord d'attaque du diffuseur, qui, contrairement à ce qu'on pourrait attendre, n'améliore pas la captation du débit secondaire, car le piège continue à fonctionner suivant le même schéma que précédemment jusqu'à des décalages très importants; en même temps se produit un effet de blocage qui tend à repousser le choc E vers l'amont;

une divergence initiale trop faible du diffuseur;

une courbure trop forte de la carène;

une longueur de piège insuffisante;

ceci évidemment pour une forme de compression supersonique donnée devant l'entrée.

La longueur de la rampe de compression joue également un rôle assez aigu dans ces phénomènes.

La forme même de la compression supersonique amont peut enfin intervenir dans la configuration interne. C'est ainsi qu'en donnant au choc de tête du faisceau de compression une certaine courbure, par un profil de rampe approprié, il peut en résulter pour une géométrie de diffuseur donnée, une accentuation de la courbure du choc (E) ce qui a pour effet de reculer à la fois la limite de pompage et de donner un écoulement plus uniforme en fin de diffuseur.

Tous ces résultats sont évidemment dépendants les uns des autres et l'on ne peut approcher une solution optimale qu'après une longue mise au point expérimentale.

6. CONCLUSION

Nous avons pu décrire qualitativement le fonctionnement d'un type de prise d'air caractérisé par une traînée de carénage externe très réduite, une efficacité optimale dans un domaine large de variation du débit du moteur, et présentant une possibilité d'adaptation automatique de ce débit, grâce au piège à couche limite interne.

En l'absence de méthode de calcul théorique, la mise au point d'une telle prise d'air, pour une application particulière, a demandé une longue étude expérimentale d'où nous avons pu dégager quelques idées directrices pour les études ultérieures.

REFERENCES

1. Mahoney, J.J. *Inlet Diffuser Design Techniques.* The Marquardt Corporation. SAE Paper 586 D, Octobre 1962.
2. Scherer, R.
et alii *Viscous Flows in Inlets.* NACA RM A58 D 17a, 1958.
3. - *AGARDograph en préparation. AGARDograph 102 - Supersonic Inlets, May 1965.*
4. Obery, L.J.
Cubbison, R.W. *Effectiveness of Boundary-Layer Removal near Throat of Ramp Type Side Inlet at Free Stream Mach number 2.0.* NACA RM E54 I 14, 1954.
5. Leynaert, J.
Brasseur, J.M. *Problèmes D'aérodynamique Interne Posés par L'avion de Transport Supersonique "Mach 2".* Vème Congrès Aéronautique Européen, Venise, septembre 1962. La Recherche Aéronautique n° 91, 1962.
6. Leynaert, J. *Aspects Aérodynamiques des Problèmes de Prises d'Air et de Sorties de Réacteur pour un Avion de Transport Supersonique.* Bulletin de l'association technique Maritime et Aéronautique, Session 1964.
7. Carriere, P. *Aérodynamique Interne des Réacteurs, Deuxième Partie - Tuyères et Jets.* Ecole Nationale Supérieure d'Aéronautique, Paris.
8. Talbot, J.E. *A Fully Integrated Propulsion System for a Supersonic Transport.* Pages 513-538 AGARDograph 103 ci-joint, 1965.
9. Hardy, J-M *Possibilités Actuelles d'Etude Théorique d'une Tuyère Supersonique à Double Flux.* Pages 445-478 AGARDograph 103 ci-joint, 1965.

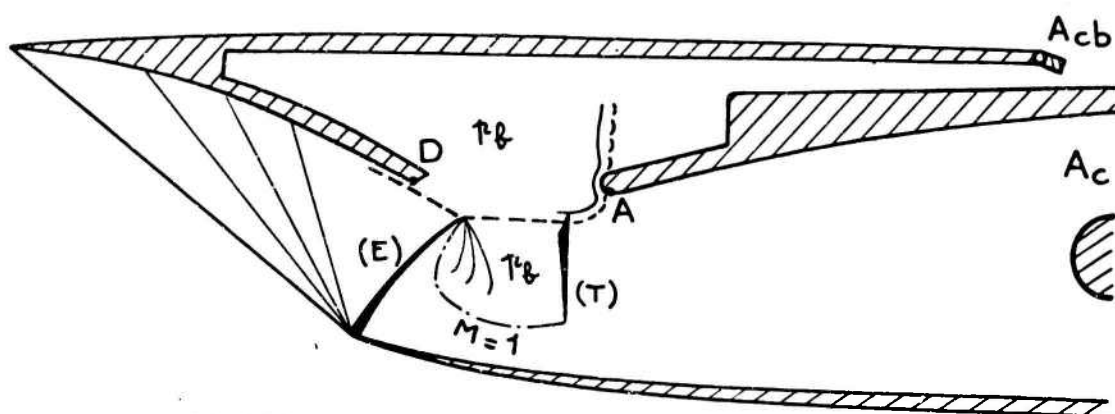


Fig. 1(a)

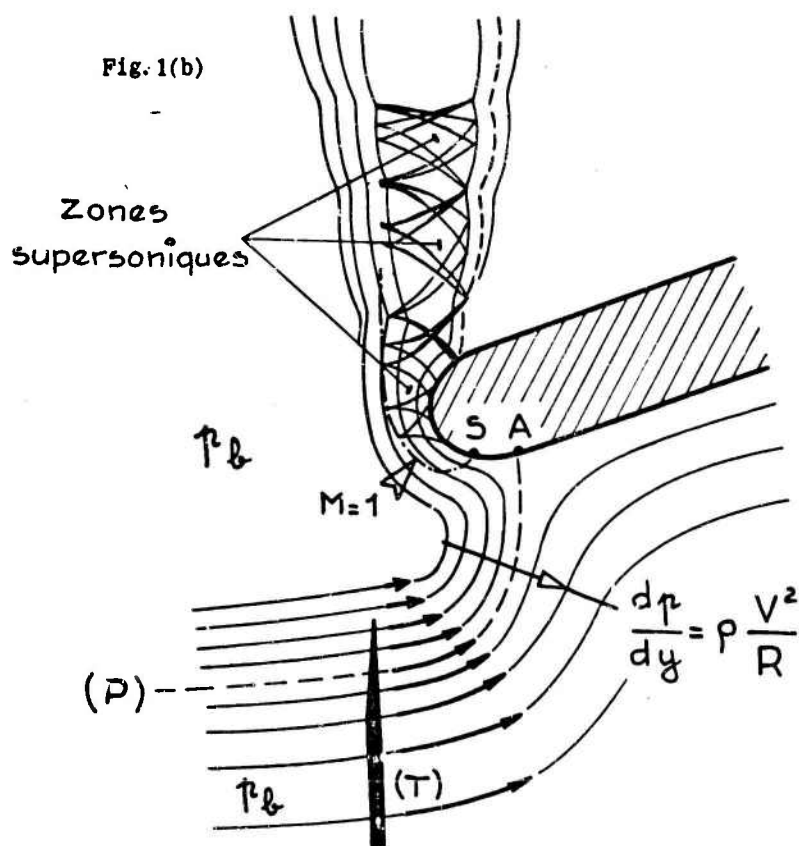


Fig. 1 Description générale de l'écoulement et du débit du piège

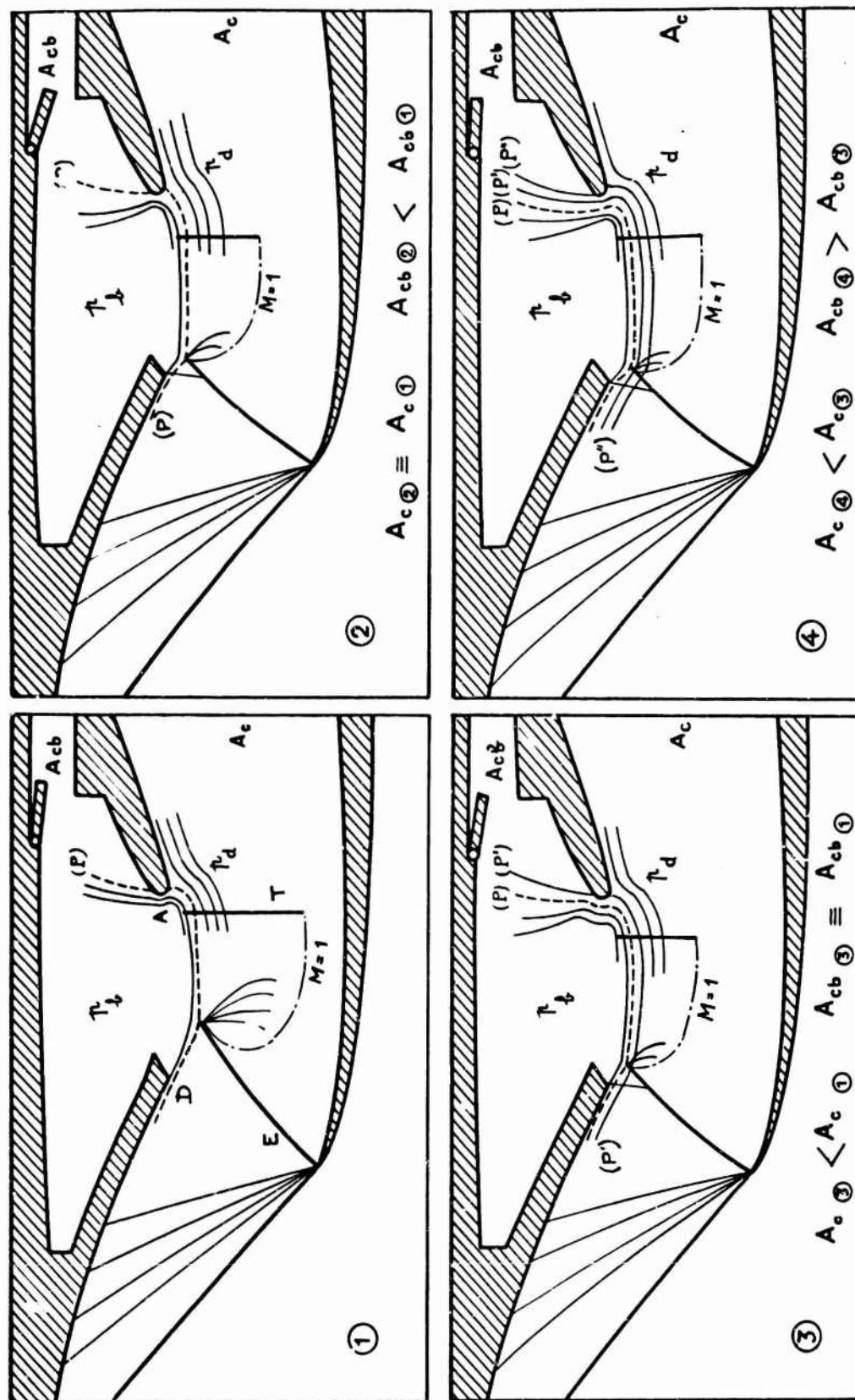


Fig. 2 ①-② Réglage de la section critique du piège ③-④ Effet de by-pass automatique ③-④ Effet de by-pass contrôlé

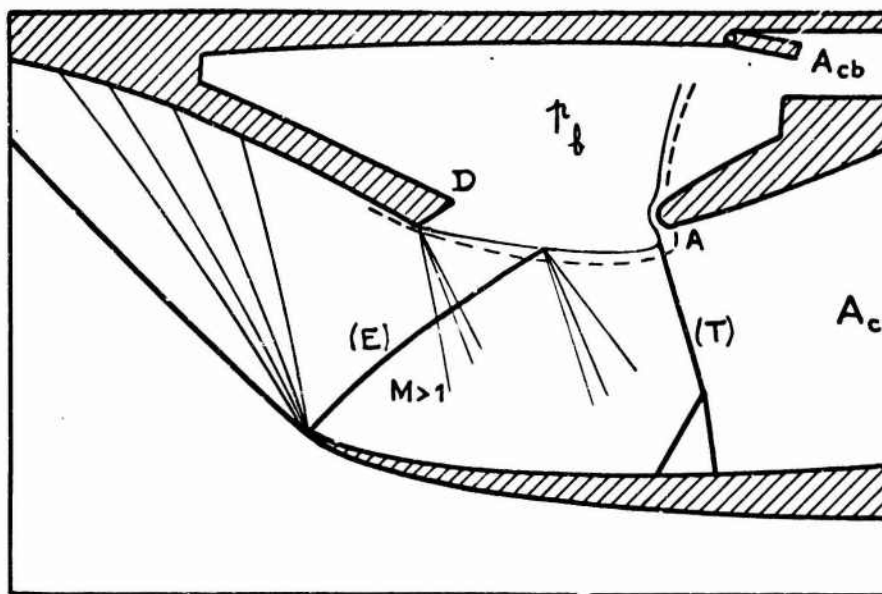


Fig.3(a) Régime supercritique

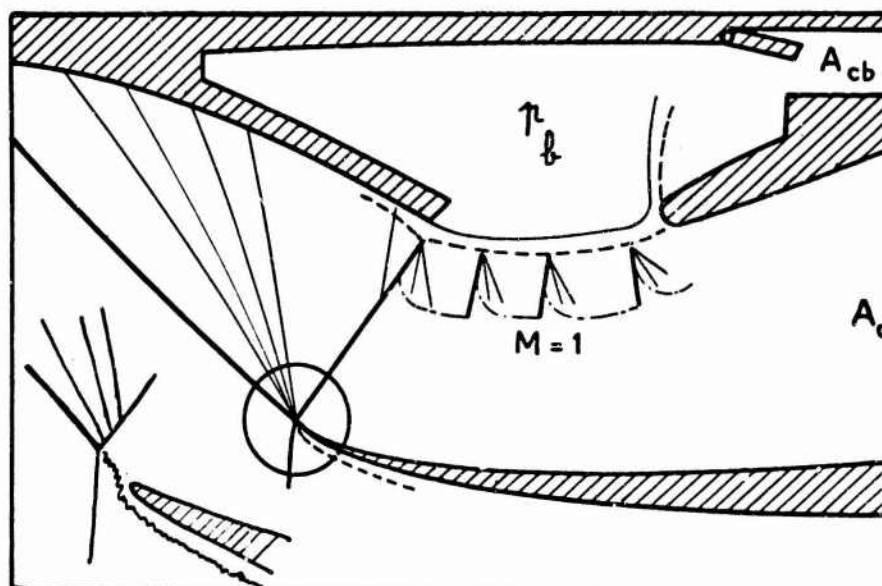
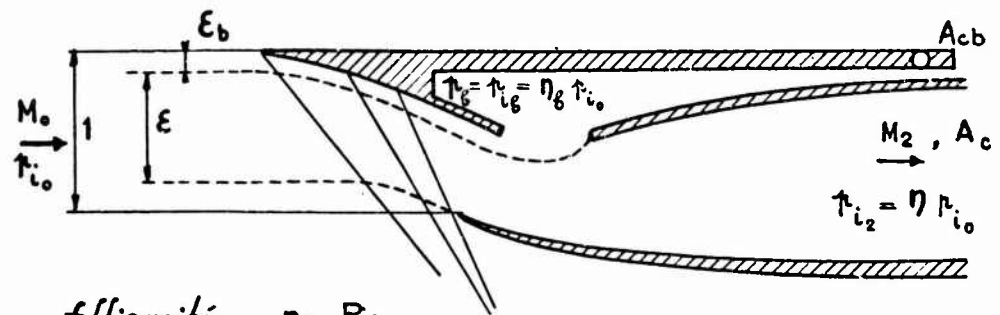
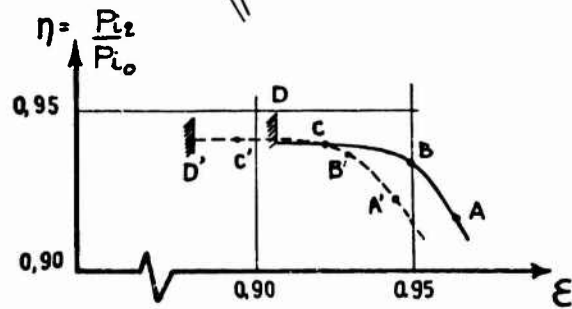


Fig.3(b) Régime critique et limite de pompée

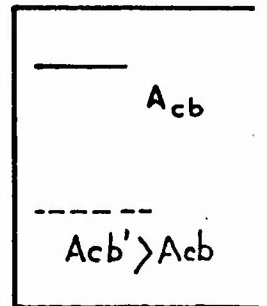
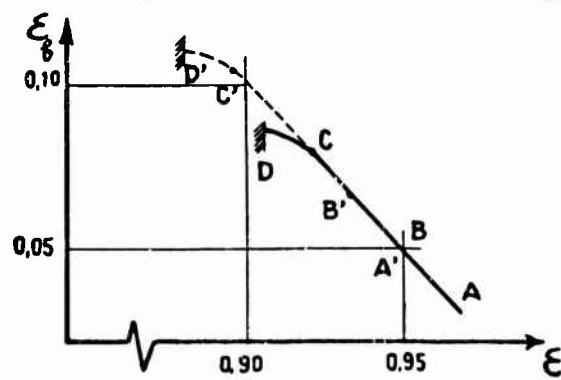
Fig.3 Limites de variations de p_b dans le domaine de fonctionnement correct



efficacité



Coefficient de débit du piège



Efficacité du piège

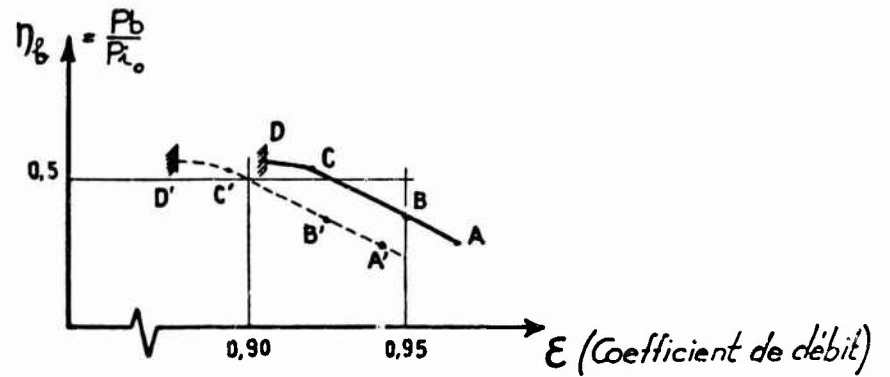


Fig. 4 Courbes caractéristiques globales

A GENERAL METHOD FOR CALCULATING LOW SPEED FLOW ABOUT INLETS

by

John L. Hess and A. M. O. Smith

Douglas Aircraft Company, Long Beach, California.

SUMMARY

A set of digital computer programs has been developed that can calculate with high accuracy the inviscid incompressible flow about arbitrary two-dimensional, axisymmetric, and three-dimensional bodies. This paper describes how these programs can be used as design tools in problems involving inlets or power-plant installations in general and illustrates their effectiveness in these applications. The basic method is outlined, and the techniques used to apply it to inlets, shrouds, and ducts are described. The ability of the method to predict real flow is exhibited by comparing calculated and experimental pressure distributions on a variety of configurations. Finally, several applications of this method to design problems are presented, both with and without experimental correlations. It is evident that this method can usefully supplement wind-tunnel tests, and in some cases can replace them.

SOMMAIRE

Une série de programmes de calculateur a été établie permettant de déterminer avec une haute précision l'écoulement incompressible non-visqueux autour de solides de forme arbitraire bidimensionnels, de révolution, et tridimensionnels. On montre comment ces programmes peuvent être utilisés comme outils de calcul dans les problèmes en général et des exemples sont donnés de leur utilité dans ces applications. On expose à grands traits la méthode dans son ensemble ainsi que les techniques utilisées afin de l'appliquer aux prises, carénages et canalisations. On montre qu'à l'aide de cette méthode il est possible de prédire l'écoulement instantané par la comparaison des répartitions de la pression obtenues par le calcul ou expérimentalement, pour des configurations très diverses. Pour terminer, on présente plusieurs applications de cette méthode aux problèmes à résoudre en cours de conception, avec ou sans corrélations expérimentales. Il est évident que cette méthode peut constituer un complément utile des essais en soufflerie et, dans certains cas, les remplacer.

SUMMARY

A set of digital computer programs has been developed that can calculate with high accuracy the inviscid incompressible flow about arbitrary two-dimensional, axisymmetric, and three-dimensional bodies. This paper describes how these programs can be used as design tools in problems involving inlets or power-plant installations in general and illustrates their effectiveness in these applications. The basic method is outlined, and the techniques used to apply it to inlets, shrouds, and ducts are described. The ability of the method to predict real flow is exhibited by comparing calculated and experimental pressure distributions on a variety of configurations. Finally, several applications of this method to design problems are presented, both with and without experimental correlations. It is evident that this method can usefully supplement wind-tunnel tests, and in some cases can replace them.

SOMMAIRE

Une série de programmes de calculateur a été établie permettant de déterminer avec une haute précision l'écoulement incompressible non-visqueux autour de solides de forme arbitraire bidimensionnels, de révolution, et tridimensionnels. On montre comment ces programmes peuvent être utilisés comme outils de calcul dans les problèmes en général et des exemples sont donnés de leur utilité dans ces applications. On expose à grands traits la méthode dans son ensemble ainsi que les techniques utilisées afin de l'appliquer aux prises, carénages et canalisations. On montre qu'à l'aide de cette méthode il est possible de prédire l'écoulement instantané par la comparaison des répartitions de la pression obtenues par le calcul ou expérimentalement, pour des configurations très diverses. Pour terminer, on présente plusieurs applications de cette méthode aux problèmes à résoudre en cours de conception, avec ou sans corrélations expérimentales. Il est évident que cette méthode peut constituer un complément utile des essais en soufflerie et, dans certains cas, les remplacer.

LIST OF FIGURES

	Page
Fig. 1 Approximation of bodies by surface elements	358
(a) Two-dimensional and axisymmetric bodies	
(b) Three-dimensional bodies	
Fig. 2 Three fundamental flows for inlets using artificial afterbodies	359
Fig. 3 Two fundamental flows for propeller shrouds	360
Fig. 4 Comparison of calculated and experimental pressure distributions on a propeller shroud with centerbody in static operation	361
Fig. 5 Comparison of calculated and experimental pressure distributions on an inlet at a mass flow ratio of 0.752 with a free-stream Mach number of 0.5	362
Fig. 6 Comparison of calculated and experimental pressure distributions on the exterior of the forward portion of an inlet at 6° angle of attack for two mass flow ratios	363
Fig. 7 Adjusted DC-8 wing-pylon-nacelle combination	364
Fig. 8 Comparison of calculated and experimental pressure distributions on a DC-8 pylon in the presence of the nacelle and wing at a free-stream Mach number of 0.825 for the zero-lift condition	365
Fig. 9 Experimental and calculated shroud configurations	366
Fig. 10 Comparison of calculated and experimental pressure distributions on a shroud configuration for an aft-shroud displacement of one inch and a dynamic pressure ratio $q_0/q_1 = 0.976$	367
Fig. 11 Variation of shroud mass flow ratio with aft-shroud displacement	368
Fig. 12 Variation of shroud thrust ratio with aft-shroud displacement	368
Fig. 13 Calculated pressure distributions on two noise suppression cowls with interior bullet in static operation	369
Fig. 14 Calculated isobars in a radial diffuser	370
Fig. 15 Calculated velocity distributions in a bifurcated duct	371

NOTATION

A_p	internal area of a shroud (Fig.9)
A_∞	area that fluid passing through a shroud occupies at an infinite distance downstream (Fig.9)
$A_{\infty 0}$	value of A_∞ for zero aft-shroud displacement
C_p	pressure coefficient, difference between local and free-stream static pressures divided by free-stream dynamic pressure
d	displacement of aft shroud from forward shroud (Fig.9)
M	Mach number
p	local static pressure
p_∞	static pressure at infinity
q_0, q_1	dynamic pressures exterior and interior to shroud configuration (Fig.9)
q_{ref}	dynamic pressure at reference location
V	local fluid velocity
V_1, V_2	velocities at control locations of inlet (Fig.2)
V_∞	free-stream velocity

A GENERAL METHOD FOR CALCULATING LOW SPEED FLOW ABOUT INLETS

John L. Hess and A. M. O. Smith

1. GENERAL DESCRIPTION OF THE METHOD OF FLOW CALCULATION

A general method has been developed for calculating, by means of an electronic computer, the incompressible potential flow about arbitrary body shapes¹⁻³. The method of solution, which is based on fundamental theorems of classical potential theory⁴, utilizes a distribution of source density over the body surface and solves for the distribution that makes the normal component of fluid velocity take on prescribed values (usually zero) on the body surface in the presence of a given onset flow, which is usually a uniform stream. This approach is perfectly general and does not make use of any simplifying assumptions. In particular, the body is not required to be slender, and perturbation velocities due to the body are not required to be small. Both interior and exterior flows can be calculated, and multiple-body interference problems present no difficulty. The theory and the details of the method are contained in the references. Only a brief outline of the approach is given here.

The body surface is approximated by a large number of surface elements whose characteristic dimensions are small compared to those of the body. Figure 1 shows the surface elements used to approximate two-dimensional bodies, axisymmetric bodies, and three-dimensional bodies. A two-dimensional or an axisymmetric body is specified by a single profile curve. This profile curve is approximated by a polygon consisting of a large number of short straight-line segments, which in general are of unequal length. Thus the surface elements for two-dimensional bodies are thin, infinite plane strips, and those for axisymmetric bodies are frustums of cones having small slant heights. For three-dimensional bodies the surface elements are small plane quadrilaterals, which are distributed over the entire surface. On each element a control point is selected where velocities and pressures are to be evaluated. For two-dimensional and axisymmetric bodies the control points are the midpoints of the line segments that approximate the profile curve of the body. For three-dimensional bodies, points near the centroids of the quadrilaterals are used as control points. (See Reference 3 for the precise definition.)

The surface source density is assumed to be constant over each surface element. Thus there is a number of unknown values of source density equal to the number of surface elements. The velocities induced by the elements at each other's control points are computed. Because of the linearity of the problem, the velocity at any point due to an element is proportional to the unknown value of source density on that element and is thus the product of this unknown value and the velocity at the point in question due to a unit value of source density on the element. It is required that the normal velocity at each control point due to all the elements equal the negative

of the normal component of the onset flow there, so that the total normal velocity is zero. (If the normal velocity is prescribed as non-zero, the modification is obvious.) Application of a normal velocity condition at all control points produces a determinate set of linear algebraic equations for the values of source density on the elements. Once these equations have been solved, velocities and pressures are computed at the control points and, if desired, at points off the body surface in the flow field.

The procedure outlined above has two main parts: calculation of the velocities induced by the elements at each other's control points for a unit value of source density and solution of the linear algebraic equations for the values of source density. The formulas for the velocity induced by an element depend on the geometry of the element. Since different types of elements are used for two-dimensional bodies, axisymmetric bodies, and three dimensional bodies, separate computer programs have been written for these three cases. There is also a special case for an axisymmetric body, namely the flow due to a uniform onset flow perpendicular to the axis of symmetry of the body. In this case the flow is not independent of circumferential location around the body. However, it can be shown² that all quantities of interest are proportional to the cosine of the circumferential angle measured from the free-stream direction. The source density on a frustum element is assumed to be constant in the axial direction, and the velocities induced by an element at any point are computed by using the known circumferential variation of the source density. Thus this special case is handled in the same way as an axisymmetric flow, and time-consuming three-dimensional techniques are avoided.

The accuracy of the calculated flow and the required computing time depend on the number of elements used to approximate the body surface. For simple two-dimensional or axisymmetric bodies, such as a torpedo, 60 elements give good accuracy. But for inlets or ducts, 150-275 are usually required. Typical computing times for the latter type of body are 5-10 minutes on the IBM 7094. For three-dimensional bodies 500-1,000 elements are usually used, and a typical computing time is two hours. Even with these large element numbers, three-dimensional cases cannot attain the accuracy of two-dimensional and axisymmetric cases.

To compute the velocities due to an element at any point, the location of the element must be known. The present method is not efficient for problems where part of the boundary has an unknown location. In this context the boundaries include all surfaces of discontinuity. Such problems can be attacked by iteration with an assumed boundary location at each stage. Problems of this type include a finite shroud with energy addition, where a stream-line of discontinuity separates the energized and non-energized flow, and all cases of three-dimensional lift, for which there is trailing vorticity. (Two-dimensional lifting flows can be calculated in a routine manner.)

The present method calculates incompressible flow about completely general body shapes. At Mach numbers for which compressibility is important, approximations must be made, and the method is accurate if perturbation velocities are not too large.

2. APPLICATION TO INLETS, SHROUDS, AND DUCTS

Calculating the flow about a simple closed body by the present method is straightforward. For the types of interest in this paper some special techniques are required.

There are several possible approaches, all of which become equivalent in the limit of an infinite number of elements. The approaches described below obtain useable results with reasonable element numbers.

2.1 Inlets

A very common application of the present method is the calculation of flow over the forward portions of axisymmetric inlets. In such cases a complication arises from the necessity of obtaining the desired inlet mass flow ratio, the ratio of fluid flux through the inlet to the flux through the same area at free-stream conditions. This is accomplished by means of an artifice.

The forward portion of the inlet is artificially extended by means of afterbodies as shown in Figure 2. The location where the forward portion joins the afterbody is denoted the control location and it is there that flux through the inlet is evaluated. Three fundamental flows are calculated. The first two are axisymmetric flows due to a uniform onset flow parallel to the inlet's symmetry axis. For the first flow the afterbody is a very long region of constant inner and outer diameter that is open at the rear. The mass flow ratio at the control location is usually near one. For the second flow the interior of the afterbody is closed near the rear by a wall normal to the symmetry axis. Immediately forward of the wall the flow is erratic and not physically meaningful, but far upstream at the control location the flow is smooth and has significance. The mass flow ratio for the second flow is usually less than one. The third flow is that due to a free-stream perpendicular to the axis of symmetry of the inlet. For this flow it is immaterial whether the closed or the open afterbody is used, since the flow about the forward portion of the inlet is the same in either case. The third flow gives zero net flux through the control location. By linearly combining these three basic flows, the flow about the inlet at any mass flow ratio and any angle of attack may be obtained.

The first and third fundamental flows are straightforward, but the second requires some comment. The meaningless flow in front of the interior closing wall is caused by the inability of the present method to handle internal corners. This is why the wall cannot be placed at the control location and the flow through it simply specified. It might be expected that the mass flow ratio in the second flow is zero, but this is not the case. There is "leakage" out of the inlet between the control location and the closing wall. This can be corrected by curving the closing wall so that it smoothly joins the interior inlet wall and by using a very large number of elements. To conserve computing time, it is preferable to use fewer elements and to accept the non-zero mass flow ratio. The accuracy of the results thus obtained is good.

Since long afterbodies are used, it might be expected that this procedure is useful only for inlets with large chord-to-diameter ratios. Good results are also obtained for inlets with small chord-to-diameter ratios if the wake has an approximately constant diameter. In fact useable results are obtained on the forward portion of almost any inlet, since downstream effects usually do not greatly affect the flow there.

The above scheme can also be used for two-dimensional inlets and could, in principle, be used for three-dimensional inlets. However, the latter would require such a large number of elements that computing times would be impractically large. Flows about three-dimensional inlets are usually calculated from the first and third fundamental flows, and the resulting mass flow ratio is simply accepted.

2.2 Shrouds

The axisymmetric flow about a finite empty propeller shroud with zero energy addition, the so-called annular airfoil, can be calculated accurately. As illustrated in Figure 3, two fundamental flows are used. The first is that due to a uniform onset flow parallel to the body's axis of symmetry. The second is that due to an onset flow from a ring vortex interior to the shroud. This latter flow gives rise to a circulation about the shroud. These two flows are linearly combined to give smooth flow off the trailing edge of the shroud. Clearly only one mass flow ratio can be obtained.

Since energy addition and mass flow ratio cannot be accounted for, this shroud calculation seldom arises in practice. It is sometimes used to study flow near exits for cases where the effect of exit geometry is of principal interest.

2.3 Ducts

Flow in a duct is a purely internal flow that is handled in either of two ways. The first artificially extends the portion of the duct that is of interest by means of sections of constant cross-section. This configuration is then considered to be in a uniform onset flow. The second closes the extensions of the duct by means of walls across the cross section and specifies the flow through these closing walls. The second method requires long constant cross-section extensions, because the phenomena described above for the flow about a closed inlet also occurs in this case. The first method is usually used and gives good results.

3. EVALUATION OF THE USEFULNESS OF THE METHOD BY COMPARISON OF CALCULATED AND EXPERIMENTAL PRESSURE DISTRIBUTIONS

To justify the use of the present method as a design tool, its predictions were compared with experiment for a large variety of configurations⁵. Three examples of such comparisons for axisymmetric inlets are presented here. The comparisons show that under many circumstances good agreement with real flow can be obtained by neglecting viscosity and by either neglecting compressibility or accounting for it approximately. In the comparisons, pressures are given in terms of the usual pressure coefficient C_p , except for inlets in static operation where pressures are normalized with respect to a reference dynamic pressure.

Figure 4 compares calculated and experimental pressure distributions on a propeller shroud in static operation. Although the configuration is a propeller shroud, it was considered an inlet and handled by the procedure of Section 2.1 to set mass flow ratio. The centerbody was accounted for in the calculations, but the propeller itself was, of course, ignored. Despite the short chord-to-diameter ratio, the pressure distribution calculated using semi-infinite afterbodies agrees closely with experiment.

Figure 5 shows calculated and experimental pressure distributions on the exterior surface of an inlet under cruise conditions at zero angle of attack. The mass flow ratio is 0.752, and the free-stream Mach number is 0.5. Good agreement of the two pressure distributions is evident.

Figure 6 compares calculated and low-speed experimental pressure distributions on the upper (leeward) exterior surface of the forward portion of an inlet at 6° angle of attack. Comparisons are shown for two mass flow ratios. The experimental zero-angle-of-attack pressure distributions are also shown to exhibit the magnitudes of angle-of-attack effects. The calculations correctly predict the presence of a large negative pressure peak at the smaller mass flow ratio and the absence of such a peak at the larger mass flow ratio.

4. DESIGN APPLICATIONS WITH EXPERIMENTAL CORRELATIONS

This section presents some examples of design applications of the present method. In these cases experimental data were available for comparison with the calculated results. These examples indicate that judicious use of the present method gives useable results in rather extreme flow situations, which might be thought to be beyond the scope of the method.

A straightforward three-dimensional application of the method was the estimation of wing-pylon-nacelle interference for the DC-8. The configuration about which the flow was calculated is sketched in Figure 7. It consists of a short portion of the DC-8 wing, to which is attached the inboard nacelle and pylon, and the mirror image of this wing-pylon-nacelle combination. This rather complicated geometry includes both the upper and lower wing surfaces and both the interior and exterior surfaces of the nacelle. The model tested was a complete airplane. Figure 8 compares calculated and experimental pressure distributions on the pylon for the condition of zero lift on the wing. The free-stream Mach number is 0.825, and regions of supersonic flow are evident in the figure. It is felt that the agreement of calculated and experimental pressures is remarkably good under the circumstances. In particular the calculations correctly predict the important fact that the negative pressure peaks on the inboard side of the pylon are considerably more negative than those on the outboard side.

A study of propeller shrouds is presented in Reference 6. Each shroud configuration studied consists of two separate shrouds, and the aft shroud is allowed to translate axially with respect to the forward shroud. The experimental and calculated configurations are shown in Figure 9. In the wind-tunnel model the forward shroud is essentially semi-infinite upstream. The dynamic pressure q_0 of the exterior flow and the dynamic pressure q_1 of the flow through the shroud can be varied independently. Tests have been conducted for various displacements d of the aft shroud from the forward shroud, including the case of zero displacement, where the two shrouds are in contact. The calculated configuration consists of two separate finite propeller shrouds, and the flow is calculated in the manner described in Section 2.2. Both shrouds have circulation about them, and these are adjusted to give smooth flow from both trailing edges. The calculation is strictly applicable only to the case $q_0/q_1 = 1$.

One shroud configuration from Reference 6 has been selected. Calculated and experimental results are compared for this shape. Figure 10 shows the shroud configuration and compares calculated and experimental pressure distributions for an aft-shroud displacement of one inch at a value of q_0/q_1 nearly equal to one. Experimental pressures are for the inner surface of the forward shroud and the outer surface of the aft-shroud. The final area A_w that the fluid passing through the

shroud occupies at an infinite distance downstream (Fig. 9) can be determined both by calculation and by experiment. Figure 11 shows calculated and experimental values of the ratio of A_w for any aft-shroud displacement and A_{w0} , which corresponds to zero aft-shroud displacement. Various experimental values of q_0/q_1 were used, and it can be seen that this dynamic pressure ratio has little effect on the ratio A_w/A_{w0} . One-dimensional theory can be used to relate the shroud thrust ratio to the dynamic pressure ratio q_0/q_1 and the area ratio A_w/A_p , where A_p is the internal area of the shroud (Fig. 9). Shroud thrust ratio is defined as the ratio of shroud thrust, which is the difference between total thrust and propeller thrust, and the propeller thrust itself. This relationship allows the potential flow calculation to be used to calculate a thrust. Figure 12 compares calculated and experimental shroud thrust ratios at various aft-shroud displacements for the case of static operation, $q_0/q_1 = 0$. (The formula relating shroud thrust ratio to A_w/A_p for the static case is shown in the figure.) The calculated thrust ratios are somewhat larger than the experimental, but the variation with aft-shroud displacement is predicted fairly well.

5. DESIGN APPLICATIONS WITHOUT EXPERIMENTAL CORRELATIONS

Recently a study was conducted to design a noise suppresser for engines of commercial jet aircraft. Part of the problem was to design a cowl and interior bullet that possessed favourable aerodynamic characteristics. Figure 13 illustrates how the present method was used in this study. The figure shows calculated pressure distributions for two configurations in static operation. The only difference between the configurations is that they have different internal fairings, labelled A and B in the figure. The fairing B greatly reduces the magnitude of the negative pressure peaks both on the cowl and on the bullet. Tests may finally be required in this study, but the present method insures that only good shapes will be tested.

A purely internal flow is shown in Figure 14. The body is an axisymmetric duct in which flow in a circular pipe is diffused radially outward. The calculated isobars in the flow field are shown to illustrate the ability of the method to calculate flow in the field off the body surface. Normally the design problem is to shape the curved portion of the diffuser to obtain certain favorable flow properties.

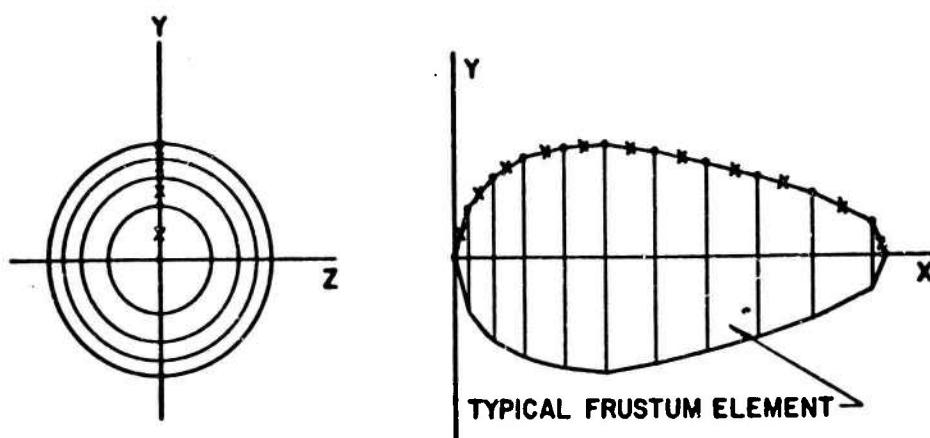
A three-dimensional duct is shown in Figure 15. It is a bifurcated duct, a modification of which is used in certain versions of the DC-8. Calculated velocity distributions are shown along two curves on the duct wall. The design problem was to shape the duct to obtain velocity distributions that do not lead to boundary-layer separation.

ACKNOWLEDGEMENT

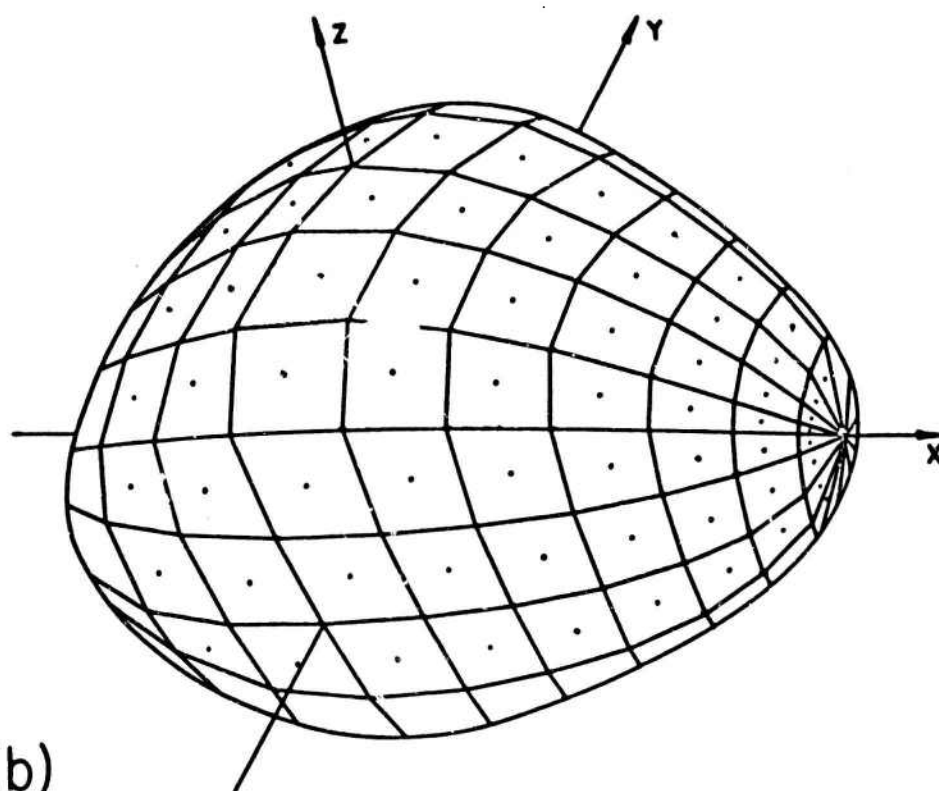
The portions of this work concerned with fully three-dimensional flows were sponsored by the United States Naval Bureau of Ships Fundamental Hydromechanics Research program Contract Nonr 2722(00) administered by the David Taylor Model Basin.

REFERENCES

1. Smith, A.M.O.
Pierce, J. *Exact Solution of the Neumann Problem. Calculation of Plane and Axially Symmetric Flows About or Within Arbitrary Boundaries.* Douglas Aircraft Company Report 26988, April 1958. (A brief summary is contained in the Proceedings of the Third U.S. National Congress of Applied Mechanics, Brown University, 1958.)
2. Hess, J.L. *Calculation of Potential Flow about Bodies of Revolution Having Axes Perpendicular to the Free-Stream Direction.* Journal of the Aerospace Sciences, Vol. 29, p. 726, 1962.
3. Hess, J.L.
Smith, A.M.O. *Calculation of Nonlifting Potential Flow About Arbitrary Three-Dimensional Bodies.* Journal of Ship Research, Vol. 8, No. 2, p. 22, September 1964. (A somewhat expanded version is contained in Douglas Aircraft Company Report ES 42522, March 1962.)
4. Kellog, O.D. *Foundations of Potential Theory Chapter 11.* Frederick Ungar Publishing Co., New York, 1929. (Also available from Dover Publications, New York.)
5. Faulkner, S.
Hess, J.L.
Giesing, J.P. *Comparison of Experimental Pressure Distributions with Those Calculated by the Douglas Neumann Program.* Douglas Aircraft Company Report LB 31831, December 1964.
6. Hoehne, J.C. *Investigation of Translating Shrouds for Ducted Propellers.* Douglas Aircraft Company Report LB 32154, April 1965.



(a)



(b)

Fig. 1 Approximation of bodies by surface elements.
(a) Two-dimensional and axisymmetric bodies.
(b) Three-dimensional bodies.

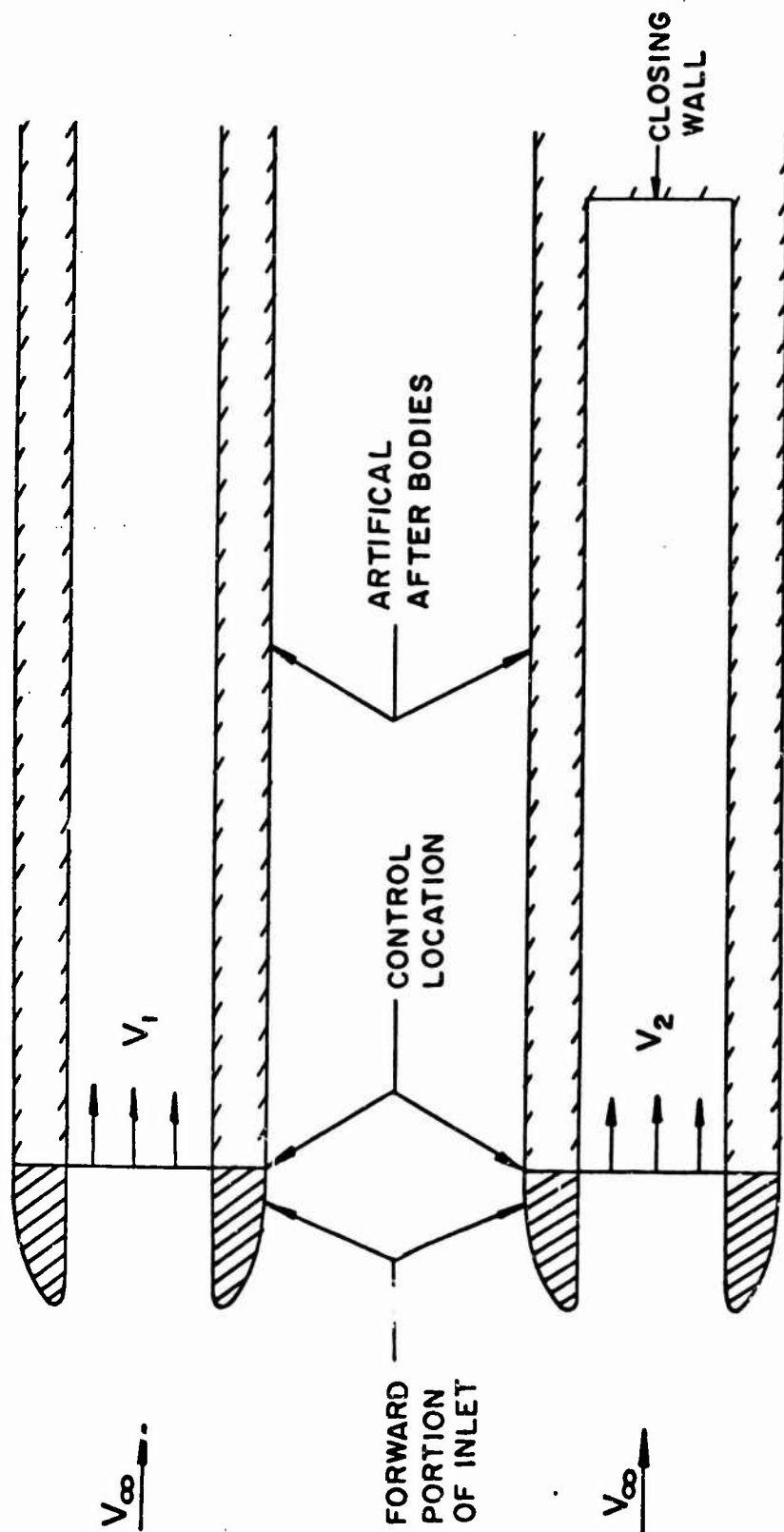


Fig. 2 Three fundamental flows for inlets using artificial afterbodies

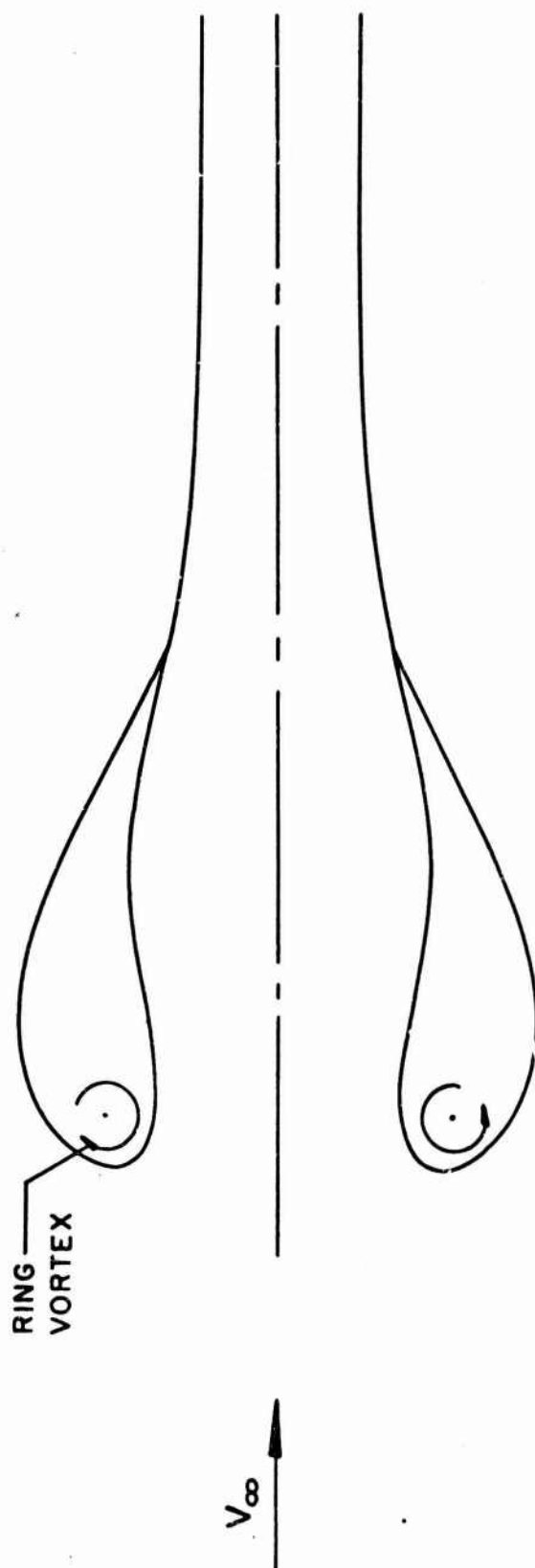


Fig. 3 Two fundamental flows for propeller shrouds

— PRESENT METHOD
 ○ ○ ○ EXPERIMENTAL

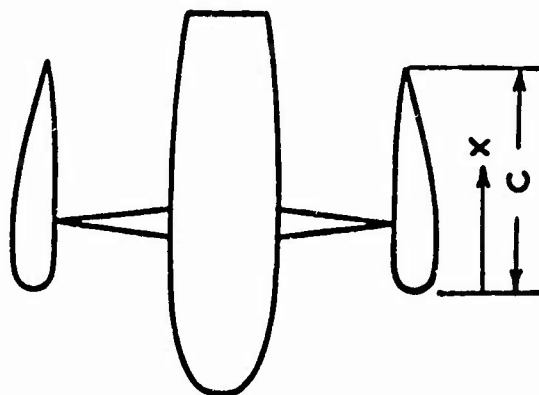
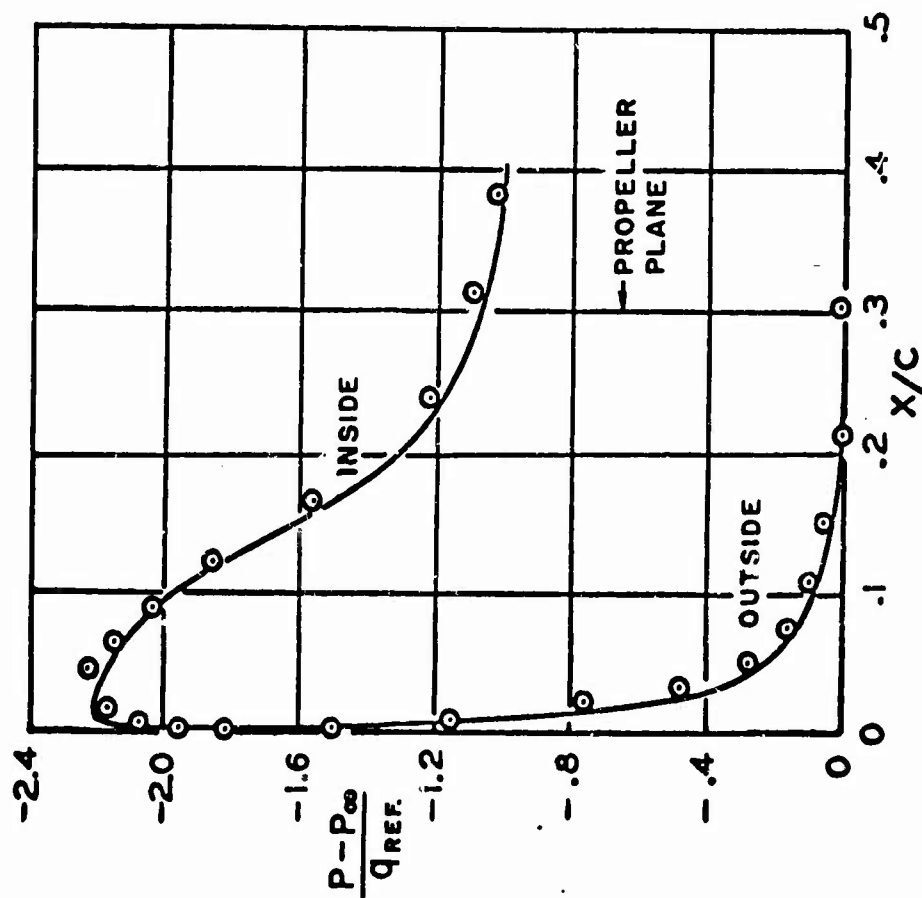


Fig. 4 Comparison of calculated and experimental pressure distributions on a propeller shroud with centerbody in static operation

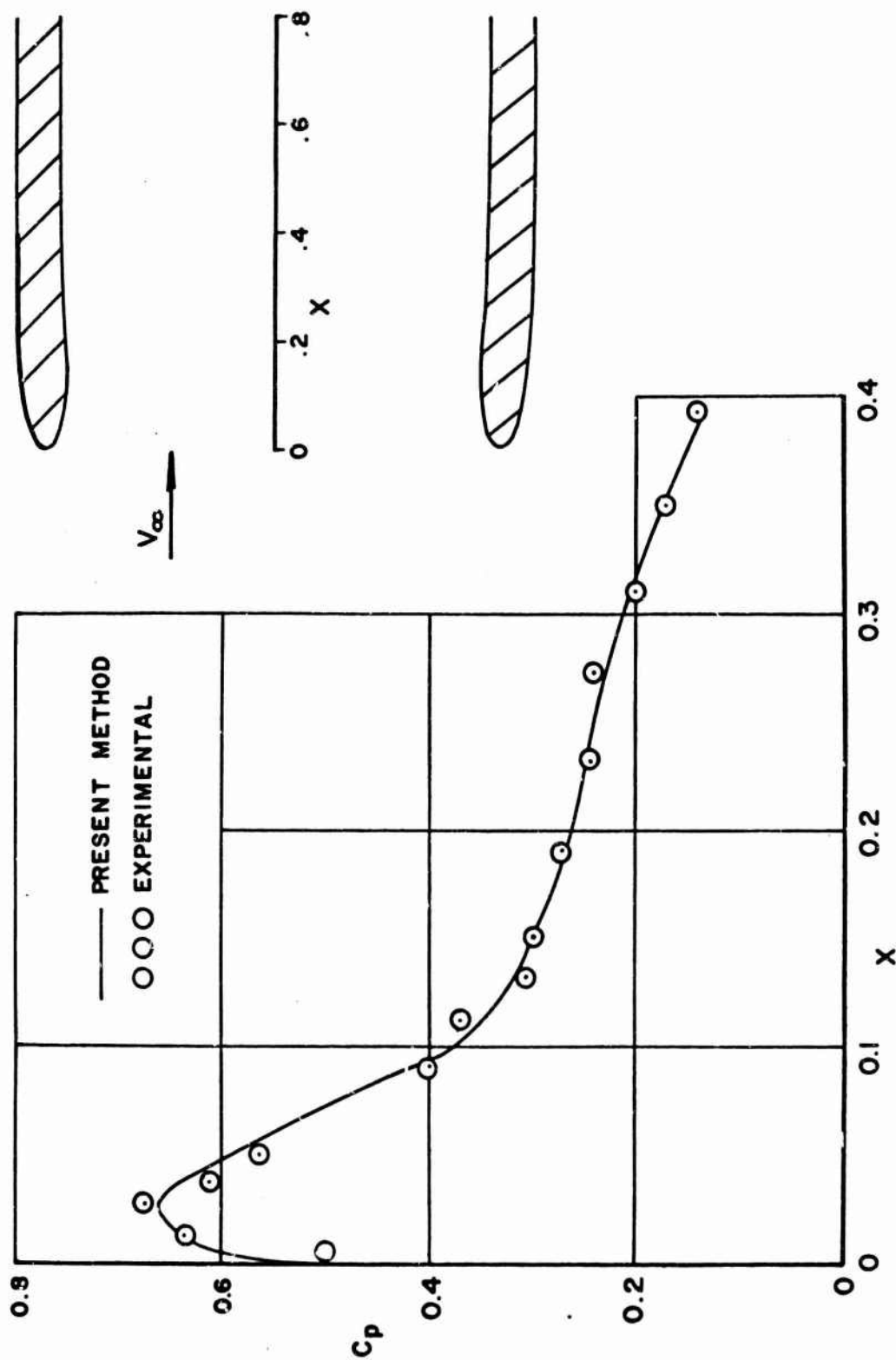


Fig. 5 Comparison of calculated and experimental pressure distributions on an inlet at a mass flow ratio of 0.752 with a free-stream Mach number of 0.5

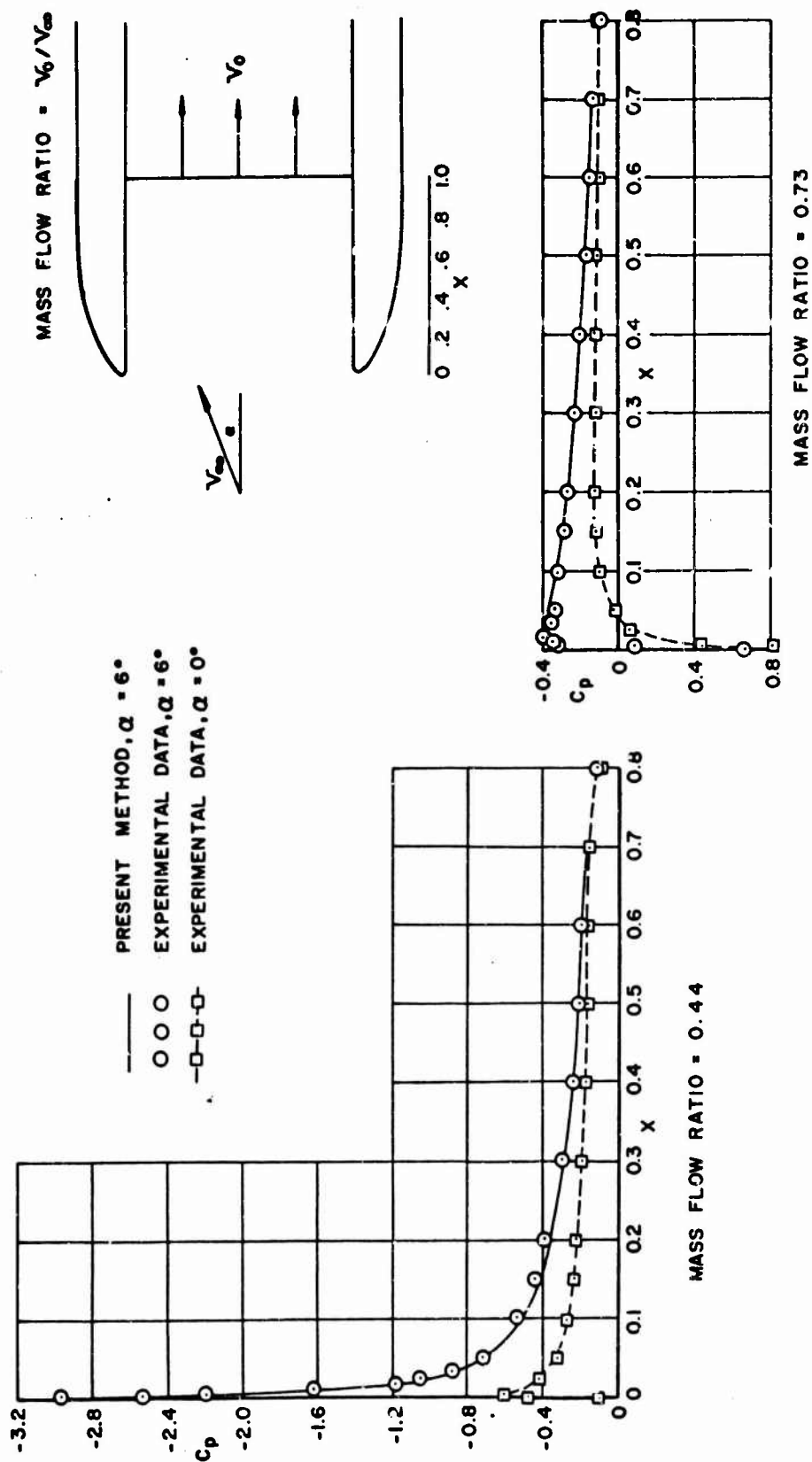


Fig. 6 Comparison of calculated and experimental pressure distributions on the exterior of the forward portion of an inlet at 6° angle of attack for two mass flow ratios

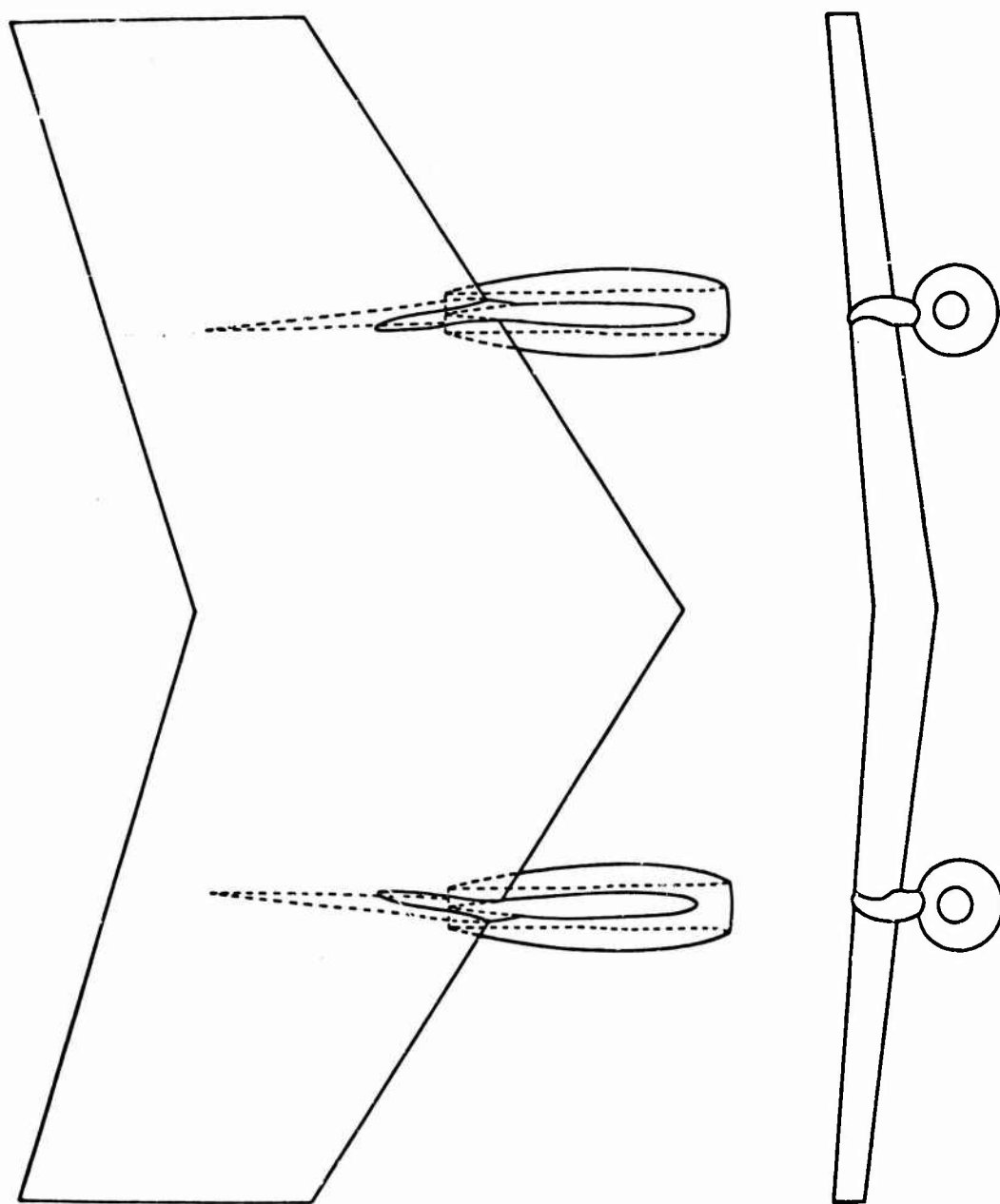


Fig. 7 Adjusted DC-8 wing-pylon-nacelle combination

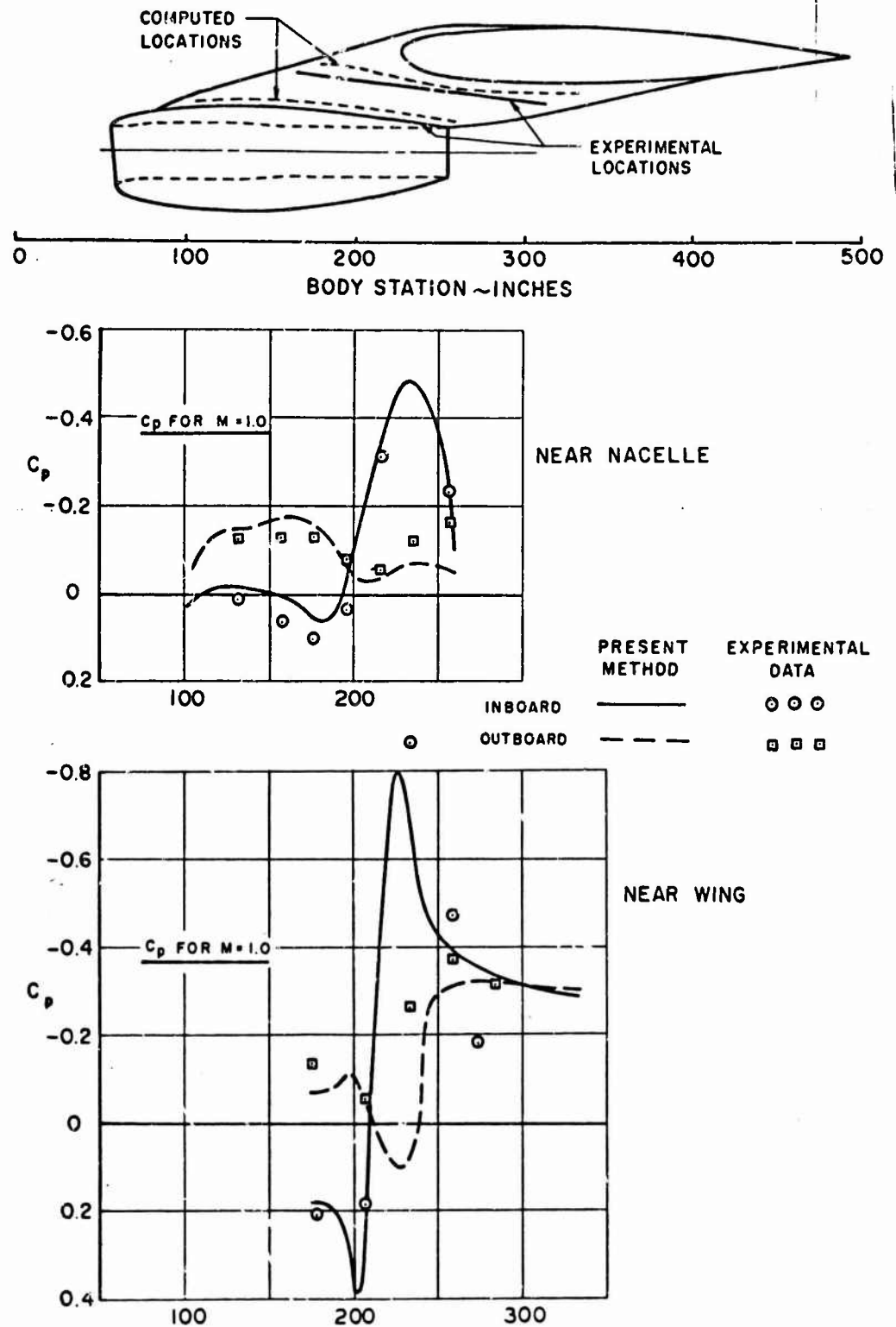
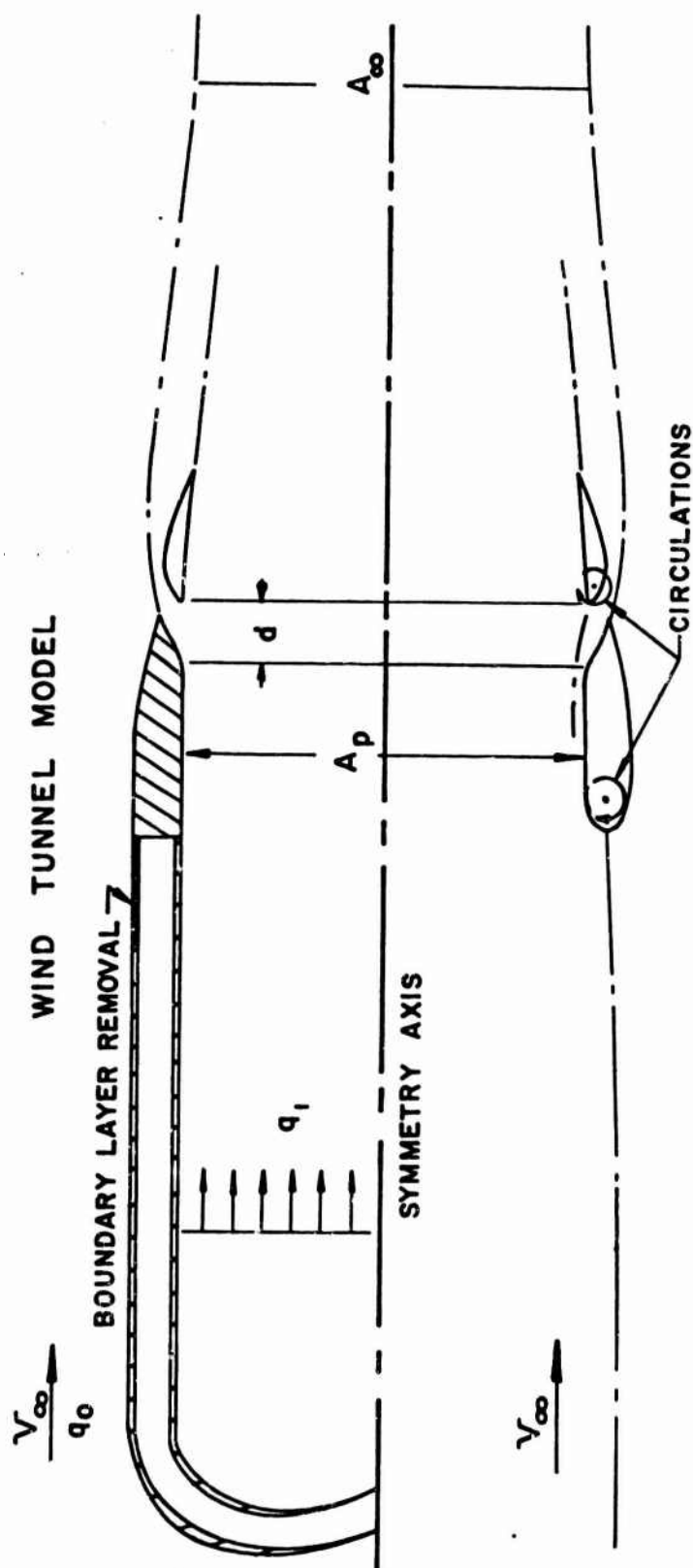


Fig.8 Comparison of calculated and experimental pressure distributions on a DC-8 pylon in the presence of the nacelle and wing at a free-stream Mach number of 0.825 for the zero-lift condition



CALCULATED CONFIGURATION

Fig.9 Experimental and calculated shroud configurations

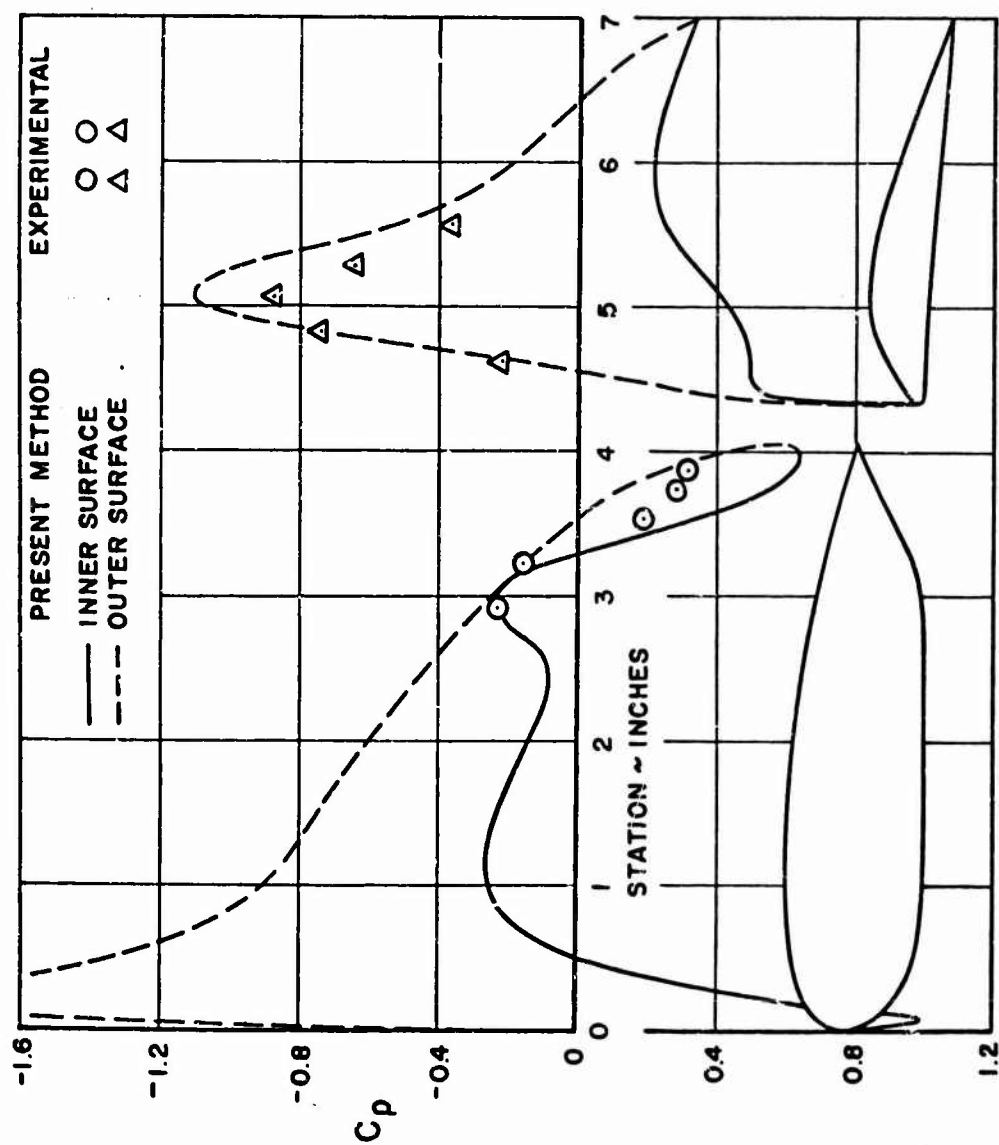


Fig. 10 Comparison of calculated and experimental pressure distributions on a shroud configuration for an aft-shroud displacement of one inch and a dynamic pressure ratio $q_0/q_1 = 0.976$

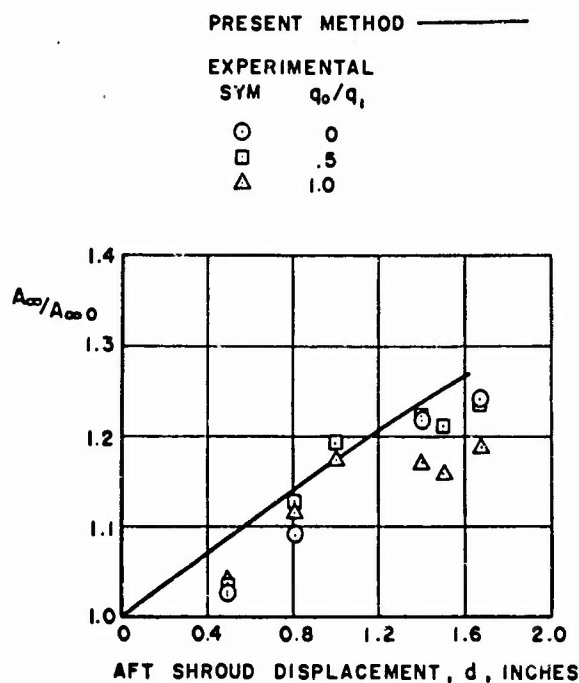


Fig. 11 Variation of shroud mass flow ratio with aft-shroud displacement

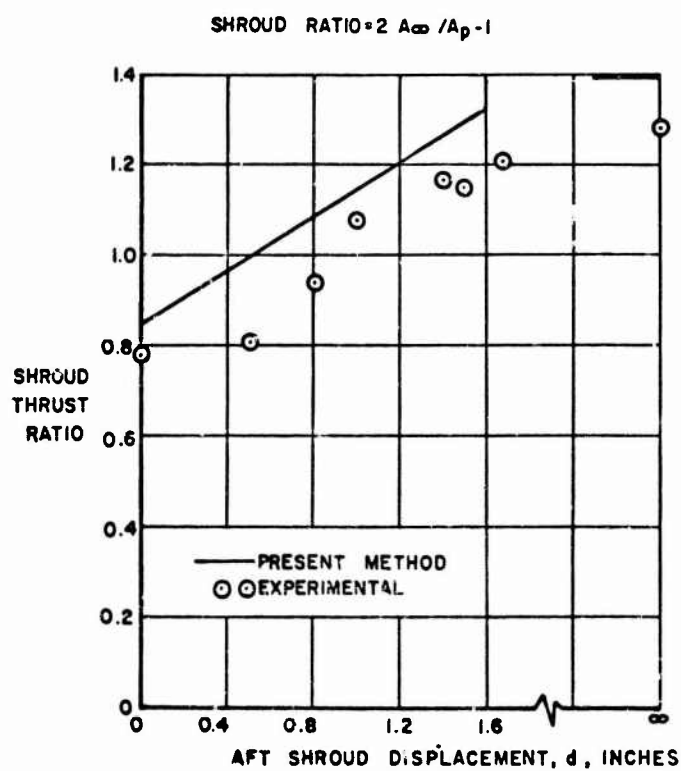


Fig. 12 Variation of shroud thrust ratio with aft-shroud displacement

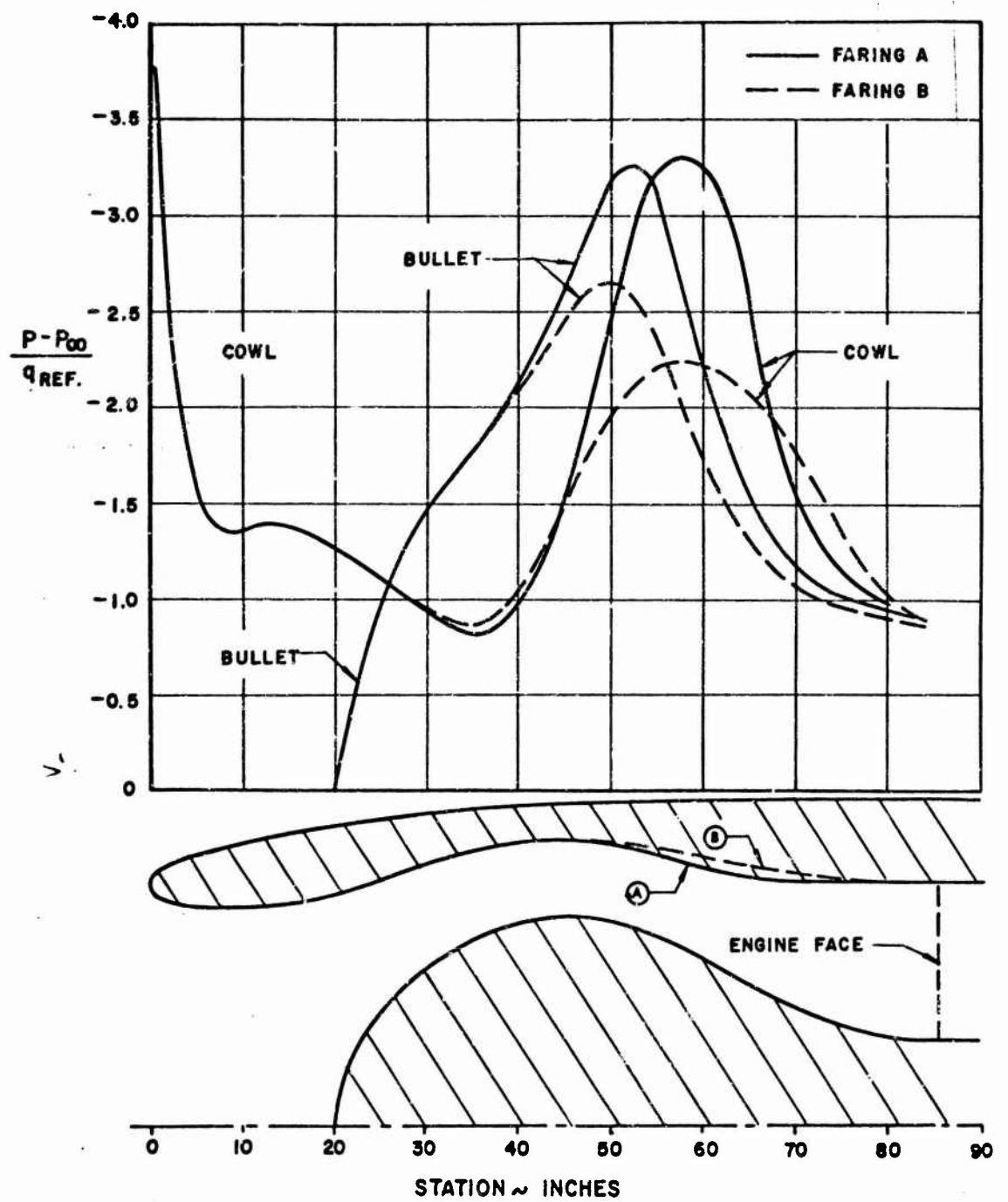


Fig. 13 Calculated pressure distributions on two noise suppression cowls with interior bullet in static operation

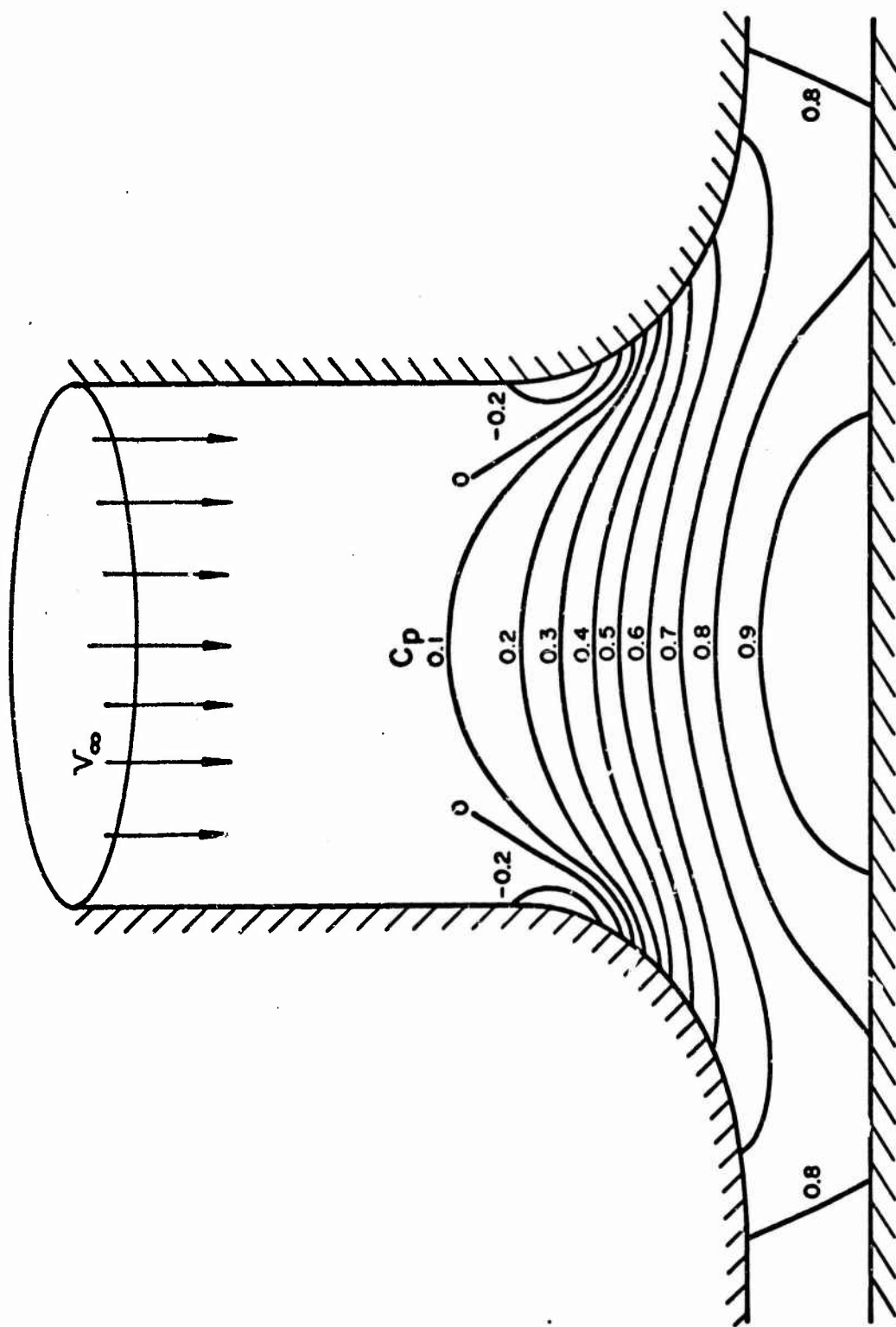
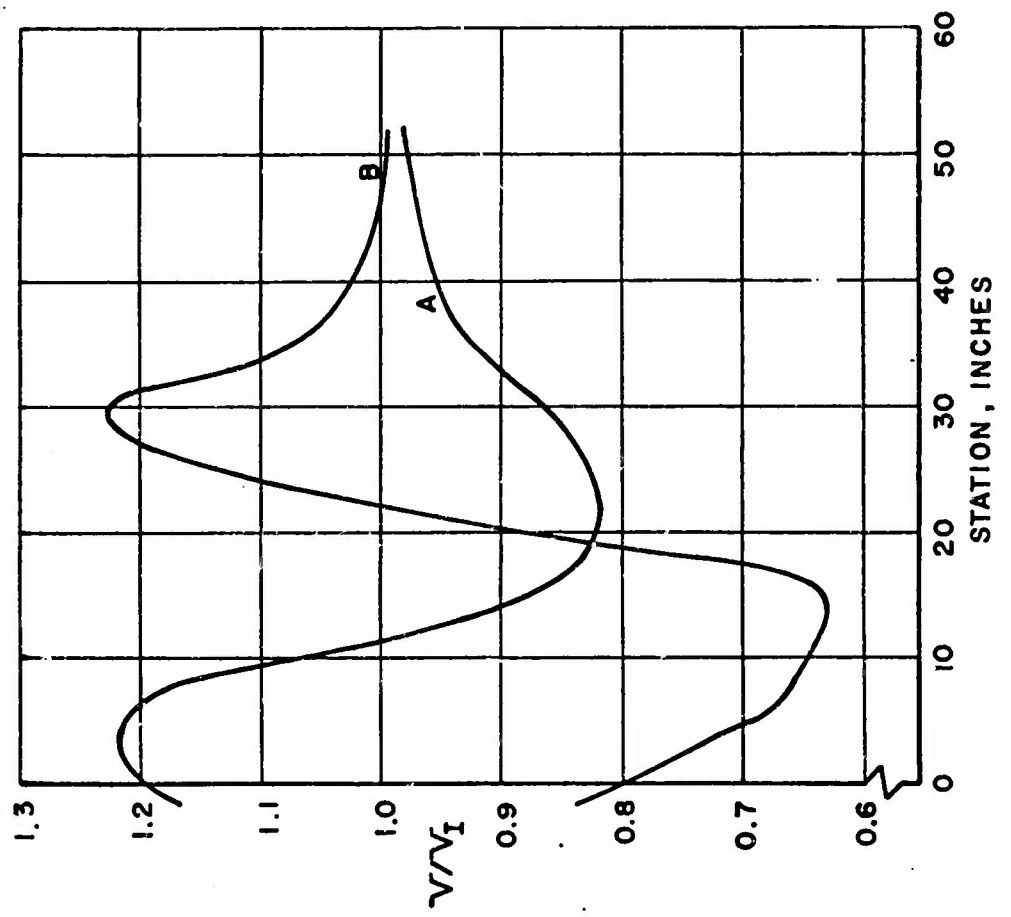


Fig. 14 Calculated isobars in a radial diffuser



V_I = AVERAGE VELOCITY AT DUCT ENTRANCE

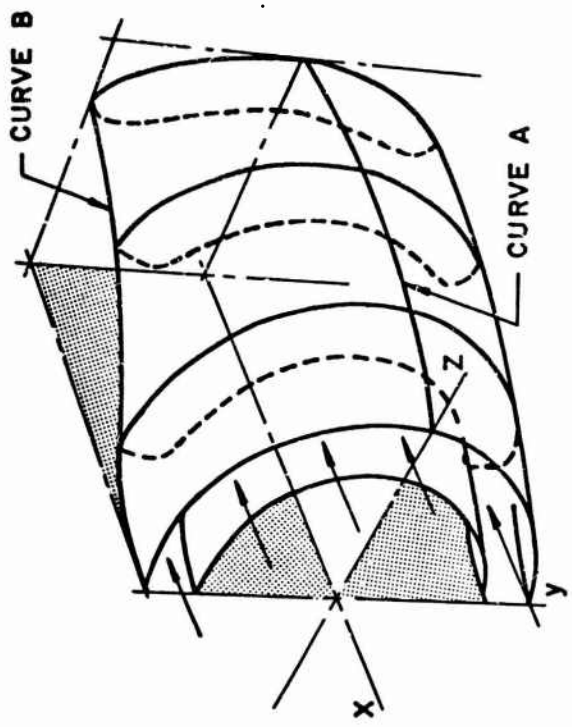


Fig. 15 Calculated velocity distributions in a bifurcated duct